An experimental and numerical investigation of the fundamental mechanisms in CO2-CH4 plasmas

Edmond Baratte

To cite this version:

Edmond Baratte. An experimental and numerical investigation of the fundamental mechanisms in CO2-CH4 plasmas. Plasma Physics [physics.plasm-ph]. Institut Polytechnique de Paris, 2023. English. NNT : 2023IPPAX016 . tel-04572933

HAL Id: tel-04572933
https://theses.hal.science/tel-04572933
Submitted on 13 May 2024

NNT : 2023IPPAX016

Thèse de doctorat

An experimental and numerical investigation of the fundamental mechanisms in CO_2-CH_4 plasmas

Thèse de doctorat de l'Institut Polytechnique de Paris
préparée à l'École polytechnique

École doctorale n°626 École doctorale de l'Institut Polytechnique de Paris (EDIPP)
Spécialité de doctorat : Physique

Thèse présentée et soutenue à Palaiseau, le 17/03/2023, par

EDMOND BARATTE

Composition du Jury :

Dr. Erik Johnson Dir. de recherche CNRS, Ecole Polytechnique, LPICM, France	Président
Dr. Gilles Cartry Professeur, Aix-Marseille Université, France	Rapporteur
Dr. Carlos Pintassilgo Associate professor, University of Porto, Dep. of Engineering Physics, Portugal	Rapporteur
Dr. Simon Dap Professeur associé, Université Paul Sabatier, LAPLACE, France	Examinateur
Dr. Carmen Guerra-Garcia Assistant Professor, MIT, USA	Examinateur
Dr. Christophe Laux Professeur, CentraleSupelec, EM2C, France	Examinateur
Dr. Paolo Tosi Associate professor, University of Trento, Dep. of Physics, Italy	Examinateur
Dr. Olivier Guaitella Ing. de recherche, Ecole Polytechnique, LPP, France	Directeur de thèse

Résumé

Le réchauffement climatique, défi majeur de ce siècle, est causé par les émissions de gaz à effet de serre issues des activités humaines, il est donc nécessaire de maîtriser ces émissions. Le recyclage du CO_2 en produit à plus haute valeur ajoutée est une solution. Une piste de recyclage est le reformage à sec du méthane par plasma, ($CO_2 + CH_4 \rightarrow 2CO + 2H_2$), qui permet de produire un mélange de CO et de H_2 utilisable dans la réaction de Fischer-Tropch (nCO + 2n+1 $H_2 \rightarrow C_nH_{2n+2}$ + nH_2O) pour produire des chaînes carbonées lourde à haute densité d'énergie brûlables comme un combustible classique. Pour y parvenir à faible coût énergétique, les plasmas froids sont une piste prometteuse: le dépôt d'énergie ciblé dans la molécule limite la perte d'énergie en chauffage du gaz.

Les plasmas froids de CO_2:CH_4 sont encore très mal compris en raison de leur complexité : ils conjuguent des phénomènes physique complexes avec une chimie organique étendue. Les processus propres aux plasmas produisent de grandes densités d'espèces excitées et de radicaux très réactifs. De plus, à cause de l'intérêt applicatif, de nombreuses études utilisent des catalyseurs et des configurations de réacteur inhomogènes (par le type de décharge plasma ou la géométrie des réacteurs), rendant difficile la compréhension de la physique sous-jacente. L'optimisation des applications requiert une meilleure description des mécanismes fondamentaux du plasma. La question qui guide donc ce travail est : quels sont les phénomènes physique et chimiques menant à la conversion dans un plasma de CO_2-CH_4? Pour apporter des élements de réponse à cette question, des réacteurs plasma de type décharge "luminescente" et "radiofréquence" à basse pression sont utilisés afin de réaliser une étude fondamentale permettant des comparaisons systématiques modèle/expérience. Les cinétiques électronique, chimique et vibrationelle sont ainsi tour à tour étudiées à l'aide de spectroscopie d'émission dans le visible et de spectroscopie d'absorption *in situ* et résolue en temps dans l'infrarouge (IR).

La première étape a été de développer des techniques simples et non-intrusives fondées sur la spectroscopie d'émission. L'actinométrie, qui permet de mesurer des densités atomiques dans le plasma, est comparée à la technique de Cavity Ring-Down Spectroscopy (CRDS) pour déterminer sa fiabilité dans les plasmas de O_2 et de CO_2. A cause des écarts sur les données de base dans la littérature, la précision de l'actinométrie est limitée mais elle permet d'obtenir un ordre de grandeur des densités atomiques (une information clé) et d'établir des tendances très robustes.Il est montré que l'actinométrie et la mesure de certaines températures du gaz peuvent même être réalisées avec un simple spectromètre en USB peu résolutif.

La cinétique chimique du plasma est étudiée dans une décharge luminescente à basse pression permettant de connaitre facilement le champ électrique, la teméprature du gaz et la densité électronique. La composition du gaz et les taux de conversion sont mesuré par spectroscopie d'absorption IR. Une modélisation de la cinétique chimique de la décharge glow est réalisée à l'aide du solveur cinétique LoKI, initialement en ne prenant en compte que les molécules avec au plus 1 atome de carbone. Les résultats numériques sont systmétiquement comparés aux mesures prises pour contraindre le schéma cinétique. Grâce à un bon accord obtenu sur une

large gamme de pressions, flux et mélanges initiaux, les chemins réactionels principaux sont mis en évidence. Les espèces excitées, souvent négligées dans l'analyse des plasmas de CO_2-CH_4, se révèlent jouer un rôle essentiel, en particulier l'état O(1D). La prise en compte de O(1D) met en évidence de nouvelles voies de réactions, habituellement remplacées par la chimie complexe des espèces C2H.
Une étude similaire est réalisée en suivant l'évolution temporelle des densités dans une décharge radiofréquence qui cette fois permet de suivre l'évolution temporelle de la chimie jusqu'à atteindre un état stationaire. Le modèle doit alors être complété avec des molécules comportant 2 atomes de carbone. L'influence de O(1D) est confirmée, ainsi que le rôle moins prépondérant des C2H par rapport à la littérature. La réaction CH_3 + O(1D) apparaît comme critique. Le rôle des surfaces apparaît aussi essentiel pour expliquer certains processus.
Enfin la cinétique vibrationnelle du CO_2, cruciale pour limiter le coût énergétique de dissociation, est étudiée dans des pulses plasmas de 5ms. Le CH_4 et ses produits de dissociation (H_2, H_2O,H) diminuent fortement l'excitation vibrationnelle du CO_2, mais celle du CO est au contraire augmente dans certains cas. A nouveau, l'implication de O(1D) dans des processus d'excitation vibrationnelle est suspectée.
L'ensemble de ces résultats permettent d'améliorer la compréhension des plasma de CO_2:CH_4 et permettent tout autant d'ouvrir la voie à de nouvelles recherches fondamentales (notamment sur les états électroniques excités), que d'identifier des piste d'optimisation des procédés de reformage à sec du méthane.

Abstract

Global warming, a major challenge of this century, is caused by greenhouse gas emissions from human activities, which imposes the urge of controlling these emissions. The recycling of methane into higher value-added products is part of the solution. One way of recycling is the dry reforming of methane by plasma, (CO_2 + CH_4 → 2CO + $2H_2$), which makes it possible to produce a mixture of CO and H_2 that can be used in the Fischer-Tropch reaction (nCO + 2n+1 H_2 → C_nH_{2n+2} + nH_2O) in order to produce heavy carbonaceous chains of high energy density that can be burnt like a conventional fuel. To achieve this at low energy cost, cold plasmas are a promising solution. Indeed, by targeting the energy deposition in the molecule, the energy loss into gas heating is limited.

Cold plasmas of CO_2:CH_4 are still very poorly understood because of their complexity: they combine complex physical phenomena with extensive organic chemistry. Plasma processes produce high densities of excited species and highly reactive radicals. Moreover, because of the applicative interest, many studies use catalytic materials and inhomogeneous reactor configurations (because of the type of plasma discharge or the reactor geometry), making it difficult to understand the underlying physics. Optimizing applications requires a better description of the fundamental plasma mechanisms. The question that guides this work is therefore: what are the physical and chemical phenomena leading to the conversion in a CO_2-CH_4 plasma? To answer this question, low pressure glow discharge and radio frequency plasma reactors are used to perform a fundamental study allowing systematic model/experiment comparisons. The electronic, chemical and vibrational kinetics are studied one by one by means of emission spectroscopy in the visible range and absorption spectroscopy in the infrared (IR).

The first step was to develop simple and non-intrusive techniques based on emission spectroscopy. Actinometry, which allows the measurement of atomic densities in plasma, is compared to the Cavity Ring-Down Spectroscopy (CRDS) technique to determine its reliability in the O_2 and CO_2 plasmas. Because of discrepancies in the literature, the accuracy of actinometry is limited, but it provides an order of magnitude of the atomic densities (a key piece of information) and very robust trends. It is shown that actinometry and the measurement of some gas temperatures can even be performed with a simple low-resolution USB spectrometer.

The chemical kinetics of the plasma is studied in a low pressure glow discharge allowing to know easily the electric field, the gas temperature and the electron density. The gas composition and conversion rates are measured by IR absorption spectroscopy. A modeling of the chemical kinetics of the glow discharge is performed with the kinetic solver LoKI, initially taking into account only molecules with at most 1 carbon atom. The numerical results are systematically compared to the measurements to constrain the kinetic scheme. Thanks to a good agreement obtained over a large range of pressures, fluxes and initial mixtures, the main reaction paths are highlighted. The excited species, often neglected in the analysis of the plasma, are shown to play an essential role, in particular the O(1D) state. Taking into account O(1D) highlights new reaction paths, usually replaced by the complex chemistry of C2H species.

A similar study is carried out by following the temporal evolution of the densities in a radiofrequency discharge which this time allows to follow the temporal evolution of the chemistry until reaching a stationary state. The model must then be completed with molecules containing 2 carbon atoms. The influence of O(1D) is confirmed, as well as the less preponderant role of C2H compared to the literature. The CH_3 + O(1D) reaction appears to be critical. The role of surfaces also appears essential to explain certain processes.

Finally, the vibrational kinetics of CO_2, crucial to limit the energy cost of dissociation, is studied in pulsed glow discharge. CH_4 and its dissociation products (H_2, H_2O,H) strongly decrease the vibrational excitation of CO_2, but on the contrary the one of CO increases in some cases. Again, the involvement of O(1D) in vibrational excitation processes is suspected.

All these results improve the understanding of the CO_2:CH_4 plasma and open the way to new fundamental research (in particular on the excited electronic states), as well as to the identification of optimization routes for dry methane reforming processes.

Contents

CHAPTER 1

Introduction

Contents

1.1 Some numbers on climate change

It is now generally admitted that climate change is one of the major challenges humanity must face in the next years. The cause of climate change is the anthropogenic emissions of green house gases such as carbon dioxide CO_2 or methane CH_4 (Masson-Delmotte et al. 2019) due to human activities and industries. Not all green house gases have the same effect on the environment, because of the spectral range on which they absorb. To compare different green house gases, each gas is attributed a "Global Warming Potential" (GWP), which represent the warming one ton of the gas would create compared to one ton of CO_2 over 100 years Ritchie et al. 2020. Methane for example has a GWP of 28, meaning that one ton of CH_4 released in the atmosphere is as harmful as 28 tons of CO_2. This allows to compute a $CO_{2\ eq}$ for each emission. The green house gases emission have constantly increased since the beginning of the industrial revolution of the XIXth century, but an acceleration has been seen over the last decades: while the summed emissions of green house gases represented 32.6 billions equivalent tons of CO_2 in 1990, the world now emits approximately 49 billions tons per year. Subsequently, the CO_2 concentration in the atmosphere has risen from 316ppm in 1959 to 408ppm in 2018. Green house gases emission have taken a large toll on the temperature, increasing it by more than 1.2° over the last 160 years.

	China	USA	India	EU
CO_2eq (in billion tons)	11.7	5.79	3.35	3.33
CO_2eq/capita (in tons)	6.77	14.52	1.01	5.93
Percentage of the world population	18.5	4.25	17.7	6.25
Percentage of the CO_2eq emission	24	12	6.84	6.8

Table 1.1: Green house gases emission in 2018. Data taken from Ritchie et al. 2020

To understand and work on reducing the emission, it is important to have a good analysis of said emissions. Most of the green house effect is due to CO_2 emission, which represent 74.4% of the emission in $CO_{2\ eq}$ in 2020 (Ritchie et al. 2020). Methane is the second contributor to greenhouse effect with 17.3 % of the emissions. The rest is due to nitrous oxide gas N_2O, which is produced when using nitrogen fertilizer and account for 6.2% of the emission and fluorided gases (such as SF_6), which account for the rest.
The largest emitters are shown in the table 1.1. In terms of total emissions, China is the world largest emitter, followed by the USA, India and the European Union, but the numbers must be nuanced. First, by looking at the per capita number, the USA are the first polluters of the globe by far, with emissions by inhabitants twice as high as the one of Europe or China. The emissions of the later are still much higher than the objective of 2t/year fixed as the Paris agreements objectives to remain below the 1.5° temperature increase. France has an estimated 4.74t/year/capita, below European average, but still too high. France still emits approximately 305Mt/year of CO_2, which is as much carbon atoms as contained in approximately 92400 Eiffel Tower made of pure diamond every year (french people like to count in Eiffel Towers) ! Second, a large part of the emissions of China and India are due to manufactured goods later shipped to Europe or the USA. The carbon footprint which measure the CO_2eq emission for a person's consumption over a year would be a better indicator of the biggest polluters but is much more complicated to compute.
The distribution of the emission of green house gases among sectors can change a lot with each country, but on a global scale, it is mostly divided in a few fields of activity: transport (road, air and naval, which sums up to 16.2% of the emissions), industry(24.2%), energy use in buildings (17.5%) and agriculture (18.4%), according to ClimateWatch n.d. This partition is similar to the one in the US (Administration n.d.).

The second gas responsible for climate change is the methane (CH_4), which is responsible for an estimated 20% of the artificial green house effect. Because the methane has a GWP of 28, small amount released in the atmosphere still have dramatic effects. There are three main sources of emission of CH_4: the agriculture, the fugitive emission and the decomposition waste which account respectively for 3.5 billion tons (in CO_2 eq tons), 3.11 billions and 1.5 billions. The emissions of CH_4 are more difficult to control because unlike CO_2 emissions, they are not concentrated. The fugitive emissions are spread over the whole pipeline network of CH_4. The waste decomposition happens everywhere. The cattle is responsible for most of the agricultural CH_4. Some solutions have been tested to extract and recycle the CH_4 emitted in indoor farms but no large-scale solution is available. The largest emitters of CH_4 are China (1.18 billion tons), Russia (687 million tons), the US (745 million tons), India (658 million tons) and Brazil (435 million tons). However, due to the nature of each sources, the emissions are unevenly distributed. 80% of the emissions of Russia are due to fugitive emissions (because it is the largest natural gas provider), the rest mostly comes from waste. In China, only 60% come from fugitive emissions, 25% come from agriculture (due to the strong economic weight of agriculture in china) and the rest comes from waste decomposition. A similar distribution is found in the US. In India and in Brazil, more than 80% of the CH_4 emissions come from agriculture.

This overview of the green house gases emissions gives an idea of the actions that need to be taken. The first action is of course a change in our behaviours, whether it comes to

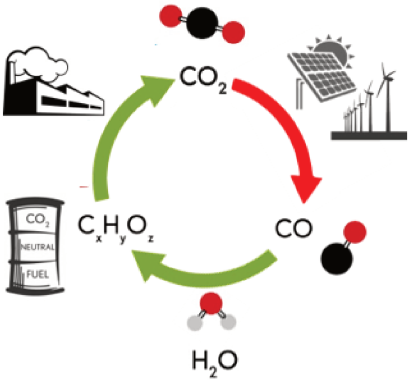

Figure 1.1: Neutral carbon cycle. Taken from A.-S. Morillo-Candas 2019

food (reducing the amount of meat in the diet and privileging short-circuit food), energy in the buildings (limit the use of heating and air conditioning), goods consumption (limit the amount of goods bought every year, be careful on the provenance) or transport (use public transportation, reduce air transport for tourism). However, a change in the behaviour is not always possible: out of the 16% of emissions due to transport globally, 12% are due to road transport, whose replacement is challenging in rural areas and not always possible. Similarly, the iron and steel industry, which accounts for 7.2% of worldwide emission, can not simply be shut down. These sectors need a transition to new technologies which will allow them to reduce their carbon emission.

1.2 Reduction of the carbon emission

Two ways are currently being investigated to limit carbon emissions from industries without going through a complete transformation: the Carbon Capture and Storage (CCS) and the Carbon Capture and Use (CCU). The first one consists in capturing the emitted CO_2 and trapping it in geological undergrounds (in Europe, the North see is the main storing site). This technology is interesting and has a relatively low cost (estimated by the french energy transition agency to about 70€/ton) but shows several limitations: for any amount of CO_2 captured, about 20% additional CO_2 is emitted. The storage sites also present limitations. They can only contain a finite amount of carbon and the ecological repercussions of storing millions of tons of carbon underground are still debated because it could pose problems of soils acidification. Finally, not all emissions can be captured. The technology is only viable if the CO_2 fraction in the mixture filtered is high enough. In France, only 51 out of the 305 Mt emitted every year could be captured (ADEME n.d.). The carbon capture and use (CCU) aims at capturing CO_2 at the output of carbon-emitting industries or straight from the air and reuse it to generate value-added products or resources, generally hydrocarbons. These hydrocarbons can then be burnt like any other fuel to reproduce energy. Burning hydrocarbon will in turn emit CO_2, which can be captured again. The CCU processes therefore aim at creating a carbon neutral cycle for fuels, as pictured on figure 1.1. CCU for other value-added products is investigated, such as for the production of graphene or carbon black. In most cases, the first step of the CO_2 recycling is to turn CO_2 into CO, which reacts more easily. Often, the second step consist of recombining CO with an hydrogenated molecule, typically H_2, to create C_XH_Y hydrocarbons chain. The first step is currently the bottleneck in CO_2 conversion because CO_2 is a very stable molecule whose dissociation is endothermic:

$$CO_2 \rightarrow CO + O, \Delta H = 5.5eV/mol \tag{1.1}$$

Several technologies are currently being developed for CCU and are presented in table 1.2. The techniques presented above all seem interesting but have major drawbacks: the artificial synthesis relies on rare materials and can only treat low volumes, the algae require a lot of

Name	Description	Source
Artificial Photosynthesis	passive system made of rare materials designed to filter CO_2 and H_2O from air and use sunlight to turn it into hydrocarbons	Q.Wang et al. 2020
Biodiesel production by micro-algae	Growth of algae in pools to filter CO_2 from air and produce biodiesel	J. Chen et al. 2018
Thermal cracking of CO_2 by solar heating	Concentrating sunlight on a CO_2- H_2O mixture to produce CO and H_2 simultaneously	Romero et al. 2012
Thermal catalysis	Heating a compressed mixture of CO_2 and another gas (like H_2) at several hundred K to trigger chemical reactions producing value added products like CH_4. The activation energy is reduced by the use of catalysts	Varvoutis et al. 2022

Table 1.2: CO_2 conversion techniques

space and water and the thermal cracking of CO_2 requires a large amount of solar energy, i.e a very large surface. The cold plasma technologies are free of theses major constraints and could therefore prove to be an efficient solution in CO_2 recycling. The cold plasmas have already demonstrated in the past efficiencies superior to thermal cracking of CO_2 (A.Fridman 2008) and are easily scalable. They are therefore an interesting lead to pursue.

1.3 CO_2 recycling by plasma

Non-thermal plasmas are an efficient way to target the energy deposition in the molecules by tailoring the electron energy and avoiding wasting energy in heating. Indeed, energy can be transferred to a single mode of the molecule via electron impact, limiting the unnecessary heating of several modes. They appear ideal to dissociate CO_2 at a low energy cost.

1.3.1 CO_2 dissociation mechanisms

It is considered that there are two main pathways to achieve CO_2 dissociation in CO_2 plasmas aside from chemistry (A.Fridman 2008): electron impact dissociation and vibrational pumping, presented on figure 1.2. First, electron impact dissociation through the following channels:

$$CO_2 + e \rightarrow CO(^1\Sigma^+) + O(1D) + e, \Delta H = 7.2eV/mol \tag{1.2}$$

Other electron impact dissociation channels also exist and produce more excited state of O_2 or CO, such as :

$$CO_2 + e \rightarrow CO(^1\Sigma^+) + O(1S) + e, \Delta H = 8eV/mol \tag{1.3}$$
$$CO_2 + e \rightarrow CO(a^3\Pi) + O(3P) + e, \Delta H = 11eV/mol \tag{1.4}$$

The second process, vibrational pumping (also called 'vibrational ladder climbing') of the molecule, consists in transferring energy to a vibrational mode of CO_2 through

$$CO_2(v) + CO_2(w) \rightarrow CO_2(v+1) + CO_2(w-1) \tag{1.5}$$

preceded by electron impact vibrational excitation of the CO_2 molecule

$$e + CO_2 \rightarrow e + CO_2(v) \tag{1.6}$$

until the molecule reaches an unstable state. The CO_2 molecule has 3 vibrational modes, represented on figure 1.3: $v1$ symmetric stretch, $v2$ bending and $v3$ asymmetric stretch. The bending mode is doubly degenerated because of the symmetry of the CO_2 molecule. An extra

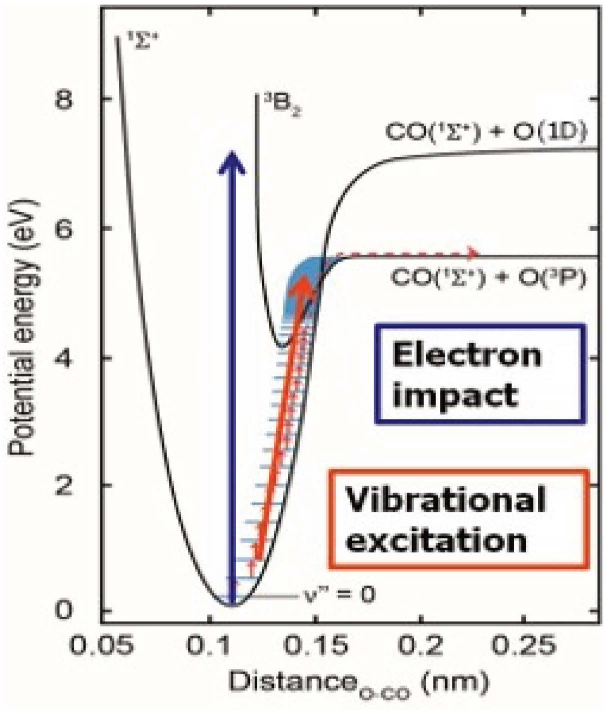

Figure 1.2: CO$_2$ dissociation mechanisms. Taken from A.-S. Morillo-Candas 2019

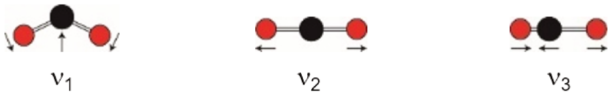

Figure 1.3: Representation of the 3 vibrational modes of CO$_2$

index $l2$ is used to describe the contribution of $v2$ to the angular momentum, with $l2 = v2,\ v2-2,\ v2-4, ..., 0$. The energy of the levels can be calculated with an anharmonic oscillator approximation, known as the Treanor approximation (Treanor et al. 1968). It must also be noted that the energy of the quantum $v1$ of the symmetric stretch is very close to the energy of two quanta of the $v2$ bending mode, leading to a Fermi resonance between the two modes, more precisely between the states $(v1, v2^{l2}, v3)$ and $(v1-1, (v2+2)^{l2}, v3)$. The first vibrational levels of CO$_2$ are shown on figure 1.4.
The CO$_2$ dissociation through pumping of CO$_2(\nu_3)$ is particularly energy-efficient and could theoretically be achieved with a minimum energy of 5.5eV/molecule. This pathway is indirect and requires electron with energy inferior to 1eV to successively transfer their energy to the asymmetric mode which could theoretically achieve vibrational dissociation if $v3$=21 is reached. At this level, the molecule would reach the potential crossing of the ground CO$_2$ (CO$_2$ ($^1\Sigma^+$)) with the excited state CO$_2$ ($^3B^2$). This state would then dissociate into CO($^1\Sigma^+$) and O(3P), both in their ground state.

Because of the lower energy cost of the vibrational ladder climbing, it would seem logical to focus on it for efficient CO$_2$ dissociation. However, as mentioned, complete ladder climbing would require the CO$_2$ to reach the level $(v1, v2, v3 = 21)$ without losing any of its vibrational quanta. This is highly unlikely because of the vibrational-to-translational (VT) energy transfers, whose rates are high: the energy of all 3 CO$_2$ vibrational modes tend to be lost to translations upon collisions with other molecules. The transfers are even higher when colliding with atoms (A S Morillo-Candas, Drag, et al. 2019a). A "partial" ladder climbing is more likely to happen. In this case, the vibrations are populated as much as possible according to processes 1.6 and 1.5, which should, using the so-called Fridman scaling (Adamovich et al. 1996), reduce the dissociation threshold for electron impact dissociation. The vibrational excitation can also

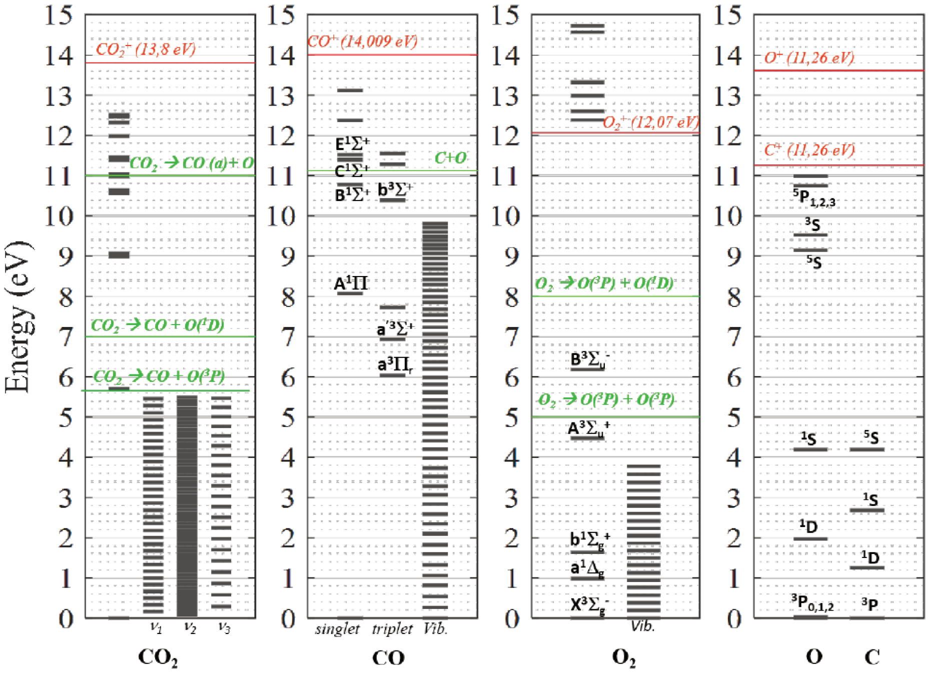

Figure 1.4: Vibrational and electronic excited levels of CO_2, CO, O_2 and atomic O. The ionization is plotted in red and the electron impact dissociation thresholds are plotted in green

reduce the activation energy of a chemical reaction involving CO_2 and therefore increase the reaction rate. Nevertheless, this "partial ladder climbing" is still limited by the V-T processes and is not easy to achieve. The rate coefficient of the VT processes are usually increased by the temperature, hence keeping a limited gas heating is favourable for partial ladder climbing. Limiting the V-T process can also be achieved by reducing the collision frequency, which is possible by lowering pressure. The "partial ladder climbing" is therefore only favoured at reduced pressure (100 mbar and below). The cost of pumping down to 100mbar might however overcome the energy gained by choosing the ladder climbing over the electron impact. Yet CO_2 vibrations remain a very important topic largely investigated, necessary to understand any CO_2 containing plasma since electrons transfer a large part of their energy to CO_2 vibrations.

1.3.2 CO_2 plasmas

The CO_2 plasmas have a long history: in the 1970's, these plasma were studied for the CO_2 lasers (W.J.Witteman 1986) and the CO lasers. The goal was to achieve population inversion between the CO_2 ground state and a lowly vibrationally excited state of CO_2 and above all to avoid CO_2 dissociation. In the 1980's, research focused on the production of new energy carriers such as H_2, investigating CO_2 dissociation for 2-stages H_2 production from CO_2 and H_2O. Experiment in supersonic wind tunnel demonstrated the possibility to achieve high CO_2 dissociation yields with good energy efficiency by using the CO_2 vibrational pumping (Asisov et al. 1985, A.Fridman 2008), sparking interest for that pathways. The vibrational pumping gained more and more interest in the study of CO_2 plasma for environmental purposes, because it appeared as a cost-effective way to recycle CO_2. Despite the lack of success in achieving CO_2 dissociation by pure CO_2 vibrations, CO_2 plasmas still appeared as an efficient way to reduce CO_2 to CO because energy efficiency above thermal cracking were demonstrated (R. Snoeckx and Bogaerts 2017). Vibrations remain a hot topic because it was theorized that the vibrational energy stored in the molecule could act as additional input energy in chemical reactions and lower the reactions activation energy. The vibrational excitation of CO_2 in plasma was investigated in numerous plasma sources: atmospheric pressure DBD, low pressure radiofrequency discharge, low pressure and atmospheric pressure microwave discharge...

The study of CO_2 plasma recently took a new turn for martian exploration and production of oxygen (Vasco Guerra et al. 2017,Premathilake et al. 2019). The martian atmosphere is indeed composed of 96% of CO_2, 2% of N_2, and a few percent of Ar. The O_2 production from CO_2 splitting is therefore a very interesting prospect for future manned mission on the red planet and the plasma solution appears more interesting than the alternatives currently used. Currently, oxygen is produced on Mars by the rovers sent there thanks to the MOXIE (Mars Oxygen in-Situ Resource Utilization Experiment) device, which relies on the solid oxide electrolysis technology. In MOXIE, a solide electrolyte is placed between porous electrodes. The CO_2 diffuses through the porous electrode and reaches the electrolyte. The CO_2 accepts two electrons from the cathode to form an O^{2-} which diffuses through the electrolyte if the temperature is high enough ($\sim 800°$) and recombines with another O^{2-} ion when it reaches the anode. MOXIE has very limited performances: with a power of 300W, it can only produce up to 10g of O_2 per hour. Estimations carried out in V. Guerra et al. 2022 showed that using non-optimized plasma technologies could produce up to 14g of oxygen per hour with the same power. In Sean Kelly et al. 2022, microwave discharges in MOXIE's operating conditions were investigated and could potentially reach O_2 production rates 30 times higher than MOXIE's. This topic is very trending and should continue to raise interest in the next years.

The study of CO_2 plasma is not limited to the CO_2 molecule. The influence of the CO_2 dissociation products on the plasma, in particular O atoms, has been at the center of many interrogations. On one hand, O atoms were claimed to help further dissociation by collision with vibrationally excited CO_2 through:

$$O + CO_2(vib) \rightarrow CO + O_2 \tag{1.7}$$

On the other hand, the recombination of CO and O is also a well-known limiting process in pure CO_2 plasmas:

$$O + CO + M \rightarrow CO_2 + M \tag{1.8}$$

This second process was found to be very effective at high gas temperature, limiting both the dissociation and the energy efficiency. At lower gas temperature, other dissociation processes can also be limiting, such as:

$$CO(a^3\Pi) + O_2 \rightarrow CO_2 + O \tag{1.9}$$

where, O_2 is produced by recombination of atomic O. The strong role of this process was recently highlighted in A S Morillo-Candas, Silva, et al. 2020. The removal of the O atoms from the plasma by the use of special membranes (Premathilake et al. 2019) is therefore a trending topic.

The CO can be beneficial for the dissociation of CO_2 in the plasma because of the resonance between CO(v) and CO(ν_3), which leads to energy transfer from CO to CO_2. CO(v) could constitute a reservoir of excitation for CO_2 vibrations. However, if too much CO is present in the plasma, the energy of the electrons is lost in electron impact vibrational excitation of CO (not transferred to CO_2 if the fraction is not high enough) or in CO dissociation to C and O. The role of CO is therefore ambivalent. The vibrational levels of CO are represented on figure 1.4, which also shows the electronic excitation thresholds of CO with the first one located at approximately 6eV. Hence all collisions of electron below 6eV with CO can only excite CO vibrationally, explaining how the CO can be efficiently vibrationally populated.

Though much work from literature investigates mechanisms taking place in pure CO_2 plasmas, a large part of literature aimed also at studying the influence of mixtures on the CO_2 dissociation. For the CO_2 laser, the impurities were crucial because they could quench the vibrational excitation. As noted in W.J.Witteman 1986, a few ppm of water can severely quench vibrational excitation and prevent lasing. On the other hand, the rare gas like He proved to be very poor quenchers of CO_2 vibrations and could be used as buffer gas to limit the CO_2 collisional quenching. The role of the mixture was also studied for CO_2 recycling: if the technology was to be ever industrialized, it would be difficult to work in pure CO_2 because it does not correspond to what industries emit (exhaust often contain large amount of air) and would require an undesirable CO_2 separation step. In this frame, CO_2-N_2 mixtures have been at the center of many studies. Luckily, N_2 was found to enhance CO_2 vibrational excitation through the resonance of N_2(v) and CO_2 (v). On the opposite, atomic oxygen and water quench efficiently the CO_2 vibrational excitation. Given the possible applications of CO_2 plasmas for Mars, measurements are also run in mixtures corresponding to martian atmosphere compositions to test whether plasma technology could achieve good yields on Mars.

In search of an efficient CO_2 dissociation, numerous types of discharges have been investigated. A complete and exhaustive review of the current state of research in CO_2 plasma was done by in L.D.Pietanza et al. 2021 and summarizes the extend of the investigation. A short overview of the discharges mentioned is given here.

- Glow discharges at low pressure have been studied repeatedly for fundamental purposes despite their low conversion and energy efficiency. Their homogeneous and reproducible features at low pressure makes them very well suited for comparison with a 0D kinetic models. That is why they have been used in particular at LPP in collaboration with IST Lisbon since 2015 for a systematic step by step validation of CO_2 plasma mechanisms. After developing diagnostics techniques to determine the composition and vibrational temperature time resolved and *in situ* in CO_2 glow discharge (Klarenaar, Engeln, et al. 2017,Klarenaar, A S Morillo-Candas, et al. 2019,A S Morillo-Candas, Drag, et al. 2019a), the vibrational kinetic was validated for the first 72 vibrational levels (Silva et al. 2018,Grofulović et al. 2018). The CO_2 dissociation by electron impact has been specifically studied in A S Morillo-Candas, Silva, et al. 2020 and Tiago Silva, Ana Sofia Morillo-Candas, et al. 2021. The chemistry of the neutral species has then been validated in A. F. Silva et al. 2020. Further studies haven then been conducted with CO2 diluted in N_2 in Terraz et al. 2019. Other groups have used similar configuration to investigate the mechanisms in CO_2 mixed with H_2O (Budde et al. 2022 and M.Damen et al. 2020), and other models have also been compared to the same glow discharge (Pietanza, Colonna, and Capitelli 2022, Naidis et al. 2022, Biondo et al. 2022). Glow discharges are also investigated at atmospheric pressure (Trenchev et al. 2019,Renninger et al. 2020) and achieve a relatively good energy efficiency of about 20% were demonstrated.
- Radiofrequency discharges, whose typical electron energy is suited for vibrational pumping, have not generated the same interest as some others because of they are usually difficult to ignite at high pressure. Nevertheless, these discharges originally designed for etching/coating have been studied in Rond et al. 2008 or in Ana Sofia Morillo-Candas et al. 2020a, where they have reached 70% of conversion. The work done in Ana Sofia Morillo-Candas et al. 2020a allowed to evidence back reaction mechanisms reforming CO_2 at relatively low gas temperature that are usually not taken into account.
- Microwave have drawn interest for their ability to deposit high power in the vibrational modes of the molecules in the plasma. They are however limited by the V-T relaxation which lead to quick thermalization. As a result, continuous microwave discharges tend to have very high operating temperature, as shown in Rooij et al. 2015. Their conversion efficiency can then depend on the O atoms transport responsible for back reaction at high temperature. However, similarly to glow discharges, a certain out-of-equilibrium degree can be maintained by going to low pressure (around 1Torr, Britun and Hnilica 2020), or with recent development of "ultra-fast" pulsing of microwave discharge in Soldatov et al. 2021 in which the CO vibrational temperature was a few thousand of Kelvin higher than the gas temperature for a few hundreds of ns.
- Nanosecond Repetitively Pulsed (NRP) discharges, consisting in short high voltage pulses of a few tens of ns are very trending for CO_2 dissociation. The very high reduced electric field they create in the reactor lead to a strong electron impact dissociation. The short

duration of this discharges however make them more challenging to investigate, requiring diagnostics with very good time-resolution (like ns-resolved OES in Maillard et al. 2022 or in Ceppelli et al. 2021). Many configurations were studied, like a cylindrical configuration in Montesano, Quercetti, et al. 2020 or a discharge in capillary tubes in Pokrovskiy et al. 2022. A Large research effort is still on-going, with most recently the modelling of these discharges in Naidis et al. 2022.

1.3.3 CO_2-H_2 plasma

The origin of research on CO_2-H_2 plasma is different. It is not derived from the research on CO_2 plasma, but rather comes from the chemistry. Methanation, also known as Sabatier reaction, is a process mixing CO_2 and H_2 to produce CH_4:

$$CO_2 + 4H_2 \rightarrow CH_4 + 2H_2O, \qquad \Delta H = -370kJ/mol \tag{1.10}$$

This process was discovered in 1897 but gained interest in the recent ecological, economic and geopolitical context: the shortage of CH_4 (main component of the "natural gas" used for domestic and industrial heating) in Europe due to cutting supplying from Russia combined with the need to recycle CO_2 emissions make this process very interesting. CH_4 is one of the most used fuel across the planet and represent one third of all fossil fuel burned every year. In the ideal case, this process uses renewable energy to transform electricity into gas, which can be stored efficiently and used when needed. The CO_2 emitted can be recaptured and re-injected in the cycle. Unlike pure CO_2 splitting, industrial thermal methanation reactors are already functioning (such as the "Minerve" demonstrator, which uses exhausts for CO_2 and green H_2 to produce CH_4) and have demonstrated industrial capacities. This process is indeed chemically achievable by compressing the mixture to a few Bars and heating to 300 to 400°C. Under these conditions, the reaction becomes exothermic. Yield enhancement of thermal methanation were demonstrated with the use of catalysts (Varvoutis et al. 2022), which are now very commonly used. Though achievable chemically, methanation could benefit from plasma: the energy efficiently deposited in the vibrations of the CO_2 molecule could lower the activation energy of the reaction and subsequently avoid wasting energy in heating the molecules. Because of its numerous advantages, methanation is currently studied for industrial purposes. Most of the work is conducted in scalable systems that will be easily translatable to industry, e.g atmospheric pressure dielectric barrier discharges (APDBD) and already includes catalysts (Dębek et al. 2019). The catalysts are necessary to achieve full hydrogenation into CH_4. Without them, plasma alone rather tends to form $C_XH_YO_Z$ molecules. The Ni-based catalyst have been found to be the most suited catalyst because their activation peaks at around 100°C and are therefore among the most studied type of catalyst (Costa et al. 2021, Sivachandiran et al. 2020). Using Ni-based catalysts, good methane yields can be obtained. Up to 80% of conversion efficiency with a 100% selectivity for methane were obtained by J.Amouroux et al. 2011. The energy efficiency of the DBD is however very low with values of only a few percents reached. Other type of discharges were studied. Low pressure RF discharges were studied in Kano et al. 2012 but have had only poor CH_4 yield and produced mostly CO. Atmospheric sparks were studied in Seán Kelly et al. 2019 and have shown to have energy efficiency up to 50%, but with only a few percent of CO_2 conversion. Similarly, Gliding Arc (GA) discharges were studied in J.-B. Liu et al. 2019 but have shown dissociation efficiency of up to 7%. Overall, CO_2-H_2 plasma meet with a similar problem as CO_2 plasma: there is an important trade-off between energy efficiency and conversion efficiency. The combination of both seems possible only through the use of catalyst, therefore orientating the heart of the ongoing research on the catalysis aspect.

1.3.4 CO_2-CH_4 plasma

An interesting way to turn CO_2 into value added product is to combine CO_2 with CH_4, which aims at achieving the Dry Reformation of Methane (DRM):

$$CO_2 + CH_4 \rightarrow 2CO + 2H_2 \tag{1.11}$$

The CO-H_2 mixture is called "syngas", which stands for "synthetic gas". CO and H_2 can indeed be recombined together to form hydrocarbons through the Fischer-Tropsch process:

$$nCO + (2n+1)H_2 \rightarrow C_nH_{2n+2} + nH_2O \tag{1.12}$$

Depending on the n chosen, many common and useful hydrocarbons can be made: C_2H_6 (ethane), C_3H_8 (propane), C_4H_{10} (Butane), C_8H_{18} (octane, main component of gasoline), and up to $C_{14}H_{30}$, one of the main component of kerosene. The DRM therefore tackles the problem of energy storage by converting electricity produced by intermittent sources (such as renewable energies) into high energy density molecules. These molecules can later be reused as any other fuel. Though the transformation of CO_2 to hydrocarbon is currently achieved in two steps (CO_2 to CO followed by CO + H_2), much effort has been recently dedicated to the production of C_2H_6, C_2H_4 and C_2H_2 (Ashford et al. 2022) in one step straight from the CO_2-CH_4 mixture, but no efficient conversion in this pathway has been demonstrated yet. The advantages of CO_2-CH_4 plasmas for DRM are therefore double: not only do CO_2-CH_4 plasma recycle CO_2 (as well as CH_4 in the best case), it also forms directly the main component needed for the Fischer-Tropsch process. The Dry Reforming of Methane can be achieved chemically Arora et al. 2016 but require both heating to several hundreds of °C and catalysts. The use of the non-equilibrium thermodynamics of cold plasmas could avoid wasting energy in heating. CO_2-CH_4 plasma are also interesting for other fields of scientific study. The atmosphere of early earth, where life appeared, was essentially composed of nitrogen and carbon dioxide, but large amounts of methane were released by volcanoes and later by micro-organisms Pavlov et al. 2000. The understanding of CO_2-CH_4 plasma could therefore help understand how some large molecules, bricks of organic molecules, could appear in the atmosphere of early Earth, but also how CH_4 dissociation could lead to large scale climate change of the planet.

The interest of using cold plasmas for DRM is quite recent (mentioned barely a decade ago by Centi et al. November 2009) and as a result CO_2-CH_4 plasmas are still an uncharted field. Indeed, despite a vast literature available on CO_2 or CH_4 plasma, the main processes at the heart of CO_2-CH_4 plasmas are still to unravel. Because of the strong industrial potential of CO_2-CH_4 plasmas, many of the research is done on industrialisable systems like atmospheric pressure dielectric barrier discharges (APDBD). Much work is also done using catalyst to enhance the performance of the discharge, making the understanding of the physical basis of CO_2-CH_4 plasma challenging. However, because the optimisation of this process will have to go through a better understanding, more and more work on the fundamental aspects of these plasmas is being done (Bogaerts et al. 2016, W.Wang et al. 2018, C.Bai 2019, Pan et al. 2022). Because of the complexity of the CO_2-CH_4 plasmas, the study of CO_2-CH_4 plasma is only at its beginnings. The level of complexity added by the CH_4 molecule comes from its intrinsic properties which are described in the next section.

1.3.5 Properties of the CH_4 molecule

The complexity of the CO_2-containing plasma has already been described before. In CO_2-CH_4 plasmas, additional difficulties arise because of the complexity of the molecule itself. CH_4 has 5 atoms shaped like a tetraedre, with an equilibrium angle of 109°. As a consequence, the molecule has 9 degrees of freedom, which translates into 4 vibrational modes, presented on figure 1.5: symmetric stretch ($v1$), symmetric bend ($v2$, doubly degenerated), anti-symmetric stretch ($v3$, triply degenerated) and anti-symmetric bend ($v4$, triply degenerated). Just like the resonance of the bending and symmetric modes of CO_2, the quanta of $v1$ and $v3$ are very close, leading to rapid transfer of energy between these modes. The quanta of $v2$ and $v4$ are also very close, leading to coupling of these modes. Finally, the quanta of $v1$ and $v3$ are almost double of the ones of $v2$ and $v4$, leading to a coupling of all modes similarly to CO_2 $v1$ and $v2$. The first vibrational levels of CH_4 are plotted on figure 1.6, where the values of the energy levels are taken from Owens et al. 2016. The vibrational levels of similar energy are grouped together

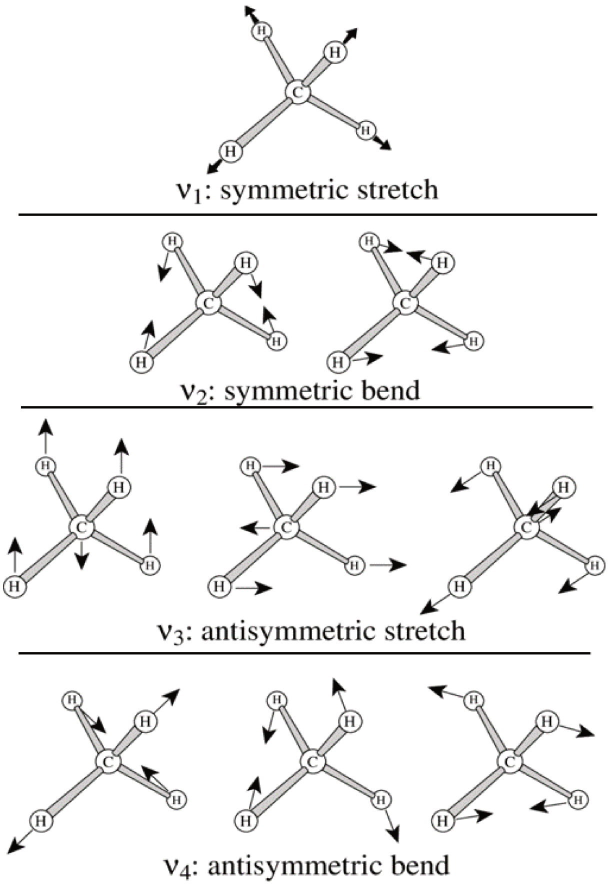

Figure 1.5: CH_4 vibrational modes. Taken from Maroni 2005

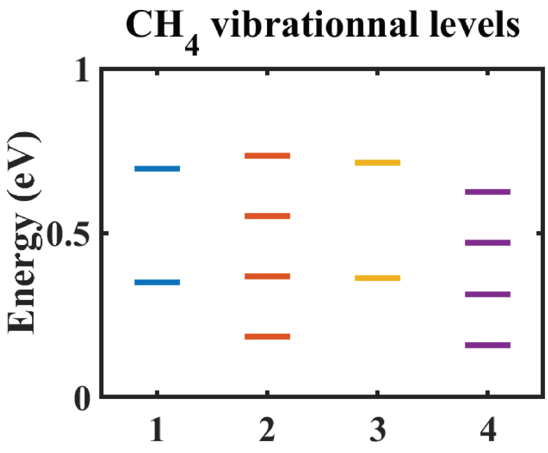

Figure 1.6: Plot of the first vibrational levels of the 4 vibrational modes of CH_4

Polyad	States grouped in the polyad
P_0	(0,0,0,0)
P_1	(0,1,0,0), (0,0,0,1)
P_2	(1,0,0,0), (0,2,0,0), (0,0,1,0), (0,0,0,2), (1,0,1,0)

Table 1.3: CH_4 polyads

Species from CO_2 plasmas	CO_2, CO, O_2, O, C, C_2...
Species from CH_4 plasmas	CH_4, CH_3, CH_2, CH, C_2H_6, C_2H_5, C_2H_4, C_2H_3, C_2H_2, C_2H, H, H_2...
Other	HCO, OH, H_2O, CH_2O, CH_2OH, CH_3O, CH_3OH...

Table 1.4: List of the neutral species expected in a CO_2-CH_4 plasma

in 'polyads' P_n (Butterworth et al. 2020), where n is the highest quantum of the states of the polyad:

$$n = v1_{max} = v3_{max} = 2v2_{max} = 2v4_{max} = v2_{max} + v4_{max} \tag{1.13}$$

The first polyads are described in table 1.3. Because of the number of possible combinations between the vibrational levels of the different vibrational modes, already several tens of vibrational levels (ν_1,ν_2,ν_3,ν_4) could be populated upon collisions with low energy electrons. The proper description of CH_4 is still ongoing in research, with new potential energy surface still being published (Nikitin et al. 2011, Owens et al. 2016).

Another sort of complexity comes from the numerous species and chemical reactions pathways in CO_2-CH_4 plasmas. A short list of molecules and radicals expected in a CO_2-CH_4 plasma is given in table 1.4. For clarity, only the neutral were given in the table, but any of the species of the table could also be found in the form of an ion (positive ion most of the time, but many negative ion can also be found) or in an electronic or vibrationally excited state. CO_2-CH_4 plasmas are an extremely interesting object of study: they rely on both the complex physical basis of CO_2 plasmas and the composite chemistry of organic molecules. Because CO and H_2 are formed in large quantities in CO_2-CH_4 plasma, studying CO_2-CH_4 plasma also sheds light on the processes driving methanation (from CO/H_2 plasma). **The study of the CO_2-CH_4 plasma has therefore much to bring even beyond the topic of DRM, but a lot remain to be understood about this complex system as shown by the current state of the art below**

1.3.6 Literature on CO_2/CH_4 plasmas

Many studies on CO_2-CH_4 plasma were conducted, both experimental and numerical, to try to understand their complexity. The number of articles on CO_2-CH_4 plasma actually keeps increasing. T. Pham et al. 2020 counted the articles published on DRM each year since 2000: while about 25 articles were written in 2001, more than 300 were published in 2019. This sums up to a few thousands of articles. This section aims at summarizing the current trends of CO_2-CH_4 plasma research.

On the experimental side, most of the work consists in study of DBD discharges with catalysts. Indeed, just like for the CO_2-H_2 plasma, the interest of CO_2-CH_4 plasma motivated the use of industrialisable reactor such as atmospheric pressure dielectric barrier discharges in plug flow configuration. Ozkan et al. 2015 studied the dissociation of CO_2 and CH_4 (in various proportions) using Argon or Helium as a carrier flow in an atmospheric pressure dielectric barrier discharge to treat large flows of CO_2. Like in most work on CO_2-CH_4 plasmas, the main products were CO and H_2, with H_2 increasing with the initial amount of CH_4. Nevertheless, C_2H_6 and C_2H_4 are found in the products, with densities close to 25% of the CO density. It was highlighted that the choice of Ar or He changed the shape of the EEDF and the proportion of high-energy electrons. Ar increased the proportion of electron available for C=0 bond dissociation whereas He favoured the C-H dissociation.

The DRM plasma system often include a catalyst which allows to increase the dissociation. Several types of catalysts have been investigated. For example, M. Pham et al. 2011 showed that the conversion of CO_2 was increased when using La_2O_3 catalyst. The most used catalyst in DRM studies are the Ni-based catalysts which have demonstrated the highest conversion in DBD. This is usually attributed to the activation temperature of these catalyst, ∼100-200°, typically the temperature reached in the DBD reactor. The synergetic effect of the catalyst was shown repeatedly, e.g in Q. Wang, Yan, et al. 2009, where the conversions of both CH_4 and CO_2 in a 1:1 CO_2:CH_4 DBD were increased by several tens of percent compared to plasma only or catalyst only. The results obtained in the packed-bed DBD of Q. Wang, Yan, et al. 2009 were compared to a ones obtained in a fluidized bed DBD in Q. Wang, Cheng, et al. 2009. The conversion did not improve in the fluidized bed compared to the packed bed but the specific energy input was found to be higher at a given voltage thanks to the better contact between the catalyst and the particles. Different types on Ni-based catalysts (several supports and Ni loading) were investigated in a 1:1 CO_2:CH_4 APDBD in H. Wang et al. 2019. Conversion of up to 60% for both CO_2 and CH_4 were reported and attributed to the catalyst structure (large surface due to a porous structure). The industrial aspect encourages the development of more pragmatical models. D.H. Mei et al. 2017 used experimental data obtained from gas chromatography at the output of a DBD reactor along with surface analysis of the Ni catalyst and power measurement from the reactor to develop a model predicting the conversion as a function of the flow, the Ni loading of the catalyst and voltage. The catalysts usually lose efficiency due to carbon deposition on their surface. An original approach was used in Kameshima et al. 2015 to take advantage of the carbon deposit on the Ni/Al_2O_3 catalyst in the packed bed reactor during the discharge operation. After flowing a 2:1 CO_2:CH_4 mixture for 1 minute, the CH_4 flow was stopped to maintain only a CO_2 plasma in the reactor. Carbon deposition was almost completely removed by the CO_2 plasma, which was attributed to the Boudouard reaction $CO_2 + C \rightarrow 2CO$ promoted by the Ni catalyst. A couple of other studies in a DBD discharge tackle the resistance of the catalyst to carbon deposition: Xu, Tian, et al. 2022 and Xu, Y. Liu, et al. 2022 show conversion rates for both CO_2 and CH_4 of about 90% in 1:1 CO_2-CH_4 mixture when using a particular catalyst, even after 10h. This is unusual as CO_2-CH_4 plasma usually deposits carbon on the wall, leading to a drop in conversion with time. The catalyst prepared in Xu, Y. Liu, et al. 2022 was pretreated with a N_2 RF discharge, which lead to a change of the crystal structure. The pore size of the catalyst carrier appeared to be larger, and the active metal (Ni again here) appeared to be better distributed on the surface with smaller particles. The exact processes leading to a lower carbon deposition are not clear but seemed to be linked to the crystal structure.

In the works on CO_2-CH_4 DBD, the measurement of the molecules densities is often done downstream by gas chromatography of mass spectroscopy. Little *in situ* diagnostics are used. Reaction pathways are sometimes proposed but remain hypothetical. The electron impact dissociation is often considered the main dissociation mechanism of CO_2 and CH_4. Chemical reactions then control the recombination into the value added-products. The role of CO_2 (v) is sometimes invoked to explain CO formation through $CO(v) + H \rightarrow CO + OH$. A review of packed-bed CO_2-CH_4 DBD for production of CH_3O and CH_3COOH was conducted in S. Liu et al. 2020a. Processes were proposed based on literature results. It was supposed that the conversion would happen in several steps. The first step happens during the filament (streamer) development itself, where electron impact dissociate CO_2 and CH_4 into CO,O,CH_3 and H, but also creates vibrationally excited CO_2 and CH_4. Both the radicals and the excited species are later adsorbed on the surface of the catalyst. The gas phase recombination of the radical yields in the after glow C_2H_6, CH_3OH or CH_2O. The production of CH_3O, precursor of CH_3OH, was attributed to dissociative adsorption of CH_4 followed by recombination of CH_3 with O at the surface.

The catalysts for conversion of CO_2 and CH_4 directly to liquid products was investigated in

L. Wang et al. 2017 and D. Li et al. 2020. In L. Wang et al. 2017, four catalysts (γ-Al_2O_3 alone or combined with Cu, Au, or Pt) were tested for DRM in a DBD at atmospheric pressure. Conversion of CO_2 or CH_4 were low (less than 20%), but the selectivity to liquid reached 60%. In D. Li et al. 2020, two catalysts (Co/SiO_2 and Fe/SiO_2) were tested in a CO_2-CH_4 mixture (with various proportions of CO_2 and CH_4) in an atmospheric pressure packed-bed DBD. The discharge products were measured at the output by gas chromatography. CO and H_2 were the main products by carbon chains between C_2 and C_5 were detected with a selectivity almost as high as the one of CO reported when using a high CH_4:CO_2 ratio. Liquid products like methanol, ethanol or acetic acid where detected in a liquid trap at the output of the reactor, once again with good selectivity ($\sim$40%). The formation of the products detected in the liquid was attributed to the catalysts but also to the packing. In these works on direct liquid production, reaction pathways were proposed but remained hypothetical due to the absence of in-situ diagnostics. The conversion of CO_2 and CH_4 can sometimes reach up to 95% (Jwa et al. 2013) when using a catalyst but comes at the price of a low energy efficiency with a specific energy input (SEI) reaching 20eV/molecule.

The DBD discharge was not the only type of discharges studied. Among the atmospheric plasmas, the study of nanosecond discharges was done in Scapinello et al. 2016 (and more recently in Montesano, Faedda, et al. 2021 in the same group), in X. Wang et al. 2019 & S.Zhang et al. 2022. The influence of the discharges parameters (in particular the time interval between nanosecond pulses) is usually explored to analyze their influence on the conversion or on the energy efficiency. Montesano, Faedda, et al. 2021 reported that the energy efficiency increased from 50% to 65% and methane conversion reached 100% when reducing the pulse interval to 40μs. This was attributed to the temperature of the gas mixture, which relaxes back to the initial conditions when the pulse interval is too long. The possible role of CO_2 (v) was here again evoked, but the vibrational temperature could not be measured to confirm this. The importance of CO_2 (v) is however supported by S.Zhang et al. 2022, where OES was used in a nanosecond discharge to fit the different vibrational and rotational temperatures. Using the fit of the C2 Swan band, it was deduced that a large part of the CO_2 is vibrationally excited.

Radiofrequency discharges were rarely studied for CO_2-CH_4 discharges, despite their potential for vibrational pumping of CO_2. Z. Liu et al. 2020 studied the vibrational excitation in a 98:1:1 Ar:CO_2:CH_4 RF discharge at atmospheric pressure. Z. Liu et al. 2020 measured the vibrational distribution of the C_2 and assuming that the vibrational temperature of C_2 evolves like the one of CO_2, highlighted that the CO_2 vibrations are populated by collision with the Ar metastables. Low pressure RF ICP discharges (between 0.1 and 0.5 Torr) were studied in H.Li et al. 2020. Conversion rates of up to 90% for CO_2 and CH_4 were found in a 1:1 CO_2-CH_4 molar ratio at a flow of 300sccm, with CO and H_2 being the main products (measured with mass-spectrometry downstream from the plasma). A reduced set of reactions was proposed to explain the observed results, though no actual model was presented. The set included CO_2 and CH_4 dissociation by electron impact followed by various recombination. Vibrations of CO_2 were assumed to be populated by low-energy electrons and to enhance dissociation of CO_2. Vibrations are unlikely to be the only responsible of the dissociation because very high gas temperatures were measured in the plasma ($\sim$4000K). CO was also estimated to be formed from oxidation of CH_3, CH_2 and CH. Because the C_2 band was observed by OES, it was assumed that C_2H_Y molecules were formed by recombination of CH, CH_2 or CH_3 radicals but were immediately destroyed by electron impact (for C_2H_6 and C_2H_2) and by chemistry for C_2H ($C_2H + H \rightarrow C_2 + H_2$). Because of the low pressure, the real flow is still low but this paves the way toward application-suited flows.

Microwave discharge also present an interesting potential for DRM. Tao et al. 2011 reported in a literature review that the microwave presented good energy efficiency and conversion compared to the DBD, with energy efficiency 10 times better than DBD for similar conversion of CO_2

and CH_4 and attributed this to both the low energy of the electrons in a microwave discharge and the high temperature. A microwave discharge was studied in Jasiński et al. 2013 and Hrycak et al. 2019 for H_2 production from a CO_2-CH_4 plasma. Thanks to the homogeneity of the plasma, large CH_4 volume (up to 6 m^3 per day) were treated. A good production of H_2 (several hundreds of liters per hour) was obtained, once again attributed to the high temperature. The rotational and vibrational temperatures of C_2 were measured by OES and estimated to be respectively between 4000 and 5700K and 5000 and 6000K depending on the microwave power. The influence of the ratio of CH_4/CO_2 was studied in the same system as showed in Hrycak et al. 2019. The selectivity of H_2 was found to increase with the CH_4/CO_2 ratio along with the carbon deposition, which created operation problems. Ni-based catalysts were also tested for microwave CO_2-CH_4 discharges in Chun et al. 2019. To avoid damaging the catalyst with the plasma high temperature (measured with the C2 Swan band to be around 6000K), the catalyst was placed outside of the plasma but were reached by the gas thanks to the circulation of the turbulent flow. The system yielded an H_2 production of ∼59g/h, close to the 60g/h usually found in the tradition steam reforming of CH_4 to produce H_2. The role of the catalyst was highlighted, almost doubling the conversion, but no processes were proposed to explain this effect. Finally, it is worth noting that microwave-assisted dry reforming of methane is currently being largely investigated. It consists in heating a CO_2-CH_4 mixture by sending a microwaves but without igniting plasma. The interest here is only to heat. A literature review was done in T. Pham et al. 2020 and highlighted the potential of Ni-based catalysts compared to more common carbon-based catalysts. The recommendations were followed in de Dios García et al. 2021 (Ni/SiC catalyst), where conversion efficiency reached 90% for both CO_2 and CH_4. Fe-based catalysed were studied in Zhang et al. 2022, where conversion as good as for Ni-based catalysts were found. This technique relies on chemistry though it is suspected that microplasmas can be ignited on the surface of the catalyst, largely increasing the conversion T. Pham et al. 2020.

The very complex chemistry of the CO_2-CH_4 plasma makes it difficult to determine the reaction pathways simply from experimental results, especially when $C_XH_YO_Z$ molecules are formed. Models must be used to understand in depth the conversion mechanisms. Pure modelling studies in CO_2-CH_4 plasmas are less common, and only a few can be enumerated. Gas phase in nanosecond repetitive pulsed discharges were modelled with a 1D fluid model in C.Bai 2019 with a "simple" cylindrical configuration. The kinetic scheme used was later updated in Pan et al. 2022 to take into account surface processes in the same configuration.

Some models are compared to experimental data to determine their validity. A 1D fluid model was done in Zhu et al. 2022 to model a packed-bed DBD reactor with Pt catalyst packing (a 1D equivalent of the 2D catalyst packing was used). The numerical results are compared with experimental results from Tu et al. 2012 and showed relatively good agreement. The Antwerp group studied high pressure CO_2-CH_4 DBD incrementally: a 1D fluid model of the CO_2-CH_4 discharge using the Plasimo's MD2D software was presented in Bie et al. 2015 for a DBD and in Bogaerts et al. 2016 for a microwave discharge. A kinetic scheme was provided as input of Plasimo's MD2D. This kinetic scheme had been previously used with a different kinetic model (Global_kin) in Ramses Snoeckx et al. 2013, also for DBD discharges. Ramses Snoeckx et al. 2013 compared the simulated energy efficiency, simulated conversion of CO_2 and CH_4 and simulated selectivity of CO and H_2 to experimental data taken from Tu et al. 2012. Further validation of the model from Ramses Snoeckx et al. 2013 was presented in R. Snoeckx, Zeng, et al. 2015. Nevertheless, the details of the reaction pathways were only discussed in depth in Bie et al. 2015. The kinetic scheme was later used with ZDPlasKin to describe a gliding arc plasmatron in Cleiren et al. 2017, where the simulated and experimental conversion of CO_2 and CH_4 were compared. The study of Cleiren et al. 2017 served as basis for the work presented in Van Alphen et al. 2021, which presented a complete model combining a gas flow approach with a 3D plasma arc model, a particle tracing model and a quasi-1D kinetic modeling of the gliding Arc plasmatrons. The kinetic scheme was later updated and used in a 0D model in W.Wang et al. 2018 for an experiment-simulation comparative study of CO_2-CH_4-N_2-H_2O plasma. Because of the interest of CO_2-CH_4 plasmas for industrial DRM, some more pragmatical models were developed to predict the maximum conversion/energy efficiency form the discharge parameters. Such model was developed for a NRP discharge at atmospheric pressure in Danhua Mei et al. 2022. A neural network was used to predict the dissociation as a function of the applied voltage, the flow rate, the CO_2-CH_4 molar ratio and the discharge length. Although this method is probably very efficient and must most certainly be investigated more as it holds a huge potential, neural network have a black box aspect and tend to be more a fit than a model. Indeed, neural network require a vast amount of input data to be accurately predictive, usually much more than what is available experimentally. However, if large volumes of experimental data can be generated, this method surely can unravel the complexity of CO_2-CH_4 plasmas. Nevertheless, the neural network used in Danhua Mei et al. 2022 showed a very good agreement with the experimental data. Possible reaction pathways were given in Danhua Mei et al. 2022 without being supported by measurements though.

Comparing the experiment and simulation is always a good idea but the complexity of the chemistry induced in CO_2-CH_4 plasma illustrated by the literature reported above, definitely impose to have quantitative comparison of model and experimental data in numerous plasma conditions in order to try to disentangle the mechanisms controlling these plasmas. The work presented here will apply as much as possible this dual approach of experiment and modelling.

1.4 What is to understand in CO_2-CH_4 plasmas

As mentioned previously, CO_2-CH_4 plasmas are very complex and much is still to understand. On the whole, CO_2-CH_4 plasma literature mostly consists in experimental values of conversion rate and efficiency of CO_2 and CH_4 and of selectivity of the various products as a function of the discharge conditions. The main focuses for the fundamental aspects are the following ones:

Electron impact cross-sections Despite their importance in plasma physics, the electron impact processes are among the first sources of uncertainty both for CO_2 and CH_4.

Several dissociation cross-sections were proposed for CO_2 (Hake et al. 1967 & Polak et al. 1976). Recent experimental results by A S Morillo-Candas, Silva, et al. 2020 have shown that in the range 10-100 Td, the Polak & Slovetsky cross-section are most suited for accurate calculation of the rate of CO_2 dissociation, but no clear conclusion could be reached for higher reduced electric field (100Td<, typically reached in NRP discharges). It was also shown in Grofulović et al. 2018 that though the Polak & Slovetsky cross-section should be used for the rate, the Phelps cross-section should be used for computation of the EEDF because it includes other energy dissipation processes that must be taken into account for the complete EEDF calculation. A proper choice of the CO_2 cross-section for CO_2-CH_4 modelling is therefore non-trivial.

CH_4 electron impact cross-section are also questioned. Until 2021, only one complete and consistent set of cross-sections validated against swarm parameters was available for CH_4 plasma EEDF computation (from IST Lisbon database, L L Alves 2014). This set however included "fitted cross-section", meaning unknown cross-section of several processes gathered together and fitted so that the whole set would math the swarm parameters. Another set was proposed by Bouwman et al. 2021, which:

- didn't include any "fitted" cross-sections
- were based on experimental results and recommendation and experimental results
- includes more processes than the IST set (previously gathered in the fitted cross-section")

This new set appeared as more legitimate, but no experimental results effectively proved one to be better than the other, making both equally legitimate. Despite this, many other cross-sections can be found in literature for specific processes, making the comparison even harder (for example the rate chosen for the modelling in C.Bai 2019 is a function of the electron temperature T_e). This illustrate the blur around the choice of the appropriate cross-sections. It goes without saying that if this problem appears for the major species, the minor species suffer from the same problem. A complete and consistent set of cross-section for water was proposed for the first time only this year Budde et al. 2022. No complete set exist for C_2H_6, C_2H_2 or C_2H_4, only scarce cross-sections for specific processes. Assembling a consistent set of electron impact cross-section is therefore a challenge that must be answered.

Determination of the chemical kinetic scheme The number of species in a CO_2-CH_4 plasma is very large. A complete set of reactions including electron-neutral, neutral-neutral, ion-neutral, electron-ion and ion-ion reactions can include more than 1500 reactions, even more if the scheme includes a complete description of the electron kinetics, the vibrational kinetics, the surface kinetics... The rate coefficient for many of the neutral-neutral reactions are often unknown or known with a large uncertainty. Most of the rates were measured for combustion (Baulch et al. 1992, W. Tsang et al. 1986) and correspond to high temperatures or do not take into account any kind of excitation. This leads to an overall important uncertainty on the reaction pathways, doubled by the possibility to do error compensation with so many coefficients. Experimental data are often taken in reactors designed for efficiency with complex geometry (Van Alphen et al. 2021 in a gliding arc plasmatron, packed bed reactor for Kameshima et al. 2015), which are complicated to model accurately. A lot of experimental data are taken with a catalyst (e.g D. Li et al. 2020 or the numerous work gathered in the review of S. Liu et al. 2020b), making the modelling and the understanding of the reaction pathways impossible without a good plasma/surface interaction model. Moreover, the use of catalyst without a proper description of the gas phase in many case prevent a good understanding of the reaction pathways, turning many studies into "try and error". The main conversion pathways are therefore not always clear and are still debated.

Excited species The role of excited species (electronic and vibrational states) is largely neglected. This is partly due to the absence of the rates of reaction between excited and ground state species. The rates used for neutral-neutral reactions mostly come from combustion sources. The absence of electron impact excitation in combustion makes the excited states far less important than they are in plasma.
The influence of a few electronically excited states of Oxygen atoms and O_2 were estimated in Konnov 2015 for combustion but were not found to be crucial, thus justifying their neglecting for combustion in general. Konnov 2015 also highlighted the role of OH* in the chemical kinetics. Baulch et al. 1992 reviewed literature to gather rate coefficient useful for combustion but only provided a limited number of rates including an excited species. Moreover, most of the rate concern excited atomic O. Rates concerning excited CO (like $CO(a^3\Pi)$) for instance are missing. Some knowledge can however be drawn from the CH_4-O_2 plasma which have been studied for plasma-assisted methane combustion or methane pyrolisis, as in Lefkowitz 2015, Mao et al. 2019 or Starik et al. 2012. In all of these papers, the influence of excited species has been highlighted for the enhancement of combustion. Lefkowitz 2015 reports the influence of O(1D) on the oxidation of CH_4 and shows that this channel is one of the main loss channels of CH_4, as relevant as electron impact deexcitation. Starik et al. 2012 reported the influence of $O_2(b^1\Sigma_g^+)$ and $O_2(a^1\Delta_g)$ on the combustion efficiency. Despite this, the effect of excited species is not studied in depth.
The same problem arise for vibrationally excited state. Vibrational excitation is generally considered beneficial for CO_2 dissociation, which shows how important is a proper description of the vibrational excitation of all the molecules in the plasma. The influence of the vibrations on the rate can be tackled by subtracting a contribution to the activation energy in the form of an Arrhenius reaction (as done in Kozák et al. 2014):

$$k(E_v, T) = A_0 exp(-\frac{E_A - \alpha EV}{T}) \tag{1.14}$$

where E_A is the activation energy of the reaction, E_v the vibrational energy and α a parameter determining the efficiency of the vibrational energy substraction. α is calculated with the Friedman-Macheret model (Adamovich et al. 1996). This contributes to describing the quenching of the vibrational excitation in the plasma. However other sources of quenching must be accounted for: the vibration to translation (VT) processes and the transfer of the vibrational excitation from one molecule to another (the so-called V-V and V-V' processes). V-T processes have been described in CO_2 plasmas (W.J.Witteman 1986) and CH_4 V-T processes are usually considered to be extremely fast. V-V processes between CO_2 and CH_4 have been described in the 70s by various sources but the rates spread over orders of magnitude, casting doubt over their real value. The vibrational excitation is therefore still a focus of research in CO_2-CH_4 plasmas. In particular CO_2 and CH_4 vibrational excitation is often claimed to be beneficial for conversion but more investigations are needed to evidence it.
The lack of data about the role of excited states on the chemistry of CO_2-CH_4 plasma is clear. As a consequence models describing CO_2-CH_4 plasma are often the combination of electron impact dissociation and ionization processes coupled with chemical sets from combustion. To know whether this is sufficient or not to accurately describe CO_2-CH_4 plasma, more *in situ* diagnostics in experiments, and more quantitative comparisons between models and experiments are necessary.

The role of the surfaces Surfaces in plasma are an everlasting problem, whose study has been going on for decades in some case (like for O_2 plasma, J. P. Booth et al. 2019). CO_2-CH_4 plasma are no exception, with many atomic species (O, H) and radicals (OH) which can be physisorbed or chemisorbed at the wall and react there. One of the issue faced in the understanding of CO_2-CH_4 plasma is the recombination rate of atomic species, which have been measured in a CO_2 plasma in A S Morillo-Candas, Drag, et al. 2019a, or in Hydrogen plasma A.Rousseau et al. 2001. These recombination probability also depends on many parameters of the surface itself (roughness, chemical composition...) and of the plasma (gas and wall temperatures, atoms diffusion and flux ...). The problem in CO_2-CH_4 plasma does not stop there and the complexity of the CO_2-CH_4 plasma unfortunately catches up with surfaces: it is a widely known problem that when the CH_4 proportion is high enough, carbon deposition will start to appear on the walls of the reactor or the electrodes (limiting in the second case the ability to restart a plasma). The characterisation of the carbon deposition is challenging because they are complex chains of C,H and O, thus making the tracing of surface process complex. Surfaces are all the more important that a large part of the research on CO_2-CH_4 plasma focuses on the use of catalysts to improve conversion.

1.5 Approach of this thesis

CO_2-CH_4 plasmas are a very interesting lead to tackle the problem of efficient energy storage. Before jumping to large scale plasma technologies and efficiently face this issue, the fundamental basis of CO_2-CH_4 must be better understood. This work aims at answering or at least provide insights into some of the main unknowns presented above. In particular, the following questions will be addressed:

- What are the mechanisms controlling the dissociation of CO_2 and CH_4 in CO_2-CH_4 plasma ?
- What are the back reaction mechanisms limiting their conversion?
- Is the chemistry induced in a plasma really making a difference compared to the conversion by thermal reactions ?
- How is the vibrational excitation of CO_2 affected by CH_4 and its by-products ? Is the vibrational excitation only affecting the electron energy or also the chemistry induced in the plasma ?

All in all, this work aims at identifying the basic physical and chemical phenomena happening in a low pressure CO_2-CH_4 plasma. Dedicated experimental setups and approaches have been designed in an attempt to disentangle the questions listed above. It also includes the need for developing measurement techniques that are reliable, yet simple enough to be applied in large parametric studies to provide enough information to dig into the complexity of CO_2-CH_4 plasmas.

Because of everything mentioned above, the use of complex discharges must be discarded to get insights on fundamental mechanisms driving CO_2-CH_4 plasmas. For this reason, the main system studied in this work is a low pressure glow discharge taking place in a cylindrical pyrex reactor. The low pressure system "slows down" the characteristic times of all phenomena by lowering the collision frequency. Phenomenon that would happen in one nanosecond at atmospheric pressure can be slowed down to a few millisecond, making the observation and the measurement much easier (the lower time-resolution needed allows for the use of more instruments). The glow discharge is probably among the worst discharges for efficient CO_2 splitting but has several incomparable advantages for a fundamental study. First, it is supposed to be spatially homogeneous, which avoid the necessity to use space-resolved diagnostics and allow the use of line-of-sight averaged diagnostics. Second, the glow discharge is reproducible: as it fills the whole volume between electrodes, no problems of spatial reproducibility are met (unlike for nano-second discharge, filamentary DBD or plasmatron where the discharge channel constantly changes). Third, several key physical quantities are easily accessible: the electron density (n_e) is proportional to the imposed current and the electric field (E) can be easily obtained by inserting two pins in the plasma and measuring the voltage drop across the positive column (assuming spatial homogeneity, the field is simply obtained by $E = \frac{\delta U}{d}$ where d is the distance between the pins). These parameters (n_e, E) are critical to understand the behaviour of the plasma. The spatial homogeneity and the easy access to physical quantities makes the glow discharge ideal for comparison with a 0D model, which is often required to fully understand the plasma kinetics.
Finally, the cylindrical pyrex reactor is symmetrical and has no sharp edges which avoids geometrical edge effects. The pyrex is one of the most studied material and many coefficients and rates are available in literature when it comes to plasma surface interaction, such as recombination of atomic species (A S Morillo-Candas, Drag, et al. 2019a).

The glow discharge is used in two complementary ways but always with a gas flow, *i.e.* in "plug-flow" configuration. The first use of this discharge is to measure parametrically the dissociation products at the output of the discharge to constraint the chemistry. Secondly, the vibrational excitation is measured in the pulsed glow discharge in a configuration where the mixture composition is considered stable during the pulse. This allows to constraint the vibrational kinetics of CO_2-CH_4 plasmas by using a 0D model.

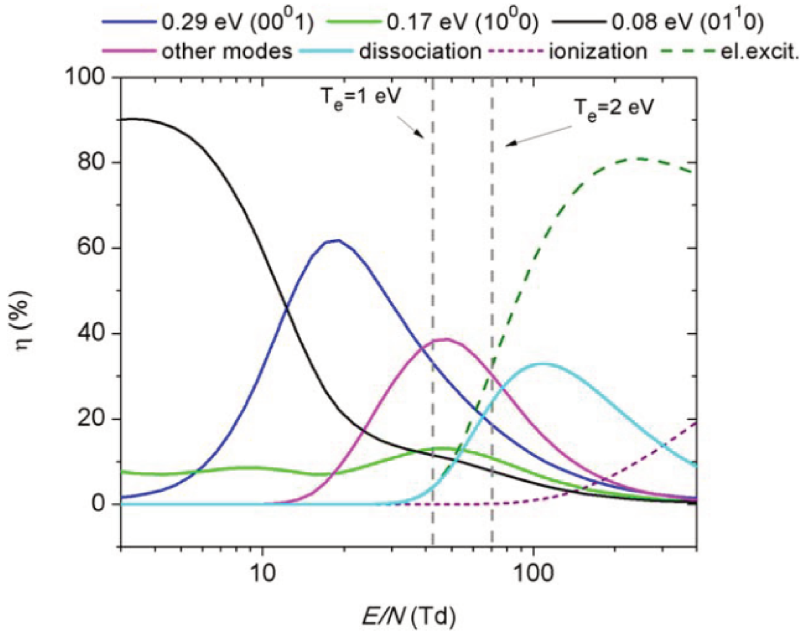

Figure 1.7: Repartition of the energy between different modes in a pure CO_2 discharge as a function of the reduced electric field. taken from Grofulović et al. 2018

However, given the strong ecological and technological interest of CO_2-CH_4 plasma, it would be foolish not to try to understand and optimize the production of CO and H_2 from CO_2 and CH_4 in a discharge more suited for CO_2 conversion. For this reason, the behaviour of CO_2-CH_4 plasma is also investigated in a low pressure radiofrequency discharge, though still from a fundamental point of view. The reduced electric field in a radiofrequency, lower than in most other discharges, is suited for CO_2 dissociation : it correspond to the field required for vibrational pumping. The following graph 1.7 taken from Grofulović et al. 2018 shows how the electron energy is splitted between different modes in an CO_2 discharge. When the reduced electric field is of a few tens of Td, most of the energy is transferred to vibrations because the typical electron energy is not too far from the vibrational quantum of CO_2. This is completed by a large electron density compared to other discharges, meaning that more electron can actually be used for vibrational pumping. The RF discharge is however not spatially homogeneous and offers no easy way to measure E/N and ne, making it challenging to study. Yet the RF discharge figures as an ideal candidate for efficient CO_2-CH_4 conversion, and the kinetics of the Radiofrequency discharge and the reaction pathways will be studied in this work in a closed-reactor configuration ("batch configuration"). In this configuration, the evolution of the densities of IR-active species is measured in a closed-reactor (i.e without any flow) giving a chance to follow the chemical kinetics from initial reactants until complete steady state. This will allow to test the kinetics scheme devised with the glow discharge even further.

Finally, to obtain as much information as possible from the experiments to constrain the models, developments of measurement method will be necessary. Automation of the measurements will also be necessary to increase the amount of data available to test the models.

The main goals of this work are therefore the following:

- Develop experimental tools to complete the data obtained in each condition measured in the parametric study that will be conducted. The reliability of actinometry will be assessed. Method to determine the rotational ad vibrational temperatures of CO will also be tested.
- Constrain the kinetics of the electrons and the main species of the plasma using a plug flow configuration in the glow discharge for which parameters driving the plasma behaviour (Electric field, electron density and gas temperature) can easily be determined.
- Constrain further the kinetics scheme developed by using a more complex discharge configuration (RF plasma in batch reactor) which however allow to follow the evolution of chemical composition until steady state
- Constrain the vibrational kinetics of CO_2-CH_4 plasmas with time resolved *in situ* measurements of CO_2 and CO vibrational temperatures in various mixtures

The primary concern of each of these goals is to place ourselves in conditions that allow us to make quantitative model/experiment comparisons in order to understand the complex kinetics involved.

1.6 Outline

This work is structured into four main parts but the first one is subdivided in two.

The first part focuses on the use and the development of diagnostics. The main diagnostic used in this work is the Fourrier Transform InfraRed (FTIR) spectroscopy, but no development were made on this diagnostic. A focus is done on OES-based diagnostics, like the determination of the temperature (rotational or vibrational) with through OES or actinometry. Actinometry is compared to Cavity Ring Down Spectroscopy to find the best parameters to use to obtain robust results from this very simple diagnostic. The second part, which can be seen as a subpart of the first one, is dedicated to the adaptation of optical emission spectroscopy to the use of a simple low spectral resolution USB spectrometer in order to be able to use this diagnostics as "routine" in all our next experiments.

The third part focuses on the kinetic scheme of CO_2-CH_4 plasma. FTIR spectroscopy and OES are used to follow the evolution of the rotational temperature and densities of IR active species in a glow discharge. A parametric study is used to explore a large range of pressure, mixture and total flow conditions. These results are then used as basis for comparison with 0D model using a "simple" kinetic scheme (containing only molecules with up to one carbon atom). This first experiment allows to validate the first part of the kinetic scheme. The reaction pathways are discussed.

The fourth part aims at understanding the reaction pathways in a CO_2-CH_4 RF discharges in closed reactor (without any flow). Plasma pulses are ignited in the reactor and are followed by FTIR measurements to obtain the evolution of the densities of IR active species as a function of the number of pulses (and indirectly of the plasma ON time). Because less information are available than in the glow discharge, a parametric study is first conducted to draw as many information as possible from experimental results. The previously established kinetic scheme is then extended to simulate the RF discharge, where molecules with 2 carbon atoms are detected.

The last part focuses on the vibrational excitation of CO_2-CH_4 plasmas and aims at answering the following question: what is the effect of CH_4 and its by-products on the vibrational excitation of CO_2 and CO ? The pulsed glow discharge is used in flowing conditions (plug flow). This allows to obtain a system in which dissociation is compensated by gas renewal, ensuring a stable composition, even during a pulse. The so-called step-scan function of the FTIR spectrometer is used to study the influence of CH_4 and some of it's by products in various conditions of mixing and pressure during a 5ms plasma pulse. The V-V processes are explored through the "Single Pulse" experiment, which increases the renewal of the gas to always ignite in fresh gas. This allows to follow the vibrational excitation in a controlled medium.

CHAPTER 2

Actinometry for O atom density measurements in low-pressure O containing discharges

Contents

2.1 Introduction

Among the many diagnostics used for CO_2 plasma, none are supposedly simpler than actinometry. Actinometry is an OES-based diagnostic, which aims at measuring the density of a specie (often atomic species) by comparing the intensity of an atomic emission line of interest with the intensity of the emission line of an actinometer, a gas whose density remains known in the plasma (a noble gas is typically admixed, usually Ar). Actinometry has been widely used over the last decades to measure absolute densities of various species. Indeed, despite low degree of dissociation in Nitrogen plasmas, actinometry to detect N was reported in Czerwiec et al. 2005 in an ICP discharge at 10^{-7}Torr. N was also measured in Ricard et al. 2007 for experiments in N_2-O_2 and N_2-H_2 microwave discharge. More recently, actinometry was applied in D. V. Lopaev et al. 2017 in RF discharges at 0.2Torr, using Kr as actinometer. D. V. Lopaev et al. 2017 also uses actinometry for F atoms and O atoms. Actinometry for O atoms densities measurements has been reported many times in pure O_2 and O_2/N_2 discharges. The measurement of O atoms by actinometry was reported in Pagnon et al. 1995 where it was compared with VUV measurements in a O_2 glow discharge at a few Torr. In Tsutsumi et al. 2017, O atom density and reduced electric field were simultaneously investigated in O_2 RF plasma, using Ar for O actinometry at 40Pa. In Britun, Belosludtsev, et al. 2017, O actinometry is used in HiPIMS Ar-O_2 discharges and compared to TALIF measurements between 3 and 20mTorr. Actinometry for O atoms is also of high interest in CO_2 containing plasma (hence for DRM). It was used in A S Morillo-Candas, Drag, et al. 2019b in a CO_2 low pressure glow discharge (1 to 5Torr). Finally, actinometry on H atoms, also of great interest for CO_2-CH_4 plasmas, has been repeatedly investigated: in Dyatko et al. 1998, Ar and Kr were used as actinometers to measure H densities in pure H_2, Ar-CO-H_2 and Kr-CO-H_2 mixtures. In Gicquel et al. 1998, H atom densities are measured in a H_2-CH_4 microwave discharges for diamond deposition. More recently, H actinometry was put forward in Krištof et al. 2016 in RF discharges at 1-10Pa. Simultaneously, A. Bernatskiy et al. 2015, A. V. Bernatskiy, V N Ochkin, et al. 2016 and A. V. Bernatskiy, Lagunov, et al. 2016 investigated H, OH and water traces in a He:Ar:Xe glow discharge containing traces of water vapor. Interestingly, A. Bernatskiy et al. 2015 used OH bands in the UV (318nm) for actinometry to investigate water densities and compared results to absorption spectroscopy. In A. V. Bernatskiy, V N Ochkin, et al. 2016, Xe and Ar were simultaneously used as actinometer to double-check the validity of the results.

Actinometry is so used because it is a powerful diagnostic for measuring atomic species densities: with a good detector, a limited acquisition time is required, allowing to follow temporal variations. Because actinometry only requires sampling light, it can be used for spatial profiles. For the same reason, actinometry is quite simple to set: in the simplest configuration, only a lens and a spectrometer are required. But most importantly, actinometry is a non-perturbative in-situ diagnostic. However, actinometry relies on a certain number of physical constant and basic collision data like excitation cross-sections or complete sets of cross-section for EEDF computation. These basic data must be reliable to get accurate measurements. Many versions of the basic data are available in literature and choosing the right one can be problematic, leading to large mistakes on the measured densities in the worst cases. The goal of this chapter is to shed light on the problems that can rise from actinometry and to provide a reliable set of parameters to perform actinometric studies.

To do so, actinometry was compared with Cavity Ring Down Spectroscopy (CRDS), assumed to be much more reliable. Measurements were taken simultaneously, first in a O_2 glow discharge and then in an CO_2 discharge at pressure between 1 and 5 Torr.

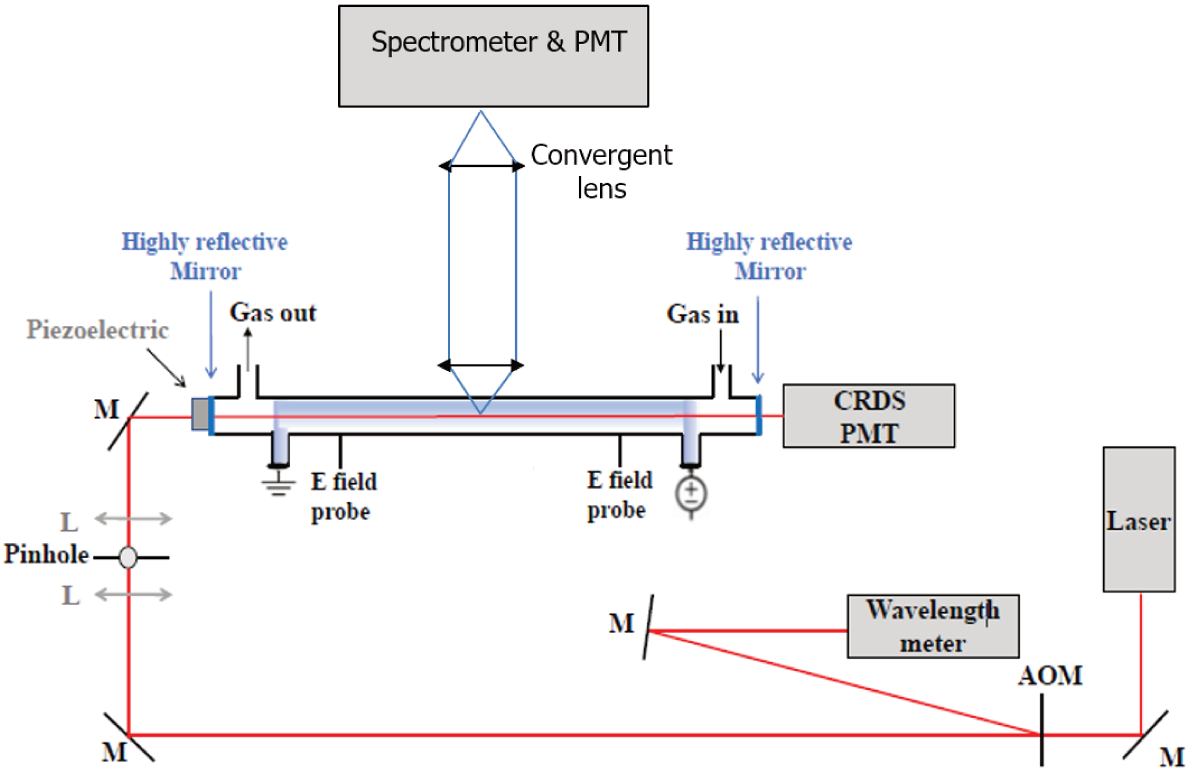

Figure 2.1: Experimental Set-up

2.2 Experimental Setup

A glow discharge was chosen for the reasons brought up in the introduction: it is reproducible, homogeneous in the positive column and important quantities like E and n_e are easily measurable. A schematic of the setup is shown on figure 6.1. The glow discharge is ignited at low pressure in a 65-cm long cylindrical pyrex reactor of radius 1cm. The electrodes are perpendicular to the axis of the tube to measure only the positive column. The gas is supplied in the reactor thanks to 2 Bronkhorst flowmeters and the ensemble is pumped down by an Edwards XDS pump. The tube is closed on both side by two highly reflective mirrors (R>0.99999) which constitute the optical cavity of the CRDS system. The mirror on one side is moved at the edge of tube of an amplitude close to the wavelength of the laser used with the help of a piezo electric motor, ensuring that the cavity length is periodically an integer multiple of the laser wavelength. The glow discharge is powered by a FUG power supply. A lens of 5cm focal length is positioned on the side of the tube, with its focal point at the center of the tube. This lense is used to create parallel beam which is then focalized on the entrance slit of a PI Isoplane spectrometer by another lens of focal length 3.5cm. An almost identical setup was used in J.-P. Booth, Chatterjee, Guaitella, D. Lopaev, et al. 2022.

2.3 Actinometry

2.3.1 Equations and principle

Actinometry relies on the comparison of the intensity of the line belonging to a specie of interest with a line belonging to a specie whose density is known (the actinometer).
Assuming that excitation is due mainly to electron impact, the intensity of a line can be computed by making the product of the excitation and deexcitation terms. The intensity I of an emission line of specie x between level i and level j at wavenumber ν is given by

$$I_x = C_\nu * h\nu_{ij}^x * k_e^i * n_e * a_{ij}^x [n_x] \tag{2.1}$$

where ν_{ij} is the wavenumber of the transition, C_ν is the response coefficient of the observation device at wavenumber ν, k_e^i is the rate coefficient of electron impact excitation from the ground state to level i, n_e the electron density, n_x the density of specie x and a_{ij}^x the effective branching ratio. The effective branching ratio represent the probability of radiative deexcitation through the observed line compared to all other deexcitation channels. The branching ratio can be written as:

$$a_{ij}^x = \frac{A_{ij}^x}{\sum A_i^x + \sum_Q k_Q^i [n_Q]} \tag{2.2}$$

where A_{ij} is the Einstein coefficient of transition ij, $\sum_i A_i$ is the sum of all Einstein coefficients of radiative transitions from level i, n_Q is the density of specie Q and k_Q^X is the collisional quenching coefficient of level i by specie Q. The electron impact excitation rate coefficient k_e^i from equation 2.1 is given by:

$$k_e^x = (\frac{2e}{m})^{1/2} \int_{\epsilon_{th}}^{\infty} \sigma_i(\epsilon) f(\epsilon) \epsilon d\epsilon \tag{2.3}$$

where σ_i is the excitation cross-section of level i, ϵ_{th} is the energy threshold of the cross-section and f is the electron energy distribution function.

If equation 2.1 is valid for both the specie of interest and the actinometer, actinometry can be used. This means the excited level i must be populated mainly by electron impact and not by radiative cascade from another excited state. Using an actinometer A transitioning from i' to j', the density of specie X can be obtained by making the ratio of two line intensities following equation 2.1:

$$[X] = \frac{I_X}{I_A} \frac{C_A}{C_X} \frac{h\nu_{i'j'}^A}{h\nu_{ij}^X} \frac{k_e^A}{k_e^O} \frac{a_{i'j'}^A}{a_{ij}^O} [A] \tag{2.4}$$

Ideally, the excitation cross-sections of level i of specie X σ_i and i' of the actinometer A, $\sigma_{i'}$ must be as close as possible, both in shape and in excitation threshold (i.e $\epsilon_i \sim \epsilon_{i'}$) to minimize the potential errors in the computation of the EEDF.
A is usually a noble gas so that its density remains constant in the plasma, but some cases have used molecules from the plasma such as H_2 in Krištof et al. 2016.

2.3.2 Case of O actinometry with Ar as actinometer

For the actinometry on O atoms, two strong emission lines are usually chosen. The first one, referred to as 777, is a triplet centered around 777.4 nm (the three lines are very close and often convoluted on the spectras, therefore no distinction is made between them), corresponding to the radiative deexcitation of O excited level $O(3p^5P)$ to level $O(3s^5S)$. The second one, referred to as 845, is also a triplet, centered around 844.63nm and correspond to the deexcitation of level $O(3p^3P)$ to $O(3s^3S)$. The excitation threshold of the excited levels radiating lines at 777nm and 845nm are very close, with respectively $\epsilon_{thO(3p^5P)} = 10.8eV$ and $\epsilon_{thO(3p^3P)} = 11eV$.
The level $O(3p^5P)$ radiating 777 is not only populated by electronic impact, but also by dissociative excitation of O_2. As a consequence, the emission of the 777 line is given by

$$I_{O777} = C_{777} * h\nu_{777}^O * n_e * a_{777}^O * ([O] * k_e^O + [O_2] * k_{de}) \tag{2.5}$$

This second source of excitation is negligible in the condition of the glow discharge at a few Torr in O_2 or CO_2 compared to electron impact excitation, as it was shown in Pagnon et al. 1995 and A S Morillo-Candas, Drag, et al. 2019b. In this work, this term was taken into account for intensity calculations but did not make a significant impact. It only accounted for up to 5% of the calculated oxygen density. It was therefore chosen to neglect it for actinometry calculations.

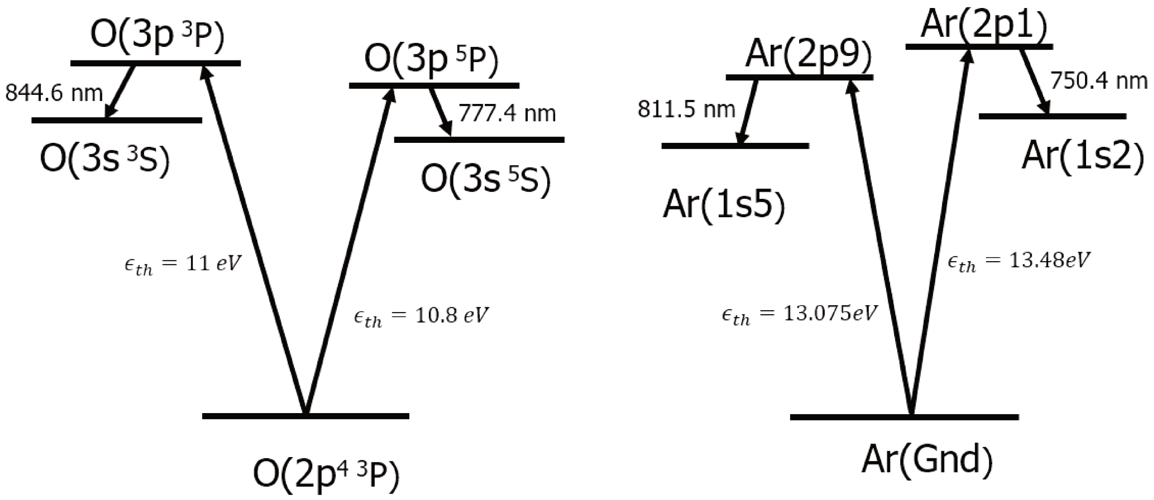

Figure 2.2: Atomic species levels used for O on Ar actinometry

For Argon, two lines are used here: the 750.4nm, corresponding to the deexcitation from Ar(2p1) ($4p[\frac{1}{2}]_0$ in Racah notation) to Ar(1s2), and the 811.5nm, corresponding to the deexcitation from Ar(2p9) ($4p[\frac{5}{2}]_3$ in Racah notation) to Ar(1s5). The 750nm line is the line usually used in literature when using Ar as an actinometer. The energy threshold of the excited levels radiating 750 and 811 are respectively $\epsilon_{thAr(2p1)} = 13.75eV$ and $\epsilon_{thAr(2p9)} = 13.48eV$. The level 2p9 of Ar requires caution as it could be populated by metastable states of Ar. It is however not a problem in O_2 discharges because the metastables are very efficiently quenched by atomic O. The spontaneous emission coefficients A_{ij} for all these levels are taken from the NIST database (Kramida et al. 2021) and are given below in table 2.1, along with the collisional quenching coefficients. As shown in equation 2.2, each excited state in the plasma should have its own collisional quenching coefficient for each individual quencher, but they are not always available in literature. The ones used here are therefore the one for O_2 as a quencher, using the approximation $\sum_q k_q n_q \sim k_{O_2} * N$, with N the gas density. This approximation is supported by the measurement of the collisional quenching coefficients in CO_2 and in O_2 in A S Morillo-Candas, Drag, et al. 2019b, which showed that the coefficients were very close for different collisional partners (such as CO_2 and O_2).

Level	Line	A_{ij} (s^{-1})	k_Q (m^3s^{-1})	Source
Ar2p1	750	$4.45.10^7$	$7.6.10^{-16}$	A S Morillo-Candas, Drag, et al. 2019b
Ar2p9 ($4p[\frac{5}{2}]_3$)	811	$3.31.10^7$	$5.9.10^{-17}$	Jelenak et al. 1993
$O(3p^5P)$	777	$3.69.10^7$	$10.6.10^{-16}$	Niemi et al. 2005
$O(3p^3P)$	844	$3.22.10^7$	$9.4.10^{-16}$	Tsutsumi et al. 2017

Table 2.1: Einstein coefficients and collisional quenching of the level used

2.4 Cavity ring down spectroscopy

Cavity Ring Down Spectroscopy (CRDS) is a very powerful diagnostic allowing to measure the atomic density of oxygen and the gas temperature. The functioning of this technique was described in Berden et al. 2009. CRDS was used for example in J. Booth et al. 2000 for fluor-containing species in a low pressure RF plasma. This techniques can be tuned for numerous species, like in Stancu, Kaddouri, et al. 2010, where CRDS was used to measure $N_2(A)$ in atmospheric pressure nanosecond discharges. The CRDS bench used in this work was installed by Jean-Paul Booth and his students Abbudhay Chatterjee, Andrey Volynets and Cherif Si Moussi.

2.4.1 CRDS principle

CRDS is a very sensitive technique allowing to detect even absorption transition having a very weak transition probability. The technique is derived from Cavity Enhanced Absorption spectroscopy (CEAS). In CEAS, a cavity is formed by using highly reflective mirrors to increase the path traveled by a laser pulse, which increases the absorption according to Beer-Lambert law ($I=I_0 exp(-\alpha l)$). In CEAS, the intensity at the output of the cavity is measured to deduce the density. In CRDS, the sensitivity is increased by observing the decay of the output signal when the laser pulse is turned off.

Let us assume a cavity of length L, closed by 2 mirrors of reflectivity R (and of transmitivity T=1-R). If a laser pulse is injected into the cavity with a duration shorter than the round trip of the light in the cavity, a fraction (1-R) of the laser pulse will enter the cavity through the first mirror, go through the cavity and a fraction (1-R) will exit the cavity through the second mirror. If the cavity contains an absorbing sample of length d, the intensity at the exit of the cavity is given by :

$$I_{1stpassage} = I * T * T * exp(-\alpha d) \tag{2.6}$$
$$= I_0 \tag{2.7}$$

by including both transmissions and the absorption through the sample by the Beer-Lambert law. The part of light that is reflected goes through another round trip. When reaching the end of the cavity, the light intensity at the exit of the cavity is given by :

$$I_1 = I * T * e^{-\alpha d} * R * e^{-\alpha d} * R * e^{-\alpha d} * T \tag{2.8}$$
$$= T^2 * e^{-\alpha d} * R^2 * e^{-2\alpha d} \tag{2.9}$$
$$= I_0 * R^2 * e^{-2\alpha d} \tag{2.10}$$

It is easily deduced that after n round trips, the intensity is given by

$$I_n = I_0 * R^{2n} * e^{-2\alpha n d} \tag{2.11}$$

Replacing the discrete n by a continuous parameter $t = n * \frac{2L}{c}$ and using $R^{2n} = exp(2nln(R))$:

$$I(t) = I_0 * exp(\frac{t * c}{L} * ln(R)) * exp(\frac{-\alpha * d * c}{L} * t) \tag{2.12}$$
$$= I_0 * exp(t * \frac{c}{L}(ln(R) - \alpha d)) \tag{2.13}$$
$$R \sim 1 \rightarrow ln(R) \sim -(1 - R) \tag{2.14}$$
$$I(t) = I_0 exp(t * \frac{c}{L}(R - 1 - \alpha d)) \tag{2.15}$$
$$I(t) = I_0 exp(-t * \frac{c}{L}(1 - R + \alpha d)) \tag{2.16}$$
$$\tag{2.17}$$

Using the form $I = I_O exp(\frac{-t}{\tau})$

$$\tau = \frac{L}{c(1 - R + \alpha d)} \tag{2.18}$$

The observed decay of at the exit of the cavity is therefore an exponential decrease with a constant τ which depend on the absorption by the medium. Because both the absorption and the reflexion by the mirror are wavelength-dependent, τ can be rewritten:

$$\tau(\nu) = \frac{L}{c[1 - R(\nu) + \sum_i \sigma_i \int_0^d N_i(x)dx]} \tag{2.19}$$

with i the species which absorb at wavenumber ν, σ_i the absorption cross-section of specie i and N_i the density of specie i. In case there is only on absorbing specie at wavenumber ν, the decay time is :

$$\tau(\nu) = \frac{L}{c[1 - R(\nu) + \sigma \int_0^d N(x)dx]} \tag{2.20}$$

The asset of the glow discharge is to be homogenous in the positive column , meaning that $N(x) = N \forall x$, finally rewriting previous equation as :

$$\tau(\nu) = \frac{L}{c[1 - R(\nu) + \sigma * d * N]} \tag{2.21}$$

The choice of the line of absorption is crucial. It depends on the specie, but must not be saturated. For oxygen, the forbidden transition $O(^3P_2) \leftrightarrow O(^1D_2)$ was chosen because despite being a forbidden transition (therefore very weak), the absorption cross-section is well known. Scanning the decay at the exact wavenumber of the absorption line provides information on the oxygen density. Scanning the whole line profile brings the temperature information because the spectral resolution is better than the Doppler broadening. For any wavenumber, the absorption is given by :

$$\alpha(\nu) * \frac{d}{L} = \frac{1}{c} * (\frac{1}{\tau} - \frac{1}{\tau_0}) \tag{2.22}$$

where τ_0 is the decay time of the empty cavity. The absorption profile (i.e the line profile) can be easily reconstructed by varying the wavenumber of the laser. The temperature can then be deduced by measuring the full width at half maximum (FWHM) and assuming that the broadening is due only to the temperature.

The CRDS is considered as a reliable diagnotic because the determination of the atomic density relies on only one absorption cross-section. For the transition $O(^3P_2) \leftrightarrow O(^1D_2)$, the integrated cross-section used in this CRDS scheme is given in J.-P. Booth, Chatterjee, Guaitella, D. Lopaev, et al. 2022:

$$\sigma_{int} = \int \sigma_{low}^{up} d\nu = \frac{g_{up}}{g_{low}} \frac{A_{low}^{up} \lambda^2}{8\pi} = 2.9810^{-23} cm^3 \tag{2.23}$$

with A_{low}^{up} the Einstein coefficient of the transition, g_{up} is the degeneracy of the upper level $O(^1D_2)$, g_{low} the degeneracy of the lower level $O(^3P_2)$. The total density of the $O(^3P)$ state was deduced from the population of $O(^3P_2)$ using:

$$[O(^3P)] = \frac{\sum_j g_j e^{-E_j/kT} * [O(^3P_2)]}{g_2} \tag{2.24}$$

The uncertainty on the results is limited to the uncertainty on the cross-section.

2.4.2 CRDS Setup

In practice, the light source of the CRDS setup is a tunable diode laser (Toptica Laser). The laser beam passes through an opto-acoustic modulator (whose role is to chop the beam) and further through a beam-spliter. One part of the beam is sent into a wavelength meter to constantly monitor the wavelength of the laser. The other beam is sent to the cavity and goes through a first highly reflective mirror. The "entrance" mirror is mounted on a piezo-electric translator which periodically moves with an amplitude of one λ, so that at least once per piezo oscillations, length of the cavity is exactly $n\lambda$, with n an integer. The beam exit the cavity through a second highly reflective mirror and is sent onto a Photo-multiplier Table (PMT), where the intensity is monitored. When the exit intensity goes over a certain threshold (meaning that enough intensity accumulated in the cavity for detection), the decay time is measured. On the contrary, when the intensity injected into the cavity is not sufficient, the event is discarded. The density of atomic oxygen is inferred using from the measured decay time on the intensity in the cavity with the equation 2.22.

2.4.3 CRDS correction for the dead volume

CRDS is a line-of-sight averaged diagnostic and the plasma does not occupy the whole cavity. To avoid exposure of the mirror to plasma that could damage it, dead volumes are left on both sides of the plasma. A correction factor must therefore be applied, to take into account the dead volume. One can calculate the "correction" C to apply to the measured O density $[\mathrm{O}]_m$ to obtain the actual value of the oxygen density in the plasma $[\mathrm{O}]_p$. Using L the length of the cavity, l_d the length of the dead volume, $[\mathrm{O}]_d$ the atomic oxygen density inside the dead volumes and l_p the length of the plasma, one gets:

$$[O]_m = \frac{l_p}{L} * [O]_p + \frac{l_d}{L} * [O]_d$$

using $[O]_p = C * [O]_m$ with C the correction factor

$$\begin{aligned}
\frac{[O]_p}{C} &= \frac{l_p}{L} * [O]_p + \frac{l_d}{L} * [O]_d \\
(\frac{1}{C} - \frac{l_p}{L})[O]_p &= \frac{l_d}{L}[O]_d \\
\frac{[O]_p}{[O]_d} &= \frac{l_d}{L * (\frac{1}{C} - \frac{l_p}{L})}
\end{aligned}$$

The obvious limit is of course if $C = \frac{L}{l_p}$. Here,

$$\begin{gathered}
L \sim 60cm \quad \& \quad lp \sim 10cm \\
\rightarrow C_{max} = 1.2
\end{gathered}$$

A correction factor that varies with pressure could be taken into account. A priori, the diffusion of O atoms from the plasma to the dead volume indeed changes with pressure. The pressure increase will also likely increase the temperature difference between plasma and the dead volume, in turn impacting the diffusion of O atoms. TALIF measurements were performed on an identical system in by Tat Loon Chng (unpublished) to measure the densities of oxygen in the tube in order to compare CRDS and TALIF. TALIF can be performed perpendicularly to the tube, allowing to measure the axial profile of O atom in the tube. The TALIF measurement in the dead volume showed that $[O]_d$ was about 10 percent of $[O]_p$ at 1Torr, while the density was negligible at 5Torr. This means that $C = 1.17$ at 1Torr and $C = 1.2$ at 5Torr. Out of simplicity, a constant C is chosen for O densities at all pressure, with C=1.18.

2.5 Challenges of actinometry

Previous comparisons between actinometry and other diagnostic method, considered as more reliable, such as CRDS or TALIF have shown discrepancies. In Pagnon et al. 1995, actinometry was compared to VUV absorption spectrometry in a low pressure O_2 glow discharge. The agreement was surprisingly good: at 2 Torr, the $[\mathrm{O}]/[\mathrm{O}_2]$ fraction was 0.19 with VUV absorption spectroscopy versus 0.22 for actinometry, giving credit to actinometry. The agreement was equally good at lower pressure with similar differences between actinometry and VUV at 0.36 Torr. However, a comparison of the cross-section shown in Pagnon et al. 1995 and supposedly drawn from Laher et al. 1990 with the original cross-section from Laher et al. 1990 showed a shift in the threshold for both O lines. The good agreement apparently comes from a mistake in the cross-section as it will be discussed in section 2.8. In A S Morillo-Candas, Drag, et al. 2019b, actinometry measurement performed in a CO_2 glow discharge measured an oxygen fraction of 12%, while TALIF measured up to 19%, showing a 50% uncertainty on the [O]/N. In A. V. Bernatskiy, V N Ochkin, et al. 2016, absorption spectroscopy of water was compared with OH

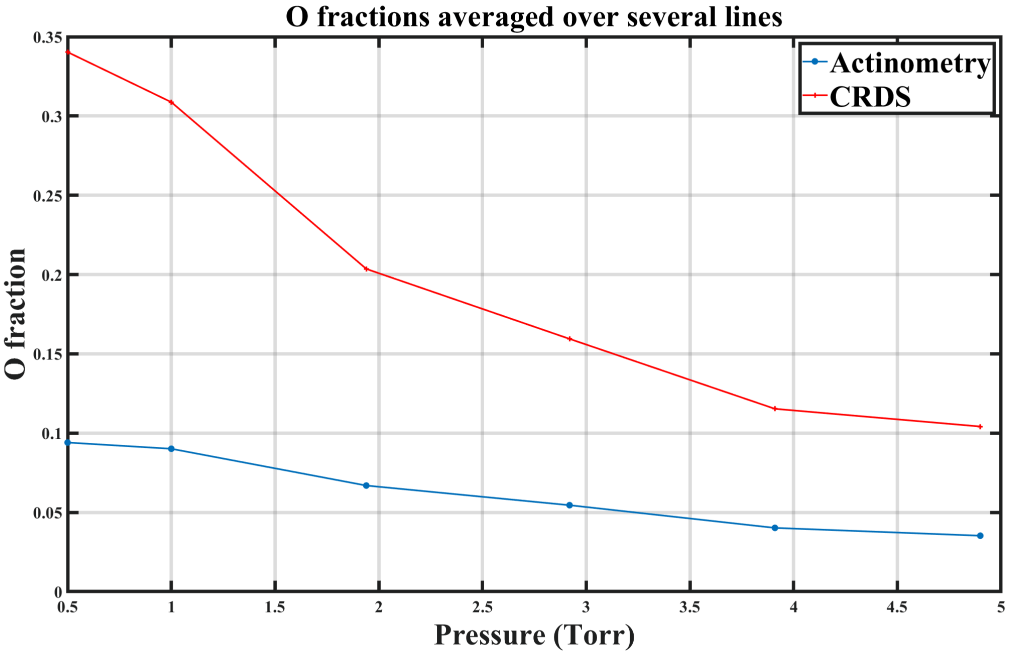

Figure 2.3: First comparison of the measured fraction of atomic O by CRDS and actinometry in an 85:15 O_2:Ar mixture at 40mA as a function of pressure. The IST Lisbon set is used for the computation of EEDF, the Laher cross-section is chosen for O excitation and the Zatsarinny cross-section is chosen for Ar. This constitutes the "initial set of parameters"

actinometry (using here not excitation but electron impact dissociation of water), which yielded good results over a current variation (2-10mA) at 0.5mbar: the maximum error was of 25% on the absolute density. However, this last measurement exhibited different trends between actinometry or absorption spectroscopy as a function of current, raising a doubt on the validity of actinometry for a wider current variation. In Britun, Belosludtsev, et al. 2017 and in Britun and Hnilica 2020, TALIF and actinometry were compared, but unlike A S Morillo-Candas, Drag, et al. 2019b where TALIF was calibrated with Xe fluorescence, Britun, Belosludtsev, et al. 2017 used a point of O actinometry for calibration of the TALIF, which therefore necessarily gave good agreement. The trends of TALIF and actinometry during a radiofrequency pulse were compared and proved to be somewhat close, but a factor 2 could be found between the two methods at the beginning of the pulse. It is important to mention that using TALIF as a reference for densities obtained from actinometry can also introduce additional incertainties. Indeed, absolute values with TALIF require a calibration (made with Xe for TALIF on O atoms) which suffers from the accuracy of the absorption cross section. In the case of Xenon, it has been shown that a factor 2 on the final O atoms density can be due just to the error on the Xe cross section Drag et al. 2021. Therefore even for O atoms which have been extensively studied with actinometry, comparison with other measurement techniques gave contradictory results on absolute densities.

In this work we have chosen CRDS which *a priori* leads to lower uncertainties on absolute values. Our experiment comparing CRDS and actinometry with our "initial set" of parameters (see below) as a function of pressure for an O_2-Ar discharge is shown on figure 2.3. The current is set to 40mA and the gas composition is 85:15 O_2:Ar. A factor 2 to 3.5 is obtained (depending on the pressure) in the range investigated. The difference between actinometry and CRDS is not constant, showing that the trend of actinometry is also a problem. The question of the source of the discrepancy obviously arose.

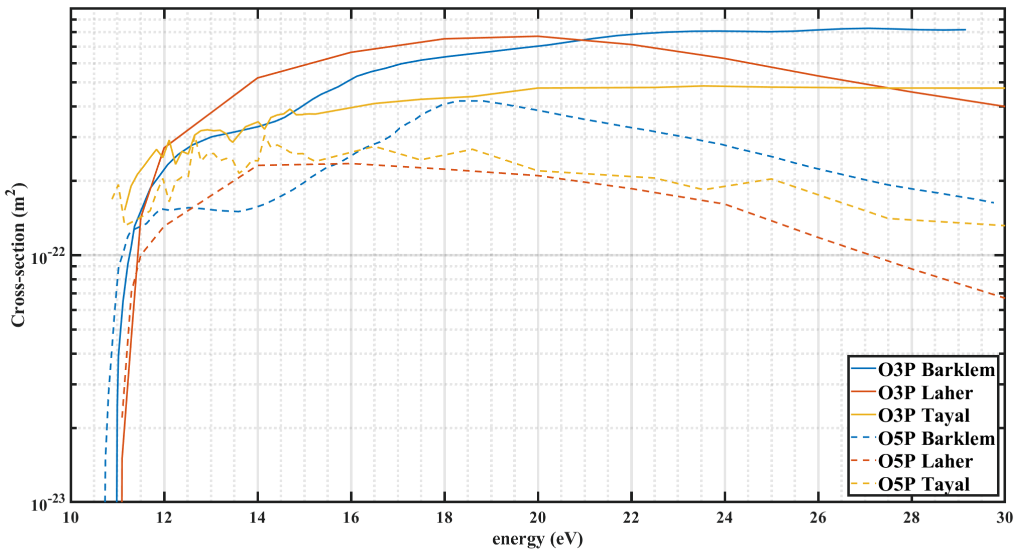

Figure 2.4: Excitation cross-sections available for oxygen

Rewriting the intensity of one line, one gets:

$$I_x = C_x * h\nu_{ij}^x * (\frac{2e}{m})^{1/2} \int_{\epsilon_{th}}^{\infty} \sigma_i(\epsilon) f(\epsilon) \epsilon d\epsilon * n_e * \frac{A_{ij}^x}{\sum A_i^x + \sum_Q k_Q{}^x [n_Q]} * [n_x] \tag{2.25}$$

As opposed to CRDS, actinometry relies on a great number of basic physical data that were measured or modeled in literature. The results of an actinometry measurement can therefore be largely influenced by uncertainties on the data used for analysis. The results can also be worsened by the fact that the data for the specie of interest and of the actinometer can be inconsistent. The most sensitive data for the proper line intensity calculation are the following ones (shown in red in equation 2.25):

- the electron impact excitation cross-section of the level radiating
- the set of cross-section used for the computation of the EEDF
- the quenching coefficients

The sensitivity of the results to each of these parameters will be analysed in the following sections.

2.5.1 The excitation cross-section σ_{exc}

Numerous excitation cross-section for O and Ar levels are available. For Oxygen, three cross-sections are available and are shown on figure 2.4.

The first cross-section for electronic excitation of O(3P) to the excited states O(3p^{3}P) and O(3p^{5}P) were calculated in Julienne et al. 1976 by the method of the unitarized distorted wave including exchange, described in Davis et al. Nov. 1974. A peak value of the direct excitation cross-section is given, as well as the cascade contribution from other levels, which, in the case of O(3p^{3}P) and O(3p^{5}P), are very weak.
The cross-section proposed by Laher and Gilmore in 1990 are built upon literature review. The cross-sections are based on the direct measurement performed in Erol E. Gulcicek et al. 1987 (which measured the value of the electron excitation cross-section at 30eV) and in E. E. Gulcicek et al. 1988 (which extended previous measurements to more energies: 13.8eV close to the threshold, 20eV, 50eV and 100eV). These two sources are compared with the work of

Julienne and Davis, which yield results approximately 25% lower. Based on the measurement, the following approximation was proposed by Laher and Gilmore:

for O(^{3}P → 3p^{5}P)	for O(^{3}P → 3p^{3}P)
direct measurement of	direct measurement of
Gulcicek et al for E < 30eV	Gulcicek et al for E < 100eV
$\sigma(E) = 1.10 * 10^{-16} * E^{-1}$ for $E > 30eV$	$\sigma(E) = 1.81 * 10^{-14} * E^{-3}$ for $E > 100eV$

In the end, the cross-sections proposed by Laher and Gilmore contains much more points than the direct measurement they are based on. The profile of the cross-section must have been extended by interpolation between the experimental points and by extrapolation down to the threshold (11eV while the measurements start at 13.8 eV), but the methods of interpolation and extrapolation are not given in Laher et al. 1990. For a glow discharge whose bulk electron energy is at 2.5eV, energies higher than 10 eV are in the tail of the EEDF. This means that in our case, the part of cross-section above 15 eV is far less relevant as only very few electrons have that energy. Hence, the cross-section of Laher, when applied to a low pressure glow discharge, only relies on one experimental point, the value measured in Erol E. Gulcicek et al. 1987.
The theoretical cross-section proposed by Barklem in Barklem, P. S. 2007 is computed using a 38-state R-Matrix in L-S coupling and was calculated to interpret emission spectras in astrophysics. It was also compared to the work of E. E. Gulcicek et al. 1988, which had 5 points between 0 and 200 eV and showed large deviation (40% with the 13.87eV point from Erol E. Gulcicek et al. 1987).
The theoretical cross-section of Tayal proposed in Tayal et al. 2016 was calculated with the B-spline R Matrix method between 11 and 200 eV and was compared with experimental measurement by Vaughan et al. 1988 and Kanik et al. 2001. However, both of these experiment presented only a limited number of points on the studied range (3 points for Vaughan et al. 1988 and and approximately 20 points for Kanik et al. 2001) with large uncertainty. The matching between the calculated cross-section and the experiment is therefore to consider with caution.
The Laher and Gilmore (further referred to as Laher) cross-section is the one usually favored for O actinometry (Viegas et al. 2021, A S Morillo-Candas, Drag, et al. 2019b) or for collisional radiative model of oxygen (Fiebrandt et al. 2020, Caplinger et al. 2020) because Laher and Gilmore were the first one to propose a theoretical and experimental review of the work on O excitation for these levels. Their work also proposes cross-section for numerous excitation processes of O, making the use of their work more convenient for O atom radiative model. The Barklem and Tayal cross-sections are however much more recent and are therefore worth being considered as well.

For Argon, the cross-sections from Biagi, Chilton & Boffard, Puech and Zatsarinny can be found for both Ar2P1 and 2P9. Additionally, the cross-sections from Bretagne (Bretagne et al. 1986) and Hayashi (Hayashi 1981) are available for 2P1 only. For this work, only sources which provided cross-section for both levels of Ar were kept and plotted on figure 2.5.
The Biagi cross-sections are transcribed from the Magboltz Fortran code developed by S.F.Biagi, which is a Monte Carlo code evaluating the trajectory of the electrons in a magnetic and/or electric field.
The Zatsarinny cross-section was computed using the B-spline R-Matrix in JK Coupling in Zatsarinny et al. 2014. They were compared with experimental data from Chutjian et al. 1981, Chilton et al. 1998, Filipovic et al. 2000a and Filipovic et al. 2000b. A relatively good agreement was found with the measurements of Chutjian and Cartwright, but the discrepancies lead the authors to question the absolute normalization accuracy.
The Puech cross-section is taken from a complete set of cross-section assembled by Puech and Torchin in Puech et al. 1986 based on literature. The cross-sections are taken from various sources: the momentum transfer are taken from Frost et al. 1964, and the inelastic processes with threshold above 20eV are taken from a set developed in Bretagne et al. 1986 and based on

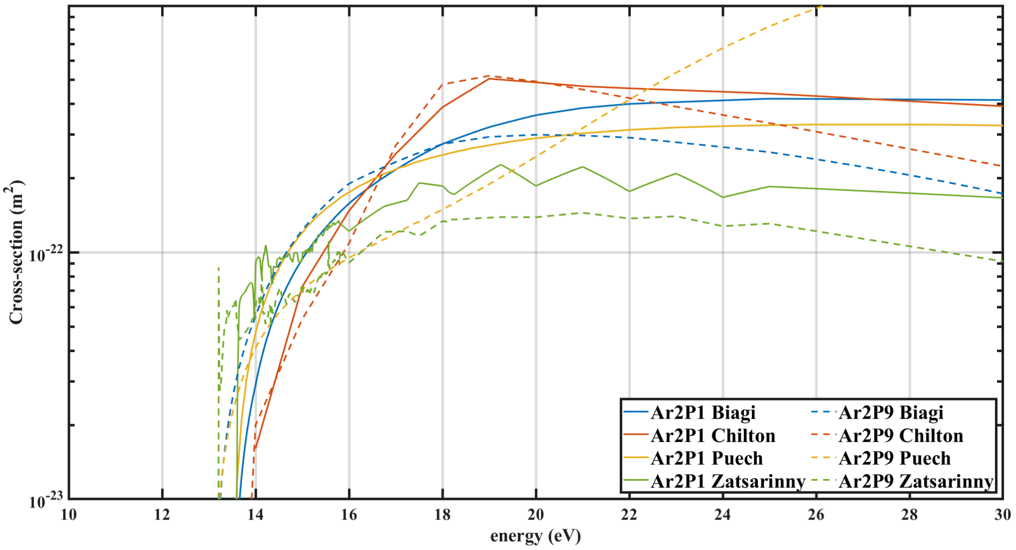

Figure 2.5: Excitation cross-sections available for Argon

the measurement by Chutjian and Cartwright. For lower energies, the set is based on measurement by Schaper et al. 1969.
Finally, the Chilton et al cross-section is proposed in Chilton et al. 1998 and was determined experimentally between 0 and 300eV through Fourier-Transform Spectroscopy (FTS). All emissions in the range 650-1100nm were measured with FTS, which allowed the authors to separate the cascade contribution from the direct excitation contribution, making the measured value supposedly more accurate. Previous measurement by Ballou et al. 1973 could only estimate the cascade contribution. The Chilton cross-section is the one used in the IST-Lisbon set for Ar.

2.5.2 The accuracy of the EEDF and the set of cross-sections used for computation σ_{EEDF}

The accuracy of EEDF is critical, especially because the threshold of excitation (∼ 10-13 eV) correspond to the tail of the EEDF for a glow discharge whose mean electron energy is around 2.5 eV. To our knowledge, only one complete and consistent set of cross-section exists for a proper description of the EEDF in O_2, which is the IST Lisbon set (Gousset et al. 1991). The IST set is validated against swarm parameters by construction: after grouping the cross-sections for known processes, other cross-sections for unmeasured processes were added, and the shape and values of the cross-sections were chosen so that the set is validated against swarm parameters. No other set proposed in literature compares well against swarm parameters. However we will also use for this work the set proposed by Biagi with his code MagBoltz. The Biagi set has two drawbacks : the ionization coefficient is not well reproduced as a function of the electric field compared to available swarm measurements (Price et al. 1972 and Price et al. 1973, Corbin et al. 1974), which in this particular case is a problem, because O_2 ionization threshold is around 11eV, precisely where the O777 and O845 excitation take place. Overall, this means that the Biagi set is less likely to reproduce accurately the EEDF in this region. Second, the Biagi set includes an extremely weak O_2 attachment cross-section (with an order of magnitude of $10^{-42}m^2$), leading to a strong disagreement on the reduced Townsend attachment coefficient. This second drawback can be very easily solved by removing the attachment cross-section from the set, leading to an excellent agreement on the reduced Townsend attachment coefficient and leaving the other swarm parameters untouched. In the rest of this work, the attachment will always be removed from the Biagi set. It was verified that this has no influence on the results presented here.

Figure 2.6 shows the comparison of the simulated swarms using the IST Lisbon set, the

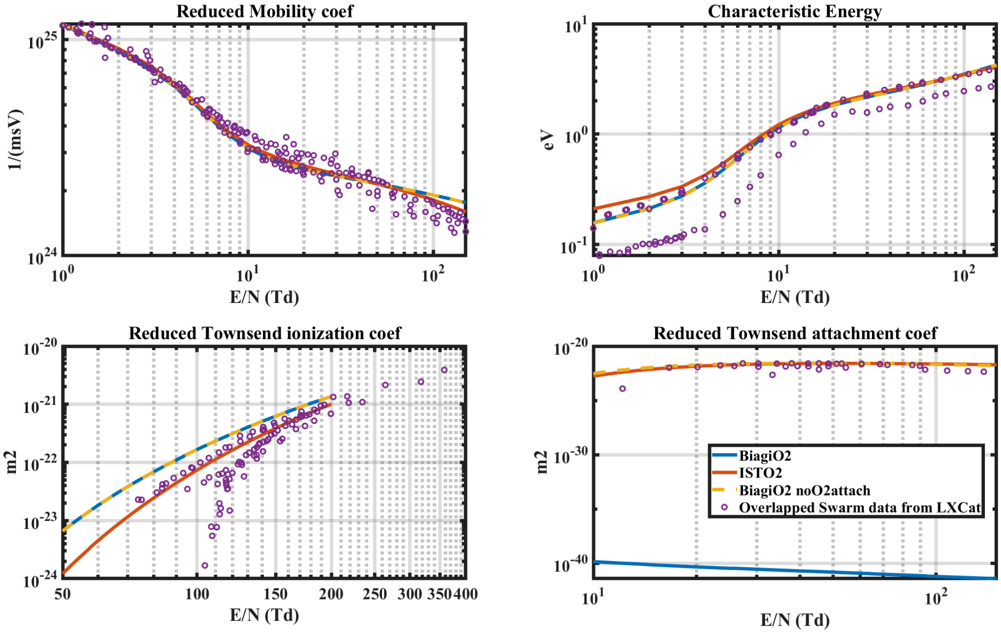

Figure 2.6: Comparison of simulated swarms (lines) with all experimental data (scattered points) available on LXCAT for pure O_2. The Biagi set without attachment cross-section is plotted in dashed line and overlaps perfectly with the Biagi set for reduced mobility, ionization and characteristic energy. The reduced ionization coefficient simulated with the Biagi set does not match with experimental values

Biagi set and the Biagi set without attachment with all experimental data available on LXCat. Appart from the reduced Townsend coefficient for the Biagi set, all swarms are well reproduced. The same problem arise for Argon. Though Ar is less critical in our experiment as it represent at most 15% of the gas, it is non-negligible. Several sets are available in literature (Yanguas-Gil et al. 2005 from IST Lisbon, Puech et al. 1986, Chilton et al. 1998). In this study, only one set of Ar cross-section is investigated because the Ar set is not expected to make a strong impact. The IST set, validated against the swarm parameters, is chosen.
Eventually, the problem appears for atomic oxygen, which can make up to 30% of the gas mixture. No set is validated against swarm parameters for mixtures of atoms and molecules, so the effect of O processes cross-sections on the EEDF is hard to evaluate. One solution is to ignore the atomic O in the computation of the EEDF, which will be shown later. This solution can only assess the error of including O cross-section but not correct it.

2.5.3 The accuracy of the quenching coefficients

With a lesser importance, the quenching coefficients are also sensitive data. Their values can vary by a factor 2 from one source to another : for example, the rate found for O(3p^{3}P) in Meler et al. 1986 is twice as low as the one found in Dagdigian et al. 1988 (respectively $3.7.10^{-10} cm^3 s^{-1}$ vs $7.8.10^{-10} cm^3 s^{-1}$). This second value is close to the value reported in Niemi et al. 2005 and to the values remeasured in A S Morillo-Candas, Drag, et al. 2019b by TALIF and therefore will be kept for the rest of this study. Their influence increase with pressure and they can therefore change the trend of emission line with pressure. It was however verified that to observe a real difference, a factor 10 was needed on the rate, which is unlikely given the number of experimental measurement of these rates. The current values, despite their small uncertainty, will not be changed.

An "initial" set of parameters is defined for O actinometry, corresponding to the most used parameters in literature: IST-Lisbon O_2 set for EEDF computation, IST O set for computation EEDF computation, the Laher cross-section for O excitation and the quenching coefficients of Niemi and Tsutsumi.

Reference set of parameters for line emission analysis in the following:

- σ_{EEDF}^{IST} sets for O_2 and O atoms in EEDF calculation
- σ_{exc}^{Laher} for excitation of emitting states (Laher et al. 1990)
- k_q from Niemi (Niemi et al. 2005) and Tsutsumi (Tsutsumi et al. 2017)

2.6 Line intensity simulations

Actinometry is a line ratio method already introduced in section 2.3.1. Testing the excitation cross-section of the levels of interest σ_{exc}, the EEDF accuracy with σ_{EEDF}^{set} and the quenching coefficients k_q just with line ratios would lead to numerous combination and possible error compensation. In litterature, only line ratios are usually compared to other measurement techniques which is probably one of the reason for the contradictory conclusions reported. It is therefore better to assess the accuracy of each individual lines intensity separately before using two of these line intensities in a ratio for "actinometry calculations". To achieve this and test the accuracy one by one of the parameters σ_{EEDF}^{set} and σ_{exc}, an intensity calculation algorithm was developed. The principle is to determine the absolute number of photons emitted for each transition of interest using the data (absoluyte oxygen density and gas temperature) obtained with the CRDS measurements assumed to be accurate. The simulated intensity can then be compared to the one measured with the spectrometer used for emission measurements. The algorithm is summarized on fig 2.7.

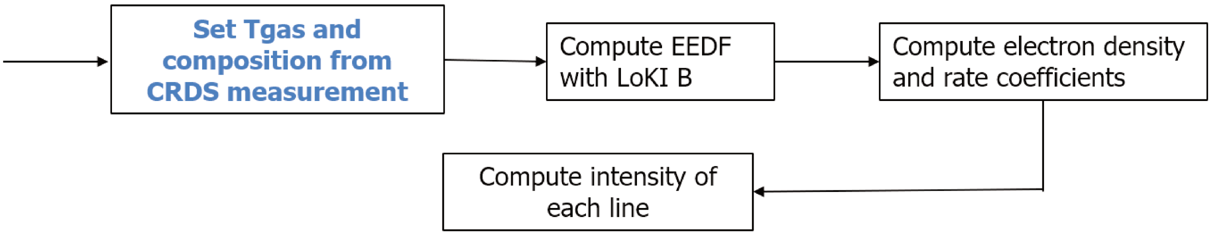

Figure 2.7: Principle of the absolute emission intensity computation

The experimental conditions (gas temperature and composition) are drawn from CRDS measurement and are used as input for the Boltzman solver LoKI-B (Lisbon Kinetics solver Tejero-del-Caz 2019, Tejero-del-Caz 2021). A set of cross-sections is provided for the computation of the EEDF and excitation cross-sections are provided for the computation of the rate coefficients. The electron density is computed by using the reduced mobility computed by LoKI-B and the current set during the experiment:

$$n_e = \frac{\frac{C}{\pi r^2}}{q * E/N * \mu_{red}} \tag{2.26}$$

where C is the current, r the radius of the tube and μ_{red} is the reduced mobility ($\mu_{red} = \mu * N$ where μ is the mobility). The value of the coefficient C(ν) from equation (2.1) is obtained by calibration of the spectrometer using a calibrated lamp, whose emission spectrum is known. The correction factor used in this work are given in the table 2.2. The spectrum detected by the spectrometer is then corrected by the function C(ν) to match the lamp spectrum. Finally, using equation (2.1), the intensities are computed for the 4 lines of interest. The simulated intensities are then compared with the experimental values.

Wavelength	Sensitivity of the spectrometer compared to 777
750	0.81
777	1
811	1.3
845	1.51

Table 2.2: Isoplane spectrometer calibration (Ireal = S*Imeasured)

A scaling of the simulated intensity with the measured intensity is necessary. The measured intensity in the experiment is given in volts at the output of the PMT while the simulation yield an absolute number of photons. A complex calibration would be required to precisely establish the relationship between the voltage at the output of the PMT and the number of photons sampled from the discharge. The solid angle of collection of the light would also be required. Instead, the intensities of both experiment and simulation normalized on the value of the O777 line at 1 Torr. This way, two things can be compared at once: first the evolution of the trend with pressure (i.e indirectly with varying E/N) for the O777 line, informing on the validity of the chosen excitation cross-section σ_{exc}. Second, the consistency of the O845 emission with the O777 line can be checked: even if the normalization is done on the O777 line, the O845 line should match the simulation if the cross-sections are consistent for both levels.

> In the following, [O] and T_g obtained from CRDS are used to calculate individual line intensity of $O(3P)$ and $O(5P)$ with LOKI instead of comparing line ratios as done in actinometry.

2.6.1 Line intensities in pure oxygen plasma

In a first part, we compare simulated intensities and experiment in a pure O_2 discharge to avoid Ar influence on the EEDF calculation. The O_2 flow is set to 10 sccm and the current to 40 mA. Two sets of cross-sections for EEDF computation σ_{EEDF} are tested, as well as 3 excitation cross-sections σ_{exc} for the specific O levels.

σ_{EEDF}^{set}		σ_{exc}
IST Set		Laher
	x	Barklem
Biagi Set		Tayal

Table 2.3: σ_{EEDF}^{set} and σ_{exc} tested for the comparison of the simulated and measured line intensities

The set of cross-sections used for atomic O in the EEDF calculation is not changed. Only the one of IST-Lisbon is used but the influence of adding or not O atoms in the EEDF calculation will also be tested. In the following, unless mentioned otherwise, it is implicit that for all measurements the atomic O cross-sections from IST are used for the EEDF. Figure 2.8 shows the comparison of the simulation and experiment for the two Oxygen lines for all combinations of σ_{EEDF}^{set} and σ_{exc}. The experimental values of the intensities correspond to the voltage taken from the PMT during the measurement, corrected by the factors in table 2.2 to take into account the sensitivity of the optical system at a given wavelength. For both lines, the simulated intensities decrease with pressure like the experimental ones. The decrease of the intensity with pressure has two sources. First, the decrease of the reduced electric field with pressure, which drops from 62Td at 1Torr to 47 Td at 5Torr, leading to less electrons exciting the radiating levels. Second, the increase of the collisional quenching with pressure. First looking at the O777 line, two groups clearly appear: the group of the Biagi set (using σ_{EEDF}^{Biagi}) on top, with a general better agreement with the experiment and the group of the IST set using σ_{EEDF}^{IST} (bottom group). In each group,

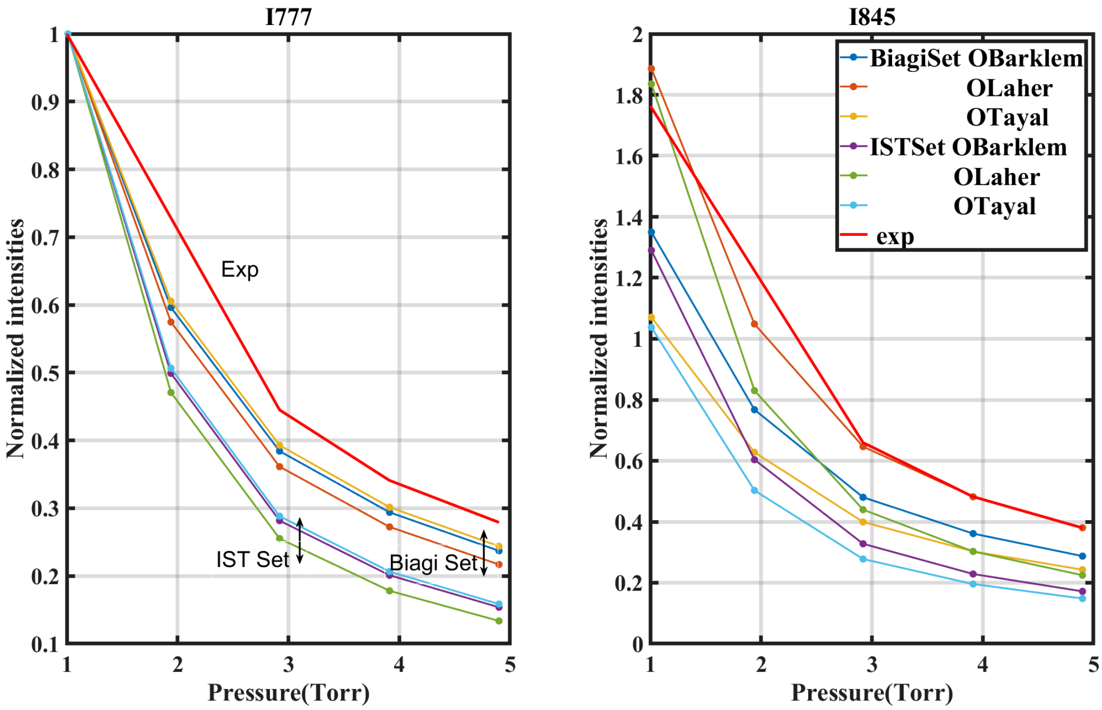

Figure 2.8: Comparison of the experimental trends of line O777 and O845 as function of pressure with several combination of EEDF set and excitation cross-section in a pure O_2 plasma. The current is set to 40mA and the flow to 10sccm

the order of the lines are the same: the Tayal cross-section seems to give the best agreement, followed by the Barklem, the Pagnon, and the Laher cross-section. The general agreement of the Biagi set is however good enough generally, and all 4 cross-sections could be used in this particular case. Looking at the O845 line, it appears that the agreement is quite different. This time, the agreement depends more on the consistency of the O845 cross-section compared to the O777 in the chosen source rather than the EEDF set used. Indeed, looking at the 1Torr point (the normalization point), it can be seen that the Laher cross-section gives a good agreement with both sets σ_{EEDF}^{Biagi} and σ_{EEDF}^{IST}, indicating that the ratio of the two excitation cross-sections proposed by Laher is likely correct. No other source for σ_{exc} give a good value of the O845 intensity at 1Torr, indicating that the ratio $\sigma_{exc}^{0845}/\sigma_{exc}^{O777}$ is wrong for Barklem and Tayal. For the 845 line, the experiment is in very good agreement with the combination $\sigma_{EEDF}^{Biagi} + \sigma_{exc}^{Laher}$ (i.e the EEDF set of Biagi and the cross-section of Laher), making it seemingly the most suited combination for proper actinometry. This is once again questionable as the Biagi set is not expected to describe properly the EEDF in this region.

Best parameters so far to reproduce O atoms lines intensities in pure O_2 plasma:

Biagi Set for EEDF σ_{EEDF}^{Biagi} + Laher cross-section σ_{exc}^{Laher}

Effect of $O_2(a)$

So far, the density of the $O_2(a)$ metastable state of O_2 was neglected in the computation of the EEDF despite its relatively high density. Indeed, comparison of VUV measurement and IR data from J.-P. Booth, Chatterjee, Guaitella, Sousa, et al. 2020, taken in the same configuration as the present work showed that the density of $O_2(a)$ is about one tenth of the O_2 density in the plasma (the real $O_2(a)/O_2(X)$ is given in table 2.4).

Pressure	$\frac{O_2(a)}{O_2(X)}$ at 20mA	$\frac{O_2(a)}{O_2(X)}$ at 40mA
0.5	0.0873	0.113
1	0.0843	0.111
2	0.0746	0.0941
3	0.0647	0.0820
4	0.0594	0.074
5 (extrapolated)	0.053	0.068

Table 2.4: O2(a) fraction in a pure O_2 plasma. Taken from J.-P. Booth, Chatterjee, Guaitella, Sousa, et al. 2020

The effect of the inclusion O_2(a) in the computation of the EEDF are shown for both oxygen lines on figure 2.9.

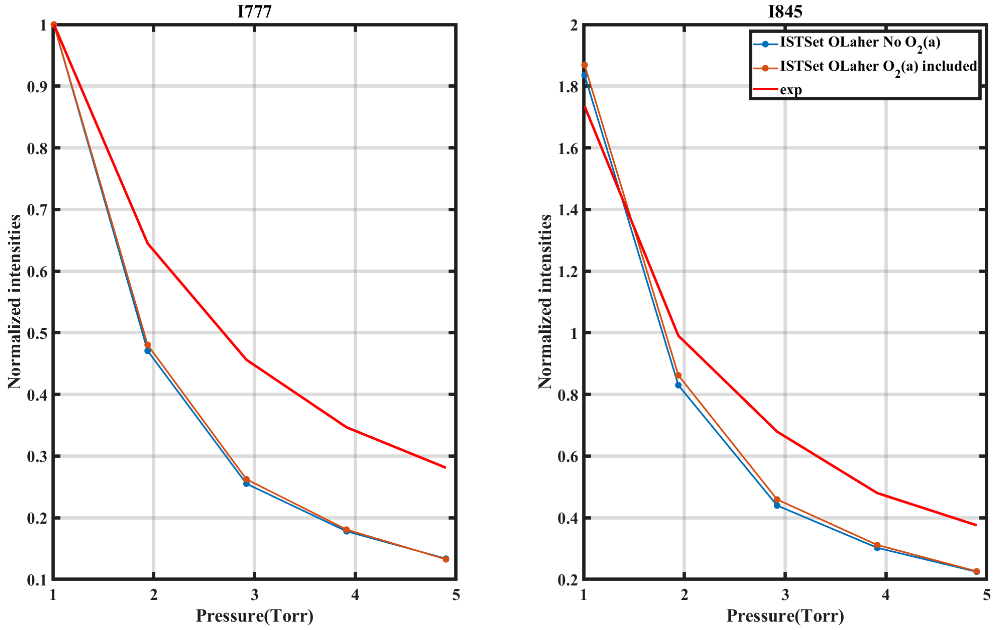

Figure 2.9: Effect of inclusion of the measured O_2(a) fraction in the computation of the EEDF for a pure O_2 plasma. The computation is done with the IST lisbon set and the Laher cross-section. The lines are compared with pressure.

Inclusion of O_2(a) in this case give a slightly better agreement between experiment and simulation (in orange on figure 2.9). The effect is however very small, which does not mean that the EEDF does not change, but rather that the bulk of the EEDF (at low energy) is modified, probably due to the low energy of the O_2(a) state (close to 1eV), leaving the tail mostly untouched. The O_2(a) state will be neglected during the rest of this work.

Including O_2(a) or not do not significantly change the calculation of absolute intensities of O777 and O845 in these conditions

Effect of atomic Oxygen cross-sections in the EEDF

As explained above, the cross-sections of electron impact with atomic O cannot be tested against the swarm. An uncertainty therefore lies in their use. So far, the computation of the EEDF included a complete and consistent set of cross-section for O_2 and some cross-sections for atomic O (the IST set from IST Lisbon database), which were not validated against the swarms.

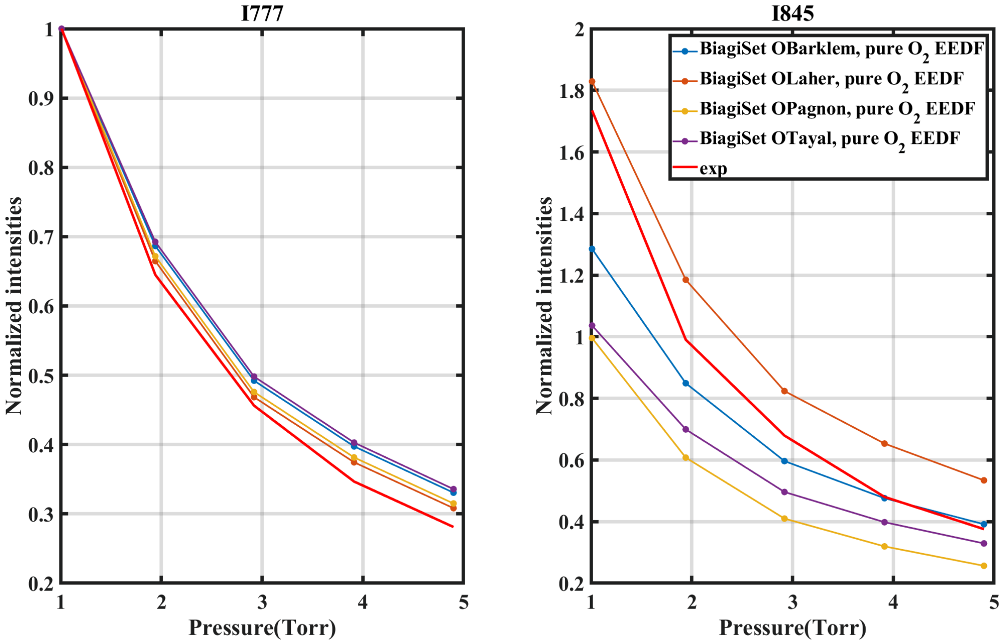

Figure 2.10: Comparison of the experiment and the simulation as a function of pressure in a pure O_2 plasma using the Biagi set assuming a pure O_2 EEDF. The current is set to 40mA and the flow is 10sccm

A way to evaluate the uncertainty of the inclusion of O atom cross-sections is to neglect the atomic oxygen in the EEDF and to assume a pure O_2 composition. First, the comparison of the experimental and simulated intensities for the Biagi set of cross-section assuming a pure O_2 plasma is shown on figure 2.10. The agreement between experiment and simulation remain very good for the O777 line, but the trend noticeably changed: while the simulated decay with pressure was previously too strong compared to the experimental one, the opposite is now obtained. The O845 line, previously in good agreement for the Laher cross-section, now show the same issue as the O777 line: the simulated trend is now flatter than the experimental one, leading to no good agreement for the O845 line.

The comparison for the same condition (pure O_2 plasma assuming a pure O_2 composition for the EEDF) is shown for the IST lisbon set on figure 2.11. For all excitation cross-section, the agreement of line O777 is now relatively good, with a trend well reproduced. The agreement of the 845 line with the Laher cross-section is excellent with a trend perfectly reproduced, which once again goes in favor of the Laher cross-section. This however raises the question of the influence of the atomic oxygen on the EEDF. The comparison of the O777 and O845 for both IST and Biagi sets with and without accounting for atomic O are shown on figure 2.12. In both cases, the Laher cross-section is used. In both cases, removing the atomic oxygen from the EEDF flattens the trend. The set of cross-section of atomic oxygen used in the computation of the EEDF is shown on figure 2.13 along with the O_2 set of IST Lisbon. The O_2 excitation are shown in blue and the O cross-sections in orange. For both species, the cross-section of individual excitation processes are shown in plain line and the summed cross-sections for all excitation processes of the specie is plotted with '+' markers. The elastic cross-section were not included in the sum. The amplitude of the summed cross-sections of O is much higher than the one of O_2 up to 6eV. After 6eV, the amplitude of the summed O_2 cross-section becomes larger than the one of atomic O. This means that including the O atoms in the EEDF computation will deplete the bulk of the EEDF and increase the tail of the EEDF above 6eV (the excitation to $O(3p^3P)$ and $O(3p^5P)$ take place at 11eV).

The calculations using the Biagi set show equally good results when removing the atomic oxygen from the EEDF computation (the results presented on figure 2.12 show that the decay with

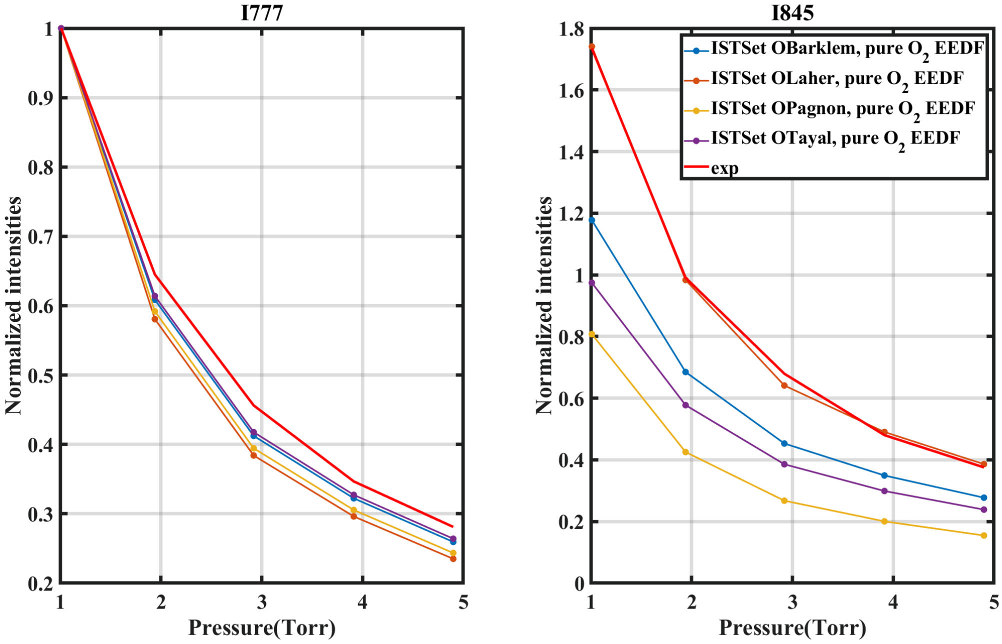

Figure 2.11: Comparison of the experiment and the simulation as a function of pressure in a pure O_2 plasma using the IST set assuming a pure O_2 EEDF. The current is set to 40mA and the flow is 10sccm

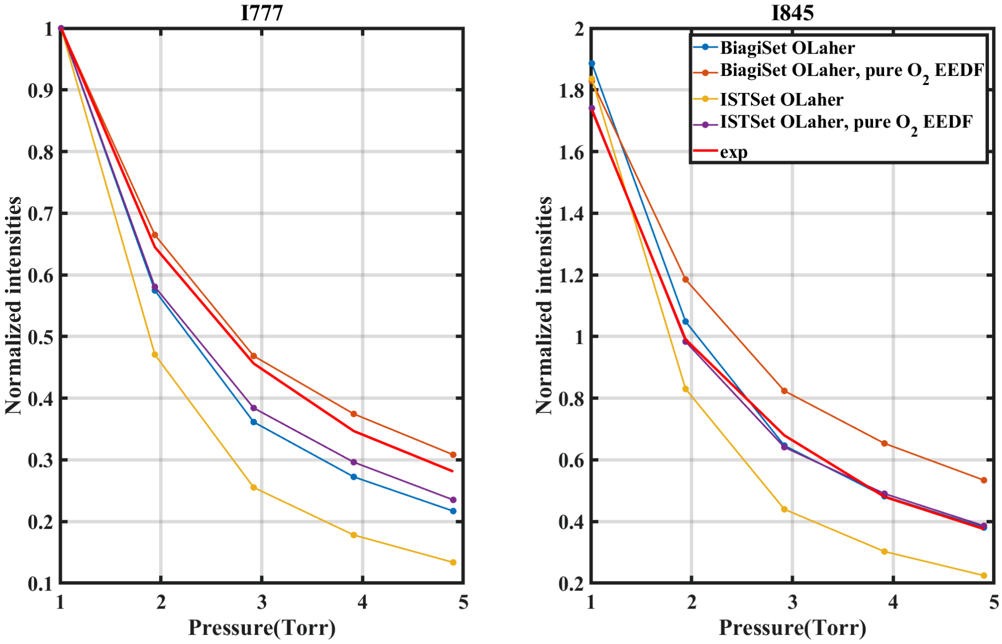

Figure 2.12: Comparison of the line intensities in a pure O_2 when accounting for dissociation in the EEDF. The curves without atomic Oxygen in the EEDF are indicated by "pure O_2 EEDF"

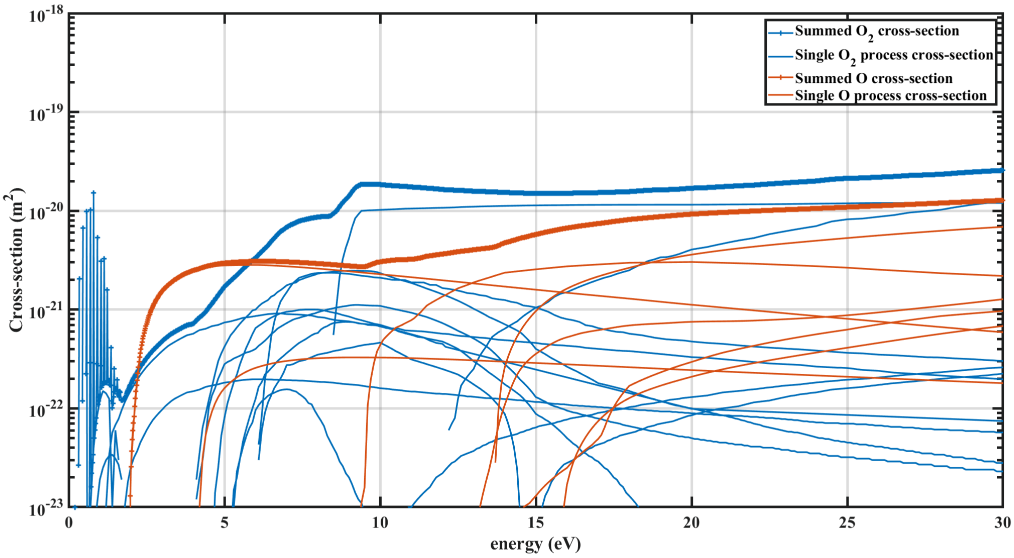

Figure 2.13: Cross-sections of O_2 and atomic oxygen used in the computation of the EEDF with Loki. The atomic cross-sections are in dashed lines

pressure of line O777 is well reproduced when using a pure O_2 EEDF whereas the decay of O845 is well reproduced when accounting for the atomic oxygen in the EEDF). For the rest of this work, the atomic O will be included in the EEDF computation when using the Biagi set for O_2. On the other hand, a large improvement is obtained when removing the atomic O from the EEDF computation if using the IST set for O_2.
In the rest of this work, the EEDFs computed using the IST set mostly do not include the cross-sections of atomic O, they are referred to as "IST set pure O_2 EEDF" or "IST set without atomic oxygen".

Two sets of parameters gives satisfactory results for both O atoms lines:

- The combination of σ_{EEDF}^{Biagi} + σ_{exc}^{Laher} already identified before
- the combination of the IST set for O_2 without atomic O cross-sections $\sigma_{EEDF}^{IST-noOatoms}$ with the Laher excitation cross-section σ_{exc}^{Laher}

This second combination allows for the best agreement between the experimental and simulated O777 and O845 in pure O_2 plasma but it requires removing O atoms from EEDF calculation.

Comparison of the best combinations of σ_{EEDF}^{set} and σ_{exc}

So far, two combinations have reproduced the experimental trend in a satisfying manner : Biagi set + Laher cross-section, and the IST set without atomic oxygen + Laher cross-section. The question of their common features naturally arise: what are the common points of the EEDF computed with these sets, leading to good agreement ?
We compare here the EEDFs at 1 and 5 Torr for these "best" cases. The comparison is plotted on figure 6.32, with the 1Torr EEDF in dashed lines and the 5Torr EEDF in plain line. The EEDF of a case with unsatisfying agreement (namely the IST set σ_{EEDF}^{set} with O atoms + σ_{exc}^{Laher}) is also shown for comparison. No common feature appears for the two satisfying combination (in blue and yellow). The EEDF obtained using σ_{EEDF}^{Biagi} decays slower than the one obtained using $\sigma_{EEDF}^{IST-noOatoms}$, leading to a higher tail of the EEDF when using the Biagi set. Because the

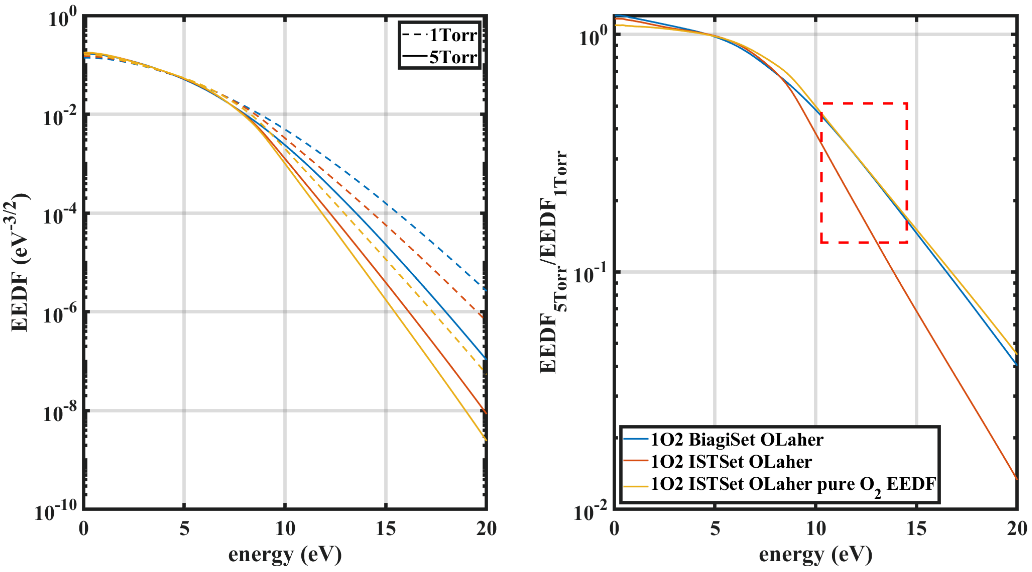

Figure 2.14: left:Graph of the EEDF of the best cases, compared with EEDF of a case with bad experimental-simulation agreement (IST set + Laher)
right: evolution of the ratio of the EEDF at 5 and 1 Torr with electron energy. In both theses graphs, the conditions giving good agreement with experiments are in yellow and blue while the orange one is unsatisfying.

comparison done before are based on a normalization at 1 Torr for O777, the absolute values of the EEDFs do not bring much information. Therefore, a second plot on figure 6.32 shows the ratios of the EEDF at 5 Torr over the EEDF at 1 Torr as a function of the electron energy in order to reveal the trend of the evolution of the EEDF with E/N, likely more important. On figure 6.32, the two combinations that yield good agreement between experiment and simulation are plotted in yellow and blue, while the unsatisfactory one is orange. The area of importance for the excitation of the two levels is around 11eV and is marked by a red dashed rectangle. It appears that in this area, the ratios of the 5Torr EEDF over the 1Torr EEDF overlap quite well for two satisfactory combinations, while for the unsatisfactory case $\sigma_{EEDF}^{ISTwithOatoms} + \sigma_{exc}^{Laher}$ drops much faster. The experimental decay of the line intensities can be reproduced well with the simulation if the EEDF computed decays not too quickly with pressure. It is difficult to pinpoint exactly one or several processes which will allow this. However the increasing pressure goes with a decrease of the reduced electric field in our conditions, meaning that the process with low energy threshold become more important at higher pressure. A good set for the computation of the EEDF for actinometry must describe properly the low energy processes.

The best results are obtained with EEDF that do not decrease to fast between 10 and 15 eV when the E/N is reducing with pressure

2.6.2 Line intensities in O_2-Ar plasmas

In the previous section, the best combinations of $\sigma_{EEDF}^{set} + \sigma_{exc}$ have been determined based on the experimental variation with pressure of O777 and O845 in pure O_2. We now check if these conclusions are still valid when adding Ar in the gas mixture as it is needed for actinometry. The variation with pressure of both the oxygen intensities and the Ar intensities with pressure (and therefore E/N) can now be compared to calculations.

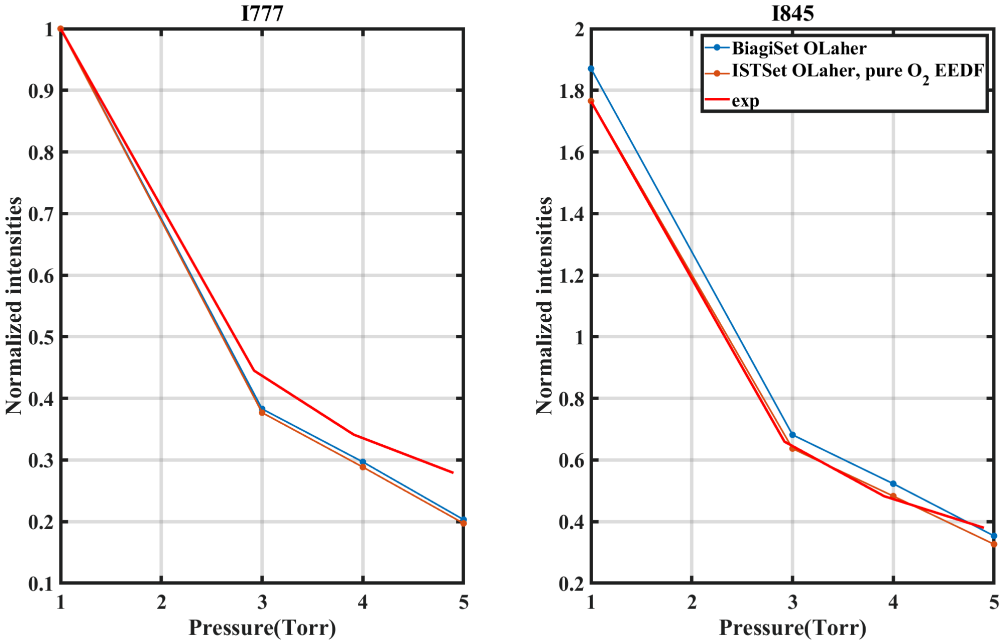

Figure 2.15: Comparison of experimental and simulated intensity trends of the Oxygen lines in a 95:5 O_2:Ar plasma using the previously identified conditions: Biagi set + Laher & IST without atomic O + Laher

2.6.2.1 Low Ar percentage

The first mixture studied is a 95:5 O_2:Ar plasma. A first test must be done: looking only at the O lines, it must be verified that the addition of Ar does not influence the parameters previously identified. Figure 2.15 shows the comparison between simulated and experimental intensities for the two oxygen lines in a 95:5 O_2:Ar plasma, using the combinations for which a good agreement between experiment and simulation was found in O_2 ($\sigma_{EEDF}^{Biagi} + \sigma_{exc}^{Laher}$ or $\sigma_{EEDF}^{ISTnoOatoms} + \sigma_{exc}^{Laher}$) . The agreement of the 777 line is not as good as previously with an error of almost 50% at 5 Torr compared to the experiment ($\frac{I777_{exp}(5Torr) - I777_{sim}(5Torr)}{I777_{sim}(5Torr)} = 0.5$), while the error in pure O_2 was below 20%. However the agreement with the 845 line remains very good, especially in the case of the IST set without atomic oxygen. This means that the 845 line will more likely yield good results when used for actinometry.

- Addition of 5% of Ar in the mixture has a detrimental effect on the agreement between simulation and experiment.
- The O777 is more affected than the O845
- the best parameters for $\sigma_{EEDF}^{set} + \sigma_{exc}$ previously identified for O lines remain valid

It can be easily checked that the choice of the Ar excitation cross-section does not influence the O lines parameters either, because of the lower amplitude of the cross-section compared to the O excitation and the higher value of the excitation threshold. Figure 2.16 shows the comparison of the Argon line intensities Ar750 and Ar811 between experiment and simulation for the 4 Ar cross-sections, using the Biagi set σ_{EEDF}^{Biagi} and Laher cross-section σ_{exc}^{Laher}. The intensities for both Ar and Oxygen are normalized by the value of O777 at 1 Torr. It is important to remind here that by normalizing all intensities for both O and Ar on the same line (the O777), it allows to assess the consistency between the excitation cross sections used for O atoms and the ones used for Argon.

Independently of the chosen excitation cross-section for Ar, the simulated intensity of Ar

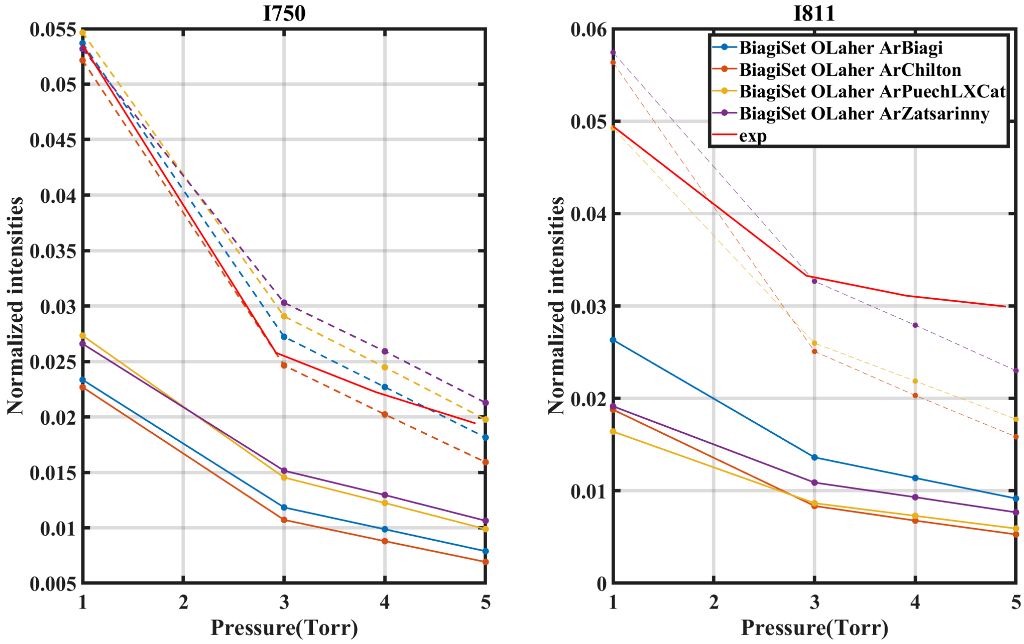

Figure 2.16: Comparison of experimental and simulated trends as a function of pressure in a 95:5 O_2:Ar mixture, for several Ar cross-sections, using the Biagi set and Laher cross-section. The original curve of Ar750 (in plain lines) have been multiplied by a factor 2 or 2.3 depending on the cross-section and plotted in dashed line. The dashed curves of Ar811 have been multiplied by a factor 3

seems to be underestimated for both lines, by a factor close to 2 for the Ar750 line and a factor close to 3 for the Ar811 line. The agreement of the simulated line Ar750 is good if a factor 2 is used for the Puech and the Zatsarinny cross-section (plotted in dashed lines on figure 2.16), while the agreement is very good with the Biagi and Chilton cross-sections if a factor 2.3 is used (plotted in dash & point lines on figure 2.16). There is therefore no way to discriminate the "good cross-section" to use in this case: all 4 underestimate the intensity of line Ar750, with various factors. For the Ar811 line, no choice of cross-section can reproduce the experimental decay with pressure, which is always flatter than the simulated decay. The least wrong cross-section giving the least underestimation for both lines is the Zatsarinny. Because the Ar750 line reproduces the trend, it is likely that using it for actinometry will give good results, if not for the absolute values (which might be underestimated, because the ratio I_O/I_{Ar} is off by a factor 2 compared to experiment), at least for the trend. Using the Biagi set, the best ratio to use for actinometry is likely to be O845/Ar750.

The results are also verified for the other case where a good agreement between simulation and experiment was obtained in pure O_2, i.e IST set without oxygen $\sigma_{EEDF}^{IST-noOatoms}$ and Laher cross-sections σ_{exc}^{Laher}, on figure 2.17. The results are very similar to the previous case. Both lines are underestimated compared to the experimental value. for Ar 750, the trends are good but the line is underestimated by a factor between 3.5 and 5 (3.5 for the Puech and Zatsarinny cross-sections, 4.5 for the Biagi excitation cross-section and 5 for the Chilton cross-section, plotted in dashed lines on figure 2.17). The correction factor in this case is larger than the one used in the case of the Biagi set. Similarly, the Ar811 line, in addition to being largely underestimated, has a trend which does not match the experimental one for any excitation cross-section. To have simulated intensity of Ar811 at the same level as the experimental one, the simulated values were multiplied by a factor 6 (and plotted on figure 2.17 in dashed lines). The conclusion when using this set of parameters ($\sigma_{EEDF}^{ISTnoOatom} + \sigma_{exc}^{Laher}$) are the same as before, with simply a different correction factor for both lines: both lines are underestimated, but the trend of the

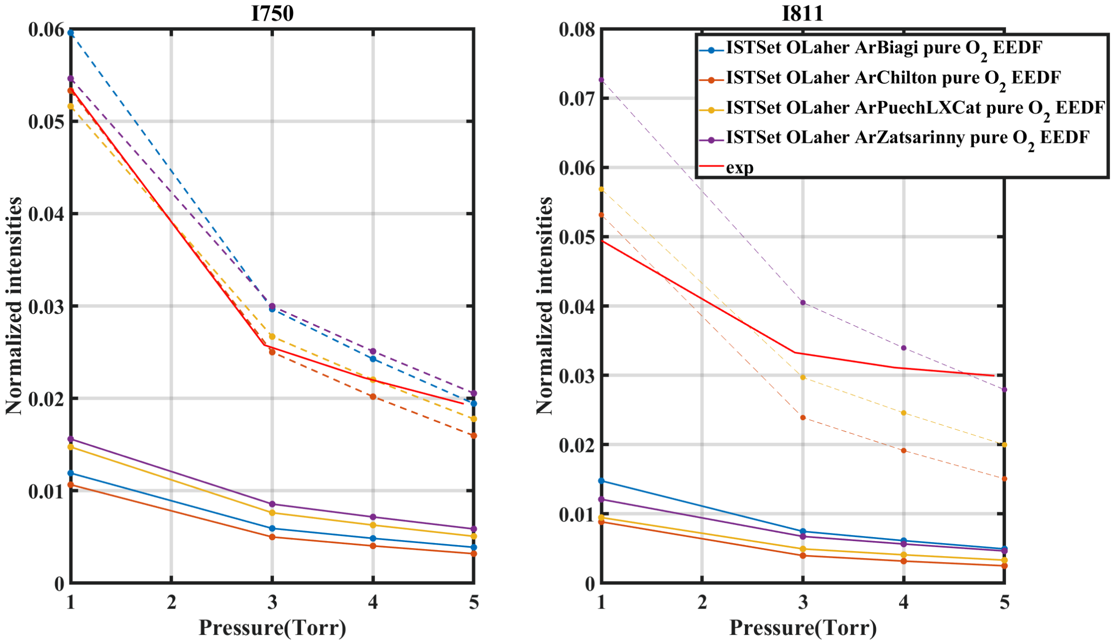

Figure 2.17: Comparison of experimental and simulated trends of the Ar lines Ar750 and Ar811 as a function of pressure in a 95:5 O_2:Ar mixture, for several Ar cross-sections using the IST set (without atomic oxygen) and Laher cross-section. The original curve of Ar750 (in plain lines) have been multiplied by a factor 3.5 to 5 depending on the cross-section and plotted in dashed line. The dashed curves of Ar811 have been multiplied by a factor 6

Ar750 line is the good one, while the simulated 811 trends with pressure are steeper than the experimental one. No clear choice of excitation cross-section for Ar appear, the only difference being a correction factor to use. However, in this case again, the cross-section yielding the least underestimation is the Zatsarinny's cross-section, making it the least wrong one. Once again, because the 750 line reproduces well the experimental trend if multiplied by a factor 2, it is likely that for the purpose of actinometry, good results might be given by the O845/Ar75O couple when using the IST set for computation of the EEDF.

- large inconsistency between Oxygen and Argon lines in all cases
- Zastarinny's excitation cross-sections for Ar are the "least wrong" ones, but there are no large differences with the others and none is really satisfying.

Similarly to the O excitation cross-sections, the Ar excitation cross-section will be noted σ_{exc}^{Ar}.

2.6.2.2 Influence of the Ar percentage

The percentage of Ar in the mixture is varied to study the influence of the actinometer. Two additional data sets are taken: a 90:10 O_2:Ar and a 85:15 O_2:Ar mixtures are studied at 40mA, 10sccm. The following figure 2.18 is a matrix of intensities, with each line corresponding to a different condition (5% Ar on the first line, 10% on the second and 15% on the third). On each line, the 4 emission intensities (O777, O845, Ar750 and Ar811) are plotted as a function of pressure. The experimental trend (in red) is compared to two simulated intensities: the combination $\sigma_{EEDF}^{Biagi} + \sigma_{exc}^{OLaher} + \sigma_{exc}^{ArZatsarinny}$ (Biagi set + Laher for O excitation + Zatsarinny for Ar excitation) (in orange) and the combination $\sigma_{EEDF}^{IST-noOatoms} + \sigma_{exc}^{OLaher} + \sigma_{exc}^{ArZatsarinny}$ (IST set without atomic oxygen + Laher + Zatsarinny).
The analysis of the behaviour of the lines must be separated in 2 parts: the 0.5 Torr point,

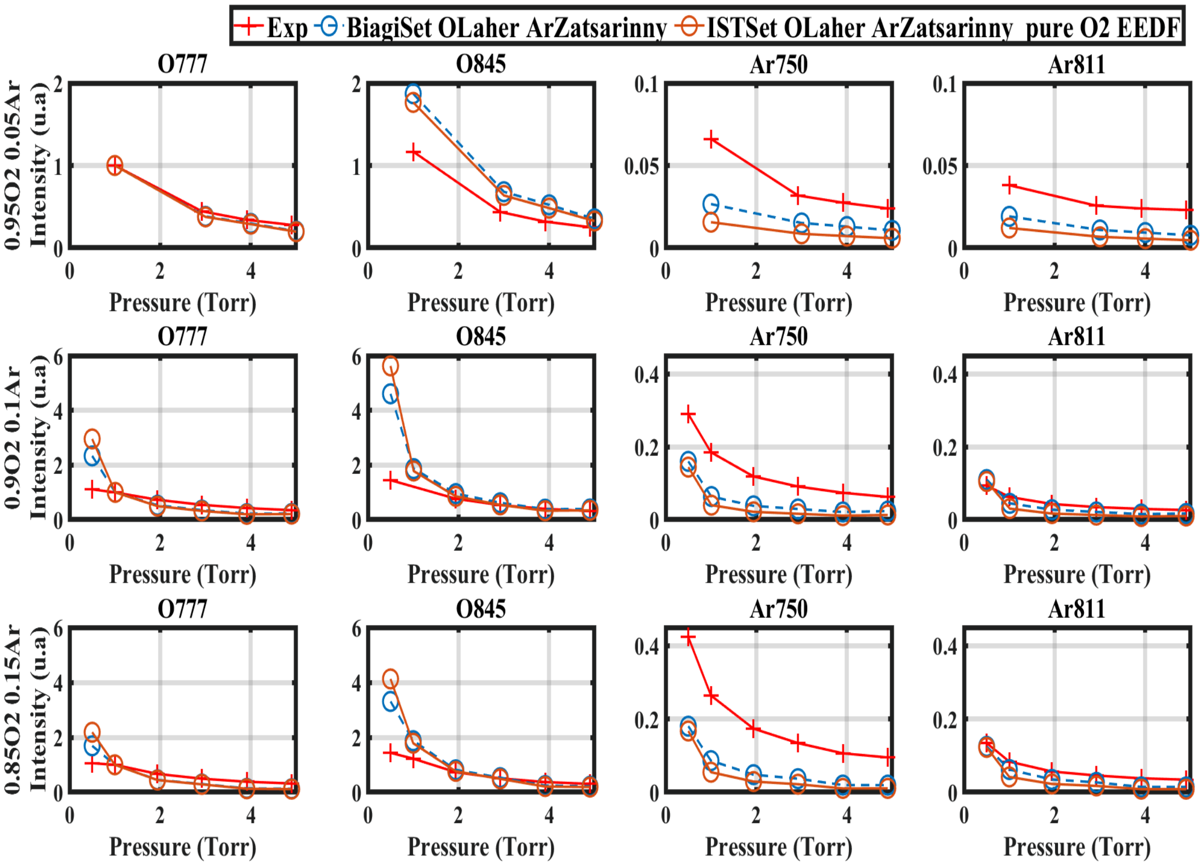

Figure 2.18: Comparison of the experimental and simulated intensity for the 4 lines of interest in 3 different O_2:Ar mixtures: 95:5, 90:10 and 85:15

where the reduced electric field is significantly higher than in the other conditions (up to 90 Td at 0.5Torr, ~65Td at 1Torr and ~48Td at 5Torr), and the points at 1Torr and above.
For pressure between 1 and 5 Torr, the agreement of the O777 line, very good at 5% Ar, is progressively worsened with Ar content. The point at 1 Torr is the normalization point and therefore does not change, but the gap between the simulated and experimental values at 5 Torr increases with pressure (0.20 vs 0.28 for the simulation vs experimental value at 5% Ar and 0.11 vs 0.32 at 15%Ar). On the other hand, the agreement of the line O845 improves with Ar percentage. The gap at 1Torr remains the same in all conditions (1.15 experimentally vs 1.75 simulated), but the points at 5Torr are in better agreement at 10 and 15%Ar than at 5%. The values of the Ar intensities are significantly changed by admixture of Ar, as well as the gap between simulated and experimental values. This means that the relevant values to compare is the evolution of the ratio between experiment and simulation at a given pressure. For Ar750, comparing experiment and simulation $\sigma_{EEDF}^{IST-noOatoms}+\sigma_{exc}^{OLaher}+\sigma_{exc}^{ArZatsarinny}$ (in yellow) shows that at 1 Torr, the ratio between experiment and simulations remains close to 6 in all conditions, while at 5Torr, the ratio between experiment and simulation increases from 4 at 5% Ar to 9 at 15% Ar. This means that the more Ar is added, the worse the agreement at 5 Torr for Ar750 is. It must be noted that while a constant multiplicative factor (on the whole pressure range) could match experiment and simulation at 5% Ar ($I_{exp}/I_{sim}(5\%Ar, 1Torr) = I_{exp}/I_{sim}(5\%Ar, 5Torr)$, it is no longer the case at 10% Ar ($I_{exp}/I_{sim}(10\%Ar, 1Torr) \neq I_{exp}/I_{sim}(10\%Ar, 5Torr)$). A similar behaviour is observed for Ar811: at 5 Torr, the ratio experiment over simulation goes from 3 at 5% Ar to 4 at 15%Ar. Overall, the agreement of the Ar lines is worsened by admixture of Ar. Apart from the O845 line, admixture of Argon seems to be detrimental for a correct description of the lines. The gap between experiment and simulation (or rather the ratio of experiment over simulation) increases with Ar percentage, leading to think that the factor 2.5 previously needed in the 5% Ar case to match experiment and simulation could already be a consequence of an improper description of the EEDF in the 13eV area due to the 5% Ar.
The EEDFs at 1 and 5 Torr for gas mixtures going from pure O_2 to 85:15 O_2:Ar are plotted on figure 2.19. The EEDFs are computed using the IST set without O atoms $\sigma_{EEDF}^{IST-noOatoms}$. At 1Torr, increasing the Ar content increases the tail of the EEDF (>6eV), though the EEDF in the 90:10 and the 85:15 mixtures are very close. The effect of the Ar content is not as clear at 5Torr. The tail of the EEDF at 5Torr is increased when going from pure O_2 to 95:5 O_2:Ar and further to 90:10 O_2:Ar. Upon further increase of the Ar content to 15%, the tail of the EEDF decreases and overlaps very well with the pure O_2 case. As a result, the ratio of the EEDF at 5Torr over the EEDF at 1Torr are very different for all the mixtures. It can be seen on the second plot of figure 2.19 that the more initial Ar in the mixture, the lower the ratio $EEDF_{5Torr}/EEDF_{1Torr}$ in the tail of the EEDF. The ratio $EEDF_{5Torr}/EEDF_{1Torr}$ too low in the tail had been seen in the pure O_2 case for the case giving poor agreement between experiment and simulation. The ratio of the EEDFs decreasing too fast with increasing Ar content likely indicate that the tail of the EEDF is not properly described in O_2:Ar mixtures. It can therefore be concluded that for actinometry purpose, the Ar percentage should be kept as small as possible, necessarily below 5% (which seemingly already induces error) to avoid inaccurate description of the tail of the EEDF. An interesting solution would be to use a more intense noble gas, such as Xenon, whose emission line can be very intense even at 1% of the total gas density. The advantages are both to limit the influence of the actinometer on the EEDF and to limit error while integrating the line on the spectrometer (low lines are more sensitive to noise or integration limits).

The 0.5Torr point left aside on figure 2.18 must also be discussed. For all the lines, the simulation sees a sudden increase of the line intensity below 1 torr for all combinations of σ_{EEDF}^{set} and $\sigma_{exc}^{O,Ar}$. For both oxygen lines, the experimental trend is much flatter than the simulated one. Even though no point at 0.5 Torr is available for 5% Ar, the experimental trend is flatter than the simulated one on the range 1-5 Torr, despite the good agreement in the values. It is likely that the simulated point at 0.5Torr would see the same increase as in the other cases, while the experimental one would be lower.

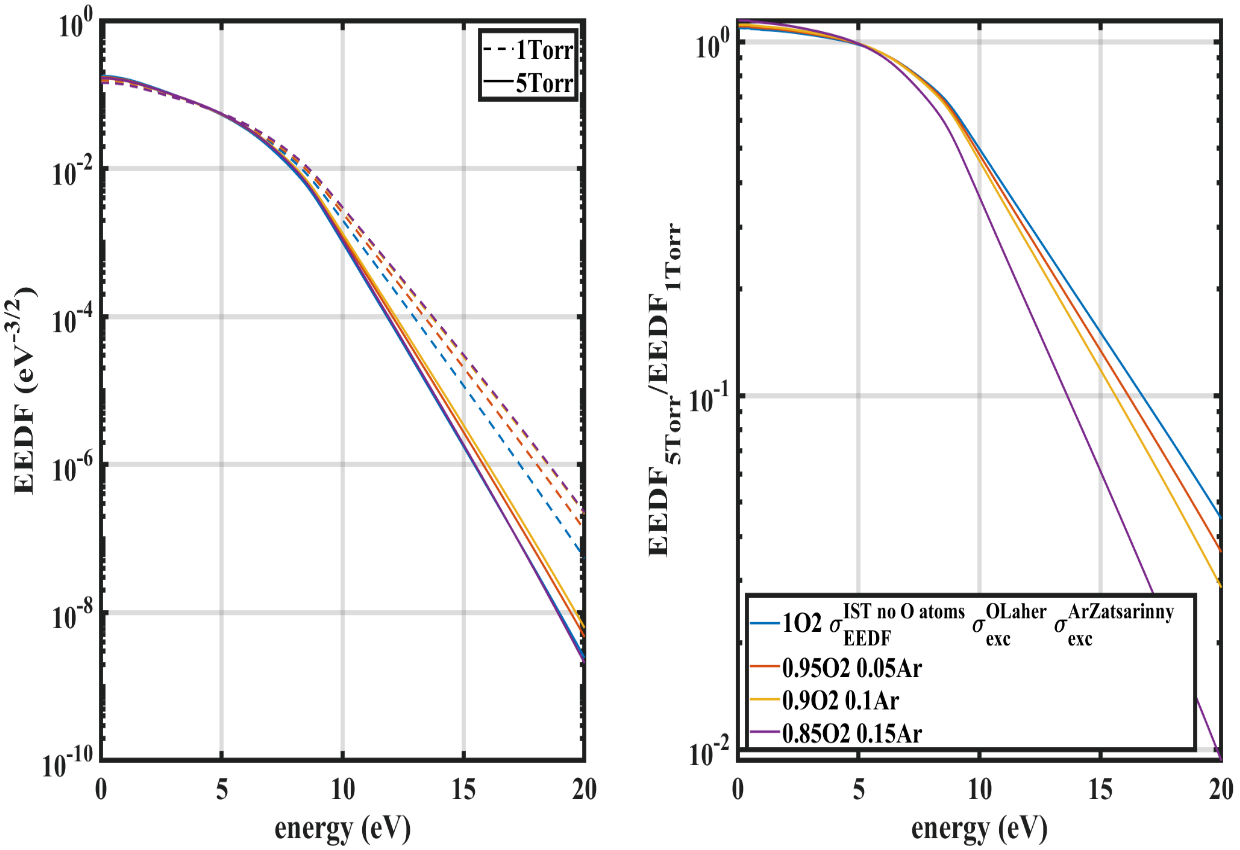

Figure 2.19: Left: comparison of the EEDFs at 1 and 5Torr for different gas mixtures (pure O_2, 95:5, 90:10 and 85:15 O_2:Ar). The EEDFs at 1torr are plotted in dashed line, the ones at 5Torr are in plain lines.
Right: Comparison of the ratio of the EEDF a 5Torr over the EEDF at 1Torr for different mixtures

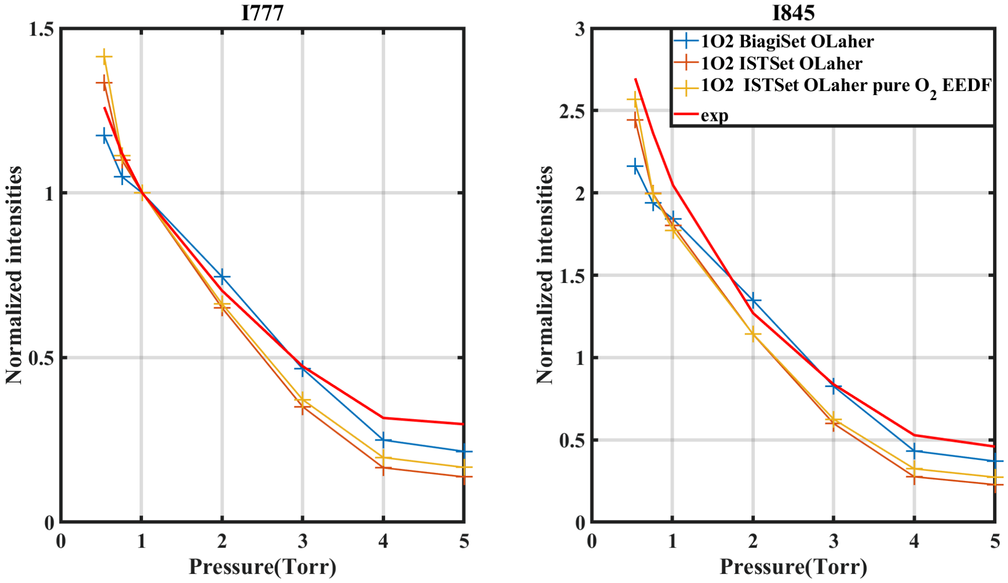

Figure 2.20: Comparison of the simulated and measured intensities of O777 and O845 lines in a pure O_2 plasma. The current is set to 40mA and the flow to 7.4sccm

In pure oxygen, the simulated trends are quite similar to the experimental one: it is impossible to say whether or not the same behaviour as in O_2:Ar would take place. It is therefore difficult to know if the trend and in particular the point at 0.5 Torr are due to the influence of Ar on the EEDF or to a miscalculation of an excitation process of oxygen, or to both phenomena entangled. A measurement at 0.5Torr in a pure O_2 discharge would bring insight on the cause of this issue.

For Ar lines, a strong increase is seen when going down from 1 to 0.5 Torr. The increase is not as steep as predicted by the simulation, but it is clearly visible. It could be that the Ar excitation processes are well-described (thus explaining the sudden increase) and that the observed difference between experiment and simulation is only due to an inaccurate description of the EEDF. In this case, this would mean that the excitation of atomic Oxygen at low presure is not properly described. The dissociative excitation was ruled out by computation, but maybe something else is missing.

- Increasing the Ar percentage is detrimental to the agreement between experiment and simulation probably because the EEDF calculation accuracy (or at least the tail) is worsened with increasing Ar admixture
- A larger error is made at low pressure *ie* higher E/N, but the reason for it remains unclear

2.6.2.3 Additional measurements in a pure O_2 plasma

An additional set of measurement in pure O_2 with points at 0.75 and 0.5Torr was taken very recently in the same setup. In this supplementary measurement, the total flow was set to 7.4sccm (different from the 10sccm in the previous ones). This should increase the O_2 dissociation but keep the temperatures and the reduced electric field similar, which does not however matter for the purpose of comparing CRDS and actinometry. CRDS and actinometry measurements were taken simultaneously. The intensities of lines O777 and O845 computed using the CRDS data are compared with the intensities obtained from the spectrometer. The comparison is shown on figure 2.20. Using the conclusions of the data in pure O_2 presented above, three different cases of collision data are tested: $\sigma_{EEDF}^{IST-noOatoms} + \sigma_{exc}^{OLaher}$, $\sigma_{EEDF}^{IST} + \sigma_{exc}^{OLaher}$ and

$\sigma_{EEDF}^{Biagi} + \sigma_{exc}^{OLaher}$. The intensities are still normalized by the intensity of O777 at 1Torr. For the three cases simulated and presented on figure 2.20, the decay of the intensity with pressure is in good agreement with the experiment. The strong increase experimentally observed below 1Torr is also reproduced in the simulation, indicating that the tail of the EEDF in pure oxygen is well described. This answers the question raised by the set of data previously shown about the validity of the tail of the EEDF in pure O_2 and allow to finally draw the conclusion that the discrepancies observed in the O_2-Ar mixture are due to a problem in the EEDF computation with the O_2-Ar mixture and not to a problem with O_2 itself.

Similarly to what had been seen before, the Biagi set leads to a very good agreement on the O777 line over the whole pressure range and to good agreement between experiment and simulation for the O845 line. For the O845, the intensity at pressure above 1Torr are underestimated by approximately 25% with the Biagi set, but the intensity at 1Torr and above are in good agreement with the experiment. Overall, the Biagi set allows to obtain a good agreement between experiment and simulation. The two cases using $\sigma_{EEDF}^{IST-noOatoms}$ (in yellow on figure 2.20) and σ_{EEDF}^{IST} (in orange on figure 2.20) are close. The difference caused by the inclusion/withdrawal of O atoms is not as strong as in the previous dataset, where a factor two could be seen at 5Torr between the two cases. This is because despite the higher residence time in this new set of measurement, the oxygen density is actually lower. This is attributed to the change of the state of the surface of the reactor wall (the new measurement was conducted 1.5 year after the first one), which increases the recombination probability γ_O and lowers the O atom density. Nevertheless, the case $\sigma_{EEDF}^{IST-noOatoms}$ shows a better agreement with experiment than the case σ_{EEDF}^{IST} for pressures between 0.75Torr and 5Torr. For the O845 line, the case $\sigma_{EEDF}^{IST-noOatoms}$ gives a better agreement on the whole pressure range investigated. Overall, the conclusion drawn from this additional series are the same as the one before: the combination that give the best agreement between experiment and simulation are $\sigma_{EEDF}^{IST-noOatoms} + \sigma_{exc}^{OLaher}$ and $\sigma_{EEDF}^{Biagi} + \sigma_{exc}^{OLaher}$.

This additional set of data will not be used again and will not serve for actinometry calculations presented below .

- Discrepancies between experiment and simulation at low pressure are due to the computation of the tail of the EEDF in the Ar:O_2 mixture and not to a problem in the description of the O/O_2 processes
- the new set of measurements extended to lower pressure confirms the previous conclusions on the best set of parameters which are either ($\sigma_{EEDF}^{IST-noOatoms} + \sigma_{exc}^{OLaher}$) or ($\sigma_{EEDF}^{Biagi} + \sigma_{exc}^{OLaher}$)

2.6.3 Actinometry measurements

After analyzing all parameters one by one and drawing a "best working combination of basic collision data" to determine individually line intensity variation with pressure (*ie* E/N), the actual actinometry method based on line ratios can be performed to determine O atoms densities. The actinometry algorithm used is described in figure 2.21. First, an Oxygen fraction is assumed. From this, an O_2 and Ar fraction can be computed as well (see appendix). The temperature and reduced electric field are still required from another diagnostic (namely CRDS and floating potential probes). They are provided to the Boltzman solver LoKI-B, along with the fractions, and are used to compute the EEDF and ultimately the rate coefficients. These are then used with the intensity ratio from the spectrometer given in table 2.2 and the Einstein coefficients given in table 2.1 to compute the O fraction in the plasma. The computed O fraction is compared with the assumption. If the difference exceeds a 0.5% of the gas density, the computed fraction is used as assumption of the oxygen fraction and the algorithm loops. If the assumption and the computed fraction are close enough, the value is kept and the final O_2 density is computed. However, because it was previously demonstrated that neglecting the dissociation might improve the results in some conditions, direct actinometry (without looping

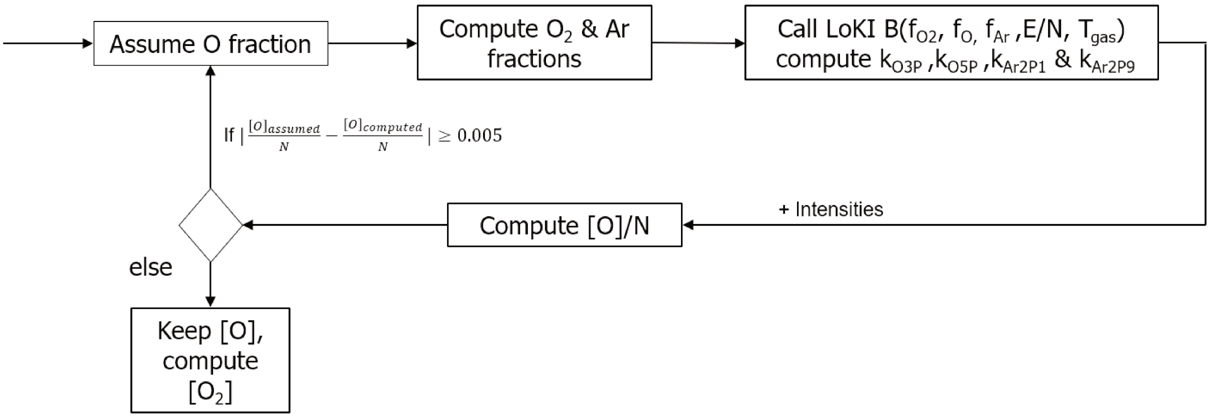

Figure 2.21: Principle of the actinometry algorithm

on O fraction) will also be performed. In the following sections, we present direct comparison of CRDS and actinometry measurements in a glow discharge at 40mA for two conditions: 95:5 O_2:Ar and 85:15 O_2:Ar.

2.6.3.1 Actinometry in a 95:5 O_2:Ar mixture

The Biagi Set (using a complete loop on O atoms fraction) is first tested. Figure 2.22 shows the comparison of the O fraction measured by CRDS and the O density measured by actinometry in 95:5 O_2:Ar at 10sscm, 40mA between 1 and 5 Torr. The 4 available line ratios are used (O777/Ar750, O845/Ar750, O777/Ar811 and 0845/Ar811). For all line ratios, the actinometry results are plotted in plain line and the CRDS measurement is plotted in red. In dashed lines are plotted the actinometry results adjusted to match the CRDS results at 1 Torr. This allows to check if despite the mismatch in absolute values, the trend are well reproduced or not. First of all, looking at all plain lines on figure 2.22, for all combinations used, the O fractions measured by actinometry are way below the CRDS measurement (in plain red line): the O fractions measured with actinometry are always twice or three times too low compared to the CRDS. This was expected because despite the relatively good agreement observed for the Oxygen absolute intensities in this mixture, a factor at least 2 was necessary to match the experimental and simulated Ar intensities. Obviously this factor is found again in actinometry. In this mixture, the agreement for intensities was particularly good with the 845 line. It was also shown that the Ar750 line could not match the experimental intensity but was reproducing the trend with pressure rather well. Therefore, the combination O845/Ar750 should be the most suited one for actinometry. Looking at the dashed line in the O845/Ar750 figure, we can see that the CRDS trend is very well reproduced, especially using the Biagi or Puech excitation cross-section for Ar2P1. No particular Ar cross-section was put forward in the previous section, so the actinometry measurement follow the line intensity predictions. As reminded, the agreement of the O845 line was excellent, and the agreement of the Ar750 line was very good as well if a factor ~2 was used. This factor 2 is found again here, as the CRDS fraction is about twice the actinometry fraction. Looking at the other lines, it can be found that the CRDS trend can be reproduced rather well by the O777/Ar811 ratio. However, in this case, this appears to be simply error compensation because the absolute intensity of line Ar811 was off by a factor 3.5 to 5 and did not reproduce the experimental intensity trend very well.

The same figure is presented using the IST set (and assuming a pure O_2 EEDF without looping on the oxygen fraction) on figure 2.23. Very similar results can be observed again in this configuration. Once again, the fractions calculated via actinometry (in plain lines) are much lower than the one via CRDS for all combinations. As predicted with absolute line intensities, the O845/Ar750 ratio reproduces the measured trends of CRDS very well, using the Biagi excitation cross-section of Ar. Actinometry underestimates O atoms densities by a factor

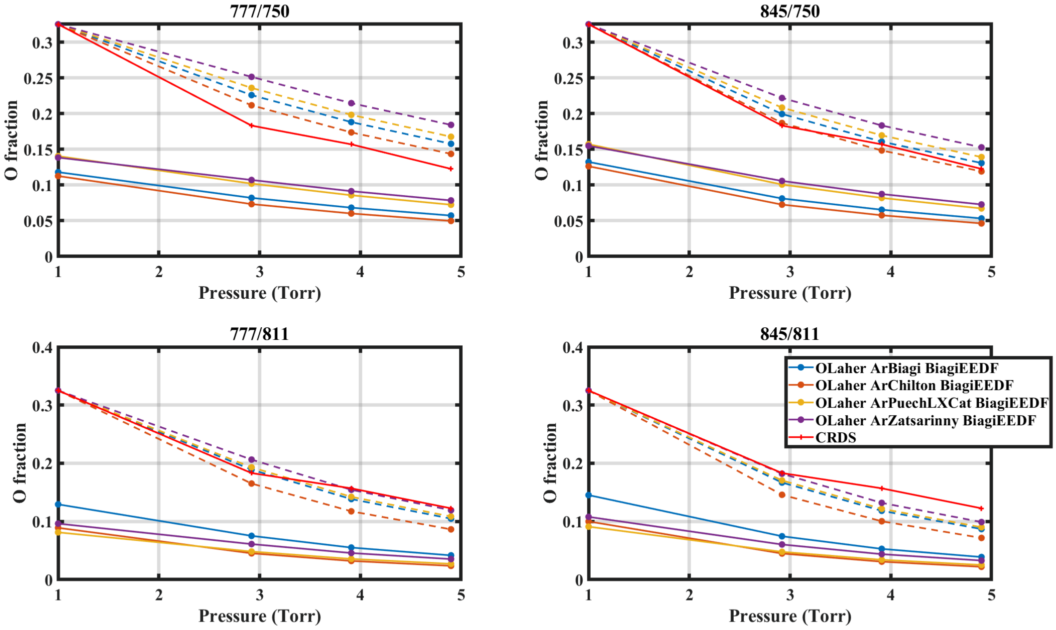

Figure 2.22: Actinometry vs CRDS measurement using several Ar excitation cross-sections in a 95:5 O_2:Ar mixture at 40mA, 10sccm. The 4 possible couple are used. The Biagi set is used for the computation of the EEDF. The CRDS lines are in red, the actinometry measurement in plain line and the actinometry results normalized by the CRDS fraction at 1 Torr (to observe the evolution of the trend) are in dashed line

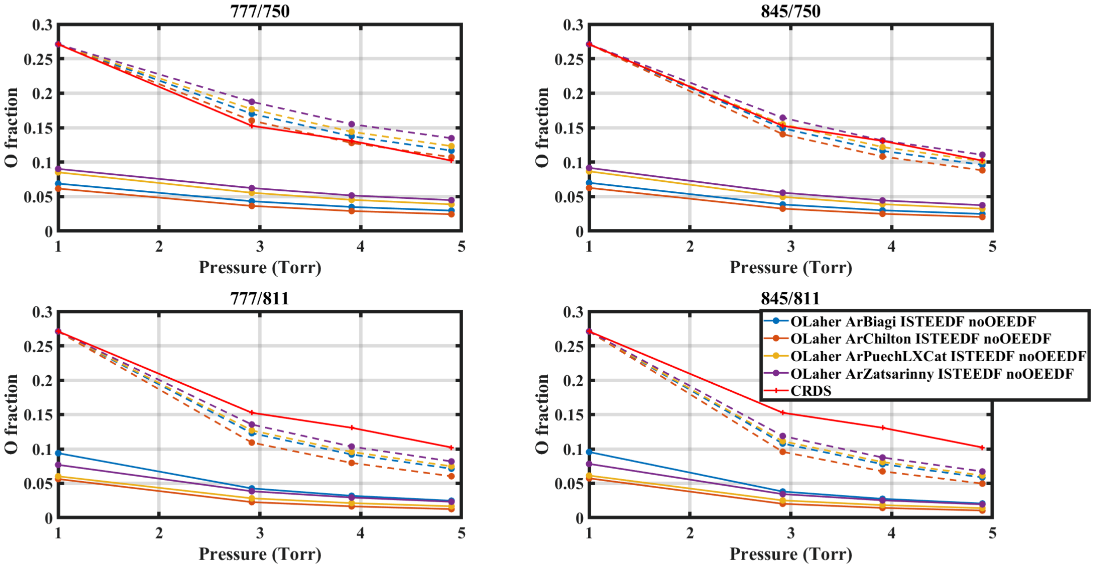

Figure 2.23: Actinometry vs CRDS measurement using several Ar excitation cross-sections in a 95:5 O_2:Ar mixture at 40mA, 10sccm. The 4 possible couples are used. The IST set is used for the computation of the EEDF

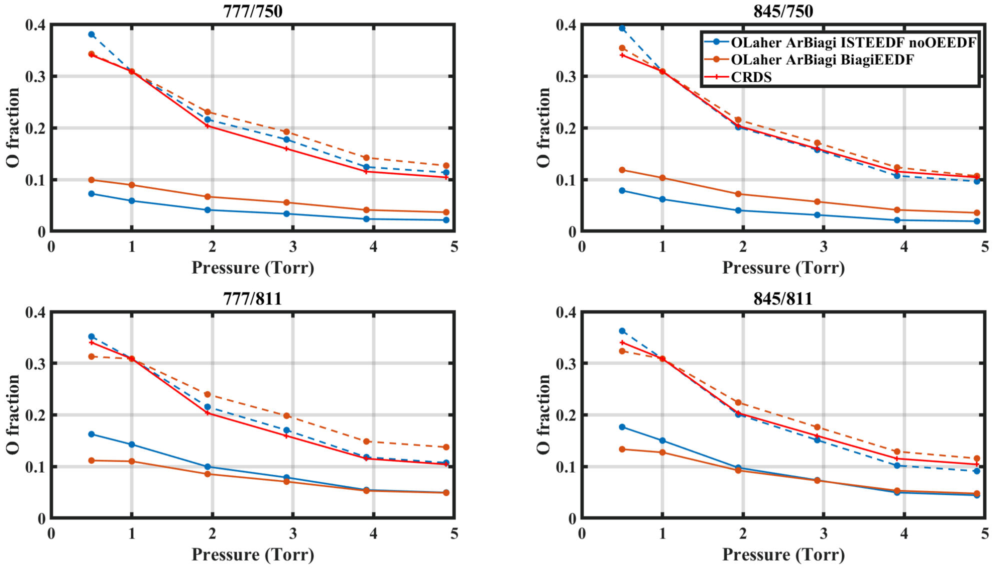

Figure 2.24: Actinometry vs CRDS measurement using several collision data combination in a 85:15 O_2:Ar mixture at 40mA, 10sccm. The 4 possible couples are used.

2.5, as seen already with the Ar line intensities. This time, the O777/Ar750 is also a good match despite no good agreement in the simulation of the O777 line. This means that the good agreement of the trend is due to error compensation. No other couple of lines reproduces the trend.

No Ar excitation cross-section was clearly identified in the intensity calculation process: all sources yielded rather good results for the 750 line and poor results for the 811 line. After analyzing the trend, it seems that the Ar Biagi cross-section for Ar(2P1) excitation is the best suited one for actinometry measurements

When using line ratios to determine O atoms density (actinometry):

- O845/Ar750 reproduces the trend of [O] the best when using either $\sigma_{EEDF}^{IST-noOatoms}$ or σ_{EEDF}^{Biagi} with $\sigma_{exc}^{OLaher} + \sigma_{exc}^{ArBiagi}$
- O777/Ar750 and O777/Ar811 are less trustable and rely on error compensation
- Even with a good set of parameters O fraction is underestimated by a factor 2 to 2.5

2.6.3.2 Actinometry in a 85:15 O_2:Ar mixture

Having chosen a final combination of $\sigma_{EEDF}^{set}; \sigma_{exc}^{O}; \sigma_{exc}^{Ar}$ to use, it can be used in another gas mixture, with pressure going down to 0.5Torr (*ie* with reduced electric fields up to 90Td). The collision data chosen just above were kept. Figure 2.24 shows, like in the previous mixture, the results yielded by the 4 possible couples (in plain lines) and the trends (normalized to the CRDS measured fractions, in dashed lines).

Looking at the O845/Ar750, the actinometry O fractions are underestimated by a factor 3 to 4 depending on the set used for the computation of the EEDF. The trends (in dashed lines) are very similar to the CRDS trends. This comes as a surprise because the absolute intensities trends were not good in this mixture due to a probably inaccurate computation of the EEDF (especially at 0.5 Torr). This illustrates one of the strength of actinometry: despite problems with basic collision data preventing an accurate determination of each individual excitation

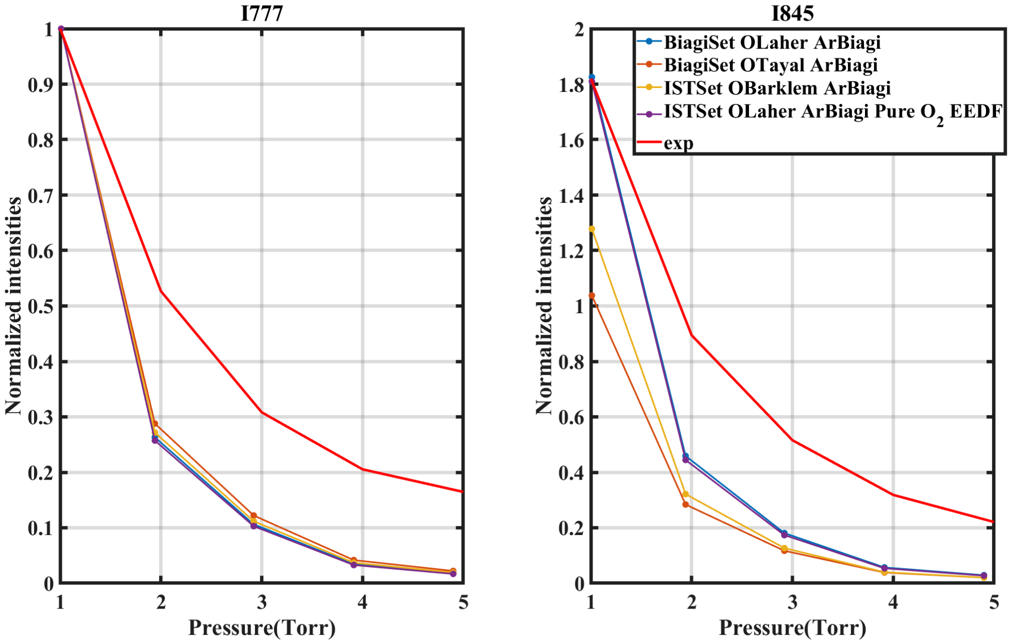

Figure 2.25: Comparison of the simulated emission (for several O_2 EEDF set and Ar excitation cross-sections) and experimental emission intensities of the O777 and 845 lines in a 95:5 CO_2:Ar plasma. All simulated intensities are normalized by the value of the experimental I777 line at 1Torr

process, the trends are very well reproduced. The densities, despite being a factor 3 too low, give a good idea of the actual order of magnitude of the O atom density. The good trend is due to error compensation, however different from the one seen previously: while it was due a choice of excitation cross-section in the case of the 95:5 mixture, it appears here that the good trend is reproduced for all ratios. The inaccuracies of the EEDF are compensated when doing the ratio.

2.7 A test on CO_2 plasma

After bench-marking the available collision data in an O_2 discharge, the choices made can be tested in another O-containing discharge of obvious interest for this work with the CO_2 plasma. A CO_2 glow discharge is ran in the same reactor with the same experimental set-up, at 7.8sccm, 40 mA, with a 95:5 CO_2:Ar mixture. Similarly to the O_2 case, the emission intensities are checked first. It was previously identified that the description of the EEDF was less accurate in a mixture of two different gases. The problem is likely to be seen here again, because CO_2 plasma creates a mixture of CO_2, CO and O_2 (and atomic O). The simulated emission intensity for the 2 oxygen lines are shown on figure 2.25. Four cases were represented: the combination of Biagi set with all three O excitation cross-sections, and the combination IST set (without atomic O) with the Laher cross-section. In general, for all 4 cases, the trends of both oxygen lines are not well reproduced, probably because of the computation of the tail of the EEDF in the mixture. While experiment and simulation overlap at 1Torr, there is almost a factor 10 between experiment and simulation at 5Torr. Looking more in details, we can see that the cases using σ_{EEDF}^{Biagi} or $\sigma_{EEDF}^{IST-noOatoms} + \sigma_{exc}^{OLaher}$ (i.e Biagi or IST sets with Laher excitation) or are now very close, proving the limited importance of the O_2 set in the EEDF. It was also verified (but not shown here) that when using the IST set, including or excluding the atomic O cross-sections is no longer critical. Comparing the 3 cases using the Biagi set, it appears that the Laher cross-section is once again the one giving the best trend for both oxygen lines, though the experimental trend is like in O_2 flatter than the simulated one.

]

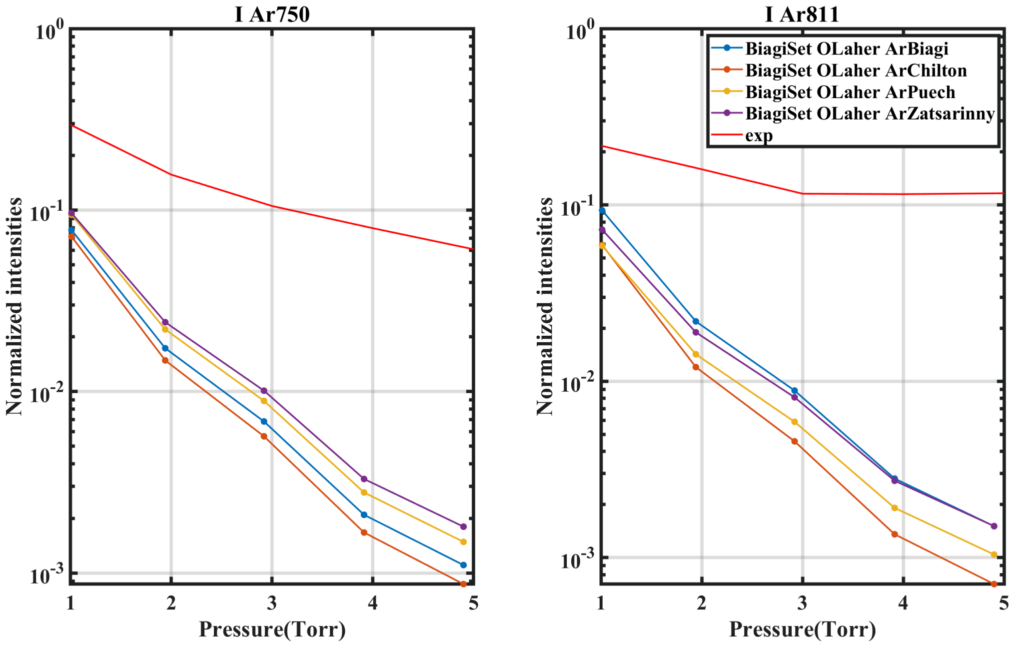

Figure 2.26: Comparison of the simulated emission (for several O_2 EEDF set and Ar excitation cross-setions) and experimental emission intensities of the Ar750 and Ar811 lines in a 95:5 CO_2:Ar plasma. All simulated intensities are normalized by the value of the I777 line at 1Torr

Figure 2.26 shows the intensities of Ar using the Biagi set for EEDF, the Laher excitation cross-section of oxygen and several Ar cross-sections. The Ar intensities are plotted in log scale. The simulated trends are completely different from the experimental ones, decaying much faster and falling to very low intensities at 5 Torr. The simulation at 5 Torr are one order of magnitude lower than the experiment while they are only a factor 2 lower at 1Torr, for all Ar excitation cross-section. Indeed at 5 Torr the difference between experiment and simulation is of a factor 10 to 15 (depending on the chosen cross-section), which is somewhat close to what was observed for oxygen lines (where a factor 8 at 5 Torr is observed). The mixture of all the different gases is probably the cause of the inaccurate tail of the EEDF. O actinometry in CO_2 plasmas is unlikely to give an accurate trend of the O atom density because the ratio of I_{sim}/I_{exp} is very different for O and Ar.

Having said this, the proper actinometry calculation can still be carried on. The results for 4 different combinations of collision data ($\sigma_{EEDF}^{Biagi}/\sigma_{EEDF}^{IST} + \sigma_{exc}^{OLaher} + \sigma_{exc}^{ArBiagi}/\sigma_{exc}^{ArZatsarinny}$) are shown on figure 2.27. The 4 available couples are shown. Here again, the actual actinometry results are plotted in plain lines, and the actinometry results normalized to the CRDS measured density are shown in dashed line (to see the trends). First, looking at the real actinometry values in plain lines, it appears that the actual values measured by actinometry are much lower than the one measured by CRDS: at 1Torr, the actinometry is about 3 times lower than CRDS for all lines but at 5 Torr, the actinometry is about 4.5 times lower than CRDS when using the Ar750 line and about 10 times lower than CRDS if using the Ar811 line. This points toward a conclusion already shown in O_2: the Ar750 line is more appropriate for actinometry than the Ar811.

Comparing the trends of actinometry and CRDS, it appears that the trends are not very well reproduced when using the Ar811 line and are better using Ar750. Though O845 seems to give slightly better results than O777, the difference is not very strong. Hence, the conclusion on CO_2 is the same as in O_2: actinometry, using the good combination collision data, can give a good idea of the trends and of the orders of magnitude because the errors made in the description of the EEDF are compensated when doing a ratio, but cannot be trusted for absolute values.

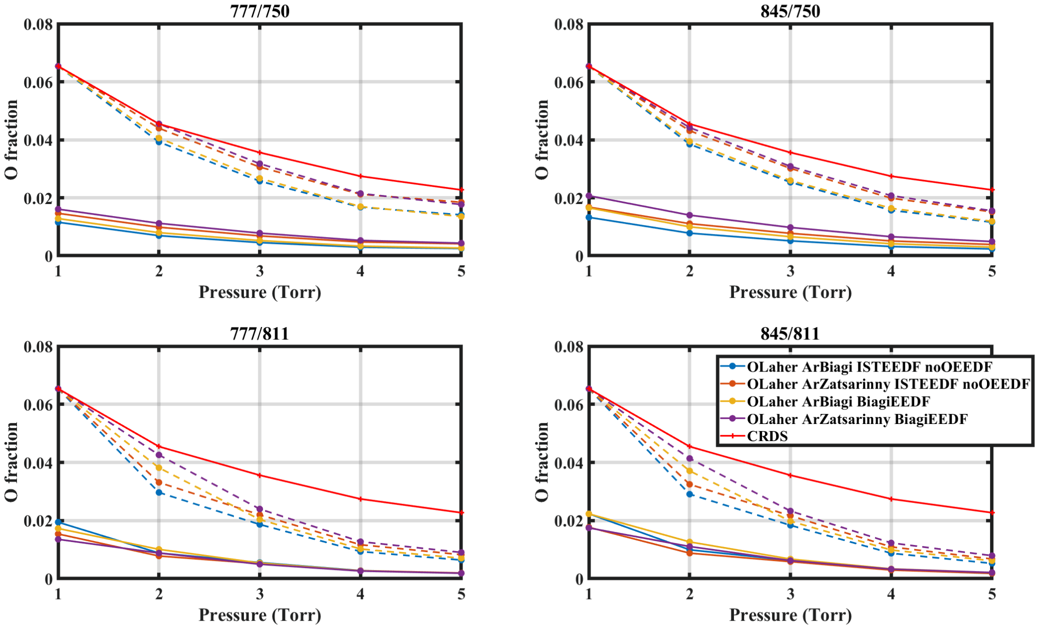

Figure 2.27: Comparison of the actinometry (for 4 different combinations) and CRDS measured O densities in a 95:5 CO_2:Ar. The CRDS lines are in red, the actinometry measurement in plain line and the actinometry results normalized by the CRDS fraction at 1 Torr (to observe the evolution of the trend) are in dashed line

In the case of CO_2, using a different set of collision data might yield better agreement between CRDS and actinometry, but this would be only more uncontrolled error compensation.

- in pure CO_2, the error on [O] from actinometry is larger than in pure O_2, perhaps because of larger inaccuracy of the EEDF calculation
- O845/Ar750 remains the most reliable ratio for O atoms density determination by actinometry even in pure CO_2 plasma

2.8 On Pagnon's cross-sections

As mentioned earlier, one of the first work comparing actinometry measurement with another diagnostic was done in Pagnon et al. 1995, using VUV spectroscopy as reference diagnostic. In this work, Pagnon claimed to use the Laher cross-section for both O levels excitation cross-sections and the Puech cross-section for Ar(2P1) excitation (the Ar(2P9) level was not used in Pagnon's work). However, comparing the cross-sections given in Pagnon et al. 1995 with their original sources showed a difference (a shift on the electron energy axis). Given the good results in terms of measured density shown by Pagnon, these cross-sections are worth investigating.

2.8.1 95O_2:5Ar case

The emission intensities obtained when using the Pagnon cross-sections are studied on figure 2.28, in the 95O_2:5Ar case.

Only the IST set is used here. Starting with the O777 line, it appears that using the Pagnon cross-section is very close to using the Laher one. Using Pagnon's cross-setion for O845 yields a worse agreement than Laher. The Pagnon cross-section predicts close absolute intensities for both O levels, whereas in reality the absolute intensity of the O845 line should be twice as high as the O777 line. For the Ar line, the direct calculation is presented in

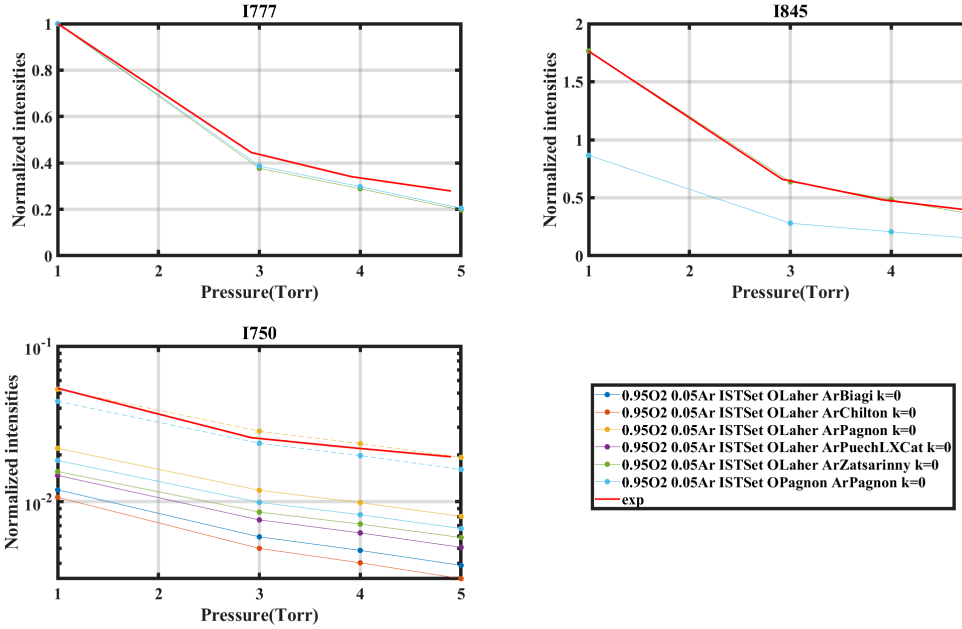

Figure 2.28: Comparison of the experimental emission intensities and the simulated including the Pagnon cross-section. The points using Pagnon's cross-section are plotted with '+' markers

plain line. In dashed is showed the direct calculation multiplied by a factor 2, allowing for comparison of the trends of the two lines. Because of the lower threshold, changing the O excitation cross-section will impact the Ar line. Therefore two combinations must be checked: both the case $\sigma_{EEDF}^{IST-noOatoms} + \sigma_{exc}^{OLaher} + \sigma_{exc}^{ArPagnon}$ (i.e Pagnon's cross-section for Ar only) and $\sigma_{EEDF}^{IST-noOatoms} + \sigma_{exc}^{OPagnon} + \sigma_{exc}^{OPagnon}$ (i.e Pagnon's cross-section for both O and Ar) are shown. In both cases, the direct calculations yield better results than with the other lines, predicting a line intensity closer to the experimental one. The results are the best when keeping the Laher cross-sections for O excitation and using the Pagnon cross-section for Ar. In both cases, however, the trend of the line with pressure (and therefore with reduced electric field) are very well reproduced (like for the other cross-sections). Hence, using the Pagnon Ar cross-section for actinometry calculation might yield better results (because the ratio I_O/I_{Ar} is closer to experiment). The actinometry calculations are shown on figure 2.29. The values yielded by actinometry are plotted in dashed lines, while the O fraction normalized by the CRDS measured O fraction at 1 Torr is shown in dashed line (to compare trends). As expected, Pagnon's cross-section yield much better results than other cross-sections. For the O777/Ar750 ratio, the Laher for O excitation and Pagnon for Ar excitation yields better results than the others, though the trends are not as good. Suprisingly, for the O845/Ar750 ratio, the values obtained using Pagnon's cross-section for both Oxygen and Argon gives good agreement with CRDS, better than the $\sigma_{exc}^{OLaher} + \sigma_{exc}^{ArPagnon}$. However the trends are in this case not as good as for any other combination. In conclusion, using the combination $\sigma_{EEDF}^{IST-noOatoms} + \sigma_{exc}^{OLaher} + \sigma_{exc}^{ArPagnon}$ for the O845/Ar750 ratio could be a good trade off despite the opacity of the method used to get $\sigma_{exc}^{ArPagnon}$. Though the O fractions trends are not as good as with the previous "best choice", the values of fraction are much better.

- The cross sections given in Pagnon et al Pagnon et al. 1995 is often used in literature foractinometry on O atoms but they do not corresponds to the ones given in initial sources for O atoms (Laher et al. 1990) and Ar (Puech et al. 1986)
- Despite this problem, using the combination $\sigma_{EEDF}^{IST-noOatoms} + \sigma_{exc}^{OLaher} + \sigma_{exc}^{ArPagnon}$ provides good actinometry results

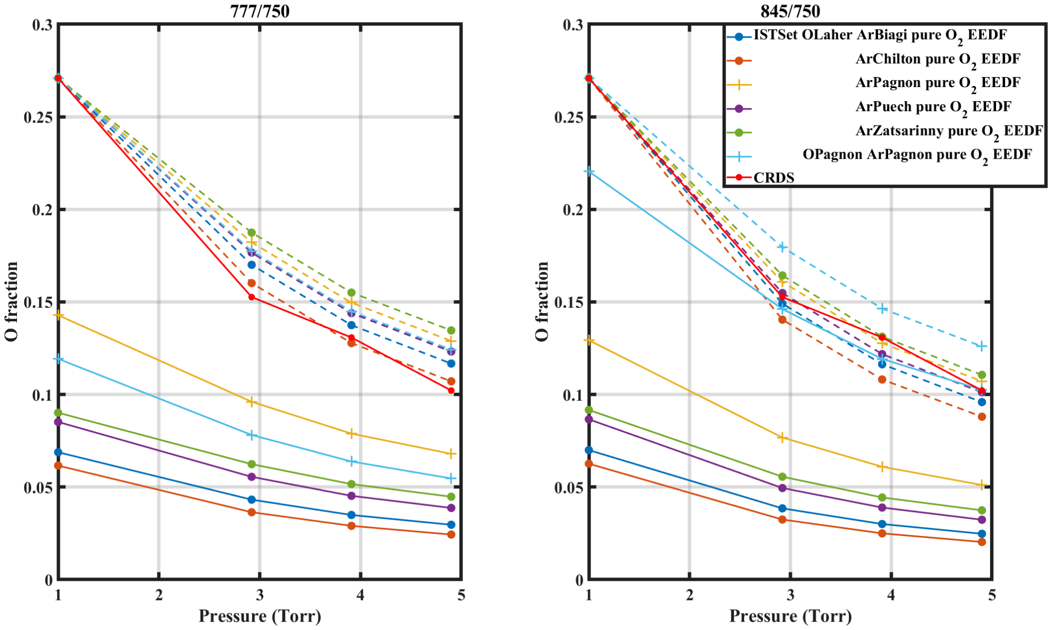

Figure 2.29: Comparison of the O fraction measured by actinometry with different set of parameters (including the Pagnon cross-sections) and by CRDS in a 95:5 O_2:Ar discharge. The CRDS is in red, the points using Pagnon's cross-section are plotted with '+' markers'

2.8.2 95CO_2:5Ar case

The line intensities are not shown here because they are very similar to the previous case: using Pagnon's cross-sections for O yield an emission of the O777 similar to the Laher one, but an emission of the O845 line much lower. Similarly, the difference between experiment and simulation is reduced for the 750 line when using Pagnon's cross-section for Ar. However the trends of the 3 lines O777, O845 and Ar750 remain similar to the one shown on figure 2.26 because the tail of the EEDF remains inaccurate in the CO_2:Ar mixture. We therefore show directly the actinometry calculation on figure 2.30. The conclusion are once again similar to the O_2 case: looking at the direct results of actinometry, the values given when using the Pagnon cross-section (either for Ar or for both gases) are better than with other cross-sections. In particular, the case of O845/Ar750 gives again a good agreement between CRDS and actinometry. The trend of ratio O845/Ar750 is best reproduced when using the Pagnon cross-sections for both gases. Using it only for Argon still give better results than with other sources. As this goes against the prediction of line intensities, this points toward a good error compensation.

Despite resulting from an error, the Pagnon's cross-section seem to be best suited for actinometry. Unfortunately, only the excitation cross-section for Ar(2P1) is available. Despite the good values given by the ratio O845/Ar750 using both Ar cross-section, the trend not well reproduced seem to indicate that this agreement is due to error compensation and is therefore less trustable. Hence, the combination IST + Laher for O + Pagnon for Ar seem to be the best one so far. The results (not presented here) are also very good when using the Biagi set for computation of the EEDF.

2.9 general conclusion on O actinometry with Ar

Actinometry is a powerful OES-based technique. Its accuracy depends on collision data available in literature and even the works reporting comparison with other diagnostics methods are sometimes contradictory. When comparing only the results of lines ratios with other measure-

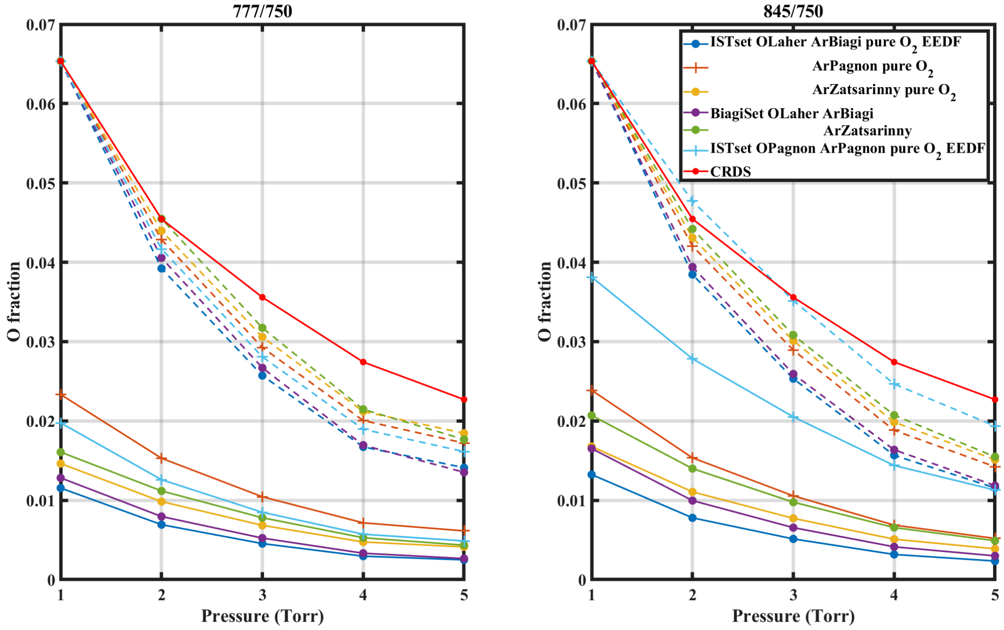

Figure 2.30: Comparison of the O fraction measured by actinometry with different set of parameters (including the Pagnon cross-sections) and by CRDS in a 95:5 CO_2:Ar discharge. The CRDS is in red, the points using Pagnon's cross-section are plotted with '+' markers'

ments, an ambiguity can arise due to error compensation on whether the set of cross sections is correct or not. An original approach has therefore been used in this work by analysing directly the variation of each individual line intensity with pressure (*ie* E/N) thanks to the O atoms density and gas temperature obtained from CRDS measurements. After analyzing the experimental intensities with the ones computed using a basic excitation scheme and several versions of the collision data, we could draw a particular set that seemed to reproduce rather well the trends. However, both in the emission intensity an later in the proper actinometry calculation, the predicted data were off by a factor 2 compared to experimental values in O_2. We attributed this to a problem on the computation of the Ar excitation, likely due to an inaccurate computation of the tail of the EEDF in an O_2:Ar mixture. It was indeed also shown that the more Ar in the mixture, the worse the agreement between experiment and simulation, leading to suspicions on the accuracy of the EEDF in the mixture. The suspicions were later confirmed with the simulation of the emission in a CO_2 discharge. Despite this offset, selecting the good parameters allow to reproduce rather well the trends and gives a correct estimation of the order of magnitude of the atomic density in the plasma. If one single combination should be used, the recommendation would be to use the IST set (and assuming no atomic Oxygen in the EEDF), with the Laher excitation cross-section for O($3p^3P$) (radiating at 84nm) and the Biagi excitation cross-section for Ar(2P1) (radiating at 750nm). **Therefore, it can be concluded that actinometry is a very powerful tool allowing to get a fast and reliable estimation of the orders of magnitude and trends of atomic density in the plasma. However, accurate O atom density measurement are challenging and probably require a better description of the tail of the EEDF.**

The diagnostic was however only tested in a limited range of E/N (from 40 to 90 Td). Given the sentivity of the EEDF to the reduced electric field, the comparison between actinometry and another diagnostic should be extended to a higher range of E/N. This might be difficult as reaching a high E/N in the glow discharge requires to lower the pressure, but it should nevertheless be investigated.

On the work done about actinometry for O atoms density determination:

- An original method has been used to constraint collisional data by calculating individual emission line intensity from CRDS data to compare with measured ones
- Trends of both individual lines and [O] atoms densities are well reproduced with the combination of $(\sigma_{EEDF}^{IST-noOatoms} + \sigma_{exc}^{OLaher} + \sigma_{exc}^{ArBiagi})$
- The addition of Argon in the mixture seems to make the calculation of the tail of the EEDF less accurate, affecting in turn the accuracy of O atoms density determination by actinometry
- The diagnostic was tested in a limited range of E/N (from 40 to 90 Td) which should be extended in future work.

2.10 H actinometry

Oxygen atoms are by far the most studied species by actinometry, which was useful for the whole validation study described above. However, in the context of this thesis on CO2/CH4 plasmas, oxygen atoms are not the only important atomic species that can be measured by actinometry. Indeed, actinometry could also be used in principle to compute the density of atomic hydrogen in the mixture as done in Krištof et al. 2016. This might however reveal more challenging than in the case of Oxygen. Indeed, the line often chosen for the H actinometry is the Hα line at 656nm from the Balmer series. This lines radiates from the H(n=3) level to the H(n=2) level of the hydrogen atom. Following the actinometry scheme proposed in Krištof et al. 2016, the upper level can be populated by electron impact and by dissociative excitation of H_2 (radiative cascade from higher levels can be neglected). It was checked that the cases studied in this work (CO_2-CH_4 low pressure glow discharges), electron impact is the main population mechanism of the upper level, i.e $k_{dissociativeExcitation}$*$[H_2]$«$k^e_{exc}$*[H]. The excitation threshold of the H(n=3) level is located at approximately 12.1eV (using the Rydberg formula), thus making the excitation threshold of the H closer to the Ar then the O. In theory, this should make the H actinometry using Ar more reliable than the O actinometry as the difference between the threshold are smaller, thus minimizing the error due to the EEDF. However in our conditions, a great number of species are present in the plasma (CO_2, CO, CH_4 and its by-products CH_3, CH_2, CH..., H_2, H, H_2O, OH...) and many of them do not have a complete and consistent set of cross-section to describe them. The EEDF calculation accuracy can therefore be difficult to assess. Two solutions arise: either to neglect the least important species and keep only the major species whose cross-sections are deemed trustable, or to use all electron impact cross-sections for this species available in literature. We have chosen the first option, but both solutions pose issues on the validity of the EEDF, especially in the tail. Hence, the frame of the use of the H actinometry is the same as for O actinometry: H actinometry is very suited for measuring trends and orders of magnitude, but is unlikely to be accurate for absolute H density. For accurate quantitative measurement, other diagnostics must be used, such as Two photon Absorption Laser Induced Fluorescence (TALIF). No comparative study of the parameters, similar to the work done for O actinometry, has been done for H actinometry as it mainly served for orders of magnitude. A few results of H atoms measurements by actinometry will be shown in the Chapter 4.1 that will be anlalysed using the collisional quenching coefficient given in table 2.5.

Specie	Ar	Kr	H_2	O_2	H_2	CO	CO_2
collisional quenching of H(n=3) $(10^{-16} m^3/s)$ from Bittner et al. 1988	4.6	11	19.9	26	11	29.7	35

Table 2.5: Collisional quenching coefficients used for H actinometry

2.11 Optical measurement of the reduced electric field

A variant of actinometry consists in using the ratio of two line intensities, not to determine the density of an atomic species, but to deduce the value of E/N. Theoretically, by using equation (2.1) for 2 lines of the same species and making the ratios,one gets:

$$\frac{I_1}{I_2} = \frac{C_1}{C_2} * \frac{\nu_1}{\nu 2} * \frac{k_1}{k_2} * \frac{a_1}{a_2} \tag{2.27}$$

$$\frac{k_1}{k_2}(E/N) = \frac{I_1}{I_2} * \frac{C_2}{C_1} * \frac{\lambda_1}{\lambda_2} * \frac{a_2}{a_1} \tag{2.28}$$

In other words, the ratio of the rate coefficients of two excited levels of the same specie can be expressed as a function the ratio of the line intensities, the wavelengths and the effective branching ratio. The measurement of the ratio of the rate coefficients is done by simply measuring two lines. But this ratio can also be computed with a Boltzmann solver, using the temperature, the composition and the reduced electric field. At constant composition, if the levels 1 and 2 are properly chosen, then k_1/k_2 is a monotonous function of E/N. Therefore, by simulating the EEDF for a large number of E/N and comparing the simulated and experimental ratio of the rate coefficients, the discharge reduced electric field can be found. This method is similar to the one used in Tsutsumi et al. 2017, the main difference being that in Tsutsumi et al. 2017 the tested parameter is the electron energy (and not the reduced electric field). Another way to challenge the accuracy of the collision data used for actinometry would be to compare the E/N obtained from line ratios with the one measured from E at the tungsten pins and from gas temperature obtained with CRDS. To be successful, this technique requires both calculated rate coefficient to be accurate. The technique was tested in the pure oxygen discharge. It was previously shown that a good computation of both oxygen lines (and therefore rate coefficient) could be achieved in the pure O_2 discharge if a pure O_2 EEDF using the IST set was used. One advantage is that because the O atoms is neglected, the knowledge of the dissociation degree in the plasma is not necessary. In the case of oxygen, independently of source chosen for the excitation cross-sections, the function k_{845}/k_{777} is a growing function of E/N. This technique however poses a problem when using the oxygen lines because the variation of the ratio on a large range of E/N is limited. This is visible on figure 2.31 where the evolution of the ratio as a function of E/N between 20 and 80 Td is plotted for a pure O_2 EEDF at 5 Torr.

Between 40 and 80Td, the ratio varies only of 15% (from 1.7 at 40Td to approximately 2.04 at 80Td), which means that for the optically measured E/N to be accurate within ∼10%, the intensities measured must be very accurate within less than ∼3% (which is very complicated in case of convolution of the bands in N_2/O_2 mixtures for example).

Moreover, it was concluded from line intensities simulation that the calculation of the rate coefficient was inaccurate and not in good agreement with the experiment, which means that the curve of the ratio of the simulated rate coefficient will likely be inaccurate as well. Considering the low variation of the curve over a range of reduced electric field of interest, together with the fact that calculating ratios of excitation coefficients is too inaccurate makes the reduced electric field measurement unreliable. The example is visible on figure 2.31 where the optically measured ratio of the rates is shown (yellow line). The measured reduced electric field at the pins is shown in yellow, from which can be inferred the expected value of the ratio of excitation coefficient. The optically measured ratio is 1.69, yielding a reduced field of approximately 40 Td, while the value of the ratio using the measured value is 1.95 corresponding to an E/N of 68 Td. The difference on the ratio of excitation coefficient is only of 13%, but the electric field is off by almost 30 Td. Finally, this technique is extremely dependant on the excitation cross-sections. Figure 2.32 show the E/N deduced from the ratio of emission lines as a function of the reduced electric field measured at the pins for different combinations of $\sigma^{set}_{EEDF}\sigma_{exc};\sigma_{exc}$. The red line if the curve E/$N_{line\ ratio}$=E/$N_{pins+CRDS}$. No combination allow to reproduce well the E/N measured with the pins and the CRDS, even using the combination which previously yielded the best results for intensity calculations. Both the values and the trends are off, often

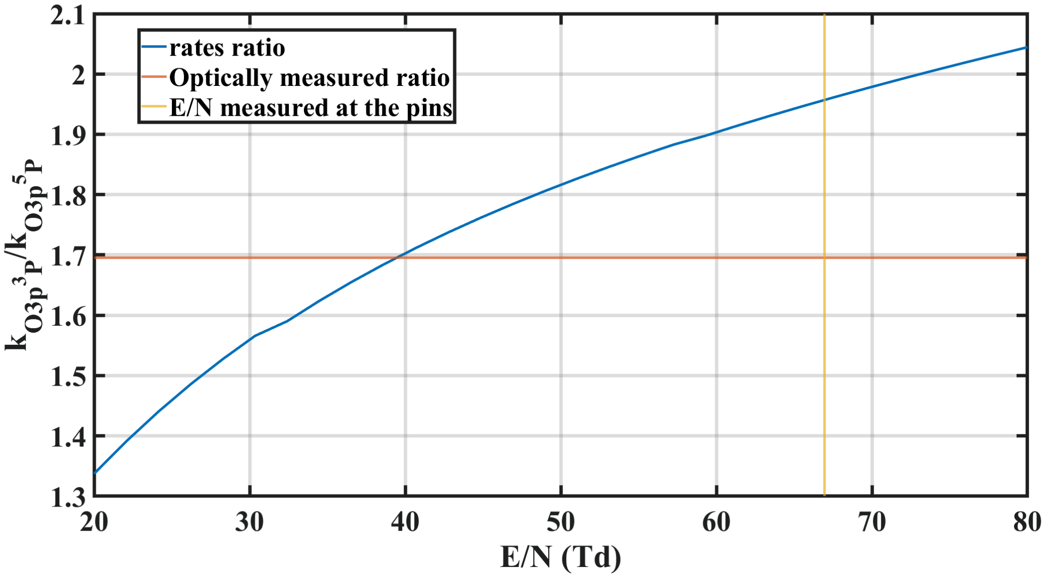

Figure 2.31: Ratio of the oxygen excitation rate coefficients as a function of the reduced electric field for a 1Torr EEDF assuming pure O_2, using the Laher excitation cross-sections. The yellow line indicates the value of the electric field measured at the pins, the orange one the value of the "optically" measured value of the ratio of the rate coefficient

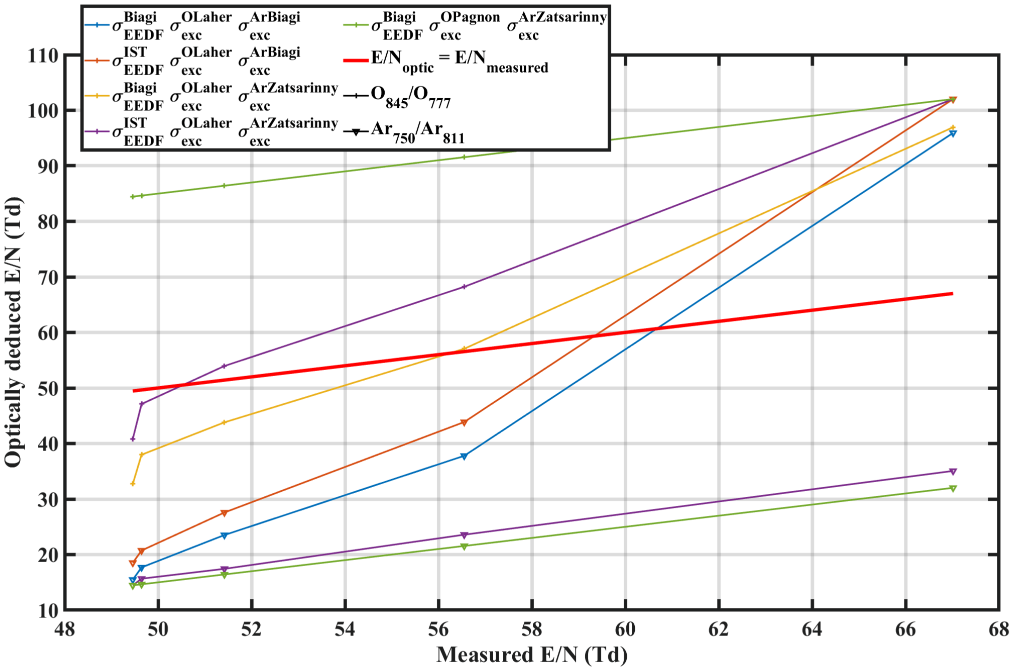

Figure 2.32: Plot of the E/N deduced from line ratio (optically deduced) as a function of the E/N measured with the pins and the CRDS temperature for different combinations of $\sigma^{set}_{EEDF}\sigma_{exc};\sigma_{exc}$. The red line is E/N$_{line\ ratio}$=E/N$_{pins+CRDS}$. The + marker are curves obtained using O_{845}/O_{777}, the triangle markers are obtaines using Ar_{750}/Ar_{811}

by several tens of Td. For O atoms as well as for Ar line ratios, this technique is unreliable in our reduced electric field range.

Another valuable electron properties information which could be obtained would be the shape of the EEDF. This technique was reviewed in Donnelly 2004: traces of different rare gases are admixed in the plasma. Emissions corresponding to levels with different excitation thresholds of all the rare gases are measured and the shape of the EEDF is reconstructed from the intensity of the various peaks. This technique is very interesting because a system of equations is built from the emissions values, with the only unknown being the EEDF. The EEDF can then be fitted. The huge asset of this technique is that it does not rely on the EEDF computation with a Boltzmann solver (which was showed to be unreliable in some cases). However, this technique also has two major drawbacks: first, the computation is very costly if the shape of the EEDF is free. For computations doable with a normal computer, a shape (often Maxwellian) must be assumed. Second, this technique is dependent on the excitation cross-sections of each level, i.e have a large uncertainty. Nevertheless, applying this technique and comparing it to the computed EEDF could help constraining the EEDF computation by a Boltzmann solver and identify the cause of the mismatch discussed in previous sections.

Despite its apparent simplicity, it appears that actinometry in our glow discharge conditions in CO_2/CH_4 can be used only for trends of O and H atoms densities. This will be exploited in chapter 4.1. Beyond atomic densities obtained by actinometry, optical emission spectroscopy, even with poor spectral resolution, can provide other valuable information for CO_2/CH_4 as it will be described in the next chapter.

Appendix: Fraction computation

When the dissociation fraction is taken into account in either the actinometry or the absolute intensities calculations, the fractions of various gases must be calculated once the O fraction is assumed. This section aims at showing how the calculation is done. The goal is to solve:

$$CO_2 + O_2 + X \rightarrow CO + ?O + ?O_2 + X \tag{2.29}$$

as a function of known parameters, leaving only one unknown parameter. X is a specie that will not be dissociated (Ar, N_2...). It is assumed here that the dissociation degree of CO_2, α, is known. A similar quantity, β can be used to describe the O_2 dissociation degree.

$$\alpha = \frac{[CO]}{[CO]+[CO_2]} \rightarrow [CO_2] = \frac{1-\alpha}{\alpha}[CO] \tag{2.30}$$

$$\text{Hence } [CO]+[CO_2] = [CO] + \frac{1-\alpha}{\alpha}[CO] = \frac{1}{\alpha}[CO] \tag{2.31}$$

$$\beta = \frac{[O]}{[O]+[O_2]} \rightarrow [O_2] = \frac{1-\beta}{\beta}[O] \tag{2.32}$$

$$\text{Similarly } [O]+[O_2] = [O] + \frac{1-\beta}{\beta}[O] = \frac{1}{\beta}[O] \tag{2.33}$$

$$\tag{2.34}$$

To simplify the notation in the calculation, we also define g (fractions of initial species that will lead to atomic O creation) and j (share of CO_2 in these species) through:

$$g = \frac{[CO_2]_{ini} + [O_2]_{ini}}{[CO_2]_{ini} + [O_2]_{ini} + [X]_{ini}} \tag{2.35}$$

$$j = \frac{[CO_2]_{ini}}{[CO_2]_{ini} + [O_2]_{ini}} \tag{2.36}$$

The atom conservation can also be used:

$$\text{Carbon conservation : } [CO_2]_{ini} = [CO_2] + [CO] \tag{2.37}$$

$$\text{Oxygen conservation : } 2[CO_2]_{ini} + 2[O_2]_{ini} = 2[CO_2] + 2[O_2] + [O] + [CO] \tag{2.38}$$

$$\rightarrow 2([CO_2]+[CO]) + 2[O_2]_ini = 2[CO_2] + 2[O_2] + [O] + [CO] \tag{2.39}$$

$$\rightarrow [CO] + 2[O_2]_{ini} = 2[O_2] + [O] \tag{2.40}$$

Using g and j:

$$[O_2]_{ini} = \frac{1-j}{j}[CO_2]_{ini} = \frac{1-j}{j}([CO_2]+[CO]) \tag{2.41}$$

$$[X] = \frac{1-g}{g}([CO_2]_{ini} + [O_2]_{ini}) \tag{2.42}$$

$$= \frac{1-g}{g}(1+\frac{1-j}{j})[CO2]_{ini} \tag{2.43}$$

$$= \frac{1-g}{g}(1+\frac{1-j}{j})([CO2]+[CO]) \tag{2.44}$$

$$= \frac{1-g}{gj}([CO2]+[CO]) \tag{2.45}$$

To express the fractions, the density must first be calculated:

$$N = [CO_2] + [CO] + [O_2] + [O] + [X] \tag{2.46}$$

Using α, β, j and g (with only β unknown), the density can be expressed only as a function of [O] an [CO]:

$$
\begin{aligned}
N &= \frac{1-\alpha}{\alpha}[CO] + [CO] + \frac{1-\beta}{\beta}[O] + [O] + \frac{1-g}{gj}([CO2] + [CO]) && (2.47)\\
&= \frac{1}{\alpha}[CO] + \frac{1}{\beta}[O] + \frac{1-g}{\alpha g j}[CO] && (2.48)\\
&= \frac{g(j-1)+1}{\alpha g j}[CO] + \frac{1}{\beta}[O] && (2.49)
\end{aligned}
$$

Finally, [O] must be expressed as a function [CO]. Using Atom conservation, one gets:

$$
\begin{aligned}
[O] + 2[O_2] &= [CO] + 2[O_2]_{ini} && (2.50)\\
[O] + 2\frac{1-\beta}{\beta} &= [CO] + 2\frac{1-j}{j}([CO_2] + [CO]) && (2.51)\\
\frac{2-\beta}{\beta}[O] &= [CO](1 + \frac{2-2j}{j\alpha}) && (2.52)\\
\frac{2-\beta}{\beta}[O] &= \frac{j(\alpha-2)+2}{j\alpha}[CO] && (2.53)\\
[O] &= \frac{\beta}{2-\beta}\frac{j(\alpha-2)+2}{j\alpha}[CO] && (2.54)
\end{aligned}
$$

Finally,

$$
\begin{aligned}
N &= \frac{g(j-1)+1}{\alpha g j}[CO] + \frac{1}{\beta}[O] && (2.55)\\
&= (\frac{g(j-1)+1}{\alpha g j} + \frac{j(\alpha-2)+2}{(2-\beta)j\alpha})[CO] && (2.56)\\
&= \frac{2 - gj\beta + g\beta - \beta + gj\alpha}{gj\alpha(2-\beta)}[CO] && (2.57)\\
& && (2.58)
\end{aligned}
$$

From there, the fractions are easily computed:

$$
\begin{aligned}
f_{CO} &= \frac{[CO]}{N} && (2.59)\\
&= \frac{gj\alpha(2-\beta)}{2 - gj\beta + g\beta - \beta + gj\alpha} && (2.60)\\
f_{CO_2} &= \frac{1-\alpha}{\alpha} f_{CO} && (2.61)\\
&= \frac{gj(1-\alpha)(2-\beta)}{2 - gj\beta + g\beta - \beta + gj\alpha} && (2.62)\\
f_O &= \frac{\beta}{2-\beta}\frac{j(\alpha-2)+2}{j\alpha} f_{CO} && (2.63)\\
&= \frac{g\beta * (j\alpha - 2j + 2)}{2 - gj\beta + g\beta - \beta + gj\alpha} && (2.64)\\
f_{O_2} &= \frac{1-\beta}{\beta} f_O && (2.65)\\
&= \frac{g(1-\beta) * (j\alpha - 2j + 2)}{2 - gj\beta + g\beta - \beta + gj\alpha} && (2.66)\\
& && (2.67)
\end{aligned}
$$

In the algorithm, the O fraction is not fitted properly speaking, but rather the β quantity. The fractions are then calculated from β.

CHAPTER 3

Optical emission spectroscopy for CO_2-CH_4 plasma. Emphasis on USB devices

Contents

3.1 Introduction

CO_2 containing plasma shows emission bands over a very wide spectral range from the UV to the IR, in particular because of the CO bands and the O atomic lines. When adding CH_4, H atoms lines appears and possibly other molecular bands. To obtain spectrum with a high spectral resolution from 250 to 900nm, the acquisition can be time consuming, not always easy to calibrate in intensity, and it requires to have a proper set of gratings available.It can therefore be interesting to compromise spectral resolution in order to use simpler spectrometers (described below as "USB spectrometers") allowing the acquisition of the entire visible range at once. In addition, the automation of OES acquisition and consequently its implementation as a routine diagnostic for all measurements, which will be presented in the next chapter, is greatly simplified. Therefore, in this chapter, some of the useful information that can be derived from low resolution spectra will be presented and their accuracy and validity will be discussed by comparing them either to better resolved spectra or to other techniques.

USB spectrometers are low resolution compact spectrometers, usually powered by the computer to which they are connected via the USB port. Instead of a turret which rotate to change the light sent on the exit slit in the usual spectrometers, the whole light diffracted by grating is sent on a CCD chip which record the whole spectrum at once. The resolution is limited by the short focal distance and the number of pixels on the detector. The temporal resolution is limited by the response time of the detector (usually on the order of magnitude of the ms). Light is usually sampled with the help of a collimator and is sent inside the USB spectrometer via an optical fiber. Because of their limited temporal and spectral resolution, USB spectrometers

are not fit for all applications. They are very ill-suited for several applications like nano-second discharges or broadening measurements. Despite the spectral and temporal limitations of these devices, this chapter aims at showing that, with caution, some useful information for the study of the low-pressure CO_2 plasmas can be drawn from the analysis of the spectra obtained with a USB spectrometer.
These instruments have two considerable assets. First, they are extremely easy to set-up: they can often be used with an optical fiber, connected on one side to the spectrometer and on the other side to a collimator. The collimator is simply placed in front of the area to probe. Second, they can capture a broad spectrum (from 300 to 900nm in the case of the spectrometer used in this work) in a relatively short time (down to 1ms). This can be exploited in two ways: first, it is an excellent routine diagnostic to control the plasma (any impurity or change in the plasma will be immediately visible on the spectrum), second, this allows to measure processes which take place on a large emission range. Because of their low resolution, the spectra obtained with USB spectrometer are not always straight forward to analyze. Several examples of the use of the spectra obtained with USB spectrometers in this work are shown in this chapter. In this work, the USB spectrometer used is an Ocean Optics Maya 2000 with a spectral resolution of 0.3nm.

3.2 Plasma composition monitoring

One of the first use that can be made of the USB spectrometer is the routine check of the plasma composition and the apparition of impurities. Because of the large spectral range they probe, USB spectrometers are suited for the detection at the same time of strong atomic lines from many atoms such as H, O, Ar and He among others. They can also detect the strong molecular systems like the ones of N_2 (third positive), the angstrom band of CO, the O_2(b) system. This can be used for the determination of the presence of some species in the plasma, like dissociation products in low-pressure CO_2 discharges or impurities in the gas line. One possible source of air leaking from the room inside the gas line in our setup, was coming from the pipe upstream the flowmeters before the low pressure part. Teflon pipes are typically use to connect the output of the pressure reducer to the flowmeters which will admit gas in the desired proportion in the low-pressure part of the gas line. The pressure reducer or the connection of the teflon pipe can be faulty which results in air being mixed with the gas sent in the reactor. Though air in the plasma would usually change its color to pink (due to the nitrogen), the leak can be small and undetectable with the naked eye. However, the N_2 has a very distinguishable spectrum with very strong molecular bands: the First Positive System (FPS, 700-1060 nm), the Second Positive System (SPS, 280-440 nm) and finally the N_2^+ First Negative System (FNS, 386-470 nm). At low pressure, these bands have a strong intensity even at low N_2 content and can be used to determine the presence of a leak.

The effective identification of the N_2 lines can however be difficult because other molecules have bands in the same areas, like CO. To facilitate the identification of the bands, an identification software was designed using the Matlab Application editor. The application can plot one or several spectra and plot vertical lines corresponding to line positions referenced in literature. By no mean is the application aimed at simulating the line: it only plots a vertical line at the positions associated to a certain species with data from literature. Several sources were used for the line positions. For the atom, the positions were taken from NIST (A. Kramida et al. 2022). For CO, several sources were used: Pearse et al. 1976 and Poncin-Epaillard et al. 2002 for the 4th positive system, Robinson et al. 1958 for the 3rd positive system and the angstrom band, Slanger et al. 1971 for the Asundi system, Conway 1981 and Wallace 1962 for the Cameron system, Wallace 1962 and Slanger et al. 1971 for the CO triplet system. Conway 1981 was also used for the CO^+ first negative system. For the nitrogen, Cicala et al. 2009 was used for the First Positive System, Second Positive System and First Negative System. Additionnally, the positions from Pearse et al. 1976 were also used for these systems, along with the 4th positive,

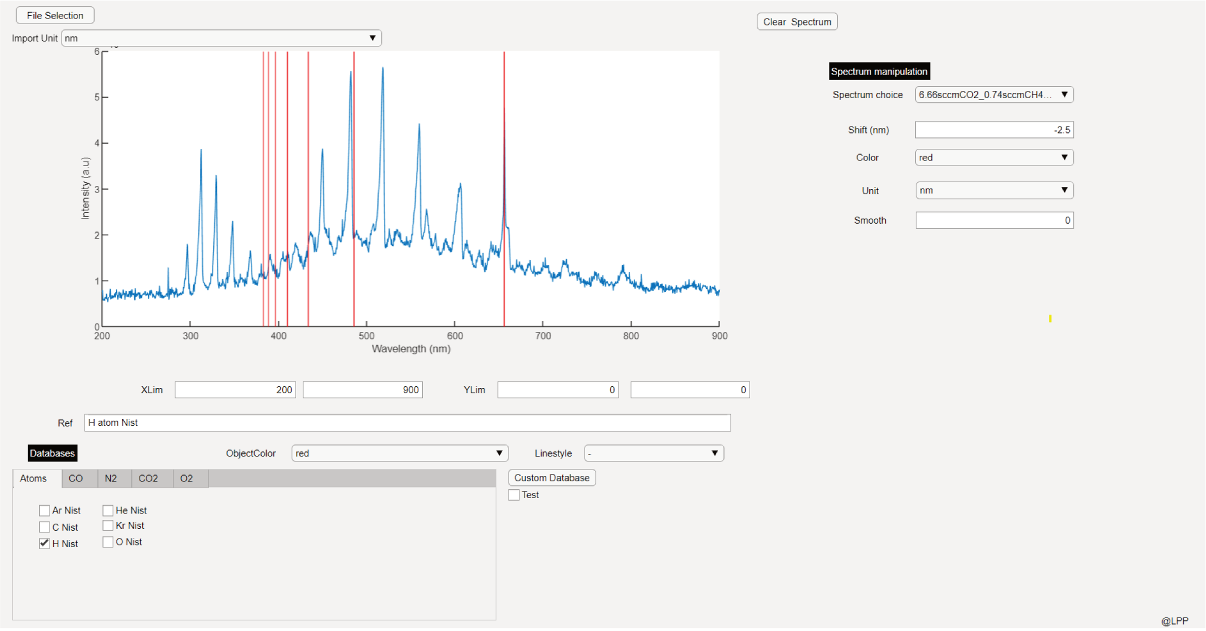

Import Unit: nm

Spectrum choice: 6.66sccmCO2_0.74sccmCH4...

Shift (nm): -2.5

Color: red

Unit: nm

Smooth: 0

XLim: 200 900

YLim: 0 0

Ref: H atom Nist

ObjectColor: red

Linestyle: -

☐ Ar Nist
☐ C Nist
☑ H Nist
☐ He Nist
☐ Kr Nist
☐ O Nist

☐ Test

Figure 3.1: Identification of the atomic H lines (in red) in a 90:10 CO_2:CH_4 plasma at 5Torr, 40mA. The lines are taken from the NIST database. The interface is the application interface.

5th positive, the Kaplan systems and several others. Finally, the lines of CO_2^+ from Gauyacq et al. 1979 were included. The application should include more species in the future. An example of the identification of the CO systems is shown on figures 3.1, 3.2 and 3.3, where a spectrum of a 90:10 CO_2:CH_4 discharge at 5Torr was measured using a USB spectrometer.
This application can conveniently be used to detect N_2 emissions. An example is given below for the identification of the lines in an homogeneous CO_2 dielectric barrier discharge at 100mbar which was taken during a test measurement campaign. The pure CO_2 conversion in DBD is notoriously low R.Snoeckx et al. 2017, so little CO was expected. Using an HRS500 spectrometer, the emission spectrum between 310 and 410 nm was observed where bands were found. This region corresponds to the CO 3^{rd} positive system, but also to the N_2 second positive system. The line identification application graph is shown on figure 3.4, where the CO 3^{rd} positive is plotted in plain black lines and the N_2 SPS lines are plotted in red. The peak position match perfectly N_2 SPS positions taken from Pearse et al. 1976, while almost no peaks are seen on the expected positions of the CO 3^{rd} positive system, indicating that not only the conversion degree of CO_2 is very low, but also that there is a leak in the gas line.

The implementation of the Ocean Optic Maya spectrometer as a routine measurement for all the conditions studied in the chapter 4 allowed us to ensure the absence of any air leak during all the acquisitions.

3.3 Determination of the rotational temperature

The determination of the rotational temperature through the fitting of the CO Angstrom band is a common technique that was repeatedly carried out in literature (Tiago Silva, Britun, et al. 2014, Y.Du et al. 2017, S.Yamada et al. 2021). The angstrom band is a transition from the CO($B^1\Sigma^+$) state to the CO($A^1\Pi$) state, with bands visible between 350 and 500nm. The v=0 → v'=1 is usually fitted to determine the temperature. The method presented here is taken from Y.Du et al. 2017.

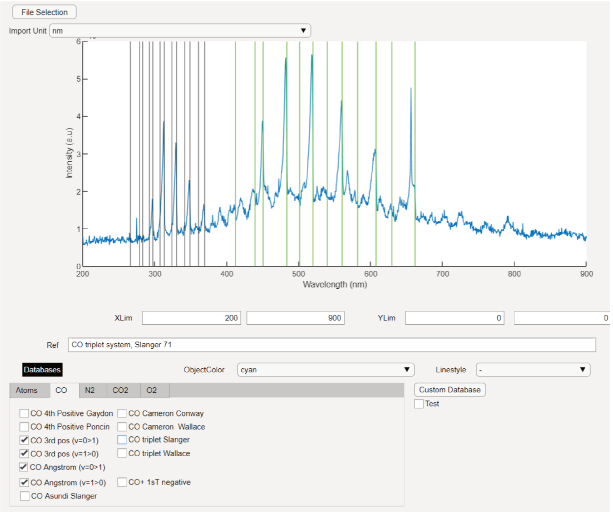

Import Unit nm

XLim 200 900 YLim 0 0

Ref CO triplet system, Slanger 71

ObjectColor cyan

Linestyle -

☐ CO 4th Positive Gaydon
☐ CO 4th Positive Poncin
☑ CO 3rd pos (v=0>1)
☑ CO 3rd pos (v=1>0)
☑ CO Angstrom (v=0>1)
☑ CO Angstrom (v=1>0)
☐ CO Asundi Slanger
☐ CO Cameron Conway
☐ CO Cameron Wallace
☐ CO triplet Slanger
☐ CO triplet Wallace
☐ CO+ 1sT negative

☐ Test

Figure 3.2: Identification of the Angstrom system (in green) and of the 3^{rd} positive (in black) in a 90:10 CO_2:CH_4 plasma at 5Torr, 40mA

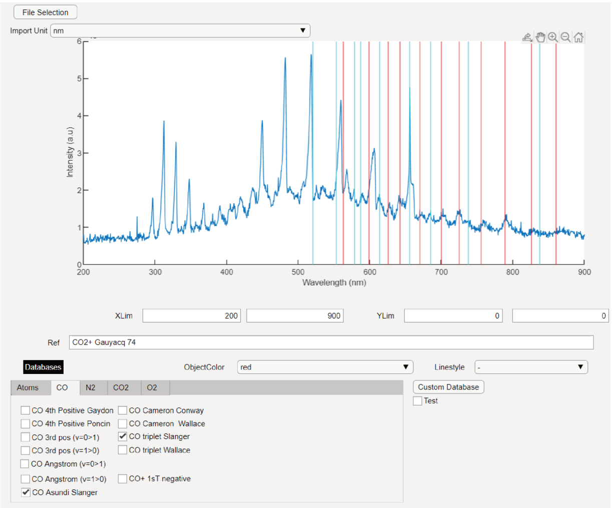

Import Unit nm

XLim 200 900 YLim 0 0

Ref CO2+ Gauyacq 74

ObjectColor red

Linestyle -

☐ CO 4th Positive Gaydon
☐ CO 4th Positive Poncin
☐ CO 3rd pos (v=0>1)
☐ CO 3rd pos (v=1>0)
☐ CO Angstrom (v=0>1)
☐ CO Angstrom (v=1>0)
☑ CO Asundi Slanger
☐ CO Cameron Conway
☐ CO Cameron Wallace
☑ CO triplet Slanger
☐ CO triplet Wallace
☐ CO+ 1sT negative

☐ Test

Figure 3.3: Identification of the CO Triplet system (in red) and of the Asundi system (in cyan) in a 90:10 CO_2:CH_4 plasma at 5Torr, 40mA

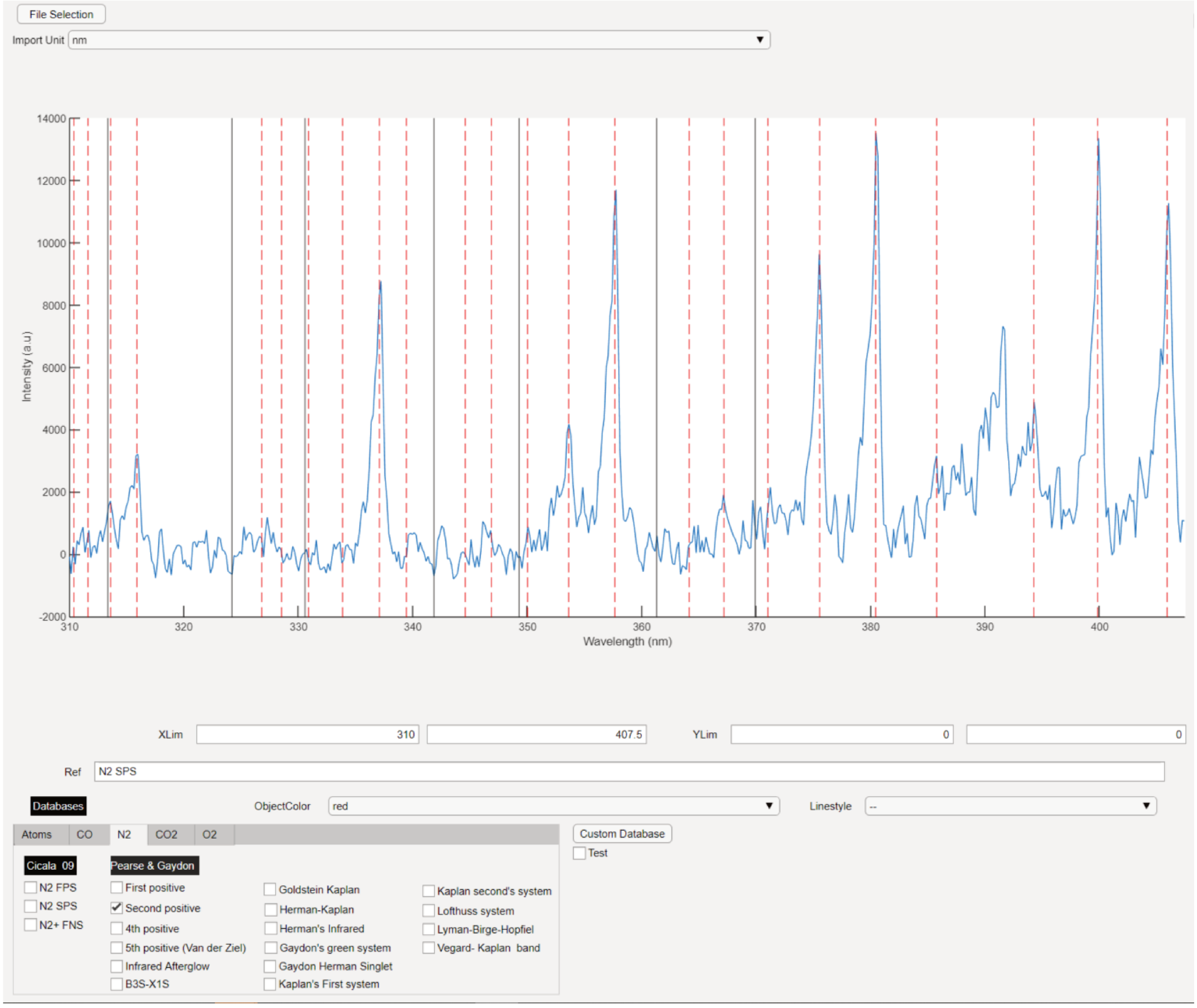

Import Unit nm

XLim 310 407.5 YLim 0 0

Ref N2 SPS

ObjectColor red

Linestyle --

☐ N2 FPS
☐ N2 SPS
☐ N2+ FNS

☐ First positive
☑ Second positive
☐ 4th positive
☐ 5th positive (Van der Ziel)
☐ Infrared Afterglow
☐ B3S-X1S
☐ Goldstein Kaplan
☐ Herman-Kaplan
☐ Herman's Infrared
☐ Gaydon's green system
☐ Gaydon Herman Singlet
☐ Kaplan's First system
☐ Kaplan second's system
☐ Lofthuss system
☐ Lyman-Birge-Hopfiel
☐ Vegard- Kaplan band

☐ Test

Figure 3.4: Identification of lines observed between 310 and 410nm in a pure CO_2 homogeneous DBD at 100mbar. The CO 3rd positive lines are plotted in plain black lines, the N_2 Second Positive System is red dashed lines. The peak positions match the N_2

3.3.1 Equations

Using a Boltzmann distribution, the intensity of a peak corresponding to the transition ($B^1\Sigma^+$, v=0, J → $A^1\Pi$, v'=1, J') is given by :

$$I_\nu = \nu^4 * S_{ij} * exp(-\frac{F_v(J) * hc}{T_{rot} * k_b}) \tag{3.1}$$

where ν is the frequency of the transition, S_{ij} is the line strength of the transition, Trot the rotational temperature, k_b the Boltzmann constant and F_v(J) the energy of the rotational level. It must be noted that this equation involves the rotational temperature of the CO($B^1\Sigma^+$) state (and not the rotational temperature of the ground state) and that is is assumed that the rotational temperature of the B state is at equilibrium with the ground state. It was shown in Y.Du et al. 2017 that this is most often the case when the CO(B) state is populated through electron impact excitation of CO which conserves the rotational distribution (which is the case in our discharge), but some types of discharges might not conserve the distribution. In the case of an NRP, the distribution must probably be recalculated (it is when deducing the temperature from N_2(C) in Ceppelli et al. 2021). F_v(J) can be calculated with :

$$F_v(J) = B * J * (J+1) - D * J^2 * (J+1)^2 \tag{3.2}$$

where B and D are the rotational constant of the emitting level. B_0 and D_0 are taken from Y.Du et al. 2017:

$$B_0 = 1.94808 cm^{-1} \ \& \ D_O = 6.33.10^{-6} cm^{-1}$$

The line strength depends on the initial and final electronic state and from the initial and final rotational level. Here, for the selected transition, $\Delta\Lambda$=1, so the lines strength for the branches P,Q and R can be computed with :

$$S_{P(j)} = \frac{(J-\Lambda-1)(J-\Lambda)}{2J} \tag{3.3}$$

$$S_{Q(j)} = \frac{(J-\Lambda)(J+\Lambda+1)(2J+1)}{2J(J+1)} \tag{3.4}$$

$$S_{R(j)} = \frac{(J+\Lambda+1)(J+\Lambda+2)}{2(J+1)} \tag{3.5}$$

$$\tag{3.6}$$

Where Λ is the orbital angular momentum of all the electrons of the initial state. The formula is taken from Kovács et al. 1969. In this case, $\Lambda = 1$, which yields:

$$S_{P(j)} = \frac{(J-1)}{2} \tag{3.7}$$

$$S_{Q(j)} = J + \frac{1}{2} \tag{3.8}$$

$$S_{R(j)} = \frac{J}{2} + 1 \tag{3.9}$$

$$\tag{3.10}$$

The line positions used in equation (3.1) are taken from D.Coster et al. 1934, but they can vary in literature. Some positions (for low J) are not given for all branches in some sources. Comparison were done with line positions given in Tiago Silva, Britun, et al. 2014 and it was concluded that the positions from D.Coster et al. 1934 yielded better results. Finally, a Voigt profile (a convolution of a Gaussian and of a Lorentzian profile) is assumed for each transition

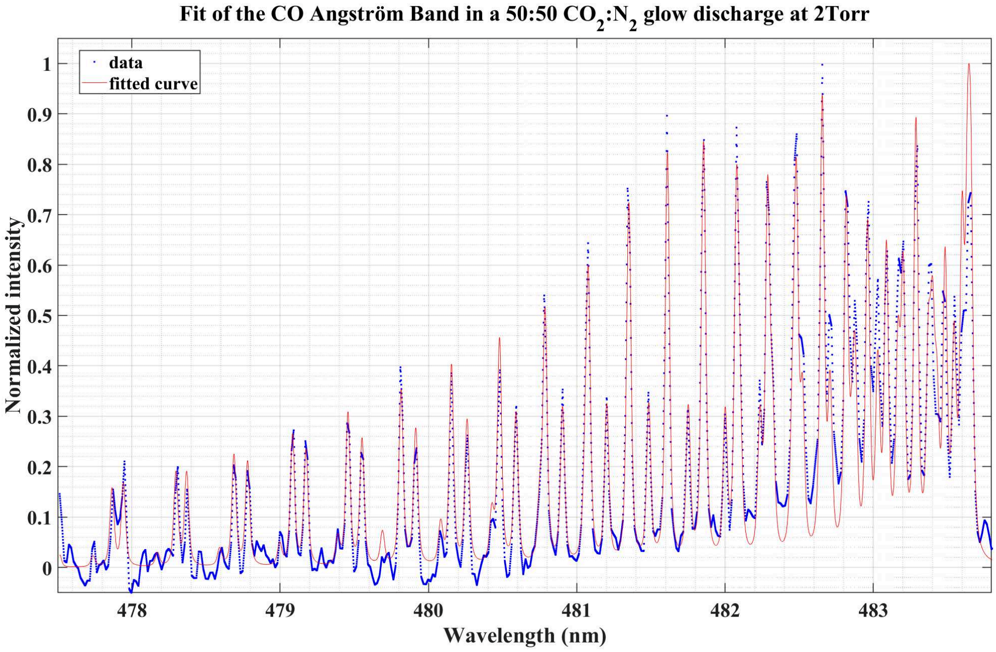

Figure 3.5: Fitting of the CO Angstrom Band in the emission spectrum of a CO_2 N_2 low pressure glow discharge. The discharge is ignited at 2Torr, 40mA in a 50:50 CO_2 N_2 mixture.

at frequency ν:

$$V_\nu(\lambda) = G(\lambda) \otimes L(\lambda) \tag{3.11}$$

$$V_\nu(\lambda) = \int_{-\infty}^{+\infty} G(\lambda - k)L(k)dk \tag{3.12}$$

$$V_\nu(\lambda) = \int_{-\infty}^{+\infty} (\frac{1}{\sigma} * \frac{1}{\sqrt{2\pi}} * exp(-\frac{(\lambda-\nu-k)^2}{2\sigma^2} * I_\nu) * \frac{\frac{L}{2\pi}}{k^2 + \frac{L^2}{4}} dk \tag{3.13}$$

$$\tag{3.14}$$

Where σ is the gaussian standard deviation and L is the Lorentzian width. The determination of the temperature by fitting is done with the help of the Matlab fit function, based on the method of the least square. Three parameters are left free in the fit: the rotational temperature T_{rot}, the gaussian deviation σ and the Lorentzian width L.

3.3.2 Validation of the temperature obtained from CO Angström band

An example of a fit of the CO Angström band is shown on figure 3.5, for a spectrum taken with a Princeton Instrument HRS500 spectrometer. The high resolution of this device allows to resolve most of the peaks of the band. To assess the validity of the fit, the results are compared with Fourier Transform Infrared spectroscopy (FTIR) measurements. The FTIR measurement is considered more reliable because the FTIR measures the rotational temperature of the ground state. The ground state rotational temperature has more time to be at equilibrium with the gas temperature and is therefore usually a more reliable measurement of the gas temperature T_g. The details of the temperature measurements by FTIR are given in Klarenaar, Engeln, et al. 2017. Several mixtures are studied: pure CO_2, 75:25 and 50:50 CO_2:N_2. For each mixtures, several pressures are investigated. The CO_2:N_2 was chosen because this diagnostic was developed in the frame of measurement done with another PhD student, Chloé Fromentin, working on CO_2-N_2 during her stay at LPP. The comparison of the temperatures measured by FTIR and OES are shown on figure 3.6. The agreement between the two techniques is relatively good. The pure CO_2 case shows the biggest difference: at 0.6 Torr, OES is about

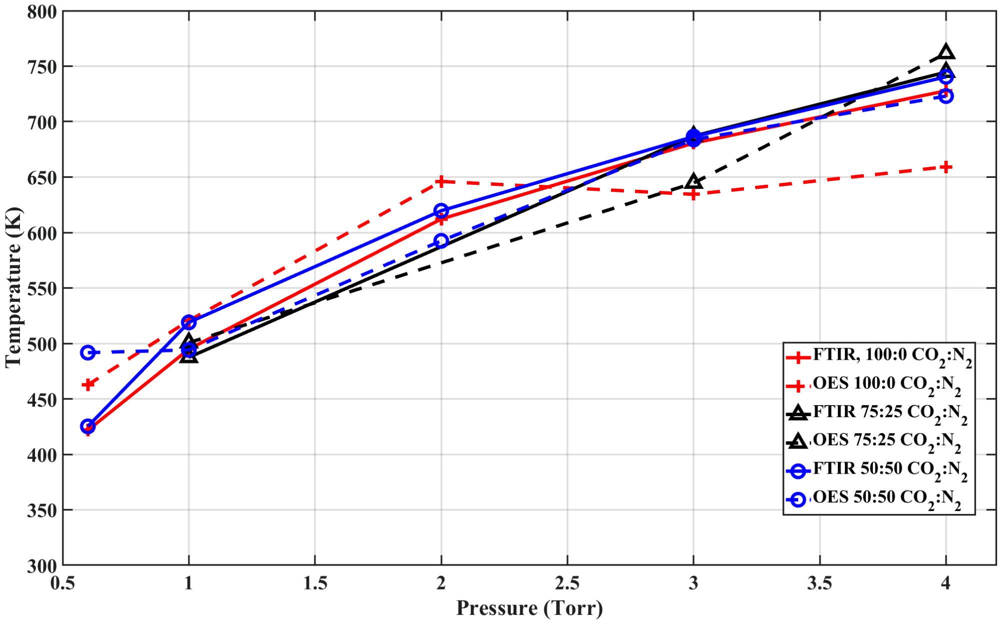

Figure 3.6: Comparison of the rotational temperatures measured with FTIR or OES in 3 different mixtures at various pressure. Each color is a mixture. The plain lines represent the FTIR measurement, the dashed line the OES

30K higher than the FTIR. The trend is parallel until 3 Torr, where the OES temperature is about 50K lower than the FTIR. At 4Torr, the gap increases to 60K. The agreement remains relatively good because the error bar of the FTIR were estimated in A.-S. Morillo-Candas 2019 to approximately 30K. The maximum difference between FTIR and OES in the 75:25 case is 50K at 3Torr. The FTIR trend is in this case correctly reproduced. Finally, the 50:50 CO_2:N_2 OES temperature is in very good agreement with the FTIR, except for the 0.6 Torr case, where the OES is 65K higher than the FTIR (whereas it was lower than the FTIR for all the other points). Overall, a good agreement (within $\sim$ 60K) is found between the two diagnostics for all the cases investigated, proving that the fitting of the CO angstrom band is a reliable technique for the determination of the rotational temperature in our glow discharge.

All results showed until here were obtained using a well-resolved spectrometer. the question of the validity of the technique with a USB spectrometer arises. The comparison of the FTIR and OES with a USB spectrometer was checked only in a pure CO_2 plasma. An example of fitting is shown on figure 3.7. The fitting is challenging when using a USB spectrometer because the band is not resolved at all, as seen on figure 3.7. One of the difficulties is the estimation of the spectral shift. When using a well resolved spectrometer like on figure 3.5, the shift can be estimated using the band head, which is not precisely defined on the spectrum taken with the USB spectrometer. A strong atomic line like the O777 line is therefore used and a constant shift over the whole spectral range assumed. With a well calibrated shift (-1.6nm used here), a good approximation of the rotational temperature can be obtained, as shown on figure 3.8. The trends are different: while the OES underestimates the rotational temperature at low pressure, it overestimates the rotational temperature at high pressure. The difference $|T_{OES} - T_{FTIR}|$ is of 65K at 1 Torr and 60K at 7Torr. Hence, over the whole pressure range, $|T_{OES} - T_{FTIR}| < 65K$, with FTIR error bars of 30K. The estimation of the rotational temperature by OES with an USB spectrometer is therefore relatively reliable and can be used in plasmas where other diagnostics are challenging to set up (upon verification that the rotational distribution of the CO(B) state is the same as the rotational distribution of the ground state) .

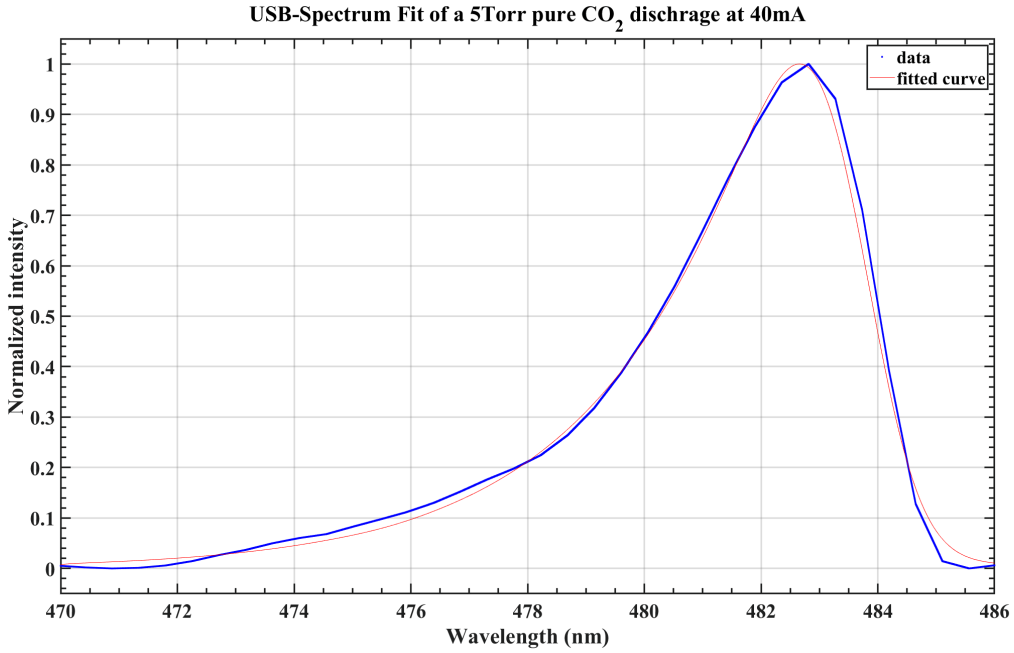

Figure 3.7: Fit of the CO Angstrom band as observed with USB spectrometer in a CO_2 glow discharge at 5Torr, 40mA

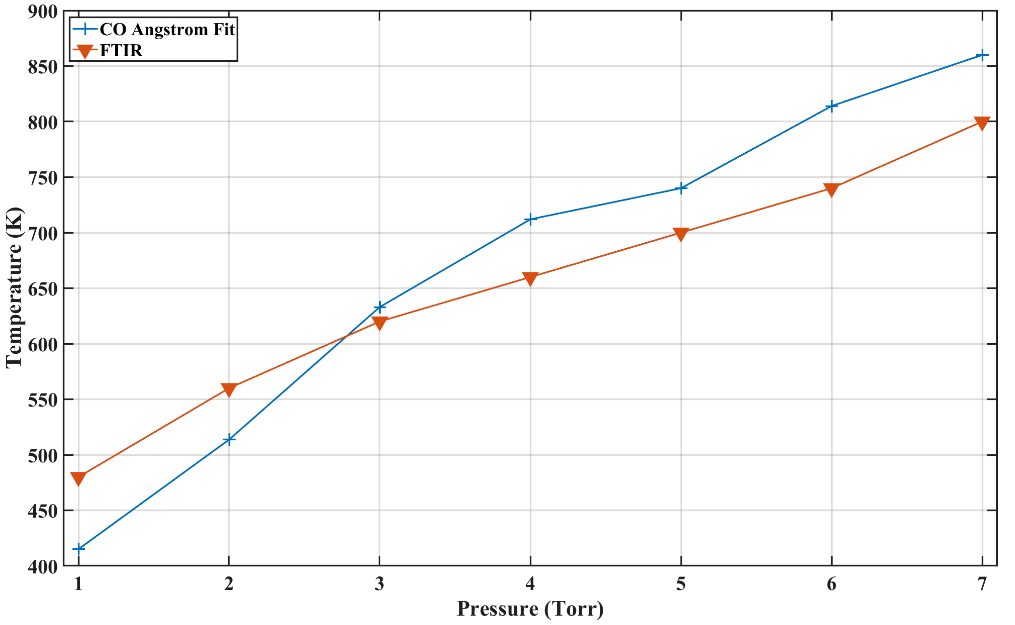

Figure 3.8: Comparison of the rotational temperature measured by FTIR and OES in a CO_2 discharge at low pressure

- Rotational temperature of CO(B) state is in equilibrium with ground state rotational temperature (T_{rot}) and therefore a good way to obtain the gas temperature (T_g)
- The temperature measured from CO(B) state emission detected with Ocean Optic Maya 2000 gives T_{rot} with an error smaller than 65 K

3.4 Measurement of the CO vibrational temperature

Now that we have shown that the fitting of a rotational band can be correctly done using a USB spectrometer, it could be assumed that other rotational bands could also be fitted. Fitting several rotational band of the Angstrom Band for different vibrational transitions (for example $B^1\Sigma^+$, v=1, J → $A^1\Pi$, v'=1, J', visible between 428 and 440nm) could bring information on the vibrational temperature if a certain distribution is assumed. A serious problem is met when trying to fit individually each band: the peak positions of the v=1→v'=1 band are only available in literature for peaks up to J = 23 (Kpa et al. 2014), which is not enough to cover the whole observed band. The peak positions could be computed from their energy with equation (3.2), replacing B_0 and D_0 by B_1 and D_1, but these calculations tend to need further corrections for high J. Another method was proposed in Drake et al. 2009: instead of resolving each rotational peak of the band, the whole band could be integrated. Assuming a maxwellian distribution (even if the CO usually shows a Treanor distribution A.-S. Morillo-Candas 2019), the ratio of two bands is given by:

$$\frac{I_1}{I_0} = C\frac{q_1}{q_0}\frac{\lambda_0^4}{\lambda_1^4}exp(-\frac{\Delta E_{10}}{k_b * T_{vib}}) \tag{3.15}$$

$$\text{rewritten as: } T_v = \frac{\Delta E_{10}}{k_b}\frac{1}{ln(C\frac{I_1\lambda_1^4 q_0}{I_0\lambda_0^4 q_1})} \tag{3.16}$$

where C is a constant depending on the optical system, I_1 is the intensity of the band v=1→v'=1, I_0 the intensity of the band v=0→v'=1, q_0 ad q_1 the Franck Condon factors of the two bands, λ_1 and λ_0 the wavelengths of the respective band heads, T_{vib} the vibrational temperature and ΔE_{10} the energy difference between the two vibrational levels. The values of the constants are given in table 3.1. The two bands measured are ~40nm apart so the spectral sensitivity calibration of the USB spectrometer was performed using an Ocean Optics DH3 Plus emission lamp whose spectrum is known. The ratio of the known spectrum of the lamp over the measured spectrum with the USB spectrometer as a function of the wavelength gives the spectral sensitivity calibration of the USB spectrometer.

	v=0	v=1
q	0.25	0.18
λ	483.65nm	439.41nm
ΔE_{10}=0.2691J		

Table 3.1: Vibrational constants of the CO(B,v) state

This method has only been used in Drake et al. 2009 where it is not detailed nor compared to other diagnostics. It therefore required a validation, which was done by comparing temperatures obtained with the USB spectrometer and with the FTIR. This was done in a pure CO_2 glow discharge at pressures between 2 and 5 Torr, for currents ranging from 10 to 50mA. In some conditions, namely low current or high pressure, the 1-1 band is not visible enough and therefore the estimation is not plotted. The comparison of the CO vibrational temperature deduced from

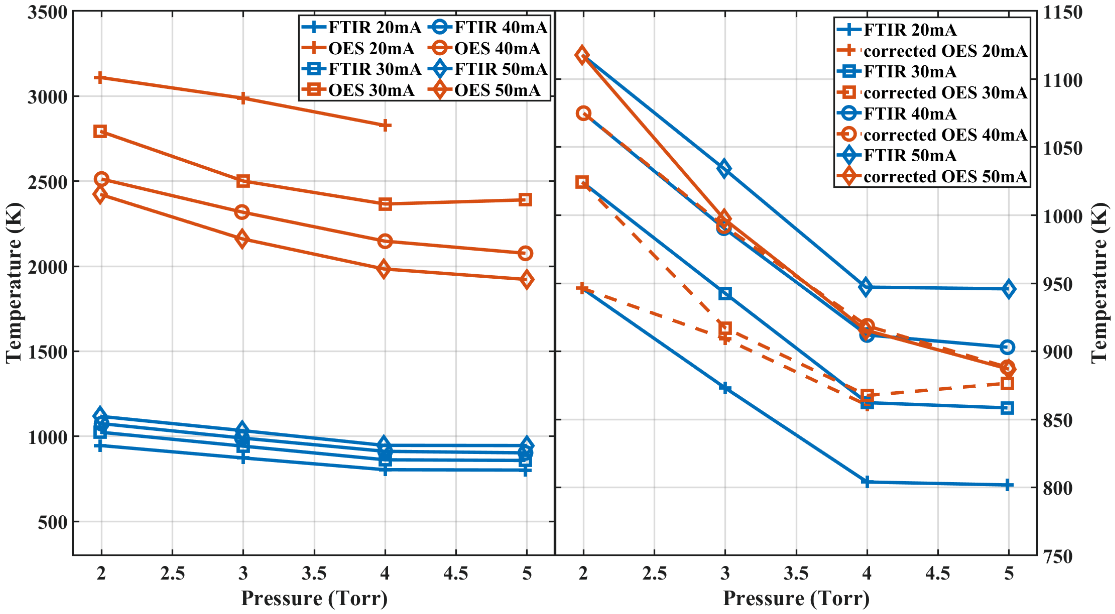

Figure 3.9: Comparison of the FTIR and OES measurements of the CO vibrational temperature. The brute results are plotted on the left panel and the OES temperature normalized by FTIR value are plotted on the right. Each current is represented by a different symbol. FTIR temperature is in blue and OES in orange

USB OES vs FTIR is plotted on figure 3.9. The results are plotted on the left panel. The CO vibrational temperature is plotted as a function of pressure for 4 different currents. Each current is represented by a different symbol. The orange curves are the OES results and the FTIR results are plotted in blue. The estimated OES temperature is between 2000 and 3000 K for all currents, while the FTIR measured temperature is between 750 and 1150 K. This method therefore yields an error of 1000 to 2000K on the vibrational temperature. However, the trends are excellent. The right panel of figure 3.9 shows the OES vibrational temperature normalized by the FTIR temperature at 2Torr:

$$Tv_{OES.corrected} = T_{OES} * \frac{T_{FTIR}(2Torr)}{T_{OES}(2Torr)}$$

The results in this case are excellent: for 30 and 40mA, the results are in almost perfect agreement with the FTIR. In the 50mA case, OES underestimates the vibrational temperature by 60K, which corresponds to the FTIR error bar on T_{CO} Klarenaar, Engeln, et al. 2017. At 20mA, the error on T_{CO} is of 63K at 4 Torr, and is the maximum discrepancy observed. At 20mA, the OES likely deviates from the FTIR measurement due to the weakening intensity of the 1-1 band. This excellent matching is due to a correction which seems to depend on the current (the correction factors as a function of current are reported in table 3.2). For one current, the correction seems to be the same over the whole pressure range (where both Trot and T_{CO} vary), meaning that the correction does not depend on the temperature. Varying the current boils down to changing the electron density but there is no clear reason why the electron density would have any effect. A clear trend is visible on the correction factor as a function of current, leading to believe that it corresponds to a real physical phenomenon. A simple explanation would be that the vibrational temperature of the CO(B) state radiating the Angstrom band is just different from the vibrational temperature of the ground state. However, the CO(B) is usually considered to have a vibrational temperature close to the ground state vibrational temperature (Vladimir N Ochkin 2009), which can be confirmed analytically. The vibrational distribution of the electronic excited B state can be computed from the distribution

Current (mA)	Correction factor
20	3.29
30	2.73
40	2.34
50	2.17

Table 3.2: Correction factor to match OES-determined and FTIR-determined CO vibrational temperature

v $\backslash v'$	0	1	2	3
0	0.599	6.56*10^{-3}	5.16*10^{-4}	3.43*10^{-6}
1	6.9*10^{-3}	0.591	7.32*10^{-3}	1.43*10^{-3}

Table 3.3: Franck Condon factors for the transition CO($X^1\Sigma_g^+$,v)→CO($B^1\Sigma^+$,v')

of the ground state with the Franck-Codon method developed in Stancu, Leroy, et al. 2016. The population density of a vibrational state is given by:

$$[CO(B^1\Sigma^+,v')] = n_e * k_X^B * \tau_{B,v'} * \sum_{v=0}^{v_{max}} [CO(X^1\Sigma_g^+,v)] * q_{X,v}^{B,v'} \tag{3.17}$$

Where n_e is the electron density, k_X^B the electron impact excitation rate coefficient,$\tau_{B,v'}$ the radiative lifetime of the excited vibrational level, [CO($X^1\Sigma_g^+$,v)] the population of the vibrational level v of ground state and $q_{X,v}^{B,v'}$ the Franck-Condon factor of the transition from ($X^1\Sigma_g^+$,v) to ($B^1\Sigma^+$,v'). In the present case, only the population up to v'=1 needs to be calculated. The Franck Condon factors are taken from the supplementary information of Qin et al. 2017 and are given in table 3.3. It can be noted that the non-diagonal matrix element are very weak, i.e $q_{X,v}^{B,v'}(v \neq v') << q_{X,v}^{B,v'}(v = v')$. In our case, because the population densities of levels v=0 and v=1 do not have 2 orders of magnitude of difference, equation 3.17 can be simplified:

$$[CO(B^1\Sigma^+,0)] = n_e * k_X^B * \tau_{B,0} * [CO(X^1\Sigma_g^+,0)] * q_{X,0}^{B,0} \tag{3.18}$$

$$[CO(B^1\Sigma^+,1)] = n_e * k_X^B * \tau_{B,1} * [CO(X^1\Sigma_g^+,1)] * q_{X,1}^{B,1} \tag{3.19}$$

The radiative lifetimes are available in literature. The values given in Rogers et al. 1970 are very close for (B,v=0) and (B,v=1) : $\tau_{B,0} = 26.3ns \sim \tau_{B,1} = 23.3ns$. The Franck-Condon are also very close: $q_{X,0}^{B,0} = 0.599 \sim q_{X,1}^{B,1} = 0.591$. Then:

$$\frac{[CO(B^1\Sigma^+,1)]}{[CO(B^1\Sigma^+,0)]} = \frac{\tau_{B,1}}{\tau_{B,0}} * \frac{q_{X,1}^{B,1}}{q_{X,0}^{B,0}} * \frac{[CO(X^1\Sigma_g^+,1)]}{[CO(X^1\Sigma_g^+,0)]} \sim \frac{[CO(X^1\Sigma_g^+,1)]}{[CO(X^1\Sigma_g^+,0)]} \tag{3.20}$$

If the CO($B^1\Sigma^+$,0) state is populated by electron impact excitation from the ground state, the vibrational distribution of the CO($B^1\Sigma^+$,0) state is close to the ground state distribution. Because of the relatively high energy of the CO($B^1\Sigma^+$,0) state (~9eV), it is unlikely to be populated by cascade from a higher level. The dissociative excitation of CO_2 forming CO($B^1\Sigma^+$,0) is very minor. It can thus be assumed that CO(B) and CO(X) have a common vibrational distribution and should share a common vibrational temperature.

The multiplicative factor on Tco observed on figure 3.9 observed is all the more strange because of its mathematical implications. Using equation (3.9) would mean that the measured quantity is:

$$\frac{I_1}{I_0} = C\frac{q_1}{q_0}\frac{\lambda_0^4}{\lambda_1^4}exp(-\frac{\Delta E_{10}}{k_b * c * T_{vib}})$$

$$\frac{I_1}{I_0} = C\frac{q_1}{q_0}\frac{\lambda_0^4}{\lambda_1^4}\sqrt[c]{exp(-\frac{\Delta E_{10}}{k_b * T_{vib}})}$$

This means that the multiplicative factor cannot be due to an error on one of the constant used. The reason for this remains unclear for the moment and will require further investigation. To this aim, similar measurements in CO_2-N_2 and CO_2-O_2 mixtures are planned at different mixing ratios and currents. The admixtures will change the gas temperature for a given current. It can then be checked 1) if the overestimation is still observed 2) if the correction by FTIR values is still correct 3) if the correction factor depends on the mixture or only on the current. In parallel, preliminary work has been started on fitting the rotational bands of the 3rd Positive system (280-350nm) similarly to the rotational bands of the Angstrom band. This second method has already yielded interesting results, with CO temperatures a few hundred K higher than measured with FTIR. Only one current was tested so far and supplementary work is required, but the method is promising. Nonetheless, the CO vibrational temperature trend is extremely well reproduced, already making the USB spectrometer a valuable tool.

3.5 USB spectrometer for actinometry

Actinometry is a very interesting diagnostic, at least for getting trends of atomic species if not absolute values, as discussed in the previous chapter. It is already quite easy to set-up with a well-resolved spectrometer, but using a USB spectrometer makes it even easier. This section aims at showing when a USB spectrometer can be used for actinometry.
Emission signal taken simultaneously with a USB spectrometer and an Isoplane spectrometer in a O_2 discharge at low pressure are compared for the atomic lines used for actinometry (777 and 845nm for O, 750 and 811nm for Ar). To compare the spectrometers despite their different sampling of the light and detectors, the ratios of important lines are presented. Four ratios are presented on figure 3.10: the ratio of the strong oxygen lines $\frac{I_{845}}{I_{777}}$, the ratio of the oxygen line over the two Ar line $\frac{I_{845}}{I_{750}}$ and $\frac{I_{845}}{I_{811}}$, and finally the ratio of the oxygen line with the 758nm krypton line sometimes used for actinometry (D. V. Lopaev et al. 2017). Because of the poor resolution of the USB spectrometer (0.3nm), the peak value is chosen for the intensity whereas the line is integrated to obtain a value from the Isoplane signal. The peak value is chosen for the USB spectrometer because the spectral resolution of the Maya 2000 USB spectrometer used in this work is lower than the spacing between the lines of the triplets of the oxygen at 777 and 845nm. The light emitted in the 3 transitions of the triplet is sent on the same pixel of the USB spectrometer CCD. If a more resolved spectrometer were used, the integrated value of the line would be more suited for calculations.

S everal data corresponding to different O_2:Ar:Kr mixtures at 20 or 40mA are overlapped. The isoplane points are represented with a circle and the USB points are plotted with a cross. The line ratio of oxygen is presented in the first plot. It can be seen that for almost all conditions, the agreement between the isoplane and the Maya USB spetrometer is very good, with less than 5% difference between the Isoplane value of the ratio and the USB one. A single case shows a discrepancy, 9:0:1 O_2:Ar:Kr at 20mA (in purple), where the USB value is overestimated by 15% compared to the isoplane. An excellent agreement is also obtained for the ratio $\frac{I_{845}}{I_{750}}$, plotted on the top right figure. The error in this case is once again below 5% of the measured ratio with the isoplane. This is surprising as the 750.4 line would be expected to be convoluted with the neighbour 751.5nm Ar line due to the poor resolution of the USB spectrometer, but it appears that using the peak value limits the effect of the convolution with this line. The comparison is not good for the $\frac{I_{845}}{I_{811}}$ ratio, plotted on the bottom left figure. A factor up to 2 can be found in the 9.5:0.5:0 O_2:Ar:Kr case (in light blue). The Ar811 line is also convoluted with a another Ar line at 810.4nm. It appears that in this case, the distance is not sufficient enough to guarantee the absence of convolution effect on the ratio. Finally, the ratio with the Kr is also showing poor agreement with the Isoplane measurement, with a factor close to 2 at 1Torr in the 9:0:1 O_2:Ar:Kr case (in purple). In this case, the convolution of the Kr line with a very close Kr line is again to blame. Overall, it appears that for strong lines, the USB spectrometer is very well suited but for weak lines, a check must be done to ensure that the observed line is not

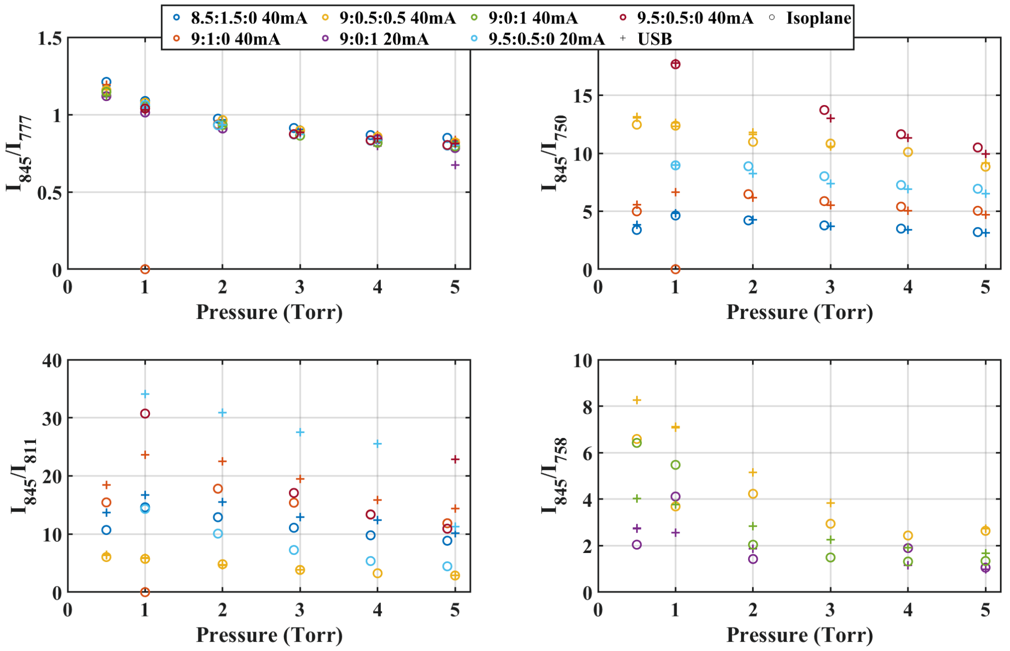

Figure 3.10: Comparison of the ratios of emission lines $(\frac{I_{O845}}{I_{O777}}, \frac{I_{O845}}{I_{Ar750}}, \frac{I_{O845}}{I_{Ar811}}$ and $\frac{I_{O845}}{I_{Kr758}})$ taken with the PI Isoplane spectrometer or with a Maya 2000 USB spectrometer. Several conditions of O_2:Ar:Kr mixture are studied for the 4 ratios presented.

convoluted with another line. In these conditions, the peak value of the line observed with the USB spectrometer is within 5% of the integrated value of measured with a well-resolved spectrometer.

In the previous chapter it has been shown that the best results for actinometry on O atoms were obtained with the ratio of O845/Ar750. The results shown here suggests that USB spectrometers (at least the Ocean optic Maya 2000) is sufficient to use this ratio of line in our glow discharge conditions.

Actinometry on O atoms can be performed with reasonable accuracy from low resolution spectra obtained with Ocean optic Maya 2000 using the O845 and Ar750 lines

3.6 The broadband emission in CO_2 plasma

One of the assets of the USB spectrometer is to record at once spectra over very large spectral range, giving access to broadband emissions that remain often unnoticed. In CO_2 plasmas an underlying broadband emission ranging from 300 to 700nm can be seen. An example is plotted in blue dotted line on figure 3.11. This emission could be thought to arise from the convolution of the peaks, but the relatively good fitting of the Angstrom band shown above for the rotational temperature indicates that it is rather a real broadband emission. This kind of emission was already observed in CO_2 plasma (Rond et al. 2008) and was attributed to CO_2 recombination chemiluminescence based on combustion literature. Similar emission is often found in hydrocarbon flames (Gupta et al. 2011) and is usually attributed to recombination reaction:

$$CO + O + M \rightarrow CO_2 + M + h\nu \tag{3.21}$$

The rate of process 3.21 was repeatedly measured in Pravilov et al. 1978, Slack et al. 1985 and Kopp et al. 2015. However this emission was also observed in our glow discharge in CO_2-CH_4 mixtures at high initial CH_4 percentages (in orange on figure 3.11). In these plasmas, the O atom lines at 777 and 845nm do not appear (which is very visible on the example provided on

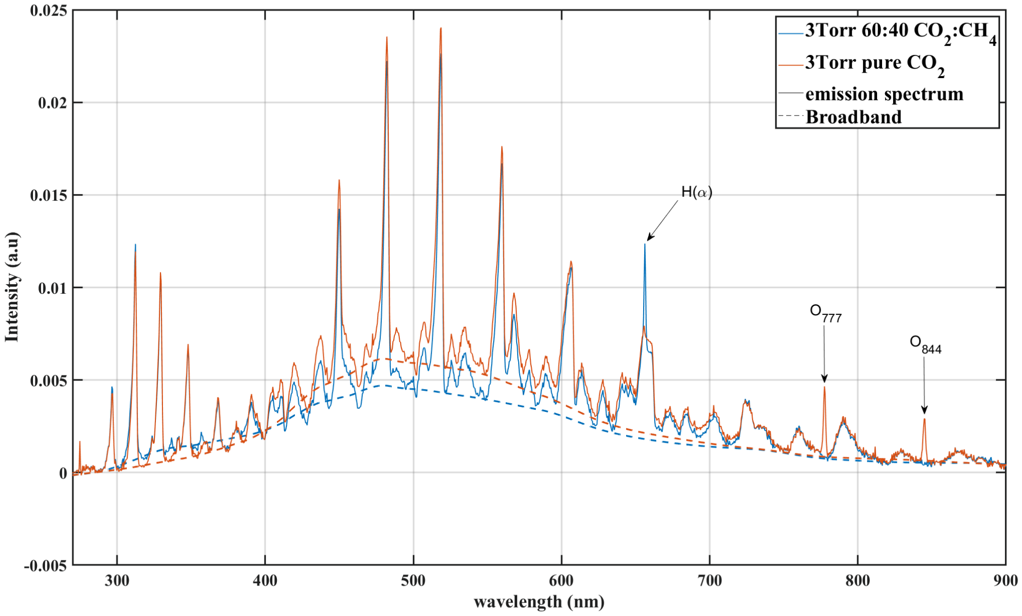

Figure 3.11: Visible emission spectra in a pure CO_2 plasma and in a 60:40 CO_2:CH_4 plasma at 40mA. The pressure is set to 3Torr and the flow is set to 7.4sccm in a 23cm long reactor. The dashed line represent the broadband emission as extracted with the msbakadj matlab function

figure 3.11), indicating that the O atom density is very low. This was latter confirmed with actinometry measurements where the O lines were below noise but not the Ar lines. The absence of O atom is contradictory with the usual explanation of the broadband emission. Moreover, the broadband described in literature peaks between 350 and 400 nm, while the broadband observed in our plasma peaks at 485nm. The shape of the broadband emission is plotted on figure 3.11 in dashed lines. The spectra were taken using an OceanOptics Maya spectrometer with a resolution of 0.3nm. A proper substraction of the broadband emission is difficult with such a low resolution because the convolution of the peaks prevents from finding the local minima. The broadband emission was therefore approximated using the matlab function 'msbackadj' (two examples are plotted on figure 3.11). The predicted baseline does not always go through the local minima but still allows to have a good idea.

It was verified that the broadband emission observed in CO_2-CH_4 and in pure CO_2 was the same in both cases by comparing the shape of the emission in various conditions of CO_2-CH_4 mixture, which are plotted on figure 3.12. The spectra were taken at 3Torr and 7.4sccm for conditions between pure CO_2 and 60:40CO_2:CH_4. The broadband intensities are plotted on the left of figure 3.12. The ordering of the different conditions on figure 3.12 does not show a clear trend. At the peak wavelength (485nm), the pure CO_2 case has the highest broadband intensity. The intensity drops upon admixture of 10% of CH_4 in the initial mixture. The intensity then goes back up for the 80:20 and 70:30 CO_2:CH_4 cases, before going back down in the 60:40 case. However, the normalized broadband intensities, plotted on the right panel of figure 3.12 clearly show that the emission has a similar profile in all cases. The contributions of the hydrogenated species can be seen between 300 and 420 nm (where the pure CO_2 case in green can be seen much lower than the other cases) and between 680 and 770 nm. On the opposite, a shoulder seen in pure CO_2 between 500 and 550nm tends to disappear when increasing the initial CH_4 percentage in the mixture, hence due to a specie found in CO_2 plasmas but not in CO_2-CH_4 plasmas, meaning O or O_2 (which will be shown in the chapter 4). Despite this, the majority of the emission remains similar in all mixtures, proving that the emission is due to the same phenomenon in all cases. The two only species found both in pure CO_2 plasma and in 60:40 CO_2:CH_4 plasma are CO_2 and CO. For more information, the intensity of the

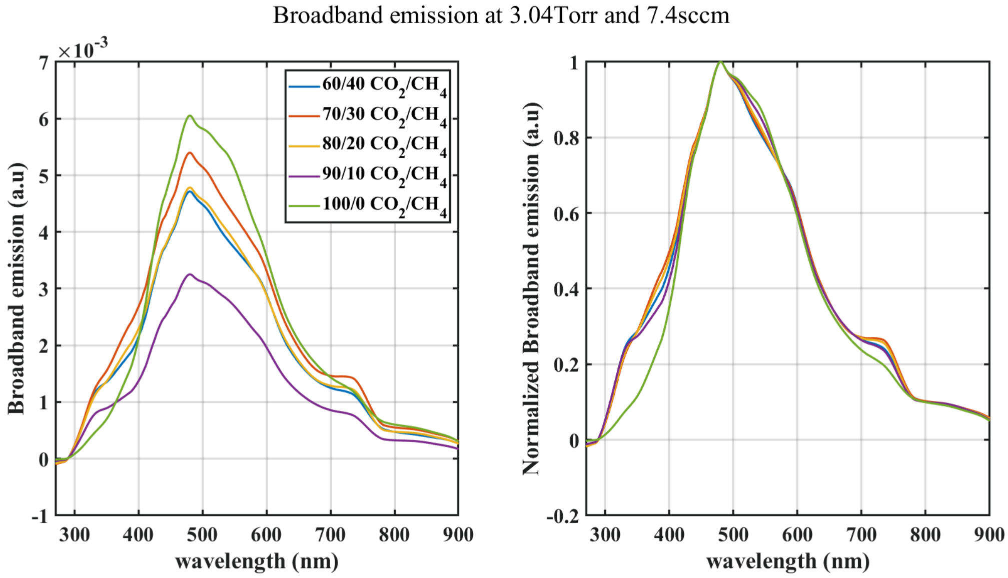

Figure 3.12: Comparison of the broadband intensities (left) and normalized broadband intensities (right) in various conditions of CO_2-CH_4 mixtures. The pressure is 3Torr, the flow is set to 7.4 sccm and the current to 40mA

broadband emission was measured in a serie of pure CO_2 plasma OES measurements. Three parameters were varied: the flow, the pressure and the current. The flow controls the residence time of the gas in the reactor and will directly influence the dissociation and the composition but it was observed that the temperatures are almost not impacted (in the range varied here). The pressure modifies the temperature while having only a small impact on the dissociation fraction, hence keeping the composition relatively steady. Finally imposing the current changes the electron density, which in turns impact both the temperatures and the composition.

The shape of the broadband emission is shown in a pure CO_2 plasma at 7.4sccm and 40mA for several pressures on figure 3.13. The intensity of the broadband emission is shown on the left graph. The intensity decreases with increasing pressure, which could be due to the increase of quenching with pressure. The normalized intensity (normalized by the value at $\lambda = 485nm$, the peak of the broadband emission) on the right show a generally speaking similar shape for all pressures. A shift on the right side of the intensity (wavelength above 500nm) can be seen with the increasing pressure.
The broadband excitation for a flow variation is plotted next on figure 3.14. The flow is varied between 7.4sccm and 1.85sccm. The residence time of the gas in the reactor increases with decreasing flow. The broadband emission intensity, presented on the left, shows that the intensity increases with the decreasing flow, i.e increases with the residence time. The increasing residence time increases the density of dissociation products in the mixture (due to longer exposure to the electron impact processes). This means that the broadband emission is related to a dissociation product rather than to a reactant, i.e CO. The shape of the broadband emission, normalized on the left of figure 3.14 remains the same independently of the flow.
Finally, the broadband emission intensities when varying the current are shown on figure 3.15. The broadband emission intensity, presented on the left, shows that the intensity increases with growing current, which is expected: increasing the current increases the electron density, leading to more excitation and more light emission. The shape of the broadband, shown by the normalized intensity on the right panel, remains unaffected by the increase of the current. The results of these variations are summed up in table 3.4. Except for the E/N, the shape of the broadband emission seems generally unaffected by the various change of experimental parameters. The broadband intensity does not increase with pressure (hence with temperature), so the process emitting this broadband is not temperature activated. The broadband intensity

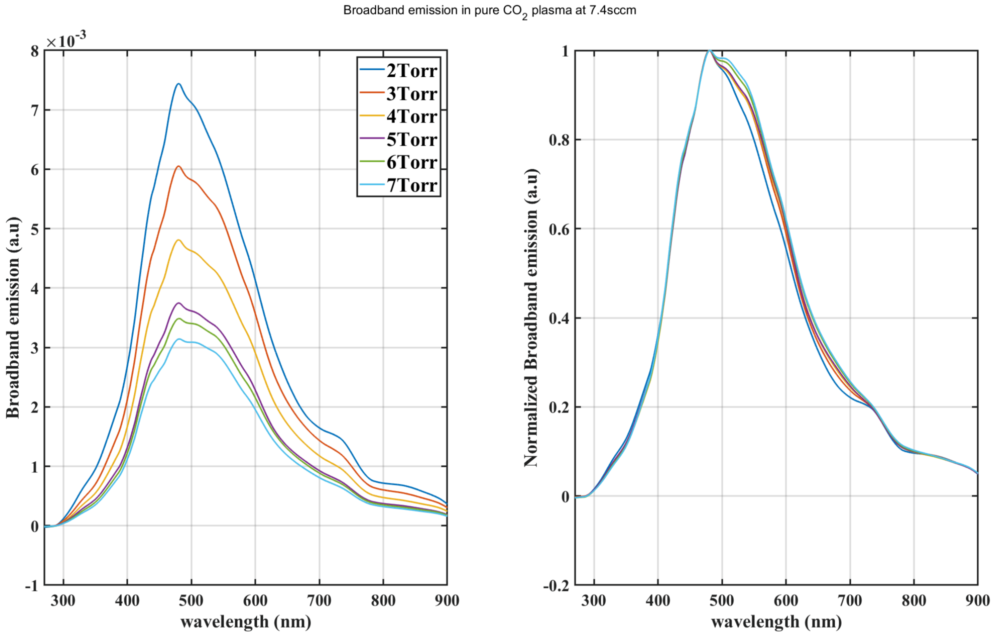

Figure 3.13: Evolution of the broadband emission in a pure CO_2 plasma as a function of pressure at 40mA. The absolute intensity is presented on the left and the intensities normalized to their maximum are presented on the right

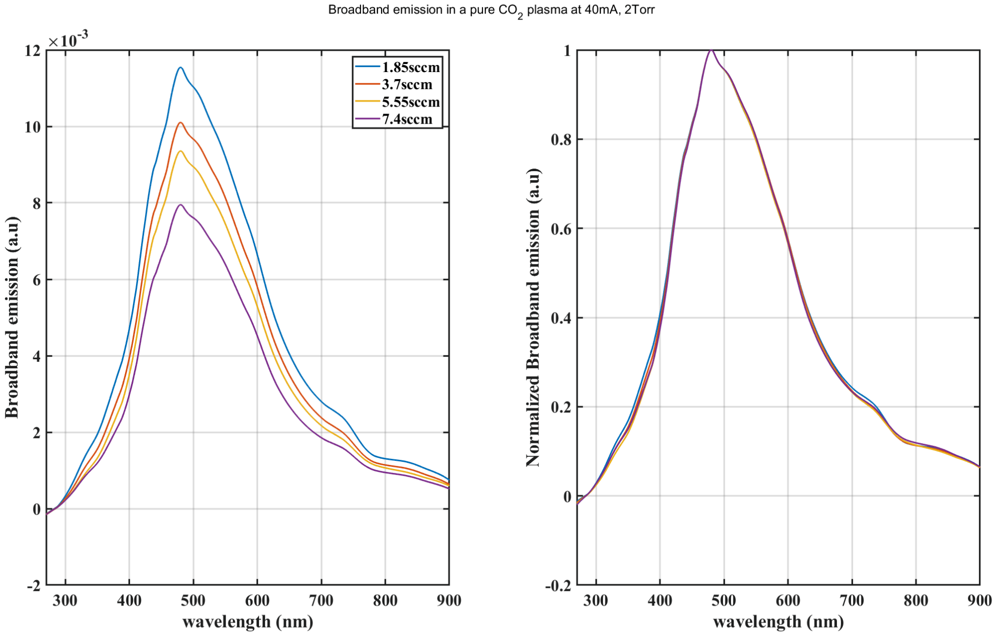

Figure 3.14: Evolution of the broadband emission (absolute on the left, normalized to their maximum on the right) in a pure CO_2 plasma as a function of the flow at 2Torr, 40mA

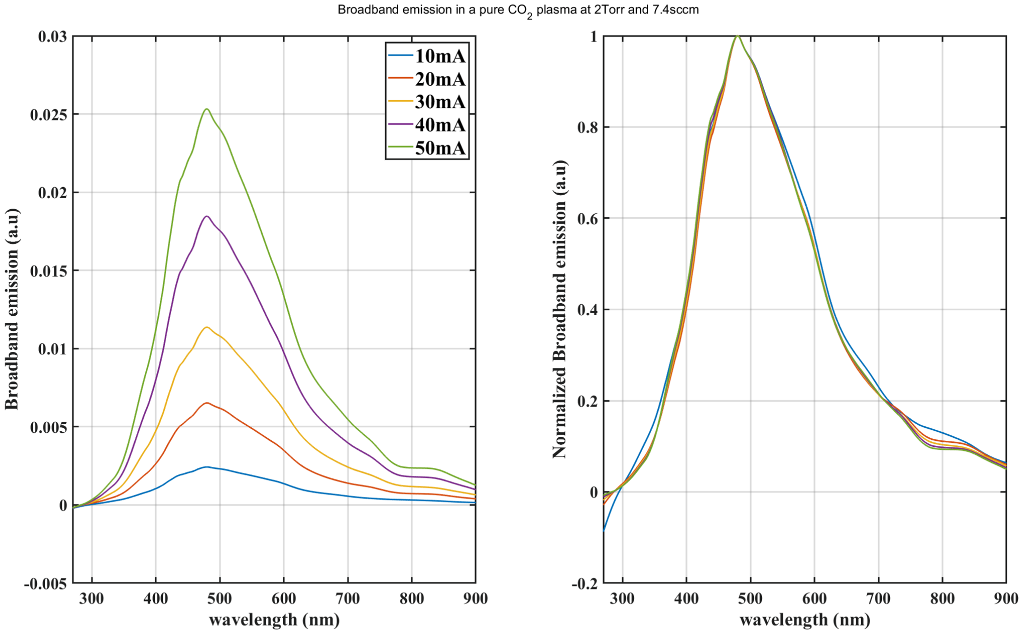

Figure 3.15: Evolution of the broadband emission in a pure CO_2 plasma as a function of the current at 2Torr, 7.4sccm

	Change of composition	Change of temperature	change of E/N	Effect
Flow Variation (1.85 - 7.4sccm)	strong	no	no	Intensity increases with residence time. No change of shape
Current Variation (10-50mA)	strong	strong	weak	Intensity increases with current. No change of shape
Pressure Variation (1-5Torr)	very weak	strong	strong	appearance of a shoulder above 500nm. Intensity decreases with pressure

Table 3.4: Effect of the experimental parameters on the plasma and the broadband intensity

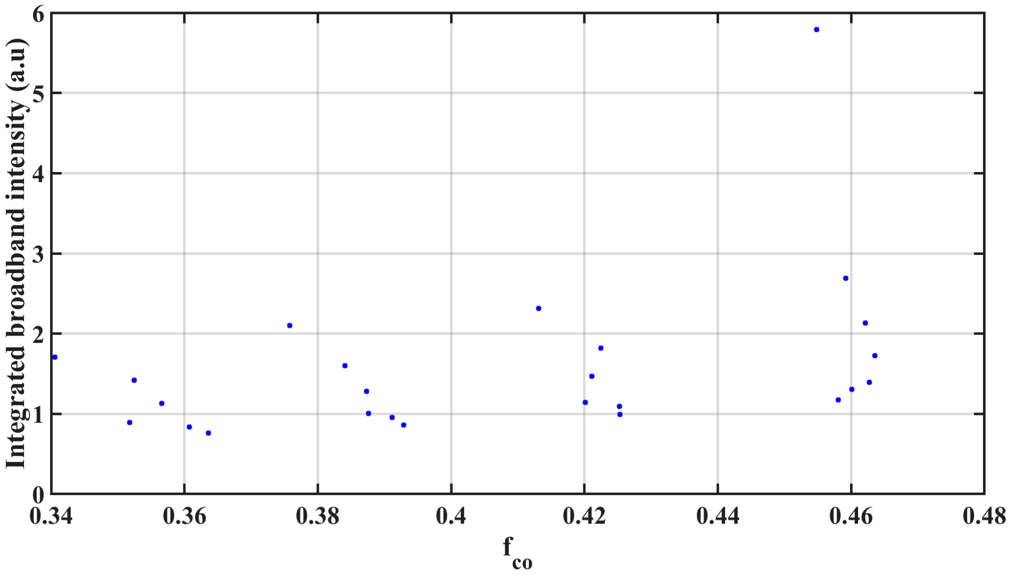

Figure 3.16: Plot of the broadband integrated intensity as a function of the CO fraction in the gas. The points used here are gathered from the pressure variation and from the current variation which were done successively.

increases with both the current and the flow variation, it must therefore be correlated to the CO fraction. Gathering all the available data, the integrated intensity of the broadband was studied as a function of several parameters. The intensity is plotted as a function of the CO fraction (I=f([CO]/N)) on figure 3.16. It does not exhibit any conclusive trend. For all the cases presented, the following relation was found for the broadband integrated intensity :

$$I = a * f_{co} * T_{co} \tag{3.22}$$

where f$_{CO}$ is the fraction of CO in the mixture and Tco the vibrational temperature of CO. The gathered data of the current and pressure variation is presented on figure 3.17. Equation (3.22) is particularly strange for several reasons

- It was verified that the intensity depends on the fraction of CO and not on the density which is surprising
- The presence of Tco as a multiplicative factor is rather odd. If the broadband emission is indeed a process activated by the vibrational temperature of CO, the influence of Tco would have been expected to be of the form $e^{-Ea/kTco}$.
- The bands related to a vibrational distribution usually show a change of shape on the high energy side (i.e on the small wavelengths) when the CO temperature is increased, due to higher energy levels being populated.

The correlation found here could simply be a coincidence. To investigate further the broadband, emission spectra should be taken in different mixtures. A CO$_2$-Ar could allow to keep the same temperature while changing the CO fraction: Ar indeed act as a buffer gas in the CO$_2$ glow discharge. On the other hand, the CO temperature could be increased by including N$_2$ in the mixture, whose vibrational excitation is usually transferred to CO and CO$_2$ via the vibrational resonances. Both of these experiments could bring additional points to the curve plotted here.

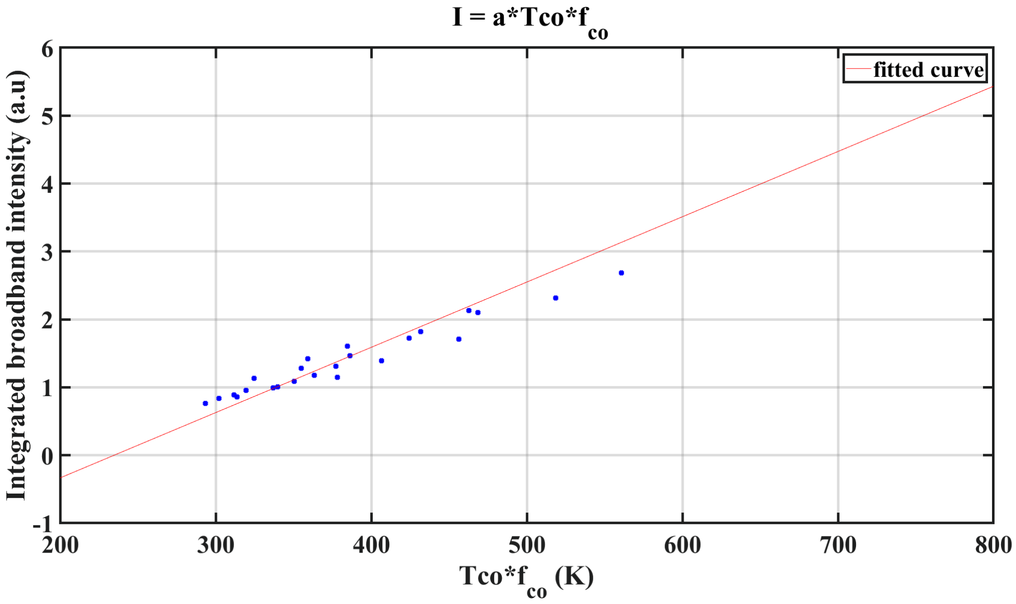

Figure 3.17: Fitting of the data of the integrated broadband intensity as a function of f_{CO}*Tco. The data are plotted in blue points and the fit is plotted in red. The data correspond to the pressure and the current variations. The "lonely" point on the right is not an error but corresponds to the only point taken at 1Torr in this study

> So far, we have not been able to determine the exact origin of the broadband emission. After studying it in different conditions, it appears that this is related to CO, but not via the usually reported process in combustion CO+O+M → CO_2 + M. A correlation with the fraction and the vibrational temperature of CO was found but the exact process responsible for the emission is still unclear.

3.7 Conclusion

USB spectrometers are convenient tools that have several applications. A USB spectrometer can be used as a routine diagnostic to detect possible leaks or just check the presence of certain gases in the mixture. If the spectrometer is resolved enough (0.3nm for the Maya 2000 USB spectrometer used in this work), some information can be drawn from the fitting of the spectra. In pure CO_2 glow discharge, the estimation of the rotational temperature through the fitting of the CO Angstrom band is reliable, with an estimated error of ±60K . The estimation of Tco in low pressure CO_2 discharges through the fitting of the Angstrom or the 3rd positive system shows the necessity to use an un-understood correction factor to obtain the right values. The trends obtained are however very good. Additional data in different mixtures (such as CO_2-N_2 or CO_2-O_2) is necessary to validate promising preliminary results. For actinometry purposes, the intensities picked up by the USB spectrometer showed similar trends for the evolution of the main peaks, indicating that the USB spectrometer can be used for actinometry estimations if the intensity of the actinometer line is sufficient. Finally, the broadband emission of CO_2 plasmas, usually attributed to the CO+O recombination, could be investigated using a USB spectrometer. The cause of this emission was not found yet but a correlation is found with the vibrational temperature of CO Tco and the fraction of CO [CO]/N.
The use of the USB spectrometer is a trade-off between simplicity of the technique and complexity of the analysis since much information is lost due to the poor spectral resolution. The Maya 2000 spectrometer will be used as routine diagnostic tool all along the next chapter dedicated to the chemistry induced in a CO_2/CH_4 glow discharge.

CHAPTER 4

Conversion mechanisms in the low-pressure glow discharge

Contents

4.1 Introduction

The two previous chapters were dedicated to the study of the diagnostics that could bring important information in the CO_2 containing plasma. These diagnostics, along with others, can now be used in CO_2-CH_4 plasma for DRM. As explained in the introduction, DRM is a process combining CO_2 and CH_4 to produce CO and H_2:

$$CO_2 + CH_4 \rightarrow 2CO + 2H_2 \tag{4.1}$$

It could be achieved by plasma, playing on the non-equilibrium characteristics of cold plasmas to avoid heating of the mixture and subsequent energy waste. Despite this, the physical basis of CO_2-CH_4 plasmas are still uncharted. A few publications discussed in the introduction chapter have started digging in the fundamental mechanisms, but the chemical kinetics of CO_2-CH_4 plasmas remains mostly uncharted. Among the reaction pathways explored in the different literature work for different type of discharges, complex chemistry of molecules with up to 3 carbon atoms is often considered important, even though the molecules are not always measured. The role of excited states, which was found to be critical in pure CO_2, is also often neglected, which can be interrogated. The chemistry of the CO_2-CH_4 plasma is therefore still an open question. This chapter aims at answering the following question:

What are the fundamental physical and chemical processes driving the chemical kinetics in a CO_2-CH_4 plasma ?

In this chapter, we use a low pressure glow discharge similar to the one of the two previous chapters, which is the simplest discharge to serve as basis for validation of a 0D kinetic model. The model itself will be kept as simple as possible also by including only molecules with up to one carbon atom in order to bring insights on the key processes allowing conversion in a CO_2-CH_4 plasma and analyse if these small molecules are sufficient or not.

The procedure of comparison of the glow discharge with 0D kinetic model coupling electron kinetics and chemistry is similar to what had previously been done for pure CO_2 in A. F. Silva et al. 2020, whose kinetic scheme was the starting point of this work. As presented in the introduction of the thesis, the glow discharge is chosen for its reproducibility and homogeneity, ideal for comparison with a 0D model, as well as for the easy access to key quantities of the plasma (the electron density n_e and the reduced electric field E/N). The goal of this study is to provide insights on the basic processes occurring in CO_2-CH_4 plasmas at low pressure by using the minimum set of reactions possible in order to minimize the number of reactions with unreliable rates.

4.2 Experimental setup

The discharge used for this study is a glow discharge at low pressure (between 1 and 7 Torr). The reactor is made of two identical pyrex cylinders, of inner radius of 1cm, attached together in a shape of an L, as visible on fig 4.1. The reactor uses the same material, radius and electrodes than the one used in the chapter 2 for actinometry and CRDS. The L-shape configuration allows for direct measurement of the post-discharge area, assuring that the gas travels only a few centimeters (corresponding to 2 to 3 seconds) between the plasma area and the measurement area. The travelling time is much longer than the recombination processes of excited species ensuring that no excited species (ions, excited states or radicals) reach the measurement cell. This also ensures that the gas is in contact with nothing else than pyrex between plasma and the measurement point (especially with no metal which could have a catalytic effect). Gas is flowed in the reactor with 3 Bronkhorst flowmeters, with a total flowrate kept between 1.85 and 7.4sccm, and pumped by an Edwards XD10 pump. The pressure is measured at the entrance of the reactor by a Pfeiffer pressure gauge. A continuous plasma is turned on in the reactor with a FUG Power supply. The reactor is in plug flow configuration, meaning that the gas is continuously supplied and pumped. The gas is constantly renewed. The total gas flow determines the pseudo steady state (where dissociation is compensated by gas renewal). The

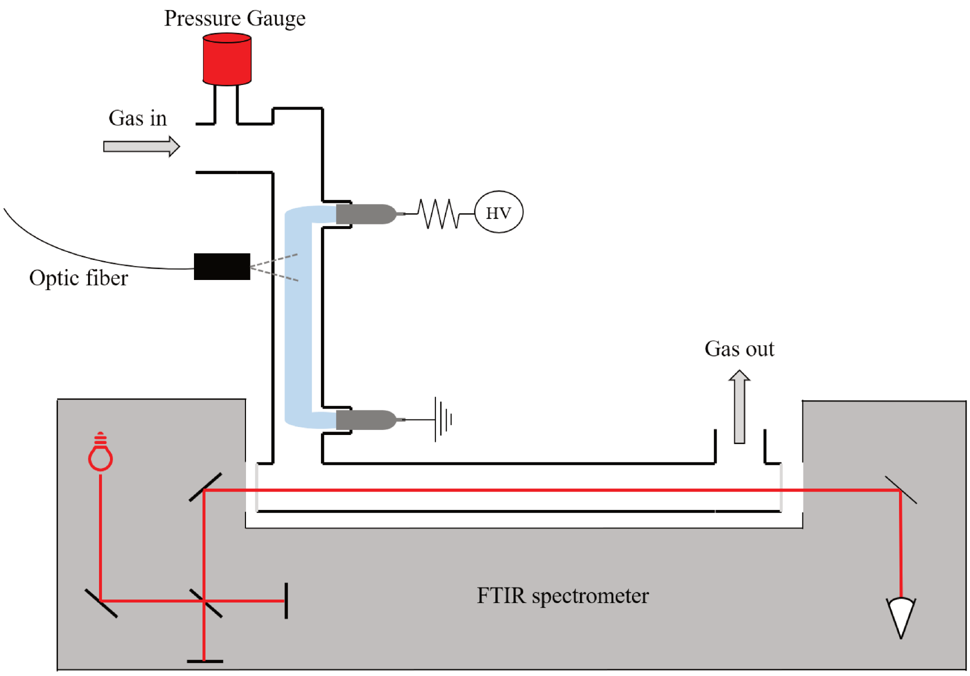

Figure 4.1: Experimental Setup

measurement area of the reactor is placed in the sample compartment of a Brucker Vertex 70 FTIR, where the IR spectra can be measured. Optical emission spectroscopy is performed simultaneously: a collimator is used to acquire light from the plasma and sends it through an optical fiber to a Ocean Optics Maya USB spectrometer (the one used in chapter 3).

For each condition measured, the gas is supplied in the line for 5 minutes before turning on the plasma to ensure a good mixing of the different gases on the whole gas line. A first FTIR measurement is taken before the plasma is turned on to check the ratio of initial gases. The initial mixture has been varied between 100:0 and 60:40 CO_2-CH_4. The proportion of CH_4 is kept below 40% to avoid significant carbon deposition on the walls (which happens when the CH_4 proportion increases). However, when the plasma is run for a long time (several hours) and for long residence time (5-7 seconds), some deposition is observed near the high voltage electrode. When carbon deposition is observed, the reactor is cleaned with an oxygen plasma until no CO or CO_2 can be measured with the FTIR in the measurement cell. Despite the small carbon deposition, it will be shown further that the carbon balance is nearly fulfilled in the chosen working conditions. Once the plasma is ON, the IR spectrum is measured after 8 minutes, corresponding to the stabilization time of CO_2-CH_4 plasma in our conditions as seen on IR and OES spectra. An important part of this work has been dedicated to the development of the automation of the whole setup in order to be able to run larger systematic set of parametric studies. All the steps of the acquisition are automated. The list of measured conditions is given in table 4.1.

Pressure	[1;7] Torr
Current	40mA
Initial CO_2-CH_4 fractions	60:40 / 70:30 / 80:20 / 90:10 / 95:5 / 1:0
Total flows	1.85 / 3.7 / 5.55 / 7.4 sccm

Table 4.1: Conditions used for the parametric study of chemical conversion in the CO_2/CH_4 glow discharge

4.2.1 Rotational temperature measurement by OES

The optical emission spectra are used to measure the temperature of the plasma through the fitting of the CO Angström band, as described in chapter 3. Like in CO_2 low-pressure glow discharge, the rotational temperature is assumed to be at equilibrium with the gas temperature. The accuracy of the temperature measurement is limited by the instrumental broadening of the USB spectrometer. In chapter 3., the comparison of OES and FTIR showed a relatively good agreement of the two methods, with a discrepancy of only 60K.

4.2.2 Densities measurement by FTIR absorption spectroscopy

The infrared spectrum are fitted with modified version of the algorithm presented in Klarenaar, Engeln, et al. 2017. The algorithm was previously designed to fit the out of equilibrium vibrational and rotational temperatures and dissociation fraction in CO_2 plasmas. The algorithm is modified to fit individually each molecule in the IR spectrum at equilibrium and determine the density of each species whose data on the measured range [1000;4000]cm^{-1} is available on NIST. For all the species in the reactor, the gas temperature is assumed to be at equilibrium with the rotational temperature, as was previously assumed for CO_2 in Klarenaar, Engeln, et al. 2017 and verified in A.-S. Morillo-Candas 2019 for the low pressure CO_2 glow discharge. A gas temperature is first assumed in the mixture. For each species X in a state s with quantum numbers (ν_s,j_s), the population of level s ic calculated with:

$$N_{s,X} = N_X * \Phi_{rot,j_s} * \Phi_{vib,\nu_s} \tag{4.2}$$

where N_X is the density of species X, Φ_{rot,j_s} is the fraction of molecules in rotational state j_s and Φ_{vib,ν_s} the fraction in state ν_s. Assuming that the rotational distribution is a maxwellian, Φ_{rot,j_s} can be obtained using:

$$\Phi_{rot,j_s} = \frac{g_{rot(j)}}{Zrot} * exp(-\frac{Erot(j)}{k_B T_{rot}}) \tag{4.3}$$

where $g_{rot}(j)$ is the degeneracy of level j, Zrot the rotational partition function (available on NIST), Erot(j) the energy of level j taken from NIST and Trot the rotational temperature. Φ_{vib,ν_s} is obtained in the same manner. With all populations computed, the linestrengh of all transitions available on the HITRAN database for the species chosen are computed. The linestrengh of a transition i is computed using:

$$S_i = \frac{I_a g_u A_{u1}}{8c\pi\nu_i^2} * (\frac{N_1}{g_1 N} - \frac{N_u}{g_u N}) \tag{4.4}$$

where I_a is the abundance of the isotope studied, g_1 and g_u are the degeneracies of the lower and upper levels. N_1 and N_u are the populations of the lower and upper level of the transition computed with the equations presented above, ν_j in the transition frequency. A_{1u} is the Einstein coefficient. Using the calculated linestrength for all transitions of all the species, a transmittance profile as a function of the wavelength is computed using:

$$T(\nu) = \prod_X exp(-L * N_X \sum_{lines \quad i} \sigma_i(\nu)) = \prod_X exp(-L * N_X \sum_{lines \quad i} S_i(Trot) * V(\nu_i)) \tag{4.5}$$

where X are the different species of densities N_X, L is the length of absorption and $V(\nu_i)$ is a voigt profile centered around the transition wavelength ν_i. $V(\nu_i)$ includes different broadening like the Doppler and collisional broadening. For each line, a self broadening and an air broadening FWHM is given in HITRAN. The fitting is done with the matlab lsqcurvefit function based on the least square method and using the densities N_X as fitting parameters. Trot could be also left as a fitting parameter but this can prevent good fitting. Indeed, if the pressure is not accurately known, the fitting of the rotational temperature will compensate the pressure error, leading in turn to errors on the densities. To avoid this error, the measurement is done

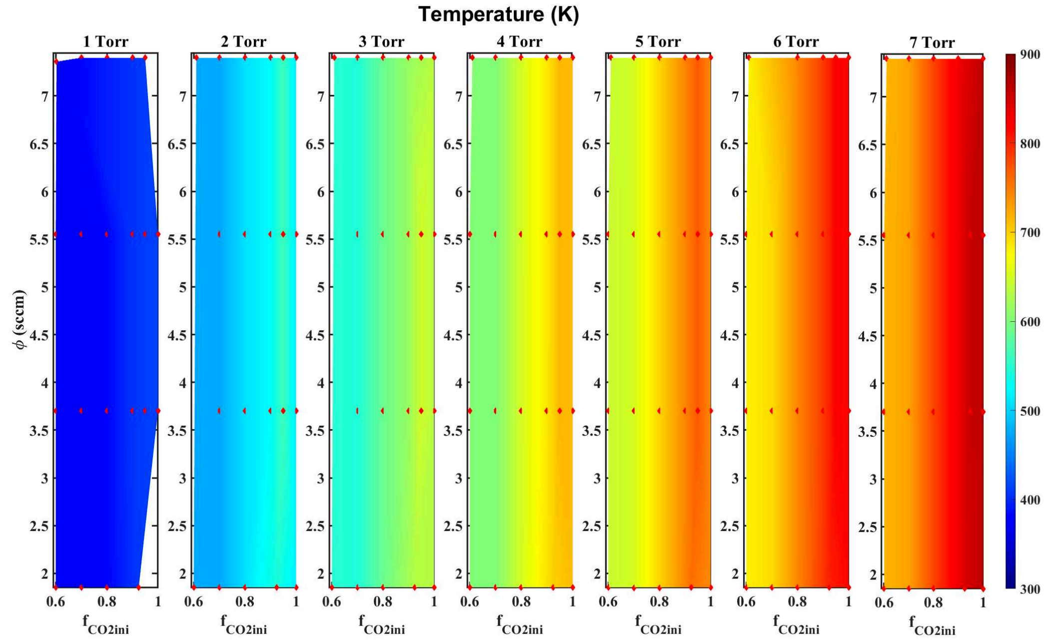

Figure 4.2: Evolution of the gas temperature obtained by OES in the measured conditions as a function of pressure, initial mixture and residence time. Each image shows for one pressure a colormap of the temperature as a function of the initial CO_2 percentage and of the residence time. The measured points are represented with red squares, while the rest is interpolated

downstream of the plasma, where the pressure can be measured with a pressure gauge and the temperature is 300K. The densities of CO_2, CO, CH_4, H_2O, C_2H_6, C_2H_4 and C_2H_2 can be measured with a sensitivity of 1‰of the total density ($\sim 10^{20}m^{-3}$). The algorithm was tested in controlled mixture, i.e in a gas mixture without any plasma. The precision in the controlled mixtures was found to be limited by the flowmeters (which have a precision of 5% of their total range).

4.2.3 Measurement of the electric field

The reduced electric field E/N, a key parameter for the understanding of the plasma behaviour has also been measured. The electric field is measured in the same conditions in an identical reactor which integrates tungsten pins at floating potential in the plasma area. The measurement of the potential at the pins allows to determine the electric field assuming the homogeneity of the electric field across the positive column. Combined with the previous measurement of temperature, this yields the reduced Electric Field E/N.

4.3 Experimental Results

4.3.1 Evolution of the temperature with CH_4

In this work, 3 parameters are investigated: pressure, flow and initial mixture. An adequate representation must be chosen to clearly show the behaviour of physical quantities like temperature with the 3 parameters. Temperature "maps" for different pressure are plotted on the figure 4.2. For each plot corresponding to a given pressure, a temperature surface is plotted as a function of the initial CO_2 fraction (on the x-axis) and of the initial flow (y axis). The plot is replicated for each pressure. For a given pressure and initial CO_2-CH_4 mixture, the temperature appears to be independent from the flow. This was already observed in pure CO_2 and is due to the characteristic time of gas heating, which are much smaller ($\sim$ few ms, see chapter 6) than the residence time of the gas in the plasma ($\sim$ few s).

For a given pressure and flow, the temperature decreases with the increase of CH_4 percentage. In these measurements, the current is kept at 40mA and the power supply voltage, monitored, vary by less than 5% over the initial mixture variation, which means that the power supplied is relatively constant over the mixture variation. The temperature decrease, therefore not due to lower heating, must be due to better heat loss. The main heat loss in our low-pressure glow discharge is the cooling at the walls as shown in T. Silva et al. 2020. The CH_4 has a thermal conductivity twice as high as the CO_2, and the H_2 (dissociation product of CH_4) tenfold the one of CO_2. The temperature decrease is therefore attributed to the excellent thermal conductivity of CH_4 and its by-products like H_2 and the better heat conduction to the walls.

4.3.2 Evolution of the reduced Electric Field

The evolution of the electric field as a function of pressure measured from the voltage drop in the positive column of the glow is plotted in dashed lines on figure 4.3 for various CO_2-CH_4 initial percentages. Figure 4.3 presents the electric field for a flow of 3.7 sccm but the change of flow (and therefore of residence time) has a very small impact on E. The maximum increase when going from 7.4 to 3.7sccm for a given mixture and pressure is observed at high pressure and is of about +4% (from 51V/cm to 53V/cm at 7Torr at 90:10 CO_2:CH_4). The same order of magnitude is seen at low pressure, with an increase from 25 to 26 V/cm at 2Torr for the same mixture.

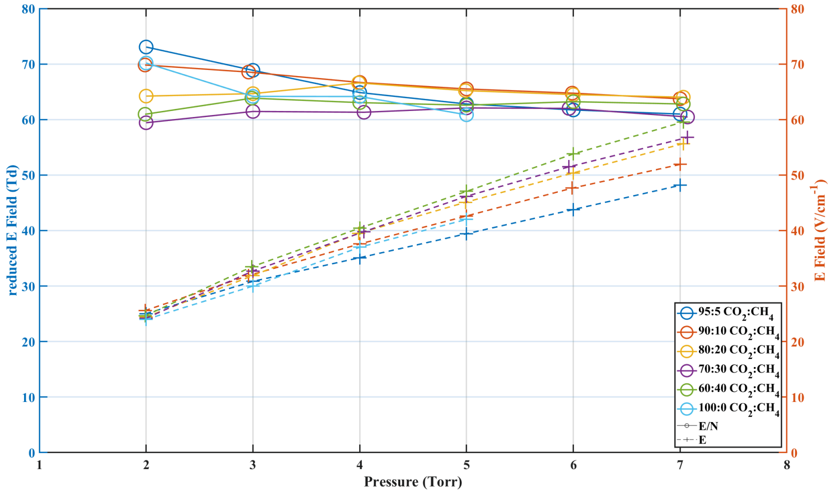

Figure 4.3: Evolution of the electric field (in dashed lines) and reduced electric field (plain lines) with pressure for various initial CO2%

Starting from the pure CO_2 case, the electric field decreases upon addition of 5% of CH_4 in the initial mixture for a given pressure. Upon further addition of CH_4 in the initial mixture, the reduced electric field increases.

The reduced electric field is shown in plain lines on figure 4.3 for several initial CO_2 percentage. Because it was seen that both the electric field and the temperature are very weakly impacted by the flow, the reduced electric field is also relatively stable with the flow. As opposed to the pure CO_2 case, the reduced electric field does not always decreases with pressure. For low initial CH_4 percentage (95:5 and 90:10 CO_2:CH_4), a decrease is observed with pressure, but the decrease of the 95:5 case (from 73 Td at 2Torr to 61Td at 7Torr) is more pronounced that the one of the 90:10 case (from 70Td at 2Torr to 64Td at 7Torr). For the 80:20, 70:30 and 60:40 CO_2:CH_4, no clear trend is exhibited and the reduced electric field seems flat with pressure. The trend of the reduced electric field with pressure for initial CH_4 content above 20% can be explained by a competition between 2 quantities. On one hand, the electric field increases with pressure.

On the other hand, the high proportion of CH_4 and its dissociation products lead to better thermal conductivity and stronger heat loss, limiting the temperature increase with pressure. The density increase is therefore stronger than in pure CO_2. The simultaneous increase of E and N with pressure lead to a flat E/N. Nevertheless, the inaccuracy of the temperature measurement could also flatten the E/N curve with pressure. As presented in chapter 3 in pure CO_2, the OES tends to underestimate the temperature at low pressure (-20K) and to overestimate at high pressure (∼60K) compared to the FTIR measurements, considered more reliable. If it is considered that the OES temperature measurements are off by the same values in CO_2-CH_4 (-30K at 2 Torr and +60 at 7Torr), the E/N evolution with pressure is not flat anymore and a decreasing trend (similar to CO_2) is observed, though only a few Td between 2 and 7Torr. No correction will be used in the rest of this work and the values measured and plotted on figure 4.3 are kept.

4.3.3 Evolution of the main species in the downstream gas mixture

As showed in section 4.2.2, the FTIR measurement yields densities of IR active, but the fractions are discussed here to be able to compare different pressures. The densities are measured downstream of the plug flow reactor and not *in situ*. The densities downstream are comparable to the ones in the plasma because few recombination takes place in the post-discharge (as will be shown in chapter 5). Additional composition measurement by mass spectrometry were carried out further down the gas line (in the far post-discharge) by Carolina Garcia-Sotto in the same setup for the same conditions and show good agreement with the FTIR measurements. This indicates that little chemistry happens in post-discharge on the long time scale and support the possibility that no recombination happens shortly after the discharge.
Before detailing each species, a general overview of the plasma composition must be given. While CH_4 seems almost completely dissociated in our conditions, some CO_2 remains. The main products of the CO_2-CH_4 low pressure glow discharge are CO and H_2, as often reported for CO_2-CH_4 discharges (M.Scapinello et al. 2016 for NRP, Ghorbanzadeh et al. 2007 for atmospheric glow, or more recently in Van Alphen et al. 2021 GA discharge). In this work, water is obtained as well (up to 15% of the gas density). C_XH_Y molecules are found only in traces. When heavier hydrocarbons are found, C_2H_6 or C_2H_4 are the dominant ones, whereas C_2H_2 is usually reported as the main C_XH_Y molecule with X>1 (M.Scapinello et al. 2016, Van Alphen et al. 2021). Little O_2 (deduced from O atom balance) is found downstream if the CH_4 percentage is above 10%: in a 90:10 mixture at 3Torr, the O_2 fraction is typically around 5%, and drops below 1% in the 80:20. No O or H atoms are expected downstream because their characteristic recombination time is much shorter (respectively tens of ms and ms) than the time it takes for the gas to travel from the reactor to the measurement cell.
Similarly to the temperature maps, the fraction of the main species in the gas mixture downstream the plasma are plotted versus the initial % of CO_2 and versus the total gas flow for each pressure in the following figures. For more readability, an interpolated surface is plotted in colour, while the measurement points are plotted as red diamonds. The number of point for the interpolation is chosen so that the interpolant gives the measured values at the measured conditions.

The CO_2 fraction in the plasma is shown on figure 4.4. For all pressures and residence times, the CO_2 fraction strongly increases when changing from 100:0 to 95:5 CO_2-CH_4, before going back down when increasing the CH_4 content. This phenomenon, very visible between 2 and 7 Torr, is less clear at 1Torr. For a given pressure, the CO_2 fraction decreases with the residence time (as expected due to longer exposure to electron impact processes). Hence for a given pressure, CO_2 is always minimal at high CH_4 percentage and low flow (high residence time), while it is always maximum at 95:5 CO_2-CH_4. The value of the minimum final fraction is however stable for all pressure, remaining at 15% of the total density, while the maximum fraction of CO_2 increases from 1 to 3 Torr before stabilizing at approximately 70% of the total plasma density.

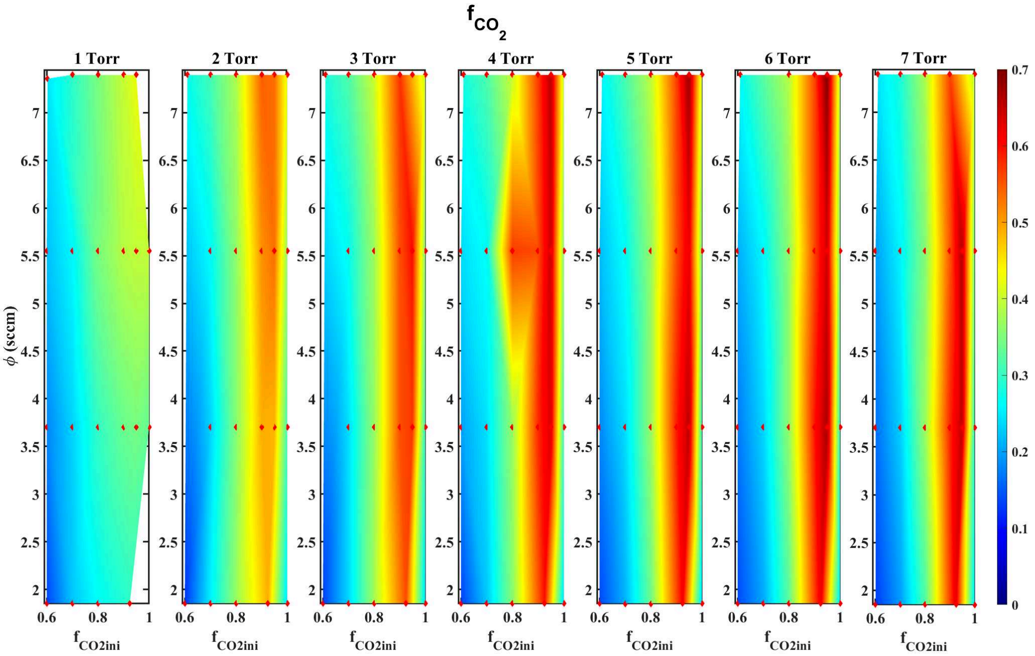

Figure 4.4: Evolution of the fraction of CO_2 in the measured conditions as a function of pressure, initial mixture and residence time. Each image shows for one pressure a map of the CO_2 final fraction as a function of the initial CO_2 percentage and of the residence time. The measured points are represented with red squares, while the rest is interpolated

The CO fraction in the plasma is represented on figure 4.5. For a given pressure, the CO fraction is maximal for low flow (high residence time) and high initial CH_4 %. For pressures between 2 and 7 torr, the CO fraction shows a drop of almost a factor 2 when changing from 100:0 to 95:5 CO_2-CH_4, then goes back up upon addition of more methane in the initial mixture, mirroring the previously shown CO_2 fraction on figure 4.4. This is visible for all measured residence times. For a given pressure and initial CO_2-CH_4 mixture, the final CO fraction increases with the residence time. For a given pressure and initial mixture, the fraction decreases with the residence time. The large fractions of CO observed (~25% at f_{CO2ini}=0.6 for instance) show that a large part of the CO comes from oxidation of CH_4 and not only from the dissociation of CO_2.

CH_4 is efficiently converted, with little to no CH_4 remaining. The final CH_4 fractions, represented on figure 4.6, show a linear trend with the initial CH_4 fraction and with the residence time: CH_4 is fully dissociated at low initial CH_4 percentage and at low flow (high residence time). The behavior of CH_4 is similar for all pressures: around 10% remain in the case 60:40 CO_2:CH_4 for all pressures and for high flows (7.4sccm, top right corner of the maps). Increasing the residence time in the same mixture leads to final CH_4 percentage close to 4%. For any other mixture, the final amount of CH_4 is decreased below 1% for all residence times.

H_2 is not measured in the plasma (because it has no IR signature). The fraction of H_2 in the plasma is deduced from H atoms balance assuming that all non-detected H atoms are recombined into H_2. The fraction of H_2 in the gas represented on fig 4.7 increases with the initial CH_4 percentage and with the residence time at a given pressure. The H_2 fraction is thus always maximum on right side of the maps for any pressure. The maximum fraction of H_2 is relatively stable with pressure, remaining in the range 32-45% of the total gas density, with a peak at 4Torr.

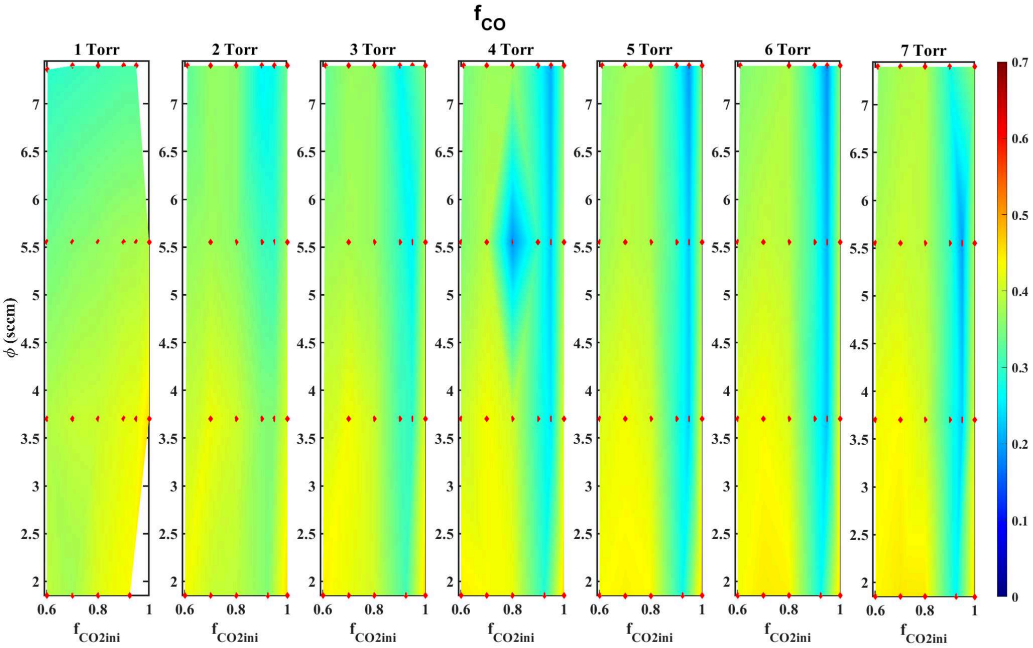

Figure 4.5: Evolution of the fraction of CO in the measured conditions as a function of pressure, initial mixture and residence time

The fraction of water (which is measured by FTIR but not represented here) has a limited range of variation. For 5% of initial CH_4, approximately 5% of water are formed for all residence times. This amount increases slightly when more CH_4 is added but remains between 8% for low residence times, and up to 11% for higher residence time. This stays true for all pressures

The fraction of O_2 is not represented here as it falls to 0 when the initial CH_4 ratio is higher than 90:10. Similarly to H_2, O_2 is not measured directly but deduced from the O atom balance assuming that all O atoms missing from the balance are recombined into O_2. Traces of C_2H_6, C_2H_4 and C_2H_2 are found but are negligible (their sum account for less than one percent in the best case). Despite the weak densities, it is worth noting that C_2H_6 peaks at 1 Torr, suggesting that surface processes could be at play here, while C_2H_4 systematically peaks in the 60:40 CO_2-CH_4 case and always at high flow. The high flow corresponding to a short residence time in the plasma, this could suggest that C_2H_4 is an intermediate in the chemistry, destroyed on long time-scales.

The deposition of carbon on the walls of the reactor has been calculated as well. To do so, the number of C, O and H atoms in the measured molecular species is calculated. Before the plasma, the total number of carbon atoms in the reactor (including the carbon atoms in molecular forms) is given by:

$$C_{initial} = [CH_4]_i + [CO_2]_i \tag{4.6}$$

Similarly, the number of O and H are given by :

$$H_{initial} = 4 * [CH_4]_i$$
$$O_{initial} = 2 * [CO_2]_i$$

Summing all the carbon atoms in CO_2, CO, CH_4 and C_2H_6 gives a density of measured carbon atoms (bonded in molecules) in the reactor $C_{measured}$

$$C_{measured} = [CH_4] + [CO_2] + [CO] + 2 * [C_2H_6] + 2 * [C_2H_4] + 2 * [C_2H_2] \tag{4.7}$$

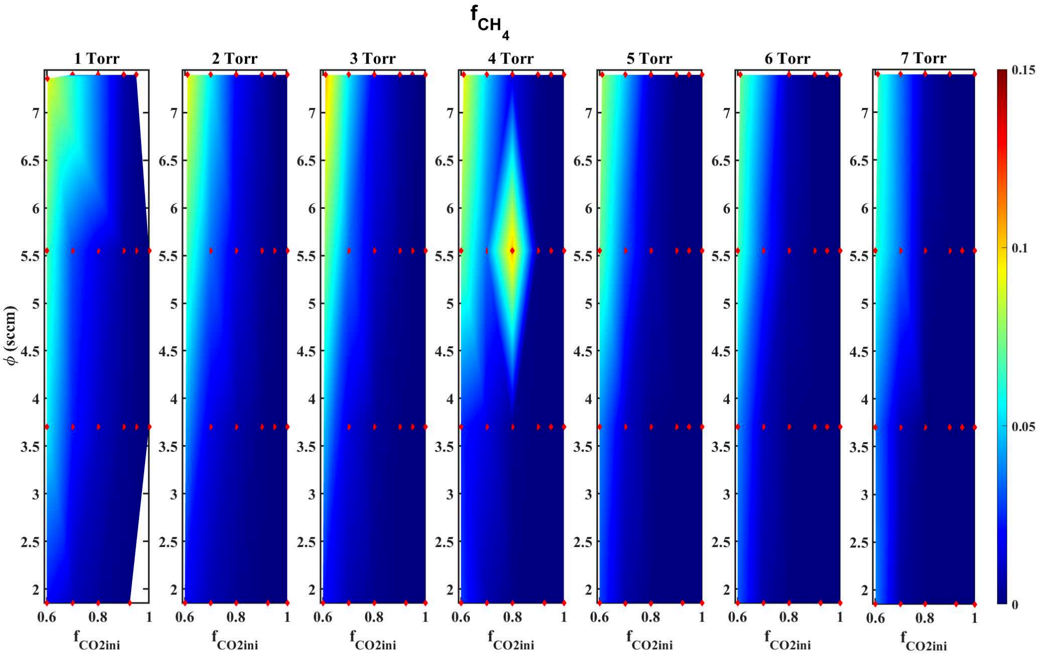

Figure 4.6: Evolution of the fraction of CH_4 in the measured conditions as a function of pressure, initial mixture and residence time

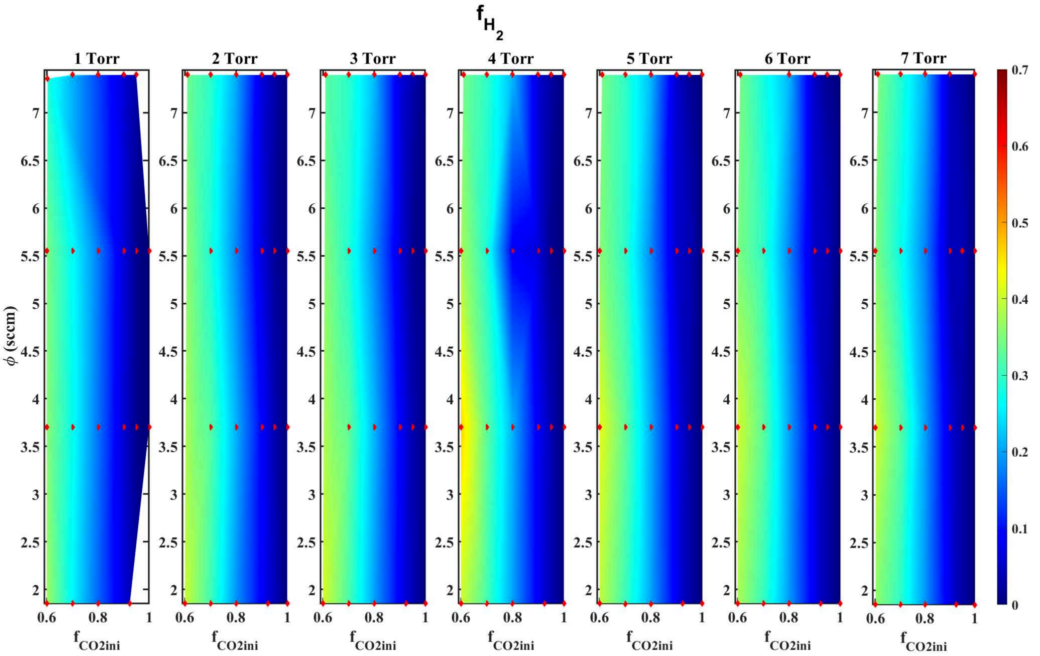

Figure 4.7: Evolution of the fraction of H_2 in the measured conditions as a function of pressure, initial mixture and residence time

The density of measured O atoms bonded in molecules in the reactor O$_{measured}$ is obtained with:

$$O_{measured} = 2 * [CO_2] + [CO] + [H_2O] \tag{4.8}$$

Similarly the density of measured H atoms is obtained with:

$$H_{measured} = 2 * [H_2] + 2 * [H_2O] + 6 * [C_2H_6] + 4 * [C_2H_4] + 2 * [C_2H_2] \tag{4.9}$$

The densities of H_2 and O_2 can be computed assuming that

$$N = [H_2] + [CO] + [CO_2] + [CH_4] + [H_2O] + [C_2H_6] + [C_2H_4] + [C_2H_2] + [O_2] \tag{4.10}$$

If $\frac{O_{measured}}{C_{measured}} < \frac{O_{initial}}{C_{initial}}$, the number of O atoms measured in all the molecules do not account for the initial amount of the O atoms sent in the reactor. Assuming that the remaining O atoms recombined into O_2, the O_2 density can be estimated. If $\frac{O_{measured}}{C_{measured}} > \frac{O_{initial}}{C_{initial}}$, it indicates that some carbon atoms were lost from the gas phase. Assuming that the deposition on the wall of the reactor are pure Carbon, the percentage of C atoms deposited at the wall can be computed. The result is plotted on figure 4.8. The carbon deposition starts once CH_4 reaches 30% of the initial mixture and is stronger at lower flow. In the worst case (60:40 CO_2:CH_4 at 4Torr), less than 15% of the total C atoms are lost. In most cases, the deposition remains around 10%. The percentage of C atom deposited being low enough, the deposition will be neglected for further analysis.

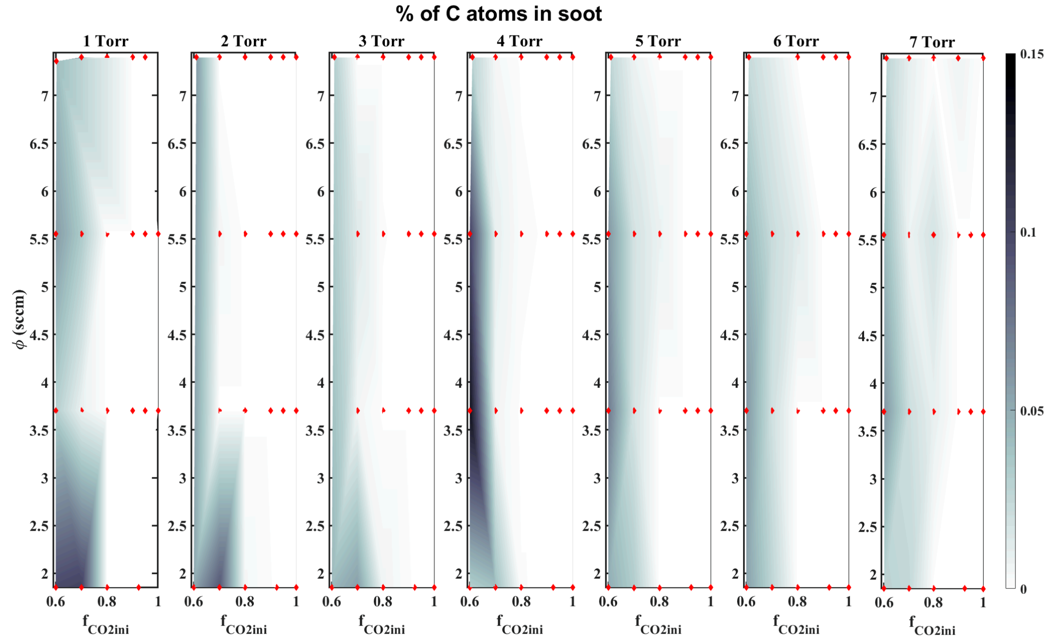

Figure 4.8: Fraction of C atoms lost in carbon deposition at the walls

4.3.4 Estimation of the atomic densities by actinometry

The atomic species play a key role in the plasma. An estimation of their densities is therefore crucial to understand the plasma mechanisms. The densities of atomic H and O in the plasma are measured by actinometry, whose validity was assessed in chapter 2 and verified for a maya 2000 USB spectrometer in chapter 3. The atomic lines O777 and O845 are used for the computation of O atom density and the H656 was used for H density. 5% of Ar was introduced in the gas flow to serve as actinometer and the Ar750 line is used as discussed in Chapter 2 and 3.

The evolution of the emission lines H656 and O777 with the change of initial mixture are shown on figure 4.9 for a pressure of 4Torr and a constant flow of 1.85sccm. The O line intensity drops

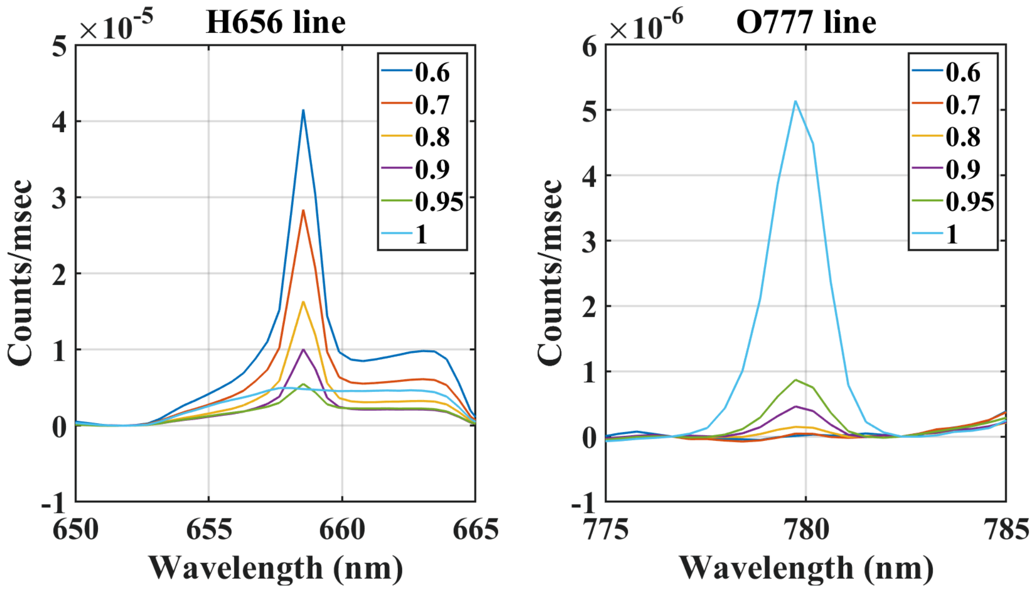

Figure 4.9: Evolution of the emission of atomic H and O at 4 torr with diffirent initial mixtures

with small amount of CH_4. When CH_4 makes up for more than 10 % of the initial mixture, the O line is below noise level. Because of this, the ratio $\frac{I_O}{I_{Ar}}$ is close to 0 for initial CH_4 content above 10% and it is estimated that the atomic O makes up for less than 0.1% of the total mixture in these cases, making it negligible. Using the actinometry equations for O with Ar actinometer presented in chapter 2, the fraction of O atoms is estimated to be close to 4% of the gas density in the 95:5 CO_2:CH_4 plasma and 1 percent of the gas density in the 90:10 CO_2:CH_4 case.

Though the H line is convoluted with a larger emission band from the CO Angström system, it is nonetheless possible to see the evolution of the line, whose intensity increases with the CH_4 content. We can also notice that the emission from the Angström band initially decreases upon admixture of CH_4, before going back up, confirming the general trend of CO. The H density is computed following the method described in chapter 2. The role of dissociative excitation ($e + H_2 \rightarrow e + H + H(n = 3)$) must be checked. Using the actinometry hypothesis, the intensity is indeed given by :

$$I_{H656} = C_{656} * h\nu_{ij}^H * (k^{elec} * [H] + k_{DE} * [H_2]) * n_e * \frac{A_{ij}^H}{\sum A_i^H + \sum_Q k_Q^H [n_Q]} \tag{4.11}$$

$$= C_{656} * h\nu_{ij}^H * (k^{elec} * [H] + k_{DE} * [H_2]) * n_e * a_{ij}^H \tag{4.12}$$

$$\tag{4.13}$$

where C_{656} is a constant depending on the experimental setup, ij correspond to the upper and lower level of the transition radiating the 656nm line, k^{elec} the electonic excitation rate coefficient, k_{DE} the dissociative excitation rate coefficient, ne the electron density, n_H the atomic hydrogen density and a_{ij}^H the efficient branching ratio of the transition. The ratio $\frac{k^{elec}}{k_{DE}}$ was computed for a 60:40 CO_2:CH_4 mixture at various pressures using the LoKI B solver and the composition, temperature and reduced electric field measured above. The ratio was found to be close to 4.10^3 in our conditions. Neglecting dissociative excitation, the H atom density was computed

$$[H] = \frac{I_H}{I_{Ar}} * \frac{k_e^{Ar}}{k_e^H} * \frac{a_{Ar}}{a_H} * [Ar] \tag{4.14}$$

Using the coefficients given in table 4.2, this estimation yields that for an initial CH_4 content of 30%, the atomic H density should remain below 1% of the total mixture. Because $k^{elec} * [H] >> k_{DE} * [H_2]$, the hypothesis of neglecting the dissociative excitation is consistent. The atomic H

species	Wavelength (nm)	Emitting State	A(s^{-1})	$k_Q(m^3.s^{-1})$ averaged over all quenchers
Ar	750	2P1	$4.5e^7$	$7.6e^{-16}$
H	656	Alpha	$6.45e^7$	$2.5e^{-15}$

Table 4.2: Values of the coefficient used for actinometry calculations

density computed here is only an order of magnitude because the basis of the line is convoluted with the CO Angstrom band which prevents exact calculations.

4.3.5 Summary

- the gas temperature (T_g) increases with pressure but decreases with initial CH_4 percentage because of the thermal conductivity of CH_4 and mostly H_2
- At high initial CH_4 percentage the reduced electric field does not change with pressure.
- The main species measured downstream the low pressure CO_2-CH_4 glow discharge are CO, H_2, CO_2, CH_4 and H_2O by order of fraction of the gas. The densities of C_2H_Y molecules are very low and accounts for less than 1%
- CH_4 is very efficiently destroyed even for large initial percentage
- Atomic densities of O and H are weak and accounts at most for a few percent of the gas density
- An increase in the CO_2 density is seen when going from pure CO_2 to 95:5 CO_2:CH_4
- a significant part of the CO necessarily come from oxidation of CH_4 and not only from CO_2 dissociation
- carbon deposition on the wall remain low (below 15% in the worst case)

In the following sections, a minimal kinetic scheme is developed to propose a model that accounts for each of these observations.

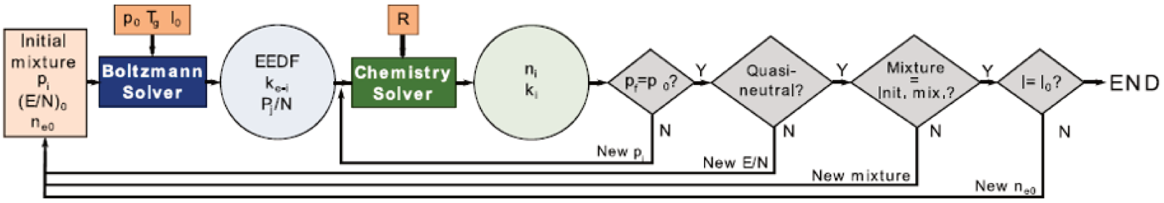

Figure 4.10: Workflow of the LoKI kinetic solver. E/N is the reduced electric field sustaining the discharge, p$_o$ is the input reactor pressure, p$_i$ the pressure in the beginning of the simulation (p$_i$ = p(t = 0)), p$_f$ is the steady state pressure of the simulation, n$_e$0is the initial guess for electron density, R is the radius of the reactor, Tg is the gas temperature k$_{ei}$ is the rate coefficient for collision i of electrons with a given heavy-species, P$_i$/N is the reduced power spent/gained by electrons in collision i, n$_i$ is the density of species i, k$_i$ is the rate coefficient of reaction i, I is the electron current calculated using equation 4.15 and I0 is the experimentally measured current, given as input. This figured is reproduced from A. F. Silva et al. 2020

4.4 Modelling

4.4.1 Overview of the LoKI simulation tool

Because the number of possible interactions in a CO_2-CH_4 plasma is too large to draw a simple chemical scheme from the experimental results, the measurement done in the glow discharge are compared with a 0D kinetic model. The Lisbon Kinetic tool (LoKI) is used both for the solving of the Boltzmann equation and for the 0D chemical solver. The solver takes as input the working conditions: an initial composition, a gas temperature, a pressure, an electron density and a guess value of the reduced electric field and computes a final composition and a reduced electric field. Because the solver assumes a cylindrical geometry, a radius must be provided. The solver aso takes into account a set of electron impact cross-sections. The functioning of this solver was previously detailed in A. F. Silva et al. 2020 for similar work on pure CO_2. The workflow of the LoKI kinetic solver is detailed on figure 4.10, taken from A. F. Silva et al. 2020. The input parameters are used to compute the EEDF using the Boltzman Solver module. The solver also computes the rate coefficients of all the electron impact reactions.The output of the Boltzmann solver, along with a set of chemical reactions (whose rate coefficient must be given as well) are used as inputs of the chemistry solver. The chemistry solver solves the rate balances equations for all heavy species in the plasma:

$$\frac{\partial n_s}{\partial t} = \sum_i C_{s,i} - D_{s,i}$$

where n_s is the density of the species s, and $C_{s,i}$ and $D_{s,i}$ are respectively the creation rate and destruction rate of species s in reaction i. The solver is run iteratively by adjusting the pressure at the beginning of the simulation until the final pressure matches the working conditions provided in input. The positive and negative charges are compared to ensure quasi-neutrality. If the plasma is not quasi-neutral, the guess value of the reduced electric field is modified and both the Boltzmann solver and the chemistry solver are run again. Once quasi-neutrality is ensured, the global cycle is run. The global cycle ensures that the final mixture has been reached. If not, the whole process is restarted. An additional loop, not included in LoKI, must be added to ensure that the electron density provided matches the experimental current. At the end of the global cycles of LoKI, the current is recomputed from the electron density, the electron mobility (obtained from the Boltzmann solver) and the reduced electric field:

$$I = n_e * \pi r^2 * q * E/N * \mu_{red} \tag{4.15}$$

where I is the current, r the radius of the tube and μ_{red} is the reduced mobility ($\mu_{red} = \mu * N$ where μ is the mobility). In this work, a tolerance criterion of 1mA is chosen. If $|I_{exp} - I_{sim}| >$

$1mA$, the electron density is modified and the whole process is run again. The simulation tools gives in the end a complete overview of the plasma parameters (EEDF, electron density, self-consistent reduced electric field and density of all the species included in the model) in the stationary state, as well as the evolution of densities between ignition of the plasma and steady state.

4.4.2 Resolution of the Boltzmann equation for electron kinetics

The EEDF is computed by the Boltzmann solver of LoKI, which has already been extensively described (Tejero-del-Caz 2019 and Tejero-del-Caz 2021). As CO_2, CO, O_2, CH_4, H_2 and H_2O are the main products, it is assumed that the EEDF in the plasma can be well described by using only these molecules in the Boltzman solver. It would not necessarily be an improvement to use more species, as they often do not have a set of complete and consistent cross-sections validated against the swarm parameters. Including other species in the EEDF would thus bring more uncertainty because of the validity of the sets employed.

The CO_2, CO, O_2 and O sets of cross-sections were taken from A. F. Silva et al. 2020, whose work in pure CO_2 serve as basis for this work. The cross-sections sets used in A. F. Silva et al. 2020 were taken from the IST Lisbon database on LXCat. The various processes included in the sets on the IST-Lisbon LXCat sets were described in Marija Grofulović et al. 2016 for CO_2, in Gousset et al. 1991 and in Luis Lemos Alves et al. 2016 for O_2 and O and in Ogloblina et al. 2019 for CO. For the computation of the EEDF, elastic collisions, electronic excitation, vibrational excitation and dissociation are included in the sets. The water cross-sections are taken from Budde et al. 2022, where a set of complete and consistent H_2O cross-sections was validated against the swarm parameters for the first time. The CH_4 cross-section are taken from D.Bouwman et al. 2021. Two complete and consistent sets of cross-section validated against swarm parameters are available for CH_4 to our knowledge: L L Alves 2014 (IST Lisbon database) and D.Bouwman et al. 2021 (Community database). The choice of D.Bouwman et al. 2021 was made for several reasons: first this sets include more dissociation cross-sections of CH_4, which in turn will give a better picture of the chemistry. Second, this sets does not include any 'fitted' cross-section (cross-section gathering several unknown processes fitted to match the swarm parameters). This avoid mixing two reactions in the same cross-section, making it easier to reuse the same set for the chemistry part.

4.4.3 Chemical kinetic scheme

The chemistry set is an input of the chemistry solver, independent of the input of the sets of cross-sections provided for the computation of the EEDF, which consists in a set of reactions along with their rates (which can be temperature dependant). Two types of reactions can be included: reactions involving electrons whose rate are calculated from the EEDF and provided cross-sections, and chemical reactions whose rate coefficients must be provided.

The pure CO_2 part of the chemical kinetic scheme, which was previously developed in A. F. Silva et al. 2020, was completed with CH_4 and by-products reaction. Because it was found experimentally that the molecules with two carbon atoms are only a minor product of the plasma, the C_2H_Y molecules were neglected to limit the complexity of the model. This CO_2-CH_4 kinetic scheme including only molecules with up to one C atom is referred to as the "simplified scheme" (a more complete scheme will be developed in the chapter 5). The list of species included in the model are presented in table 5.3. In A. F. Silva et al. 2020, the vibrational chemistries of CO_2, CO and O_2 were taken into account for the computation of the EEDF but not for the chemical part (the rates of vibrational excitation were simply not included in the chemistry solver), which still yielded good agreement between experimental dissociation and simulated one. The same choice is done in this work and is applied to CH_4 and water, whose vibrational excitation is removed from the chemistry set. Several reasons justify this choice. First, our measurements of the vibrational excitation of CO_2 and CO in a CO_2-CH_4 discharge (which will be presented in chapter 6) show that CO and CO_2 vibrational excitations are very efficiently

	neutral species	ions	excited states
Pure CO_2 case (validated in A. F. Silva et al. 2020)	CO_2, CO, O2, O	CO2+, CO+, O2+, O+, O-	CO(a^3P), O(1D), O2(b1Sg+), O2(a1Dg)
Simplified CO_2-CH_4	CH_4, CH_3, CH_2, CH, H_2, H, OH, H_2O, HCO, CH_2O	CH_4^+, CH_5^+, CH_3^+, CH_2^+, CH^+, H_2^+, H^+, H_3^+	

Table 4.3: List of species included in the chemistry scheme of the model

quenched by CH_4 and its by-products, leading to vibrational temperatures lower in CO_2-CH_4 than in pure CO_2. Second, recent studies on the vibrational relaxation of CH_4 have shown that the VT processes take place on a very short time-scale (Butterworth et al. 2020), leading to think that no vibrational excitation of CH_4 can build-up in our plasma and that the population of vibrationally excited CH_4 in the plasma is negligible. Third, the VV and VT rates coefficients between the various by-products of CO_2-CH_4 mixtures are very poorly known, with values in literature ranging over several orders of magnitude (D.F. Starr et al. 1974, Roger C. Millikan 1965a), making it difficult to accurately simulate the populations of the various levels.
For the simplified CO_2-CH_4 chemistry including only single-carbon molecules, the added chemistry totalizes 140 neutral-neutral reactions, 40 electron impact reactions and 40 ion-neutral reactions. All the reaction rates with their sources are given in the annexe 7. Most of the rate coefficients are taken from the NIST chemical kinetic database for the neutral species chemical reactions or from the UMIST database for the ionic reactions. Most of the ions were included because they could be obtained straight from electron impact on one of the major molecule of the plasma (CH_4, H_2 or H_2O). CH^+,H^{3+} and CH_5^+ were believed to play an important role in the plasma according to previous CO_2-CH_4 modelling in literature (C.Bai 2019). The kinetic scheme also include inflow and outflow reaction. The flow of gas is assumed to work in the following way: new reactant molecules enter the reactor and an equal number of particles from the gas mixture exits the reactor. All the species are concerned by the outflow. The inflows and outflows are simply added as creation or loss terms in the balance equation 4.16:

$$\left.\frac{\partial n_{[CO_2]}}{\partial t}\right|_{inflow} = \frac{f_{CO_2}}{f_{CO_2}+f_{CH_4}} * \frac{4.477962 * 10^{17}}{V_{reactor}} \tag{4.16}$$

$$\left.\frac{\partial n_{[CH_4]}}{\partial t}\right|_{inflow} = \frac{f_{CH_4}}{f_{CO_2}+f_{CH_4}} * \frac{4.477962 * 10^{17}}{V_{reactor}} \tag{4.17}$$

$$\tag{4.18}$$

for the inflow, where f_{CO_2} and f_{CH_4} are the flows of CO_2 and CH_4 in sccm, $4.477962*10^{17}$ is the number of particles in one sccm and $V_{reactor}$ the volume of the reactor. The outflow for a species s is given by

$$\left.\frac{\partial n_s}{\partial t}\right|_{outflow} = \frac{-n_s}{N} * f * \frac{4.477962 * 10^{17}}{V_{reactor}} \tag{4.19}$$

where n_s is the density of species s, N the gas density and f the total flow in sccm.

4.4.4 Diffusion and Recombination of atomic species at the walls

In the model, the diffusion and recombination of atomic species at the wall is taken into account. The characteristic loss frequency of a species ν_s at the wall is given by

$$\nu_s = \frac{\Lambda^2}{D_s} + \frac{V}{A} * \frac{4-2\gamma_s}{\gamma_s v_{ths}} \tag{4.20}$$

where V/A is the ratio of the reactor's volume over area, v_{th} the thermal velocity, γ_s the probability of loss, Λ the characteristic diffusion length and D the diffusion coefficient. In a cylindrical reactor of length L and radius R, Λ is given by

$$\frac{1}{\Lambda^2} = (\frac{2.405}{R})^2 + (\frac{\pi}{L})^2 \tag{4.21}$$

$$\sim (\frac{2.405}{R})^2 \text{ if L » R} \tag{4.22}$$

D is the diffusion coefficient computed according to Hirschfelder et al. 1964. One of the hypothesis of this model is the value of the atomic recombination probability. For Oxygen, the recombination has arbitrarily been chosen equal to the one in pure CO_2 at 2Torr, measured in A S Morillo-Candas, Drag, et al. 2019a. However, the oxygen recombination probability has a limited impact because the atomic oxygen density is expected to be negligible for cases with an initial CH_4 content higher than 10%. The recombination of H atoms at the wall is expected to be more important, though only a small amount of H is present in the plasma. Little work is available on the H recombination on a pyrex wall but the atomic H is expected to be very short-lived due to very fast recombination at the wall. In A.Rousseau et al. 2001, the loss probability of atomic H in a quartz tube at pressures between 1 and 5Torr is found to be one order of magnitude higher than the one for O_2 measured in A S Morillo-Candas, Drag, et al. 2019a. Previous calculations carried out in K.E.Shuler et al. 1949 support the hypothesis of a large recombination probability. The H recombination at the wall is therefore fixed one order of magnitude higher than the one of O_2, with a γ_H at 0.002. The effect of the recombination probability will be investigated further.

4.4.5 Charged species transport

The main loss of charges in the positive column of the glow discharge is the recombination at the wall. The transport of charged species in the plasma is therefore critical because it will impact the density of charged species and in turn the E/N chosen by the solver to reach quasi-neutrality. Because the E/N controls key processes through the EEDF like electron impact dissociation, the main dissociation channel in our plasma, an accurate description of the diffusion of charged species is necessary.

The ambipolar diffusion controls the transport of charged species in the plasma. In the low pressure glow discharge, the radial diffusion length is one order of magnitude higher than the positive ions mean free path λ_+, which is close to the high-pressure transport limit where the classical ambipolar diffusion is valid. However, the limit being not reached, the classical ambipolar diffusion scheme tends to overestimate the electron diffusion. The effective ambipolar diffusion scheme developped in Self et al. 1966 and Ferreira et al. 1983 and valid for the whole pressure range studied here for an electropositive gas was used instead. The model was generalized in Coche et al. 2016 for several positive ions.

The validity of the diffusion scheme can be questioned if negative ions are present in the plasma. The model developed in Coche et al. 2016 accounts for negative ions but only if the ratio of the diffusion length over the ion mean free path is below one, which is not the case as stated higher. The presence of negative ion can therefore raise issue on the validity of the scheme used. In this work O^- is the only negative ion included in the model and has a low density (as will be shown on figure 4.19 of section 4.5.3 leading to a very low electronegativity $(\frac{n_{negativeions}}{n_e})$ between 0.001 and 0.02. The effective diffusion scheme is therefore considered valid. The influence of the diffusion scheme used (classical or effective ambipolar diffusion) was already discussed in A. F. Silva et al. 2020 for the pure CO_2 glow discharge. The classical ambipolar diffusion was found to overestimate the self-consistently computed E/N compared to the one obtained with the pins/FTIR measurements, especially at low pressure. The effective ambipolar diffusion yielded better agreement between experiment and simulation on the reduced electric field, which in turn improved the agreement on the dissociation fraction of CO_2 and the atomic oxygen density. However, the reduced electric field remained overestimated, especially at low pressure, even with the effective ambipolar diffusion. Because of this previous results in the CO_2 low pressure glow discharge from A. F. Silva et al. 2020, the effective ambipolar diffusion scheme is used in this work.

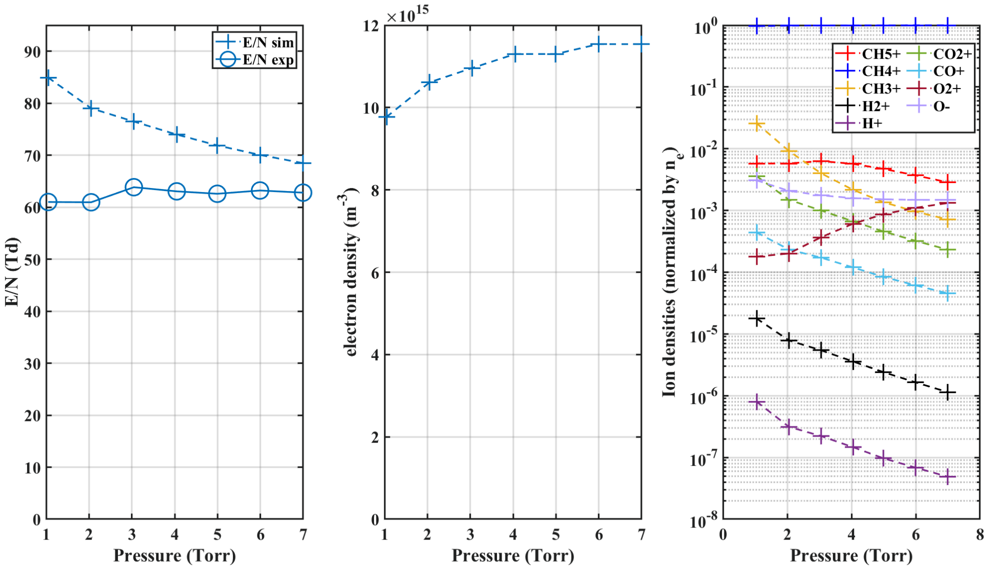

Figure 4.11: Electron kinetics for a pressure variation at 1.85sccm in a 60:40 CO_2:CH_4 mixture. The simulated and experimental reduced electric field are compared on the first graph. The evolution of the electron density and ion densities are plotted next. The simulation is plotted in dashed lines and the experiment in plain lines

4.5 Comparison of modeling and experimental results

General Comparison

It is shown *a posteriori* by the model that the composition *in situ* is very close to the composition downstream due to limited reactions in the post-discharge (which will be confirmed experimentally in chapter 5). This is due to the low density of reactive species (such as radicals or excited states) in the plasma. We therefore compare *in situ* simulation and downstream measurement.

A set of reactions concerning all the species from table 5.3 was assembled and is given in annexe 7. The model was first implemented using only rates from literature for the reactions of the set. The validation of the kinetic scheme proposed here is done through comparison of the measured quantities from the plasma (E/N and densities of the main species) with the simulated ones.
The electron kinetics part of the scheme is assessed first through comparison of the measured E/N (with the electric field from the pins and the gas temperature from the OES) with the E/N calculated self-consistently (from the quasi-neutrality cycle) in LoKI. It is the most direct way to check the good description of the electron kinetics in our model.

The reduced electric field from LoKI is compared to the experimental one on the first graph of figure 4.11 for a pressure variation at a flow of 1.85sccm and in a 60:40 CO_2:CH_4 mixture. The simulation clearly shows a trend not visible in the experiment: the simulated E/N increases with decreasing pressure while the experimental one stays steady. The experiment-simulation difference is about 8 Td at 7 Torr but it increases, reaching 17 Td at 2Torr. The gap at 1Torr is about 25Td and the insights obtained from the model at this pressure should therefore be taken with caution. Several hypothesis could explain this inconsistency. For example, if the diffusion of the charges to the wall at low pressure is not well accounted, the global charge could be ill-estimated. The choice of the diffusion scheme made for the charge diffusion to the wall could hence increase the electric field, which is likely to be the main reason of the difference. However, surface phenomenon could also play a role in the inaccuracy of the E/N. Indeed,

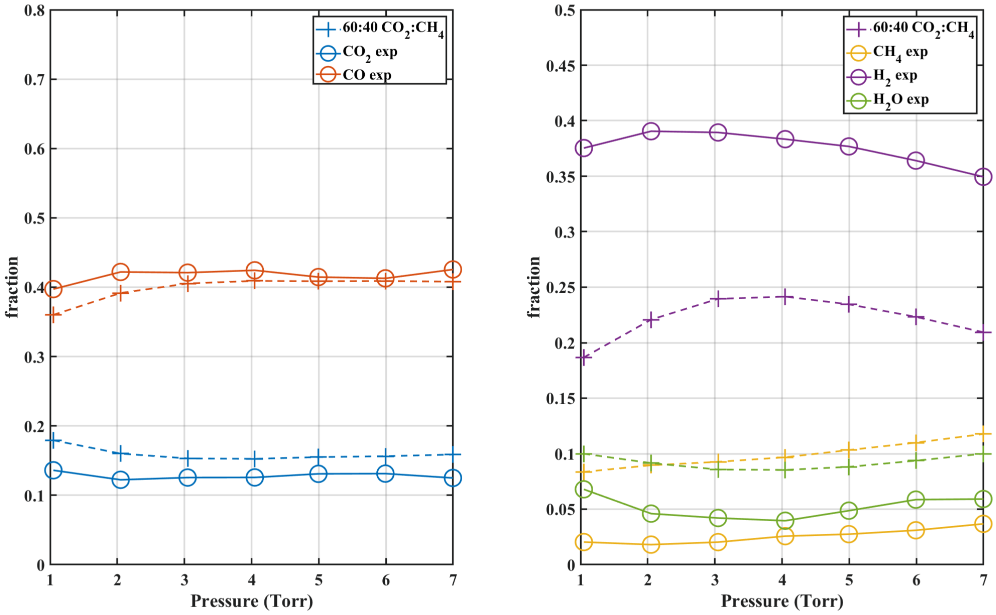

Figure 4.12: Comparison of the simulation and the experiment for a pressure variation at 1.85sccm in a 60:40 CO_2:CH_4 mixture. The simulation is plotted in dashed lines and the experiment in plain lines

surface processes becomes very important at 1Torr (A S Morillo-Candas, Drag, et al. 2019a) and unaccounted processes could affect the chemistry. Because of the large discrepancy in the computed reduced E field, the case of 1 Torr will not be discussed in the next section.

The second graph of figure 4.11 shows the electron density variation. The electron density increases with pressure but in a limited range. The electron density at 4 and 5 Torr are almost equal, which is due to the tolerance in the algorithm: in LoKI, the electron density is provided as input and the current is computed in the end as a function of the electron density and the reduced mobility. The algorithm then loops on the electron density until the simulated current matches the experimental one. Here, the tolerance criterion on the final value of the current ($|C_{sim} - C_{exp}|$ <1mA) is large enough so that the same electron density is a good fit for both the 4 and 5 Torr cases. The same thing is observed for 6 and 7 Torr. Finally, the 3rd graph of figure 4.11 shows the simulated ion densities normalized by the electron density. Over the whole pressure range, the main ion is CH_4^+, as opposed to what can be found in literature (which will be discussed in section 4.5.3), and accounts for almost 99% of the electron density. This ion is formed on one hand by ionization of CH_4, but also by charge transfer from other ions such as CO_2^+. The O^- ion, the only negative ion included in the model, only makes up for 0.1-0.5% of the electron density, which confirms that the plasma can be considered electropositive and that the effective ambipolar diffusion scheme can be applied.

The relatively good agreement between the experimental and simulated E/N above 1Torr ensures a proper description of the electron kinetics which gives confidence in looking now at the densities of the main neutrals species. The main species (CO_2, CO, CH_4, H_2 and H_2O) are compared in the same condition (1.85sccm and 5Torr with a mixture variation) on figure 4.12. The first graph on the left shows the CO and CO_2 densities, simulated in dashed lines and experimental in plain lines. The two species are well reproduced both in trends and value. On the second graph, the experimental CH_4 follows the same trend as the experimental CH_4, but is too high by a factor close to 3 on the whole pressure range. The CH_4 is under-dissociated in the model. The H_2 simulated density (in purple) shows a trend different from the experiment: though they both go through a maximum, it happens at 2Torr in the experiment while it is shifted at 4Torr in the simulation. The simulated values of H_2 fraction are very far from the experimental ones,

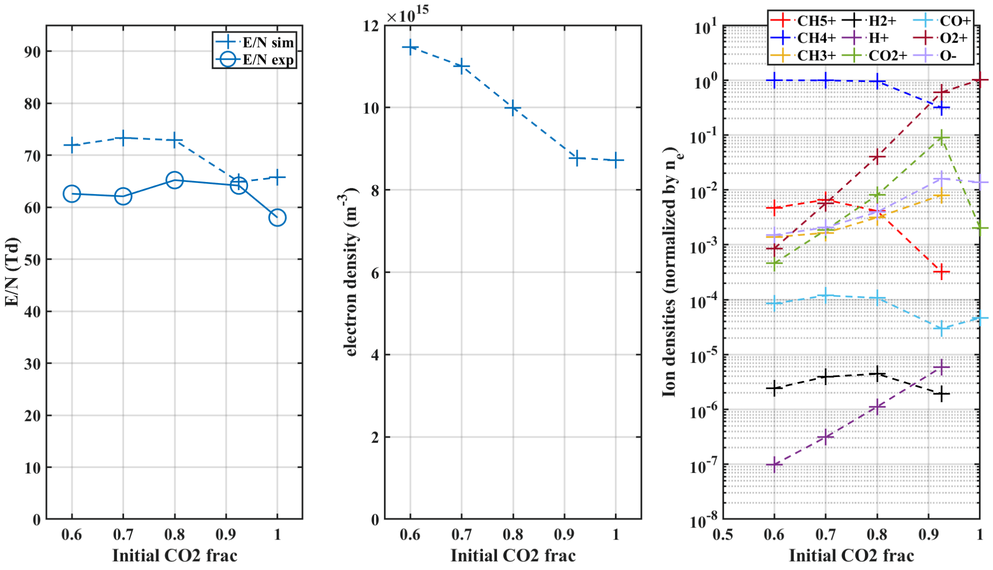

Figure 4.13: Electron kinetics for a mixture variation at 1.85sccm and 5Torr. The simulated and experimental reduced electric field are compared on the first graph. The evolution of the electron density and ion densities are plotted next. The simulation is plotted in dashed lines and the experiment in plain lines

with the simulations being too low by a factor 1.5 (with a peak value at 24% versus 37% in the experiment). Finally the simulated water density (in green) shows a good trend but is overestimated by a factor 2. This is surprising as a under-dissociation of CH_4 would predictably leave less hydrogen available to form water.

The following figure 4.13 shows the comparison between experiment and simulation for a mixture variation: the flow is kept at 1.85sccm and the pressure is fixed at 5Torr (where $|E/N_{sim} - E/N_{exp}| \sim 8Td$). This time, the agreement of the self-consistent E/N from LoKI compares well with the experimental one, keeping on the whole range of explored mixtures $|E/N_{sim} - E/N_{exp}| < 12Td$. No clear trend is visible neither in the experiment nor in the simulation. The electron density is plotted on the second graph of figure 4.13 and increases with initial CH_4 content. The electron density does not vary much between the 95:5 and the 100:0, just like the simulated reduced electric field. The main ion, O_2^+ in pure CO_2, quickly changes to CH_4^+ upon admixture of CH_4: at 5% of CH_4 in the initial mixture, CH_4^+ already accounts for 30% of the total ion density, and rises to close to 100% in the 80:20 mixture. This is likely due to the difference in ionization energy of the molecules. The ionization energy of CO_2, CH_4 and O_2 are respectively $\epsilon_{ionization}(CO_2) = 13.77eV$, $\epsilon_{ionization}(CH_4) = 12.6eV$ and $\epsilon_{ionization}(O_2) = 12.06eV$. In pure CO_2 plasmas, O_2 is the easiest molecule to ionize. Its density however drops upon admixture of CH_4 in the plasma, as seen in section 4.3.3. CH_4 becomes the easiest molecule to ionize, making CH_4^+ the main ion. The densities of the main species are shown on figure 4.14. Just like for the pressure variation, the CO_2 and CO are well reproduced, both in trends and in values. The peak in CO_2 (and the corresponding deep in CO), visible on the CO_2 maps 4.4, are also reproduced. Concerning the hydrogenated species, the same conclusions are drawn as in pressure variation: the CH_4 is under-dissociated, with a density overestimated on the whole range by a factor 3, leading in turn to an underestimated H_2 fraction. The H_2 fraction is underestimated by a factor 1.5. Once again, the water trend is reproduced, going through a maximum at 80:20 CO_2:CH_4 in both the simulation and the experiment, but the simulated values are overestimated.

In both pressure and initial mixture variations, the simulated CO and CO_2 show relatively good agreement with the experimental values, but the hydrogenated species are not well reproduced.

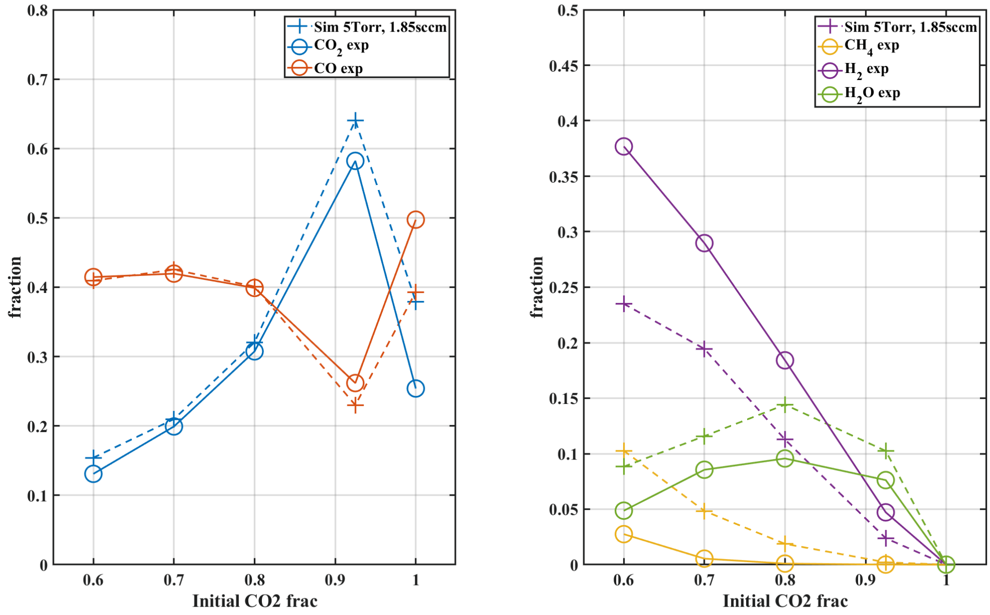

Figure 4.14: Comparison of the simulation and the experiment for a mixture variation at 1.85sccm, 5Torr. The simulation is plotted in dashed lines and the experiment in plain lines

The underdissociation of CH_4 seems to be the reason of the underestimation of H_2. The possible causes of the under-dissociation of CH_4 are investigated next.

4.5.1 Effect of CH_4 dissociation cross-section

As mentioned earlier, electron impact is one of the main dissociation process of CO_2 and CH_4 in our plasma. Because the simulated density of CH_4 is constantly overestimated, the hypothesis that the electron impact dissociation cross-section of CH_4 through the channels $e + CH_4 \rightarrow e + CH_3 + H$ and $e + CH_4 \rightarrow e + CH_2 + H_2$ could be underestimated arose. The dissociation cross-section for these two channels is taken from D.Bouwman et al. 2021 where they are not measured directly but estimated from total dissociation cross-section and branching ratios. Though the cross-sections eventually chosen in D.Bouwman et al. 2021 are the best fit for the validation against the swarm parameters, some experimental values of these cross-sections available in literature (Makochekanwa 2006) do show a factor of 2 compared to the one used in our range of interest ($\epsilon < 15eV$). The CH_4 dissociation cross-sections were therefore kept as such for the computation of the EEDF (to keep a set of cross-sections validated against swarm parameters) but the dissociation cross-sections were multiplied by a factor 2 in the chemistry part. This of course introduces an inconsistency between the Boltzmann solver and the chemistry solver but this has already been proved to be a good solution in some cases, for example for CO_2 dissociation (Marija Grofulović et al. 2016). The effect of this change on the electron kinetics, not shown here, is very minor. The effect of the doubling of CH_4 cross-section on the chemistry is shown on figure 4.15. The CO_2 and CO are only minorly modified by this change. The trends of the hydrogenated species are still reproduced for all conditions and the values are slightly improved by the doubling of the cross-section: the CH_4 percentage, previously at 11% in the 60:40 CO_2:CH_4 case, decreases to 9% (leaving still a factor 3 compared to the experimental value). In the same mixture, the H_2 goes from 23% without the doubling to 26% with, thus improving, while remaining far from the experimental 38% . Finally, still in the same mixture, the water density sees a minor improvement, going from 8.8% to 8%. The impact of doubling the CH_4 cross-section is therefore very limited but is still positive. However, given the improvement and given that a factor 2 correspond to the upper values available in literature for CH_4 dissociation cross-sections, this change is kept in the model for the rest of this work.

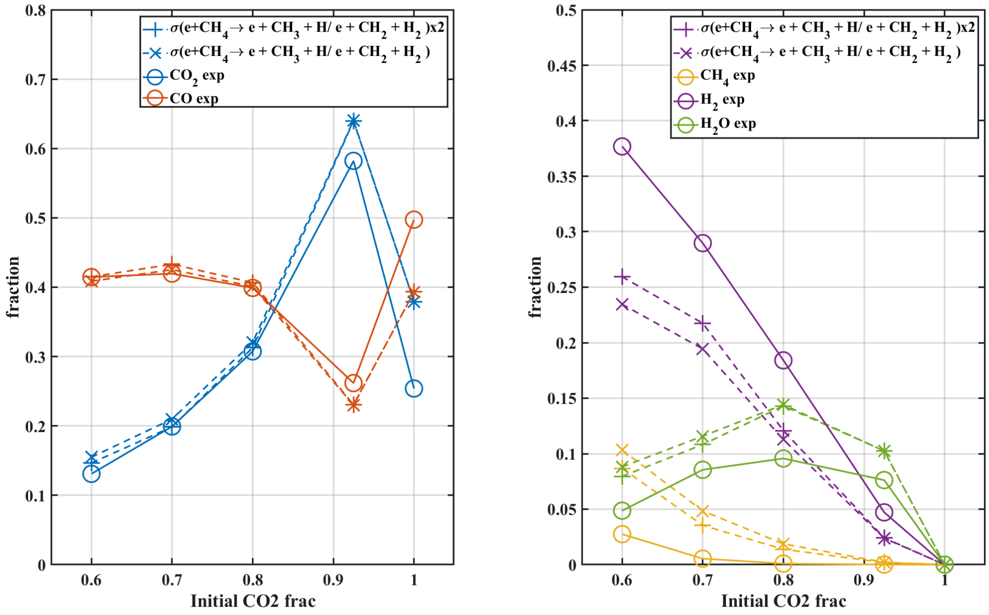

Figure 4.15: Study of the effect of the doubling of the CH_4 dissociation cross-section on the main products fractions at 1.85sccm, 5Torr. The simulation is plotted in dashed lines and the experiment in plain lines

4.5.2 Role of the O(1D) state in limiting CH_4 backreaction

The previous subsection proved that the overestimation of CH_4 and underestimation of H_2 were not explained by an underestimation of the CH_4 dissociation. The problem can therefore be taken the other way around: the back-reaction of H_2 could reform CH_4, lowering the H_2 density and increasing the CH_4 density. A back-reaction mechanism indeed exists and is taken into account in the model

$$H_2 + CH_3 \rightarrow CH_4 + H, \quad k = 2.52e - 20 * (\frac{T}{300})^{3.21} e^{-\frac{4380}{T}} m^{-3} s{-1} \tag{4.23}$$

It is the main cause of formation of CH_4 at this stage. The value of the rate is taken from W. Tsang et al. 1986, but other values given in Baulch et al. 1994 or Warnatz 1981 give values of the same order of magnitude. Several other values for this reaction are available on the NIST kinetic database but all give higher values of the rate, the 3 values quoted are at the bottom of the range of rates available. It is therefore unlikely that the back-reaction rate is overestimated. This could mean the reactants should be consumed in another reaction with a higher rate (presumably CH_3, because H_2 is underestimated in the model). The possibility of the reaction forming C_2H_6 from CH_3 ($CH_3 + CH_3 \rightarrow C_2H_6$) arise. However, the density of C_2H_6 that would have to be formed to obtain a good agreement on the CH_4 would add up about 2.5% of the gas density, which would be detected with the FTIR measurement but is not for the cases presented here. Though the formation of C_2H_6 could contribute to a better agreement, it does not seem to be the mechanism involving CH_3 that would prevent the backreaction.
It was noted that the O(1D) excited state of atomic oxygen played an important role in the plasma with reactions of O(1D) with CH_4, H_2 and H_2O (which will be discussed in section 4.6). For example, the production of OH is patly due to

$$CH_4 + O(1D) \rightarrow CH_3 + OH \tag{4.24}$$

The rate coefficients of these reactions are usually several orders of magnitude higher than the rate coefficients of the same processes with the O(3P) ground state. No rate coefficient is available in literature for the interaction of CH_3 with O(1D) and this reaction was not included

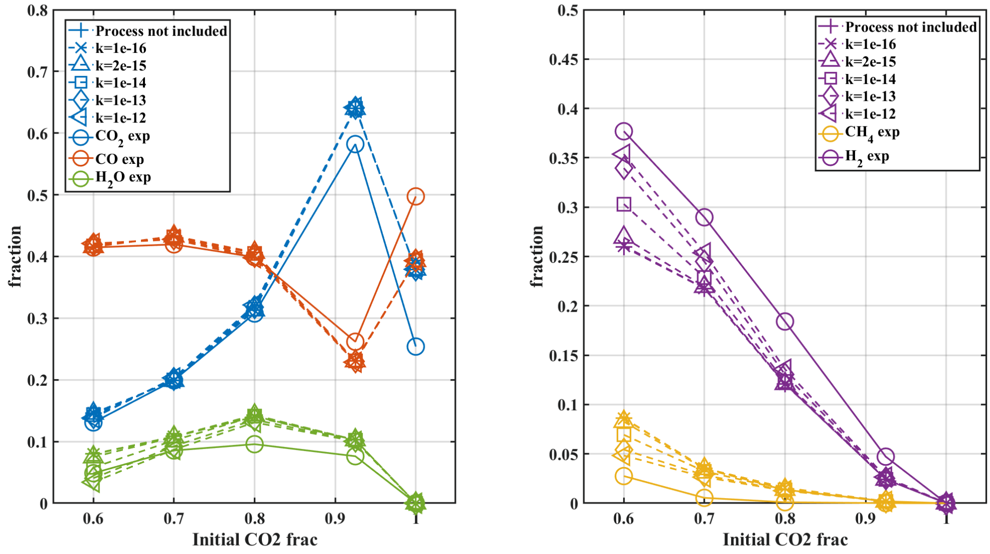

Figure 4.16: Study of the effect of the addition of process (4.25) on the main products fractions at 1.85sccm, 5Torr. The simulation is plotted in dashed lines and the experiment in plain lines

so far. As a test to assess the sensitivity of the results to a possible stronger oxidation of CH$_3$, one process was added to the kinetic scheme:

$$CH_3 + O(1D) \rightarrow CO + H_2 + H \tag{4.25}$$

Its counterpart exists for the ground state O(3P). This process is very likely to occur in our plasma, because both CH$_3$ and O(1D) are direct dissociation fragments of the two input gases:

$$e + CH_4 \rightarrow e + CH_3 + H \tag{4.26}$$
$$e + CO_2 \rightarrow e + CO + O(1D) \tag{4.27}$$

These two channels are the most probable dissociation channels for CO$_2$ and CH$_4$ in our plasma. The reaction 4.25 could therefore very well happen. This raise the question of the rate of the reaction. The next figure (4.16) shows the influence of process(4.25) on the chemistry with different values of the rate coefficient, varied between k$_{4.25}$=1e-16m^{-3} and k$_{4.25}$=1e-12m^{-3}. The lower value k$_{4.25}$=1e-16m^{-3} is the order of magnitude of the same process with O(3P) at 600K. Because of the electronic energy of the O(1D) state (∼1eV), the rate coefficient k$_{4.25}$ is expected to be higher than the one for O(3P). The various simulations are plotted in dash lines and the experiment is in plain lines. In this plot, due to the great number of curve overlapping, the water fraction was plotted with the CO and CO$_2$ fractions. First, the CO$_2$ and CO remain unchanged by this new process, and both trends and values are well reproduced. Looking at the CH$_4$ in yellow, the simulated fractions are significantly improved by the addition of the process. In the case of the 60:40 CO$_2$:CH$_4$ mixture, a very minor difference is seen on the CH$_4$ fraction (of the order of 0.04%, from 8.63% to 8.59%) for k=1e-16. In this same mixture, increasing k$_{4.25}$ to 1e-14 decreases the CH$_4$ fraction to 6.9%. Finally, adding two extra orders of magnitude (k$_{4.25}$=1e-12) bring the CH$_4$ fraction down to 4.8% . This value is still far from the 2.8% of CH$_4$ measured experimentally, but this process, depending on its rate coefficient, allows to greatly improve the CH$_4$ fraction. The amelioration can be seen for all mixtures but with a lesser importance. Similarly, in a 60:40 CO$_2$:CH$_4$ mixture, the H$_2$ fraction is also increased with the rate of 4.25: the value without (26%) is raised to 30% with k$_{4.25}$=1e-14 and to 35% with k$_{4.25}$=1e-12, not so far from the experimental 37%. The amelioration is also here seen for all percentages. Finally, looking at the water fraction at high CH$_4$ initial percentage (60:40 CO$_2$:CH$_4$), the simulated initial value (7.9%) is improved with k$_{4.25}$=1e-14 down to 5.7%,

Process	Value with O(3P)	at 300K	at 600k	value with O(1D)
$CH_4 + O \rightarrow CH_3 + OH$	$2.26e\text{-}18*(\frac{T}{300})^{2.2}exp(\frac{-3819}{T})$	6.69e-24	1.79e-20	1.35e-16
$H_2 + O \rightarrow OH + H$	$3.4e\text{-}19*(\frac{T}{300})^{2.67}exp(\frac{-3159}{T})$	9.08e-24	1.12e-20	1.2e-16
$H_2O + O \rightarrow OH + OH$	$1.84e\text{-}17*(\frac{T}{300})^{0.95}exp(\frac{-8570}{T})$	7.25e-30	2.23e-23	2e-16

Table 4.4: Comparison of the rate coefficients of the reaction involving O(3P) and O(1D) available in literature. The source of the rate coefficients are available in supplementary information

close to the experimental 4.8%. However when k is increased above 1e-14, the water fraction is underestimated, dropping below the experimental value (with 4% for $k_{4.25}$=1e-13 and 3.4% with $k_{4.25}$=1e-12). The 60/40 mixture is the only case where this is observed; in all other mixtures, increasing k brings experiment and simulation closer. It therefore appears that a large value of the rate coefficient is largely beneficial for the agreement of CH_4 and H_2, and for the one of H_2O until a certain point, showing the interest of adding that process to the model. However, a reasonable value of the rate must be chosen. To this aim, the rates coefficient available in literature for reactions with O(1D) and O(3P) are compared in table 4.4. It appears that the rate coefficient with O(1D) can range from 1000 to 10000 time the one of O(3P). The model seems to point toward a high value of the rate, therefore a factor 1000 will be kept. Hence, we choose

$$CH_3 + O(3P) \rightarrow CO + H_2 + H,\, k = 2.8e - 17m^3/s$$
$$CH_3 + O(1D) \rightarrow CO + H_2 + H,\, k = 2.8e - 14m^3/s$$

In our conditions,the gas kinetic rate coefficient for O and CH3 is of the order of 10 15m3s 1. The large rate coefficient needed to achieve good agreement, higher than the gas kinetic rate coefficient, suggests that the reaction is an effective process hiding several processes. These other processes could involve other excited states like higher electronically excited O states or excited OH radicals. The process is nevertheless kept in the model with the rate give above. This remains of course a rough approximation and further work would be needed to prove the rate of this particular process but its existence seems plausible and its influence on the results is very beneficial to match the experimental densities.

This illustration of the possible importance of the O(1D) state highlights the lack of data (even the absence!) for other excited states. O(1D) is one of the very few excited states for which rate coefficients can be found for the interaction with hydrogenated species. No rate can be found for instance for the reaction $C_XH_Y + CO(a^3\Pi)\ \forall X\&Y$ despite the crucial role of $CO(a^3\Pi)$ in pure CO_2 plasmas put forward in A. F. Silva et al. 2020. The other excited states could also improve the model if properly taken into account.

It was verified that the addition of reaction (4.25) does not change the electron kinetics. The self-consistent reduced electric field at 1.85sccm, 5 Torr is shown below on figure 4.17 along with the experimental reduced electric field. The agreement found earlier is maintained with the same gap: $|E/N_{sim} - E/N_{exp}| < 12Td$. The trend with pressure must also be verified. The following figure 4.18 shows the comparison on the main species fraction and the reduced electric field for experiment and simulation. First, looking at the third graph of figure 4.18 (showing the reduced electric field), it appears that the addition of process (4.25) and the doubling of the CH_4 cross-section only has a minor impact on the electric field, which conserve a similar agreement as before. The divergence between experiment and simulation is still seen at low pressure. The 2Torr measurement, which previously showed $|E/N_{sim} - E/N_{exp}| \sim 20Td$ now shows a difference of 21Td, showing the little impact overall. The fractions of CO_2 and CO, shown on the first graph of figure 4.18 are in very good agreement, both in trend and values. The CH_4 fraction is still overestimated by a factor slightly smaller than 2, but the trend is well reproduced and the gap only correspond to a few percent of the total gas density. The H_2

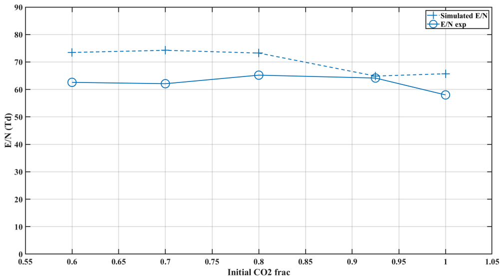

Figure 4.17: Comparison of the experimental and simulated reduced electric field (after inclusion of process 4.25 with the chosen rate) for an initial mixture variation at 1.85sccm, 5Torr. The experiment is in plain line and the simulation in dashed line

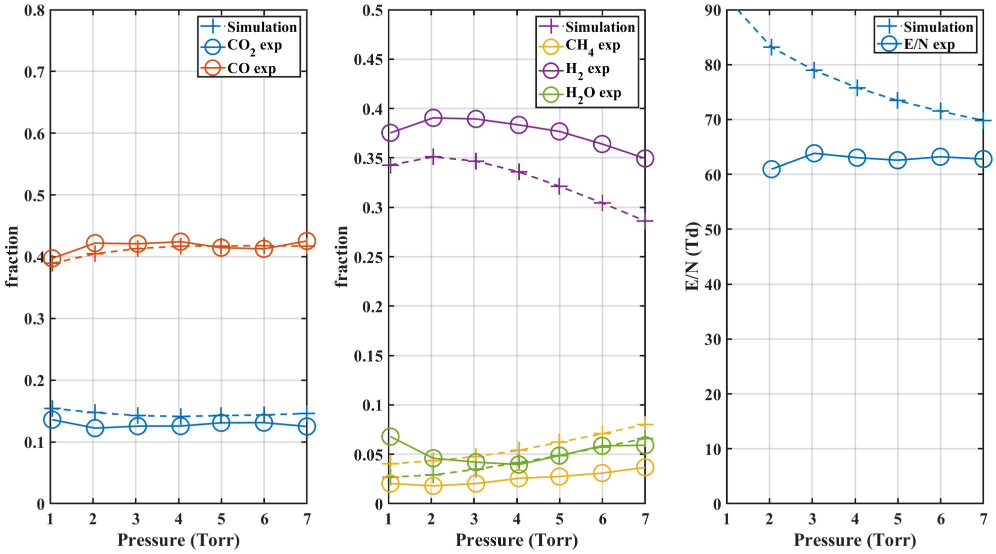

Figure 4.18: Comparison of experiment and simulation for the E/N and the main products densities (after inclusion of process4.25 with the chosen rate) for an pressure variation at 1.85sccm in a 60:40 CO_2:CH_4 mixture. The experiment is in plain line and the simulation in dashed line

Reaction	Rate coefficient (m^3s^{-1})	Reference
$CH_4^+ + CH_4 \rightarrow CH_5^+ + CH_3$	$1.5.10^{-15}$	D.Smith et al. 1977
$CH_4^+ + H_2 \rightarrow CH_5^+ + H$	$4.89.10^{-17} * \frac{T}{300}^{-0,14} * exp(-36.1/T)$	D.Smith et al. 1977

Table 4.5: CH_5^+ main reaction mechanism

results are now in much better agreement. The maximum, previously shifted to 4 Torr in the simulation is now at the same pressure as the experimental maximum, though the simulated values are still a bit lower than the experiment.

- A set of chemical reactions including only molecules with one carbon atom is sufficient to reproduce reasonably well all the species observed in the downstream of a low pressure glow discharge in CO_2/CH_4 mixtures
- the main issues are the overestimated E/N at low pressure (maybe due to improper charge diffusion scheme) and lack of dissociation of CH_4 corresponding to a lack of H_2 production in the model
- An increase of the rate of CH_4 electron impact dissociation, as well as for all CH_4 direct oxidation processes seem insufficient to explain the very low fraction of CH_4 in the experiment
- only a strong reduction of CH_3 density by adding an efficient oxidation process with O(1D) (reaction 4.25) would be able to account for the observed CH_4 and H_2 in all pressures and gas mixtures studied, but the rate for this reaction is unknown
- given the strong rate coefficient attributed to reaction 4.25 (above the gas kinetic rate coefficient), the reaction is likely an effective process, hiding other processes.

The kinetic scheme proposed until now includes the highest electron impact dissociation rate from literature as well as the additional reaction 4.25 to achieve good agreement between measured and modelled fractions. Other important choices/hypothesis had to be made in this model and their influence on the results will now be discussed.

4.5.3 Effect of the CH_5^+ ion

In the model presented here, CH_4^+ is the main ion when the initial proportion of CH_4 is higher than 10%. It is usually found in literature that CH_5^+ is the main ion, as shown both in Bie et al. 2015 and C.Bai 2019, where it is the most abundant ion in two different types of discharge. The main reaction forming CH_5^+ in these discharges are listed in the table 4.5 with their rate coefficients. The rate coefficients are taken from the UMIST database (like in Bie et al. 2015 and C.Bai 2019). The effects of the two reactions on the simulation with the present kinetic scheme has been tested and is shown on figure 4.19. Only a minor impact is seen on the plasma chemistry, not shown here: the fractions are shifted by 1%, in the good direction for CH_4 and H_2 but in the wrong direction for CO_2 and CO. They have however a strong effect on the electron kinetics (both the reduced electric field and the ion densities), which are shown on figure 4.19. On the first graph of figure 4.19, the experimental reduced electric field is plotted in plain line and the simulated one is in dashed line. The case where the two reactions of table 4.5 are included is shown with x marker, the case without is plotted with + markers. A significant improvement is seen when the reactions are removed, with an improvement of about 8∼9Td, reducing the gap between experiment and simulation to 11Td in the 60:40CO_2:CH_4 (vs 20Td when the reactions are included). The reason of this improvement probably lies in the very high value of the rates of these CH_5^+ production reactions. The rate coefficients for these reaction are one order of magnitude higher than the typical rates of ion reactions, leading to a change of the main ion when they are added to the model, as visible on the second graph on figure 4.19:

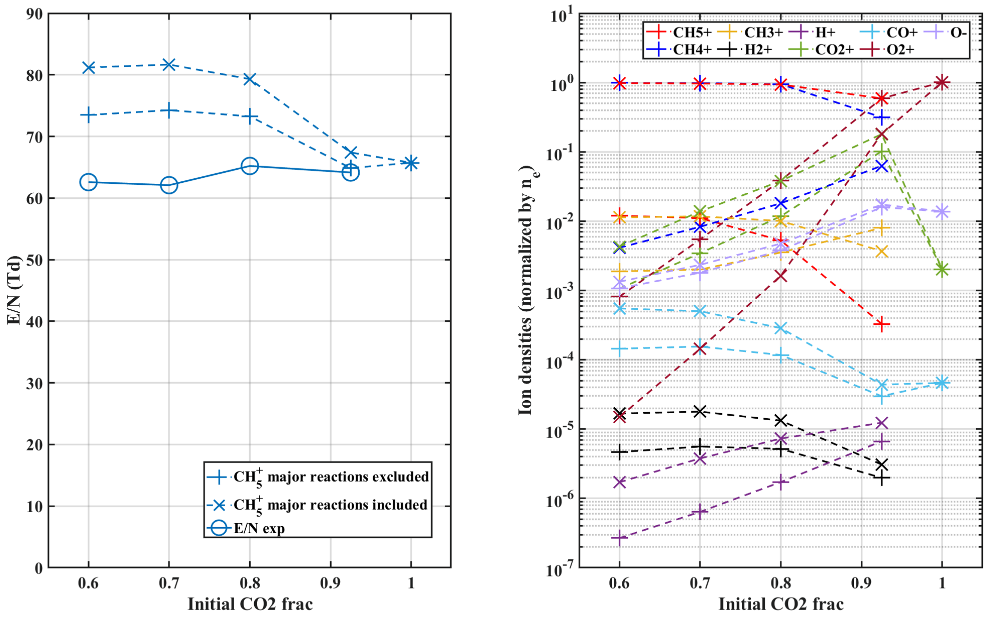

Figure 4.19: Effect of the CH_5^+ production reactions of table 4.5 on the electron kinetics in the case of a initial mixture variation at 1.85sccm and 5 Torr. The case where the reactions are included are plotted with x markers, the case where they are not included are plotted with + markers

when the reactions are added (with x markers), CH_5^+ (in red) is the main ion whereas it only accounts for 1% of the ion density when the reactions are not here (with + markers). The CH_4 is first ionized forming CH_4^+, followed by an efficient production of CH_5^+ (due to the high rate). However, CH_5^+ is much more easily destroyed than CH_4^+. First the higher reduced mobility of the CH_5^+ ion is about 1.5 times higher than the one of CH_4^+ (Viehland et al. 1995), leading to higher diffusion and loss to the wall. The main CH_5^+ recombination reaction is

$$e + CH_5^+ \rightarrow CH_4 + H \tag{4.28}$$

The rate coefficient of this reaction, computed with LoKI, is one order of magnitude higher than the rate coefficient of any CH_4^+ recombination reaction. When the reactions of table 4.5 are included, charges are quickly transferred to CH_5^+ and lost. In turn, the reduced electric fields increases to ionize more CH_4 and compensate for the loss of CH_5^+. The improvement of E/N when the reactions are removed points toward an overestimation of the rates of creation of CH_5^+ (they are one order of magnitude higher than typical rates of ion productions). They were originally determined in D.Smith et al. 1977 by mass spectrometry. Another experimental determination, again by mass spectrometry, from F.H.Field et al. 1957 gives a rate coefficient of approximately $4e^{-16}$ for the first channel in our conditions (versus $1.5e^{-15}$) in D.Smith et al. 1977). Because of the large spread of the values and their impact on the reduced electric field and the dominant ion, it was decided not to include these reactions in the model.

4.5.4 Effect of H recombination

The H atom in the plasma play an important role. Along with CH_3, they are the main dissociation product of CH_4 and will therefore be involved in many reactions. It is essential that they are correctly simulated. One of the main loss of H atom is the recombination of H into H_2 at the walls. As mentioned in section 4.4.4, the wall recombination of H atoms in the plasma is estimated based on literature measurement. The H atom recombination is expected to be faster than the O atom recombination, giving an indication of the minimum value expected

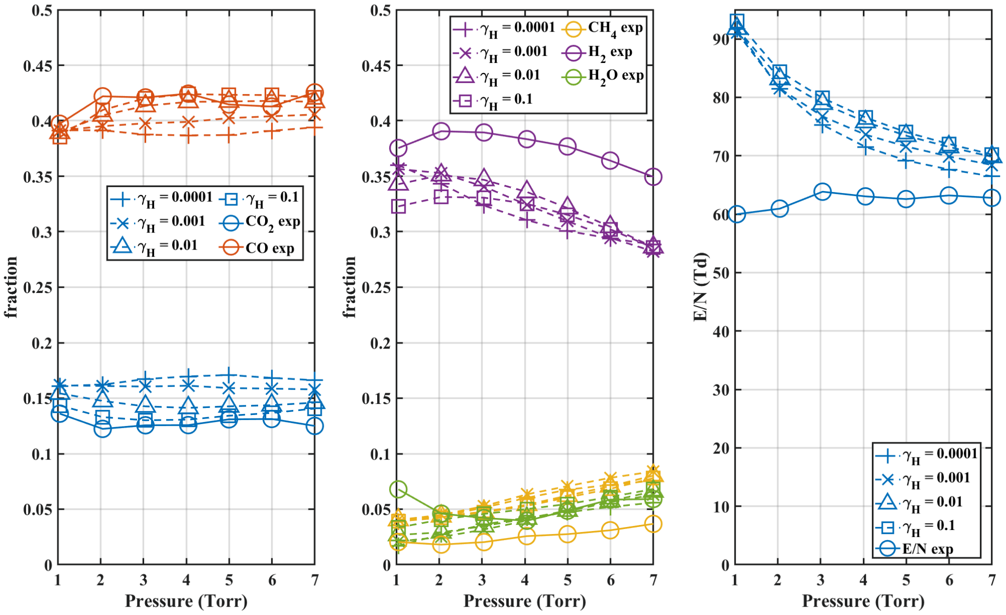

Figure 4.20: Study of the influence of the H wall recombination probability γ_H as a function of pressure in a 60:40 CO_2:CH_4 mixture at 1.85sccm. The measurement are shown in plain line, the simulation is plotted in dash lines

for the H recombination probability. The real value however remains uncertain. A study of the influence of the recombination probability of H atoms at the wall, γ_H, is presented on figure 4.20 as a function of pressure in 60:40 CO_2:CH_4 mixture at 1.85sccm. The influence of γ_H on the reduced electric field and main products fractions is presented for γ_H ranging from 10^{-4} (order of magnitude of the value chosen for O in pure CO_2 plasmas) to 10^{-1}. The influence on the reduced electric field is shown on the third plot of figure 4.20. The gap between experiment and simulation is increased with the value of the recombination probability. The difference between model and experiment however varies with pressure. The largest increase is seen at 4 Torr, where the value jumps from 71.5Td for γ_H=10^{-4} to 76.5Td for γ_H=0.1, farther from the experimental 63Td. At other pressure, the increase in E/N is closer to 2∼3Td, always increasing the difference between experiment and simulation. As for the chemistry, presented on the first 2 graphs of figure 4.20, the effect of the increasing γ_H is non monotonous and depends very much on the pressure. For H_2 between 2 and 7 Torr, using γ_H=10^{-2} always gives the highest H_2 density, with the best agreement with experimental H_2. The ordering of the H_2 densities obtained with γ_H=10^{-3} or γ_H=10^{-1} are not very clear and change with pressure. This is probably due to a balance between electron impact dissociation processes producing the atomic H and the back-reaction mechanism 4.6.1 ($CH_3 + H_2 \rightarrow CH_4 + H$). The increase of γ_H indeed increases the reduced electric field, in turn increasing electron impact dissociation of CH_4 and formation of atomic H through 4.26. H_2 formed by recombination of atomic H can react with CH_3 to reform CH_4. A balance of these processes probably explains the observed evolution of the H_2 density with γ_H. It must also be noted that the experimental trend of H_2 (with a maximum at 2Torr) is only reproduced for $\gamma_H = 10^{-2}$ and $\gamma_H = 10^{-1}$. No clear trend can be established for the effect of the increase of γ_H, but it can be concluded that for all species showed here, the variation of γ_H over 4 orders of magnitude can change the fraction by ±4%. The expected value of the recombination probability for Hydrogen is 10^{-3}, value proposed in A.Rousseau et al. 2001 for low pressure hydrogen microwave discharge, or 10^{-2}, 10 to 100 times higher than O from values drawn from A S Morillo-Candas, Drag, et al. 2019a for O. γ_H=10^{-2} is kept for the rest of this work. It must also be well noted that the wall recombination probability is expected to vary with pressure, as shown for O atoms in A S Morillo-Candas, Drag, et al. 2019a where the γ_O,

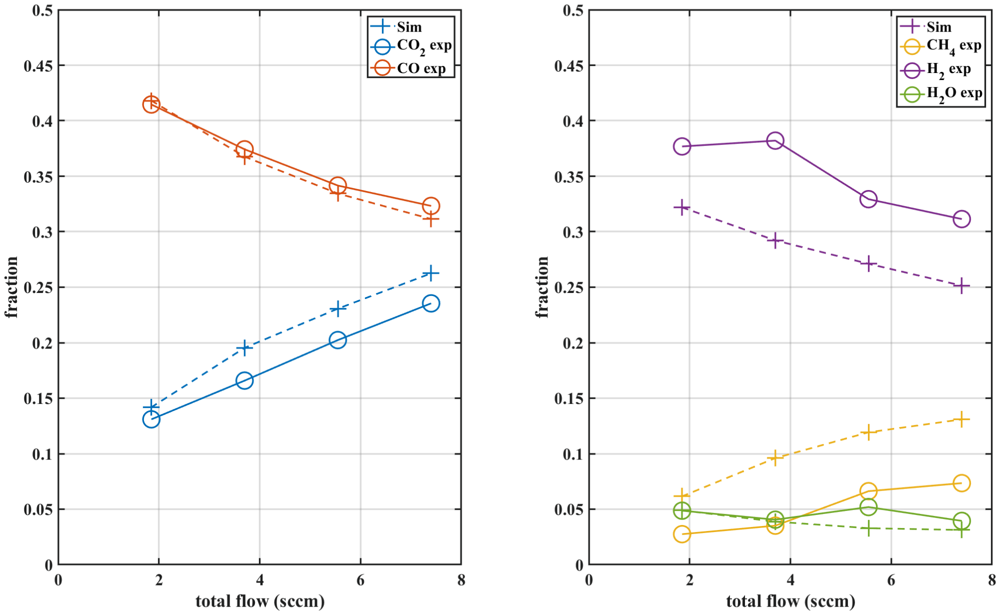

Figure 4.21: Comparison of the simulated and experimental fractions of the main species as a function of the flow for a 60:40 CO_2:CH_4 mixture at 5Torr

the recombination probability of atomic O in a O_2 plasma can vary by a factor 4.5 between 2 and 5 Torr. Keeping a constant value of γ_H with pressure is an approximation, which should be refined in further work. Though this does not change the heart of the results of the model, this is one of the blind spot of the model, whose experimental investigation should be pursued.

4.5.5 Effect of the flow

So far, only the pressure and gas mixture variation had been investigated. The validity of the model for different flow must be tested. The effect of the flow variation is shown on figure 4.21, where the flow is varied from 1.85 to 7.4 sccm at 5Torr in a 60:40 CO_2:CH_4 mixture. Decreasing the flow increases the residence time of the gas in the plasma and therefore increases the energy input in the gas via electron impact reactions. It is therefore expected that decreasing the flow increases the dissociation for both CO_2 and CH_4. This is observed on figure 4.21, where the fractions of CO_2 and CO show an almost linear trend with the flow. The evolution of the main hydrogenated species CH_4, H_2 and H_2O in the simulation generally reproduce the trends observed experimentally, though the simulated values can show differences (up to a factor 2 for the CH_4 at low flow, as presented in the previous section). The lower flows emphasize the role of the chemistry because less gas is renewed, lowering the influence of the inflow and outflows on the final balance. Because of that, the rest of the discussion will focus on the case of 1.85sccm

4.5.6 Conclusions on the presented model

Overall, the model provides a good agreement between experiment and simulation over the whole range of parameters explored (pressure from 1 to 7Torr, from pure CO_2 to 60:40 CO_2:CH_4 and for flows going from 7.4sccm to 1.85sccm). The simulated points at low pressure show a discrepancy in the reduced electric field, indicating that the electron processes, driving the dissociation in our plasma, are not well accounted for at low pressure (likely because of the diffusion scheme of the ions used). Therefore, the insights taken from the model on the behaviour of the plasma at low pressure (1Torr or below) should be taken with caution.
It must be kept in mind that the addition of the process (4.25), seemingly necessary for good agreement between the experiment and the simulation, does not allow perfect agreement between

experiment and simulation. It significantly improves the results but still leaves some discrepancy between experiment and simulation. It is probable that solving the remaining difference requires the use of the chemistry of the C_2H_Y molecules (especially because in some conditions C_2H_4 is detected at high flow, meaning at low residence time, pointing toward the intermediate role of this species). However, this demonstrates that if the electronic states are properly described, the role of the C_2H_Y molecules might not be prominent. The models without supporting measurement of the densities of these species (C.Bai 2019,Bie et al. 2015) might overestimate their impact. Indeed, none of these models include the process 4.25, and sometimes do not include O(1D) at all. It is of course expected that when operating at higher pressure, O(1D) is quenched by collision very quickly (which also happens here, see section 4.6) and its density is lower. This does not mean that it can be neglected in models: despite the quenching, part of O(1D) react and can still impact the other species (see 4.6). In a model computing the temperature self-consistently (like Van Alphen et al. 2021), the conversion of electronic excitation to translational excitation must be taken into account. To clearly determine the role of O(1D) compared to the one of large molecules, the present model must be improved with an additional set of reaction including the C_2H_Y molecules. This will be presented in chapter 5.
A limit of the model must be explicited: the present test data only cover a limited range of E/N and pressure. The limited range of E/N prevents us from drawing general conclusions on the electron impact processes at high electron energy. As underlined prevously, the factor 2 on the CH_4 dissociation cros-section is only valid in our range of interest (ϵ<15eV). The relatively low E/N compared to other plasma experiment reduces the influence of the electron processes compared to the chemical processes. The same model used for NRP experiment might underestimate or overestimate the electron impact processes, and further work should be conducted on a different range of E/N to validate the model outside of the present conditions. Moreover, the limited pressure range (below 7Torr) used here does not allow to fully validate the 3-body processes which will take place at higher pressure. The 3-body reactions are included in the model, but their rate is not considered validated as the present conditions limit their influence. Further work at higher pressure should also be conducted to verify their influence.

- A good agreement was found for the model over the whole range of pressure, flows and gas mixture investigated
- Doubling the CH_4 electron impact dissociation cross-section for the chemistry set only was found to improve the results but insufficient to explain fully the CH_4 conversion
- The addition of process $CH_3 + O(1D) \rightarrow CO + H_2 + H$, not described in literature, was found to significantly improve the results. The rate coefficient was estimated based on the rate of the same reaction with O(3P) and on literature values for rates with O(1D). The rate coefficient used here is however higher than the gas kinetic rate coefficient, leading to believe that this process is an effective process hiding other reactions (likely involving other excited states).
- The CH_5^+ ion, usually main ion in CO_2-CH_4 plasma in CO_2-CH_4 plasma literature, was found to be formed by a single reaction whose rate could be overestimated. Removing the single CH_5^+ creation reaction made CH_4^+ the main ion with a significant improvement on the electron kinetics
- After testing several value, the probability of recombination of atomic H was fixed to γ_H=0.01
- The present model is validated in a limited range of E/N and pressure, limiting the validation of the electron processes to low energy and the validation of the 3-body reactions

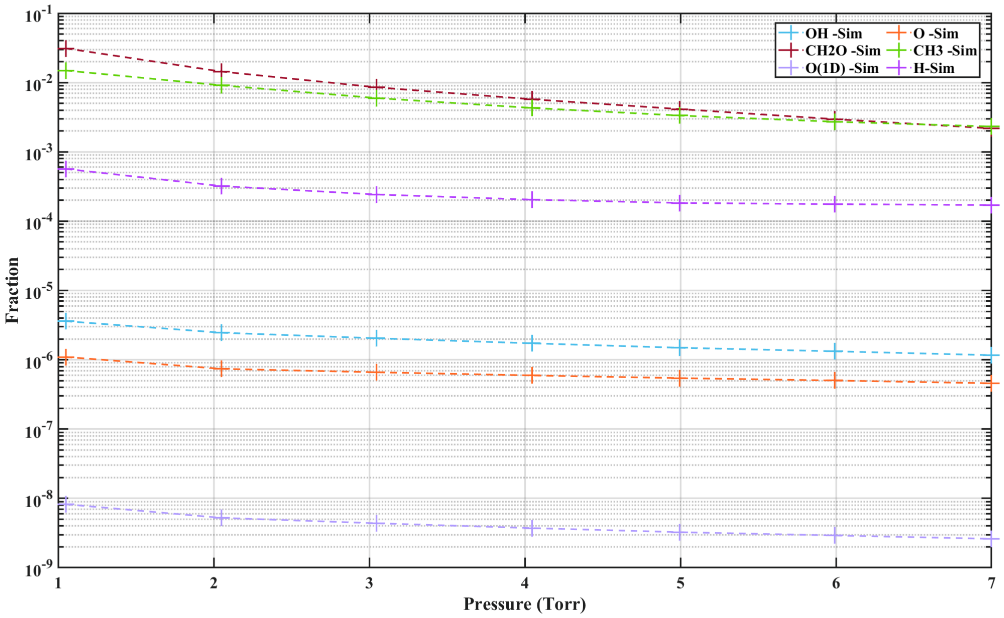

Figure 4.22: Evolution of the simulated fractions of minor species with pressure in a 60:40 CO_2:CH_4 mixture at 1.85sccm.

4.6 Discussion of the reaction pathways

Now that the validity of the model has been verified by comparison with the experiment, it is used to understand more in details the processes of formation of the main species, as well as the role of the minor and/or unmeasured species such as the OH radicals, the CH_2O or the excited state O(1D), whose role was highlighted in the previous section. The mechanisms depend on the parameters explored (pressure and mixture), therefore the influence of each parameter is discussed separately.

4.6.1 Effect of pressure on CO_2-CH_4 plasmas main products

Varying the pressure in our glow discharge changes mostly the gas temperature from 300 K to ∼700K at 7 Torr. As seen previously, the reduced electric field remains stable with pressure when the initial CH_4 percentage is above 10%. For most of the major species, the densities evolve in a limited range with pressure, as visible on figure 4.18. For all pressures, CO_2, H_2O and CH_4 remain respectively around 12, 5 and 4%, while CO evolve in a larger yet still narrow range between 36 and 44% of the total plasma density. The experimental variation of H_2 is also restrained in the range 35-40% of the plasma density. This limited evolution with a strongly increasing temperature (from 400K to 700K) proves already that the thermal dissociation of CH_4, which starts above 500K(J.R.Fincke et al. 2002), is not a major contributor to the dissociation in our conditions. This illustrates the interest of cold plasmas to achieve DRM.

Before discussing the reaction pathways explaining the major species, the fractions of the minor species must be known. The following figure 4.22 shows the evolution of the minor species with pressure in a 60:40 CO_2-CH_4 mixture at 1.85sccm. The minor species plotted include atomic O and H, the formaldehyde (CH_2O), the excited state O(1D) (whose role was highlighted higher), and the radicals OH and CH_3. For clarity, the other CH radicals (CH_2, CH and C) were not plotted but are computed in the model. Firstly, unlike the major species, the fraction of the minor species are not stable with pressure: CH_2O varies by an order of magnitude between 2 and 7 Torr (from 1.4% at 2Torr to 0.2% at 7Torr), like CH_3. The CH_2O, though

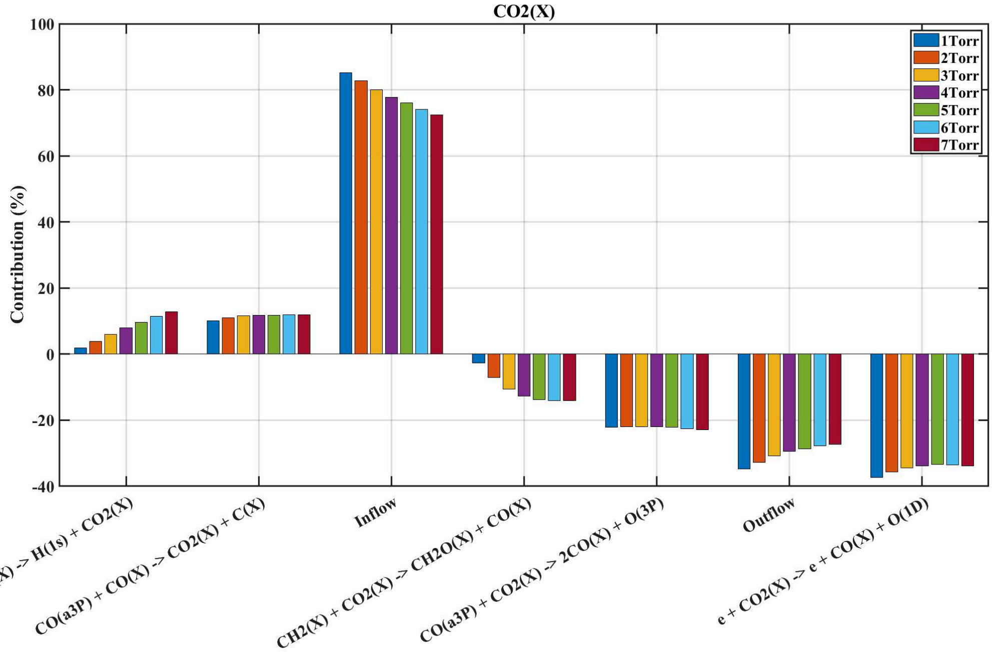

Figure 4.23: Evolution with pressure of the contribution of the main creation and destruction of CO_2 in a 60:40 CO_2:CH_4 plasma at 1.85sccm. The positive contribution represent the creation, the negative the destruction processes. Each pressure is plotted in a different color

IR active, is not fitted in our experiment. The lines are convoluted with CH_4 lines and have a weaker line-strength. Because of the low fraction of CH_2O, the convolution with CH_4 lead to large uncertainty on CH_2O. CH_2O represents in our conditions between 3 and 0.2% of the total density depending on the conditions. This is similar to Bie et al. 2015 where the CH_2O was also the highest 'minor species', representing ~0.1% of the density. Bie et al. 2015 modelled that in conditions with up to 30% of initial CH_4, the CH_2O density was close to the CH_3OH density, not included in the present model and whose inclusion is a lead for future work. The least varying species is the OH, decreasing only by a factor 3 from 1 to 7 Torr. The decrease of the radical density with pressure is expected due to both the increase of the gas temperature (which increases the rate coefficients of recombination reactions) and the increasing collision frequency (and therefore recombination reactions) with pressure. The simulated O fraction is about 1e-4%. This is very low but possible as O is below our actinometry detection level in the 60:40 CO_2:CH_4 condition studied here. The H fraction varies between 0.05 and 0.01%, one order of magnitude lower than actinometry estimation, which could be due to the wall recombination probability (whose order of magnitude is unknown). Having a good picture of the fractions, the reaction pathways can be discussed.

The aim of this section is to understand the evolution of the main processes driving conversion in CO_2-CH_4 plasmas as a function or the pressure, even if they vary a lot with pressure. It is hard to draw a general trend, but some constant phenomena can be observed, for example in CO_2. The evolution of the processes creating and destroying CO_2 with pressure is shown on figure 4.23 in a 60:40 CO_2:CH_4 plasma at 1.85sccm. The processes are represented in a form of a bar graph, with the contribution of each process (in %) at steady state. The positive contribution represent the creation, the negative the destruction processes. Each pressure is plotted in a different color.

In this condition (60:40 CO_2:CH_4 at 1.85sccm), CO_2 is destroyed through 3 main channels independently of pressure: the outflow accounts for about as mush as the electron impact dissociation forming CO and O(1D). The third important destruction channel of CO_2 involves

$CO(a^3\Pi)$ as described in A. F. Silva et al. 2020 and Ana Sofia Morillo-Candas et al. 2020b:

$$CO(a^3\Pi) + CO_2 \rightarrow 2CO + O(3P) \tag{4.29}$$

The main source of CO_2 is the inflow, showing that the state reached in the reactor is only a pseudo-steady state where the dissociation is compensated by the renewal of the gas. The creation of CO_2 is also steadily assured by recombination of $CO(a^3\Pi)$ through:

$$CO(a^3\Pi) + CO \rightarrow CO_2 + C \tag{4.30}$$

This process is critical in pure CO_2 (as shown in A. F. Silva et al. 2020 or in Ana Sofia Morillo-Candas et al. 2020b) and seems to play here a non-negligible role but is not mentioned in any of the CO_2-CH_4 plasma model from literature. In pure CO_2 plasmas, the $CO(a^3\Pi)$ also strongly contributes to the reformation of CO_2 with the back-reaction

$$CO(a^3\Pi) + O_2 \rightarrow CO_2 + O \tag{4.31}$$

This reaction is negligible in the 60:40 CO_2:CH_4 plasma because of the very low density of O_2. However, the interaction of $CO(a^3\Pi)$ is in this work only taken into account with CO_2 and CO and O_2. This once again points toward the importance of excited species and the necessity to obtain rates in particular for reactions of $CO(a^3\Pi)$ with hydrogenated species which to the best of our knowledge are not reported. With rising pressure, the contribution of the back-reaction :

$$CO + OH \rightarrow CO_2 + H \tag{4.32}$$

largely increases with pressure. This back-reaction mechanism (representing approximately 10% of CO_2 creation) was identified in Bie et al. 2015 in a DBD with a contribution of 9%, close to the one computed here. The reaction was not identified in nanosecond discharges in C.Bai 2019, but Danhua Mei et al. 2022 (also in NRP) claimed that the inverse process (CO_2+H) helped dissociation. However, the model in Danhua Mei et al. 2022 does not focus on the reaction pathways (no reaction rate is given) and process 5.13 is just a lead to explain the results. In J.-L. Liu et al. 2022, where DRM is studied in a gliding arc plasmatron, the inverse process (CO_2+H) is the main dissociation process of CO_2. Similar results for a gliding arc were found in Cleiren et al. 2017, where up to 90% of the dissociation was attributed to CO_2+H at high initial CH_4 content. This could be due to the higher temperature in the GA (>2500K) compared to the glow (<1000K). The comparison of the rate coefficient of CO+OH (taken from Baulch et al. 1992 in our work) with the rate coefficient of CO_2 +H (taken from W. Tsang et al. 1986 in our work) show that the first one is several orders of magnitude higher than the second at temperatures below 1000K, but that the rate coefficient of CO_2 + H becomes higher than the one of CO+OH at temperature above 2400K. This explains why the reaction reforms CO_2 in our discharge but dissociate it in the GA. Despite the numerous processes at play, the destruction and production of CO_2 are relatively steady with pressure.

Similarly, the destruction of CH_4 is quite steady with pressure,as visible on figure 4.24

For all pressures, CH_4 at pseudo-steady state is lost mostly through outflow and electron impact dissociation:

$$e + CH_4 \rightarrow e + CH_3 + H \qquad (4.26)$$

$$e + CH_4 \rightarrow e + CH_2 + H_2 \tag{4.33}$$

with the first one being twice as important as the second one. CO_2 main loss was the outflow, before electron impact dissociation but it is the opposite for CH_4, for which electron impact dissociation is dominant, with approximately 60 to 70% of CH_4 lost by electron impact. The two species have very close dissociation threshold (around 7.5eV) and the difference is therefore explained by the greater amplitude of the CH_4 dissociation cross-section. In Bie et al. 2015, the electron impact yielding CH_3 and H (process 4.26) contribute to 33% of CH_4 destruction

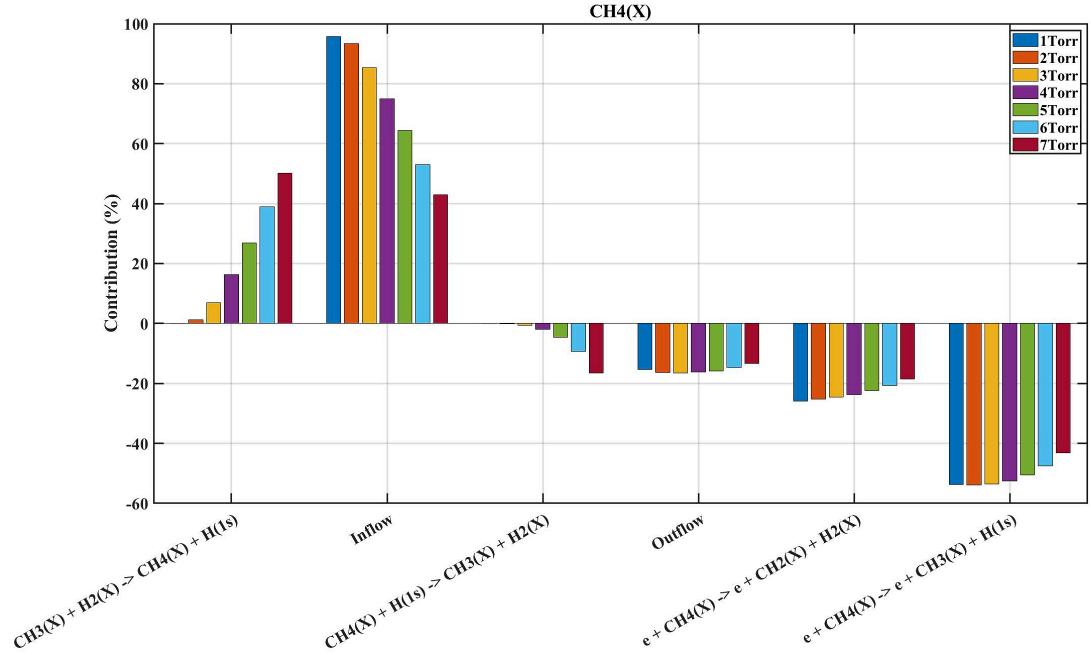

Figure 4.24: Evolution with pressure of the contribution of the main creation and destruction of CH_4 in a 60:40 CO_2:CH_4 plasma at 1.85sccm. The positive contribution represent the creation, the negative the destruction processes. Each pressure is plotted in a different color

(not too far from the 40-50% simulated in our conditions) whereas the channel yielding CH_2 accounts for only 6% (a factor 4 lower, compared to a factor 2 for us). This likely comes from the CH_4 dissociation cross-section: R K Janev et al. 2001 was used in Bie et al. 2015 whereas D.Bouwman et al. 2021 was chosen in our case. As discussed in section 4.5.1, the more recent source D.Bouwman et al. 2021, is a set of cross-sections validated against the swarm parameters and based on experimental measurements. The cross-sections proposed in R K Janev et al. 2001 is based on calculations and analytical fitting of experimental ionization cross-sections. Both source yield different branching for CH_4 cross-section. The cross-sections from D.Bouwman et al. 2021 were chosen but the chemistry with the branching ratio proposed by R K Janev et al. 2001 should also be tested in future work. Dissociation of CH_4 mostly by electron impact was also observed in the ns discharges of C.Bai 2019, where it is expected due to the very high electric field of the nanosecond discharge. The loss of CH_4 via ion recombination is very weak in our model, as opposed to Bie et al. 2015, where 18% of the loss of CH_4 is attributed to the production of CH_5^+: $CH_4^+ + CH_4 \rightarrow CH_3 + CH_5^+$. This reaction is very weak in our work due to the low production of CH_5^+ as discussed in section 4.5.3. A last main loss process of CH_4 is the reaction:

$$CH_4 + H \rightarrow CH_3 + H_2 \tag{4.34}$$

However, the contribution to CH_4 formation by the inverse reaction

$$CH_3 + H_2 \rightarrow CH_4 + H \tag{4.35}$$

is higher. Overall the net balance of these two processes lead to formation of CH_4. The contribution of this process strongly increases with pressure, becoming the dominant CH_4 creation channel at 7Torr. This could change with the value of the H atoms recombination probability γ_H chosen. The other creation channel of CH_4 in our plasma, is the inflow. In Bie et al. 2015 (a plug flow configuration as well), 30% of CH_4 production is attributed to electron impact dissociation of C_3H_8, 27% to dissociation of C_3H_6 and 16% to dissociation of C_2H_6, underlining the importance that these species can have if the plasma description relies on C_XH_Y.

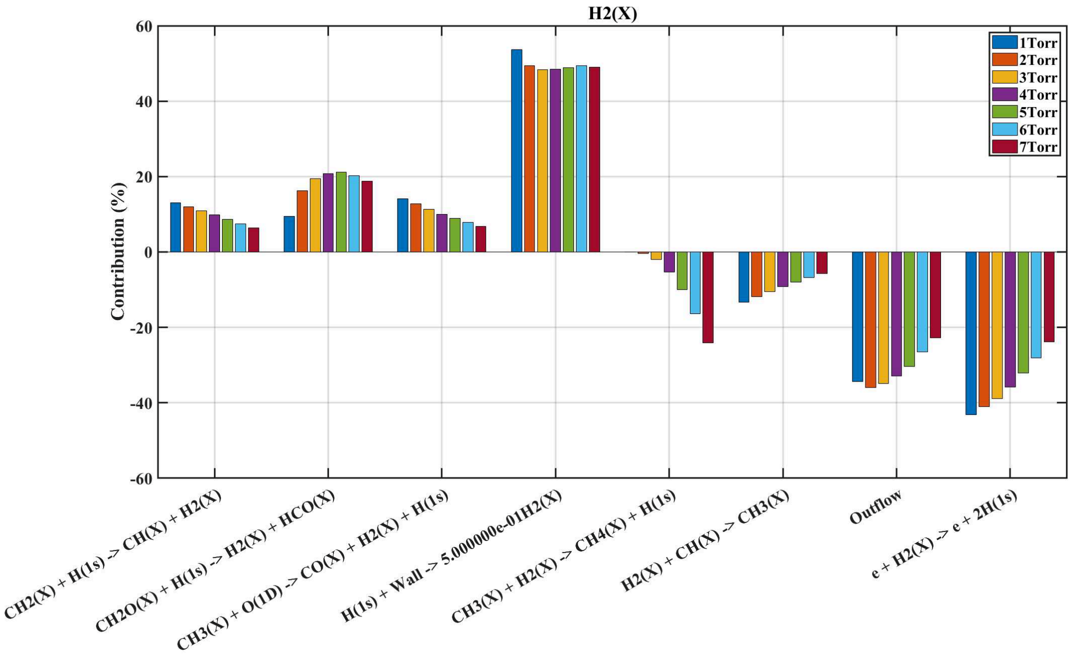

Figure 4.25: Evolution with pressure of the contribution of the main creation and destruction of H_2 in a 60:40 CO_2:CH_4 plasma at 1.85sccm. The positive contribution represent the creation, the negative the destruction processes. Each pressure is plotted in a different color

The processes forming and destroying H_2 vary a lot with pressure, as shown on figure 4.25. One thing draw the attention: at all pressures, almost 50% of H_2 is produced by wall recombination, which is understandably not described in the other CO_2-CH_4 plasma models available. The importance of the walls compared to other literature results is due to the low operating pressure of our reactor, favoring the wall reactions. It is by the way seen that the contribution of the wall to H_2 production increases when the pressure decrease (as for O recombination at similar pressure in A S Morillo-Candas, Drag, et al. 2019a). In the 60:40 CO_2:CH_4 mixture shown on figure 4.25, the other H_2 formation channels are of course the process 4.25 (discussed in depth before), and 2 recombination channels of H with CH_2 or CH_2O. These 3 channels each account for 10 to 20% of the formed H_2. In Bie et al. 2015, H_2 formation is attributed to electron impact of C_2H_Y and C_3H_Y molecules, totaling 60% of the H_2 production and highlighting the role attributed to large C_2H_Y molecules. This once again points toward the uncertain role of these large molecules in the kinetic scheme. In C.Bai 2019, H_2 formation is mostly attributed to CH_4 electron impact dissociation. This difference could find its root in the very high electric field applied in the NRP. With such an electric field, the electron impact dissociation would be greatly enhanced, explaining the importance of this channel. For all pressure, the outflow and the electron impact dissociation of H_2 are in the 60:40 CO_2:CH_4 mixture major channels. In Bie et al. 2015, a plug flow configuration, the in- and outflows are not taken into account: there, electron impact is responsible for 90% of the H_2 loss while in our case, it's responsible for half of the loss. However, if we do not count the outflow, electron impact of H_2 is indeed 90% of its loss. At high pressure, the back-reaction to CH_4 (4.6.1) becomes as important as the two other destruction channels. Destruction of H_2 is not mentioned in C.Bai 2019.

The evolution of the processes involving water with pressure must also be evoked. They are presented on figure 4.26. The creation of H_2O is far from being constant with pressure: the most important process at 1Torr ($CH_2O + OH \rightarrow H_2O + HCO$) is completely negligible at 7 Torr (following the evolution of CH_2O which is lowest at 7Torr). At 7Torr, $H_2 + OH \rightarrow H_2O + H$ is the main process. It is interesting to note that all the processes leading to formation of water involve OH. The water losses in the 60:40 CO_2:CH_4 plasma are however very steady with

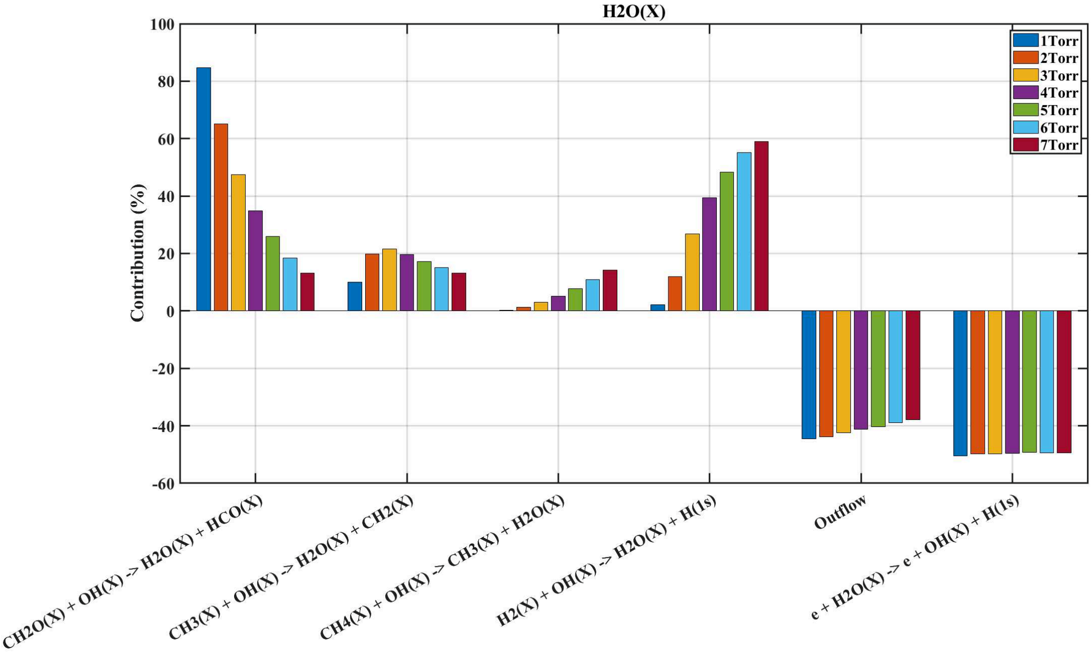

Figure 4.26: Evolution with pressure of the contribution of the main creation and destruction processes of H_2O in a 60:40 CO_2:CH_4 plasma at 1.85sccm. The positive contribution represent the creation, the negative the destruction processes. Each pressure is plotted in a different color

pressure: electron impact accounts for half of the loss, while the other half is carried away by the outflow. The electron impact dissociation leads to OH formation, thus establishing an equilibrium between OH and H_2O in the steady state. Because water is not identified as an important product in the other models, its main production or loss processes are not described. In Bie et al. 2015, the measurement supporting the model seem to indicate that the water fraction is close to 1e-4, far from our 10%. This could be linked to the high pressure, which will efficiently quench the excited state necessary to form water (see next section).

Varying the pressure do not affect strongly the fractions of all the species. The fraction of minor species tend to decrease with pressure as expected with faster recombination/reactivity at higher collision frequency. The fractions of major species are relatively stable in the explored range of pressures (1-7Torr). In our conditions the balance of the main species is controlled only by a few major processes. Though their contributions vary slightly, the dominant processes remain the same independently of the pressure. This can help future efforts of kinetic scheme reduction, giving insights for each species on a limited number of main processes to include. Knowing that the dominant process remain the same with pressure, the effect of the CH_4 percentage in the initial mixture is studied at 5Torr.

4.6.2 Effect of the initial mixture

The last parameter changed in the experiment is the initial mixture variation, changed from a pure CO_2 plasma to a 60:40 CO_2:CH_4 plasma. As can be expected, this last parameters is the one that induces the more changes in the plasma chemistry. In pure CO_2 plasmas, the main species are CO_2, CO, O_2 and atomic O. When a small fraction of CH_4 is introduced in the gas mixture, H_2, CH_4 and H_2O start appearing at levels higher than O_2 and O. The evolution of the processes driving the conversion when changing from pure CO_2 to CO_2-CH_4 is studied here. Before using the model to look reaction pathways in details, the evolution of the fractions of minor species with the initial CH_4 content must be examined. The simulated fractions of minor and unmeasured species as a function of the initial mixture are shown on

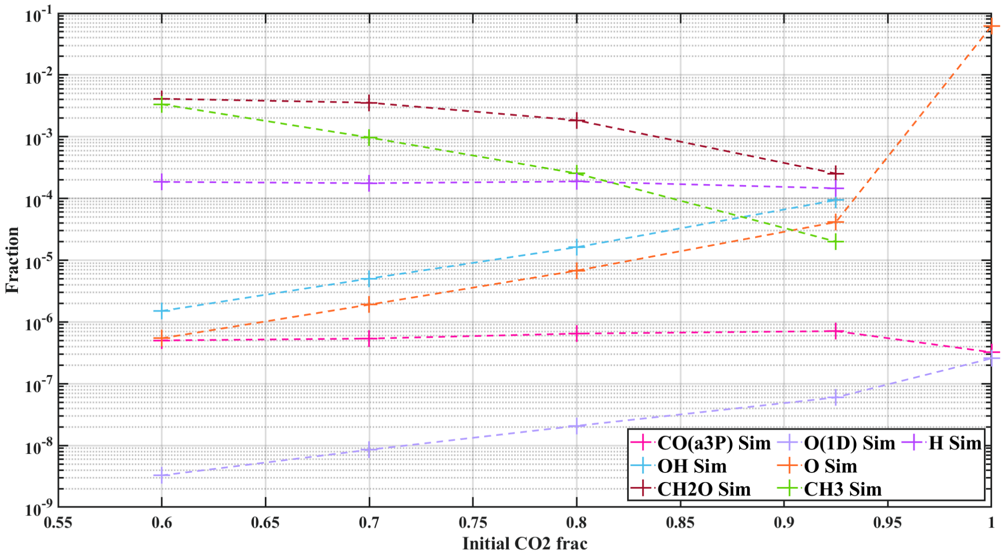

Figure 4.27: Evolution of the simulated fractions of minor species with initial CO_2:CH_4 ratio at 1.85sccm and 5Torr

figure 4.27. The CH_3 and CH_2O fractions increases with admixture of CH_4 in the initial mixture as expected. The simulated H remains stable with the increase of initial CH_4 content because the loss of H is dominated by H recombination at the wall. The density of atomic H is in this case controlled by the diffusion of H to the walls. The OH density decreases with admixture of CH_4, surprisingly because the peak of H_2O is reached at 80:20 and as seen in the previous section, the OH and H_2O are related through several processes. It can be noticed that OH and O densities have similar behaviours, both decreasing with increasing initial CH_4 content. The decrease of the O density matches the experimental actinometry results. The O(1D) decreases with the increasing CH_4 similarly to O atoms, due to both the decreasing fraction of CO_2 and to the high chosen rate of reaction 4.25. Finally, the $CO(a^3\Pi)$ sees a slight increase when going from pure CO_2 to low initial CH_4 content. The CO(a) density remains stable upon further admixture of initial ($7.10^{-7}\%$ in the 92:8 CO_2:CH_4 condition, $5.5^{-7}\%$ at 60:40 CO_2:CH_4. The increase of the $CO(a^3\Pi)$ density when going from pure CO_2 to 95:5 CO_2:CH_4 is likely due to the drop of the O atoms density. O atoms have indeed the strongest quenching coefficient of $CO(a^3\Pi)$.

Because the densities of the main species are not monotonous with the increase of the initial CH_4 content (deep in CO_2 conversion at CH_4 percentage, peak in water fraction...), the processes controlling the plasma composition are expected to be quite different at low or high initial CH_4. One of the most noticeable behaviour is the peak in CO_2 fraction observed on figure 4.4 in the 95:5 CO_2:CH_4 mixtures for all pressures and all flows. To shed light on the processes driving CO_2 dissociation as a function of the initial CH_4, the rates of the main CO_2 loss and creation processes at "pseudo" steady state are plotted on figure 4.28 as a function of the initial mixture. Each initial mixture is plotted with a different color. The positive reaction rates represent creation processes, the negative are loss processes. One difference is to note with the previous section (for pressure variation): while the contribution in % was plotted in the previous section because the rates scale with pressure, it is now the rates that are plotted because the pressure is kept constant at 5Torr. The rates are plotted for a total flow of 1.85sccm.

For each process (each x-axis tick), the rate of the process in the 60:40 mixture is plotted first on the left, followed by the 70:30, 80:20, 92:8 and finally the 100:0 mixtures.

- *Creation and loss processes of* CO_2

Four processes mostly destroy CO_2, independently of the initial mixture. The three main

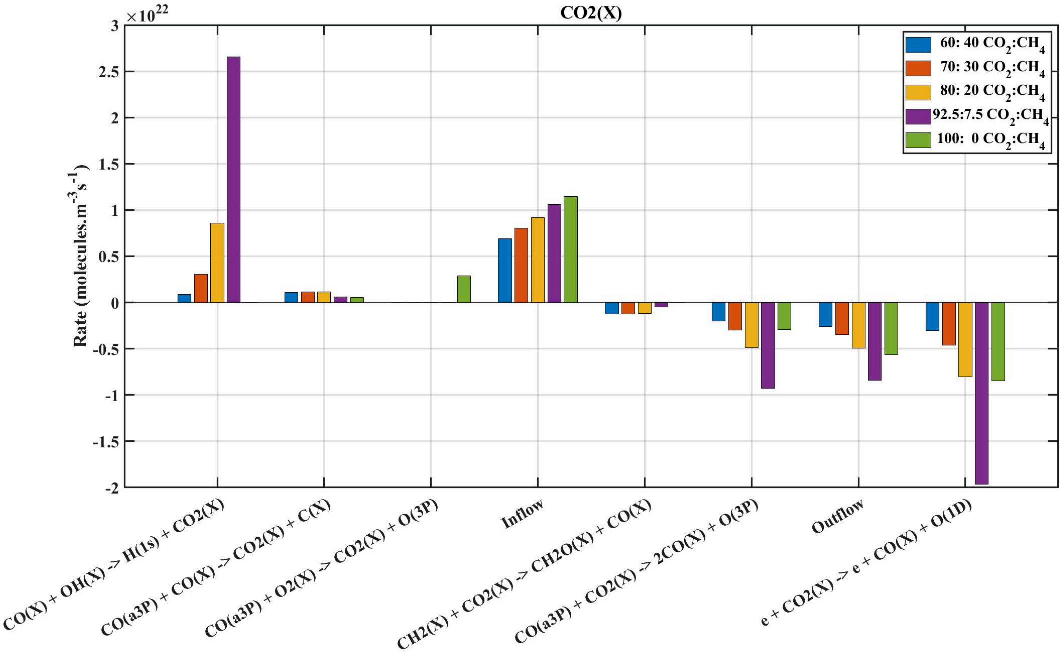

Figure 4.28: Evolution with initial mixture of the reaction rates of the main creation and destruction processes of CO_2 at pseudo-steady state at 1.85sccm, 5Torr. The positive rates represent the creation, the negative the destruction processes. Each initial mixture is plotted in a different color

ones (electron impact on CO_2 4.27, outflow and dissociation by $CO(a^3\Pi)$ 4.31). The rates of these 3 processes follow the evolution of the CO_2 density (which peaks in the 92:8 mixture). The fourth process is

$$CH_2 + CO_2 \rightarrow CH_2O + CO \tag{4.36}$$

The rate of process 4.36 increases with the initial amount of CH_4 because the limiting reactant in this process is the CH_2, a direct dissociation product of CH_4.
The inflow reaction is a good representation on how the rates are decreased due to the initial CO_2 decrease. The rate of dissociation by $CO(a^3\Pi)$ (process 4.29) can be compared of the rate of creation of CO_2 by $CO(a^3\Pi)$ (process 4.31). The process (4.31), negligible for most conditions, account for 10% of the CO_2 production at 60:40 CO_2:CH_4. In this condition, $CO(a^3\Pi)$ dissociate twice as much CO_2 as it produces (the reaction rate of 4.31 is 1e21 $cm^{-3}s^{-1}$ versus 2e21 for 4.29 at 60/40). In the other gas mixtures, the rate of 4.29 is always higher than the one of 4.31, meaning that in all the mixture $CO(a^3\Pi)$ is beneficial for CO_2 dissociation.
Two processes stand out for the formation of CO_2: the inflow and the back-reaction (5.13) previously identified. The latter shows a very strong rate in the 92:8 mixture and is the main source of formation of CO_2 in this condition. This means that the back-reaction (5.13) ($CO + OH \rightarrow CO_2 + H$) is responsible for the peak in CO_2 fraction observed in this condition on figure 4.4, which is consistent with the OH density being maximum in the 92:8 CO_2:CH_4 condition.

- *Creation and loss processes of CH_4*

The processes creating and destroying CH_4 are more straight forward. A plot showing the reaction rate of the main CH_4 processes in the pseudo-steady state as a function of the initial mixture (at 5torr, 1.85sccm) is shown on figure 4.29. Independently of the initial mixture, CH_4 is created by two processes: the inflow, and the back-reaction mechanism (4.6.1) ($CH_3 + H_2 \rightarrow CH_4 + H$). This process logically increases with CH_4 initial %, because more CH_3 and H_2 are available. The loss of CH_4 happens mostly through 4 mechanisms: outflow, the two electron

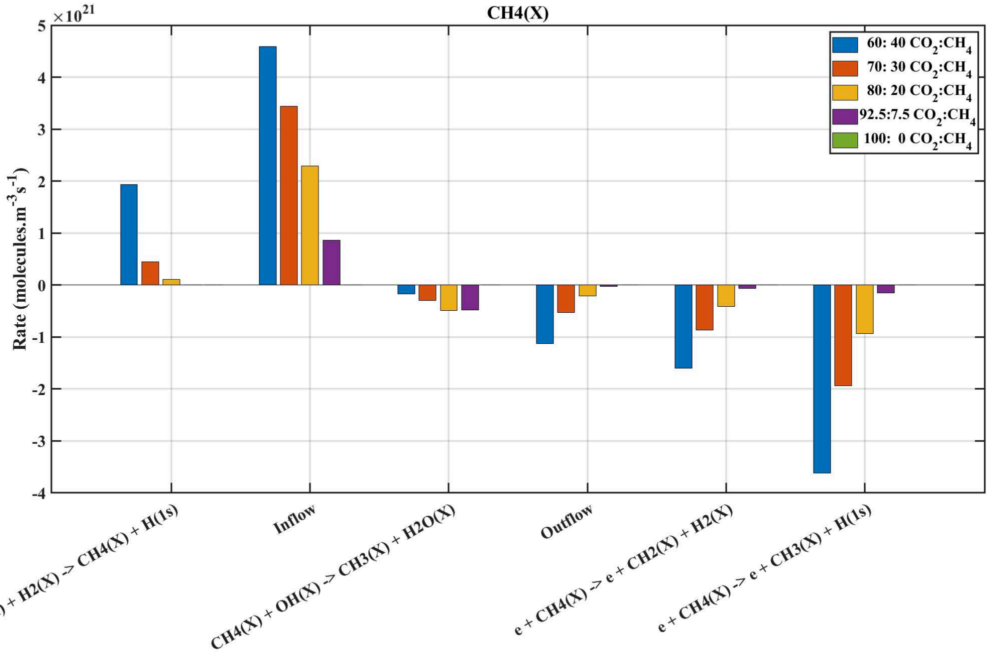

Figure 4.29: Evolution with initial mixture of the reaction rates of the main creation and destruction processes of CH_4 at pseudo-steady state in a 60:40 CO2:CH4 plasma at 1.85sccm, 5Torr. The positive rates represent the creation, the negative the destruction processes. Each initial mixture is plotted in a different color

impact dissociations and the reaction

$$CH_4 + OH \rightarrow CH_3 + H_2O \tag{4.37}$$

This last process is the only direct oxidation process of CH_4. It is also the only one that is not linear with CH_4 initial %. This process producing water is also maximum in the 80:20 CO_2:CH_4 mixtures (where the water fraction peaks). It would however be too simplistic to attribute the peak of H_2O solely to process 4.37.

- *Creation and loss processes of H_2O and OH*

This of course raises the question of the water creation processes. The most important ones in the steady state are presented on figure 4.30. Water is created through 3 main processes in the steady state:

$$CH_3 + OH \rightarrow H_2O + CH_2 \tag{4.38}$$
$$H_2 + OH \rightarrow H_2O + H \tag{4.39}$$
$$CH_2O + OH \rightarrow H_2O + HCO \tag{4.40}$$

Out of these 3 processes, the last one is the only one peaking in the 80:20 CO_2:CH_4 mixture, the other are linear with the CH_4 admixture. The process(4.40) peaks at 80:20 because it is where the product of the density of OH times the density of CH_2O is maximum (OH decreases with increasing CH_4 percentage while CH_2O increases). Figure 4.31 show the temporal evolutions of the reaction leading to the equilibrium reached for OH and CH_2O in the 80:20 CO_2:CH_4 mixture (the figure describes the evolution of the rates in the reactor over time, from the plasma breakdown to the pseudo-steady state). For each species, the top graph shows the evolution of the density over time. The bottom graph show the reaction rates of the main reactions. The creation processes are plotted with plain lines and the destruction processes are plotted with dashed lines. The density of OH, plotted in the top left graph goes through a maximum (at

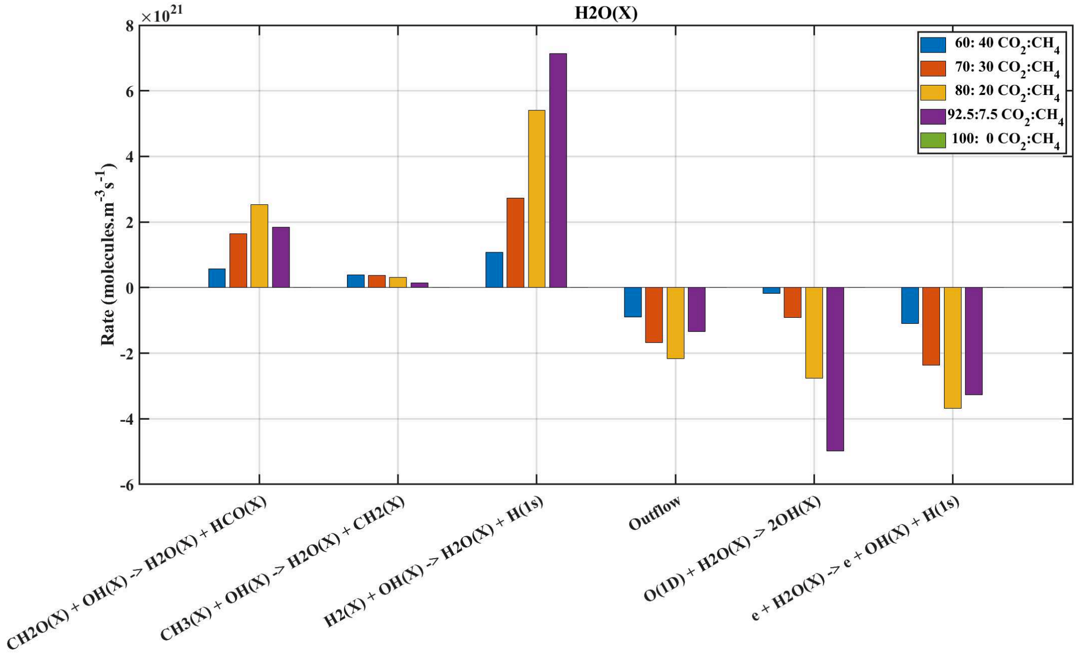

Figure 4.30: Evolution with initial mixture of the reaction rates of the main creation and destruction processes of H_2O at pseudo-steady state at 1.85sccm, 5Torr. The positive rates represent the creation, the negative the destruction processes. Each initial mixture is plotted in a different color

1ms) before oscillating toward its final values (i.e it is possible to tune the products by changing the plasma duration). OH is initially produced through:

$$CH_4 + O(1D) \rightarrow CH_3 + OH \tag{4.41}$$

The rate of this reaction is taken from Atkinson 1992. This production channel was not identified in any CO_2-CH_4 plasma model, but was put forward in Lefkowitz 2015 (which compared experiment and simulation for CH_4-O_2 mixtures in nanosecond discharges). In Lefkowitz 2015, process 5.9 was the most important loss channel of CH_4 (accounting for 40% of the loss), above electron impact dissociation (all channels sum up to 38%) despite the very high electric field and electron density of nanosecond discharges. The electron impact dissociation cross-section used in Lefkowitz 2015 is the one taken from R K Janev et al. 2001, lower than the one used in this work, which could partly explain the difference. Lefkowitz 2015 did not take into account the reaction of O(1D) with CH_3 (process 4.25) which ultimately increased the amount of O(1D) available to react with CH_4, also explaining the difference. This however shows in another way the importance of the O(1D) state: if not taken into account, it might not be possible to explain the initial building up of OH and eventually the peak in the water fraction. Process 5.9 builds up the OH density until 1ms. Between 1ms and 1s, the OH density is reduced because OH reacts with CH_2O and produces water (explaining the peak of water in the 80:20 CO_2:CH_4 mixture). Once enough water is accumulated, water and OH reach an equilibrium through 6 processes, 3 of them forming OH, the other 3 destroying it

$$O(1D) + H_2O \rightarrow 2OH \tag{4.42}$$

$$e + H_2O \rightarrow e + OH + H \tag{4.43}$$

$$H + O + M \rightarrow OH + M \tag{4.44}$$

$$H_2 + OH \rightarrow H_2O + H \tag{4.45}$$

$$CH_2O + OH \rightarrow H_2O + HCO \tag{4.46}$$

$$CO + OH \rightarrow CO_2 + H \qquad (4.32)$$

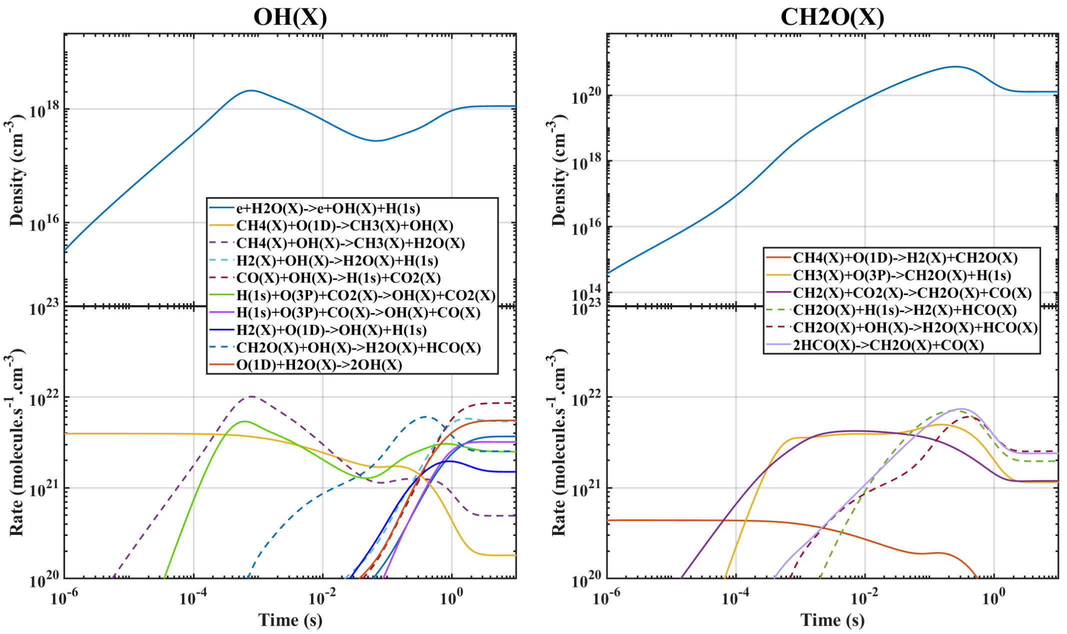

Figure 4.31: Top: Temporal evolution of the densities of OH (Left) and CH_2O (right) in a 80:20 CO_2:CH_4 mixture at 5Torr and 1.85sccm. t=0 is the break-down of the plasma. A pseudo-steady state is reached when the dissociation is compensated by the gas renewal. Bottom: Temporal evolution of the reaction rates of processes involving OH (left) and CH_2O (right). The creation processes of the concerned species are plotted in plain line, the loss processes are plotted in dashed line. t=0 correspond to the plasma break-down

The most important ones are found on figure 4.30. This is only possible because enough CH_2O is available in the plasma.

- *Creation and loss processes of CH_2O*

Similarly to OH, the density of CH_2O (plotted on the top right graph of figure 4.31), goes through a maximum around 0.1s. The density of CH_2O is initially built up by the reaction:

$$CH_4 + O(1D) \rightarrow CH_2O + H_2 \tag{4.47}$$

This reaction was also identified in Lefkowitz 2015 and had a reaction rate about 10 times lower than the other channel involving CH_4 and O(1D) (5.9), which is similar to our observations. When CH_4 starts being dissociated enough (around 10^{-4}s), the CH_2O production is assured by :

$$CH_3 + O \rightarrow CH_2O + H2 \tag{4.48}$$
$$CH_2 + CO_2 \rightarrow CH_2O + H \tag{4.49}$$
$$2HCO \rightarrow CH_2O + CO \tag{4.50}$$

These reactions later balance with water production (4.40), as seen above.

- *Creation and loss processes of H_2*

The evolution of the main processes involving H_2 as a function of the initial mixture at 5Torr, 1.85sccm, are shown on figure 4.32. The majority of H_2 is produced by wall recombination of hydrogen atoms, highlighting the critical dependence of the model to the recombination

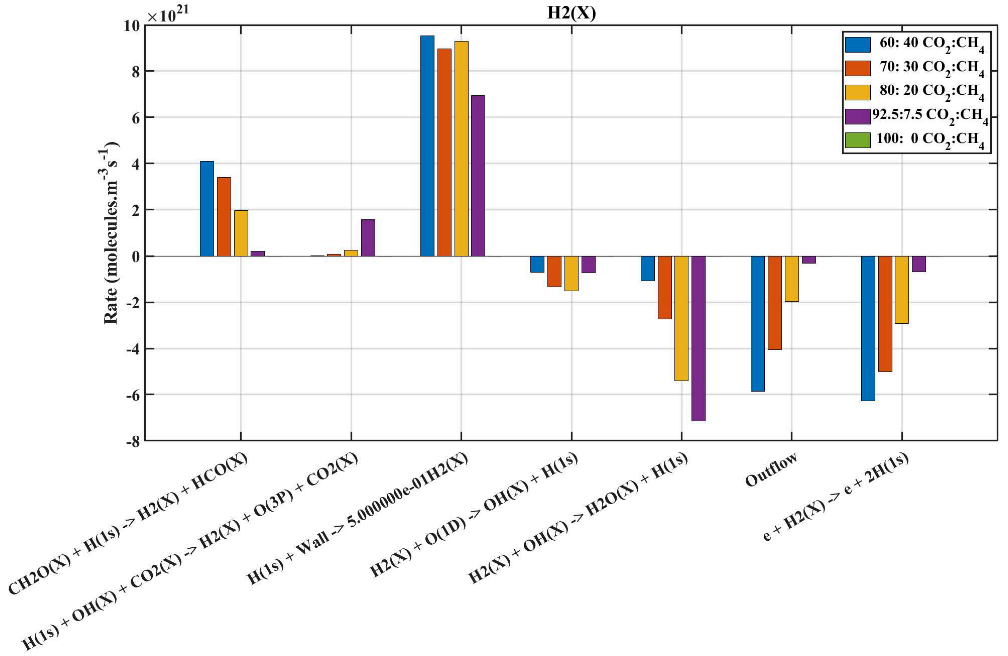

Figure 4.32: Evolution with initial mixture of the reaction rates of the main creation and destruction processes of H_2 at pseudo-steady state at 1.85sccm, 5Torr. The positive rates represent the creation, the negative the destruction processes. Each initial mixture is plotted in a different color

probability γ_H. The rest of the hydrogen is mostly produced by

$$CH_2O + H \rightarrow H_2 + HCO \tag{4.51}$$

underlining the important role of CH_2O in our plasma. With low CH_4 percentage mixtures, the 3-body process H + OH + M is also a source of H_2. In these mixtures, the production of water through

$$H_2 + OH \rightarrow H_2O + H \tag{4.52}$$

is the main destruction channel of H_2. With high initial CH_4 percentages mixtures, H_2 is destroyed by outflow and electron impact. Finally, in all the conditions, the dissociation of H_2 through collision with O(1D) is non-negligible, representing about 10% of H_2 loss.

- *Creation and loss processes of O(1D)*

A constant of all the variations presented above is the importance of O(1D). Though processes involving O(1D) are rarely the most important ones, non-negligible processes involving O(1D) can be found impacting the final balances and densities for all mixtures and all pressures (it could be that H_2O does not appear important in other models simply because no O(1D), which ultimately cascade to H_2O, is included. The question of the production and loss of O(1D) must be addressed. Figure 4.33 pictures the evolution of the reaction rates of processes involving O(1D) in the pseudo steady state as a function of the initial mixture at 5Torr, 1.85sccm. In pure CO_2 plasmas, O(1D) is produced not only through electron impact dissociation of CO_2, but also through electron impact dissociation of O_2 and through electronic excitation of O(3P). Because of the very low level of atomic O and O_2 in CO_2-CH_4 plasmas, these last two channels are negligible in CO_2-CH_4 plasmas and O(1D) is produced only by electron impact dissociation of CO_2. In pure CO_2 plasmas, O(1D) is mainly lost by collisional quenching with CO_2. This channel is not the dominant loss of O(1D) anymore when the initial CH_4 percentage is higher than 10. Apart from simple quenching, O(1D) is lost through 3 main channels:

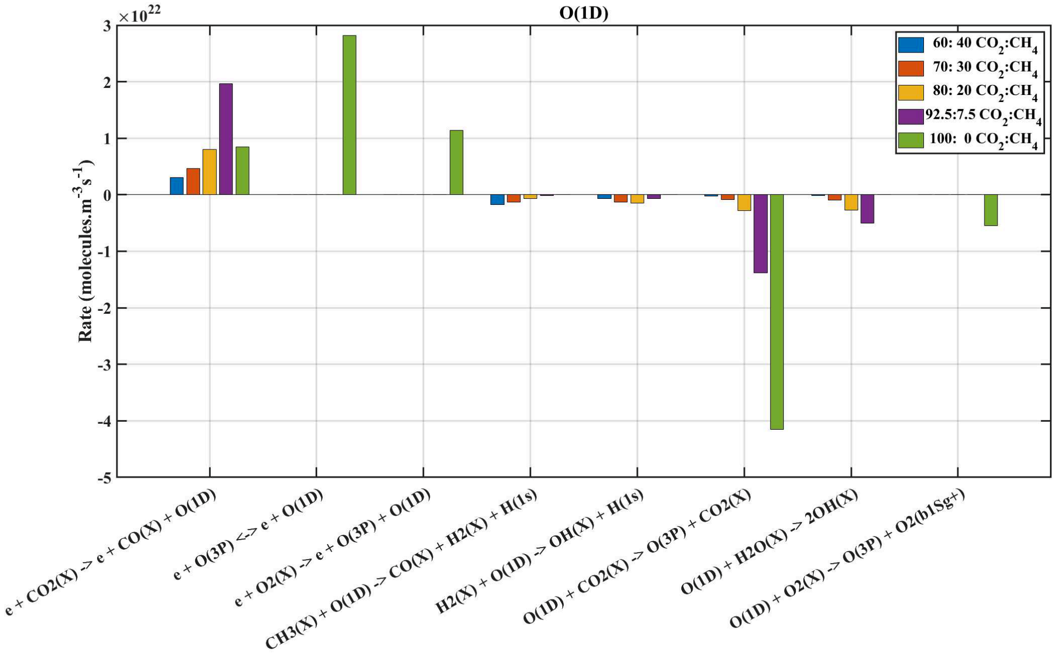

Figure 4.33: Evolution with initial mixture of the reaction rates of the main creation and destruction processes of O(1D) at pseudo-steady state at 1.85sccm, 5Torr. The positive rates represent the creation, the negative the destruction processes. Each initial mixture is plotted in a different color

$$
\begin{aligned}
CH_3 + O(1D) &\rightarrow CO + H_2 + H \\
H_2 + O(1D) &\rightarrow OH + H \\
H_2O + O(1D) &\rightarrow 2OH
\end{aligned}
$$

The splitting between these channels is dependant on the rate coefficient chosen for the first one, which is still subject to interrogation. With the rate chosen here, 1/3rd of the O(1D) at 20% initial CH_4 is lost in (O(1D) + H_2O), 1/3 by colisional quenching and the other third is split between H_2+O(1D) and CH_3+O(1D). When increasing the initial CH_4 percentage to 30%, the loss of O(1D) is more or less equally parted between the 4 channels. At 40 % initial CH_4, 2/3rd of the O(1D) is lost through process (4.25), highlighting the critical stake of obtaining through other methods a value of this rate to clarify the importance of the interaction between CH_3 and O(1D) and therefore obtain a better picture of a CO_2:CH_4 plasma.

4.7 Conclusion

A low pressure glow discharge has been set up and used to test a OD kinetic model for CO_2-CH_4 plasmas, using the LoKI simulation tool.The model takes into account a simple chemistry including only molecules with one carbon atom, as well as CH_4 and its derivative. A relatively good agreement has been found between the model and the experiment, allowing to use the model to gain insights on the key processes of CO_2-CH_4 plasmas. It has been shown that in our conditions, electronic impact dissociation of CO_2 and CH_4 are the main channels to produce the main products, CO and H_2, but that some highly reactive species also play a key role. O(1D) and OH oxidation of CH_4 have shown to be important loss mechanisms of CH_4, emphasizing the role of excited state in the chemistry of CO_2-CH_4 plasma. The parametric study performed here strongly suggest that the interaction between O(1D) and CH_3 is necessary to explain the level of conversion of CH_4 and the production of H_2. It would be also important to quantify the reaction rates of the CO(a3Π) state (critical in pure CO_2 plasmas) with hydrogenated species. The good but not perfect agreement in trends and values between the experiment and the model leaves room for improvement: firstly, by better taking into account the vibrational excitation of CO_2 and CO, which are key processes for CO_2 dissociation in pure CO_2 plasmas. More effort is required to properly include the vibrations, but a first lead could be to simply use the so-called Friedman scaling for all available cross-sections (note that in chapter 6 it will be shown that vibrations of CO_2 are probably less important in mixture of CO_2/CH_4). Secondly, though it seems that they are not essential for CO_2-CH_4 chemistry in our conditions the larger hydrocarbons species need to be taken into account in the model as it is not so clear whether their influence on the chemistry is comparable to the one of excited states or not. Finally, this models only takes into account the gas phase. For DRM purposes, it will be useful to have a better understanding of the processes taking place on the surfaces because as shown, they could be of interest to produce value-added chemicals such as C_2H_6. This comparison of experiment and model brings insights of the chemistry of CO_2-CH_4 plasmas in the gas phase.

CHAPTER 5

Reaction pathways in the low-pressure CO_2-CH_4 RF discharge

Contents

5.1 Introduction

So far, CO_2-CH_4 plasmas have been investigated in a very simple discharge, which presented numerous advantages but was not very suited for dissociation. The next step seems therefore quite naturally to use a more adapted discharge to achieve DRM. The radiofrequency discharge pose as a good candidate, because it is already appropriated to CO_2 dissociation: in the RF discharge, the energy acquired by the electron following the field oscillations is adapted to vibrational pumping of CO_2 (A.Fridman 2008). However the goal of this chapter is not yet to find out an optimal way to achieve DRM in the radiofrequency discharge, but rather to understand the fundamental processes leading to CO and H_2 formation in such discharge.

Beyond focusing on another type of plasma discharge that is *a priori* more efficient, the approach developed in this chapter complements that of the previous chapter in an attempt to specify a more complete kinetic scheme of the complex chemistry induced in CO_2:CH_4 plasmas. Indeed, the previous chapter made it possible to establish solid bases for a kinetic scheme based on the comparison with a discharge in which the electric field, the electronic density and the temperature of the gas were known. On the other hand, the conversion of the reactants (CO_2 and CH_4) was limited by the relatively short residence time of the gas in the plasma. In this chapter, on the contrary, the temporal evolution of the conversion of the reactants will be studied from the beginning until reaching a true steady state. However this will be obtained at the expense of a larger uncertainty on the parameters controlling the plasma (E, n_e, T_g).

The general question addressed in this chapter remain therefore close to the one in the previous chapter: What are the fundamental physical and chemical processes taking place in a CO_2-CH_4 discharge suited for efficient dissociation ?

The RF discharges was repeatedly investigated for CO_2 dissociation. In Capezzuto et al. 1976, the dissociation in a low pressure RF discharge ($\sim$ 20Torr) showed that a dissociation mechanism involving vibrational excitation was among the dominant conversion mechanisms. In Spencer et al. 2011, an RF discharge was turned on at 0.3Torr and showed excellent dissociation of CO_2 (up to 90%) but with poor energy efficiency. More recently in Ana Sofia Morillo-Candas et al. 2020b, a pure CO_2 RF discharge at low pressure was studied (in the same setup as the one presented here) and a detailed analysis of the processes leading to dissociation and back-reaction in a pure CO_2 plasma in closed reactor was given. To our knowledge, only a couple of paper investigated DRM in RF plasmas, as presented in the introduction. Vibrational excitation of CO_2 was studied in Z. Liu et al. 2020 in a Ar-CO_2-CH_4 ICP discharge at atmospheric pressure which put forward the increase of the CO_2 vibrational excitation thanks to the Ar metastables. H.Li et al. 2020 studied RF ICP discharges between 0.1 and 0.5 Torr and showed conversion rates of up to 90% for CO_2 and CH_4 in a 1:1 CO_2-CH_4 molar ratio at a flow of 300sccm. A gas temperature of 4000K was however measured in the plasma, making vibrational pumping unlikely to be the source of the high dissociation. This will be further investigated in the chapter 6 on vibrational kinetics conclusions of the chapter. Because of its performance for CO_2 conversion compared to other discharges (R.Snoeckx et al. 2017), the RF discharge remains interesting to study.

Following the method described in Ana Sofia Morillo-Candas et al. 2020b, the time evolution of the RF discharge will be studied in a closed reactor, without any flow. This uncommon configuration in plasma studies presents the great advantage to allow following in time the evolution of the plasma composition providing much stronger constraints to the model. In a "plug flow" configuration like in the previous chapter, the inflows and outflow were major reactions for the main species (CO_2, CO, CH_4, H_2O and H_2), proving that the pseudo-steady state was far from being a real steady state.On the contrary in a closed reactor, the plasma can be run as long as necessary to achieve a real steady state. An additional advantage is that knowing the time evolution of all species, it is then possible to get an idea of the residence time needed in a flowing reactor to optimize the conversion.

5.2 Experimental Setup

The experimental setup is described here. It is the same as the one used in Ana Sofia Morillo-Candas et al. 2020b The discharge takes places in a cylindrical Pyrex tube of inner diameter 2cm and of length 23cm (same dimensions as the pyrex tube used for the glow discharge). The reactor has a gas inlet and a gas outlet which can both be closed by teflon valves to prevent any flow circulation in the reactor. The inlet and outlet are connected with a by-pass. The system by-pass + reactor can be closed by a couple of metal valves located upstream and downstream of the by-pass. The gas is flowed in by 3 Bronkhorst flowmeters and is pumped by an Edwards XDS Pump. The pressure in the line is controlled by a Pfeiffer pressure gauge, located in the by-pass. The mixtures is done with flow and once the correct proportion of each gas are present in the flow, the metal valves are closed. The pressure in the by-pass and reactor is first adjusted

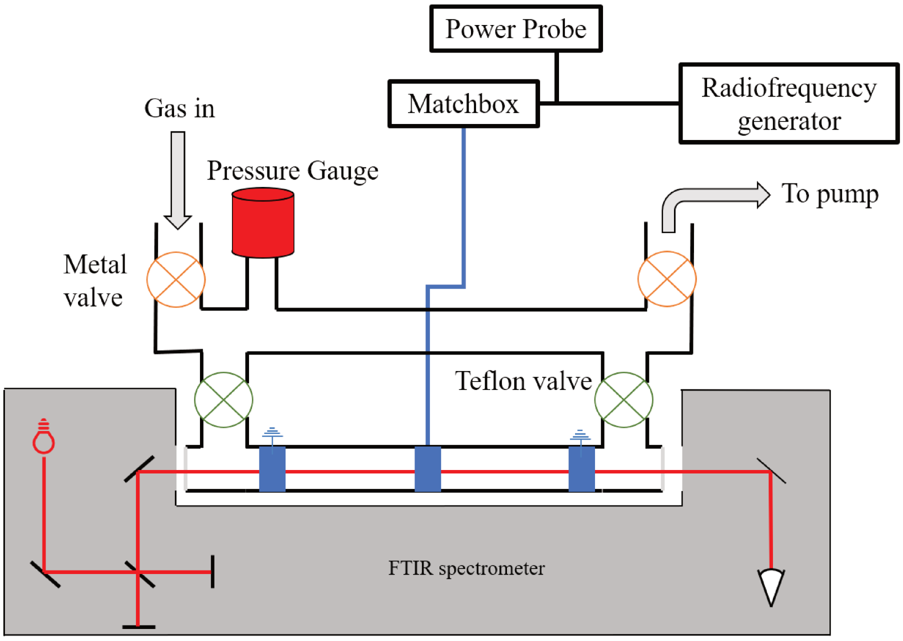

Figure 5.1: Experimental setup

Pressure	2 & 5 Torr
Mixture (CO_2:CH_4)	100:0 / 95:5 / 90:10 / 75:25 / 65:35 / 50:50
Power	40W

Table 5.1: Conditions studied

with the downstream valves and the Teflon valves are then closed, ensuring the correct mixture at the correct pressure in the reactor.

The discharge is ignited in the plasma thanks to 3 cylindrical electrodes placed against the outer wall of the reactor to avoid contact between the plasma and the metal. The central electrode is connected to the matchbox and the RF generator, while the side electrodes are grounded: this system allow a better control of the plasma volume. The matchbox is custom-made. The RF generator is a 13.56MHz generator, which allows fast on/off switching of the RF voltage (with a rising time of a few nanoseconds). A Solayl power probe is connected to the matchbox to measure the power sent to the plasma and the power reflected to the generator. The matchbox power calibration was done according to the method described in V.A.Godyak et al. 1990. The calibration curves of power sent in the reactor are shown on figure 5.2. It was computed that about 70% of the power sent is coupled into the plasma. In the present configurations, 2 parameters related to the gas content were investigated: the pressure and the mixture. The pressure was set to 2 or 5 Torr and the mixture was varied from pure CO_2 to 50:50 CO_2:CH_4. The power, which was shown to influence the steady state in pure CO_2 plasma in Ana Sofia Morillo-Candas et al. 2020b, was kept constant to 40W.

The diagnostic used here is a Fourier Transform InfraRed (FTIR) spectrometer Brucker Vertex 70. The reactor is placed in the sample compartment of the FTIR, as visible on figure 5.1. The FTIR is used in the so-called "rapid scan" mode: the FTIR follows a serie of instructions defined by the user, with Fourier transform computed at the end of the experiment to allow "fast" chain of event. The FTIR allows for measurements of the density of IR active species in between the plasma pulses. The detected species are CO_2, CO, CH_4, H_2O, C_2H_6, C_2H_4 and C_2H_2. Because the reactor is closed, the absolute number of atoms is known. By calculating the initial amount of H atoms and O atoms in the mixture, the densities of H_2 and O_2 (the only undetected molecules) can be calculated at any time. This also allows to follow the number of carbon atoms in the reactor and check that no carbon is deposited on the wall.

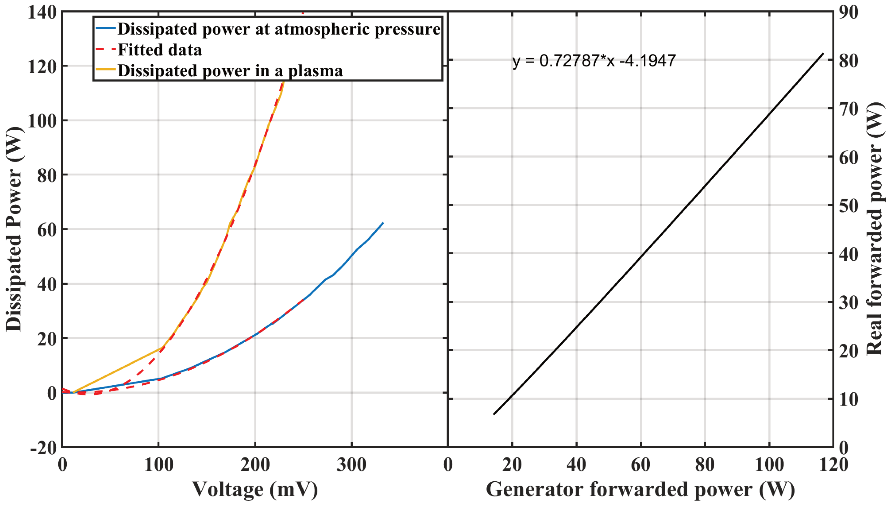

Figure 5.2: Calibration of the RF matchbox according to the method described in V.A.Godyak et al. 1990. The left plot shows the power dissipated read on the generator as a function of the voltage both in a CO_2 plasma and at atmospheric pressure, without plasma. The graph on the right shows the real power forwarded as a function of the power sent by the generator

In this experiment, a pulsed RF discharge is used. The pulses are organized in "trains" of plasma pulses, sent successively. A train is typically constituted of 10 pulses (which is the number of pulses per train noted $n_{p/train}$), each with a 5ms of plasma ON (t_p^{ON}) and 10ms of plasma OFF (t_p^{OFF}), but all these parameters (duty cycle ratio, number of pulses, the pulse duration) can be changed to study various effects. Between each train, an FTIR measurement is taken. The measurement takes about 1.5s (time to complete a full swipe of the IR spectrum between 1000 and 4000 cm^{-1}). In practice, the FTIR takes a measurement, then sends a trigger signal to a pulse generator connected to the RF power supply. The pulse pattern is schematized on figure 5.3.

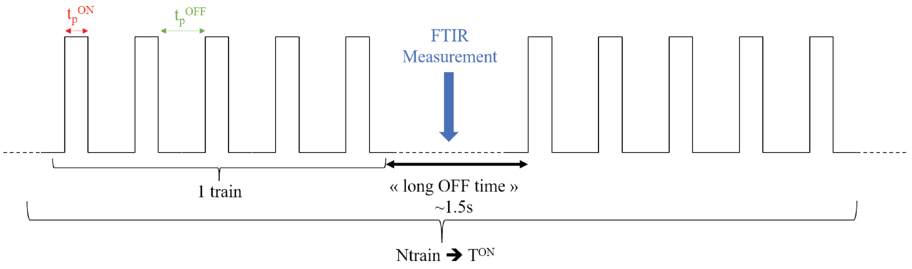

Figure 5.3: Pulse setup

A measurement usually counts several hundreds of trains. The range studied for each train settings is shown on table 5.2. Changing the pulse settings allow to single out process depending on their characteristic times. The only constant parameters in our experiment is the total plasma ON time T^{ON}, which corresponds to the total time when the plasma was turned on during a measurement: it is the sum of the plasma ON time per pulse multiplied by the number of pulses per train multiplied by the number of trains sent:

$$T^{ON} = (\sum_{1train} t_p^{ON}) * N_{train} \tag{5.1}$$

$$T^{ON} = n_{pulses/train} * t_p^{ON} * N_{train} \tag{5.2}$$

In our experiment, the total plasma ON time is always 25s. For the rest of this work, the pulses

	Number of trains (Ntrain)	pulses per train $n_{p/train}$	time on per pulse (t_p^{ON})	time off per pulse (t_p^{OFF})	total plasma ON time (T^{ON})
Typical measurement	500	10	5ms	10ms	25s
Range	100-1000	1-100	0.1-50	1-50	25s

Table 5.2: Pulses settings investigated

settings will be noted in the following way:

$$Npulses * Npulses/train * t_p^{ON} - t_p^{OFF}$$
$$\text{for example } 500 * 10 * 5 - 10$$

meaning 500 trains of 10 pulses, each pulse being 5ms on and 10ms off. The 500*10*5-10 is the reference condition in the rest of this work.

It is well-known in CO_2-CH_4 or CH_4 plasma in general that carbon deposition can occur if the CH_4 proportion becomes too large in the initial mixture. A procedure was then developed to clean the wall surface in case of carbon deposition and make the experiment reproducible. Before each measurement, the surface was treated during 20 minutes with an Oxygen plasma (pure O_2) at 1 Torr to oxidize possible $C_XH_YO_Z$ accumulated onto the surface. After that, the mixture used in the measurement was flowed in the reactor for 10 minutes without any plasma. This procedure was found to be efficient, making measurement reproducible over several months and thus proving that the initial state of the surface was well controlled in our experiment. The procedure was necessary as the repeatability could not be obtained if one of the two steps was skipped. It is interesting to note that for the second step, flowing a mixture of CO_2 and CH_4 or with pure CO_2 did not affect the repeatability. The physical effect of flowing the gas without any plasma after Oxygen plasma are not clear. It must also be noted that despite using proportions of methane up to 50:50, no significant carbon deposition was visible on the reactor walls. Moreover, FTIR measurements were taken during the cleaning phase with O_2 plasma. The CO_2 and CO were below the FTIR detection limit (<100ppm).
This experiment is called the "Building-up" experiment in the following.

5.3 Reminder of previous work on pure CO_2

A short reminder of previous work done in our group with a similar setup in pure CO_2 plasma is presented here. It illustrates the interest of such method with pulsed plasma in a closed reactor to isolate and identify the role of certain processes before applying the same method to the CO_2:CH_4 gas mixture.

This configuration was used in A S Morillo-Candas, Silva, et al. 2020 to study the evolution of a pure CO_2 plasma over 25s of "plasma-On" time. The plasma source used was a glow discharge and not an RF discharge but the rest of the setup is identical. The conclusions are summarized here. A S Morillo-Candas, Silva, et al. 2020 showed that in pure CO_2 plasma, the first second of the evolution of the CO and CO_2 densities is controlled by electron impact dissociation mechanism, mostly :

$$e + CO_2 \rightarrow e + CO + O(1D) \tag{5.3}$$

The slope of evolution of the density during this time is simply determined by

$$\frac{d[CO_2]}{dt} = -k_e^{diss} * n_e * [CO_2] \tag{5.4}$$

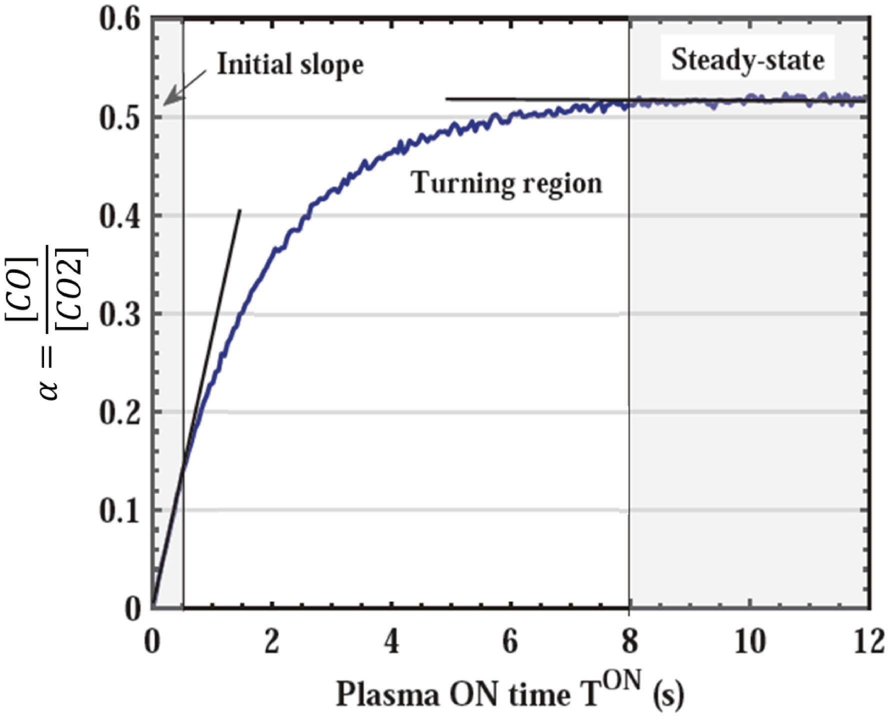

Figure 5.4: Evolution of the dissociation fraction α as a function of plasma ON time in a pure CO_2 RF discharge at 5Torr. Reproduced from A.-S. Morillo-Candas 2019

where k_e^{diss} is the electron impact dissociation rate coefficient and n_e the electron density (which was inferred from the glow discharge current). Varying the initial conditions changes the E/N, therefore modifying the value of k_e^{diss}. By measuring this in numerous conditions, a curve k_e^{diss}(E/N) was obtained. This curve was used to validate the dissociation cross-section of CO_2 in the range 0-100 Td. After the first seconds, the gas goes through a transitory phase when the chemical processes start modifying the plasma. Finally, the plasma reaches a final steady state where the electron impact dissociation is balanced by the back-reaction mechanisms. The evolution of the dissociation fraction α ($\alpha = \frac{[CO]}{[CO_2]+[CO]} = \frac{[CO]}{[CO_2]_i}$), which indirectly represent the evolution of the CO fraction is plotted on figure 5.4 as a function of the total plasma ON time (T^{ON}, the sum of all plasma pulses duration). The three regimes are visible as well as the initial slope of the dissociation fraction.

The measurements from A S Morillo-Candas, Silva, et al. 2020 were also modeled in Tiago Silva, Ana Sofia Morillo-Candas, et al. 2021, where they were used to validate a whole kinetic scheme for pure CO_2 plasmas: it was indeed shown that though the electron impact mechanisms were dominant in the first seconds, the plasma chemistry plays a crucial role on longer time-scale. The effect of the excited state CO($a^3\Pi$) was shown to be crucial, being involved either in dissociation or back-reaction through the mechanisms:

$$CO(a^3\Pi) + CO_2(X^1\Sigma^+) \rightarrow 2CO(X^1\Sigma_g^+) + O(^3P) \tag{5.5}$$

$$CO(a^3\Pi) + O_2(X^3\Sigma_g^-) \rightarrow CO_2(X^1\Sigma^+) + O(^3P) \tag{5.6}$$

CO($a^3\Pi$) therefore promotes dissociation or back-reaction depending on the stage at which it is formed. The negative ion O^- could also recombine with CO to form CO_2 through the reaction:

$$O^- + CO(X^1\Sigma^+) \rightarrow e + CO_2 \tag{5.7}$$

At the steady state of a discharge at 1Torr, reaction 5.6 contributed to half of the formation of CO_2 and reaction 5.7 contributed to 23% of CO formation, highlighting the importance of these two reactions.

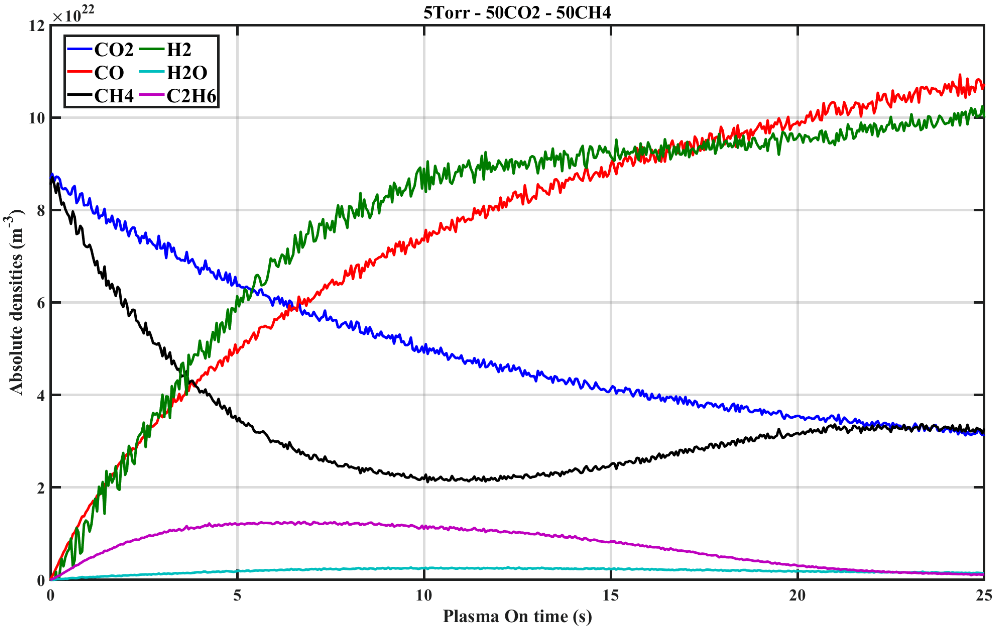

Figure 5.5: Evolution of the densities of the detected species with plasma ON time corresponding to the sum of all plasma pulses duration ($T^{ON} = \Sigma t_p^{ON}$) in a 50/50 CO_2:CH_4 plasma in the configuration 500*10*5-10

Because their simulation requires a good understanding of both the electron impact mechanisms cross-sections and of the chemistry rate coefficients, these measurement are ideal for constraining a kinetic scheme. This experiment will therefore allow to complete the numerical model proposed in the previous chapter.

Similar measurements were also performed in pure CO_2 RF discharge in A S Morillo-Candas, Silva, et al. 2020. Similarly to what will be done here, various parameters were varied to obtain information on both the electronic processes and the chemistry. The results will be commented further.

5.4 Typical experiment

This experiment is very different from the ones described in the previous chapters and the output of a typical measurement must therefore be presented. The typical output is the evolution of the densities presented versus plasma ON time, T^{ON} equal to the sum of all t_p^{ON}. A typical measurement at 5Torr, in a 50/50 CO_2:CH_4 mixture in the configuration 500*10*5-10 (500 trains of 10 pulses, each pulse with 5ms of t_p^{ON} and 10ms of t_p^{off}) is shown on figure 5.5. The main features observed here and repeatedly seen in other conditions are the following:

- After 25s of plasma ON time the gas composition is still evolving in some of the CO_2:CH_4 mixtures while in pure CO_2 it was sufficient to reach a steady state

- Among the species detected, the main one are still CO_2, CO, CH_4 and H_2 like in the plug flow glow discharge, but on the other hand H_2O is not anymore the next most abundant specie. Indeed depending on the conditions, important amount of C_2H_6 (up to 5% of the total density) are found, water only comes next. The H_2 density is not measured directly but deduced from H atom balance. Because the reactor is closed, the total number of H atoms remains constant. The H_2 density is calculated by summing the number of H atoms present in the measured species and assuming that the difference with the initial number of H atoms correspond to H_2 molecules. O_2 is deduced similarly using an O atom balance. The pressure at the end of the experiment is monitored to check that the measured and calculated densities match the pressure in the reactor, which is the case for all the conditions that will be presented in the rest of this chapter.

- Traces of C_2H_4 and even C_2H_2 can be detected. This means that the model proposed in the previous chapter (which did not include molecules with 2 carbon atoms because no C_2 molecule was observed) will have to be updated to properly simulate these measurements.

Looking at the trends of each specie, it can be seen that the CH_4 is dissociated faster than CO_2. However, CH_4 can re-increase after 10s, before decreasing again. This is not observed for all conditions. C_2H_6, C_2H_4 and C_2H_2 increase at the beginning of the measurement, peak between 5 and 10 s and finally decrease below detection limit before the end of the measurement. C_2H_Y molecules always exhibit this trend whenever they are observed.
Even though the purpose of this work is to understand the discharge rather than to optimize it, the efficiency of the RF can be commented. In the glow discharge in the 60:40 CO_2:CH_4 case, the power (measured from the current and the voltage drop across the positive column) is approximately of 18W with and a residence time of ∼7s. In the RF, ∼25W are transmitted to the plasma, so it only takes ∼5s to reach the same specific energy input as in the glow discharge. The composition downstream of the glow and the composition at 5s of plasma ON time can be compared to have an idea of the best suited discharge for dissociation, though this must be taken with caution as the initial mixture compared are not the same (the 50:50 case was not checked in the glow and the 60:40 was not checked in the RF). Downstream from the glow discharge, about half of the initial CO_2 and 1/10th of the initial CH_4 are remaining, while 2/3rd of the CO_2 and 1/3rd of the CH_4 are remaining in the RF after 5s of plasma ON time, which does not seem as good as the glow. Nevertheless, the RF discharge produces less water and more C_2H_6, which is ultimately the desired products in the DRM. Moreover, in the closed reactor the pressure is largely increasing during the first 5s making the direct comparison with the glow a bit more complicated. Without saying that the RF is suited for achieving a one step production of hydrocarbons (without going through the Fischer-Tropch process - the grail -), RF already appears as a good candidate for efficient DRM.

The understanding of these CO_2-CH_4 plasma is very difficult because of the numerous reactions and pathways at play. The only way to properly understand CO_2-CH_4 plasma is through a model. However, there is an enormous number of reactions to take into account to build a complete model (the "simplified" model of the previous chapter had only 450 reactions, and this number grows exponentially with each new specie added) and as underlined in the previous chapter, reactions and rates available in literature might not be enough to build a complete model. Therefore, several measurements are performed in various conditions of pressure, mixture and pulse settings to obtain experimental insights on the plasma. A series of parametric experiments is conducted and the influence of the different parameters are analyzed below.

Reproducibility

The reproducibility of the measurement in pure CO_2 was demonstrated in Ana Sofia Morillo-Candas et al. 2020b. Here, the reproducibility in CO_2-CH_4 plasma was tested with two different RF generators, several months apart. The test was done at 2Torr (where the plasma should be more sensitive to surfaces effect than at 5Torr). The results shown on figure 5.6 are the densities of the main species in our plasma (CO_2, CO, CH_4 and H_2). No differences are seen, proving the reproducibility of the experiment.

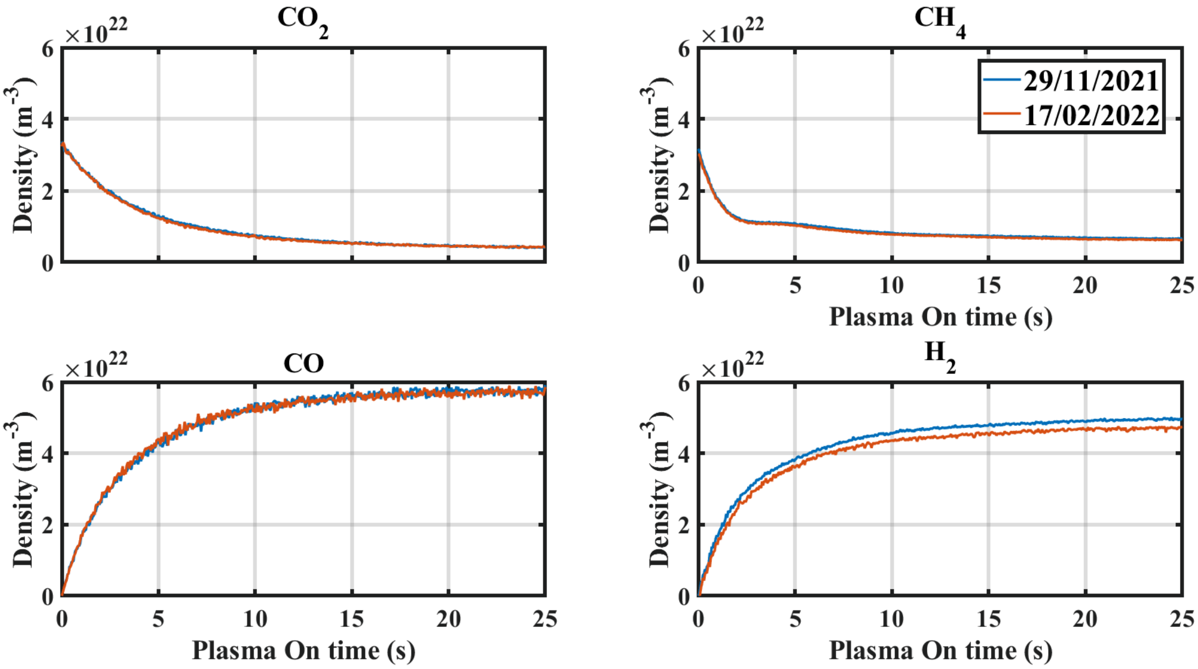

Figure 5.6: Reproducibility Test: Evolution of the densities of the main species during the experiment at 2Torr, in a 50:50 CO_2:CH_4 initial mixture, with a configuration 500*10*5-10. The two measurements were taken three months apart, using two different RF generator

5.5 Experimental results

5.5.1 Gas Mixture variation

The first parameter varied is the gas mixture. As showed in the previous chapter, the processes at play in various mixtures are very different and the mixture variation can therefore bring much information. For all conditions, the pulse settings chosen are 500*10*5-10 (500 trains of 10 pulses, each with 5m on and 10ms off).

Because of the great number of species present in the plasma, the evolution of each specie is plotted separately. The evolution of the CO_2 density with time for various initial mixtures is plotted on the left plot of figure 5.7. The density normalized by the initial value is plotted on the right. For all initial mixtures, the CO_2 density decreases with time. On the absolute densities (left plot), it can be seen that the final value of the CO_2 density in the 90:10CO_2:CH_4 and in the 95:5 CO_2:CH_4 cases are higher than the density in the pure CO_2 case, despite a lower initial density. This is a confirmation of a process already observed in the CO_2-CH_4 glow discharge (see chapter 4), where a peak in the CO_2 fraction measured downstream of the plasma was observed in the same mixtures. This process was attributed to the back-reaction

$$CO + OH \rightarrow CO_2 + H \tag{5.8}$$

because the OH formation is maximum in these conditions. It was shown that in the first few milliseconds of the discharge, the OH formation was mostly due to the reaction

$$CH_4 + O(1D) \rightarrow CH_3 + OH \tag{5.9}$$

as highlighted in Lefkowitz 2015. After increasing in the 95:5 and 90:10 mixture, the final CO_2 density starts decreasing, with a minimum logically reached in the 50:50 mixture.
The normalized density follow more or less the same ordering. This plots shows that CO_2 conversion is more efficient in CO_2-CH_4 plasmas than in pure CO_2 plasmas only above a certain

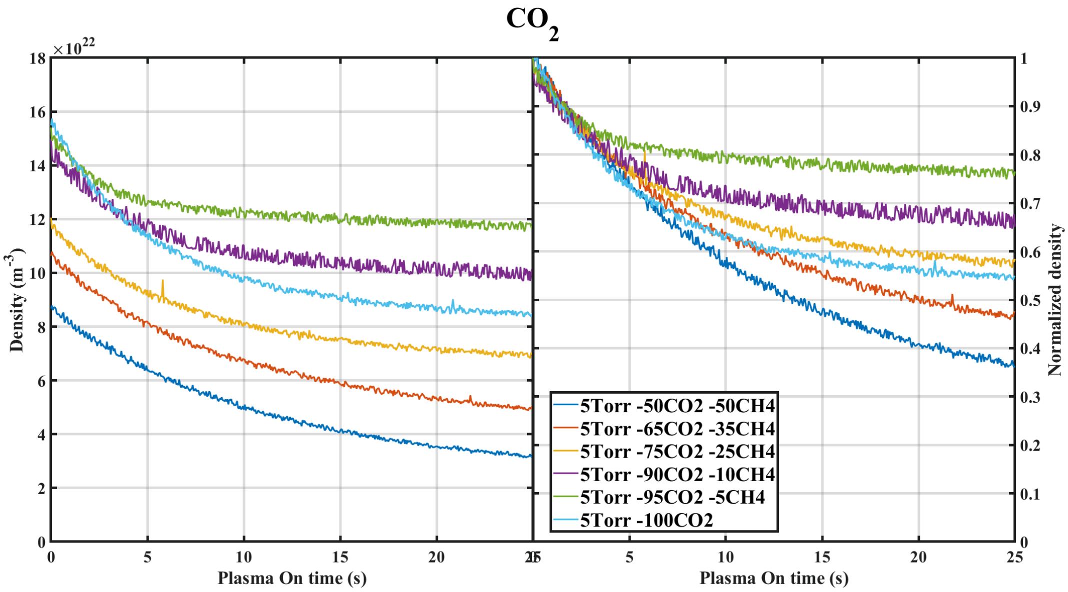

Figure 5.7: Evolution of the density of CO_2 with plasma ON time for various initial mixture at 5Torr, with a 500*10*5-10 pulse configuration. The left plot shows the absolute density as measured by the FTIR, the right plot shows the densities normalized by their initial values

initial CH_4 threshold, which is close to 20%. A particular attention must be paid to the initial CO_2 dissociation, on the first 2.5 seconds. On the right plot, it is clear that the initial decrease of CO_2 is always the same independently of the initial CO_2 fraction, meaning that the CO_2 is always dissociated by the same process. Accordingly to A S Morillo-Candas, Silva, et al. 2020 and Ana Sofia Morillo-Candas et al. 2020b, the first few seconds of the plasma ON time are driven by electron impact dissociation, which is consistent with a scaling with the initial fraction if the electron density does not vary too much between the pure CO_2 and the 50:50 CO_2:CH_4 cases. This assumption is corroborated by the values of the simulated electron density in the glow, which only varied by 15% in the glow between pure CO_2 and 60:40 CO_2:CH_4.

The evolution of the CO density as function of plasma ON time is plotted on figure 5.8. The pure CO_2 case is plotted in light blue and reaches a final CO density of about $7.10^{22}m^{-3}$, in good agreement with Ana Sofia Morillo-Candas et al. 2020b due to the good reproducibility. The finale CO density in the 95:5 CO_2:CH_4 case is plotted in green and is much lower, reaching only $4.10^{22}m^{-3}$: in the RF as in the glow discharge, the evolution of the CO with the mixture mirrors the CO_2 evolution (the lowest CO density is indeed reached in the 95:5 CO_2:CH_4 mixture where the maximum CO_2 density was reached on figure 5.7). The CO density then goes back up: in the 90:10 case, it is still below the final density of the pure CO_2 case, but quickly catches up. The final CO density keeps increasing until the 65:35 CO_2:CH_4 case, where the maximum is reached. Finally in the 50:50 CO_2:CH_4 case, the CO density goes back down to the level of the 75:25 case. The evolution of the CO density with the mixture is quite disordered and complicated to analyze, especially because the cases up to 70:30 CO_2:CH_4 seem to have reached their steady state, while the two other cases are still evolving. Once again looking at the first few seconds of plasma ON, it can be seen that the curves of the pure CO_2 and of the 50:50 CO_2:CH_4 case overlap. As previously shown in the pure CO case, CO is produced mainly by electron impact dissociation of CO_2:

$$\frac{d[CO]}{dt}_i = k_e^{diss} * ne * [CO_2]_i$$

But at constant pressure, there is twice as much CO_2 in pure CO_2 as in 50:50 CO_2:CH_4.

$$[CO_2]_{i,pureCO2} = 2 * [CO_2]_{i,CO2-CH4}$$

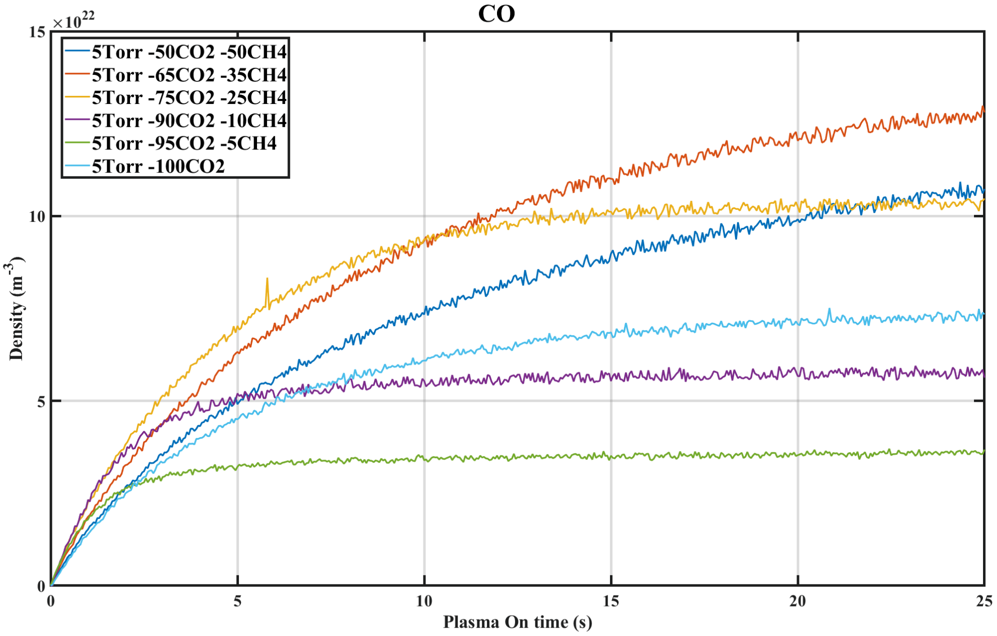

Figure 5.8: Evolution of the absolute density of CO with plasma ON time for various initial mixture at 5Torr, with a 500*10*5-10 pulse configuration

It would therefore be expected that:

$$\frac{d[CO]}{dt}_{i,pureCO2} = 2 * \frac{d[CO]}{dt}_{i,CO2-CH4}$$
$$\text{yet } \frac{d[CO]}{dt}_{i,pureCO2} = \frac{d[CO]}{dt}_{i,CO2-CH4}$$

This means that CO is quickly formed using the carbon coming from the CH_4, which implies the existence of a fast oxidation process of CH_4 or one of its direct by-product CH_3 or CH_2. To the best of our knowledge, no such process has been evoked in literature. Indeed, the quickest way to achieve significant CO formation through CH_4 dissociation are oxidation of CH_4 leading to CH_2O followed by dehydrogenation or through the reaction

$$CH_2 + CO_2 \rightarrow CH_2O + CO$$

which however requires a large quantity of CH_2. Hence, no quick pathways (in 2 or 3 steps) match the observation. This observation support the possibility of the oxidation of CH_3 by O(1D) described in the previous chapter:

$$CH_3 + O(1D) \rightarrow CO + H_2 + H \tag{5.10}$$

The necessity of this reaction to describe the results of the RF "building-up" experiment will be discussed in section 5.7.2.1.

The time evolution of the CH_4 density in all studied mixtures is shown on figure 5.9. As for CO_2, the absolute densities as a function of the plasma ON time is plotted on the left, while the densities normalized to their initial values are plotted on the right. The final density of CH_4 in the plasma is increasing with the initial percentage, similarly to what was seen in the glow discharge. For the 95:5, 90:10 and 80:20 mixtures, the CH_4 decreases monotonously until no more is detected. For higher initial CH_4 percentage, the CH_4 exhibits a different behaviour: in the 65:35 CO_2:CH_4 case, the CH_4 initially decreases, goes through a plateau and then resume decreasing. In the 50:50 CO_2:CH_4 case, the CH_4 initially decreases, re-increases after 11s and

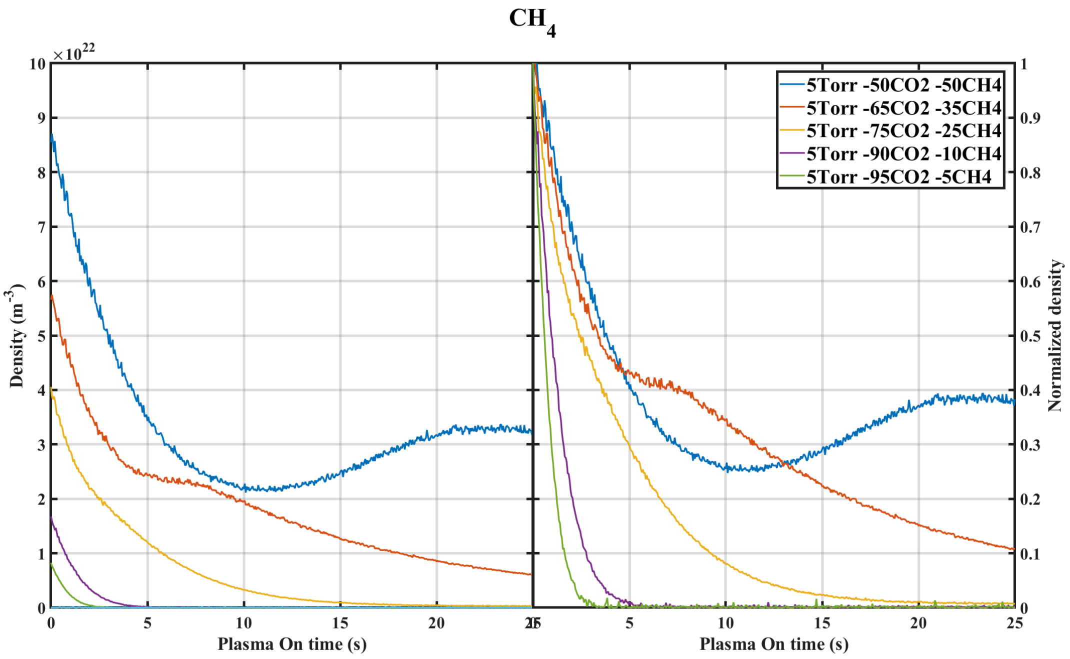

Figure 5.9: Evolution of the density of CH$_4$ with plasma ON time for various initial mixture at 5Torr, with a 500*10*5-10 pulse configuration. The left plot shows the absolute density as measured by the FTIR, the right plot shows the densities normalized by their initial values

finally resume decreasing. Looking at the first 5 seconds of CH$_4$ dissociation on the right plot, it can be seen that the initial destruction is increased with the initial CO$_2$ content. It was shown that at pseudo steady state in the glow discharge the main loss channel of CH$_4$ was electron impact dissociation at high initial CH$_4$ content (30 or 40 %) but was chemical reaction with OH in the 95:5 CO$_2$:CH$_4$ case:

$$CH_4 + OH \rightarrow CH_3 + H_2O$$

The same process could be responsible of the increasingly fast destruction of the CH$_4$ density with initial CO$_2$ fraction.

The last main specie of our discharge is the H$_2$, whose time evolution as a function of plasma ON time is plotted below on figure 5.10. The H$_2$ densities are not measured directly, but are deduced from the H atom balance in the reactor. For the 95:5, 90:10 and 75:25 mixtures, the H$_2$ densities reach a steady state after respectively 2,4 and 15 seconds. These are approximately the times at which, in the same condition, CH$_4$ is completely dissociated. This means that the H$_2$ formation is mostly dependant on the CH$_4$ dissociation. In the glow discharge, H$_2$ was formed mainly by recombination of atomic H at the wall, supplied by CH$_4$ electron impact dissociation into CH$_3$ and H. The mechanism could be the same here. In the 65:35 CO$_2$:CH$_4$ case, the H$_2$ does not reach steady state, which is consistent with the CH$_4$ not being in the steady state either. The evolution of the H$_2$ density in this condition can be separated in 2 parts: a first strongly increasing segment until 4s, followed by a second exponential curve. This break at 4 seconds, not very abrupt, corresponds to the CH$_4$ plateau observed in the same condition, linking again CH$_4$ and H$_2$. The 50:50 condition starts by a strong increase before reaching a period of very slow H$_2$ production between 10 and 15s of plasma ON time. This is followed by a small reincrease in the H$_2$ production rate after 15s (it is particularly visible because starting 15s, the 50:50 overlaps with the 65:35 CO$_2$:CH$_4$). The very slow H$_2$ production, almost a plateau between 10 and 15s, corresponds to the reincrease of CH$_4$. The last part of the H$_2$ curve, after 15s, where the production rate reincreases slightly, corresponds to the time when

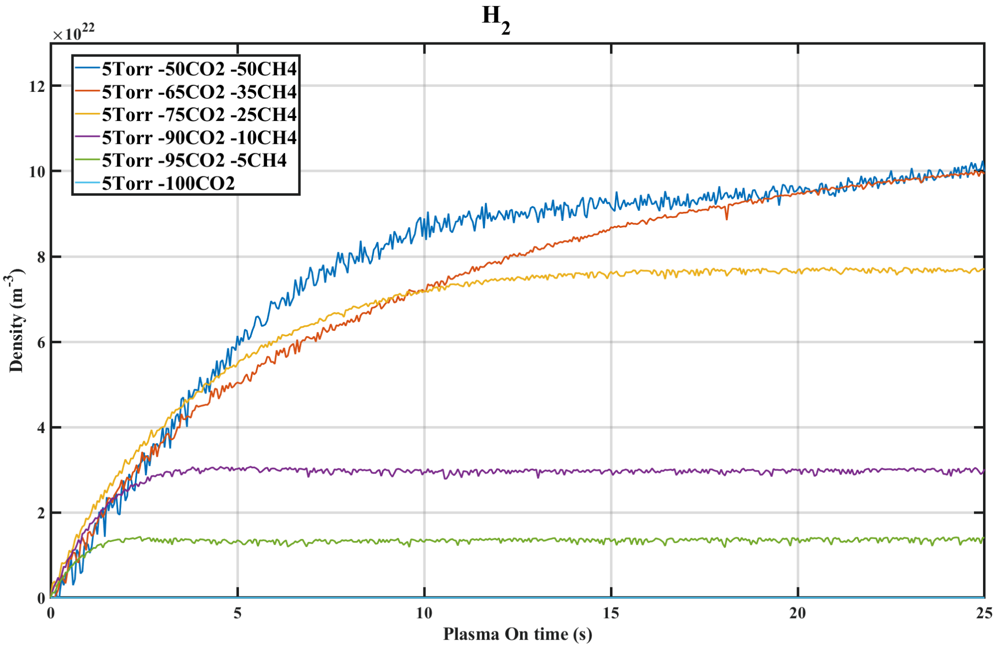

Figure 5.10: Evolution of the absolute density of H_2 with plasma ON time for various initial mixture at 5Torr, with a 500*10*5-10 pulse configuration

CH_4 dissociation resumes after the reincrease. This means that H_2 production is mostly related to CH_4 dissociation but not only.

As seen on figure 5.5, C_2H_6 can be found in the plasma, as well as C_2H_4 and C_2H_2, whose densities are presented on the figure 5.11. The densities are smoothed over 10 points for readability of the lowest ones. Each color corresponds to a condition. The C_2H_6 density is plotted in plain lines, the C_2H_4 lines in dashed lines with triangle marker and the C_2H_2 is dashed and dotted lines with + markers. For the conditions where they are observed, the ordering is $[C_2H_6] > [C_2H_4] > [C_2H_2]$. The ordering of these species in literature can vary from an experiment to the other: in Alphen et al. 2021 a model predicts that the C_2H_2 is the only molecule with 2 carbon atoms expected in a gliding arc, though none is measured. In a DBD discharge at atmospheric pressure in Bie et al. 2015, the simulation predicts that the order is $[C_2H_6] > [C_3H_6] > [C_3H_8] > [C_2H_4] > [C_2H_2]$,close to the results presented here except that no C_3H_Y is observed. In a $CO_2/CH_4/N_2$ DBD at atmospheric pressure, W.Wang et al. 2018 reports measurement of C_2H_6 and traces of C_3H_6. C_2H_6 is often the major specie with more than 1 carbon atom. It seems therefore possible that C_2H_6 is formed first and that the other ones are formed in cascade by successive electron impact of C_2H_6. Below 25% of initial CH_4, no C_2H_Y is detected. In the 75:25CO_2:CH_4 mixture, only C_2H_6 is detected, formed and destroyed in less than 5s of plasma ON time. In both the 65:35 and the 50:50 CO_2:CH_4 cases, all 3 molecules are detected, but are also intermediate molecules, destroyed (or almost) by the end of the 25s. The evolution of these molecules is to relate to the CH_4 decrease: on figure 5.5, it can be seen that the peak of C_2H_6 correspond more or less to the local minimum of CH_4. When C_2H_6 starts being destroyed, CH_4 starts reincreasing. This does not mean however that all the carbon temporarily "stored" in C_2H_6 is going back to methane, which is visible on the following figure 5.12 (showing how each type of atom is parted between the different types of molecules in the 50:50 CO_2:CH_4 case). Indeed, because the configuration is a closed reactor, the absolute number of each type of atom (C, O and H) at the beginning the experiment is known. At any instant, the fractions of H atom in a given specie (H_2 or CH_4) can be computed. These fractions are plotted on figure 5.12 for the 50:50 CO_2:CH_4 case. Initially, 50% of the carbon atoms are in CO_2, and 50% are in carbon. After 10s of plasma ON time, at the minimum of

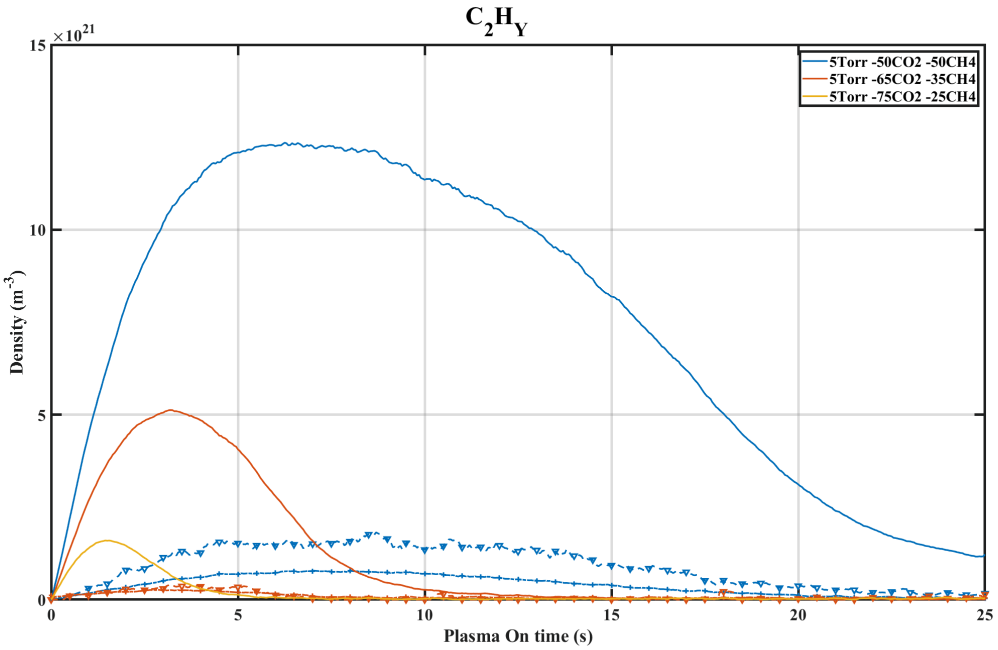

Figure 5.11: Evolution of the absolute density of C_2H_6, C_2H_4 and C_2H_2 with plasma ON time for various initial mixture at 5Torr, with a 500*10*5-10 pulse configuration. The C_2H_6 density is plotted in plain lines, the C_2H_4 lines in dashed lines with triangle marker and the C_2H_2 is dashed and dotted lines with + markers

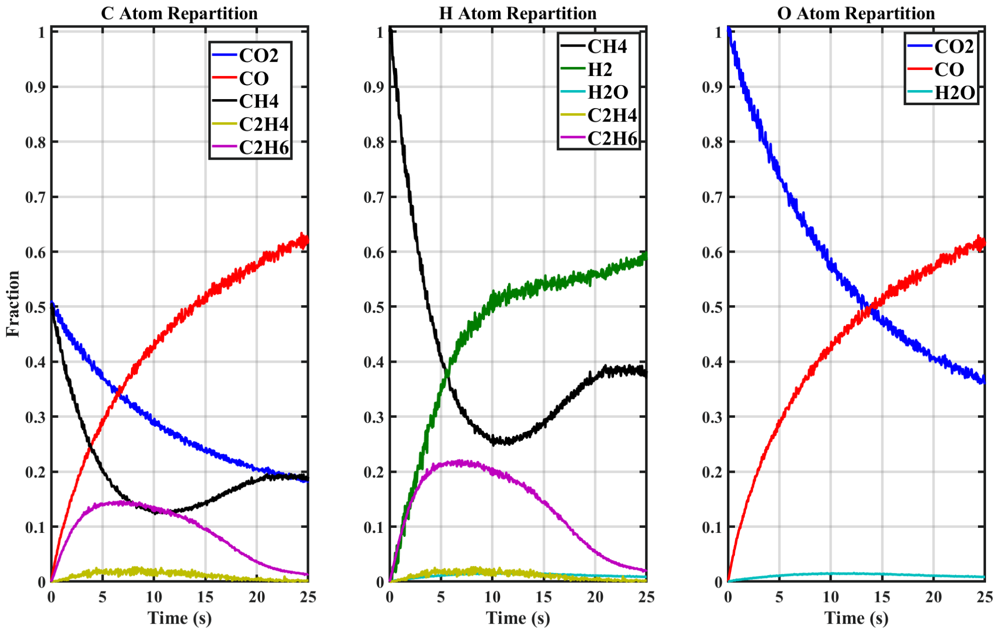

Figure 5.12: Evolution with plasma ON time of the fraction of C, O and H parted in each type molecule in a 50:50 CO_2:CH_4 mixture at 5Torr, with a 500*10*5-10. The first plot is for the carbon atoms, the second for H atoms and the third for atomic oxygen

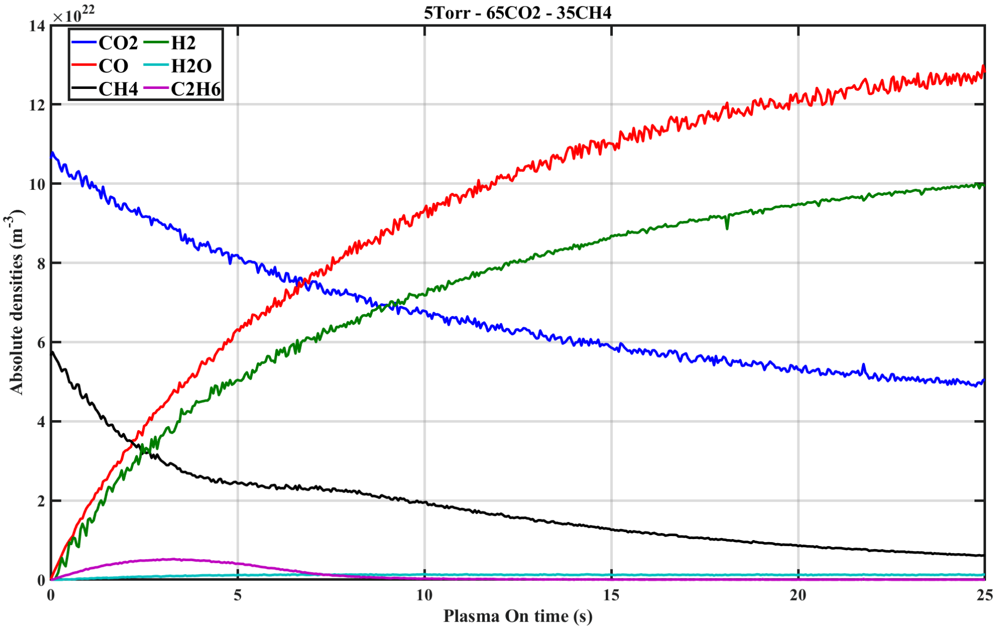

Figure 5.13: Evolution of the densities of the detected species with plasma ON time in a 65:35 CO_2:CH_4 plasma in the configuration 500*10*5-10

CH_4 density, approximately 14% of the carbons are in C_2H_6 and 13% are in CH_4. By the end of the experiment, close to 25s, 1% of the carbon is in C_2H_6, and 19% are in CH_4, meaning that out of the 13% released by C_2H_6 destruction, only 6% went to the CH_4 reformation and the rest goes to the CO. This means that the C_2H_6 destruction pathways must end up with both CH_4 and CO creation, probably in close proportions.

For H atoms, something similar can be observed: at 10s, 20% of the hydrogen are in C_2H_6, 26% are in CH_4 and 52% are in the H_2. By the end of the measurement, 2% are left in C_2H_6, 38% are in CH_4 and approximately 58% are in H_2. Out of the 18% liberated by C_2H_6 destruction , 13 went to CH_4 and 5 went to H_2. The C_2H_6 destruction process is also expected to produce H_2, again in close proportions (13% of H atoms recombining in CH_4 will give about as many molecules as ~5% recombining in H_2).

The O atoms are quite simple to analyse: almost all of it is either in CO_2 or in CO.

A similar analysis can be drawn from the 65:35 CO_2:CH_4 mixture, whose density as a function of the plasma ON time is shown below on figure 5.13. This time, no reincrease of CH_4 is observed, but a plateau in CH_4 dissociation around 5s, when the C_2H_6 starts being dissociated. When the C_2H_6 is below detection limit (close to 7.5s), the CH_4 dissociation resumes. This proves that in this case, the CH_4 rate production from C_2H_6 loss is close to the summed rates of CH_4 electron impact dissociation and CH_4 oxidation.

- The CO_2 is destroyed all along the 25s of plasma ON time. When normalizing by the initial CO_2 density, it appears that the CO_2 during the first seconds is always destroyed in the same proportion, leading to think that the CO_2 is destroyed by the same mechanism, likely electron impact dissociation
- After 25s of plasma ON time, the CO_2 is less dissociated in the 95:5 CO_2:CH_4 than in the 100 CO_2 case, as seen in the glow discharge
- The formation of CO is similar in the pure CO_2 case and in the 50:50 CO_2:CH_4 case, indicating that CO is rapidly produced from CH_4
- The normalized CH_4 densities show that the more initial CO_2, the faster CH_4 drops, indicating that CH_4 is strongly oxidized
- When the initial CH_4 percentage is high enough, the CH_4 does not decrease monotonously. In the 75:25 CO_2:CH_4 case, a plateau on the CH_4 in seen. In the 50:50 CO_2:CH_4 case, a temporary reincrease of the CH_4 is seen
- C_2H_Y molecules are measured in the plasma when the initial CH_4 content is high enough. The order observed is $[C_2H_6] > [C_2H_4] > [C_2H_2]$. The C_2H_Y molecules are intermediate species, disappearing by the end of the 25s of plasma ON time. Their characteristic time is similar to the CH_4 reincrease
- An atom balance shows that the destruction of C_2H_6 produces CH_4 but also CO and H_2.

5.5.2 Pressure variation

The next varied parameter is the pressure. This variation is expected to be less impacting because it was shown in the glow discharge that the main species are not critically changed. In the glow discharge, the dissociation of CO_2 with pressure was indeed similar (when looked in fraction of the gas mixture), and it was later shown that the main processes leading to the creation and loss of a specie were the same at high and low pressure (though their respective contribution to the final balance changed). To verify this in the RF discharge, the densities of the main species are plotted as a function of the plasma ON time on figure 5.14 for 2 and 5Torr and for different initial mixtures. The densities at 5Torr are plotted in plain lines, the densities at 2Torr are plotted in dashed line. Each color represents a different initial mixture.

For all species, no major differences of the evolution with the initial mixture are found between 2 and 5Torr. For the CO_2, a higher density is observed for the 95:5 CO_2:CH_4 than in the pure CO_2 plasma at both pressure. The CO_2 density then goes down when increasing the initial CH_4 percentage. For the CH_4, the ordering of the curves with initial CH_4 percentage is the same for both pressure, nevertheless no CH_4 reformation is observed in the 50:50 case at 2Torr. Only a plateau is visible, similar to what is seen in the 65:35 case at 5Torr. Concerning the CO, one difference can be seen: the 75:25 case, previously higher than the 50:50 case, is now lower. Finally, the ordering of the H_2 densities is the same at 2 and 5Torr. Generally, the evolutions of the densities seem to follow the same trends at 2 and 5 Torr but are more pronounced at 5Torr, probably due to the higher density of reactants. In the glow, the processes creating and destroying water proved to be very dependant on pressure, which is found again here, as seen of figure 5.15. At 5Torr (in plain lines), all the curves have different shape, trends and values. No trends as a function of the initial mixture is visible. It is however interesting to note that at 2 Torr, still no clear trend can be drawn, but the ordering of the curves as a function of the CH_4 initial content is completely different from the 5Torr case, which points toward a change of main creation and loss processes of water (like in the glow). Because no clear trend can be drawn from this plot, no indications on the mechanism creating water can be

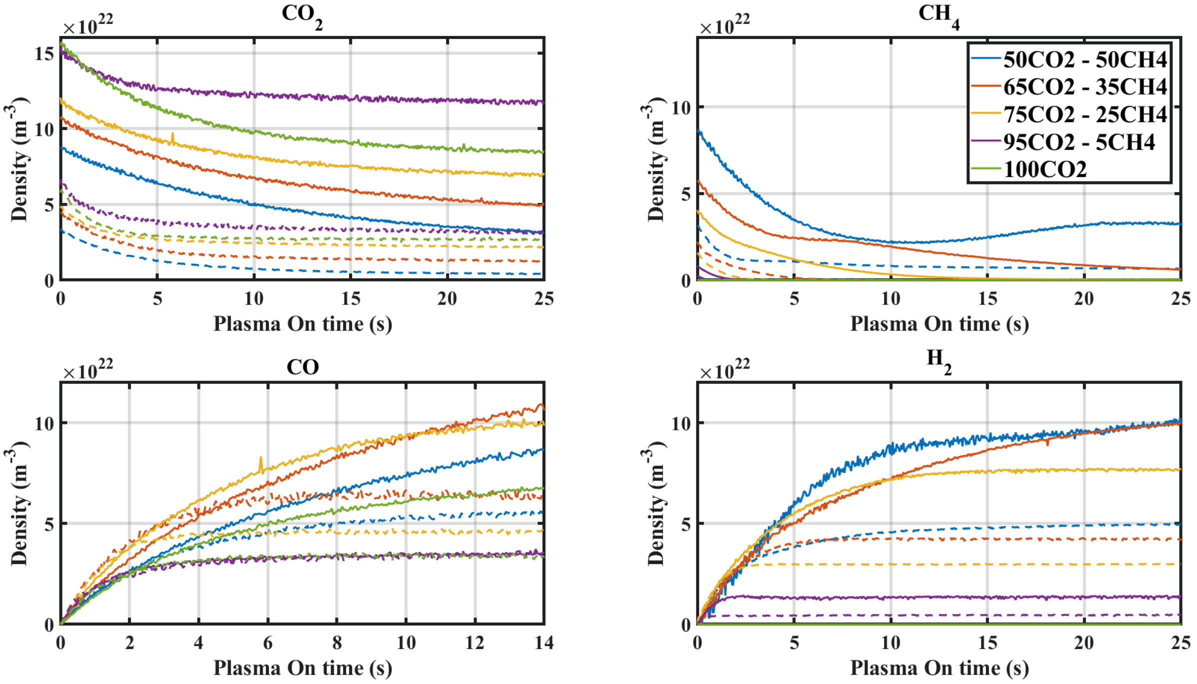

Figure 5.14: Evolution of the densities of the main species (CO_2, CO, CH_4 and H_2) over plasma ON time for different mixtures. The pulse configurations is 500*10*5-10. The densities at 5Torr are plotted in plain lines, the ones at 2Torr are in dashed lines. Each color is a different initial mixture

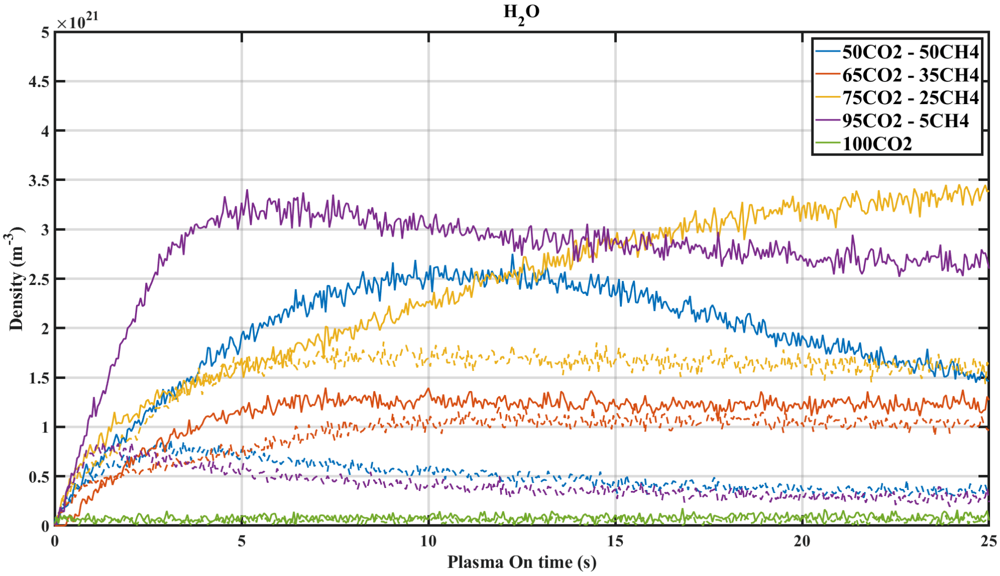

Figure 5.15: Evolution of the density of water over plasma ON time for different mixtures. The pulse configurations is 500*10*5-10. The densities at 5Torr are plotted in plain lines, the ones at 2Torr are in dashed lines. Each color is a different initial gas mixture

found without a model. Overall, it can be seen that the dissociation is much more efficient at 2Torr, a good illustration being the CO density which is the same at 2 and 5 Torr in the 95:5 CO_2:CH_4 case (in purple on figure 5.14). This is due to the specific energy input, which is 2.5 higher at 2Torr because the power coupled to the reactor is kept constant at 40W.

- The evolutions observed at 2 and 5 Torr are similar but are more pronounced at 5Torr due to higher density of reactant.
- The dissociation at 2Torr is more efficient than at 5Torr due to higher specific energy input

5.5.3 Pulse settings variation

A significant advantage of the "building-up" experiments is to provide the possibility to play with the duty cycle ratio of the plasma pulses to probe the influence of species with different lifetime or the effect of temperatures evolving over a few milliseconds. After the gas mixture variation, the effect of the pulses duration t_p^{ON} and the total number of pulses is therefore studied here. Varying the pulses settings (number and duty cycle ratio) will allow to single out processes as a function of their characteristic time such as for example the gas heating, whcich takes approximately 2ms to stabilize as shown in pure CO_2 in Klarenaar, Engeln, et al. 2017 and in chapter 6 for CO_2-CH_4 plasmas. Using plasma pulses shorter than 2ms will therefore prevent the gas heating by the plasma.

Number of trains and number of pulses per train

In this variation, the total number of trains N_{trains} is changed. The duration of the pulse (t_p^{ON}) and of the OFF time between pulses t_p^{OFF} are kept constant, the compensation is done by changing the number of pulses per train $n_{p/train}$. The configuration tested are:

$$\begin{aligned}
&Ntrains * n_{p/train} * t_p^{ON} - t_p^{OFF} \\
&\qquad\qquad 100 * 50 * 5 - 10 \\
&\qquad\qquad 500 * 10 * 5 - 10 \text{ (Normal configuration)} \\
&\qquad\qquad 625 * 8 * 5 - 10 \\
&\qquad\qquad 1000 * 5 * 5 - 10
\end{aligned}$$

In all of these experiments, the plasma undergoes 5000 pulses of 5ms. The main change is the number of 'long OFF time' (see on figure 5.2), meaning the number of times 1.5s is left between two pulses, which changes between 100 and 1000. In Ana Sofia Morillo-Candas et al. 2020b, the influence of the number of trains in pure CO_2 plasmas is discussed: lowering the number of trains slightly increase the dissociation fraction, which was attributed to long lived-species or slow surface processes. The effect of the long OFF time in the 50:50 CO_2:CH_4 experiment is shown on figure 5.16. The effect of the long OFF time are very minor. It is difficult to know if the small differences observed are due to a real effect or to imprecision in the initial mixture. Indeed, the effect of the variation seems to confirm what is seen in pure CO_2 experiment, i.e that lowering the number of train slightly increase the dissociation. However the blue and orange curves, corresponding to the smallest number of trains, also have a slightly higher initial density of both CO_2 and CH_4 (meaning that the pressure in the reactor could have been slightly higher than 5Torr), which is expected to lead to a higher CO and H_2 density. In both cases, the changes are minor enough to neglect the influence of the long OFF time. This confirms what had been seen with the glow discharge that no important chemical change happen over long time scale in the post discharge.

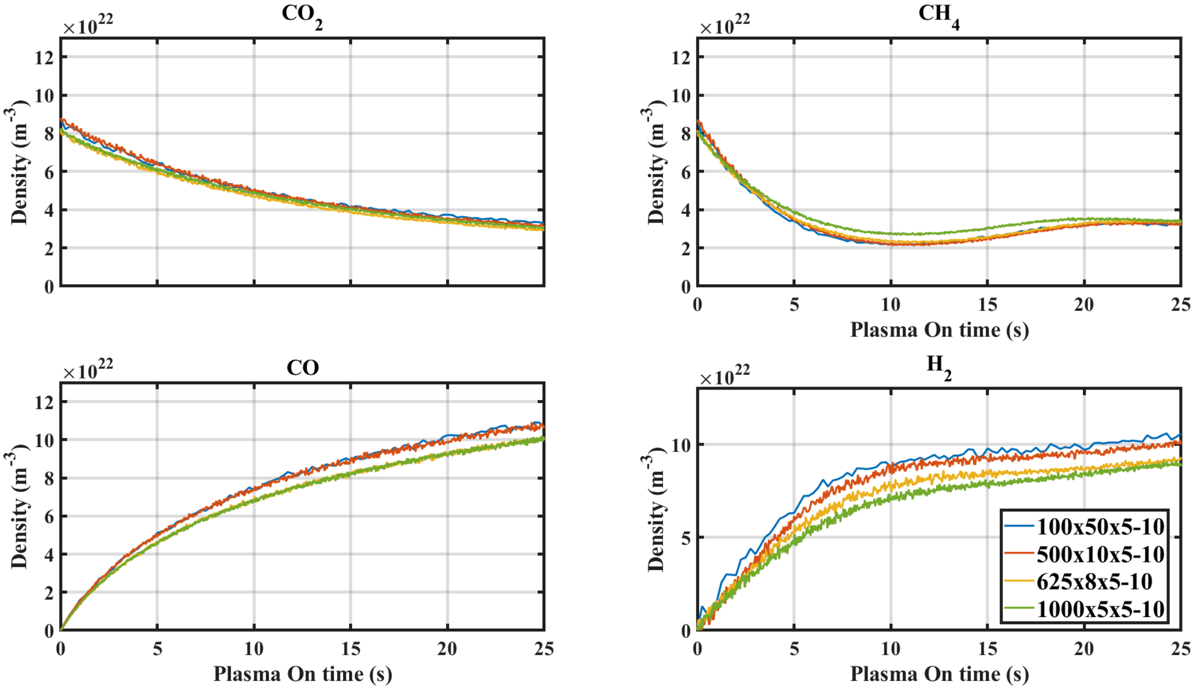

Figure 5.16: Densities of the main products (CO_2, CO, CH_4, H_2) as a function plasma ON time for several Ntrains*Npulse/train configurations in a 50:50 CO_2:CH_4 mixture at 5Torr. The total number of pulses is kept to 5000 and the pulses duration is kept at 5ms on/10ms off

> Changing the number of train and the number of pulses per train has a very minor influence, indicating that the long OFF time has a negligible influence on the evolution of the species

Interpulse (t_p^{OFF}) variation

The second parameter studied is the time between two pulses, t_p^{OFF}. This parameter is the simplest to study because it does not affect the other pulse settings, therefore its influence can be isolated. Varying t_p^{OFF} informs on the behaviour of the molecules in the early post-discharge phase, but on time scale for which no electron impact reaction happen anymore. Three values of the t_p^{OFF} are tested: 1ms, 10ms and 50ms. Varying t_p^{OFF} changes mostly the back reaction mechanisms involving radicals with life time of a few tens of ms. In pure CO_2, the main back reaction mechanism is the recombination of CO($a^3\Pi$) with O_2, which is formed by recombination of atomic oxygen. Increasing t_p^{OFF} allows for more atomic recombination, increasing in turn the back-reaction. Varying t_p^{OFF} also changes the cooling of the gas. When t_p^{OFF} is set to 1ms, the plasma does not have time to fully cool down before the next pulse whereas at t_p^{OFF} = 10ms, the plasma can fully cool down. the first back-reaction mechanism (whose characteristic time in pure CO_2 plasma is approximately 5∼10ms, according to A S Morillo-Candas, Silva, et al. 2020,Ana Sofia Morillo-Candas et al. 2020b and Tiago Silva, Ana Sofia Morillo-Candas, et al. 2021) have kicked in. At t_p^{OFF}=50ms, the gas is completely cooled down between 2 pulses and the back-reaction mechanism are expected to play an significant role. The main back-reaction mechanism in CO_2-CH_4 plasma were identified in the previous chapter and do not involve O atoms, but rather OH ($CO + OH \rightarrow CO_2 + H$) and H_2. Playing on the different time-scales could give indication on these molecules. The evolution of the densities of the main species (CO_2, CH_4, CO and H_2) are shown on the next figure 5.17 as a function of the plasma ON time at 5Torr in a 50:50 mixture. Each color represent a different value of t_p^{OFF}. Surprisingly, no

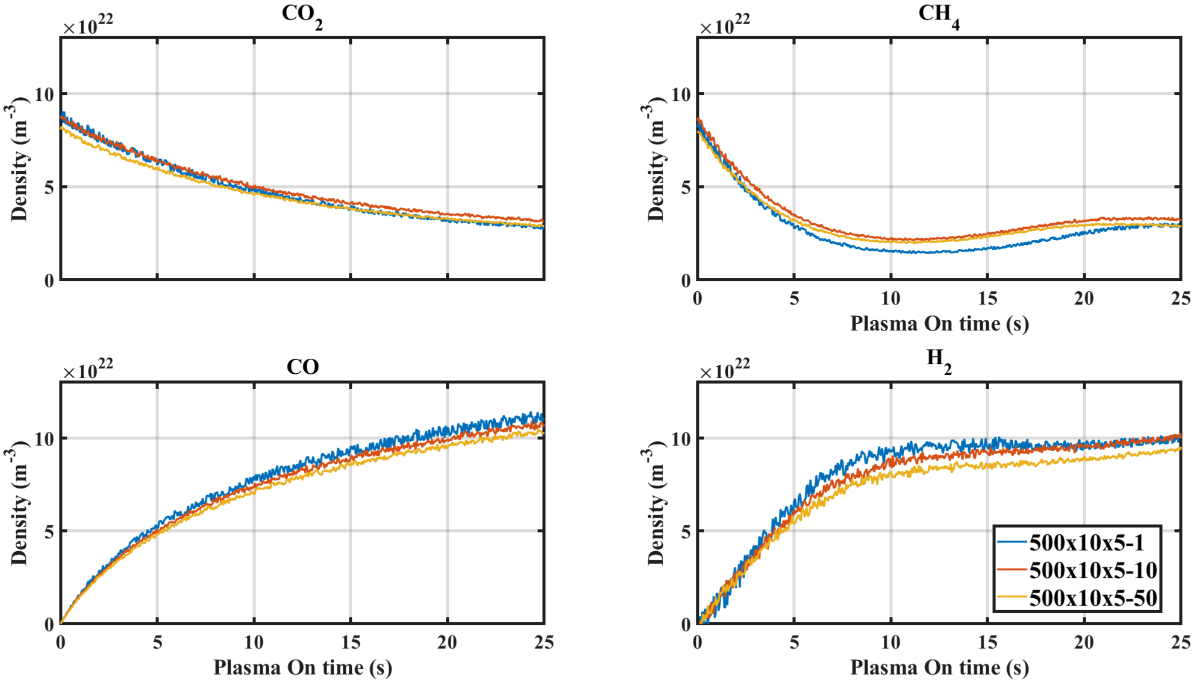

Figure 5.17: Densities of the main species (CO_2, CO, CH_4, H_2) as a function of plasma ON time for different t_p^{OFF} in a 50:50 CO_2:CH_4 mixture at 5Torr. Each color is a different t_p^{OFF}. The number of trains is kept to 500, with 10 pulses per train. The t_p^{ON} is kept to 5ms

difference is observed when varying t_p^{OFF}. The minor species (not shown here) also do not show any major difference. The few differences seen on CO or H_2 are difficult to analyze because they are within the reproducibility limit of the measurement, which requires to put the exact same mixture at the same pressure in the reactor for every measurement. The flowmeters used have a limited precision (down to 5% of the total range of the flowmeter), which could lead to small inaccuracy on the flow. A small tolerance (5e-2 Torr) is also left on the pressure at the beginning of the experiment. Though the mixture is checked by FTIR before starting the plasma, a small difference can exist between two measurements in the same condition. This is illustrated by the initial value of the absolute density of both CO_2 and CH_4, which are slightly higher in the t_p^{OFF}=1ms condition than in the t_p^{OFF}=50ms condition, eventually leading to a larger CO density in the first case. Nevertheless, a minor effect could exist: indeed the CO and H_2 densities show the same ordering:

$$[CO]_{t_p^{OFF}=1ms} > [CO]_{t_p^{OFF}=10ms} > [CO]_{t_p^{OFF}=50ms}$$
$$[H2]_{t_p^{OFF}=1ms} > [H2]_{t_p^{OFF}=10ms} > [H2]_{t_p^{OFF}=50ms}$$

On the contrary, accounting for the small offset on the t_p^{OFF}=50ms curve compared to the other ones, the densities of CO_2 and CH_4 have the opposite order:

$$[CO2]_{t_p^{OFF}=1ms} < [CO2]_{t_p^{OFF}=10ms} < [CO2]_{t_p^{OFF}=50ms}$$
$$[CH4]_{t_p^{OFF}=1ms} < [CH4]_{t_p^{OFF}=10ms} < [CH4]_{t_p^{OFF}=50ms}$$

The absence of major effect of the t_p^{OFF} brings much information. The effect of the temperature on the post-discharge is negligible. Most importantly, contrarily to the pure CO_2 case, no back-reaction or recombination mechanisms happen on the scale of the few ms/tens of ms, most recombination reactions are probably shorter. The minor effect could be explained by a minor recombination process which would take place on the tens of ms time scale and would lead to minor back reaction on that time scale.

Varying the time between the pulse induces minor changes, which could however be due to inaccuracies in the initial mixture. This indicates that unlike in pure CO_2, no recombination mechanisms happen on the scale of several ms/tens of ms. The recombination mechanisms likely happen on a timescale smaller than the ms.

pulse duration (t_p^{ON}) variation

The last pulse setting to vary is the t_p^{ON}. This variable is the most complicated to analyze because it affects directly the discharge and plays on several entangled phenomena.
Four durations of t_p^{ON} are tested. The number of trains is kept constant and the compensation for the total plasma ON time T^{ON} is done through the variation of the number of plasma pulses per train. The t_p^{ON} is kept constant at 10ms. The total plasma ON time is kept at 25s. The 4 configurations tested are:

$$\begin{aligned}&500 * 1 * 50 - 10\\&500 * 10 * 5 - 10 \text{ (reference Configuration)}\\&500 * 50 * 1 - 10\\&500 * 100 * 0.5 - 10\end{aligned}$$

Regarding the previous results, this is not the best choice of configuration: it was shown that varying Ntrains and $n_{p/train}$ while keeping a constant number of pulses did not affect the results, therefore keeping Ntrains*$n_{p/train}$ (the total number of pulses) constant in this variation might have been a better choice to fully decorelate the variations. Here, both the total number of pulses and the pulse duration are changed. Regarding previous results on the long OFF time and on t_p^{OFF}, changing the total number of pulses should have no impact and the change of t_p^{ON} should be the source of the observed changes, but both are entangled.

The plasma heating is one of the phenomena affected by t_p^{ON}. As will be shown in chapter 6 on vibrational kinetics and preplotted on figure 5.18, the plasma rotational and vibrational heating can take up to a few ms. The data reported on figure 5.18 were taken in a glow discharge and not an RF discharge so they do not exactly correspond to what happens during an RF pulse, but it was verified in A.-S. Morillo-Candas 2019 that the characteristic heating time are similar in the glow and in the RF. The estimation provided by figure 5.18 is therefore good. For pulses of 0.5 and 1ms, whose rotational temperatures by the end of the pulse are shown by the blue and orange markers, the gas temperature remains quite low during the pulse, barely reaching 500K for pulses of 1ms. Several processes could be affected by temperature, like thermal dissociation of CH_4 which at 500K J.R.Fincke et al. 2002 (though it was not a driving process in the glow discharge) or many others (see the list of the rate coefficients in the appendix). The characteristic time of vibrational heating is similar to the one of the rotational heating (see chapter 6). The vibrational excitation was neglected in the analysis of the glow discharge but it could also increase the rate of some chemical reactions.
The influence of the t_p^{ON} on the main densities is plotted on figure 5.19. The CO_2 densities can be separated in two: the 'short' pulses, 500*100*0.5-10 and the 500*50*1-10 i.e $t_p^{ON} \leqslant$1ms, are very close and almost overlap, while the long pulses ($t_p^{ON} = 5$ and 50ms) are lower. This difference between the 'short' and the 'long' pulses is also visible on the CH_4 densities: in the short pulses, the CH_4 decreases monotonously but with longer pulses (5ms or above), the CH_4 reaches a local minimum around 10s of plasma ON time, before going back up. This indicates that the CH_4 back-reaction mechanism is likely due to a short-lived specie that accumulates during the pulse, like a radical or an excited electronic state. The change of temperature is ruled out because the effect on CH_4 would be the same all along the experiment and because it was estimated in the glow that the thermal dissociation only played a minor role. Distinction between short and long pulses can also be seen in the H_2 densities, also plotted on figure 5.19. A clear difference is visible in the shape of the density, with long pulses (in yellow and purple)

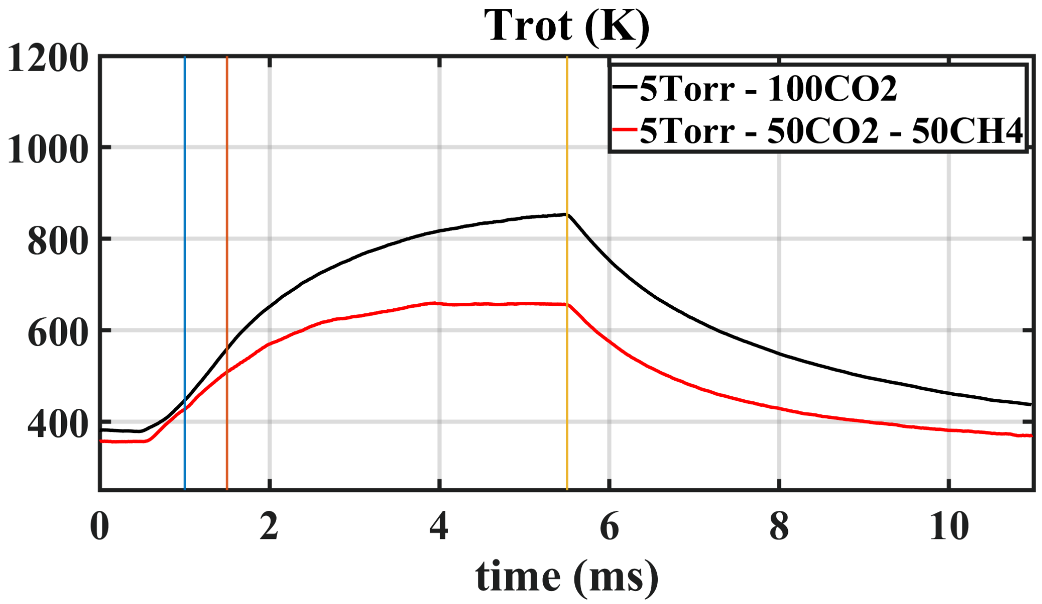

Figure 5.18: Evolution of the rotational temperature during a 5ms pulse in the glow discharge. Taken from chapter. Color markers have been added in the time corresponding to the pulse duration chosen for the RF. The 50ms temperature will be assumed to be the same as the 5ms temperature, as heating reaches steady state after 5ms

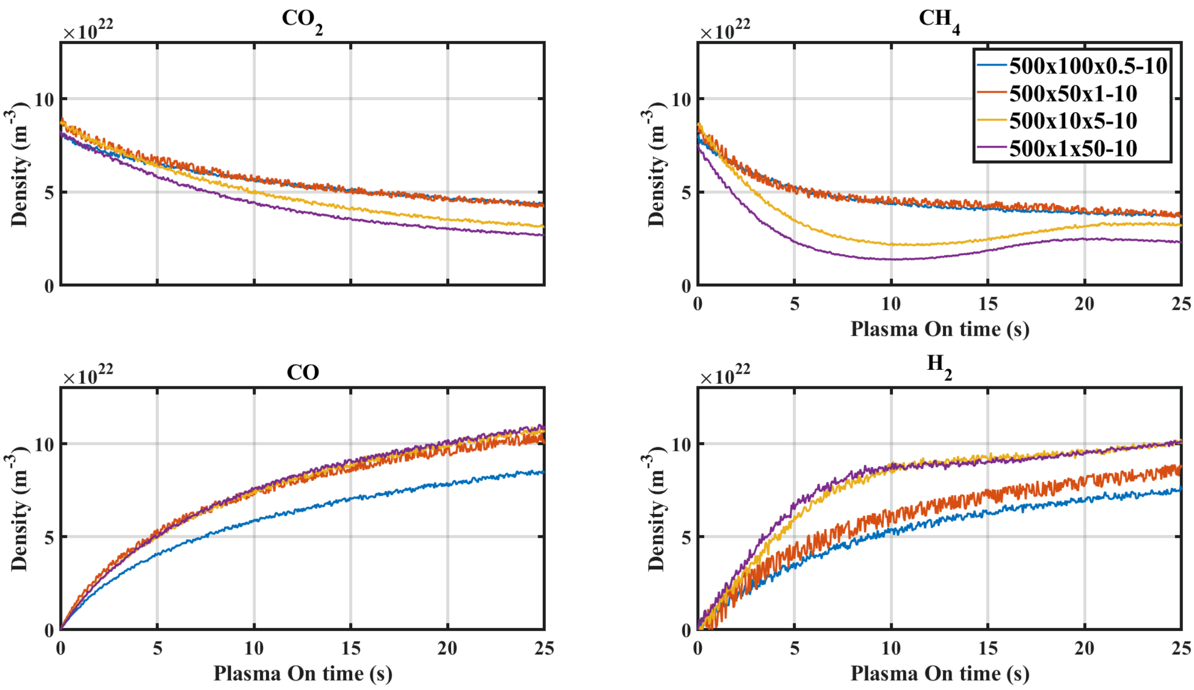

Figure 5.19: Densities of the main species (CO_2, CO, CH_4, H_2) as a function of plasma ON time for different t_p^{ON} in a 50:50 CO_2:CH_4 mixture at 5Torr. Each color is a different t_p^{ON}. The number of trains is kept to 500. The t_p^{OFF} is kept to 10ms

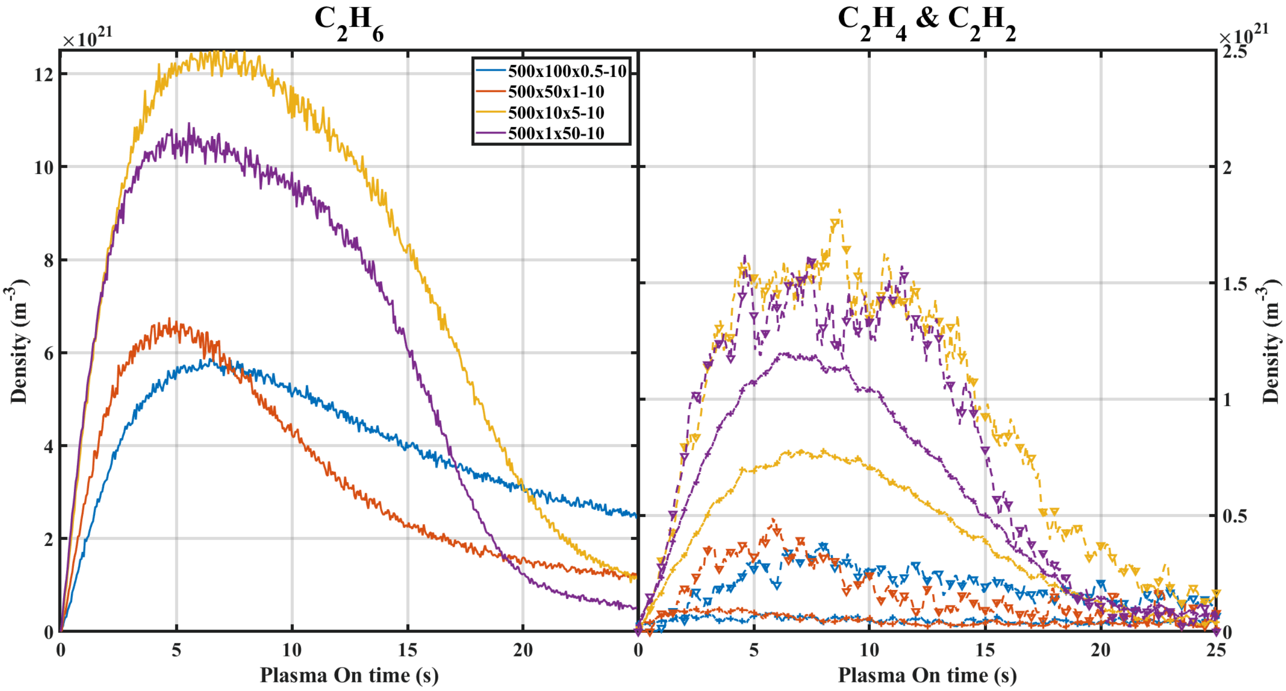

Figure 5.20: Densities of C_2H_6 (on the left), C_2H_4 (on the right with triangles) and C_2H_2 (on the right with crosses) at 5Torr in a 50:50 CO_2:CH_4 mixture for different t_p^{ON}. Each color represent a different pulse settings

exhibiting an strong change in the slope around 10s. The short pulses (in blue and orange) do not show any inflexion point. The CO densities do not show the same behaviour: the shortest pulse (0.5ms, in blue) stands alone and is lower than all the other, which overlap. The reasons behind this are not very clear, but it would points toward the existence of process leading to CO formation with a characteristic time between 0.5 and 1ms. This process would not directly be tied to CO_2 or CH_4 dissociation. No such process was identified for pure CO_2 plasma in Ana Sofia Morillo-Candas et al. 2020b and could therefore involve CH_4 or its by-products. This is left to be explored in the future using the model. The influence of pulse duration on the C_2H_Y molecules can be seen on figure 5.20. The long pulses (in yellow and purple) exhibit a similar shape with a maximum around 6s of plasma ON time. The values of the maximum are relatively close in both cases. This similarity of the curves can be found again for the C_2H_4 (dashed line with triangles on the right plot of figure 5.20), which overlap for long pulses. Finally, the C_2H_2 (dashed line with crosses on the right plot of figure 5.20) are also close for long pulses. The behaviour of the C_2H_6 density is not similar for both short pulses configuration, contrarily to the main species. The 0.5ms pulses experiment has a sharp increase, with a maximum reached at 5s of plasma ON time. The density then decreases with a linear trend until the end of the measurement. The 1ms pulses also starts with a sharp rise and reaches a maximum close to the 0.5ms configuration one but decreases with an exponential trend. These different trends are found again in the C_2H_4 (on the right plot with triangle markers), where the decrease is faster in the 1ms configuration than in the 0.5 configuration. The C_2H_2 is too close to noise to draw any information.

It can be observed that in all pulse configurations studied, the shapes of C_2H_6, C_2H_4 and C_2H_2 are very similar (with a maximum close to 6 seconds) and a decrease slower than the increase, which supports the hypothesis that C_2H_6 is first formed and that a part of it then cascades to C_2H_4 and then to C_2H_2, probably through electron impact dissociation. The dissociation of C_2H_6 could lead directly to C_2H_4 or go through C_2H_5. The fastest C_2H_6 formation channel from CH_4 or its by-products is

$$CH_3 + CH_3 \rightarrow C_2H_6 \tag{5.11}$$

as found in Bie et al. 2015. The CH_3 is mainly produced by the electron impact dissociation reaction of CH_4, but also by chemical reactions. So it seems that increasing the pulse duration both increases the electron impact dissociation and leaves more time for chemistry to happen, leading to higher dissociation. This must be confirmed by modeling.
As mentioned, the CH_4 reincrease observed in the reference configuration (500*10*5-10) and confirmed with 50ms pulses was linked to the C_2H_6 destruction, which would ultimately form CH_4, CO and H_2. The process leading to loss of C_2H_6 remains however unknown/unclear, but was attributed in the mixture variation to an accumulation of short-lived specie. The variation of the t_p^{ON} brings some information on the characteristic time of formation of this specie: with the 0.5ms pulses, the loss of C_2H_6 is very inefficient (with a linear trend), meaning that the specie responsible is not accumulating enough. On the contrary, the identical shapes of the 5ms and the 50ms pulses (in purple and yellow on figure 5.20), indicate that the specie responsible for C_2H_6 loss does not accumulate on more than 5ms. The 1ms curve is intermediate (in orange on 5.20): the decrease is not linear like in the 0.5ms case, but is not as fast as in the 5 and 50ms cases. The processes responsible for C_2H_6 loss and indirectly for CH_4 reincrease therefore appear to have a characteristic time of a few ms.

Varying the duration of the pulses lead to 2 behaviours: the short pulses ($t_p^{ON} \leqslant$ 1ms), where the CH_4 decrease monotonously and the long pulses ($t_p^{ON} \geqslant$ 5ms), where a reincrease of the CH_4 is observed. Long pulses also lead to higher CO_2 dissociation and a different H_2 trend. The process responsible for this could not be clearly identified but it should have a characteristic time of a few ms.

5.5.4 Summary of the experimental results

A brief summary of the several types of variation tested is done here.

- The initial CO_2:CH_4 proportion variation highlighted several important elements. First, the CO_2 is dissociated during the first 5s by electron impact dissociation. The CO_2 initial decay with the initial mixture is similar to the glow discharge, leading to think that the same processes are at play. The CO production relies on a fast oxidation process to convert CH_4 or its by-products to CO. Similarly to the glow discharge, CH_4 is initially oxidized. Increasing the initial CH_4 content will lead to more production of C_2H_6 and other C_2 molecules, but these molecules are only intermediate species that are destroyed and reform CH_4 in the process. The CH_4 reformation depends on the amount of C_2H_6 produced.

- The pressure was lowered to 2Torr and similar behaviours to the 5Torr case was observed, but less pronounced. The conclusion drawn here is the same as in the glow discharge: the main processes remain the same independently of the pressure (at least between 2 and 5Torr) , only their relative contribution vary.

- The pulse settings were also varied. The 'long' OFF time (the time between trains) was varied and has only a minor influence, indicating that the long processes (with a time scale of a second) have a minor influence. The t_p^{OFF} time (the off time between pulses) was varied as well and once again did not show any major influence, indicating that the recombination process happening in the post-discharge have a very short time scale. Finally, the t_p^{ON} (duration of each pulse) was varied and had a strong influence. Two cases are seen: the short pulses (t_p^{ON} $\leqslant$1ms), where little C_2H_6 is produced and no reincrease of CH_4 is observed, and the long pulses (t_p^{ON} $\geqslant$5ms), where more C_2H_6 was produced but CH_4 was later reformed, showing a strong reincrease. The H_2 density was linked to the CH_4 and C_2H_6 density, and an atom balance could show that the process reforming CH_4 is of the form $C_2H_6 + X \rightarrow ... \rightarrow CO + CH_4 + \alpha H_2$, where α is between 1 and 2. Given the evolution of the shape of the C_2H_Y, the characteristic time of the process was

	Molecular species	Ions
Pure CO_2 case (validated in A. F. Silva et al. 2020)	CO_2, CO, O2, O	CO2+, CO+, O2+, O+, O-
Simplified CO_2-CH_4	CH_4, CH_3, CH_2, CH,H_2, H, OH, H_2O, HCO, CH_2O	CH_4^+, CH_5^+, CH_3^+, CH_2^+, CH^+, H_2^+, H^+, H_3^+
Extended CO_2-CH_4	C_2H_6, C_2H_5, C_2H_4, C_2H_3, C_2H_2, C_2H, CH_3O	

Table 5.3: List of species included in the model

estimated to a couple of ms. The CO_2 and CO are also affected by the pulse duration but differently, which is not understood so far.

In the following sections, an extended version of the model presented in chapter 4 glow is presented to explain these observations.

5.6 Modeling

The model is the continuation of the model previously described for the glow discharge in the chapter 4. The LoKI solver (from IST Lisbon, Tejero-del-Caz 2019) is used for solving first the Boltzmann equation in the plasma, and then for computing the evolution of the chemistry in the gas. The list of the species included in the model are given in table 5.3: the first line describes the species included in the pure CO_2 case in A. F. Silva et al. 2020, the second line the species included in the model used to describe the glow discharge (simplified CO_2-CH_4) and the third line the species added for the description of the RF discharge (extended CO_2-CH_4). The list does not include any molecule with 3 carbon atoms because the main expected one, C_3H_8 according to literature (Bie et al. 2015) was not measured. The new molecules in the extended CO_2-CH_4 scheme add about 150 neutral-neutral reactions and 30 electron neutral reactions. All reactions involving ions (ionization, ion-neutral, ion-ion) have been neglected in the chemistry, as detailed below. No additional electronic state is included. The list of the reactions included in the model are given in the appendix, along with the rate coefficients and the sources.

Simulation procedure

The method used for modeling the "building-up" experiment is different from the computation in the glow discharge: in the glow discharge, the pressure is imposed as well as the electron density for one condition. LoKI self-consistently computed an evolution of the mixture at the imposed pressure and a reduced electric field, which was done through 3 cycles, as described in 4. The first cycle ensure that the pressures remains constant in the stationary state. The second cycle ensures that the plasma is quasi-neutral. Finally, the third cycle ensures that the gas composition is consistent with the initial mixture. The numerical procedure is different for the "building-up". All the pulses are successively simulated. For the first pulse, the initial mixture and pressure are used. For all following pulses, an initial pressure and composition, a gas temperature, a reduced electric field and an electron density are imposed. The cycles are deactivated so that LoKI only computes the new chemistry and the densities evolution during the pulse (the self-consistent reduced electric field is not computed anymore). The output from LoKI (meaning the composition at the end of the pulse and the new density) are used as input for a post-discharge run, where the reduced electric field and electron density are set to 0. For the post-discharge, the gas temperature is set back to 300K (it was seen previously in that the cooling of the gas takes only 2 to 3ms, which is often less than the t_p^{OFF}). The pressure is derived from the densities at each step and the density continuity with $P = nkT$, as drawn on figure 5.21. In the "building-up" experiment, neither the reduced electric field nor the electron

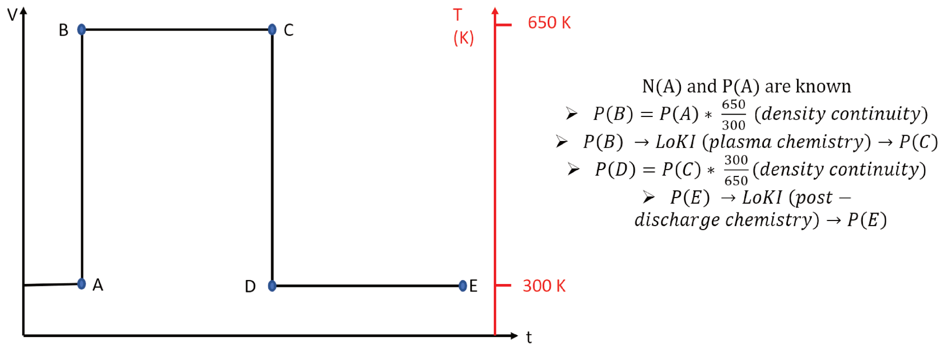

Figure 5.21: Computation of the pressure during the pulse

density are known. The electron density in the glow discharge was calculated using the current density but no such simple calculation can be performed in the RF. The electron density must therefore be guessed. The value of the glow discharge was chosen. The reduced electric field could be computed using LoKI's quasi-neutrality cycle, but this has two major drawbacks. First, there is no way to control the value obtained in the output of LoKI (unlike in the glow) and as seen in the glow, the reduced electric field is very dependant on the ion reactions included in the chemistry. Choosing manually the reduced electric field is therefore *a priori* not worse. Second, the simulation of the building-up experiment is already very long (at least 3 hours per condition) because several thousand successive simulations must be ran for a single condition. Adding 2 cycles would drastically increase the computation time. Subsequently, the reduced electric field follows a predefined temporal profile (which will be discussed more in details in section 5.7.2.2). The electron density is kept constant throughout the experiment.

For each condition, a few thousands simulation are run corresponding to the successive discharge and post-discharges. Each of these simulation has a different set of initial parameters, taken from the output of the previous one. This kind of experiment is therefore an extremely constraining test for a kinetic scheme.

Generally, the hypothesis and approximation made for the glow discharge are kept here. First, only the main species (CO$_2$, CO, CH$_4$, H$_2$) are used for the computation of the EEDF in the discharge phase, because the other species do not have a complete and consistent set of cross-section validated against the swarms, which might lead to large error on the EEDF. Because the 4 species used already account for 95% of the gas density, the error due to neglecting the other species for the computation of the EEDF is limited. In the glow discharge, the water was also taken into account but it represented up to 10% of the gas density. Here, it accounts for at most 1%, justifying its absence. Second, the wall recombination probability of atomic H is kept constant (even if it was shown in A S Morillo-Candas, Drag, et al. 2019a for O that it should change with pressure).

Vibrational excitation by electron impact was taken into account in the computation of the EEDF, like in the glow discharge. Still no vibrational excitation was taken into account for the chemistry but this is a lead of improvement for future work.

No new ion was added in the model. The main reason is there are no ways to validate the electron kinetics in these measurements. Indeed, the reduced electric field can not be easily measured and cannot be used to validate the choices made for the kinetic scheme. Thus, we have no way of controlling the relevance of adding other ions. The example of CH$_5^+$ ion illustrates this: despite being often considered as the main ion in CO$_2$-CH$_4$ plasmas, its addition to our model worsened the results in the glow discharge case because its density relies on a single creation reaction ($CH_4^+ + CH_4 \rightarrow CH_5^+ + CH_3$), whose rate usually used seems to be overestimated.

We therefore assume here that CH$_4^+$ probably remains the main ion. The C$_2$H$_Y$ ions are mostly produced through electron impact ionization of the C$_2$H$_Y$ molecule or through charge exchange between the C$_2$H$_Y$ molecule and another ion. For both these creation processes, only C$_2$H$_6$ has a density large enough. Anokhin et al. 2016 computed the ionization coefficient in a nanosecond discharge at 2Torr in pure CH_4 or pure C_2H_6 and showed that the ionization coefficient (to CH_4^+ or CH_3^+) in CH_4 is one order of magnitude higher than the ionization coefficient in C_2H_6 (to $C_2H_6^+$ or $C_2H_4^+$). It can be assumed that if the densities of C_2H_6 and CH_4 are close, the ionization will rather lead to CH_4^+ production. As for the charge exchange processes with another ion, CH_4^+ (the main ion in the glow) only has charge exchange processes with C_2H_2 and C_2H_4, which do not have a population large enough to provoke significant loss of CH_4^+ compared to the CH_4^+ creation through electron impact ionization of CH_4. In any case, the ions are not very relevant for our purpose here. Indeed in the glow discharge, they have very little impact on the plasma chemistry and are mostly used in the charge balance to compute the self-consistent reduced electric field. As for modelling the "building-up" experiments the reduced electric field is imposed and not computed through the self-consistent cycles, so the influence of the ions would be anyway limited to chemistry only and this is assumed to be very small. Another experiment would be required to study the influence of the ions, for example a glow with a residence time long enough to have formation of C_2H_6.

Simulation strategy

The simulations are very long, which is a limiting factor to explore multiple parameters. The LoKI solver takes approximately 10s to run a simulation for one pulse on an I7 2.1GHz core computer, whether for the discharge or the post discharge. In the most favorable case, the 500*1*50-10 pulse configuration (500 trains of 1 pulse), 500 pulses are sent during the 25s of experiment (followed by 500 post-discharges), meaning that at least 1000 simulations must be ran. Because the output of a simulation are the input of the following one, this can not be done with parallel computing, meaning that the simulation takes between 3h (for the most favorable case) and theoretically 300h (in the worst case, but never tested). The reference pulse configuration (500*10*5-10, 500 trains of 10 pulses) used for example in the mixture variation takes about 25h for a 25s of plasma ON time, meaning that this cannot be ran as a routine test. An efficient simulation strategy must be chosen. The shortest case (500*1*50-10) is chosen as the first test. Two measurements are available with this pulse configuration: 2Torr 50:50 CO_2:CH_4 and 5Torr 50:50 CO_2:CH_4. The latter exhibits C_2H_6, C_2H_4 and C_2H_4 formation and a CH_4 reincrease (which is not seen in the 2Torr case) and therefore seem to be a more interesting test case. The 5Torr 50:50 CO_2:CH_4 500*1*50-10 therefore serves as a test case on which the kinetic scheme and its variations are tested on this case. Once a satisfying scheme has been defined for this test, it is run on the other cases.

5.7 Step by step improvement of the model

5.7.1 Initial results

These first results are obtained using the model presented for the glow extended with the chemistry set detailed in annexe 7. Like for the precedent set, the rates are taken from the NIST chemical kinetic database. The simulation results are presented here for a 5Torr case in a 50:50 initial CO_2:CH_4 mixture with the 500*10*5-10 configuration. At first, a constant reduced electric field and electron densities are imposed for all pulses of the simulation. In the initial gas mixture variation, it has been seen that the CO_2 initial decay slope is always the same, suggesting that CO_2 is dissociated only by electron impact (like in pure CO_2 plasma). It is therefore possible to impose a value of the couple (E/N, n_e) so that the initial simulated dissociation of CO_2, given by $\frac{d[CO_2]}{dt}_i = -k_e^{diss}(E/N) * n_e * [CO_2]_i \quad m^{-3}s^{-1}$, matches the experimental one. For n_e, the chosen value is extrapolated from the glow discharge electron density. In the glow at 40mA, n_e goes from 0.87e16 in pure CO_2 to 1.15 in the 60:40 CO_2:CH_4 case. The value for this simulation is therefore chosen close to the glow discharge value: n_e=1.2e16m^{-3}. This in turns impose an initial value of the reduced electric field of 29.7Td to match CO_2 dissociation. Because the LoKI solver is designed for continuous or low-frequency fields, using an RF field requires a small correction. The RF is not a problem but the value imposed in the solver must be the root mean square value of the field, in the present case 42Td. This value is half of the value measured in the glow discharge ($\sim 60Td$), which is questionable. RF discharges are expected to have a low reduced electric field (hence their efficiency for vibrational excitation), but 30Td still appears as very low. Nevertheless, this is only the initial value (i.e corresponding to a mixture containing only CO_2 and CH_4), which is not exactly comparable to the value measured in the glow where the reactants are dissociated (the variation of the reduced electric field will be discussed further). The value of the electron density chosen could also be too high, which would increase the required value of E/N.

Based on figure 5.18, the gas temperature of 650K during the discharge is chosen (value reached in the steady state of a 5ms pulse) and the gas temperature during the post discharge is 300K. Ideally, a temporal temperature profile would be used during the pulse, but for pulses of 50ms, the approximation of a step in temperature is good enough since the gas temperature reaches a steady state in a few ms. This will not be possible anymore when simulating 5ms pulses. Similarly, for the post discharge, no profile is used, which is justified by two reasons. First, in the chosen test configuration 500*1*50-10, each train is composed of only one pulse, meaning that a measurement is taken after. The post discharge time is therefore 1.5s (corresponding to the 'long OFF time', see figure 5.2), so a gas temperature temporal profile is not needed. Second, the t_p^{OFF} variation showed that very little differences existed between a t_p^{OFF} of 1ms and one of 50ms. After 1ms, the gas temperature is still not cool down, which means that the processes at play in the post-discharge are not temperature driven. The value of the temperature in the post-discharge is therefore not very important. The temperature during the pulse is kept constant for the 25s of plasma ON time of the experiment. This is a strong approximation because the thermal conductivity of the CH_4 dissociation products is much higher than the one of CO_2 (the conductivity of H_2 is about 10 times higher than the one of CO_2). The large change of the gas composition during the experiment should favor the loss of heat to the wall and reduce the temperature reached during the pulse at the end of the experiment. We currently have no way of determining the temperature during the experiment (which would help the accuracy of the simulations) but solutions could be set-up. For example, a spectrometer triggered at each pulse could sweep over the CO Angstrom band if the pulse are long enough (which is the case in the 50ms case). For now, a temperature of 650K for all pulses is considered.

The results are presented on the figure 5.22. The experimental densities are plotted in plain lines and the simulation results are plotted in plain lines with '+' markers (only one marker every 10 points is plotted for readability). All the detected species are compared with their simulated counterpart.

These primarily results show large discrepancies with measured densities for all the species. The simulated CO_2, overestimated in the simulation, diverges quite quickly from the experimental one after the first second. On the contrary, the CH_4 density is destroyed too fast in the first seconds of the simulation but quickly stabilizes after 5s of plasma ON time. After 5 seconds, the CH_4 density is stable (decreasing very slightly). A first observation can be obtained from the evolution of these two reactants: while both of them should *a priori* mostly be destroyed by electron impact at the very beginning (T^{ON}«0.5s), CH_4 is largely over dissociated while CO_2 is largely under-dissociated. No value of the reduced electric field and/or electron density could then match both of these species simultaneously. The sole modification of the used electric field will not be sufficient to improve results. Fast chemical reactions are hence probably missing from the kinetic scheme to explain these initial slopes.

Contrarily to the experiment, the CH_4 does not reincrease. The CO density is largely underestimated, which is partly due to the under-dissociation of CO_2, but not only. Indeed, during the first half second of plasma ON time (up until the first '+' marker of the simulated CO_2), the CO_2 dissociation is correct but the CO is already underestimated by a factor 2. It was seen in the gas mixture variation (figure 5.8) that in the 50:50 CO_2:CH_4 case, CO is rapidly produced from both CO_2 and CH_4. The simulated CH_4 being destroyed more than in the experiment, the simulated CO would be expected to be overestimated but it is not the case. It seems therefore that processes which rapidly produce CO from CH_4 are missing in the kinetic scheme. The H_2

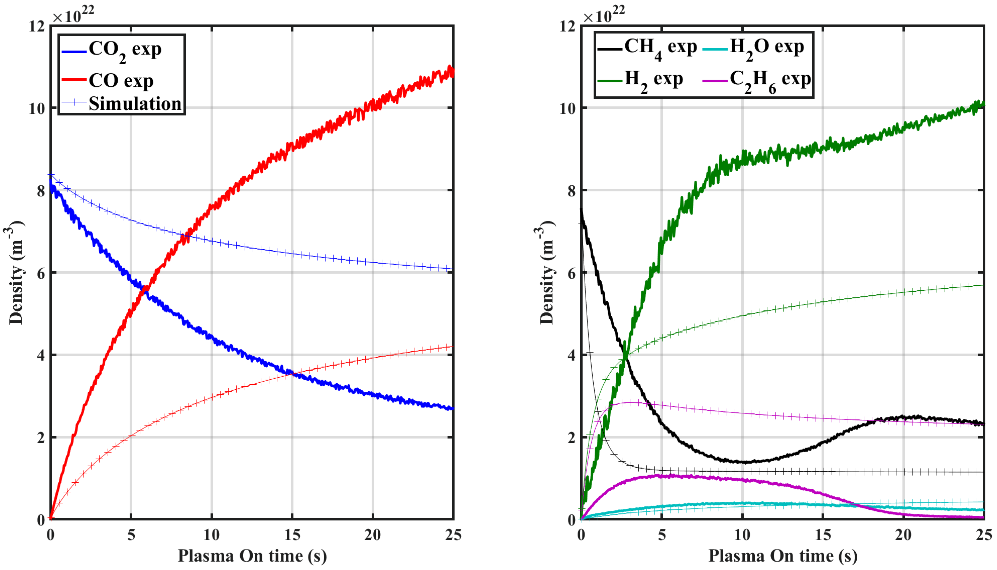

Figure 5.22: Comparison of the simulated and experimental densities of CO_2 and CO (on the left) and CH_4, C_2H_6, H_2 and H_2O (on the right) as a function of the plasma ON time. The initial mixture is a 50:50 CO_2:CH_4 at 5Torr, with a pulse configuration 500*1*50-10. These results are obtained at constant reduced electric field and using the scheme given in the annex 7

density increases rapidly at the beginning of the simulation but sees a change of slope after 2.5s. After 2.5s the density keeps increasing slowly. The C_2H_6 density increases very quickly at the beginning of the pulse until 2.5s and reaches a level much higher than the experimental C_2H_6. After 2.5s, the C_2H_6 decreased very slowly until the end of the 25s. Finally the simulated water density is quite close to the experimental one, though overestimated by the end of the 25s of plasma ON. Overall, the results are not good: some trends are reproduced (for example the C_2H_6 going through a maximum), but all of the species are very far from their experimental counterpart, meaning that the model must be improved to provide a better description of the plasma chemistry. The problem can be separated in 2 parts: the first 5 seconds, during which the CO_2 is destroyed mainly by electron impact dissociation (as seen on figure 5.7) and the rest.

5.7.2 The first 5 seconds

The first 5 seconds of plasma ON time of the experiment are very interesting because they bring 2 strong constraints: first, it was seen on figure 5.8 that during the first 2s, CO was produced quickly from both CO_2 and CH_4, indicating that some form of oxidation of CH_4 or one of its quickly produced by-products is missing from our scheme. Second, the experimental conclusion that CO_2 is almost only destroyed by electron impact dissociation over the first 5seconds can also be used.

5.7.2.1 CO production

The previous simulation shows several problem: first, no CO is produced from CH_4, and second, CO_2 density is not controlled only by electron impact dissociation. Two back-reaction mechanisms recreate CO_2 in the simulation, explaining the drift from the experiment. The mechanisms are :

$$CH_3O + CO \rightarrow CH_3 + CO_2 \tag{5.12}$$

$$CO + OH \rightarrow CO_2 + H \tag{5.13}$$

Reaction 5.13 was identified in the glow discharge as one of the main back-reaction mechanisms to reproduce CO. The CH_3O is created in three steps. First, the reactants are dissociated simultaneously by electron impact:

$$e + CH_4 \rightarrow e + CH_3 + H \tag{5.14}$$

$$e + CO_2 \rightarrow e + CO + O(1D)$$

followed by two step. First, process 5.9

$$CH_4 + O(1D) \rightarrow CH_3 + OH$$

Then:

$$CH_3 + OH \rightarrow CH_3O + H \tag{5.15}$$

Third, too much C_2H_6 is produced. The C_2H_6 is produced through electron impact dissociation (R5.14) and by process 5.11:

$$CH_3 + CH_3 \rightarrow C_2H_6 \quad (5.11)$$

These 3 problems have a common source: the CH_3 is forming C_2H_6 or forms back CO_2 (via reactions 5.15 and 5.12) instead of being oxidized to form CO. With the rates available in literature, no process is strong and fast enough to oxidize CH_3. The reaction of CH_3 + O(3P) is taken into account but leads to only a few percent of the losses of CH_3. In the glow discharge, the reaction of CH_3 with O(1D) turned out to be essential to achieve good agreement between the experiment and the simulation. This process was not taken into account in the results presented on figure 5.22. The process was:

$$CH_3 + O(1D) \rightarrow CO + H_2 + H,\, k_{5.16} = 2.8 * 10^{-14} m^{-3}/s \tag{5.16}$$

In the building-up experiment like in the glow discharge, reaction 5.16 seems to be necessary to match experiment and simulation. The value of the rate coefficient of this process is however unknown. The rate coefficient of the reaction CH_3+O(3P) is k=2.8*$10^{-16} m^{-3}/s$ (taken from W. Tsang et al. 1986), and a rate 100 time higher was chosen for the O(1D) reaction based on the usual increase when using O(1D) instead of O(3P) for other reactions on hydrogenated species measured in literature (see table 4.4 in the previous chapter, section 4.5.2). For the building-up modeling, several simulations are run with different values of the rate coefficient between $k_{5.16}$=1.$10^{-14} m^3 s^{-1}$ (close to the value chosen in the glow) and $k_{5.16}$=1.$10^{-10} m^3 s^{-1}$ which is an extreme value taken just as a test to see the effect of the process (5.16). The results are plotted on figure 5.23. The CH_4, H_2 and C_2H_6 density are greatly improved by the addition of this process. The CH_4 density underestimated in the initial results increases when (5.16) is added. For $k_{5.16}$=$10^{-14} m^3 s^{-1}$, the initial CH_4 is very close to the experiment. The more $k_{5.16}$ is increased, the more the simulated CH_4 density drifts away from the experimental one. An improvement can also be seen for C_2H_6: the higher the value of k, the more the simulated C_2H_6 decreases. While it is initially overestimated, the C_2H_6 density starts being underestimated for $k_{5.16}$ $\geqslant$1e-11$m^3 s^{-1}$.

The effect is not straight forward for CO_2, CO and H_2. For CO_2, the case without process (5.16) is better than when $k_{5.16}$=$10^{-14} m^3 s^{-1}$ or $k_{5.16}$=$10^{-13} m^3 s^{-1}$. When $k_{5.16}$=$10^{-12} m^3 s^{-1}$, the simulated CO_2 densities is the same as without the process. Finally, additional increase in $k_{5.16}$ ($k_{5.16}$=$10^{-11} m^3 s^{-1}$ or $k_{5.16}$=$10^{-10} m^3 s^{-1}$) improve the CO density (foresees more dissociation similarly to the experiment). The CO has an exactly symmetric behaviour: for low values of $k_{5.16}$, the density is largely underestimated. With $k_{5.16}$=10^{-12}, the CO and CO_2 densities are similar to the ones without process (5.16), and further increase of $k_{5.16}$ improves the CO_2 densities. This evolution of the densities with different values of the rate $k_{5.16}$ chosen result from a balances between different processes. Preventing the C_2H_6 formation (which happens at low $k_{5.16}$) considerably changes the composition of the gas mixture, impacting the rates of electron impact dissociation (for example the rates of CO_2 electron impact dissociation is lowered).

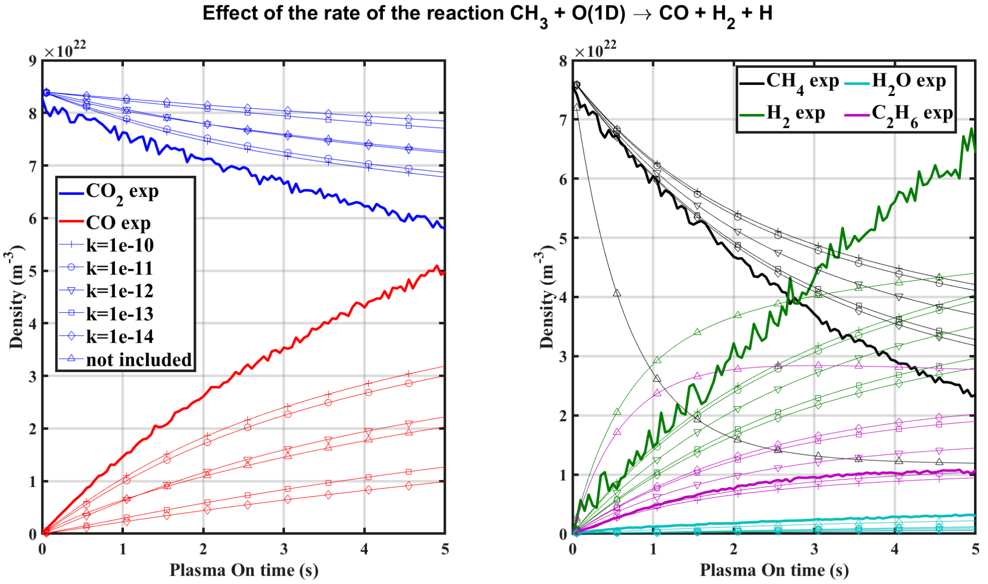

Figure 5.23: Comparison of simulated and measured densities of CO_2 and CO (on the left) and CH_4, H_2, C_2H_6 and H_2O (on the right) as a function plasma ON time in a 50:50 CO_2:CH_4 initial mixture at 5Torr, with a 500*1*50-10 configuration. The experimental values are plotted in bold lines and the simulated values are plotted with markers.

Additionally, at low $k_{5.16}$, the process (5.16) does not consume a significant part of the O(1D), which still allows the formation of OH by CH_4 oxidation, leading in turn to more back-reaction on CO. The value of $k_{5.16}$=1e-12 $m^3 s^{-1}$for process (5.16) seems appropriate because it is an intermediate value which improves all densities. This value is 2 orders of magnitude higher than proposed in the previous chapter and appears as very high, again much higher than the gas kinetic rate coefficient. It still matches the larger order of magnitude compared to the rate coefficient for the same reaction with O(3P) found in literature (it was shown in chapter 4 that the rate of a reaction involving O(1D) could be 10 000 tims higher than the rate of the same reaction involving O(3P)). The rate could also be increased by the vibrational excitation of CH_3 which is neglected here. In Kozák et al. 2014,the increase of the rates due to vibrational energy is calculated with::

$$k(E_v, T) = A_0 exp(-\frac{E_A - \alpha EV}{T}) \tag{5.17}$$

where E_A is the activation energy of the reaction, E_v the vibrational energy and α a parameter determining the efficiency of the vibrational energy subtraction. α is calculated with the Friedman-Macheret model (Adamovich et al. 1996). A high vibrational energy, favoured by the low reduced electric field of the RF discharge, could increase $k_{5.16}$. It can also be noted that according to Schlütter et al. 1993, the reaction of CH_4 with O(1D) can produce vibrationally excited CH_3, which could contribute to the high rate of CH_3 + O(1D). Nevertheless, the very high value of the rate coefficient used here points toward the same conclusion as the one of the previous chapter: though the reaction between O(1D) and CH_3 certainly happens, the process included here seems to be an effective process hiding other processes which could explain such a high rate.

An important observation that must be done is that independently of the value of the rate, the simulated CO_2 and CH_4 densities diverge more and more from the experimental value as plasma ON time goes on. At high $k_{5.16}$ values (10^{-12}) and higher), the back-reactions are very limited and the CO_2 dissociation is controlled by electron impact, which means that the insufficient dissociation is not due to chemistry anymore but rather to insufficient electron impact. The reduced electric field must increase with the plasma ON time to allow sufficient CO_2 dissociation, which will also improve the CH_4 simulated density.

- Over the first 5s of T^{ON}, electron impact dissociation alone is not sufficient to explain both CO_2 and CH_4 decay, whatever values of n_e and E/N are chosen
- CH_3 seem to be the key specie for C_2H_6 formation but also for back reaction mechanisms leading to CO_2 reformation
- Like in the glow discharge, the process CH_3+O(1D) -> CO+H_2+H improves significantly all simulated molecule densities

5.7.2.2 Reduced electric field profile over the first 5s

During the first 5 seconds, the CO_2 dissociation is controlled by electron impact dissociation (see figure 5.7). The dissociation is given by :

$$\frac{d[CO_2]}{dt}_i = -k_e^{diss}(E/N) * n_e * [CO_2]_i$$

Using this, a couple (E/N(t),n_e(t)) can be imposed during the first 5s. The electron density cannot be inferred from the fitting of the stark broadening of the H_β line (Kunze 2009) as the stark broadening is not the dominant broadening (the Doppler broadening is dominant at our pressure). Using hairpin probe could be a good way to measure the electron density, though the measurements above 1Torr are usually unreliable (Piejak et al. 2005). For future work, the electron density in a CO_2-CH_4 plasma should be measured at 1Torr and below and extrapolated. In the present case, the electron density could not be measured and therefore it is chosen close to the value in the glow (n_e=1.2.$10^{16}$$m^{-3}$). Because the electron impact dissociation was insufficient to reproduce the CO_2 dissociation, the reduced electric field should increase. The following profile of E/N is chosen for the first 5 seconds:

$$\begin{aligned} E/N(0) &= 42.5Td \\ E/N(n+1) &= E/N(n-1) + 1/10Td \sim \text{ +1 Td/10 steps} \\ \sim E/N(t) &= E/N(0) + 2 * t \text{ Td} \end{aligned}$$

The effect of the E/N profile on the first 5 seconds is plotted on figure 5.24. 3 rates for the (5.16) reaction (k=1e-11, k=1e-12 and k=1e-13) are plotted to ensure that the chosen value in the previous paragraph still hold. Using a E/N profile greatly helps reducing the divergence on the first 5 seconds. The CO_2 still diverges for k=1e-13, but for higher values the simulated and experimental trends are similar. The same is seen for the CO on the left plot of figure 5.24, directly related to CO_2 dissociation. The hydrogenated species (CH_4, H_2 and C_2H_6) exhibit similar behaviours: the divergence is reduced by using a profile of E/N. For the 5 species presented so far, using a rate k=1e-11 for process (5.16) during the first 5 seconds yields an excellent agreement. Using k=1e-12 is not as good but still yields satisfying results.

The physical reasons of the increase of the reduced electric field are complex. In the glow discharge, for a given pressure, the electric field increases when going from pure CO_2 to 60:40 CO_2:CH_4, indicating that the change of composition drives the electric field increase. For a given pressure, the reduced electric field remains constant because when going from pure CO_2 to CO_2-CH_4, the excellent thermal conductivities of the CH_4 by-products lower the temperature, maintaining E/N approximately constant with increase of CH_4 content. In the glow discharge, the electric field also increases with pressure for a given initial mixture. The reduced electric field however remains approximately constant due to the electric field increase being compensated by the density increase. In the building-up experiment, as plasma ON time goes by the mixture strongly changes with an ever increasing fraction of H_2, which according to the glow discharge results should increase the electric field. Simultaneously, the density increases because of dissociation increasing the total number of particles in the closed reactor. The variation of

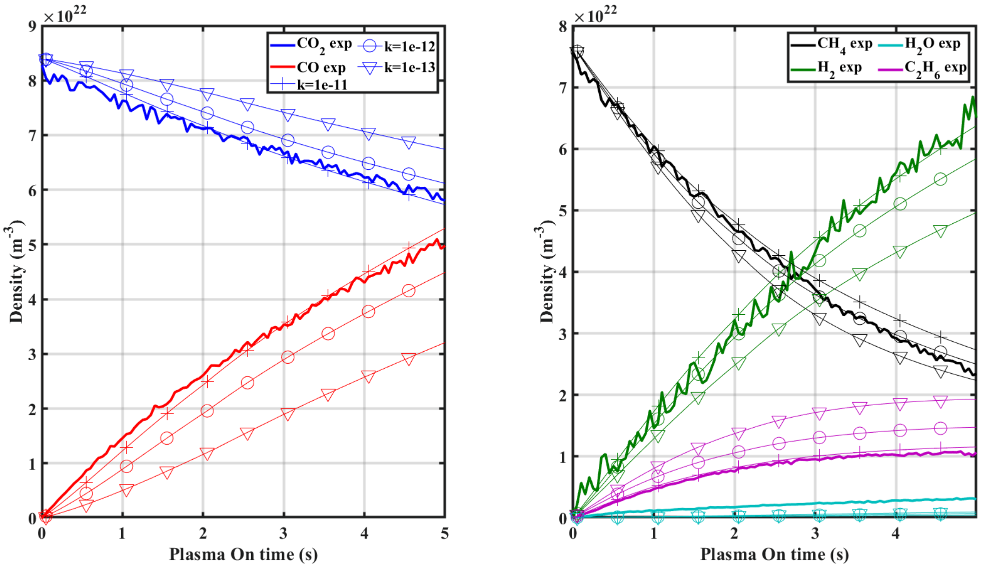

Figure 5.24: Evolution of the densities of the main species during the first 5s of plasma ON time. Several values of the rate of process (5.16) are tested. A profile of reduced electric field is used.

the reduced electric field E/N is therefore the result of a competition between two processes: on one hand, the change of composition (with growing CO and H_2 fractions) increases E and in turn E/N, while the dissociation increases N. In the case of the building-up experiment, the first could outgrow the second, leading to a rise of the E/N.
The measurement of the gas temperature in the pulses with plasma ON time could bring more information on the temporal reduced electric field. Indeed, the temperature in the pulse is expected to decrease with plasma ON time which will impact the evolution of the density in the plasma.

5.7.3 E/N profile after 5s

The increase of the reduced electric field during the first seconds is tied to the strongly increasing pressure and the change of gas composition in that period. It would therefore be relevant to take into account a temporal profile of reduced electric field for the rest of the experiment as well. Looking at figure 5.22, it can be seen that the strongest change in plasma composition goes on until 7s. After 7seconds, the plasma keeps evolving but slower than before. Finally, around 17s, the C_2H_6 density is below detection limit the CH_4 and H_2 are quite stable and only the CO_2 and CO keep evolving. Based on the results before 5s, a general shape of the reduced electric field profile can be proposed: the increase highlighted above would keep going until ∼7s. After that, the E/N would keep increasing but with a smaller slope. Finally around 17s, the E/N would stabilize. The following profile is chosen:

$$\begin{aligned} E/N(0) &= 42.5Td \\ \text{for t<7s: } E/N(n+1) &= E/N(n-1) + 1/10Td \sim \text{ +1 Td/10 steps = + 2 Td/sec} \\ \text{for 7<t<15s: } E/N(n+1) &= E/N(n-1) + 1/100Td \sim \text{+0.2 Td/sec} \\ \text{for 15<t: } E/N(n+1) &= E/N(15s) \end{aligned}$$

The shape of the E/N profile is chosen to be somewhat similar to the evolution of the densities during the plasma ON time. The reduced electric field profile is shown on figure 5.25, along with the evolution of the total density and the densities of CO and H_2, which are the main sources of the increase of E/N. The effect of the profile is shown on figure 5.26. The result presented here are the same than the ones presented on figure 5.24 but extended to 25s of plasma ON

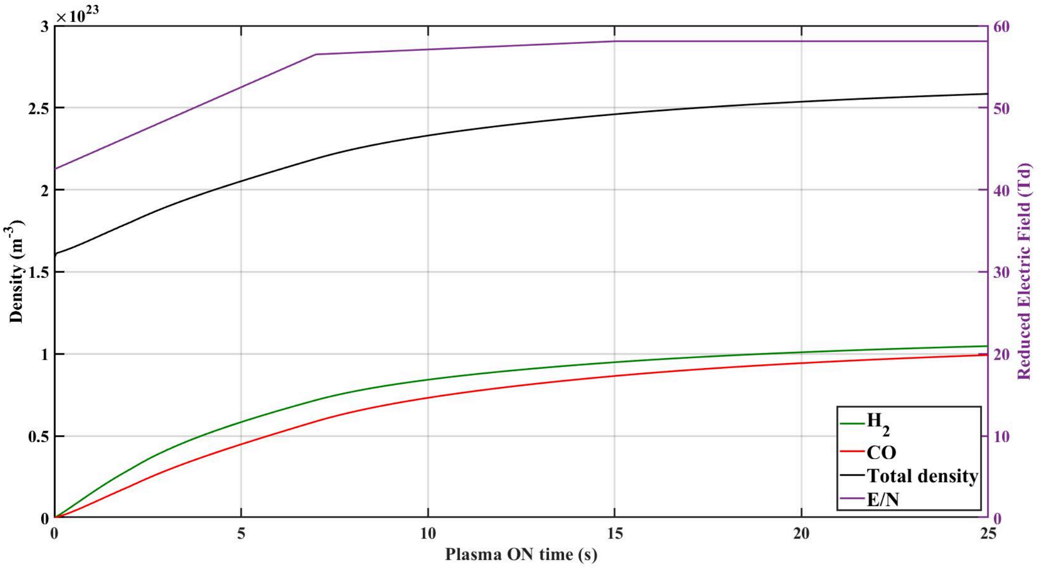

Figure 5.25: Temporal profile of the reduced electric field E/N used in the simulation (purple). The E/N profile is plotted along the gas density (black), the CO density (red) and the H_2 density (green)

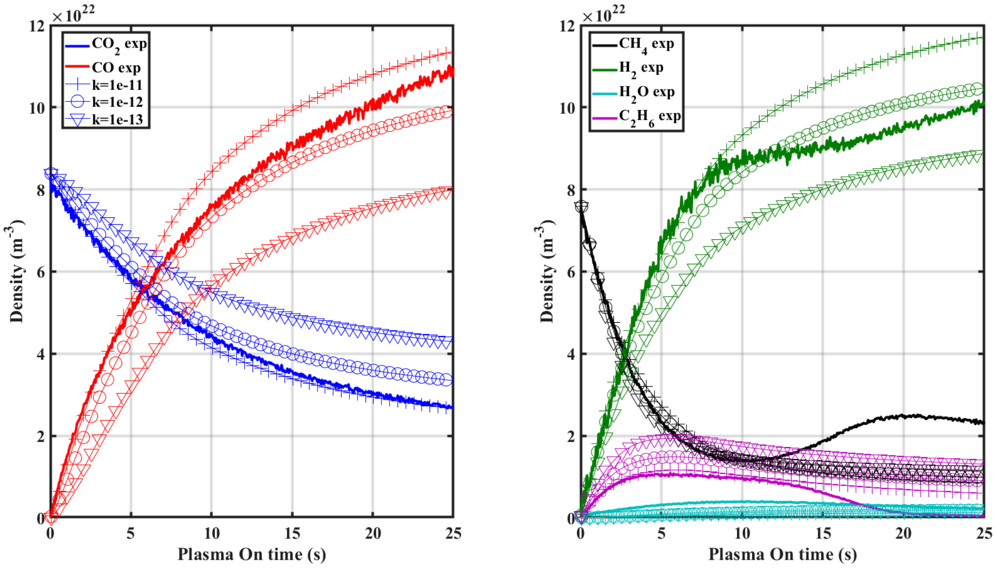

Figure 5.26: Evolution of the densities of the main species during the 25s of plasma ON time. Several values of the rate of process (5.16) are tested. A profile of reduced electric field is used.

time using the reduced electric field profile presented. The simulations are presented for several values of the rate used for process 5.16 ($CH_3 + O(1D) \rightarrow CO + H_2 + H$). It appears that using this profile of reduced electric field along with the k=1.10^{-12}m$^3s^{-1}$ for process 5.16 (with o markers) yields good results for the CO, the CO$_2$ and H$_2$. The simulated CO$_2$ density remains almost parallel to the experimental one all along the simulation, except at the end (after 20s) where a small divergence appears. This could mean that the constant electric field chosen for the last part of the profile might actually keep increasing very slowly. The CO evolution is the symmetric of the CO$_2$ one, and shows the same deviation after 20s. The final simulated density of H$_2$ is in good agreement with the experimental one for k=1.10^{-12}m$^3s^{-1}$, though the trend during the experiment are not the same: the experimental slope break at t=7s is not seen in the simulation. No rate chosen for reaction 5.16 allows to see this slope break. The CH$_4$ curves are quite close for the 3 rates tested. The simulation and the experiment are in good agreement until 10s. The CH$_4$ simulated density shows a stabilization after 10s but does not reincrease. On the contrary, the CH$_4$ keeps slowly decreasing until the end of the experiment. The 3 simulated C$_2$H$_6$ densities have the same shape, with a maximum value decreasing with increasing k. The C$_2$H$_6$ goes through a maximum at the same time during experiment and simulation but unlike the experiment, the decrease in the simulation is very slow. Several test were made on the profile of reduced electric field to check that it was not responsible for the absence of CH$_4$ reincrease. Indeed, in the final part of the simulation (15<t<25s), the electron impact processes are major for CH$_4$ and C$_2$H$_6$. CH$_4$ is mainly destroyed by reaction 5.14 ($e + CH_4 \rightarrow e + CH_3 + H$). C$_2H_6$ is destroyed through:

$$e + C_2H_6 \rightarrow e + C_2H_4 + H_2 \tag{5.18}$$

$$e + C_2H_6 \rightarrow e + C_2H_5 + H \tag{5.19}$$

C$_2$H$_6$ is formed by CH$_3$ recombination (reaction 5.11). Part of the C$_2$H$_4$ created is later transformed into CH$_3$, and the rest goes back to C$_2$H$_6$ by recombination. It could be assumed that an increase in the reduced electric field would increase the C$_2$H$_6$ dissociation without increasing the CH$_4$ dissociation and ultimately form back CH$_4$. But the dissociation cross-sections of C$_2$H$_6$ (ϵ_{th}=4.5eV) and CH$_4$ (ϵ_{th} =7.5eV) would only allow this for an EEDF with a sharp decrease between the 2 thresholds. It is not the case in our plasmas so any increase of the reduced electric field accelerates CH$_4$ dissociation. Similarly, a reduction of the electric field would have the same effect both on CH$_4$ and C$_2$H$_6$, leading to a re-increase for both. An electronic effect is therefore to exclude to explain the CH$_4$ reincrease and the C$_2$H$_6$ loss.

5.7.4 Possible explanation for the CH$_4$ reincrease

A major flaw of the model is its inability to reproduce the C$_2$H$_6$ destruction and the reincrease of CH$_4$ which happens between 10 and 15s of plasma ON time in the test case (5Torr 50:50 CO$_2$:CH$_4$ 500*1*50-10). An effect of the reduced electric field was ruled out, which only leaves a chemical effect. In the current state of the model, the pathways converting C$_2$H$_6$ to CH$_4$ start with electron impact dissociation of C$_2$H$_6$ (processes 5.18 and 5.19), followed by:

$$C_2H_5 + CH_3 \rightarrow C_2H_4 + CH_4 \tag{5.20}$$

$$C_2H_5 + CH_2 \rightarrow C_2H_4 + CH_3 \tag{5.21}$$

$$CH_3 + H_2 \rightarrow CH_4 + H \tag{5.22}$$

$$C_2H_4 + H_2 \rightarrow C_2H_5 + H \tag{5.23}$$

In other words, the only way to reform CH$_4$ is currently to destroy C$_2$H$_6$ by electron impact and to have the dissociation fragments reacting with CH$_3$ or CH$_2$ to reform CH$_4$. These pathways are visibly not sufficient to match the experimental reincrease. Several tests were done in which the rate coefficients of these pathways were boosted (which could have been the case due to vibrational excitation for instance) to check if their underestimation could not explain to the observed results but none of the tests led to a CH$_4$ reincrease. This can be explained by the fact that the reformation reactions (reactions 5.20 and 5.22) include a direct dissociation fragment of CH_4 (CH_3 or CH_2), i.e they reform CH_4 from a CH_4 dissociation fragment. Reactions 5.20 and 5.22 do not "break" a C_2H_Y molecule in two CH_X molecules. The decay of C_2H_6 simultaneous to the reincrease of CH_4 suggest a mechanism based on the C_2H_6 destruction of the type:

$$C_2H_6 + X \rightarrow CH_a + CH_b + \alpha H_c \tag{5.24}$$

Using the experimental repartition of each type of atom (figure 5.12), it was deduced that the carbon contained in the C_2H_6 did not go fully to CH_4 but also to CO. Similarly, the H atom contained in C_2H_6 are found at the end of the experiment in CH_4 and H_2. Using the atom balance presented in section 5.5.1, it can be deduced that the general pathway should be of the form:

$$C_2H_6 + X \rightarrow ... \rightarrow CH_4 + CO + H_2 \tag{5.25}$$

After the discussion on the role of O(1D) in the previous chapter, the reaction of C_2H_6 with O(1D) could be a lead. Two reaction rate coefficients for the reaction of C_2H_6 and O(1D) are available in literature and have been included in the model:

$$C_2H_6 + O(1D) \rightarrow C_2H_5 + OH \tag{5.26}$$

$$C_2H_6 + O(1D) \rightarrow CH_3O + CH_3 \tag{5.27}$$

The rate coefficients were taken from Matsumi 1993, where translationally hot O(1D) was produced by photolysis of O_3 and the products were measured by light induced fluorescence. The rate coefficients are on the order of 10^{-16}m^{-3}, much lower than the chosen rate coefficient for CH_3+O(1D). The question of the value of these rates arise. Tests with increased values of the rate coefficient (by a factor 10 and 100) were run but did not show a reincrease of the CH_4 because most of the O(1D) reacts with CH_3 rather than C_2H_6. Moreover, there are no reasons to believe that the values measured Matsumi 1993 were underestimated by a factor 100.
Using the experimental variation of t_p^{ON}, it was found that the process necessary for C_2H_6 destruction had a characteristic time of a few ms. Since it is now assumed that this process is due to chemistry (because the effect of the reduced electric field were ruled out), it can be assumed that the specie X from eq 5.25 has a characteristic formation time of a few ms. To sort out the species that could match this, a simulation of one pulse of 50ms is run using the mixture of "plasma ON time = 5s". The results are shown below on figure 5.27 Several species reach their final level on the time-scale of 3-4 ms: OH, O(1D), CH_3O, HCO and CH_4^+. The case of O(1D) was already discussed. The OH experiences the strongest variation between 0.5 and 5ms but its reaction with C_2H_6 is already included in the model:

$$C_2H_6 + OH \rightarrow C_2H_5 + H_2O \tag{5.28}$$

The rate coefficient were taken from Baulch et al. 1992 (see annexe 7). Numerous rate coefficients for reaction 5.28 are available on the NIST Kinetic database and are all in the same range ($k_{5.28}$ $\sim$ 10^{-18}-10^{-19}) for the studied range of temperature. This reaction included in the model is therefore not the cause of the CH_4 reincrease in the 500*1*50-10 configuration. The CH_3O is an unlikely candidate because first no rates were found for $C_2H_6 + CH_3O$; second it only experiences a small variation between 0.5 and 5ms and third, its density during the pulse is extremely weak (a few 10^{14}m^{-3} according to the model). The reaction of HCO with C_2H_6 is also included in the model $HCO + C_2H_6 \rightarrow CH_2O + C_2H_5$ and does not show any effect on the CH_4 reincrease. The atomic H could be a good candidate. The reaction

$$C_2H_6 + H \rightarrow CH_3 + CH_4 \tag{5.29}$$

is included in the model but has a very weak rate ($k_{5.29}$ $\sim$ 10^{-20}m^{3}molecule^{-1}s^{-1}) from R. A. Back 1983). This reaction would be however exactly the kind of mechanism expected, because the CH_3 could later react with O(1D) to form CO, H_2 and H, satisfying the experimental constraint $C_2H_6 + X \rightarrow ... \rightarrow CO + CH_4 + H_2$. Finally, CH_4^+ shows a 30% variation between

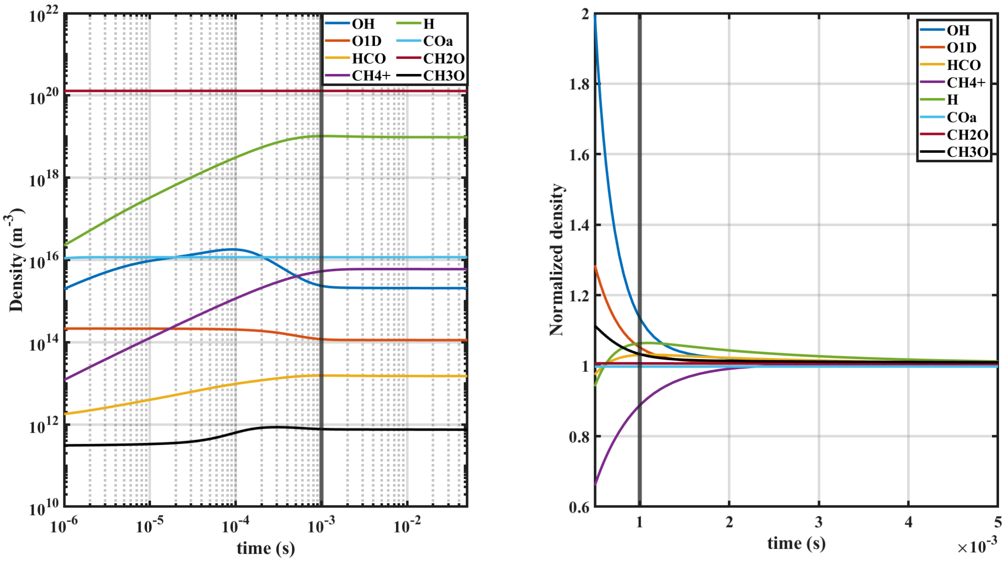

Figure 5.27: Evolution of the densities of minor species during a pulse of 50ms. The evolution during the whole pulse is plotted on the left. On the right, the densities are normalized by their value at the end of the pulse. In both case, a vertical line was plotted at t=1ms

0.5 and 5ms, but no reaction rate for $CH_4^+ + C_2H_6$ was found in literature. Out of all the minor species shown here, the atomic H seems to be the best candidate, but the rate reported in literature is too low. H atoms are lost for almost 1/3rd by wall recombination in this model. It is therefore possible that H atoms are adsorbed at the walls in our conditions. Surface mechanisms could maybe play a role in the CH_4 reincrease by enhancing the reaction 5.29.

5.7.5 Possible role of the surface production of CH_4

In pure CO_2, the surfaces were found to influence the dissociation fraction of CO_2 for long plasma ON time ($T^{ON} \geqslant 10$s, A.-S. Morillo-Candas 2019) due to adsorption of CO or CO_2 on the surfaces. So far, the surface processes have mostly been neglected, except for wall recombination of atomic O and H. The recombination of atomic species at the wall is calculated by combining the diffusion of H atoms in the reactor (using the diffusion coefficient calculated according to Hirschfelder et al. 1964) and the recombination probability of atomic H, as descirbed in chapter 4. It is however very likely that some atomic H are adsorbed on the wall of the reactor during the plasma. The atomic H could react with species at the wall and form back gas species following an Eiley-Rideal process. A complex model of the plasma-surface interaction would be required to properly describe the surface processes. The goal of this work is not to develop and include such model but rather to show with simplistic reactions the possible influence of the surfaces in this problem. Two reactions are added to the model :

$$H(1s) + Wall \rightarrow H(ads) \tag{5.30}$$

$$C_2H_6 + H(ads) \rightarrow CH_3 + CH_4 \tag{5.31}$$

Because of the way these reactions are added to the simulation, the density of H(ads) can only decrease by being consumed in the ER process 5.31. The first reaction de facto represents the probability of an H atom to be adsorbed and further involved in an ER process with C_2H_6. The second reaction 5.31 describes the ER process . it is based on the gas phase reaction 5.29. Reaction 5.31 is not described in the CH_4- H_2 plasma literature and are therefore unlikely to be found as such in the plasma. Nevertheless, the surfaces could be important: in Xinyi Li et al. 2021, the influence of the plasma treatment of a catalyst is put forward for C_2H_6 dehydrogenation by CO_2. It is shown that upon exposure to a glow discharge, oxygen is deposited

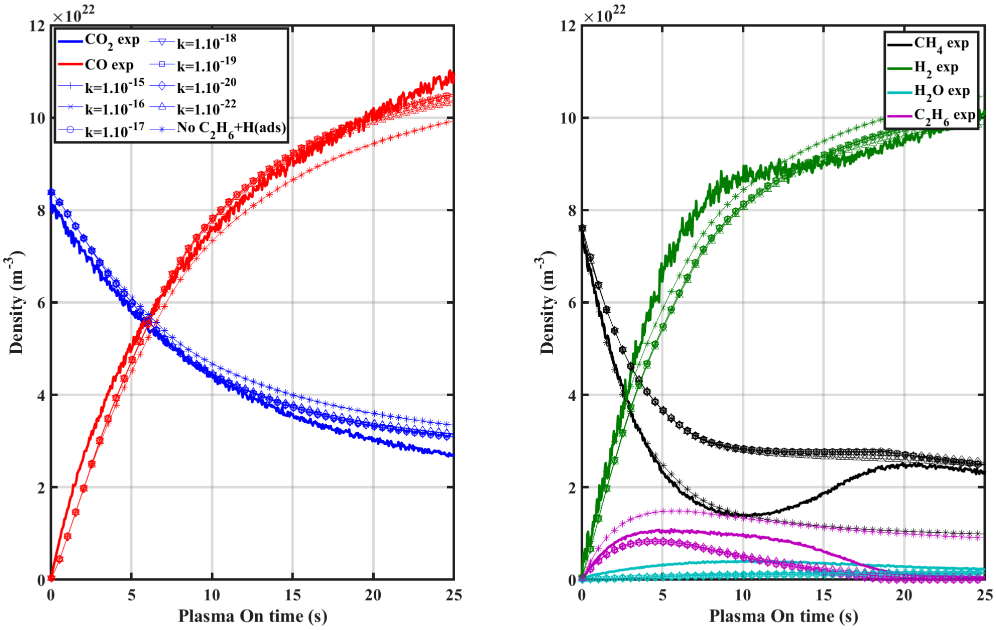

Figure 5.28: Comparison of the measured and simulated densities of the main species (CO_2, CO, CH_4, H_2, C_2H_6 and H_2O with addition of the surface processes. The rate of process (5.31) is varied. The mixture is a 50:50 CO_2:CH_4 at 5Torr

on the surface of a catalyst. When used for thermal catalysis, one of the C-H bond of C_2H_6 on the surface is weakened by the catalyst. The weakly attached H could later react with oxygen to form OH and dehydrogenate C_2H_6. This hypothesis is supported by Gómez-Ramírez et al. 2014. The mechanism described in Gómez-Ramírez et al. 2014 and Xinyi Li et al. 2021 relies on the presence of a catalyst and is not applicable in our situation but shows the role surfaces could play. The question of the rate of the surface processes arise, to which there is no simple answer.

The rate of the reaction 5.30 should correspond to the adsorption probability of H atoms multiplied by the ratio of the probability for the adsorbed H to react with C_2H_6 and the probability for the adsorbed H to react with any other molecule, i.e the ratio $\frac{H(suface)+C_2H_6}{H(surface)+X}$, X being here any other molecule than C_2H_6. This ratio is complicated to determine and would probably require an accurate calculation of H atoms diffusion to the wall since their loss are fast. This rate also depends on the probability of recombination of H into H_2 at the wall γ_H, which has not been measured but only estimated with the model in the glow discharge. The rate coefficient of reaction 5.31 will likely depend on the properties at the surface (type of adsorption site whether they are physisorbed or chemisorbed, surface atom mobility, number of adsorption sites, wall temperature...). The rate coefficient of 5.31 could also depend on the gas temperature. Because of this, keeping a constant rate all along the simulation is probably not physically correct because the pressure and the temperature vary during during the experiment but as all these parameters remain unknown, a constant rate is used. The goal of the addition of reactions 5.30 and 5.31 is only to show the possible influence of surfaces processes.

For reaction 5.30, the probability of adsorption on the surface is arbitrarily chosen equal to the probability of recombination into H_2 by reaction with an adsorbed H. This means that an atomic H in the plasma has as much chances of recombining into H_2 when reaching the wall as of being just adsorbed on the wall. The wall recombination probability, whose influence was studied in the previous chapter, was $\gamma_H = 0.01$ in the glow discharge. The same probability is kept for the RF discharge. For process (5.31), several rates are tested.

The results are plotted on figure 5.28 The addition of processes 5.30 and 5.31 has a very minor effect on CO_2 and CO (on the left plot of figure 5.28), independently of the rate chosen. The ef-

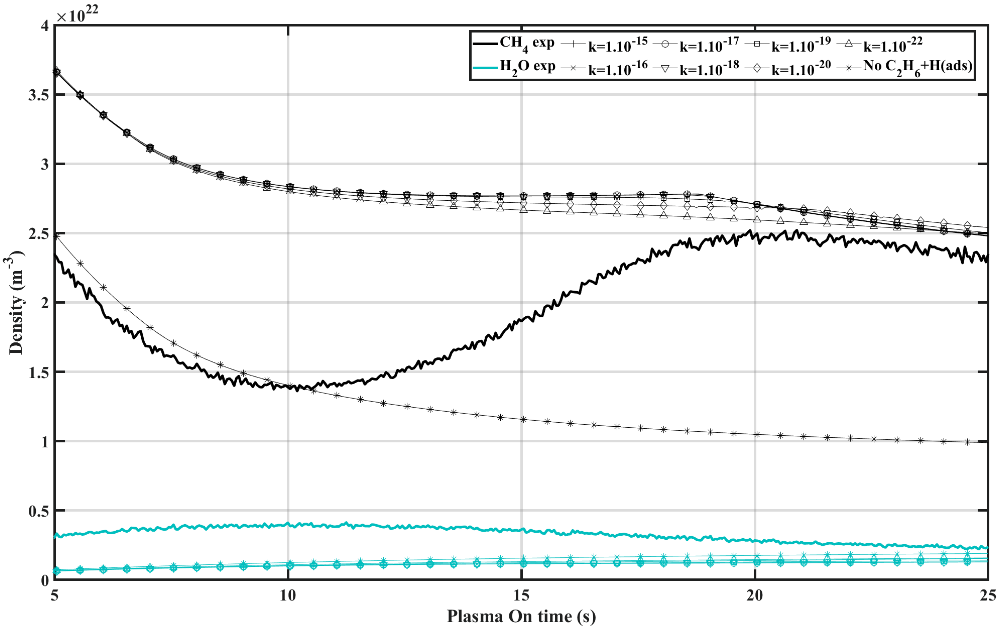

Figure 5.29: Comparison of simulation and experiment. This figure is a zoom of figure 5.28

fect seems to be beneficial for these two species, whose simulated densities seem to be in slightly better agreement with the experiment. However, the final trend of the CO density (between 20 and 25s of plasma ON Time) seems closer to the experimental slope when the two processes are not added (curve with * markers on figure 5.28). A similar phenomenon can be observed for H_2 density, whose final value with the surfaces processes coincides with the experimental values, but whose slope at 25s plasma ON time would likely lead to a worse agreement for longer simulation time. The CH_4 densities are strongly influenced by the added processes 5.30 and 5.31. Due to the CH_4 reformation, the CH_4 simulated density, previously in very good agreement with the experimental density during the first 10 seconds (curve plotted with '*' markers), are now overestimated. After 12s, if $k_{C_2H_6+H(ads)} > 1.10^{-19} cm^{-3}.s^{-1}$, a reincrease of the CH_4 density is observed until 19s, (as seen on figure 5.29, a zoom of figure 5.28) before going back down until the end of the simulation. This is linked with the C_2H_6 density. The evolution of the simulated C_2H_6 between 0 and 5s is very close to the measured one, independently of the rate for 5.31. After 5s, the simulated C_2H_6 density goes down while the experimental one is stable until 10s and goes down only after 10s. Once it reaches a density as low as 0.05 10^{22}m^{-3} (around 18-20s of plasma ON time), the CH_4 starts decreasing again. The decrease of the C_2H_6 density also probably explains the mismatching final slopes of CO_2, CO and H_2. Indeed, once all the C_2H_6 is consumed, the present model keeps adsorbing atomic H while no more reactions desorb it. The H content of the plasma is artificially lowered in the simulation, explaining the changing final slope of the H_2. The H_2 influences in turn the CO_2 and CO through a chemical balance.
The comparison of the H_2O, the C_2H_4 and the C_2H_2 is plotted on figure 5.30. No values of the rate allow a good description of the water density. However, it is very likely that surface processes are involved in the formation of water as well. A complete surface model would be needed to properly describe water formation. In the present case, the simulated values at the beginning of the experiment are an order of magnitude too low. By the end of the simulation, the simulated density is close to the experimental one, but did not go through the bump seen in the experiment. A large mismatch is found for both C_2H_4 and C_2H_2. The order $[C_2H_4] > [C_2H_2]$ is not found in the simulation. The shape of the simulated C_2H_2 somewhat reproduces the experimental shape but the simulated density is 3 orders of magnitude too low. The mismatch is worse for C_2H_4: not only is the simulated density 5 to 6 orders of magnitude too low, but the shape of the temporal density of C_2H_4 is not reproduced. This is probably due the rate of the

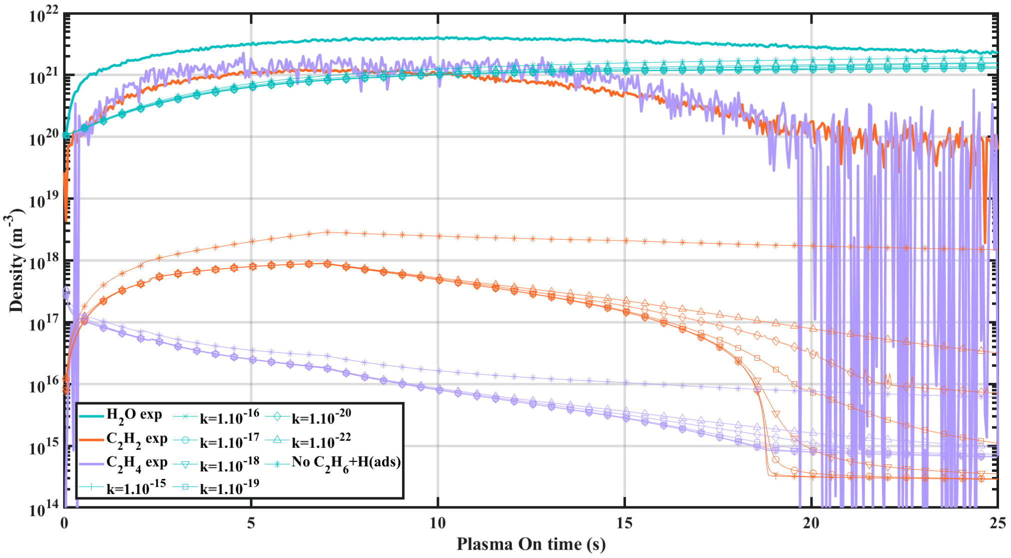

Figure 5.30: Comparison of measured and simulated densities of H_2O, C_2H_2 and C_2H_4 and with plasma ON time for several rate of process (5.31). The condition is 5Torr, 50:50CO_2:CH_4, 500*1*50-10

main loss channel of C_2H_4: $C_2H_4 + H_2 \rightarrow C_2H_5 + H$, which could be too high.

The two simplistic reactions (5.30 and 5.31) added to the model show the potential influence of the surface reactions, which can explain the CH_4 reincrease. Once again, these surface reactions are not made to be permanently included in the model but rather to provide a lead on the potential cause of the observed behaviours. It must also be noted that numerous other hypothesis were tested. The rate coefficient of the reactions susceptible to fit the type of reaction 5.24 (i.e $C_2H_6 + X \rightarrow CH_\alpha + CH_\beta X$) (like reaction 5.29 or reaction 5.27) were tested by being increased by a factor up to 100 to detect potential errors on the rate. Processes including CO($a^3\Pi$) with hydrogenated species, whose rate coefficients are not described in literature, were tested (with rate coefficients deduced similarly as the one for $CH_3 + O(1D)$ in the chapter 4). Variation of the reduced electric field profile were tested with E/N increasing or decreasing with different speed but none of these tests could reproduce the CH_4 increase. The addition of the surface processes 5.30 and 5.31 was the only case where a reincrease of the CH_4 was observed, even if it was very weak.

The reactions 5.30 and 5.31 are also tested at 2 Torr, where the influence of the surface should be higher than at 5Torr. The value of γ_H should decrease with pressure because of lower H atom flux and the lower temperature if we do not assume that the recombination is limited by diffusion to the wall. However the results from the glow discharge showed that a constant γ_H over the whole pressure range yielded good results. The adsorption (process 5.30) could also change with pressure and temperature. Hence, the influence of 3 rates must be checked. Because of the duration of a simulation, the simulation capacity is limited and only a few tests were made. They are presented on figure 5.31. The first case, plotted with 'o' markers, uses a wall recombination probability of H into H_2 of 5.10^{-3}, half of the value at 5 Torr. The adsorption probability is also chosen equal to γ_H, and the rate for the C_2H_6 dissociation is chosen $k_{5.31} = 10^{-17} m^3 s^{-1}$, in agreement with the 5Torr results.

$$\gamma_H = 5.10^{-3} \quad k_{H(ads)} = 5.10^{-3} \quad k_{C_2H_6+H(ads)} = 10^{-17} m^3 s^{-1}$$

A good agreement is found between experiment and simulation for CO and CO_2. However, the four hydrogenated specie show a very poor agreement. The C_2H_6 bump is almost non-existant and water is largely underestimated. The simulated CH_4 trend does not reproduce

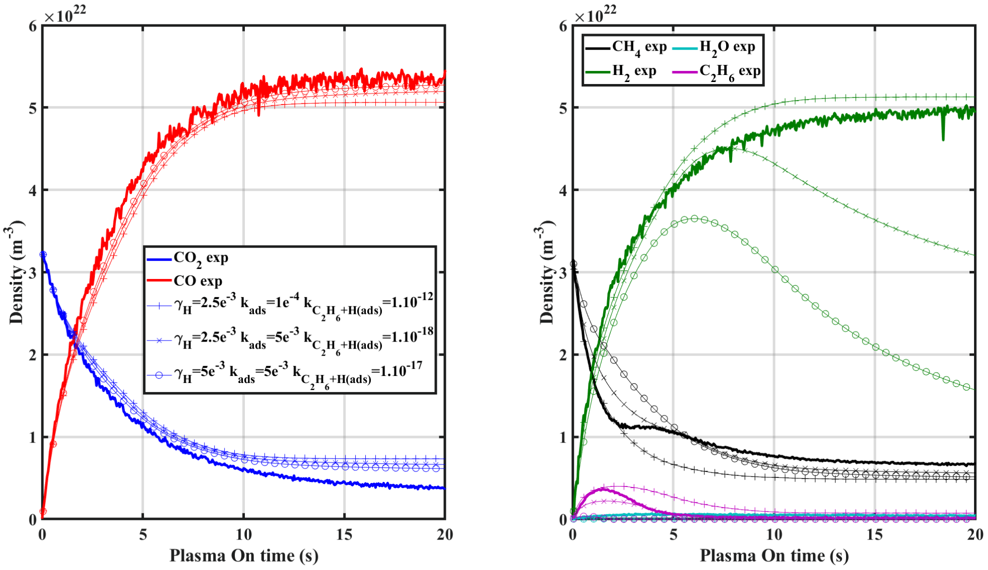

Figure 5.31: Comparison of the simulated and experimental densities in a 50:50 CO_2:CH_4 mixture at 2Torr for several combination of the added surface processes

the plateau at 3s of plasma ON time. Finally, the H_2 density initially increases but starts decreasing after 5s of plasma ON time, which is due to the strong adsorption and the lack of desorption reaction. Similar results are obtained when dividing the wall recombination γ_H and the adsorption probabilities by a factor 2 ($\gamma_H = 2.5.10^{-3}$). Two other cases are presented. In the first one, plotted with x markers, the wall recombination is kept $\gamma_H = 2.5.10^{-3}$, but the adsorption probability is now lower. The rate of process (5.31) is also lowered to allow for the building up of the C_2H_6 density.

$$\gamma_H = 2.5.10^{-3} \quad k_{H(ads)} = 5.10^{-4} \quad k_{C_2H_6+H(ads)} = 10^{-18} m^3 s^{-1}$$

The CO and CO_2 are mostly unaffected by the rate coefficients, but the influence on the hydrogenated species is strong. The C_2H_6 density now reproduces the experimental bump but only reaches a maximum value twice as low the experimental value. The CH_4 now goes through a sudden change of slope coinciding with the C_2H_6 destruction. This change of slope is not reproducing the plateau in CH_4 density but is the closest we can get. Finally, the H_2 density is correctly reproduced over the 7 first seconds but eventually goes down, similarly to what was observed in the previous case due to the absence of process balancing the H adsorption (process (5.30)). In the last case, plotted with + markers, the adsorption probability was lowered but the rate of (5.31) was increased.

$$\gamma_H = 2.5.10^{-3} \quad k_{H(ads)} = 1.10^{-4} \quad k_{C_2H_6+H(ads)} = 10^{-12}$$

Once again, the effect on CO_2 and CO is minor. The simulated H_2 density is similar to the experimental values though the inflexion is stronger in the experiment than in the simulation. The simulated C_2H_6 density initially increases before starting to decrease, but the decrease is slower than the experimental decrease. The value of the maximum densities are in good agreement. Finally, the CH_4 does not go through the plateau value nor through a slope break: the CH_4 follows an exponential trend all along the simulation. In all three cases, the H_2O density (not shown here) is underestimated by a factor 10 ($H_{simMax} \sim 0.5 * 10^{20} < H_{expMax} \sim 6 * 10^{20}$). It is probable that water formation at the wall also exists in our plasma but that we fail to take it into account properly in this situation. Despite being unable to reproduce correctly the trends of the main species, these 3 cases give a good picture of how the surfaces could influence the gas densities and how a correct modeling of the plasma surface interaction could help simulating the evolution of the densities with plasma ON time.

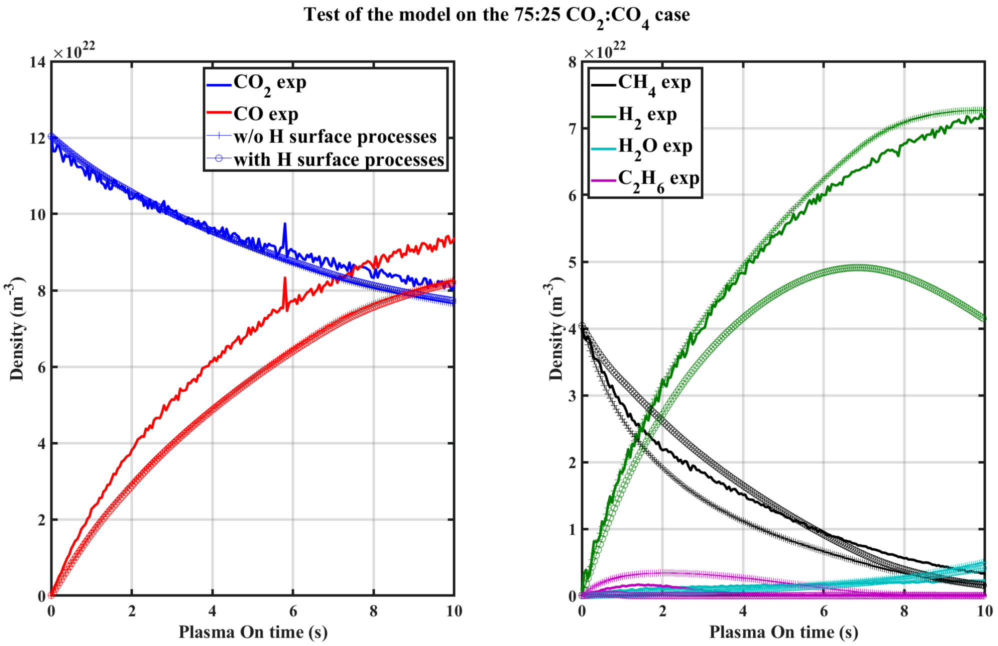

Figure 5.32: Comparison of the simulated and measured densities of the main species in the 75:25 CO_2:CH_4 mixture at 5Torr. The simulation with '+' markers includes processes 5.31 and 5.30, the simulation with 'o' markers does not.

5.7.6 Beyond the test case

After trying the model with a test case, two other cases should be tested: 75:25 CO_2:CH_4 mixture at 5Torr, with a 500*10*5-10 configuration (to see the impact of the mixture variation) and a 50:50 CO_2:CH_4 mixture at 5Torr in a 500*100*1-10 (to see if the effect of the t_p^{ON} is reproduced by the model). However, the simulation of both theses cases are extremely time-consuming (about 30h for the first case and 150h for the second case), and the second case could not be run. Because of the limitation of the desktop computer used, the model was only run for the first 10s of plasma ON time of the 75:25 CO_2:CH_4 500*10*5-10 case. The long simulation time did not allow for adjustment of the reduced electric field profile as it has been done for the test case. The same E/N profile as described in section 5.7.2.2 is therefore used. The comparison between experiment and simulation is shown on figure 5.32. Two cases are presented: the one with '+' markers includes processes 5.31 and 5.30, the one with 'o' markers does not include them. The surface processes have limited impact on the CO_2 and CO and the curves are very close in both cases. The simulated CO_2 dissociation appears to be slightly stronger than experimentally observed, which could be due to the reduced electric field imposed, whose evolution would be too fast. The CH_4, presented on the second panel of figure 5.32, decreases in both case with a relatively good agreement with experiment. The shape of the curve when excluding the H surface processes shows a similar trend with the experiment. The imposed reduced electric field could be here also the source of the over-dissociation of the CH_4 when the surface processes are excluded. When they are included, the higher CH_4 is due to process 5.31 reforming CH_4. The H_2 curve, in green shows a really good agreement when the surface processes are not included, though the derivative at 10s points a toward a disagreement for longer plasma ON time. When processes 5.30 and 5.31 are included, the H_2 starts decreasing after 7s of plasma ON time (as seen for 2Torr on figure 5.31), which correspond to the time when C_2H_6 is back to very low density. At this point, process 5.30 keeps happening but the adsorbed H is not consumed by process 5.31, leading to a sink of H_2. In both simulated cases, the C_2H_6 has a similar shape as the experimental one though it is not very visible when the surface processes are included. In this case, the C_2H_6 is destroyed very fast to reproduce CH_4. Without the surface processes, the C_2H_6 is initially over-produced compared to the experiment (likely because of the over-dissociation of CH_4 due to the imposed reduced electric field), before going back down by electron impact dissociation. The simulated water densities, plotted in light blue, are somewhat close to the experiment in terms of order of magnitude but show very different trends. At 10s of plasma ON time, the experimental density evolves with a linear trend while the simulated value show an exponential trend (with or without the surface processes). The evolution of the hydrogenated species shows overall a better agreement with experiment when the processes 5.30 and 5.31 are removed from the kinetic scheme. This shows that the surface processes are much less important in this mixture which is consistent with the lower initial amount of hydrogen. A complete run of this mixture should be done to fully check the matching of experiment and simulation until steady state but the present test already show a relatively good agreement and bring additional proof that the kinetic scheme is adapted, especially for the added process 5.16.

5.8 Discussion of the reaction pathways

In the 5Torr test case (50:50CO_2:CH_4 500*1*50-10 case), the model reproduces rather well the trends of CO_2 and CO. The values of the H_2 with plasma ON time are quite close to the experimental data but some features of the measured H_2 evolution are missing: the initial H_2 slope is too slow and the slope break at T^{ON}=7s is not found in the simulation. The CH_4 density is too high compared to the experimental one, and the CH_4 reincrease is very small compared to the clear one observed experimentally. The simulated C_2H_6 trend is somewhat close to the experimental one, with an increase followed by a decrease, but the decrease happens after 5s instead of 10. The water is not well reproduced. Though the models fails to reproduce well the CH_4 density, the reaction pathways can be discussed to identify the weaknesses of the model.

Creation and loss processes of CO_2 Figure 5.33 shows the main creation and loss processes of CO_2 during the simulation. The rate of each process is plotted. At each time, the rate plotted is the rate of the reaction at the end of the pulse, just before the post-discharge phase. The creation mechanisms are plotted in plain lines with '+' markers, the loss in dashed lines with o markers. For readability, a process is only plotted when it contributes to more than 5% of the creation or the destruction of the specie. On all the reaction rates plotted on figure 5.33, three curve breaks are seen at 2.5, 7 and 15s of plasma ON time. The breaks at 7 and 15s are due to the change of slope in the reduced electric field profile. The jump seen at 2.5s is due to the computation of the EEDF by the LoKI solver. Based on the threshold of the cross-sections used in the kinetic scheme and on the value of the reduced electric field, the solver automatically chooses a range of electron energy on which the EEDF is computed. The jump seen on the reaction rates at 2.5s of plasma ON time correspond to the step when the range of computation of the EEDF is increased from 20eV to 35eV. The different EEDFs as a function of the time step are plotted in appendix at the end of this chapter. Overall, the sudden increase of the rate due to the change of the EEDF range correspond to less than 10% of the rate and does not majorly impacts the results. This issue should however be solved in the future. During the 25s of plasma ON time, the CO_2 is mostly dissociated by 2 reactions The first is electron impact dissociation (process 5.3),

$$e + CO_2 \rightarrow e + CO + O(1D)$$

The second is process 5.5

$$CO(a^3\Pi) + CO_2 \rightarrow 2CO + O$$

Both channels were already prominent in the glow discharge. The CO($a^3\Pi$), often neglected in CO_2-CH_4 plasma models, plays a major role, weighing 1/3rd of the dissociation. This highlights again that the electronic states would deserve more investigations. This experiment could be perfect for determining the role of the electronic state if the reduced electric field and the electron

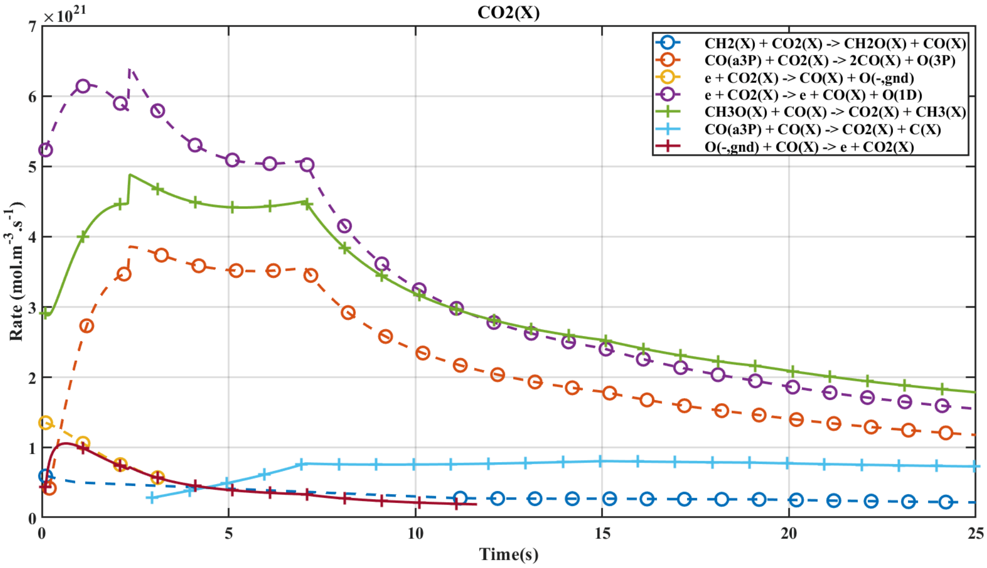

Figure 5.33: Evolution of the main creation and loss channels of CO_2 during the 25s of plasma ON time. At any time, the value plotted correspond to the value of the rate at the end of the plasma phase. The creation processes are plotted with '+' markers, the loss in dash lines with 'o' markers

density were measured and not deduced. This is probably one of the largest improvement prospect of this work. The main back reaction mechanism during the simulation is the reaction 5.12

$$CH_3O + CO \rightarrow CO_2 + CH_3 (5.12)$$

The rate of this reaction is taken from W. Tsang et al. 1986. Three separate measurements of this rate are available on the NIST Kinetic database, obtained with three different techniques (UV absorption in a shock tube, gas chromatography and LIF after photolysis) and are in good agreement on the temperature dependence, though a factor 2 can be found. In the glow discharge, the main back-reaction mechanism identified was reaction 5.13

$$CO + OH- > CO_2 + H \quad (5.13)$$

It is here of negligible importance. The CH_3O is produced by process 5.15 ($CH_3 + OH \rightarrow CH_3O + H$). This mechanisms was neglected in the "simplified kinetic scheme" because the scheme arbitrarily did not include CH_3O. Therefore it could be that the previously identified back-reaction mechanism was wrong because of this omission, but in the building-up configuration (with a closed reactor), the gas composition is also different. The accumulation of C_2H_6 (allowed by the close configuration) lead to a much stronger production of CH_3 in the RF. In the RF discharges, at 2.5s of plasma ON time, the total CH_3 production adds up to $7.05*10^{22}m^{-3}s^{-1}$ (more than half coming from C_2H_6 dissociation), while the CO creation only adds up to $3.4*10^{22}m^{-3}s^{-1}$. In the glow discharge at pseudo-steady state, at 5Torr in a 60:40 CO_2:CH_4 mixture (the closest condition from the building-up test case), the CH_3 production reaches $1.8*10^{22}m^{-3}s^{-1}$ while the CO creation rate reaches $8*10^{22}m^{-3}s^{-1}$. This means that in the glow, CH_3O would be produced in much smaller quantity than in the RF and could explain how process 5.13 is the back-reaction mechanism in the glow while process 5.12 is the main back-reaction mechanism in the RF.

Nevertheless, it must be noted that the rate of process 5.12 (CH_3O + CO) is quite strong: the creation rate of CO_2 via 5.12 during the first 5 seconds is as much as 40% of the total loss rate of CO_2, which does not match the experimental observation. It was indeed seen that the normalized initial loss of CO_2 in the building-up experiment overlapped in all the tested

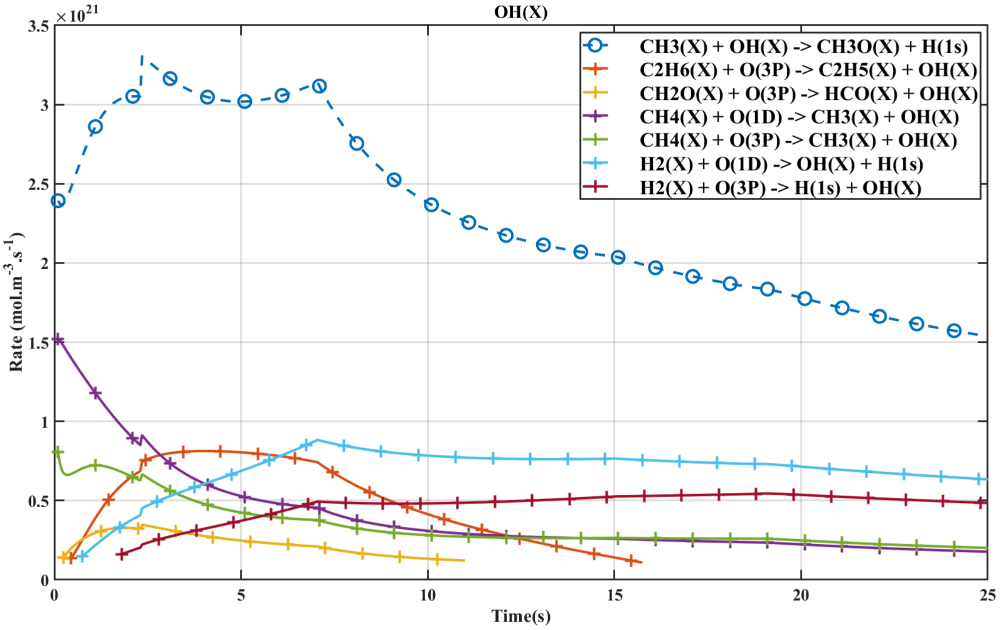

Figure 5.34: Evolution of the main creation and loss channels of OH during the 25s of plasma ON time. At any time, the value plotted correspond to the value of the rate at the end of the plasma phase. The creation processes are plotted with '+' markers, the loss in dash lines with 'o' markers

mixtures (see figure 5.7), which implied that the initial loss of CO_2 was controlled only by electron impact dissociation. The high rate of process 5.12 means that the density of CO_2 is given by

$$\frac{d[CO_2]}{dt} = -k^e_{diss} * n_e * [CO_2] + k_{5.12}[CH_3O][CO] \neq -k^e_{diss} * n_e * [CO_2] \qquad (5.32)$$

If the hypothesis that CO_2 initial density is controlled only by electron impact dissociation is not wrong (in order to explain the constant initial decay of CO_2 for all gas mixtures on figure 5.7b), then the back-reaction mechanism is overestimated. The rate coefficient for reaction 5.12 which is the main loss of CH_3O, has already been discussed. The production of CH_3O must therefore be questioned. The mechanisms forming CH_3O were given in section 5.7.2.1. CH_3O is produced by reaction 5.15 (CH_3 + OH → CH_3O +H). The creation of CH_3O is somewhat related to the field: it is due to reaction of CH_3 with OH, itself produced by reaction of O(1D) with CH_4, indirectly dependant on the electron impact. It is possible that these processes somehow compensate each other in all conditions of figure 5.7b but it seems very unlikely. The rate coefficient of process 5.15 is taken from Dean et al. 1987 and is already the lowest one available in the NIST kinetic database. It seems therefore unlikely that CH_3O production or loss are overestimated because of the rate coefficients used. The large production of CH_3O could be due to a large production of OH (which is the limiting reactant in 5.15). The rate of the mechanisms creating and destroying OH are plotted on figure 5.34. All along the 25s of plasma ON time, OH is mostly produced by oxidation of CH_4, C_2H_6 and H_2:

$$CH_4 + O(1D) \rightarrow CH_3 + OH \quad (5.9)$$

$$CH_4 + O(3P) \rightarrow CH_3 + OH) \qquad (5.33)$$

$$C_2H_6 + O(1D) \rightarrow C_2H_5 + OH \quad (5.26)$$

$$H_2 + O(1D) \rightarrow OH + H \qquad (5.34)$$

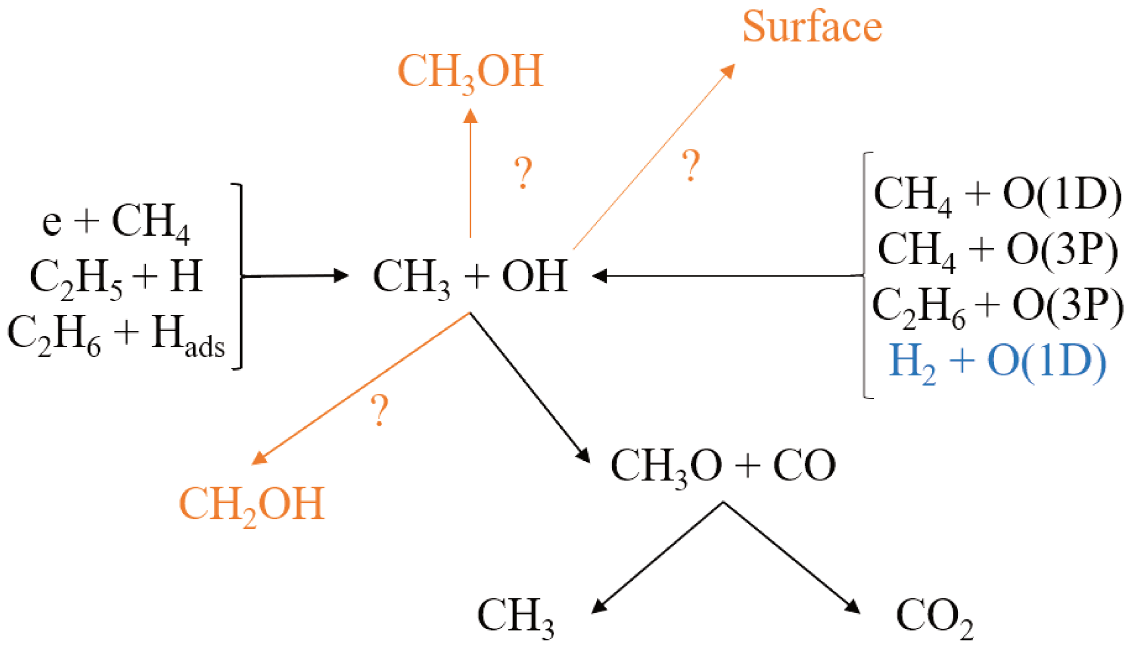

Figure 5.35: Reaction pathways leading to CH_3 and OH formation and destruction. The process in blue is the one with a large uncertainty on the rate coefficient. The arrows in orange are alternative pathways not included in the model

Their relative importance vary in time but overall maintain an approximately constant production rate of OH. The rate coefficient used for processes 5.9 is taken from Atkinson 1992, in good agreement with other values available on NIST kinetic database and with the value used in Lefkowitz 2015, where the importance of this process was highlighted for CH_4-O_2 nanosecond discharges. The rate of processes 5.33 and 5.26 are taken respectively from Miyoshi 1993 and Matsumi 1993, both in good agreement with values from the NIST kinetic database. The value of the rate coefficients available for reaction 5.34 on the NIST database are spread over several orders of magnitude, the value from Tully 1975 used here is one of the highest one. The channel 5.34 is not as strong as the three others on the first seconds of plasma ON time, so the use of an overestimated rate coefficient for 5.34 is unlikely to explain the large production of OH.
Because none of the rate coefficients seems to be satisfactory to explain why the simulated back-reaction is stronger than the one observed in the experiment, the possibility that processes concerning OH are ill-estimated must be examined. OH can be easily adsorb on surfaces, which is not taken into account here and could account for a loss of OH. In turn, this OH adsorption would lower the rate of the back reaction. However, the surface adsorption would likely not play a strong role in the first seconds of plasma ON time where the inconsistency is observed.

The combination of CH_3+OH could produce CH_3OH but it is not included in the model so far. Indeed, Fagerström et al. 1994 proposed a value for $k_{CH_3+OH\rightarrow CH_3OH}$ two orders of magnitude higher than the value of Dean et al. 1987 for $k_{CH_3+OH\rightarrow CH_3O+H}$. However, as explained, the value of Dean et al. 1987 is already the lowest available, meaning that using a different source could still lead to the same pathway even if methanol is added. It also appears that Dean et al. 1987 proposes a much higher value for $CH_3 + OH \rightarrow CH_2OH + H$ (i.e differentiating CH_3O from CH_2OH).

The possible pathways leading to the back reaction 5.12 are summarized on figure 5.35. This highlights the limits of the current model: the molecules were chosen based on the experiment results to limit the complexity but some molecules such as methanol and its precursor CH_2OH could be important intermediate species (though no methanol was measured in all our measurements). An improvement of the model would be to add these species, but they cannot be added blindly. An extremely large amount of molecules could be added and in the present case, the discussion focuses on a very specific process. This highlight the limits of the modeling alone. Pragmatically, the next step to address that issue is to measure the reduced field at the beginning of the experiment to ensure that the hypothesis drawn from experimental results (dissociation induced by electron impact) is correct and that the observed CO_2 dissociation does not result from a compensation of some sort.

- CO_2 is mainly destroyed by electron impact dissociation and reaction with CO($a^3\Pi$)
- The simulation shows a non-negligible production of CO_2 through CH_3O + CO, which doesn not match the experimental observations where the CO_2 density seems controlled only by electron impact dissociation
- This difference could be due to the reactions pathways neglected in the model which would limit the CH_3O production: formation of unaccounted molecules like CH_3OH and CH_2OH, surface processes.
- The inclusion of these processes would likely modified the deduced value of the reduced electric field, highlighting the need to properly measure the reduced electric field.

Loss and creation processes of CO The CO processes are not represented here. Because of the lack of quenching of CO(a3Π) by other species than CO_2 and CO, the CO is in a constant cycle with CO(a3Π): after few seconds, the main loss of CO is the electron impact excitation to CO(a3Π) and the main creation process of CO(X) is the quenching of CO(a3Π). Apart from this excitation cycle, the CO is mainly produced through 3 channels. The first two are processes 5.5 and 5.3

$$CO(a3\Pi) + CO_2 \rightarrow 2CO + O \quad (5.5)$$
$$e + CO_2 \rightarrow e + CO + O(1D) \quad (5.3)$$

The third one is the debated process:

$$CH_3 + O(1D) \rightarrow CO + H_2 + H \quad (5.16) \tag{5.35}$$

The rate follow: $k_{5.5} > k_{5.3} > k_{5.16}$. The second inequality is true during the 25s, the first one is only true after 2.5s, time necessary to produce CO(X), later excited to CO(a3Π). All 3 rates decrease with time because they depend on the CO_2 density (indirectly for 5.16, which relies on O(1D) creation by 5.3). CO has only one loss process:

$$CH_3O + CO \rightarrow CH_3 + CO_2 \tag{5.36}$$

This loss is due to the large production of CH_3O discussed above. This process also decreases due to the decreasing CH_3O density (see figure 5.39).

- CO is formed from CO_2 through electron impact dissociation and dissociation by CO($a^3\Pi$) and from CH_4 from process 5.16
- CO($a^3\Pi$) plays an important role for CO which might be overestimated due to the lack of reaction between CO($a^3\Pi$) and hydrogenated species

Loss and creation processes of CH_4 The CH_4 creation and destruction processes are plotted on figure 5.36. The main loss of CH_4 during the whole simulation is the electron impact

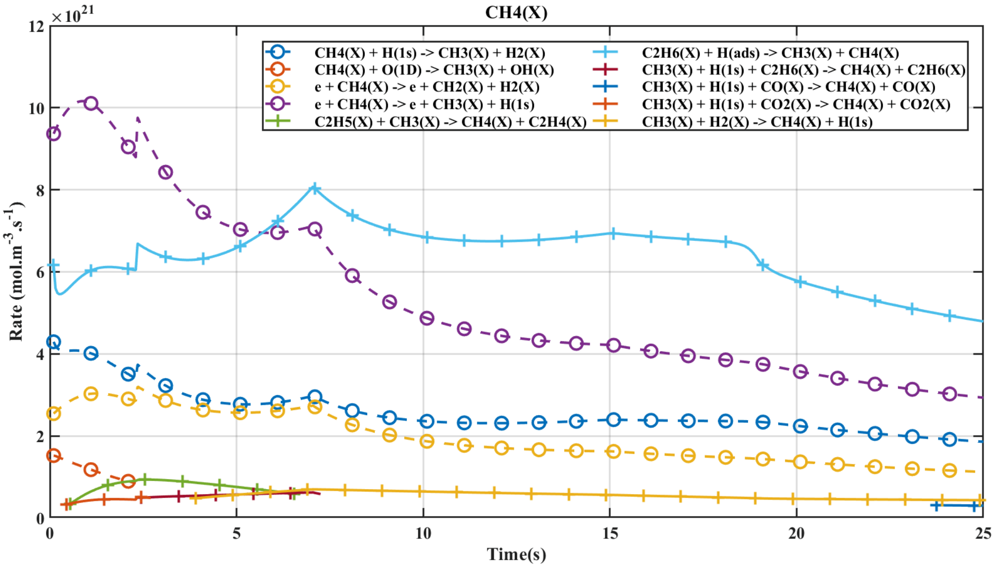

Figure 5.36: Evolution of the main creation and loss channels of CH_4 during the 25s of plasma ON time. At any time, the value plotted correspond to the value of the rate at the end of the plasma phase. The creation processes are plotted with '+' markers, the loss in dash lines with 'o' markers

dissociation:

$$e + CH_4 \rightarrow e + CH_3 + H \quad (5.14)$$

and with a lower importance

$$e + CH_4 \rightarrow e + CH_2 + H_2 \tag{5.37}$$

This is similar to what was found in the glow discharge. A new loss channel different from the glow emerges:

$$CH_4 + H \rightarrow CH_3 + H_2 \tag{5.38}$$

Negligible in the glow, the amplitude is here comparable to the second electron impact mechanism 5.37. The difference from the glow comes from the formation of C_2H_Y molecules, whose successive destruction and reformation produce H atoms (the processes relative to C_2H_Y will be discussed later). Nearly 50% of the atomic H produced at 2.5 second of plasma ON time comes from the reaction

$$C_2H_4 + H_2 \rightarrow C_2H_5 + H$$

During the first 2.5s, CH_4 is oxidized by O(1D) following reaction 5.9:

$$CH_4 + O(1D) \rightarrow CH_3 + OH$$

This mechanisms was previously identified in the glow discharge, where it played a stronger role. In this case, the rate of the process 5.16 ($CH_3 + O(1D)$) was increased compared to the glow, consuming more O(1D) and thereby reducing the importance of CH_4 + O(1D). The process CH_4 + O(1D), already weak at the beginning of the experiment, becomes negligible very quickly due to the drop of CH_4.

Over the 25s of plasma ON time, the main mechanism reproducing CH_4 is the added surface process 5.31

$$C_2H_6 + H(ads) \rightarrow CH_4 + CH_3$$

It is worth noting that the second process producing CH_4 is reaction 5.22 ($CH_3 + H_2 \rightarrow CH_4 + H$) which is pushed by the high production of CH_3 after 5s of plasma ON time thanks to process

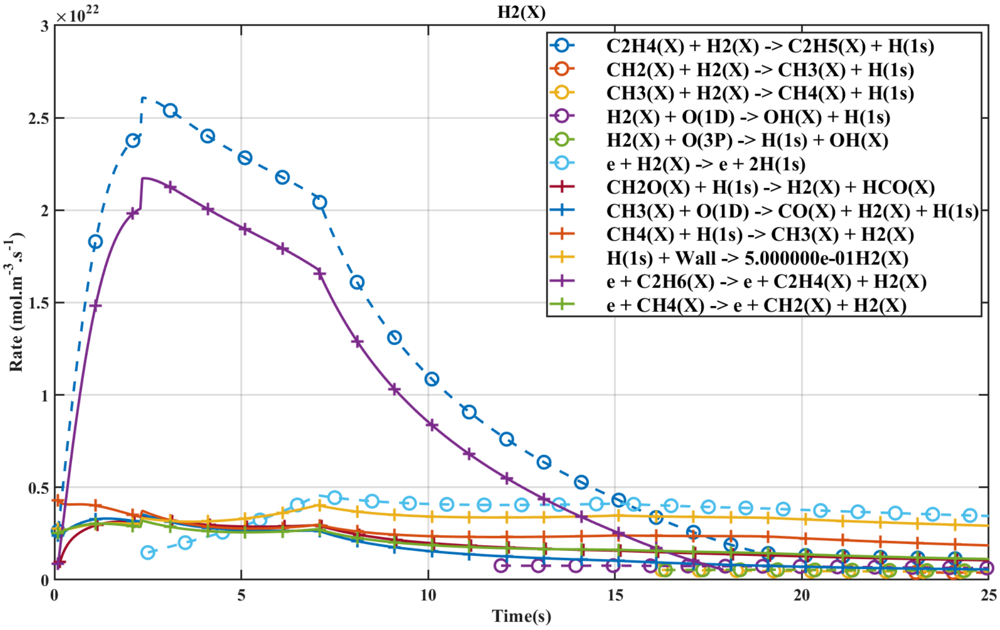

Figure 5.37: Evolution of the main creation and loss channels of H_2 during the 25s of plasma ON time. At any time, the value plotted correspond to the value of the rate at the end of the plasma phase. The creation processes are plotted with '+' markers, the loss in dash lines with 'o' markers

(5.31). The CH_4 back-reactions have different sources in other literature model: in Bie et al. 2015, CH_4 is produced by electron impact of C_3H_Y molecules , which are not measured in our plasma and therefore are unlikely to be the main formation channel of CH_4 in our plasma. The CH_4 reformation is not mentioned in the CO_2-CH_4 nanosecond DBD studied numerically C.Bai 2019. In the GA studied in J.-L. Liu et al. 2022 for DRM, only process(5.22) is mentioned but appears to have a very small rate, much lower than the destruction processes. The influence of the artificial surface process (5.31) is very strong. It clearly appears that if this process was not here, nothing would balance the CH_4 destruction: only 3 other creations processes have a non-negligible contribution to CH_4 formation but none have the potential to create enough CH_4 to induce a reincrease. This highlight the necessity to introduce a new reaction in the kinetic scheme.

- CH_4 is destroyed mostly by electron impact dissociation
- O(1D) and H (formed from the C_2H_Y) also react with CH_4
- The main CH_4 reformation channel is the surface process 5.31. None of the processes found in literature can explain the observed CH_4 reincrease after 10s.

Loss and creation processes of H_2 The rates of H_2 loss and production are plotted on figure 5.37. Two mechanisms mainly drive the H_2 formation: the electron impact process 5.18

$$e + C_2H_6 \rightarrow e + C_2H_4 + H_2 \quad (5.18)$$

and the reaction

$$C_2H_4 + H_2 \rightarrow C_2H_5 + H \quad (5.23)$$

Which holds until the C_2H_6 is destroyed. One C_2H_6 is destroyed, after ∼ 15s of plasma ON time, the main creation processes of H_2 are the wall recombination of H into H_2 and the reaction:

$$CH_4 + H \rightarrow CH_3 + H_2 \tag{5.39}$$

The H_2 production from larger hydrocarbons is found in the model of the DBD in Bie et al. 2015, where electron impact on C_2H_6 account for 36% of the H_2 formation (vs 50-55% in our case). But the C_2H_6 fraction is much larger in our case, accounting for up to 5% of the mixture (while it is less than 1% in Bie et al. 2015). Similarly, Bie et al. 2015 attribute 16% of its H_2 production to impact on C_3H_8, which is not detected in our plasma and therefore not taken into account. C_3H_8 is produced according to Bie et al. 2015 by recombination of CH_3, which is prevented in our case due to the reaction of CH_3 and O(1D). This seemingly indicates that the influence of the large hydrocarbon can be overestimated in literature (as suggested in the previous chapter) and must be balanced by the influence of the electronic state. Reaction 5.16 however remains an hypothesis and other reaction pathways could also balance the influence of the C_2H_Y. In C.Bai 2019 for the modelling of the nanosecond discharge, H is produced by electron impact of CH_4, like in the glow. In J.-L. Liu et al. 2022, H_2 is produced inside a GA by recombination of H with vibrationally excited CH_4. The rate of this reaction is low in our models but the scaling with vibrational energy could contribute to increase its importance. Outside the arc, H_2 is produced through the H exchange $C_xH_y + H \rightarrow C_xH_{y-1} + H_2$. The model of J.-L. Liu et al. 2022 does not include electron impact on large molecules, explaining the difference with ours. In our model, as long as some C_2H_6 remains in the gas phase, H_2 is consumed in C_2H_5 formation through reaction 5.23 ($C_2H_4 + H_2 \rightarrow C_2H_5 + H$) It is only once C_2H_6 disappears that H_2 is lost by electron impact. This is in strong disagreement with Bie et al. 2015, where H_2 is lot by electron impact even in the presence of C_2H_6. This could be due to a higher reduced electric field in the DBD. The loss processes in J.-L. Liu et al. 2022 are not explicited.

- As long as C_2H_Y molecules remain in the plasma, the H_2 production and destruction is driven by production and destruction mechanisms of C_2H_Y
- In literature, the importance of the mechanisms involving C_2H_Y have already been observed but in conditions with lower C_2H_Y content, maybe overestimating their importance
- Once the C_2H_Y molecules reach a low level, the H_2 production is du to CH_4 destruction. H_2 is lost by oxidation and electron impact mechanisms

C_2H_y The C_2H_6 (and the large hydrocarbon in general) formation mechanisms in DRM are unclear from literature, because the main hydrocarbon changes a lot from one source to another, as mentioned in the experimental section. Before comparisons with literature, the pathways of our own model must be explained. The C_2H_6 creation and destruction channels are plotted on figure 5.38. The C_2H_6 is almost entirely produced by recombination of CH_3 through reaction 5.11:

$$CH_3 + CH_3 \rightarrow C_2H_6 \quad (5.11)$$

This is consistent with literature when C_2H_6 is the largest C_2 molecule (Heijkers et al. 2020,Bie et al. 2015). C_2H_6 is later consumed mostly by two reactions: process (5.31 which is C_2H_6 + H on the wall) and electron impact dissociation:

$$e + C_2H_6 \rightarrow e + C_2H_4 + H_2 \tag{5.40}$$

As will be shown later, there is no rapid way to convert C_2H_4 into CH_4. This underlines the necessity to introduce another process of destruction of C_2H_6 to explain the reincrease of CH_4 observed in our experiment. The C_2H_Y radicals are shown on the right panel of figure 5.39, where

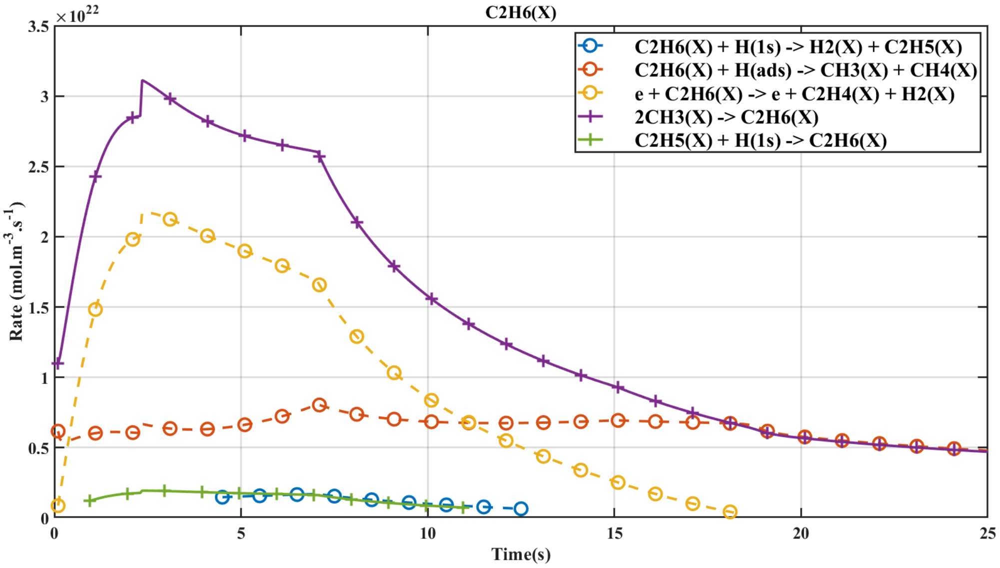

Figure 5.38: Evolution of the main creation and loss channels of C_2H_6 during the 25s of plasma ON time. At any time, the value plotted correspond to the value of the rate at the end of the plasma phase. The creation processes are plotted with '+' markers, the loss in dash lines with 'o' markers

the densities of the minor species both during the discharge and the post-discharge are shown. For each given plasma ON time, the values plotted with a '+' marker correspond to the value of the density at the end of the pulse and the value plotted with a triangle marker correspond to the density at the end of the post-discharge following the pulse. For readability, the plot has been separated in 2 panels. The species which do not have triangle markers have post-discharge densities below $10^{10} m^{-3}$. As expected, $[C_2H_5] > [C_2H_3] > [C_2H]$ but not because they directly cascade from each other, as supposed initially. The C_2H_Y pathways leading to this specific ordering are shown on figure 5.40. Only the main pathways are represented. The thickness of the arrow is relative to the importance of the process from the point of view of the reactant. On the whole, the "entrance" reaction to the C_2H_Y cycle is recombination of two CH_3 into C_2H_6. Electron impact mechanisms lead to formation of C_2H_4 and C_2H_2 (mostly the former). C_2H_4 is rapidly transformed into C_2H_5 and then into C_2H_6. The high value of these rates explain that the C_2H_4 simulated density is lower than the C_2H_2 density despite the production of C_2H_4 being much higher than the production of C_2H_2. A great number of hydrogen exchange reactions take place. These reactions are of the form:

$$C_xH_y + C_zH_w \rightarrow C_xH_{y\pm1} + C_zH_{w\mp1},\ \text{with } (w,x,y,z) \geqslant 1 \tag{5.41}$$

These exchange reactions contributes to reforming large hydrocarbons but never allow a carbon atom to transfer from C_2H_6 to CH_4 as seen in the partition of carbon atoms presented on figure 5.12 in the experimental results. The only two reactions allowing to form back CH_4 from C_2H_6 are the newly added surface process 5.31 ($C_2H_6 + H(ads) \rightarrow CH_3 + CH_4$) and the reaction:

$$C_2H_5 + H \rightarrow 2CH_3,\ k_{5.42} = 1.25.10^{-16} \tag{5.42}$$

This last process (5.42) is in direct competition with:

$$C_2H_5 + H \rightarrow C_2H_6,\ k_{5.43} = 1.10^{-17} \tag{5.43}$$

Several versions of these rates are available in literature: for $k_{5.42}$, value as low as $5.99.10^{-17}$ is found Baulch et al. 1992, while Sillesen et al. 1993 gives a value twice as high, chosen in this work. For $k_{5.43}$, the value given in Harding et al. 2005 is about 5 times higher than the value

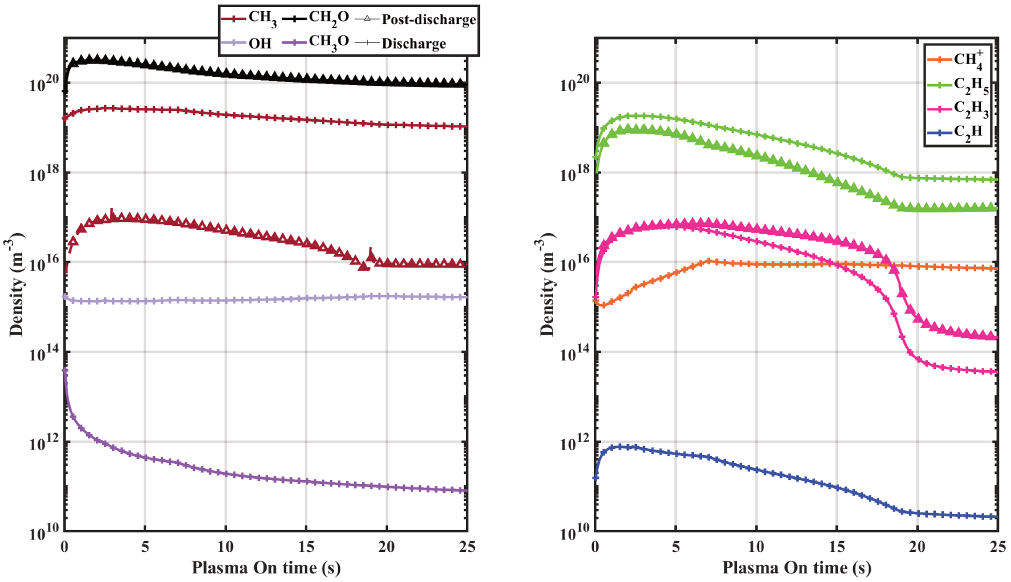

Figure 5.39: Simulated densities of the minor species in the test case (5Torr, 50:50CO_2:CH_4, 500*50*1-10). The densities during the discharge are plotted with '+' markers, the density during the post-discharge are plotted with triangle markers.

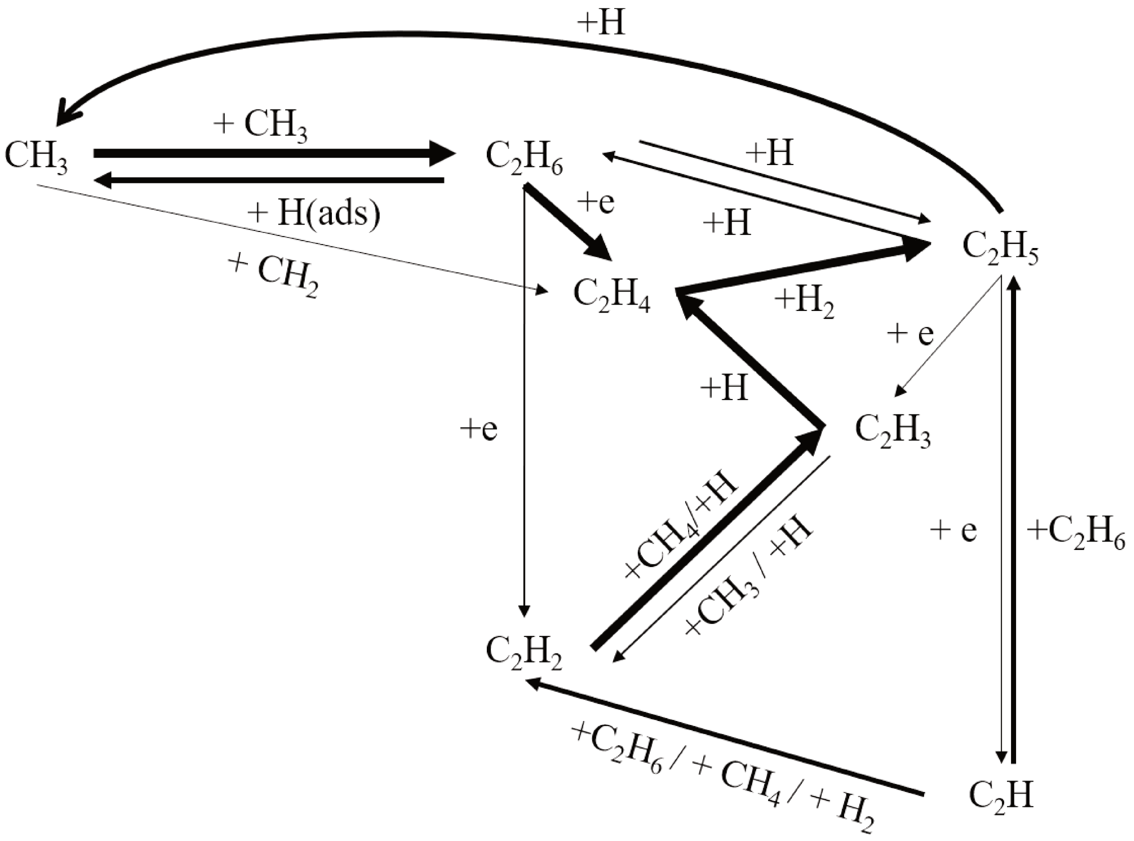

Figure 5.40: Description of the main processes between the C_2H_Y. The thickness of the arrow represent the importance of the process relatively to the total destruction rate of the specie of origin

found in Kurylo et al. 1970. The sources here were chosen to facilitate the "exit" of carbon atoms from the C_2H_Y species in an attempt to reproduce the CH_4 reincrease without needing to invoke additional surface processes. The ratio $\frac{k_{5.42}}{k_{5.43}}$ was maximized (in agreement with values available in literature), but this was not enough to explain the CH_4 reincrease, leading to the necessity to add surface process (5.31).

The CH_4 reincrease observed in the experiment is quite unusual and never found to be so important in literature. Indeed, CH_4 production is usually mostly found in methanation plasma, where it takes place thanks to a catalyst. In these plasma, the pathway of formation of CH_4 is the successive deoxidation of CO_2, followed by hydrogenation as showed in Gao et al. 2021: $CO_2- > CO- > C/CH- > ...- > CH_4$. The present case is different as CH_4 must be formed from C_2H_6. CH_4 production from C_2H_6 was reported in Thejaswini et al. 2011, where the products of Ar/CH_4, Ar/C_2H_2, Ar/C_2H_4 and Ar/C_2H_6 DBD at 300mbar were measured. It was found that after 3h of Ar/C_2H_6 plasma, CH_4 made up 11% of the gas density, but C_2H_2 accounted for 10%. In our case, little C_2H_2 is produced, pointing toward a different mechanism. In Sanchez-Gonzalez et al. 2007, the reaction pathways in an atmospheric pressure RF-driven plasma jet in Ethane:Helium and Methane:Helium are investigated experimentally and numerically. In Methane:Helium, the major stable species are $H_2 > C_2H_6 > C_2H_4$ in the post discharge area of the jet. In the $C_2H_6 : He$ jet, methane is the largest stable product, created in two steps: electron impact dissociation of C_2H_6 forming C_2H_5 followed by recombination with H through process 5.42 ($C_2H_5 + H \rightarrow 2CH_3$). The rate of reaction 5.42 in Sanchez-Gonzalez et al. 2007 was taken from Baulch et al. 1992. The value from Baulch et al. 1992 was initially used in our model before changing to the one of Sillesen et al. 1993, twice as high. In Sanchez-Gonzalez et al. 2007, the single process 5.42 however lead to a simulated CH_4 density 10 times lower than the measured one. Therefore, similarly to our case, the reactions included in Sanchez-Gonzalez et al. 2007, similar to the reactions used in our work, are not sufficient to explain the CH_4 formation. The surface processes are not expected to be important in a plasma jet so the impossibility to reproduce the CH_4 density in Sanchez-Gonzalez et al. 2007 could indicate that a chemical reaction is missing (in both our work and Sanchez-Gonzalez et al. 2007) rather than surface processes. Overall, no process can be found to efficiently reform CH_4 from C_2H_6, though it must be kept in mind that this takes about 10s of plasma ON time: such a high residence time is rarely found in literature. Still, all the processes brought up in literature to explain CH_4 reformation were already taken into account in our model. Because nothing can be found in the C_2H_6/CH_4 plasma literature, it could be that this reaction is due to a specie related to CO_2 (given that CO_2-CH_4 plasma have been much less studied). This remains an open question for future work.

Ordering of the C_2H_y molecules densities: The question of the ordering of the C_2H_Y species still remains. In Bie et al. 2015, the model for atmospheric pressure DBD predicts that CH_3 recombines into C_2H_6 and C_3H_8, whose density is higher than C_2H_4. In Cleiren et al. 2017, the same model applied to a gliding arc predicts that $C_2H_2 > C_2H_3 > C_2H_4 > C_2H_5 > C_2H_6$. This time, the C_2H_2 is produced in the arc by recombination of CH_2 radicals (obtained from dehydrogenation of CH_4) through:

$$CH_2 + CH_2 \rightarrow C_2H_2 + 2H \tag{5.44}$$

C_2H_6 and C_2H_5 are created outside the arc by CH_3 recombination 5.11 (CH_3 +CH_3 $\rightarrow$ C_2H_5 + H) or reaction :

$$CH_3 + CH_3 \rightarrow C_2H_6 \tag{5.45}$$

The two large molecules could then be successively dehydrogenated to C_2H_2. The difference between the two discharges (DBD vs GA) was attributed to the higher temperature in the gliding arc (2700 vs 300K), leading to dehydrogenation of C_2H_6. It also seems that the initial dehydrogenation of CH_4 is important. In our discharge, electron impact dissociation produces much more CH_3 than CH_2 (due to the electron impact dissociation cross-sections), which was also true in the DBD in Bie et al. 2015, leading to production of C_2H_5/C_2H_6 rather than C_2H_2/C_2H_3 like in the GA. However, the branching $\frac{k_{5.45}}{k_{5.11}}$ depends on the source chosen for the rate, as many are available. In our case, the rate of 5.11 is taken from Baulch et al. 1992 and the rate of 5.45 is taken from Sangwan et al. 2015. In Bie et al. 2015, the rate for 5.45 is taken from Baulch et al. 1992 and the rate for 5.11 is taken from Stewart et al. 1989.

Interestingly, another numerical study by J.-L. Liu et al. 2022 in a similar apparatus (a gliding arc plasmatron) did not found any C_2H_2 or C_2H_4 in the arc region but showed they were the main products outside of the arc. In J.-L. Liu et al. 2022, the radicals found are $CH_3 > CH_2 > C_2H_3 > C_2H_5 > CH$. J.-L. Liu et al. 2022 explained the formation of C_2H_2 in several steps: first, vibrationally excited CH_4 collides with H, producing CH_3. This CH_3 recombines with CH_3 to form preferentially C_2H_5 (or C_2H_6 quickly dehydrogenated to C_2H_5), which successively loses H to end up in C_2H_2. The C_2H_2 remains because the temperature is not high enough for further dehydrogenation. In this model of GA, no electron impact on the C_2 hydrocarbon is taken into account because the reduced electric field (50Td) is assumed to be low enough so that the electrons pump CO_2 and CH_4 vibrations. This is one major difference with our model despite a similar E/N in the range [42:55]Td, where C_2H_6 is destroyed by electron impact rather than thermal dissociation. The pathways are extremely different due to the temperature, key differentiating parameter. The assumption made in J.-L. Liu et al. 2022 that the electrons are only pumping the vibrations is debatable: with a similar value of the reduced electric field, electron impact dissociation of CO_2 is observed in our case. Finally, in the model presented in C.Bai 2019 for nanosecond discharges, C_2H_4 is predicted to be the main hydrocarbon (C_2H_4>C_2H_6>C_2H_2), produced by reaction of CH or CH_2 with CH_4. How CH_2 is produced is not explicited but it can be assumed that it is by electron impact of CH_4 (nanosecond discharges have very high reduced electric field, favourable to electron impact). However, it is reported that process 5.14 ($CH_4 + e \rightarrow CH_3 + H + e$) and process $CH_4 + CH_2 \rightarrow 2CH_3$ have similar rates, raising doubt on the passage from CH_3 to CH_2. Electron impact on CH_3 could form CH_2. After this, two reactions occur:

$$CH_4 + CH_2 \rightarrow C_2H_4 + H_2$$
$$CH_4 + CH \rightarrow C_2H_4 + H$$

These reactions were not included in our model (because they are not reported in the NIST kinetic database). The rates reported in C.Bai 2019 for these reactions are lower than the rates of recombination of CH_3 into C_2H_6. The high density of C_2H_4 must therefore be explained by the high production rate of CH and CH_2. It appears in this case that the reduced electric field is the key parameter for C_2 formation.

To summarize this literature review, two discharge parameters appear as key for C_2H_Y molecules formation: the reduced electric field, which determines the degree of dehydrogenation of CH_4 and the corresponding C_2 hydrocarbon formed, and the temperature, which if high enough, will lead to step-wise dehydrogenation. The glow and the DBD discharges creates CH_3 radicals, forming quickly C_2H_6. The nanosecond discharge creates CH_2, further transformed in C_2H_4. Because of its low reduced electric field, the gliding arc mainly produces CH_3 transformed into C_2H_6, but because of the high temperature, step-wise dehydrogenation transforms C_2H_6 into C_2H_2. It must be noted that the proposed analysis of E/N and of the gas temperature is based on results measured in post-discharge and therefore takes into account the post discharge. It does not apply to the pulse only. The gliding arc of J.-L. Liu et al. 2022 is a good illustration because the main C_2H_Y molecule in and out of the arc are very different due to the different temperatures and reduced electric field in and out of the arc. This analysis as a function of the E/N and of the gas temperature seems to be valid again in discharges that do not contain oxygen (i.e CH_4 discharges). In C.Bai 2019 (same model as for the CO_2-CH_4 plasma), the C_2H_4 is predicted to be the main C_2 hydrocarbon in a pure CH_4

nano-second discharge at atmospheric pressure, following the same logic as the CO_2-CH_4 case. In Hassouni et al. 2001, C_2H_2 is the main measured C_2 molecule in a 5ms pulse of a microwave discharge at ∼15Torr. This measurement is supported by kinetic modeling, which predicts that $[C_2H_2] > [C_2H_4] > [C_2H_6]$, as well as a temperature reaching up to 2800K during the pulse. Finally, in Heijkers et al. 2020, a model developed for CH_4/H_2 plasmas is applied to 4 plasmas: a DBD, a low pressure microwave at 300mbar, an atmospheric pressure microwave and a gliding arc discharge. The DBD, with the lowest temperature ($\sim 500K$) and probably highest reduced electric field, has $C_2H_6 > C_2H_4 > C_2H_2$. The production mechanisms are very similar to the one observed in our case (cascade from C_2H_6), but radical recombination (CH and CH_2) also creates C_2 molecules. When switching to GA or MW discharges, the temperature is increased and the reduced field likely lowered. The CH_X radical formation is lowered and the thermal dissociation of C_2 molecules leads to C_2H_2 being the largest C_2. For each type of discharge, the gas temperature and reduced electric field reach will depend on the individual configuration: the pulse duration, the repetition rate, the power... Montesano, Faedda, et al. 2021 showed that a memory effect could exist in CO_2-CH_4 atmospheric pressure NRP, where the first pulse could influence the dissociation in the following pulses (through several parameters such as the gas temperature). All these parameters will influence the E/N and the temperature and could be tuned to tailor the products.

- The C_2H_Y "cycle" is shown on figure 5.40. C_2H_6 is formed from CH_3 radicals recombination. Other C_2H_Y molecules are formed from successive reactions starting from C_2H_6. Few processes "break" the C_2H_Y molecules into 2 CH_X molecules, highlighting the necessity to introduce such process to explain the CH_4 reincrease
- The major C_2H_Y present in the plasma (both in this case and in literature) seems to depend on the discharge temperature and reduced electric field: High reduced electric field lead to smaller CH_X radicals that can recombine together, high temperature lead to dehydrogenation of the C_2H_Y molecules

H_2O production mechanisms The water production, presented on figure 5.41, is almost entirely due to OH reacting with the main hydrogenates species:

$$C_2H_6 + OH \rightarrow C_2H_5 + H_2O \tag{5.46}$$
$$H_2 + OH \rightarrow H + H_2O \tag{5.47}$$
$$CH_4 + OH \rightarrow CH_3 + H_2O \tag{5.48}$$

The production rates obviously align very well with the density of said species: $k_{5.48}$ is dominant initially until $k_{5.46}$ becomes dominant (following the rise of C_2H_6 density). After 12s, process 5.47, becomes dominant following the increase in H_2 density. The loss of H_2O is due to 2 processes: electron impact and reaction with O(1D). Both processes scale with the reduced electric field, as visible in their shape, with a sharp change at 7s (and 15s for electron impact), following the change in the E/N profile. The underestimation of H_2O could be due to 2 things: first, it is highly probable that water is involved in surface reactions (for example an ER process with adsorbed H and gas phase OH). Second, the loss of OH could be miscalculated, as was discussed on figure 5.35. H_2O was better reproduced in the glow discharge. The importance of the surface processes, far less important in the glow because of the short residence time, could explain the difference.

CH_3O, CH_2O, CH_3 and OH The non-measured specie with the largest simulated density is the CH_2O (in black on the left panel of figure 5.39), whose density is of the order of $10^{22}m^{-3}$. This corresponds to about 0.1% of the gas density, which would explain why this specie was not detected. The density of CH_2O does not vary much between the discharge and the post-discharge because CH_2O is a stable molecule at 300K and its reactivity is too low to make a

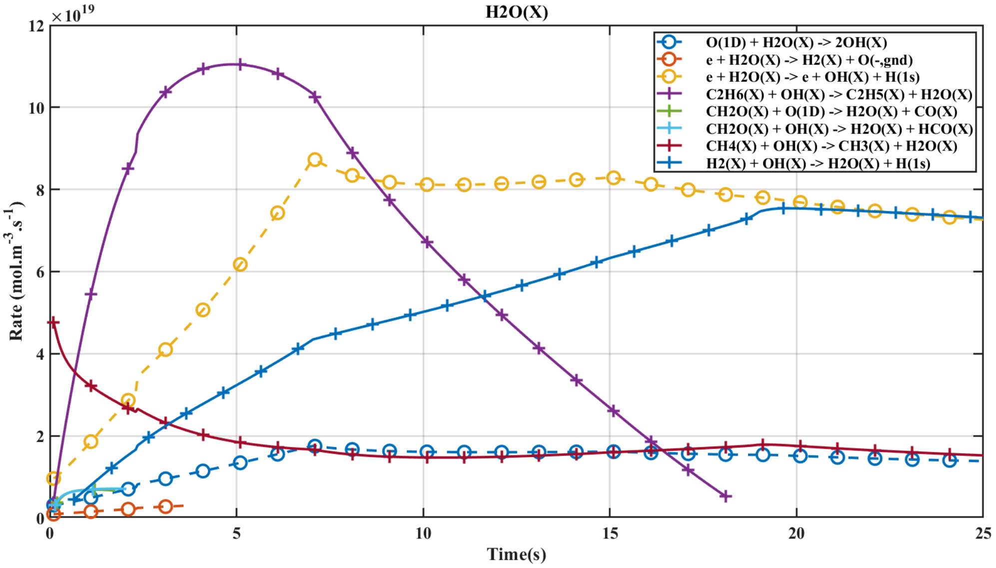

Figure 5.41: Evolution of the main creation and loss channels of water during the 25s of plasma ON time. At any time, the value plotted correspond to the value of the rate at the end of the plasma phase. The creation processes are plotted with '+' markers, the loss in dash lines with 'o' markers

difference within the few ms of cooling down of the gas temperature.

The CH_3 is the second minor species with a low varying plasma-on density over the whole simulation. At small plasma ON time, CH_3 is produced by CH_4 electron impact. Later on, the surface processes added (5.30 and 5.31) take the relay of the CH_3 production, until CH_4 is destroyed again by electron impact. There is a large difference between the discharge and post discharge value of CH_3 (from $\sim 10^{19}$ to $\sim 10^{16}$ m^{-3}) because of the strong reactivity of this radical. It is interesting to note that the CH_3 post-discharge curve shape (in brown triangle on the left panel) is very similar to the simulated C_2H_6 visible on figure 5.28. This is because electron impact mechanisms which lead to CH_3 (direct impact of CH_4 or impact of C_2H_6 leading to CH_3 through processes 5.19 followed by 5.42) only happen during the discharge phase while the CH_3 creation by $C_2H_6 + H(ads)$ happens during both plasma ON and plasma OFF phases, hence giving this shape to the CH_3 post-discharge curve. It can be noted from figure 5.39 that after each pulse, approximately $1.10^{19}m^{-3}$ of CH_3 is lost in the post-discharge (on the scale of 1ms according to the experimental results). In the post discharge, approximately 50% of the CH_3 is lost by recombination into C_2H_6, i.e $2.5.10^{18}m^{-3}$ is produced in each post-discharge. After 40pulses ($\sim$2s of plasma ON time), the CH_3 recombination in post-discharge produces $1.10^{20}m^{-3}$, which is about one tenth of total the C_2H_6 density produced at that time.

The main loss and creation mechanisms of OH were presented on figure 5.34. OH is produced by oxidation of C_2H_6, CH_4 and H_2 (processes 5.33, 5.9, 5.26 and 5.34). CH_4 + O being is initially dominant but is quickly overtaken by C_2H_6 + O(3P) when C_2H_6 density rises. When H_2 becomes the main hydrogenated specie, H_2+O(1D/3P) becomes dominant. This highlight the importance of O(1D) whose rate for a given reaction is higher than with O(3P). OH is lost through reaction with CH_3 forming CH_3O (process 5.15). This is quite different from the glow, where the OH was mostly lost in the production of water. As seen previously, OH is the main precursor of water but on the scale of OH, water production is a minor channel. The mismatch between experimental and simulated H_2O could indicate that the rate of creation of CH_3O from CH_3 and OH is too high.

The CH_4^+, main ion in the simulation and shown on the right panel in orange, initially increases before stabilizing after approximately 7 seconds of plasma ON time, which corresponds to the change of slope in the E/N profile. The CH_4^+ density appears as entirely correlated to the

reduced electric field.
The CH_3O density drops by three order of magnitude over the simulation, which is due to the increasing loss mechanism 5.12 $CH_3O + CO \rightarrow CH_3 + CO_2$ because of the CO increase over the plasma ON time. The initial CH_3O is created by reaction of CH_4 with O(1D) (process 5.9) creating CH_3 and OH, followed by process 5.15 (CH_3 + OH → CH_3O + H) as previously discussed .

5.9 Conclusion

An CO_2-CH_4 pulsed RF discharges was studied at low pressure in a closed reactor. The closed reactor configuration was chosen to be able to study the evolution of the mixture over long time-scales. These long time-scales allowed to witness the production of CO and H_2, the formation of C_2H_Y molecules as intermediate species and their destruction. Several gas mixtures and pulse configurations were studied to derive as many information as possible from the experimental results. The behaviour of several species was found to be similar with CH_4 fraction of pressure than what was observed in the glow, likely because of the somewhat similar reduced electric field and temperature. Nevertheless, several information were drawn from the experimental variations, like the rapid production of CO from CH_4. The chemistry however proved to be too complex to easily establish the reaction pathways, and a model was developed. The 'simplified' CO_2-CH_4 plasma presented for the glow discharge was completed with species up to C_2H_6 and tested here. Because of the nature of the experiment, the simulation capacity were limited and a limited number of simulation on one test case at 50:50 CO_2:CH_4 could be run. The correct modeling was made difficult by the lack of some basic data like the reduced electric field, the electron density or the temperature during the experiment. The latter was inferred from glow discharge data, but probably evolves over the course of the experiment. As for n_e and E/N, they were deduced from experimental insights. The model highlighted two interesting features: first, if only rates available in literature were used, it is impossible to match the rapid CO formation rate of the experiment, which pointed toward the lack of an essential process in the model. The reaction of the electronic excited state O(1D) with CH_3 was again brought under the spotlight and shown to be critical. Second, using only gas phase reactions, the CH_4 reformation from C_2H_6 could not be explained. The hypothesis done here is that the CH_4 reproduction is due to surface reactions, which were included in the model under the form of 2 over-simplistic reactions. Though the values remained very incorrect, the trends could be reproduced, showing the potential influence of the reactions and the necessity of developing a plasma/surface interaction model. The modeling was also useful to understand the creation mechanisms of the C_2H_Y in this discharge and in other discharges from literature. Several leads must be pursued in the future to improve these results. The most important is the measurement of the gas temperature and of the reduced electric field, which could be done by time-resolved OES. The modification of the surface using nano-structured silica fibers on the wall to increase the atomic H adsorption could also bring confirmation of the surface processes hypothesis. The development of a plasma-surface interaction model to properly include walls is also an interesting lead. The influence of the t_p^{ON} on the CO and the CO_2 also remains an open question.

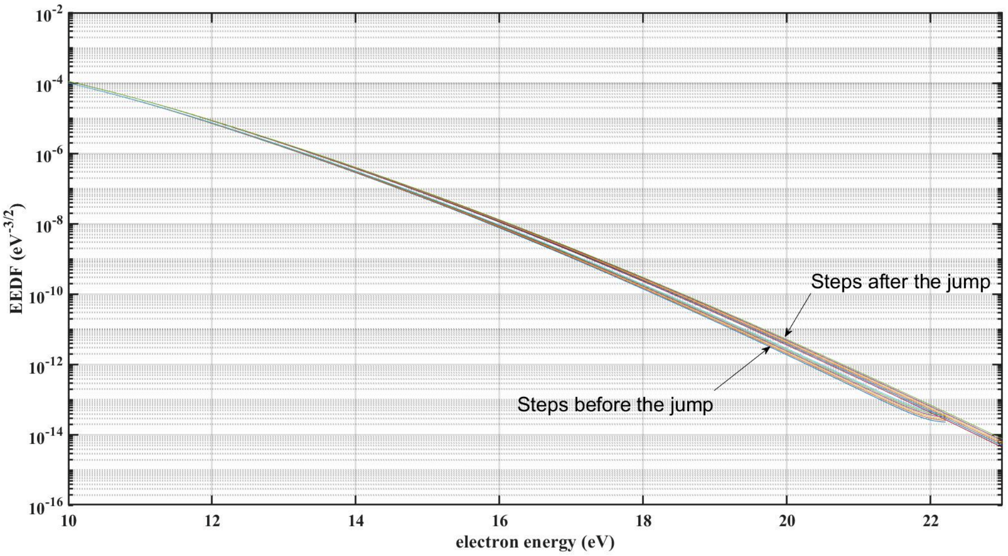

Figure 5.42: Evolution of the EEDF computed with LoKI in the test case (50:50 CO_2:CH_4, 5Torr, 500*1*50-50. The jump is occurs at step 46. The EEDF of steps 41 to 51 are plotted. Two distinctive group of EEDF are visible

Appendix

On figure 5.33, a sudden jump is seen on the rates close to 2.s of plasma ON time. The evolution of the EEDF over the steps close to the 'jump' is showed on figure 5.42. At each step, the EEDF is computed with LoKI using the output of the previous simulation as well as the reduced electric field taken from the temporal profile The jump correspond to the step when the range on which the EEDF is calculated is extended. Before the jump, the EEDF is calculated up to 22eV. At the jump, the EEDF is calculated up to 35eV. It was verified in several simulations that the jump always occurs when the EEDF calculation range is extended. The EEDF calculation range is chosen automatically by LoKI based on the electron cross-section threshold and the reduced electric field. The parameters for correct EEDF computation can be fixed but in this case, since 1000 EEDF are computed successively, it is seemingly better to let LoKI adjust to each case. The change of the total range changes the value of the rates, which in turn impact the chemistry, explaining why the jump seen of figure 5.33 is visible for all reactions, even the one which do not include electrons.

CHAPTER 6

Vibrational kinetics of a low-pressure CO_2-CH_4 plasma

Contents

6.1 Introduction

The vibrational excitation is at the heart of recent research of CO_2 conversion by plasma. The vibrational excitation has been studied since the 1970's for the CO_2 laser. The goal was to achieve population inversion with a $CO_2(v)$ level: the aim was to maintain vibrational excitation while avoiding dissociation. In the 1980's, measurements of the dissociation of CO_2 in a supersonic wind tunnel showed that an energy efficiency of 90% could be achieved A.Fridman 2008. These measurements demonstrated the interest of going through the vibrations to dissociate CO_2 instead of simply relying on electron impact dissociation. This information took a new importance in the wake of the recent effort of the community to achieve efficient CO_2 recycling for environmental purposes, which has to go through CO_2 reduction to CO. Numerous papers claim that CO_2 vibrational excitation is key to activate catalysts (S. Liu et al. 2020a) or to dissociate CO_2. It also gained interest with the relatively recent idea to use plasma for In Situ Ressources Utilization (ISRU) on Mars, where the goal is to form and collect O_2. In this

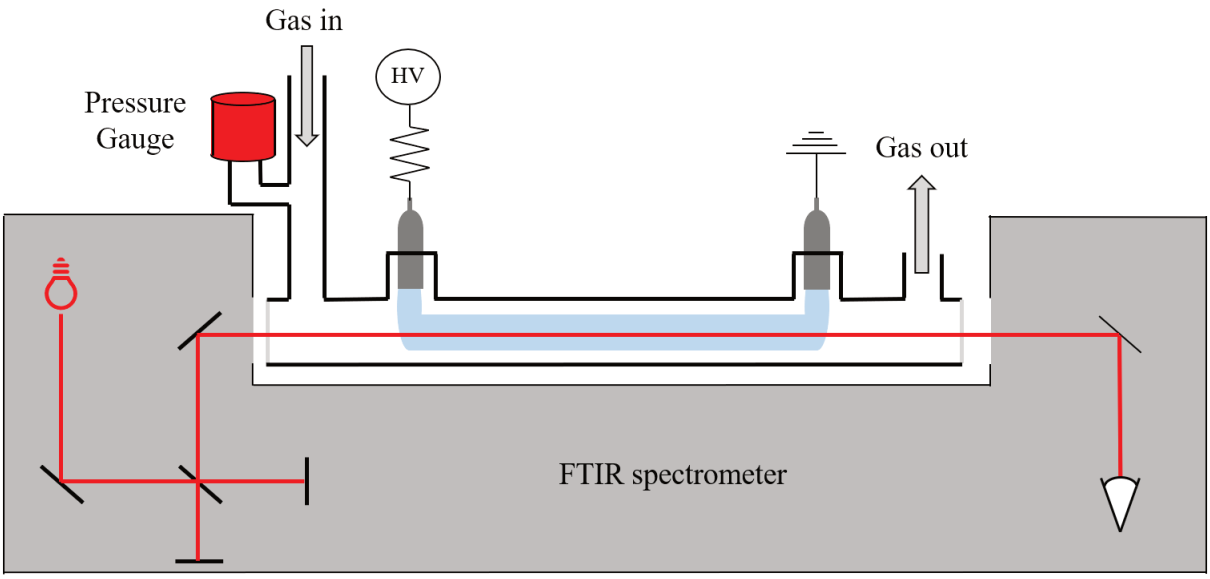

Figure 6.1: Scheme of the experimental setup

case, the low pressure environment of Martian atmosphere could help promoting vibrational excitation in plasma to help the CO_2 dissociation. Vibrational excitation is also important to describe accurately to achieve accurate calculations of EEDF. The low excitation threshold of vibrational modes will strongly impact the shape of the EEDF at low energy (<2eV), which will in turn impact the rate coefficients. A good description of any CO_2 containing plasma hence requires a good understanding of the vibrational excitation of at least CO_2 and CO. As already seen throughout this thesis, the low pressure DC glow discharge is an interesting test-discharge because of its homogeneity and because at low pressure vibrational excitation and relaxation is slowed down, meaning that the vibrational excitation can be observed with a ms temporal resolution. The vibrational excitation mechanisms in pure CO_2 discharge were explored in many works (A.-S. Morillo-Candas 2019,Pietanza, Colonna, and Capitelli 2022,Biondo et al. 2022,L.D.Pietanza et al. 2021,Kustova et al. 2021, among others). The main goals of this chapter is to explore the influence of methane and its byproducts on CO_2 and CO vibrations, and then to try to assess the influence of the CO_2 vibrations on the Dry Reforming of Methane.

What is the influence of the CH_4 and its by product (H,H_2, H_2O) on the CO_2 and the CO vibrations ?

To answer this question, the vibrational temperatures of CO_2 are studied in a low pressure CO_2-CH_4 plasma. The choice was made to measure the evolution of the temperatures during a pulse of 5ms, for several reasons: first, in pure CO_2, it is approximately the time it takes for the vibrational temperatures to reach a steady state. Second, following the time-variation gives information on the various time-scales of the processes at play, namely electronic to vibrational exchange (e-V), vibrational exchange between two different species (VV), vibrational exchanges between the modes of a specie (V-V') and vibrational to translation energy exchange (V-T) processes. Finally, using a pulse also allows to follow the relaxation when the plasma is turned off,i.e in the absence of e-V processes. In this chapter, the vibrational temperature of the mode ν_1 and ν_2 of CO_2 is noted T_{12}, the temperature of the mode ν_3 is noted T_3 and the vibrational temperature of CO is noted Tco.

6.2 Experimental Set-up and method

The experimental apparatus and the measurement method are described here. A drawing of the experimental setup is shown on figure 6.1. The reactor in this chapter is a cylindrical pyrex tube of diameter 2cm and of length 23cm like in chapters 2, 3 and 4.1. Two metal electrodes are placed on the side of the tube, each electrode being 1.5cm away from the cylindrical part

of the reactor (see figure 6.1) so that the successive dark and glow areas close to the electrodes are not in the cylindrical part of the tube. Only the positive column fills the axial part of the discharge tube. The distance between the 2 electrodes is 17cm, meaning that on each side of the plasma there is a 3cm long volume without plasma. Two channels are opened on the wall of the reactors perpendicularly to the cylinder axis. These channels serve as gas inlet and outlet. The cylinder part of the reactor is closed on both end by CaF_2 window. Gas is supplied in the reactor by 3 Bronkhorst flowmeters and is pumped by an Edward x10 pump. The pressure in the reactor is controlled by a Pfeiffer vacuum 100mbar gauge and maintained with the help of a Pfeifer automated valve (connected to the gauge).
In this study, plasma pulses of 5ms are sent. The pulses are ignited with the help of a custom made power supply, which can send square pulses of a few ms with a rising time of a few μs. The power supply is connected in serie to a 40 kΩ ballast resistor. The voltage is measured at the resistor and the current is inferred. The voltage is followed on a oscilloscope for every experiment.
The reactor is placed inside the sample compartment of a Brucker Vertex 70 Fourier Transform InfraRed (FTIR) spectrometer. The FTIR can measure the IR spectrum of the CO and CO_2 (between 2000 and 2500 cm^{-1}), from which the rotational and vibrational temperature of CO and CO_2 can be drawn, according to the procedure described in Klarenaar, Engeln, et al. 2017. In a few words, a transmittance spectrum is simulated and fitted using a custom Matlab code and the Matlab lsq (least square) function. To do so, the population of the vibrational levels are calculated for all levels of energy below 6eV, i.e up to $v_{i,max}$= [40, 70, 30, 35] for the 3 modes of CO_2 and the single mode of CO, using :

$$N_{V_i,j} = N * \Phi_{rot,J} * \prod_i \Phi_{vib,vi}$$

where v_i is the vibrational level, j the rotational level. Φ is the fraction of the population in the state (v_i,j) and N the total density of the specie whose population is calculated. The rotational fraction is calculated with a Boltzmann distribution:

$$\Phi_{rot,j} = \frac{g_{rot,j}}{Q_{rot}} exp(\frac{-hcE_{rot,j}}{k_B T_{rot}})$$

The degeneracies and energies are taken from HITEMP. The vibrational fractions are calculated using a Treanor distribution:

$$\Phi_{vib,vi} = \frac{g_{vib,vi}}{Q_{vib,i}} exp(\frac{-hc}{k_B}(v_i \frac{G_{1,i}}{T_i} - v_i(v_i-1)\frac{(\omega_e x_{e,i})}{T_{rot}}))$$

where $G_{1,i}$ is the energy difference between the first and last levels, $\omega_e x_{e,i}$ is the anharmonicity term, $g_{vib,vi}$ the degeneracy of mode v_i and Ti the temperature. $Q_{vib,i}$ and Q_{rot} are respectively the vibrational and rotational partition function, calculated so that:

$$\sum_{v_i=0}^{v_{i,max}} \Phi_{vib,vi} = 1$$

$$\sum_{j=1}^{j_{max}} \Phi_{rot,j} = 1$$

The linestrength S_k of a transition k is computed through:

$$S_k = \frac{I_a g_u A_{u1}}{8c\pi\nu_k^2} * (\frac{N_1}{g_1 N} - \frac{N_u}{g_u N}) \tag{6.1}$$

where I_a is the abundance of the isotope studied, g_1 and g_u are the degeneracy of the lower and upper levels. N_1 and N_u are the populations of the lower and upper level of the transition computed with the equations presented above, ν_j^2 in the transition energy. A_{1u} is the Einstein coefficient. Using the linestrength, a transition profile is computed through :

$$\sigma_k(\nu) = S_k * V(\nu) = S_k * G(\nu)\backslash L(\nu)$$

Where G and V are respectively a Gaussian and a Lorentzian profile, convoluted to form a Voight profile.Using Beer-Lambert's law, a transmission profile is computed:

$$T(\nu) = \prod_{n=n_{th}}^{n_{nth}} \prod_{f=f_{co}}^{f_{co_2}} exp(-Ln \sum_{j=1}^{j_{max}} \sigma_j(\nu))$$

The contribution of the CO and CO_2 in the non-plasma volume (the small 3cm long volume on each side of the plasma) is also taken into account, using three hypothesis are done. First in theses volumes, the gas has its own temperature, different from the gas temperature in the plasma. Second, the gas in this volume is thermalized (i.e Tvib=Tgas). Finally, the dissociation degree of CO_2 in this volume is the same as in the plasma (implying that CO is diffusing to that volume).

6.3 Experimental procedure

The aim of this experiment is to measure the evolution of the vibrational temperatures of CO and CO_2 during a pulse of 5ms. The FTIR can not perform this measurement over a single pulse with a good temporal resolution. To solve this problem, a reproducible system is chosen with gas continuously flowing in the reactor. A pulsed plasma is turned on, with pulses of 5ms followed by 10ms off. The system quickly reaches a pseudo steady state, where gas is flowed in and experiences during its residence time a few hundred pulses, before leaving the reactor and being replaced by new gas. Overall, the system is in a pseudo steady state where the dissociation is compensated by the gas flow. The FTIR is used in the so-called "Step-scan" mode. In this mode, the mobile mirror of the interferometer goes to a position, stabilises for 60ms and awaits for a trigger signal. After being triggered, the DC signal of the IR detector is repetitively read out with a certain period defined by the time resolution. The time-resolution and the number of time slices were set to 10 μs and 1100 respectively in most of our time-resolved experiments, which results in a measured time period of 11 ms. Each of this series per interferometer position was average four times. Subsequently, the mirror of the interferometer moves to the next position (53.323 in total), and the procedure is repeated. The Fourier transform of the 2D interferogram gives a time-resolved absorption spectrum of 10μs time resolution. Overall, the IR spectrum of the discharge is recorded over 10ms with a temporal resolution of 10μs. In practice, a pulse generator controls the triggering of the FTIR and the power supply. The pulse generator triggers the FTIR. If the FTIR is in "listening" mode (i.e after measuring and changing to the next interferometer position), the acquisition is started, otherwise the trig is ignored by the FTIR. Simultaneously, the pulse generator triggers a second slave generator which in turn sends a signal with an adjustable duration to the power supply. Because of the numerous positions that the mirror must assume, a measurement can last up to 2 hours for a single condition. Because the plasma is on the line-of-sight of the interferometer, the emission of the plasma must be subtracted to the recorded signal. To do so, a second measurement is taken but with the IR source turned off, which adds another 2 hours, totaling 4h pr condition. These measurements can be tricky because they are sensitive to any noise/malfunction over the 2*2h. Noise can appear in the interferogram due to vibrations in the vicinity of the FTIR, heating (no reliable points can be taken during the summer) or other sources difficult to control.
This type of measurement is referred to as 'repetitive step-scan'.

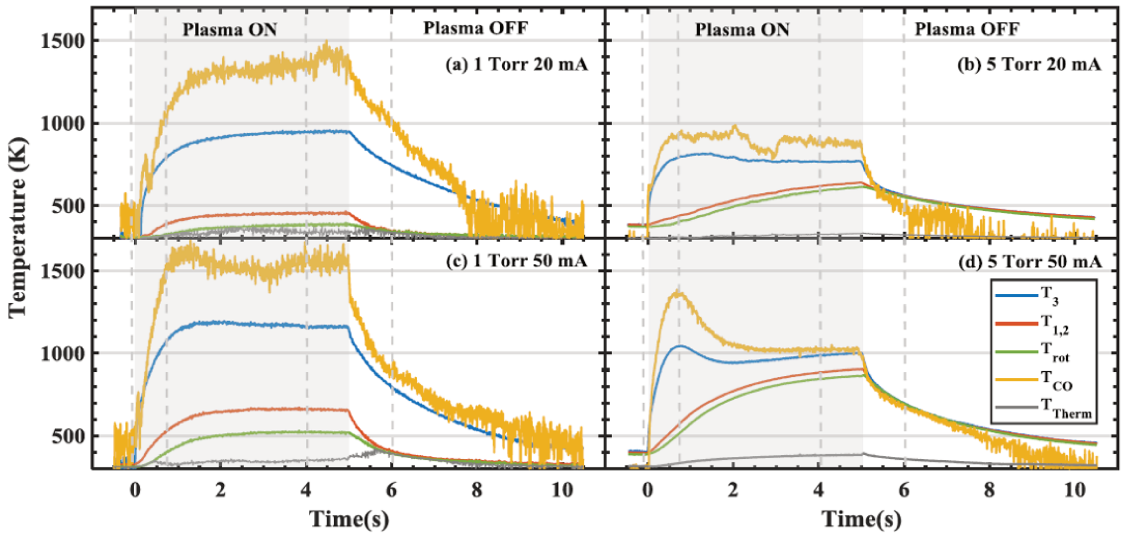

Figure 6.2: Variation of the rotational temperature of CO2, Trot, the temperature of the thermal volume TThem and the vibrational temperatures of CO2, T_{12} and T_3, and CO, Tco, versus time along a plasma pulse of 5-10 ms On-Off, for four different conditions of pressure and current: 1 Torr 20 (a) and 50 mA (c) and 5 Torr 20 (b) and 50 mA (d). Taken from A.-S. Morillo-Candas 2019

6.4 Previous work on CO_2

This experiment was previously ran in pure CO_2 (Klarenaar, Engeln, et al. 2017, A.-S. Morillo-Candas 2019). The conclusions of the work on CO_2 are summarized here. Figure 6.2, taken from A.-S. Morillo-Candas 2019, shows the evolution of the various temperatures (Trot, T_{12},T_3 and Tco) over a pulse of 5ms at 1 and 5 Torr for two different currents. In the low-pressure glow discharge, the rotational mode is at equilibrium with the translational mode, i.e Tgas=Trot. The rotational temperature, deduced from the IR spectrum fitting, is used to measure the gas temperature. First, as observed in the continuous plasma, the temperatures reached by the end of a pulse change with pressure: when going from 1 to 5Torr, the rotational temperature and T_{12} (the temperature of the first two vibrational modes of CO_2) increases and remain very close (often thermalized), while T_3 (the temperature of the third vibrational mode of CO_2) and Tco (vibrational temperature of CO) decrease with pressure. This is due to the increase of the VT (vibrational to translational) processes with pressure: the energy of v_3 is transferred to v_{12} and to the translational mode. The translational mode then mainly loses energy through cooling at the walls (main cooling mechanism in our plasmas) as shown in T. Silva et al. 2020 and A. F. Silva et al. 2020. The energy is also efficiently transferred from CO(v) to v_3 and further to the rotations because of the resonance between CO and $CO_2(v_3)$. At high pressure, Tco and T_3 go through a peak (after about 1ms) before going down and stabilizing at their final value. In A.-S. Morillo-Candas 2019, this peak was attributed to a chain of processes. Initially, the electron impact excitation increase the vibrational temperatures from the start of the pulse. The VT processes increase the gas temperature and become more and more important (the VT rate is usually increased by the gas temperature). Simultaneously, the VV processes transferring energy from CO(v) to $CO_2(\nu_3)$ take place, limiting the peak of Tco while increasing the one of T_3. A new balance is found with the electron impact processes approximately 1 ms after the peak. Information on the VT processes can be drawn from the post discharge: because there are no electron impact processes, vibrations are only quenched by the VT processes. The role of O atoms on the vibrations was clarified using this information and silica fibers. The silica fiber is a thin layer of micro-structured material placed against the inner wall of the reactor which considerably increase the available surface while keeping an identical volume and an identical reduced electric field. The fiber increases the recombination of O atoms into O_2 at the wall

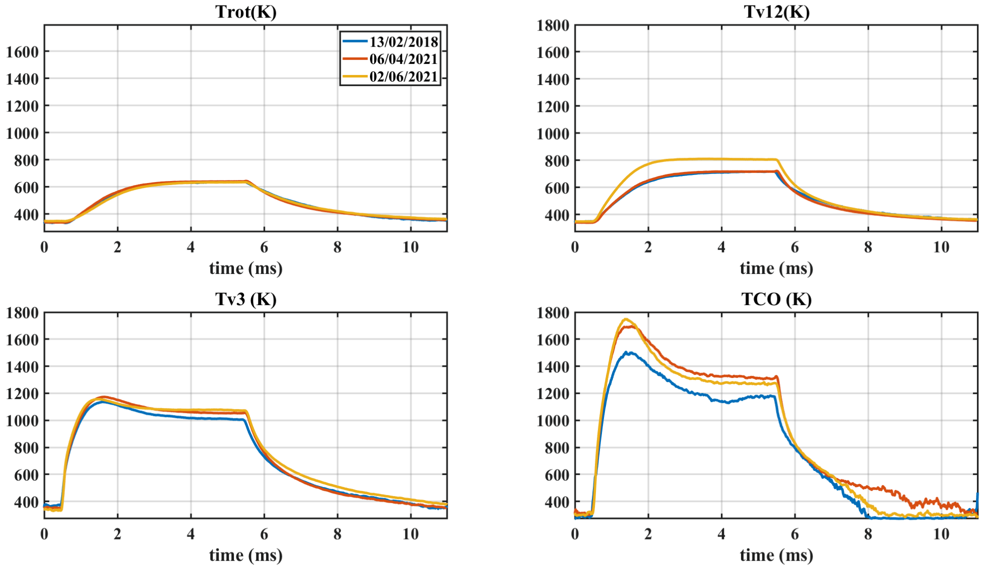

Figure 6.3: Example of the reproducibility of the repetitive step-scan measurement in pure CO_2 at 2 Torr, 50 mA

and thereby efficiently remove O atoms from the gas phase (A S Morillo-Candas, Klarenaar, et al. 2020). The comparison of the discharges and of the post-discharges in pure CO_2, in a mixture of CO_2-O_2 and using silica fibers revealed that O atoms were very efficient quenchers of the CO_2 and of the CO vibrations and that their removal from the gas phase increased the vibrational temperatures. The results of the single pulse experiment in pure CO_2 presented in Klarenaar, Engeln, et al. 2017 were later modeled in Grofulović et al. 2018 & Silva et al. 2018 and in Pietanza, Colonna, and Capitelli 2022 with two different models.
Pietanza, Colonna, and Capitelli 2022 developed a 0D time-dependant self-consistent model is a state-to-state vibrational kinetic model considering almost only the $CO_2(\nu_3)$ kinetics (ν_3^{max}=21) and a few levels of $CO_2(\nu_1, \nu_2)$. The model also included CO and O_2 vibrations. Electronic excited state of CO_2, CO, O_2 O and C were also considered. The model developed in Grofulović et al. 2018&Silva et al. 2018 (which will be reused in this work) is also a 0D self consistent model but includes a more complete vibrational kinetics of the CO_2 VV transfer while taking into account less asymmetric levels (ν_3^{max}=5). Both models were compared in Pietanza, Colonna, and Capitelli 2022 and were found to be in good agreement, though the first one seems to overestimate the electron density during the pulse, leading to higher population of excited states. The work of Grofulović et al. 2018 was recently completed by Biondo et al. 2022, which included more vibrational state as well as additional reactions concerning the electronically excited state. The model was there again compared to Grofulović et al. 2018 and to the experimental results from Klarenaar, Engeln, et al. 2017. The results reproduced correctly the gas temperature and highlighted the role of the VT in the gas heating, but also highlighted that some grey areas remain in the comprehension of the vibrational energy transfers.

The reproducibility of the results obtained in pure CO_2 was tested again during this work to ensure that the new measurements could be reliably compared with previous work. A measurement of a repetitive step-scan at 2Torr, 50mA in pure CO_2 was taken twice over several months. It is compared to the results shown in Klarenaar, Engeln, et al. 2017 (from February 2018) on figure 6.3. The blue curves on figure 6.3 correspond to a measurement taken with the same experimental setup in 2018. The yellow and red measurements were taken 4 years apart from the blue and 2 months apart from each other. The spread of the rotational temperature is about 10K. T_{12} shows a difference of maximum 80K. The reason of this difference remains unclear as the reproducibility on T_{12} is expected to be close to the one on Trot. Nevertheless, the difference remains very low. The spread of T_3 is of approximately 60K, corresponding to the error bars on T_3 measured in A.-S. Morillo-Candas 2019 for the same experiment. Tco exhibits the largest difference between the measurement taken in 2018 and the ones from 2021, with a maximum difference at the peak of 190K. At the end of the pulse, the difference between the measurement from 2018 and the one from 2021 is only of approximately 100K, which correspond to the error bars attributed to the Tco measurement in A.-S. Morillo-Candas 2019. The difference of Tco at the peak could have physical origins. The measurement from 2018 and from 2021 were taken in different reactors which had different surface states. The measurement is taken at 2Torr, where the loss of vibrational energy to the surface could still play a role. Finally, the difference is seen mainly for Tco, whose peak depends on a balance between different vibrational energy transfer, which would support a stronger loss at the wall due to the surface state in the old reactor. Overall, the reproducibility of the experiment is very good, even over several years and in different reactors.

6.5 CH_4 vibrations

One question steer this work: what is the influence of the CH_4 and its by-products (H,H_2, H_2O) on the CO_2 and the CO vibrations ? As presented in the introduction, the CH_4 vibrations are quite complex: CH_4 has 4 vibrational modes, two of them triply degenerated. Overall, the thermalisation of the different vibrational modes of CH_4 is very fast. It was estimated in Butterworth et al. 2020 that the intra-polyad relaxation (VV relaxation) at 0.1mbar are on the order of magnitude of 5μs which is very short for a pressure 10 to 100 times lower than the ones of this work. Older measurements of this rate had been done in De Vasconcelos et al. 1977 and found a VV rate of 0.4μs at atmospheric pressure. As a results, the different CH_4 vibrational modes are considered to be always at equilibrium, meaning that in cases with plasma pulses longer than 5ms, a single vibrational temperature is sufficient to describe the CH_4 vibrational distribution. Generally speaking, the vibrations of methane are quite difficult to study. To properly resolve the vibrational structure of some bands of CH_4, Louviot et al. 2015 used a hyper-sonic jet free expansion system with Ar as a carrier gas. As a result, the rotational temperature of CH_4 was cooled down to 13K, while the vibrational excitation could not efficiently relax and reached T_{vib}=2000K.
The current fitting algorithm does not include CH_4 vibrational excitation. Few data are available on HITEMP for CH_4 vibrational excitation. The highest levels are (0300),(0020) and (0004). No vibrational excitation of ν_1 is reported. No alternative solution for fitting CH_4 (v) are available to the best of my knowledge: the python code RADIS developed in Pannier et al. 2019 for fitting of out-of-equilibrium CO_2 currently does not allow for fitting of the vibrational distribution of CH_4 either. Before including the fitting of vibrationally excited CH_4 and modifying the code, indications of vibrational excitation were searched in the IR spectras. The following figure shows the methane spectrum taken in the middle of a 5ms pulse in a 50:50 CO_2-CH_4 discharge at 1Torr (where the vibrational excitation is expected to the highest among the studied conditions). The spectrum is superimposed with a simulated CH_4 spectrum at equilibrium at 440K, the rotational temperature measured from the CO_2 part of the spectrum. The simulation is very close to the experiment. A difference can however be observed around 3050 $cm^{-}1$, where four peaks emerge from the noise in the residuals. The value of the residuals is however very weak (below 0.01) compared to the absorbance measured at this peaks (close to 0.15), showing that there is no significant divergence from the Boltzmann distribution and that error done when fitting at equilibrium is very small. This indicates that the CH_4 vibrational temperatures are probably very close to the gas temperatures and that the assumption that CH_4 is thermalized can be done, in good agreement with literature results. Butterworth et al. 2020 measured VT relaxation rates of CH_4 in a microwave discharge at 25mbar (supposedly suited to create out-of-equilibrium distributions) and found a characteristic time of 15μs for VT from the second polyad P_2 to the first polyad P_1 and of 50μs for the relaxation from the first polyad P_1 to polyad 0. This means that vibrational excitation is unlikely to build-up in the plasma, confirming our

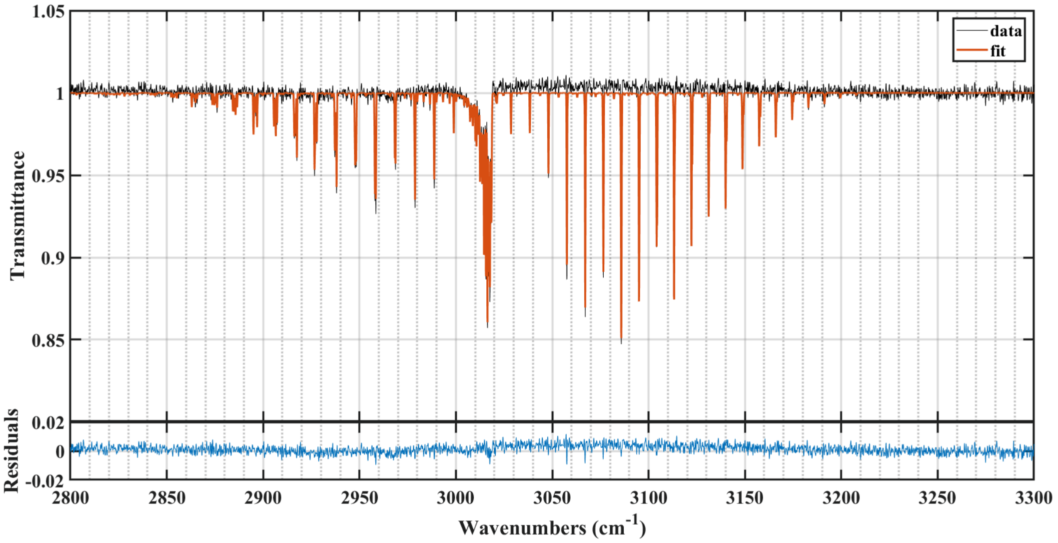

Figure 6.4: Comparison of the measured spectrum and of a simulated spectrum 4s after the beginning of the pulse during a 5ms in a 50:50 CO_2-CH_4 discharge at 1 Torr. The simulated spectrum is at equilibrium at T=440K. The residuals are plotted below

Pressure	1,2,3,5 Torr
Mixture	100:0 / 90:10 / 75:25 / 50:50 CO_2:CH_4
Current	50mA
total flow	7.4sccm
Duty cycle ratio	1/3

Table 6.1: Conditions tested in the step-scan measurement

results: the CH_4 vibrational temperature in the plasma is very likely thermalized with the rotational temperature. The CH_4 vibrations will therefore not be studied a focus of the rest of this work.

6.6 Determination of plasma composition

Before looking at the evolution of vibrational temperatures during the plasma pulses, it is important to know what is the gas composition obtained with this pulsed discharge. The plasma composition is presented more in details in the chapter 4 but to properly pursue the analysis of the vibrational kinetic, an idea of the content of the CO_2-CH_4 plasma must be given. Using a modified version of the algorithm from Klarenaar, Engeln, et al. 2017 (presented in more details in the chapter 3), the composition of the plasma is measured by fitting the spectrum before the beginning of the pulse, when all the temperatures are at equilibrium. In this work, the pressure is varied between 1 and 5Torr and the initial mixture sent in the reactor is changed. In all of these measurements, the glow discharge current is set to 50mA to maximize the vibrational excitation. It was indeed shown in Klarenaar, Engeln, et al. 2017 that increasing the current did not change the trends but mostly increased the value of the temperatures. The total flow is set to 7.4sccm, equivalent to 22.4sccm in the continuous glow discharge because here the plasma is pulsed with a duty cycle ratio of 1/3rd. The conditions tested are summarized in table 6.1. The composition of the plasma in some of these conditions is presented on figure 6.5. The fractions of the main species (CO_2, CO, CH_4, H_2 and H_2O) in the plasma are presented as a function of the initial mixture at 2Torr ('x' markers) and 5Torr (triangle markers). The composition is almost the same in both cases (and at the other pressures 1,3 and 4 Torr not plotted here): the plasma composition is little impacted by the change in pressure as already observed in pure CO_2

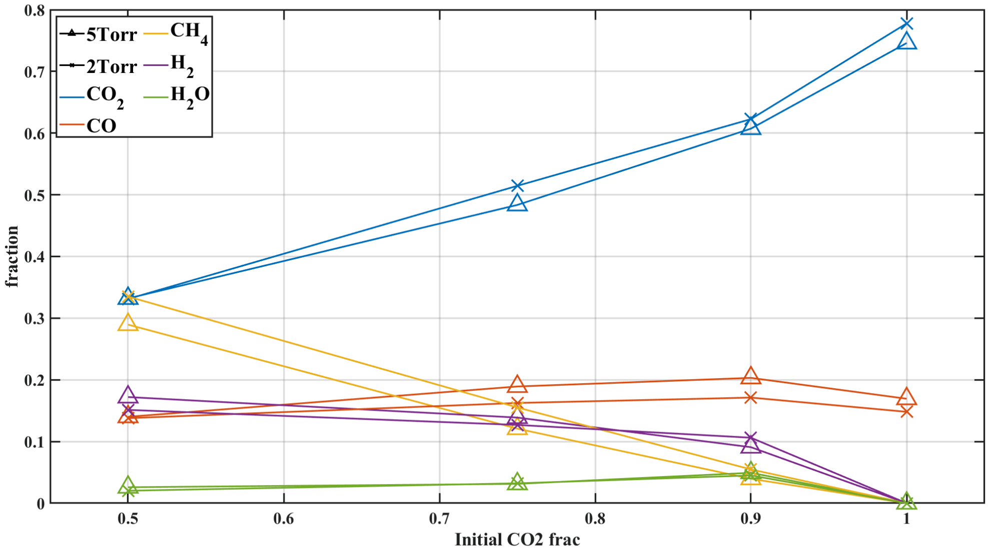

Figure 6.5: Evolution of the fractions of the main species of a CO_2-CH_4 plasma at 2 (x markers) and 5Torr (triangle markers) as a function of the initial CO_2 fraction in the gas sent in the reactor. The composition is fitted from the spectra before the beginning of the pulse.

or in chapter 3. Starting from the pure CO_2 case on the right of the plot, the CO_2 fraction in the plasma continuously decreases with addition of initial CH_4, going from 75% in pure CO_2 to 35% in 50:50 CO_2:CH_4, while the CH_4 fraction in the plasma logically continuously increases, reaching approximately 30% of the gas density in the case of a 50:50 initial CO_2:CH_4 mixture. Similarly, the H_2 fraction increases when increasing the initial CH_4 content, reaching 17% of the gas density in the 50:50 case. The CO and the H_2O both go through a maximum in the 90:10 initial CO_2:CH_4 case, before going back down for higher initial CH_4 content. The CO peaks at 20%, and the water at 4%. The atom densities were determined with actinometry. The light emission being too weak during the 5ms pulse to draw above-noise ratio, the atomic H and O were measured in the continuous case and estimated in the pulsed experiment based on the H_2(Continous)/H_2(pulsed) and O_2(Continous)/O_2(pulsed). The O atom density, up to 6% of the gas density in pure CO_2, drops upon admixture of CH_4. It accounts for less than 1% of the gas density in the 90:10 CO_2:CH_4 mixture and is below actinometry detection limit for higher initial CH_4 contents. The H atom density increases with the CH_4 content but remains lower than 1% in the 50:50 CO_2:CH_4 case.

6.7 Temporal evolutions of vibrational temperatures

The evolution of the rotational and vibrational temperatures of CO_2 and CO are studied in conditions of table 6.1. To fit the vibrational temperatures, the densities of species other than CO and CO_2 are fixed during the pulse, and the atomic densities are neglected. To explore the two dimensions varied (pressure and mixture), the effect of the mixture will first be shown at 5Torr, where the temperatures are more quickly thermalized. The pressure will then be varied.

5Torr The effect of the mixture on the rotational temperature at 5Torr is first shown on figure 6.6. The value of the temperature at the end of the pulse decreases with the increase of CH_4 in the initial mixture, going from 850K in pure CO_2 to 650K in 50:50 CO_2-CH_4. This lower temperature could results from either a lower heating or from a more efficient cooling. The heating (due to relaxing vibrations) is expected to be similar in CO_2 and CO_2-CH_4 plasmas: the reduced electric field are similar (cf chapter 4) and the excitation threshold of CH_4 and CO_2 vibrations are close. Even though the vibrational excitation cross-section of CO_2 are higher

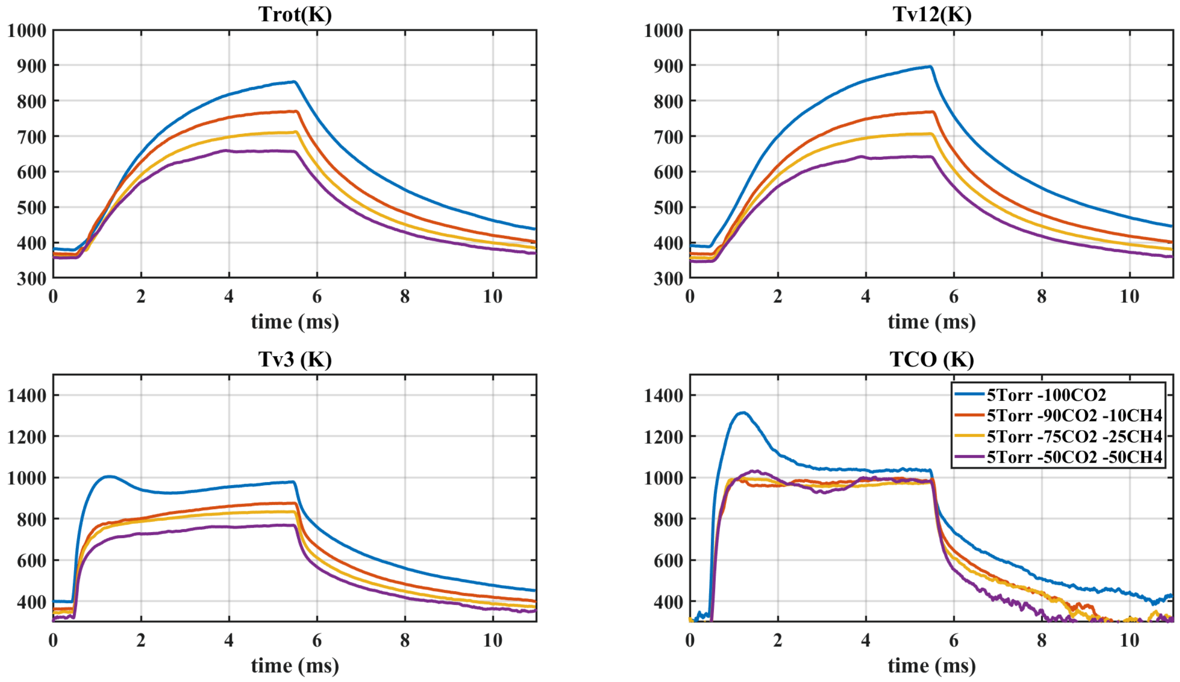

Figure 6.6: Evolution of the rotational temperature (top left), the CO_2 vibrational temperatures T_{12} (top right) and T_3(bottom left) and of the CO vibrational temperature (bottom right) during a pulse of 5ms. The pressure is set to 5Torr, the initial mixture is varied

Gas	Thermal conductivity at 500K ($mW.m^{-1}.K^{-1}$)
CO_2	33.5
CO	39.2
CH_4	66.5
H_2	230 (value at 400K)
H_2O	35.7

Table 6.2: Thermal conductivity of different gases. Taken from *Thermal Conductivity and heat transfer* n.d.

than the ones of CH_4, the strong VT relaxation should contribute to efficient heating of the gas. The efficient cooling seems more probable. As mentioned in A. F. Silva et al. 2020, the main heat loss in pure CO_2 is the cooling at the wall. If wall cooling remains the main process, this means that the heat is better evacuated to the wall in CO_2-CH_4 mixtures. The thermal conductivity of the gas mixture was therefore calculated. Out of the several formulas available for the computation of the thermal conductivity of a gas mixture, Perry's formula was used (taken from Green et al. 2019). The thermal conductivity λ of the mixture is given by:

$$\lambda = \frac{\Sigma^i yi\lambda_i M_i^{1/3}}{\Sigma^i yi M_i^{1/3}} \tag{6.2}$$

where λ_i is the thermal conductivity of gas i, M_i the molecular weight and y_i is the molar fraction of specie i. The thermal conductivity are taken from *Thermal Conductivity and heat transfer* n.d. and are given in table 6.2.

Using this approximation and the composition measurement showed on figure 6.5, the thermal conductivity of the gas in the pure CO_2 plasma at 3Torr and 50mA was estimated to be about 40.10^{-3} W/(m.K), while the thermal conductivity of the gas in the reactor in the CO_2-CH_4 plasma was estimated to be around 70.10^{-3} W/(m.K). This means that in the case CO_2-CH_4 case, the heat is much better evacuated to the wall, which is consistent with the

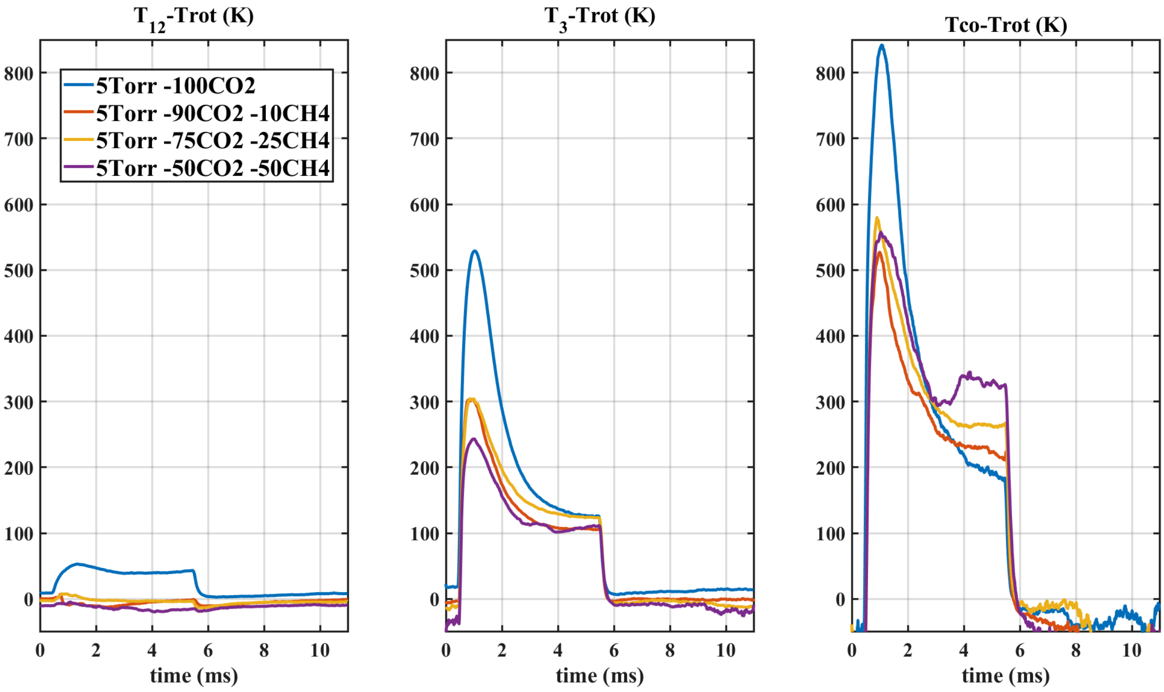

Figure 6.7: Evolution of T_{12}-Trot (left), T_3-Trot (center) and (Tco-Trot) (right) during a pulse of 5ms. The pressure is set to 5Torr, the initial mixture is varied

experimental observation. The decrease of Trot with the increase of CH_4 in the initial mixture could therefore be partially due to the thermal conductivity of the mixture. It is interesting to note that the thermal conductivity of the CH_4 is of the same order of magnitude as the CO, but that the conductivity of H_2 is one order of magnitude higher. The increase of λ is hence mainly due to H_2.

The vibrational temperatures at 5 Torr are shown on the other panels of figure 6.6. T_{12}, plotted on the top right graph, decreases with the initial CH_4 content similarly to Trot, plummeting from 900K in pure CO_2 to 650K in 50:50 CO_2:CH_4. For all cases with initial CH_4, T_{12} is thermalized with Trot, whereas it is still some 40-50K higher than Trot in pure CO_2. The decrease of the gas temperature should lower the rate of the VT processes and maintain the vibrational excitation but the opposite is seen. This probably means that the VT processes are much stronger than in pure CO_2. The thermalization of T_{12} being already seen at 10% of initial CH_4, the VT could be much stronger than in pure CO_2. T_3 (plotted on the bottom left panel) also decreases with the increase of initial CH_4 in the mixture, going from 980K in pure CO_2 to 740K at 50:50 CO_2:CH_4, probably again due to the VT. Interestingly, the peak in T_3 previously reached at 1ms in pure CO_2 disappears upon admixture of CH_4. This peak was attributed to delay between the electron impact excitation and the VT processes, which became strong enough only when Trot became high enough. When CH_4 is present in the initial mixture, the VT processes are very efficient from the start. Tco, on the right bottom graph, presents a large peak in pure CO_2, which does not appear anymore upon addition of 10% of CH_4 in the initial mixture. Contrarily to T_3, the final values of Tco are very close in pure CO_2 and in 50:50 CO_2:CH_4. A small decrease in Tco is observed between pure CO_2 and 90:10 case, but the difference is barely of 30K, below the error bars of the FTIR on Tco (70K), so the final value of Tco can be considered constant.

More information can be drawn from the difference between the vibrational temperatures and the rotational temperature $Tvib - Trot$, plotted on figure 6.7, which shows how out-of-equilibrium is each temperature during the pulse. The first graph of figure 6.7 shows the value of $|T_{12} - Trot|$. While the pure CO_2 case is slightly out of equilibrium ($|T_{12} - Trot| \sim 50K$), T_{12} is at equilibrium in all mixtures including initial CH_4. T_3-Trot is plotted on the central

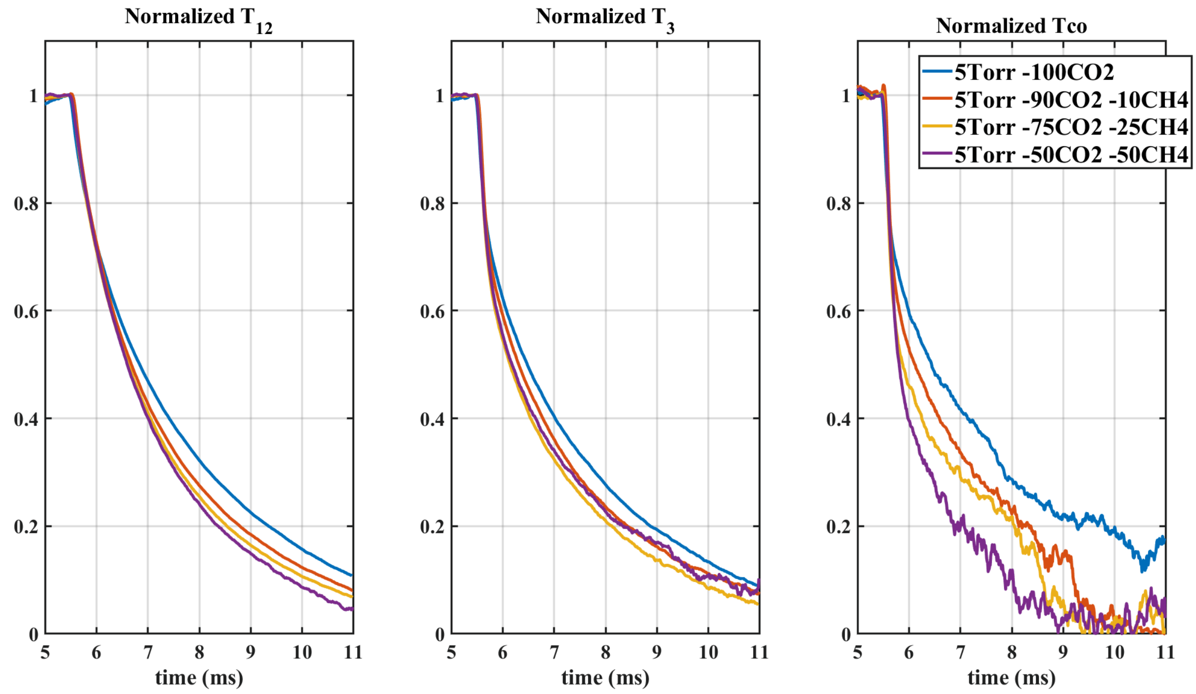

Figure 6.8: Evolution of the normalized T_{12}(left), T_3 (center) and Tco (right) during a pulse of 5ms. The temperatures are normalized on their values at the end of the pulse. The pressure is set to 5Torr, the initial mixture is varied

subplot of figure 6.7 and still shows a peak in all the measured conditions, meaning that the dynamics of electron impact excitation compensated by VT process and VV processes described in pure CO_2 is still applicable in CO_2:CH_4 plasma, but that the evolution of Trot masks it. The third panel of figure 6.7 shows the difference between Tco and Trot over time in the different mixtures. During the pulse, the difference Tco-Trot shows a peak for all the conditions, similarly to T_3-Trot. At the end of the pulse, the final value of the difference between Tco and Trot is higher in the cases containing CH_4 than in pure CO_2. It also appears quite clearly that the gap between Trot and Tco increases with the initial CH_4 percentage: 190K in pure CO_2, 220K at 90:10, 270K at 75:25 and 320K at 50:50. This means that the more initial CH_4, the more Tco is out of equilibrium. Therefore the lower Tco in CH_4 containing mixtures compared to pure CO_2 is due to the lower rotational temperature, not to a lower excitation.

Additional insights can be found when analyzing the post-discharge. The post-discharges (which has no electron impact reactions) are normalized and plotted on figure 6.8. The normalization point is the end of the pulse so that the characteristic relaxation time of the vibration can be observed. It appears quite clearly that the more CH_4 in the initial mixture, the faster the decrease of the vibrational temperatures for T_{12}, T_3 and Tco. This points toward strong VT process with CH_4 or its by-products. It is interesting to note that the collision partners of the CO_2 VT processes change in the various case. In the 90:10 CO_2:CH_4, the mixture has much more CO_2 than CO, and the hydrogenated species are mostly H_2 followed by similar amounts of CH_4 and H_2O. The densities of atomic O and H are comparable. In the 50:50 case, the CO and CO_2 densities are not very different and the main hydrogenated specie is by far CH_4. It can be considered that no more O atoms remain in the gas phase while atomic H remains. This means that all CH_4 by-products are efficient quenchers of CO_2 vibrations. This quenching is consistent with what can be found in literature. In W.J.Witteman 1986, the relaxation rate constants of T_3 with several other species are given: the rate of VT relaxation for CO_2 colliding with CO_2 is estimated to 350 $torr^{-1}s^{-1}$ and the rate of relaxation of CO_2 with H_2O is estimated to 24 $000^{-1}s^{-1}$, meaning that 1% of water would already have a very strong quenching. Other values available in literature also attribute a much higher CO_2 quenching by water than by

CO_2. Lopez-Puertas et al. 2001 also reports a 10^2 factor between the two.

The decrease of the vibrational temperatures, the decrease of the difference between the vibrational temperatures and the rotational temperature and the fast decay time in the post-discharge all point toward an increase of the V-T processes upon admixture of CH_4 in the plasma. The increase of Tco-Trot is therefore not due to less efficient quenching, but must rather be due to an excitation process of CO. It is all the more surprising because, due to the resonance between CO(v) and $CO_2(v_3)$, the vibrations of CO are expected to transfer energy to the CO_2 and the vibrational temperatures Tco and T_3 are expected to follow similar trends. So far, no clear excitation process of CO can be identified to explain this effect on Tco.

At 5Torr

- Upon addition of CH_4 in the initial mixture, the rotational temperature of the gas decreases, probably due to the high thermal conductivity of the CH_4 and of the H_2.
- Increasing the initial CH_4 percentage lowers the final values of T_{12} and T_3 but leaves the final value of Tco stable
- The decay of the vibrational temperatures in the post-discharge points toward strong VT processes between the CO_2 and the CH_4 and its by-products
- The addition of methane in the mixture seems lead to Tco being more out of equilibrium despite the strong VT

3Torr Because of the VT decrease at lower pressure, a higher vibrational excitation of CO_2 should be found at 3 Torr. The evolution of the temperatures during the pulses at 3Torr are shown on figure 6.9. Similarly to the 5Torr case, the rotational temperature decreases with admixture of CH_4 in the initial mixture, going from 700K in pure CO_2 to 570K at 50/50 CO_2:CH_4. The vibrational temperature of the CO_2 v_1 and v_2 decrease also with addition of CH_4 in the initial mixture, going from 750K in pure CO_2 to 570K in the 50:50 CO_2:CH_4 case. In this case, T_{12} seems to "saturate", i.e T_{12} is identical in the 75:25 and in the 50:50 CO_2:CH_4 case. In reality, in both these cases, T_{12} is thermalized with Trot. The reason of the similar Trot in both cases is unclear, and goes against the idea of the thermal conductivity evoked higher: the amount of H_2, excellent thermal conductor, and of CH_4, second best conductor, increases in the 50:50 CO_2:CH_4 case compared to the 75:25 CO_2:CH_4 case. The thermal conductivity should therefore be higher and the temperature would be expected to decrease further. The decrease of Trot due to the thermal conductivity of the mixture could be counterbalanced by strong VT processes in the 50:50 CO_2:CH_4 case, due for example to the large amount of atomic H or H_2O. These processes could contribute to the rotational heating of the gas and explain the similar temperatures. Like at 5Torr, T_3 decreases when increasing the initial CH_4 percentage (from 980K in pure CO_2 to 780K at 50:50 CO_2:CH_4). Contrarily to the previous case where the CO_2 T_3 peak was never visible in CO_2-CH_4, a very small peak is seen in the 90:10 CO_2:CH_4 case, but is extremely weak. The main difference is found on Tco, shown on the fourth panel of figure 6.9. On this panel, only the pure CO_2, 90:10 and 50:50 cases are presented because the Tco in the 75:25 case could not be fitted due to noise on the interferogram. In the 50:50 case, the vibrational temperature of CO is much higher than in the pure CO_2 case (1300 vs 1050K). This could be due to either efficient excitation of CO in CO_2-CH_4 plasma or to a decrease of one or several of the loss channels. The trends of Tco and T_3 with initial CH_4 % are very different despite the resonance between CO(v) and CO_2 (ν_3). This could partly come from the dilution in the CO_2-CH_4 mixture, which limits the transfers between CO and CO_2, or from a process exciting only CO. The influence of the CH_4 and its by products is once again seen on the post-discharge, normalized and plotted on figure 6.10. It is here again clear that by increasing the initial amount of CH_4 in the mixture, the vibrations of both CO and CO_2 are

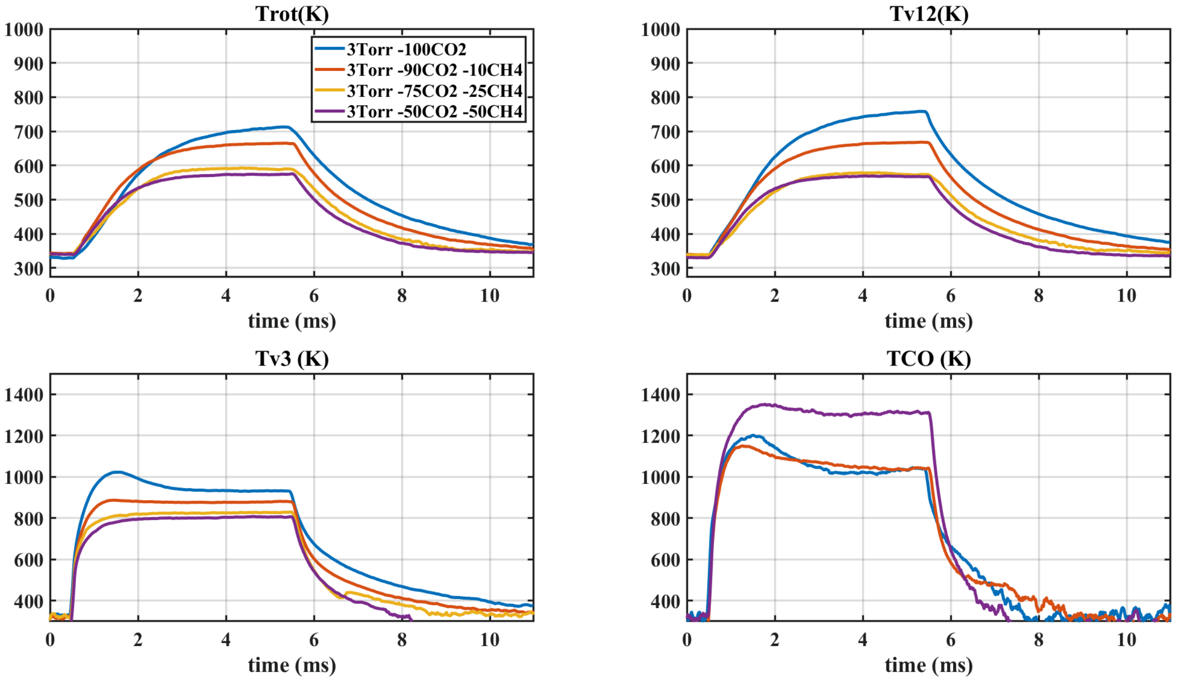

Figure 6.9: Evolution of the rotational temperature (top left), the CO$_2$ vibrational temperatures T$_{12}$ (top right) and T$_3$(bottom left) and of the CO vibrational temperature (bottom right) during a pulse of 5ms. The pressure is set to 3Torr, the current is 50mA and the initial mixture is varied

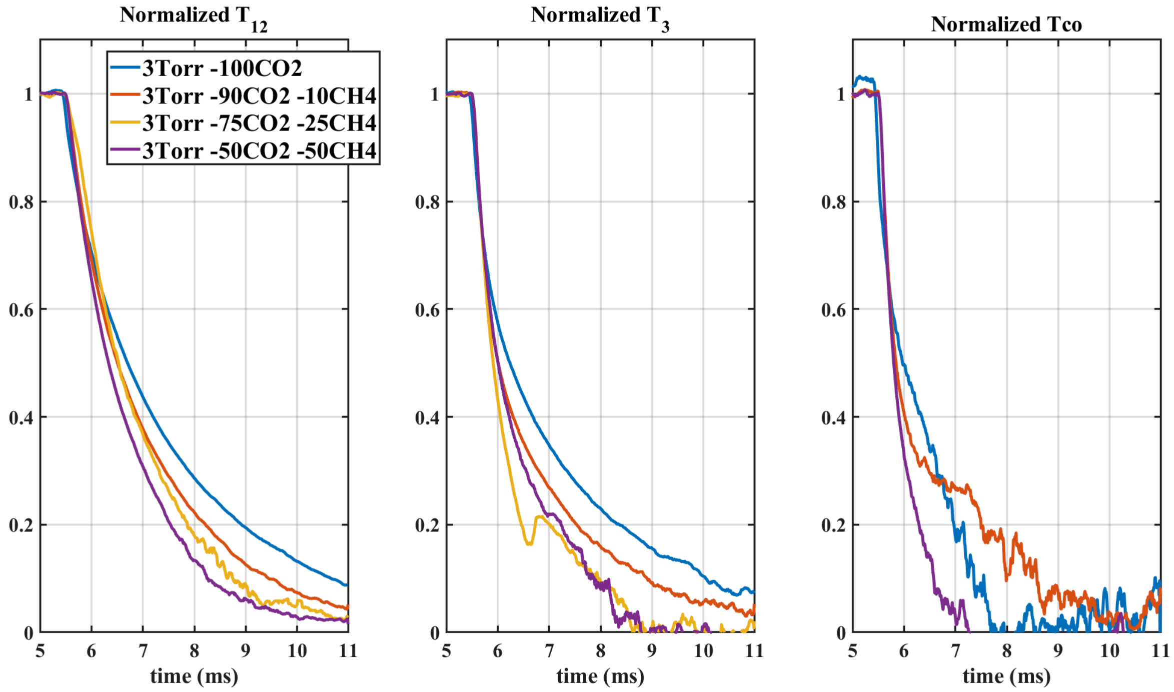

Figure 6.10: Evolution of the normalized T$_{12}$(left), T$_3$ (center) and Tco (right) during a pulse of 5ms. The temperatures are normalized on their values at the end of the pulse. The pressure is set to 3Torr, the initial mixture is varied

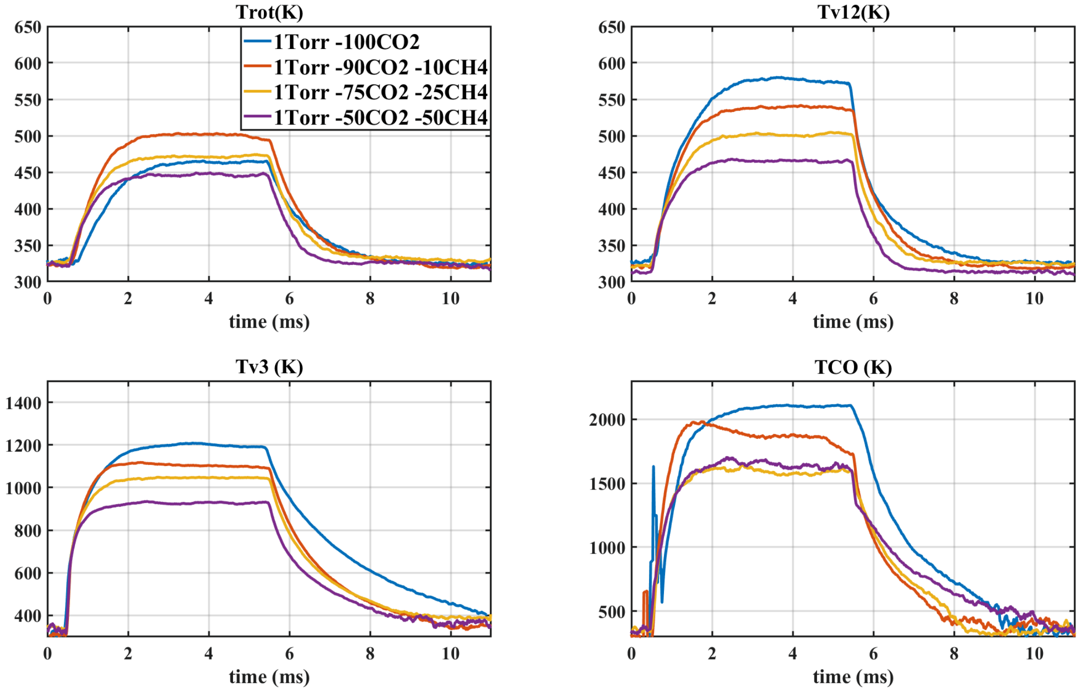

Figure 6.11: Evolution of the rotational temperature (top left), the CO_2 vibrational temperatures T_{12} (top right) and T_3(bottom left) and of the CO vibrational temperature (bottom right) during a pulse of 5ms. The pressure is set to 1Torr, the current is 50mA and the initial mixture is varied

quenched faster and faster, proving that the increase on Tco is not due to a quenching smaller in CO_2-CH_4 than in CO_2 but rather to excitation. The identification of the excitation process is very important for DRM. storing a lot of energy on excitation of products of conversion of CH_4 is detrimental to the global energy efficiency. On the other hand CO being easier to excite than CO_2 the resonnant vibrational energy transfer to CO_2 could also help achieving better conversion of CO_2. In any case, it would be interesting to understand and control the process populating CO vibrations so efficiently.

At 3Torr

- Upon addition of CH_4 in the initial mixture, the rotational temperature of the gas initially decreases but stabilizes for high initial CH_4 percentage, maybe due to the strong VT processes
- The strong VT processes are confirmed again by the normalized post-discharge
- Despite the VT processes, Tco increases in the 50:50 CO_2:CH_4 case compared to the pure CO_2 case because of an unknown excitation process.

1Torr The pressure is lowered to 1Torr, where the out-of-equilibrium degree is maximal in pure CO_2 (in our experiment). The evolution of the rotational temperature is plotted on figure 6.11. The rotational temperature does not follow the same evolution as for the other pressures. In this case the rotational temperature at 1Torr in pure CO_2 is 464K, rises to 500K in a 90:10 CO_2:CH_4 mixture before going back down to 470K in the 75:25 case. Trot then decreases to 445K in the 50:50 case. The cause of this trend is unclear but in any case, the variation is of approximately 35K, i.e in the 30K error bars on T_{rot} measured with FTIR. The pure CO_2 case has been measured many times over several years and T_{rot} in this condition was already

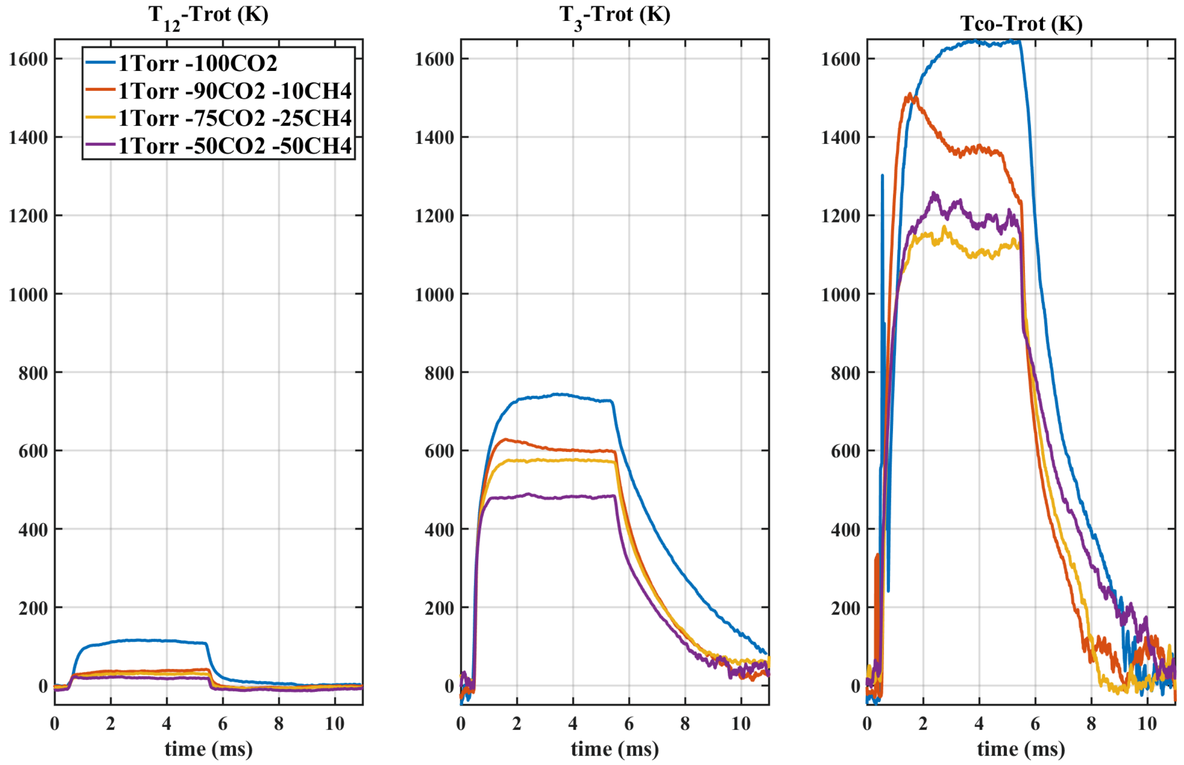

Figure 6.12: Evolution of T$_{12}$-Trot (left), T$_3$-Trot (center) and (Tco-Trot) (right) during a pulse of 5ms. The pressure is set to 1Torr,the current to 50mA and the initial mixture is varied

measured as high as 510 K. The variation observed here on T$_{rot}$ is therefore not considered significant. The vibrational temperature T$_{12}$ follow the same order as for other pressures: it decreases with the growing initial CH$_4$ content, going from 575K in pure CO$_2$ to 460K in the 50:50 CO$_2$:CH$_4$ case), which is again consistent with strong VT processes. In the CO$_2$-CH$_4$ cases, T$_{12}$ is not quite thermalized, but about 20 to 30K systematically above T$_{rot}$, even though close to the error bars. The ordering of T$_{12}$-T$_{rot}$, plotted on figure 6.12, is the same as the one of T$_{12}$, meaning that the less initial CH$_4$, the further is T$_{12}$ from equilibrium, even though it is very weak. T$_3$ is still much higher than T$_{12}$ in all the cases (like in pure CO$_2$) and follows the same trend: T$_3$ decreases with addition of initial CH$_4$ (dropping from 1200K in pure CO$_2$ to 900K in at 50:50 CO$_2$:CH$_4$). The evolution of T$_3$-Trot with the mixture is the same as at higher pressure. Finally, the effect seen at 3 Torr on Tco is no more. Tco, plotted on the bottom right plot of figure 6.11, is now higher in pure CO$_2$ and decreasing upon admixture of CH$_4$ in the initial mixture. The difference between Tco and Trot, shown of figure 6.12 does not show an increase of the out-of-equilibrium degree of CO. The more initial CH$_4$, the closer is Tco to being thermalized with Trot. Noise on the beginning of the pulse prevent further analysis of the rise of Tco in pure CO$_2$. The 90:10 mixture is the only CO$_2$-CH$_4$ case that exhibit a peak on Tco, about 1 second after the beginning of the pulse, indicating like at 3 and 5 Torr, that the VV processes are increased in CO$_2$-CH$_4$ mixtures upon addition of CH$_4$ in the initial mixture and are stronger than the ones observed pure CO$_2$.

At 1Torr

- The evolution of the rotational temperature is unclear but in a very limited range
- The strong VT processes quenching the CO$_2$ are still observed
- The excitation of CO previously observed is not seen here anymore

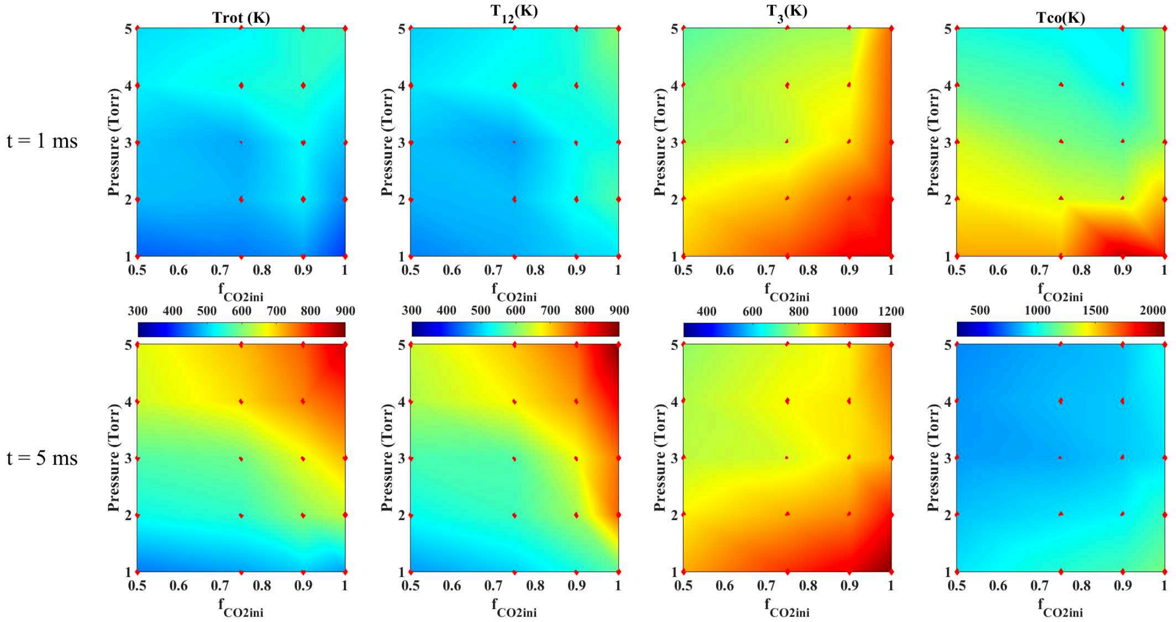

Figure 6.13: Temperature "maps" of the temperatures in the pulse at two different times: 1ms (close to the peaks) and 5ms (end of the pulse) as a function of the pressure and the initial CO_2 fraction

To summarize, the conclusion that can be drawn from the experimental pressure and mixture variation is that, for a given pressure, the rotational and vibrational temperatures reached during a pulse of 5ms are lowered when increasing the initial CH_4 percentage. The decrease of the rotational temperature could be partially due to the increase of thermal conductivity of the plasma due to the formation of very conductive H_2 but could be in some cases balanced by the strong VT processes. The vibrational temperature of CO is lowered by addition of initial CH_4 at 1Torr but shows a strong increase with increasing initial CH_4 at 2(not shown here) and 3Torr and is finally lowered again at 5Torr but remains more out of equilibrium than in pure CO_2. The decrease of the vibrational temperature is attributed to strong VT processes with one or several of the CH_4 by-products. The VT, usually less important when Trot is lower, must be in CO_2-CH_4 really strong because they quench the vibrations more, despite a lower gas temperature. The results are summarized on the two temperature "maps". The first one (figure 6.13) represent the temperatures (Trot, T_{12}, T_3 and Tco) 1ms after the beginning of the pulse (close to the peak when there is one) on the first row and at the end of the pulse on the second row as a function of pressure and initial CO_2 fraction. The second (figure 6.14) represents the "distance from equilibrium" T_i-Trot, i={12,3,co}. The data points are represented with red diamonds, the rest of the map is interpolated.

In CO_2-CH_4 plasmas, the VT seems to be much stronger despite a lower gas temperature. The question remaining is: which one of CH_4 by-products has the strongest influence ?

6.8 Literature on CO_2-CH_4 vibrational quenching

Many values of the VT coefficients are available for different collision partners of CO_2 or CO but they can spread over several orders of magnitude. A non-exhaustive literature review is presented for quenching rates relevant to CO_2-CH_4 plasmas. Most of the values found in literature were measured in the 1970's.

Experiment and model comparison Many of the measurements were made to provide data to compare with the at-the-time recent theories on the interactions of vibrationally excited

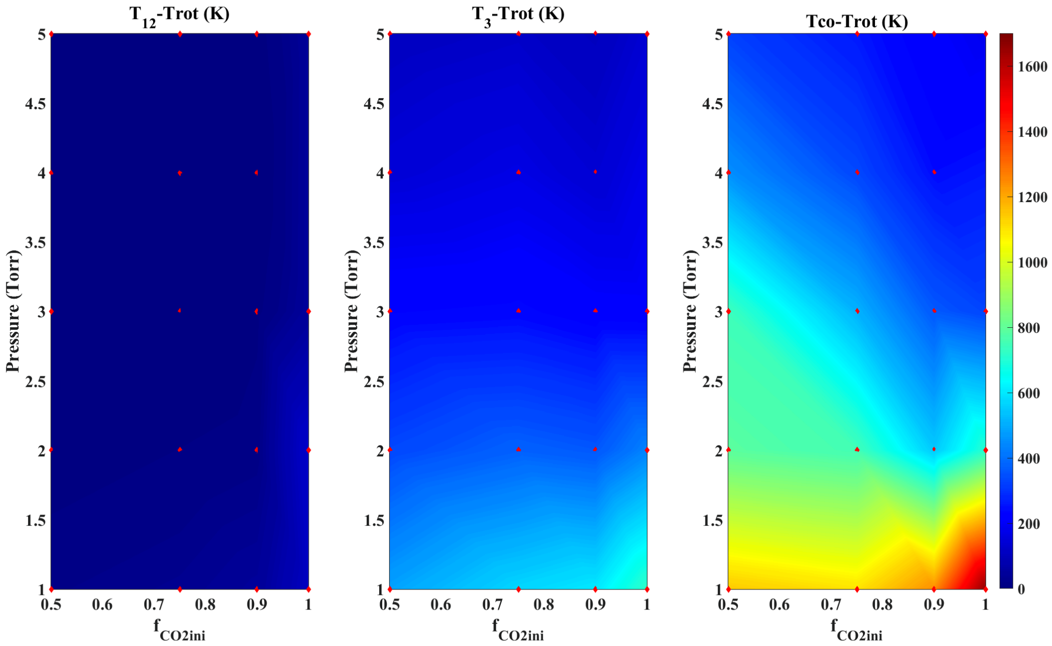

Figure 6.14: Temperature "map" of the "distance from equilibrium" T-Trot at the end of the pulse as a function of the pressure and the initial CO_2 fraction

molecules. The team of R.Millikan carried out several experiment in the 1960s on the quenching of vibrational excitation using various diagnostics like infrared emission or fluorescence. Among this work, Roger C. Millikan 1965a measured the CO-CO and CO-H_2 VT transfers,Roger C Millikan 1965b used vibrational fluorescence to measure CO-CH_4 VV transfer and Hooker et al. 1963 used infrared emission in shock tubes to study the CO-CO VV transfer as well as to remeasure the CO-CO and CO-H_2 VT transfers. Richman et al. 1975 used fluorescence to measure CO-CH_4 VV transfer (though the excited state of CH_4 was not properly identified). The CO-CH_4 or CO-CO_2 VT processes were measured in Kovacs 1973 by scattering of light due to the local VT processes. The CO was previously excited by laser pumping. The CO-CH_4 VV transfer was measured and found in good agreement with Richman et al. 1975. Matsui et al. 1975 used a Raman laser to generate IR fluorescence of CO and measured the CO-H_2 and H_2-H_2 VT transfers, but also CO vibrational pumping by H_2 ($H_2(v)+CO \rightarrow CO(v)+H_2$). Measurement of the CO-CH_4 VT transfer, the CO-CH_4 VV transfer ($CO(v{=}1)+H_2 \rightarrow CO + CH_4(\nu_2$ or $\nu_4 = 1)$) and the CH_4-M VT quenching were caried out in Yardley et al. 1970. Infrared fluorescence was used in Mehl et al. 1978 to measure CO_2 vibrational deexcitation by CH_4 and CD_4. The exact process could not be clearly identified, but it was suspected that the transfers were of the type $CO_2(001) + CH_4 \rightarrow CO_2 + CH_4(\nu_3{=}1)$ or $CO_2(001) + CH_4 \rightarrow CO_2(010) + CH_4(\nu_4{=}1)$, creating in both cases an increase of the vibrational excitation of CH_4. Similar work using infrared fluorescence was used to determine the VT transfers in CH_4-M and CD_4-M collisions (M={CH_4,H_2,CO_2,N_2,rare gases }). Interestingly though irrelevant for the present work Siddles et al. 1994 found that the CH_4 vibrations could later pump the O_2 vibrations.

The quenching of CO_2 (001) by atoms (O, H, F, Cl, N) was studied by laser fluorescence in Buchwald and Wolga 1975. The quenching of CO_2 by H was in this case found to be lower than the quenching by O.

The CO lasers The CO_2 and CO lasers were also the source of several works on vibrational quenching: in these lasers, the population inversion was done between the ground state and a vibrationally excited state. CO_2 VT quenching by CO_2, N_2, He or H_2O can be found in the Witteman book (W.J.Witteman 1986) on CO_2 laser. Some of these values were taken from

Moore et al. 1967, where the CO_2 (01^10) and CO_2 (001) vibrational relaxation with H_2O, H_2 and others were measured by laser-excited vibrational fluorescence. Using laser fluorescence, Rosser and Gerry studied the deexcitation of CO_2 (ν_3) specifically with CO_2,N_2 (Rosser Jr, Wood, et al. 1969), He, O_2, H_2O (Rosser Jr and Gerry 1969), H_2, NO (Rosser Jr and Gerry 1971) and CO (Rosser Jr, Sharma, et al. 1971). Some of these rates (CO_2-H_2, CO_2-H_2O, CO_2-CO) wear also measured in Cheo 1968. In all of these measurement, the role of water as an excellent quencher of CO_2 vibrations was identified, which motivated the study of CO-H_2O quenching for CO laser. Time-resolved FTIR spectroscopy was used B. Wang, Gu, et al. 1999 to measure the deexcitation of CO(v=1-8) by collisions with water, which was completed with ab initio calculation. This study (one of the most recent among the ones quoted here) showed that H_2O was also a good quencher of CO but quenched CO_2 faster. The interaction of CO with H atoms was studied experimentally for the CO laser using infrared emissions in shock tubes in Glass et al. 1982, using CO fluorescence in Starr et al. 1974, or more recently using ab initio calculations in Song et al. 2015 for astrophysics purposes. Stephenson and Mosburg (John C Stephenson et al. 1974) measured the CO-CO VV transfer for CO lasers using laser excited vibrational fluorescence. The CO laser was repeatedly studied and modeled in V M Shmelev et al. 1975 and Vladimir Mikhailovich Shmelev et al. 1981, using the CO-H_2O VT quenching measured by Cassady et al. 1979 and the CO-H VT measured in Rosenberg Jr et al. 1971.

Astrophysics calculations A serie of simulations of vibrational transfers involving CO and H_2 were carried out over the last decades for astrophysics measurements: CO and H_2 are among the most abundent molecular species in many interstellar environment. Quenching rates of CO(v=1-8) by atomic H between 5 and 3000K were obtained in Balakrishnan et al. 2002 using quantum mechanical scattering calculations. The rotational quenching of CO by H_2 or H, though not direct interest for the current matter, were also obtained in Yang et al. 2010 and in Walker et al. 2015. CO-H_2 VT and VV transfers cross-sections were presented in Forrey et al. 2015.

Miscellaneous An extremely complete review of vibrational quenching rates relative to CO_2-H_2O-N_2 was done by Blauer and Nickerson (Blauer et al. 1974), gathering measurement and SSH calculations. The Lopez-Puertas et al. 2001 book on non-LTE radiative transfers in Earth's atmosphere gathers numerous values of vibrational quenching of specific state of CO_2 by other molecules or atoms (CO_2, O_2, N_2...), some measured by Lopez-Puertas himself, as well as quenching of CO(v=1) by the same species. The book also reports several values for the VT quenching of CH_4 (ν_2) and CH_4 (ν_4). Finally, in the frame of the recent work on CO_2 recycling, it is admitted that pure CO_2 mixtures will unlikely be used in the application and that impurities must be taken into account. This motivated the recent study of M.Damen et al. 2020, which investigated the CO_2 dissociation upon admixture of water in a setup very similar to ours (a low pressure glow discharge with plasma pulses of 5ms) and showed that water did not have a significant impact on the e-V (meaning that the electron density was weakly affected by addition of H_2O) and on the VV transfers (the peak of T_3-Trot was also analyzed three), but admixture of water had a major impact on vibrations, efficiently quenching both CO_2 and CO. No rate was given there.

The comparison of these rates can prove to be very tedious: many of these work could not identify exactly the process measured (e.g could not measure the final vibrational state of CH_4) and thus gave a general VT process. These values are difficult to compare with mode-specific values such as the one presented in Blauer et al. 1974. A temperature dependence was also given in many of theses works, adding a dimension to compare. The comparison of specific rates will be interesting in the future, when modelling of the step-scan experiment will point out the influence of critical processes. As for now, two general conclusions can be drawn. Using the values at 300K (most of these measurements have a temperature dependence), a large spread of 1 or even 2 orders of magnitude can be found for some of the quenchings (CO-H between

Rosenberg Jr et al. 1971 and Balakrishnan et al. 2002, CO-H_2 between Starr et al. 1974 and Vladimir Mikhailovich Shmelev et al. 1981). Despite the large spreads, a general ordering of the VT quenching can be done both for CO_2 and CO. For CO_2:

$$\begin{aligned}
&k_{H_2O}(\sim 10^{-10}\text{Cheo 1968}) > k_H \sim k_O(\sim 10^{-11} - 10^{-12}\text{Blauer et al. 1974}) \\
&> k_{CO}(\sim 10^{-11} - 10^{-13}\text{Blauer et al. 1974}) > k_{H_2}(\sim 10^{-12} - 10^{-13}\text{Buchwald and Bauer 1972}) \\
&> k_{CH_4}(\sim 10^{-14}\text{Mehl et al. 1978}) > k_{CO_2}(\sim 10^{-15}\text{Moore et al. 1967})
\end{aligned}$$

For CO:

$$\begin{aligned}
&k_{H_2}(\sim 10^{-12}\text{Starr et al. 1974}) \\
&> k_H(\sim 10^{-13}\text{Balakrishnan et al. 2002}) \\
&> k_{H_2O}(\sim 10^{-13}\text{B. Wang, Gu, et al. 1999}) \\
&> k_O(10^{-13} \sim 10^{-14}\text{Lopez-Puertas et al. 2001}) \\
&> k_{CH_4} \sim k_{CO_2}(10^{-14}\text{Roger C Millikan 1965b Blauer et al. 1974})
\end{aligned}$$

For both, the order is approximate and some sources can be found in disagreement. Generally speaking, for a given specie, the quenching of CO_2 vibrations appears much stronger than the quenching of CO.
Second, most of the measurements were done in the 1970s, implying that they suffer from technological limitation. An important one is the purity of the gas, often underlined in these works: H_2O impurities were not always quantified and could have impacted the measurements. To complete these measurements and provide recent data (suited for modelling), we perform a dedicated experiment to constraint the quenching rate associated to each molecule. To this aim, the "single Pulse experiment" was used.

6.9 The single pulse experiment

The single pulse experiment (as opposed to the 'repetitive' measurement) is basically the same experiment as in the previous section but with full renewal of the gas in the reactor between two plasma pulses. The gas is still sent through the same reactor and the evolution of the temperatures is measured during a pulse of 5ms. The specificity of this experiment lies in the large gas flow which was increased to reduce as much as possible the residence time of the gas in the reactor. The pulses were also spaced so that ultimately, the gas experiences only one pulse while flowing across the tube. Because one single plasma pulse only leads to a negligible dissociation, it can be considered that the only species in the plasma are the one sent in the initial gas mixture. This experiment therefore allows to probe the vibrational interactions between the molecules sent only, without any significant contribution of their dissociation byproducts.

Several mixtures were tested: pure CO_2, CO_2-CO, CO_2-CH_4, CO_2-H_2, pure CO, CO-CH_4 and CO-H_2. Water could not be probed because it would have required liquid flowmeter. The current was still set to 50mA. The lowest pressure reachable was 3 Torr due to limitations of the equipment: indeed, the flow is increased as much as possible to renew the gas in the reactor as fast as possible and keep the time needed between two pulses not too long. However, the flow can not be too high otherwise the pumping becomes difficult to reach the targetted pressure. Hence, only measurements at 3 Torr were carried out. Because of the limitations of the pump, the time between pulses previously set to 10ms is now raised to 180ms to make sure that the gas only sees one pulse while passing through the reactor. As a result the measurements are much longer, taking up to 6 hours per measurement. Because two measurements are needed per

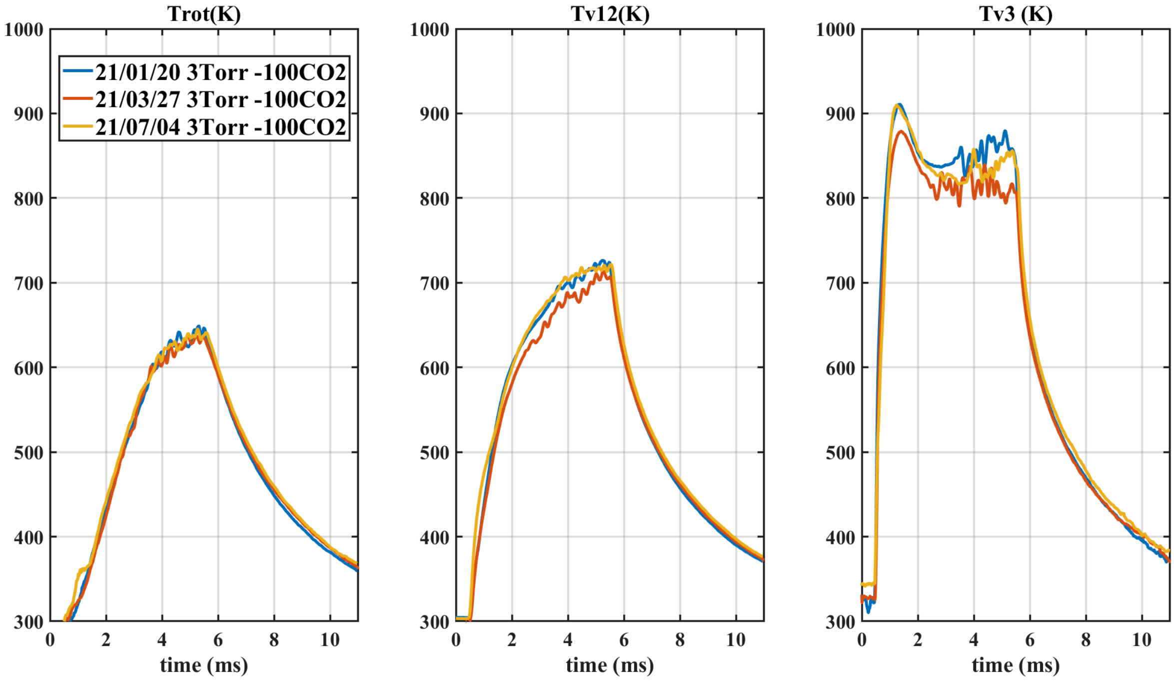

Figure 6.15: Reproducibility of the single pulse: the same condition (pure CO_2 at 3 Torr, 50mA) was measured several time over 6 months. Trot (left), T_{12} (center) and T_3 (right) are plotted and overlap very well

condition (absorption and emission), the acquisition of one condition can last up to 12h, making the single pulses more sensitive to instrumental variation (e.g heating) and to noise in general. The sensitivity of the measurement was tested: a test case (namely pure CO_2, at 3 Torr) was tested several time over 6 months. The results are plotted on figure 6.15. The reproducibility of the measurement is very good, with approximately a 20K maximum difference on Trot and about 30K on T_{12}. For T_3, the temperature at the end of the pulse spreads over 40K, though the maximum difference observed for a given time-step can reach 80K but is rather due to noise than to a real difference. The decay time in the post-discharge is also very reproducible.

For some of the measurements presented in the following, the post-discharge phase was modeled: the vibrational population of the CO_2 and CO levels were simulated during the post-discharge to quantify the influence of the VV and VT processes. The custom model was developed by Tiago Silva from N-Prime team of IST Lisbon. Because the electron impact excitation decreases as quickly as the decay time of the voltage (on the μs scale), the modelling of the post-discharge of single pulse experiments (several ms) does not require to take into account any electronic excitation. The temperatures at the end of the pulses are used as input to compute an initial vibrational distribution. Because the experiment is designed so that there is little to no dissociation, only the species sent in the reactor are taken into account (unless specified otherwise for very specific cases). The base of the model is the reaction scheme for CO_2 vibrational relaxation presented in Silva et al. 2018. This model includes CO_2 VT and VV transfers for levels up to ν_1^{max}=2, ν_2^{max}=ν_3^{max}=5 for the higher levels of respectively the symmetric, bending and asymmetric modes of CO_2. This lead to a total of 72 vibrational levels for CO_2. The transfers are already explained in details in Silva et al. 2018. In a few words, the loss of vibrational quanta (one or more) from the three vibrational modes were taken into account. The loss of quanta from different modes at once were also included. The CO_2 VT can be described by:

$$CO_2(\nu_1+n,(\nu_2+j)^{l_2+j},\nu_3+k)+CO_2 \\ \rightarrow CO_2(\nu_1,\nu_2^{l_2},\nu_3)+CO_2 \text{ with } n,j,k \geqslant 0 \quad (6.3)$$

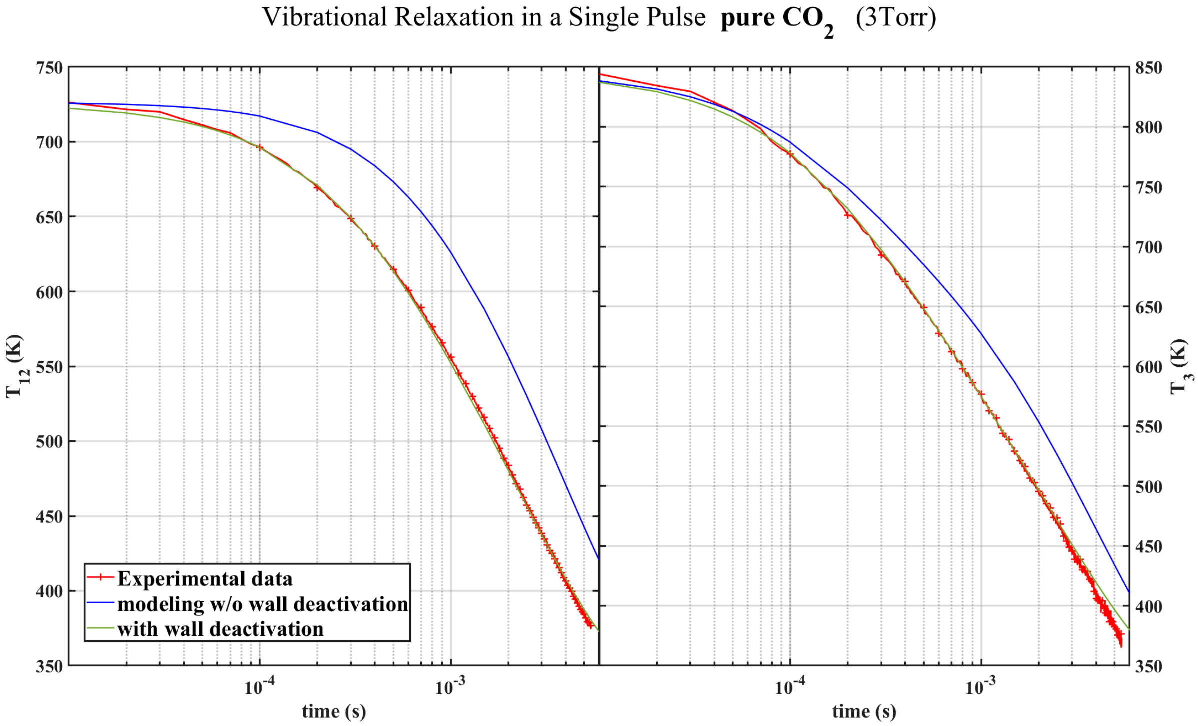

Figure 6.16: Simulation of the relaxation of T_{12} (left) and T_3 (right) during the post-discharge phase of the pure CO_2 single pulse experiment at 3Torr, 50mA. The experimental data is plotted in red

Similarly, vibrational transfers of one quanta or more from one or several vibrational modes are taken into account:

$$CO_2(\nu_1{+}n,(\nu_2{+}j)^{l_2+j},\nu_3{+}k){+}CO_2(\nu_1',\nu_2'^{l_2'},\nu_3') \rightarrow CO_2(\nu_1,\nu_2^{l_2},\nu_3){+}CO_2(\nu_1'{+}n,(\nu_2'{+}j)^{l_2'+j},\nu_3'{+}k) \tag{6.4}$$

where n,j,k ⩾0. A second type of VV transfer was taken into account:

$$CO_2(\nu_1,\nu_2,\nu_3)+CO_2(\nu_1',\nu_2',\nu_3') \rightarrow CO_2(\nu_1,\nu_2,\nu_3-k)+CO_2(\nu_1'+n,\nu_2'+j,\nu_3') \text{ with } n,j,k \geqslant 0 \tag{6.5}$$

The rates for these transfers were taken from Blauer et al. 1974 where they were measured or calculated with the SSH theory. The rates for transition from $\nu_3 \geqslant 1$ are not given in Blauer et al. 1974, they were calculated in Silva et al. 2018 using the SSH scaling method developed in Mario Capitelli et al. 2013. For this work, the model was extended with VV and VT processes of CO. The highest CO vibrational level taken into account was v=10. For each new specie tested in the experiment, the model was completed with new VT and VV processes, which will be detailed in each case. For all simulations, the t=0 is chosen at the end of the pulse.

6.9.1 Pure CO_2 Single pulses

The first measurement presented is the pure CO_2 single pulse, which was simulated to show that the CO_2 vibrational kinetics is well reproduced with the initial kinetic scheme (which had already been demonstrated in Grofulović et al. 2018 and Silva et al. 2018). The comparison of the simulated and experimental vibrational temperatures is shown on figure 6.16. The vibrational temperature of mode 1 & 2 of CO_2, T_{12} is plotted on the left, T_3 is plotted on the right The experimental measurements are plotted in red with '+' markers. When using only the 'initial' vibrational kinetic scheme (curve plotted in plain blue lines), the simulated vibrational deexcitation is too slow compared to the experiment for both CO_2 temperatures. This is corrected by completing the set with the wall deexcitation of CO_2:

$$CO_2^* + Wall \rightarrow CO_2 \tag{6.6}$$

Molecule	loss probability γ_v	Source
CO_2	0.2	L.D.Pietanza et al. 2021
CO	0.04	Black et al. 1974
H_2	0.0012	Arnold et al. 1993
CH_4	0.88	Black et al. 1974

Table 6.3: Loss probabilities γ_v for several gases used in this model

It is considered that any vibrationally excited molecule hitting the wall has a certain probability γ_v of completely losing its vibrational energy to the ground state (even if v>1). The loss frequency of vibrational excitation in a cylindrical geometry can be calculated by taking into account the deexcitation probability and the diffusion to the wall L.D.Pietanza et al. 2021:

$$\nu_{wall} = \frac{1}{D}\frac{R}{2.405}^{2} + \frac{2R(1-\gamma_v/2)}{\gamma_v\langle v\rangle} \tag{6.7}$$

where D is the diffusion coefficient calculated according to Hirschfelder et al. 1964, R the cylinder radius and $\langle v\rangle$ is the thermal velocity obtained through:

$$\langle v\rangle = \sqrt{\frac{3k_b}{m}T} \tag{6.8}$$

The various loss probabilities used in this work are given in table 6.3. When including this wall deexcitation process, the simulation (in plain green line) matches very well with the experimental values. The wall deexcitation plays a crucial role at this low pressure and is therefore included in the scheme from now on.

6.9.2 CO_2-CH_4 Single Pulse

The single pulse presented next is the CO_2-CH_4 measurements. Three mixtures are probed: pure CO_2, 90:10 CO_2:CH_4 and 50:50 CO_2:CH_4. The evolution of the temperatures is plotted on figure 6.17. In this case, only CO_2 and CH_4 are present in the reactor so Tco is not showed. The dissociation by electron impact of CO_2 into CO was measured by fitting the spectra before the beginning of the pulse and after relaxation. Weak traces of CO were detected (<0.2% of the gas density). The dissociation of CH_4 into H during a plasma pulse of 5ms was simulated and estimated to yield atomic H fraction close to 0.01% of the gas density, therefore negligible. The final value of the rotational temperature does not vary much between the different conditions, reaching 650K both in pure CO_2 and 50:50 CO_2:CH_4. The temperature in the 90:10 CO_2:CH_4 case reaches 700K, but this difference is barely higher than the error bars of the FTIR, preventing from drawing a conclusion. Despite reaching the same final value, the rise of the temperature in both CO_2:CH_4 cases is faster than in pure CO_2, indicating that the rotational heating mechanisms are faster. T_{12} is plotted on the central panel and shows almost no difference between pure CO_2 and 90:10 CO_2:CH_4, but is reduced by 80K in the 50:50 CO_2:CH_4 case. T_3 shows a similar behaviour, with final values close in pure CO_2 and in the 90:10 case and lower by approximately 60K in the 50:50 case. It can be seen that the peak of T_3 visible in pure CO_2 is cut by the addition of CH_4.
Information can be drawn from the comparison of the repetitive case (figure 6.9) and of the single pulse case (figure 6.17). The rotational temperature, as low as 580K in the repetitive case remains close to 650K in the single pulse. This supports the hypothesis that the temperature decrease is driven by the apparition of good thermal conductors (the excellent thermal conductor H_2 is absent in the single pulse measurement). In the repetitive case, T_{12} went from 750 to 550K when going from pure CO_2 to 50:50 CO_2:CH_4. In the single pulse, the temperatures in the same mixtures drops from 720K to 650K, which is due to the absence of the strongest quenchers (H_2O, H, H_2) in the single pulse. In pure CO_2, the peak in T_3 was due the competition of on one side electron impact processes and VV transfers from CO to CO_2 (ν_3) and on the other

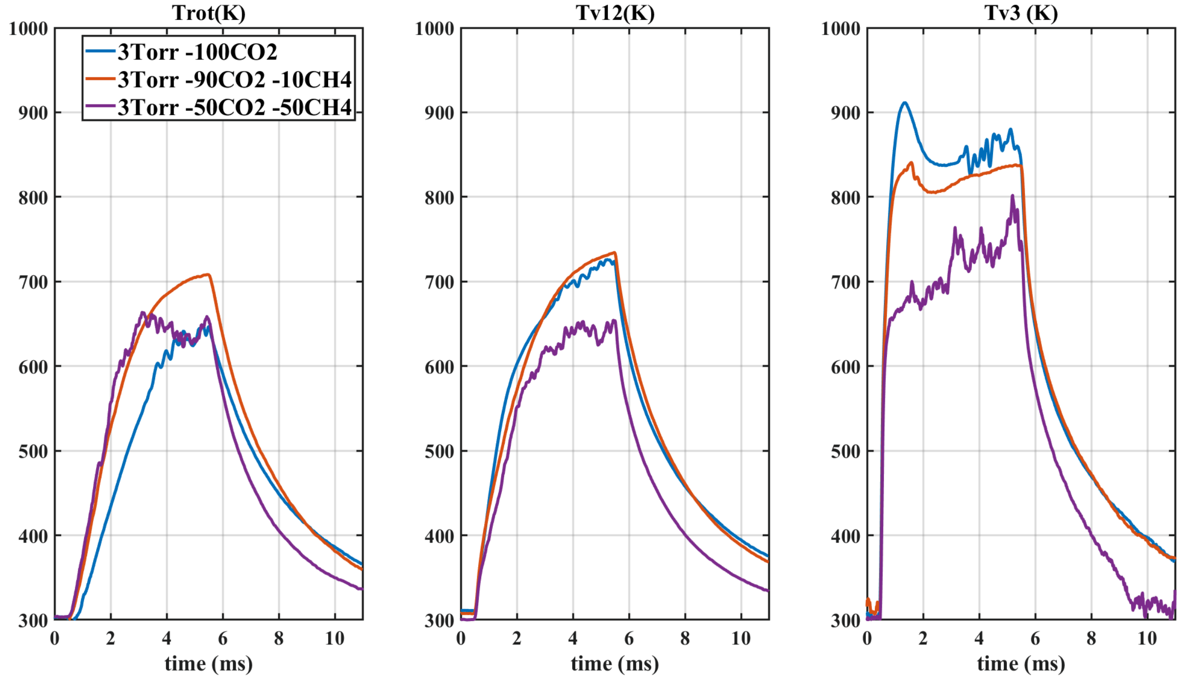

Figure 6.17: Evolution of Trot, T_{12} and T_3 in the single pulse experiment in CO$_2$-CH$_4$ (at 3 Torr, 50mA)

side the VT processes. In the repetitive measurement in CO$_2$-CH$_4$ mixtures, the peak of T_3 was not visible at all (meaning that the VT processes were very strong), whereas it is visible in the single pulse for the 90:10 case. No VV from CO take place in the single pulse, leaving only electron impact excitation. The VT are strong enough to quench electronic excitation and VV excitation in the 90:10 CO$_2$:CH$_4$ repetitive measurements but not strong enough to quench only electronic excitation in the 90:10 single pulse, meaning that the VT processes related to dissociation product are very strong. The final value of T_3, dropping from 950K to 800K when going from pure CO$_2$ to 50:50 CO$_2$:CH$_4$ in the repetitive case, only changes 850 to 800 in the same mixtures in single pulse, supporting the hypothesis that the VT processes involving dissociation products of CH$_4$ are stronger than the ones involving CH$_4$.

The variation of Tvib-Trot is plotted on figure 6.18. T_{12} is closer and closer to Trot with increasing initial CH$_4$ content, indicating that the VT processes between CO$_2$ and CH$_4$ are stronger than the one between CO$_2$ and CO$_2$. In the 50:50 CO$_2$:CH$_4$ case, T_{12} is thermalized. T_3-Trot is plotted on the last panel of fig 6.18. Once again, the more initial CH$_4$, the closer is T_3 to Trot. Both T_{12}-Trot and T_3-Trot show initial peaks (much more visible on T_3-Trot). It appears quite clearly that the peak happens earlier when there is more initial CH$_4$. The peak, "pushed" by transfer from CO(v) in the repetitive measurement, is now only pushed by electron impact, which is less and less sufficient when increasing the CH$_4$.

The post-discharge phase was modeled for the 50:50 CO$_2$:CH$_4$. The temperature at the end of the pulse was used as input. Both CO$_2$ temperatures were simulated. The results are plotted on figure 6.19. The experimental value of the temperatures (T_{12} on the left and T_3 on the right) are plotted in red plain lines with '+' markers. The green lines shows the predicted evolution of T_{12} and T_3 without including the quenching of CO$_2$ by CH$_4$. The decrease of the temperature is much slower than experimentally observed. It can be reasonably assumed that a mechanism quenching CO$_2$ vibrations is missing. The blue curves on both panels include the process:

$$CO_2(001) + CH_4 \rightarrow CO_2(v_1, v_2) + CH_4 \tag{6.9}$$

whose rate is taken from Siddles et al. 1994. The value are given there for temperature until 300K. For higher temperatures, the value were extrapolated based on the shape of the rate

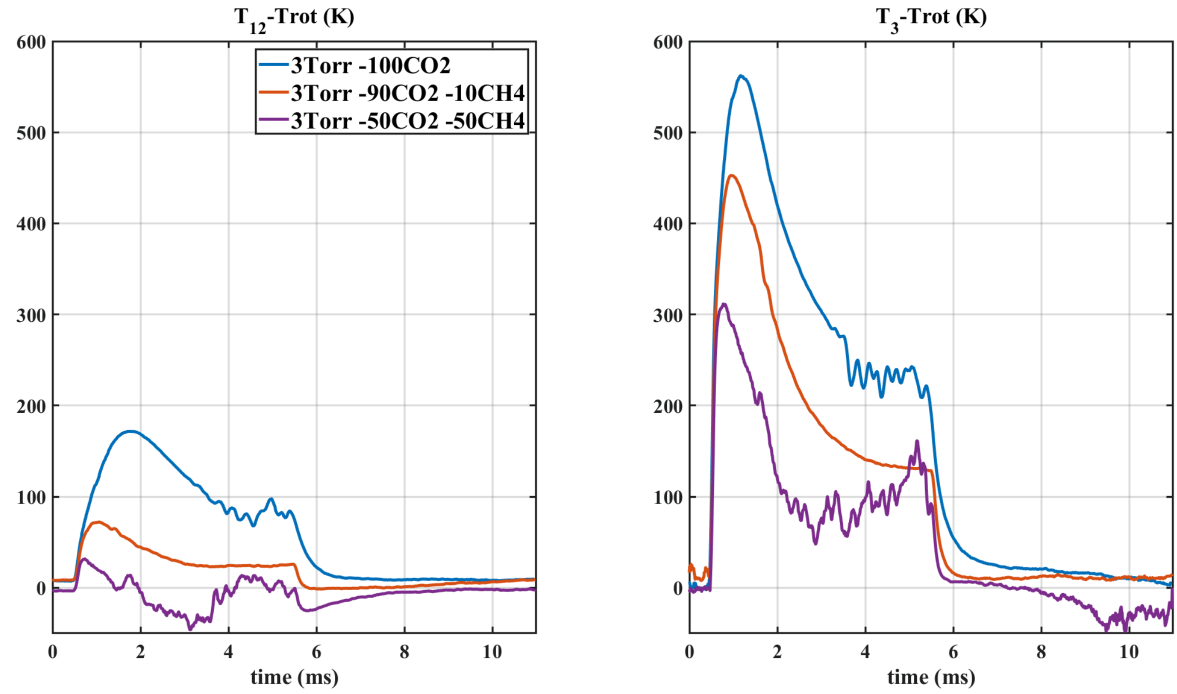

Figure 6.18: Evolution of the difference between the vibrational temperatures of CO_2 and the rotational temperature (distance from equilibrium) during a 5ms pulse in a CO_2-H_2 single pulse experiment. The pressure is 3 Torr

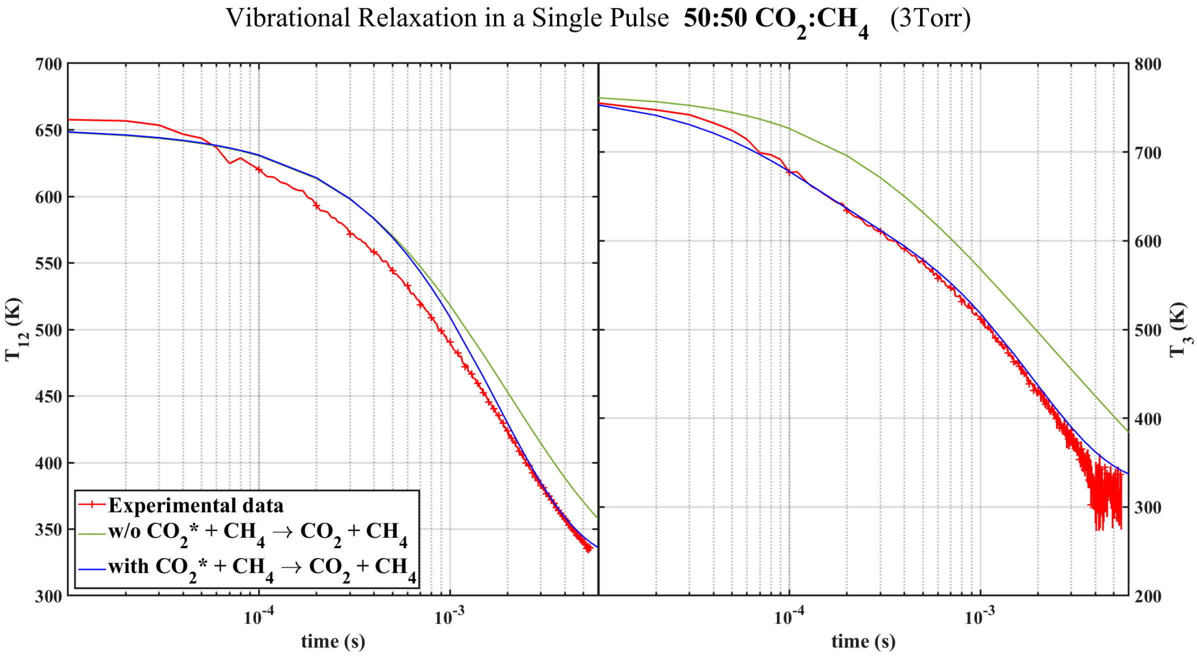

Figure 6.19: Simulation of the relaxation of T_{12} (left) and T_3 (right) during the post-discharge phase of the 50:50 CO_2:CH_4 single pulse experiment at 3Torr, 50mA. The experimental data is plotted in red

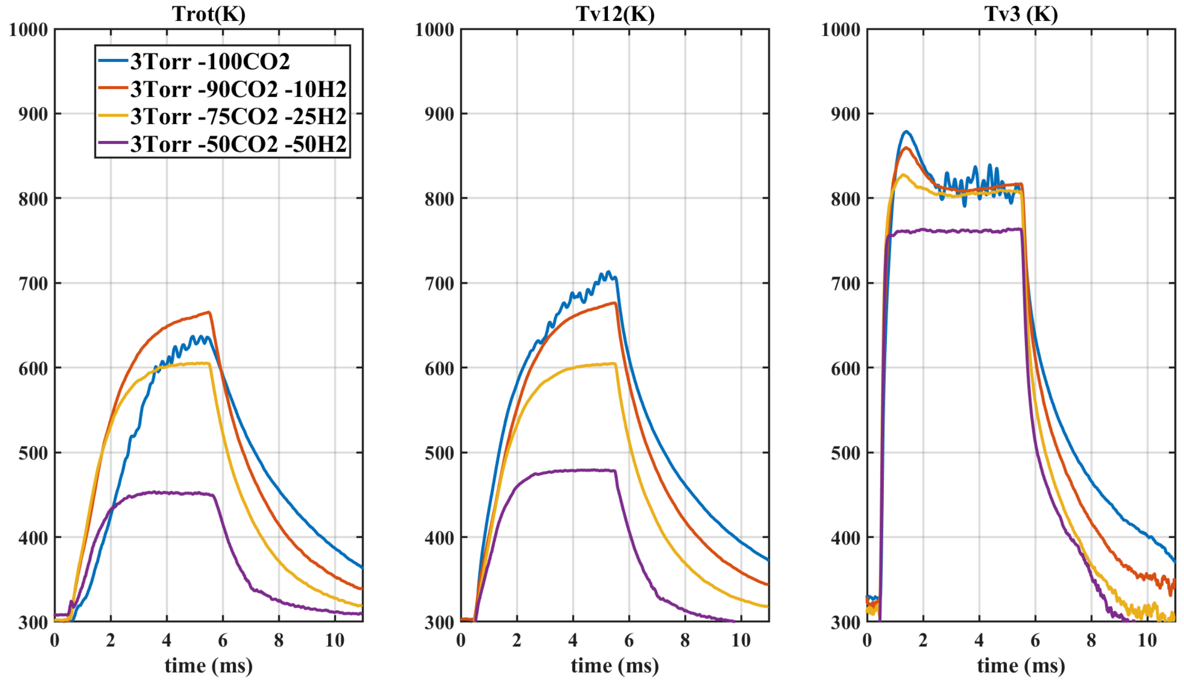

Figure 6.20: Evolution of Trot, T_{12} and T_3 in the single pulse experiment in CO_2-H_2 plasmas (at 3 Torr, 50mA)

of the similar $CO_2(001) + H_2 \rightarrow CO_2(v_1, v_2) + H_2$, which overlaps very well with the CO_2-CH_4 quenching rate at low temperatures. The rate of this process was extended to higher ν_3 according to Silva et al. 2018. Using this process allows for a much better matching of the experimental and the simulated T_3. T_{12} is also improved but the relaxation shows a small delay compared to the experiment: between 10^{-4} and 10^{-3}s, T_{12} is higher, before catching up with the experiment at 2ms. After 2ms, experiment and simulation are in good agreement. The rates proposed in Siddles et al. 1994 for the CO_2-CH_4 VT appear to be quite good values.

- The VT transfers from CO_2 to CH_4 become more and more visible with increasing CH_4 content in the single pulse experiment experiment
- Comparison of the single pulse and the repetitive experiments show that the VT are however stronger with CH_4 dissociation products than with CH_4
- The inclusion of the transfer from CO_2 (ν_3) to CO_2 (ν_1,ν_2) upon collision with CH_4 is necessary to reproduce the post-discharge. The rate of the process is extrapolated from the rate of the same process with H_2 in Siddles et al. 1994.

6.9.3 CO_2-H_2 Single Pulse Experiment

The interactions of CO_2 and H_2 were also studied in the single pulse measurements. Four different initial mixtures were probed: pure CO_2, 90:10, 75:25 and 50:50 CO_2:H_2. The dissociation of H_2 into atomic H due to electron impact was estimated using the kinetic model developed in chapter on the glow discharge. After 5ms, atomic H is 0.02% of the gas density and H_2O makes up for 0.06%. This remains extremely small, but it can be found in literature (W.J.Witteman 1986) that the quenching coefficient of CO_2 vibrations by H_2O is 3 orders of magnitude higher than the one by CO_2. In this case, even traces of water might not be negligible. The effect of H_2 on the temperatures of CO_2 is plotted on figure 6.20. The rotational temperature is plotted on the first panel. The final values reached during the pulse in the pure CO_2, the 90:10 case

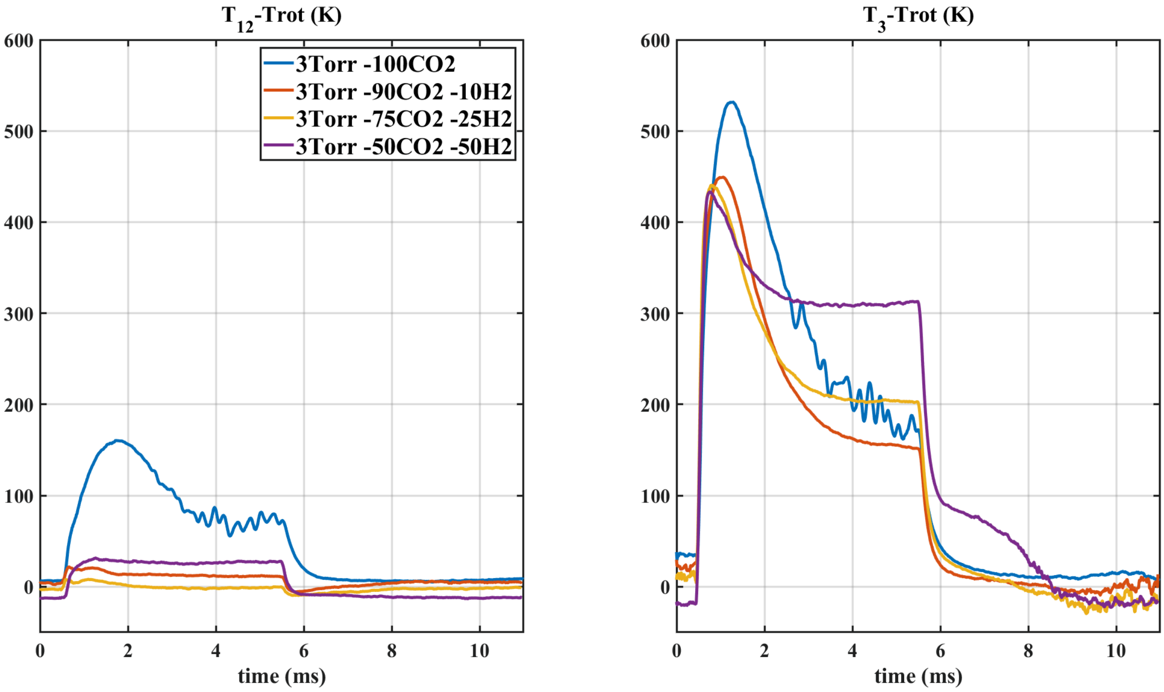

Figure 6.21: Evolution of T_{12}-Trot and T_3-Trot (distance from equilibrium) in the single pulse experiment in 50-50 CO_2-H_2 plasmas (at 3 Torr, 50mA)

and the 75:25 case are very close and they spread over 60K which could still be in the error bar of the FTIR. However, Trot in the 75:25 case being 60K lower than the 90:10 case, it is likely that a small, but real temperature decay with CH_4 content exists. The final value in the 50:50 case is 150K lower than in the 75:25 case, showing unambiguously a real effect of the H_2. The thermal conductivity is probably one of the processes explaining this, but not only. The evolution of the rotational temperature, with a faster rise in CO_2:H_2 than in pure CO_2, could here again witness fast VT processes. T_{12}, plotted on the second panel of figure 6.20, shows a different behaviour. In this case, the pure CO_2 case exhibits the highest T_{12}, reaching 700K. T_{12} decreases upon addition of H_2 in the initial mixture, reaching only 675K in the 90:10 mixture, 600K in the 75/25 case and 450K in the 50:50 case. Given the proximity of the pure CO_2 and the 90:10 cases, it is hard to say for sure that a decrease is seen but the trend with the other cases tend to back up this idea. The lower T_{12} suggests strong CO-H_2 VT processes for v_2. The final value of T_3 appears to be the same in the pure CO_2, the 90:10 and the 75:25 CO_2:CH_4 cases. In the 50:50 case, T_3 seems to be about 50K lower. However, there seem to be an offset of approximately 35K in the fit (visible right before the beginning of the pulse), which lead to think that the temperature is underestimated by a few tens of K and that the final temperature reached by the end of the pulse is the same as in the other cases. The main difference between the conditions is the peak of T_3 at approximately 1ms, which progressively disappear as H_2 is added to the initial mixture. The constant final value T_3 could indicate that H_2 efficiently quenches the first two vibrational modes of CO_2, but not the 3rd one. The differentiated excitation as a function of the mode is clearer on figure 6.21, where the difference between the vibrational temperatures and the rotational temperature T_{12}-Trot and T_3-Trot is plotted respectively on the left and on the right. T_{12} is out of equilibrium only in the pure CO_2 case. In the other cases, Trot-Tv_{12}<30K so T_{12} can be considered thermalized. On the other hand, T_3, on the second graph, is still very much out of equilibrium. By the end of the pulse, the difference between T_3 and Trot is the same in pure CO_2, in the 90:10 and in the 75:25 CO_2:CH_4. In the 50:50 CO_2:CH_4 case, T_3 appears to be more out of equilibrium than in pure CO_2, because of the lower Trot and the similar T_3. Yet at the beginning of the pulse, a similar behaviour to the CO_2-CH_4 single pulses is observed: T_3-Trot goes through a maximum.

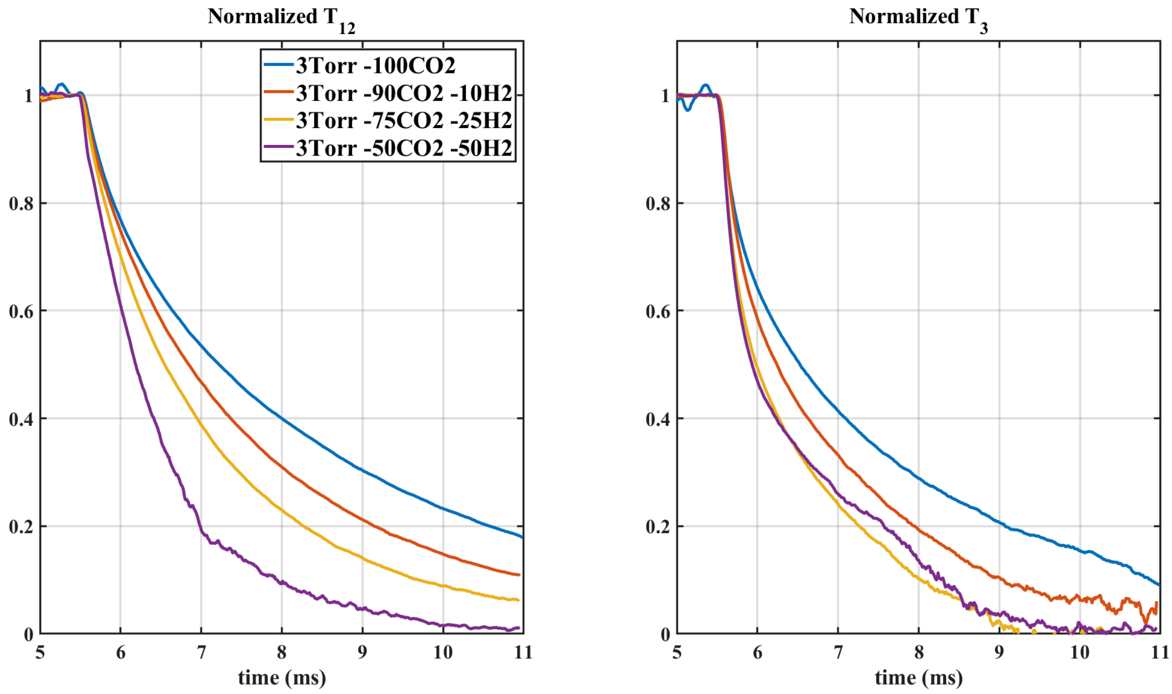

Figure 6.22: Evolution of the normalized temperatures T_{12} and T_3 in the post-discharge of a single pulse experiment in 50-50 CO_2-H_2 plasmas (at 3 Torr, 50mA)

This peak, lower than in pure CO_2 is attributed to the competition between electron impact excitation and VT deexcitation. Like in CO_2-CH_4, the more initial H_2, the sooner the peak, seemingly indicating that the VT process are actually stronger in CO_2-H_2 (even despite the lower Trot, which should decrease the VT processes). This is confirmed by the normalized post discharge, plotted on figure 6.22. For both vibrational temperatures, the more H_2, the faster the quenching of the vibrational excitation. However, T_{12} is at equilibrium, meaning that the observed normalized decay of T_{12} is actually the decay of the gas temperature. The main gas cooling channel is the loss at the wall, so the increasingly fast decay of T_{12} with H_2 simply means that the loss to the wall is much higher when the H_2 content increase. The decay of T_3, at equilibrium, is due to the VT processes. The decay of T_3 becomes faster upon addition of H_2 in the initial mixture. The decay time stabilizes above 25% of H_2, remaining identical in the 50:50 and 75:25 CO_2:H_2 cases. The fast decay of T_3 in CO_2-H_2 plasma shows that the increase of excitation of T_3 (observed on figure 6.21) is due to an excitation process and not to an inefficient quenching. This excitation process is related to H_2. The similar decay time in the 75:25 and in the 50:50 CO_2:H_2 single pulse measurements could be explained by the simultaneous increase of the VT processes and of the CO_2 (ν_3) excitation process.

The post discharge in the 50:50 CO_2:H_2 case was modeled and compared to experiment on figure 6.23. The experimental T_{12}, plotted on the left panel with '+' markers, is rather well reproduced when only including the VT process :

$$CO_2(0,0,1) + H_2 \rightarrow CO_2(\nu_1,\nu_2) + H_2 \tag{6.10}$$

(in plain blue line) The value from Rosser Jr and Gerry 1971 is used in this work. The rate was here also extended to ν_3=5 using the method developed in Silva et al. 2018. This additional single quenching reaction does not allow to reproduce T_3 (in plain blue line on the right panel of the figure), which decreases too fast compared to the experiment. The excitation of T_3 by H_2 was reported in literature (Bott 1976).

$$H_2(v=1) + CO_2(00n) \rightarrow H_2(v=0) + CO_2(00n+1) \tag{6.11}$$

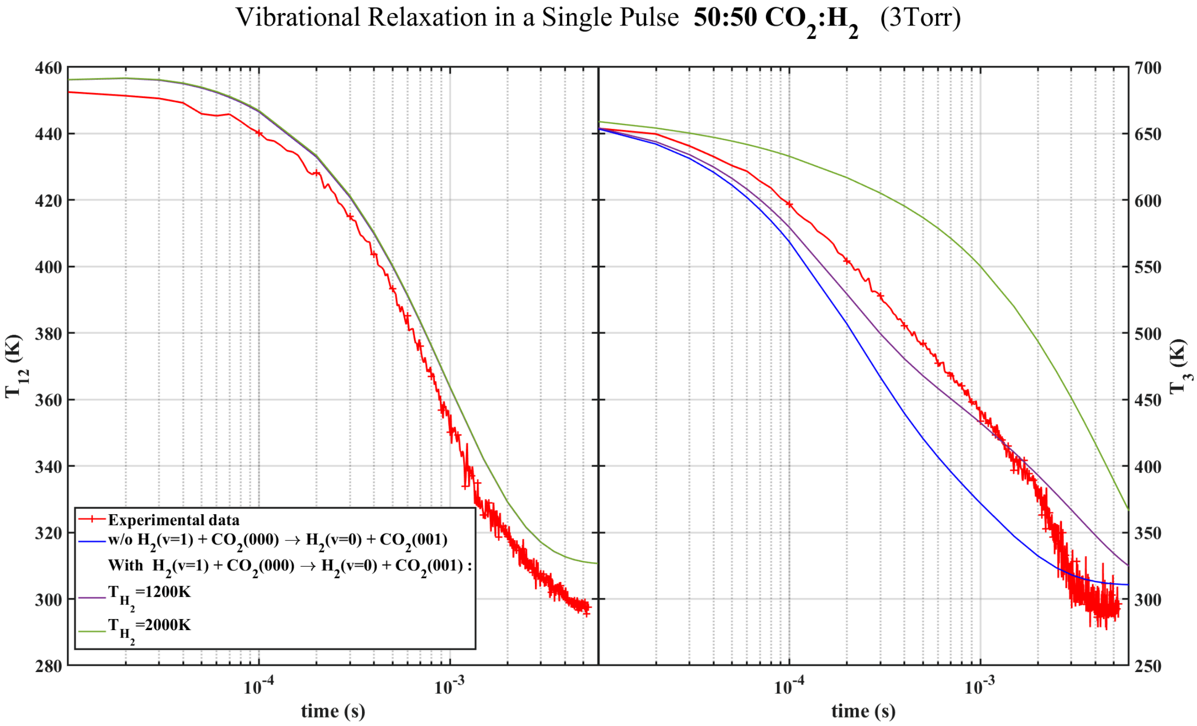

Figure 6.23: Simulation of the relaxation of T_{12} (left) and T_3 (right) during the post-discharge phase of the 50:50 CO2:H_2 single pulse experiment at 3Torr, 50mA. The experimental data is plotted in red

Its addition counteract the fast quenching of T_3. Three rates for $CO_2(000)$ to $CO_2(001)$ from Bott 1976,Miller et al. 1977 and Grimley et al. 1979 were compared. All of these rates have similar values at 300K. The value at 600K was extrapolated. For the rates for ν_3>1, the rate was scaled to v using $k_{v=1\rightarrow v=2} = 2 * k_{v=0\rightarrow v=1}$. For the H_2, only the two first vibrational levels (v=0 and v=1) are taken into account. Additionally, two quenching of H_2 are included: the wall deactivation using the loss probability γ_{vH_2} given in table 6.3 and the VT process $H2(v = 1) + H_2 \rightarrow 2H_2$, whose rate was taken from Blauer et al. 1974. The simulated T_3 (when including the pumping process) is showed for 2 different H_2 vibrational temperatures (1200K in plain purple lines and 2000K in green purple lines). As visible, these process have very limited impact on T_{12} and make almost no difference. Using Tv_{H_2}=1200K yields good results for T_3, with a simulated temperature being slightly under the experiment until 2ms after the end of the pulse. After that, the measured T_3 falls faster than the simulated one. Using Tv_{H_2}=2000K keeps T_3 too high for too long. The value of Tv_{H_2}, approximately 1200K in the simulation, seems quite high compared to the rotational temperature (450K), but similarly to N_2, H_2 has a quite high dissociation threshold (14.68 eV) and has on the other hand low vibrational excitation threshold. The diatomic geometry of the molecules also prevents vibrational quanta transfers between different mode of the molecule, maintaining a high temperature for the only vibrational mode (Tco in this work reaches temperature higher than 1200K). The H_2 vibrational temperature could therefore be 1200K.

This process necessary to fit the post-discharge confirms what was seen in the discharge: the VT processes are stronger but a specific excitation process pumps CO_2 (ν_3), leading to T_3 being more out of equilibrium when the initial H_2 increases.

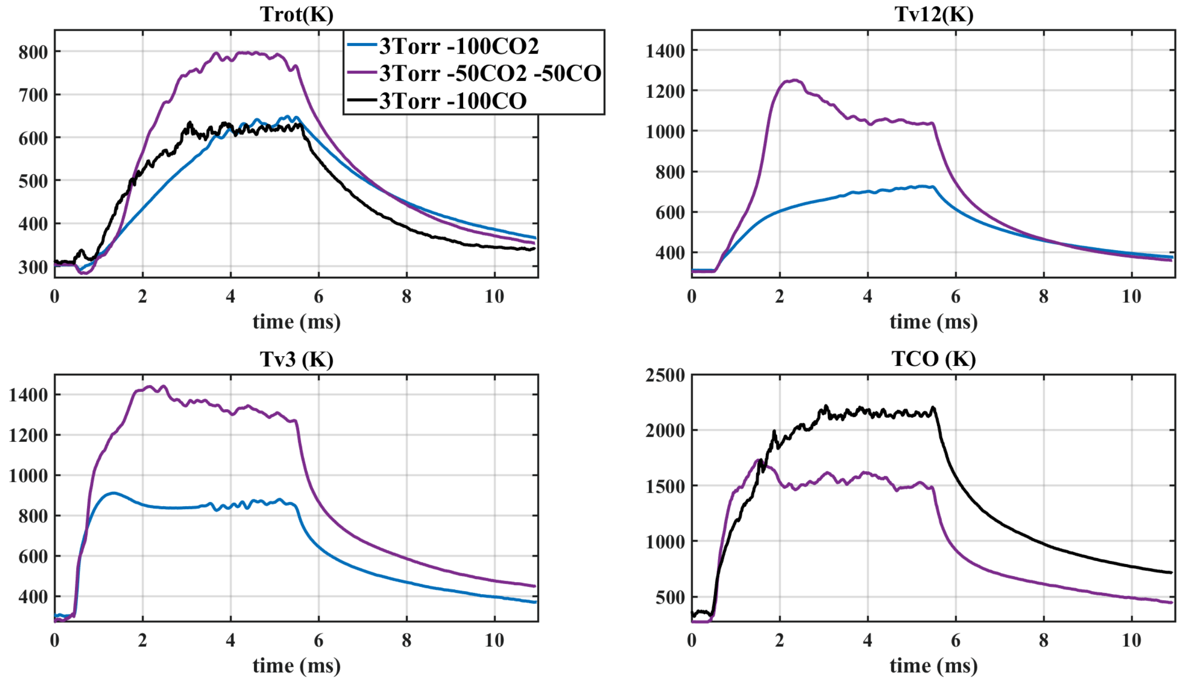

Figure 6.24: Evolution of the rotational and vibrational temperatures Trot, T_{12}, T_3 and Tco in the post-discharge of a single pulse experiment in 3 cases: pure CO_2, 50:50 CO_2:CO and pure CO. The pressure is set to 3 Torr and the current to 50mA

- The discharge values of T_{12} and the post-discharge decays highlight strong VT processes between CO_2 and H_2
- However, increasing initial H_2 content leads to T_3 being more and mor out of equilibrium due to an excitation process
- The inclusion of VV transfer from H_2 to CO_2 (ν_3) improves the matching of experiment and simulation for T_3 using the rate from Bott 1976
- The vibrational quenching of H_2 taken from Blauer et al. 1974 is also necessary

6.9.4 CO_2-CO and pure CO Single Pulses

The vibrational interaction between CO_2 and CO are critical because of the resonance between $CO_2(\nu_3)$ and CO(v). Figure 6.24 shows the evolution of the temperatures in 3 different cases: pure CO_2, 50:50 CO_2:CO and pure CO. The rotational temperature reaches the values of 620K in both pure CO and pure CO_2. In the 50:50 CO_2:CO case, the value reaches 800K. The comparison of T_{12} and T_3 for the pure CO_2 and the 50:50 CO_2:CO case is plotted next: it appears that $T_{12CO2:CO}>T_{12CO2}$ and $T_{3CO2:CO}>T_{3CO2}$. This is attributed to the pumping of the vibrational mode ν_3 of CO_2 by the VV transfers from CO(v). This effect is for instance visible in the bump of T_3, previously observed in other mixtures. The bump, visible soon after the beginning of the pulse, happens earlier in the pure CO_2 case. In the CO_2:CO case, it is delayed due to the pumping of ν_3. The VV' transfers from $CO_2(\nu_3)$ to $CO_2(\nu_1, \nu_2)$ then increase T_{12}. This had already been observed in A.-S. Morillo-Candas 2019. The comparison of Tco for pure CO and 50:50 CO_2:CO, confirms that. The rise at the beginning of the pulse is indeed very similar in both cases until $Tco_{CO_2:CO}$ starts going down, about 1ms after the beginning of the pulse, when the energy transfers to ν_3 start playing an important role in CO_2:CO. This corresponds to the characteristic time of the VV processes depopulating CO(v). The simulation

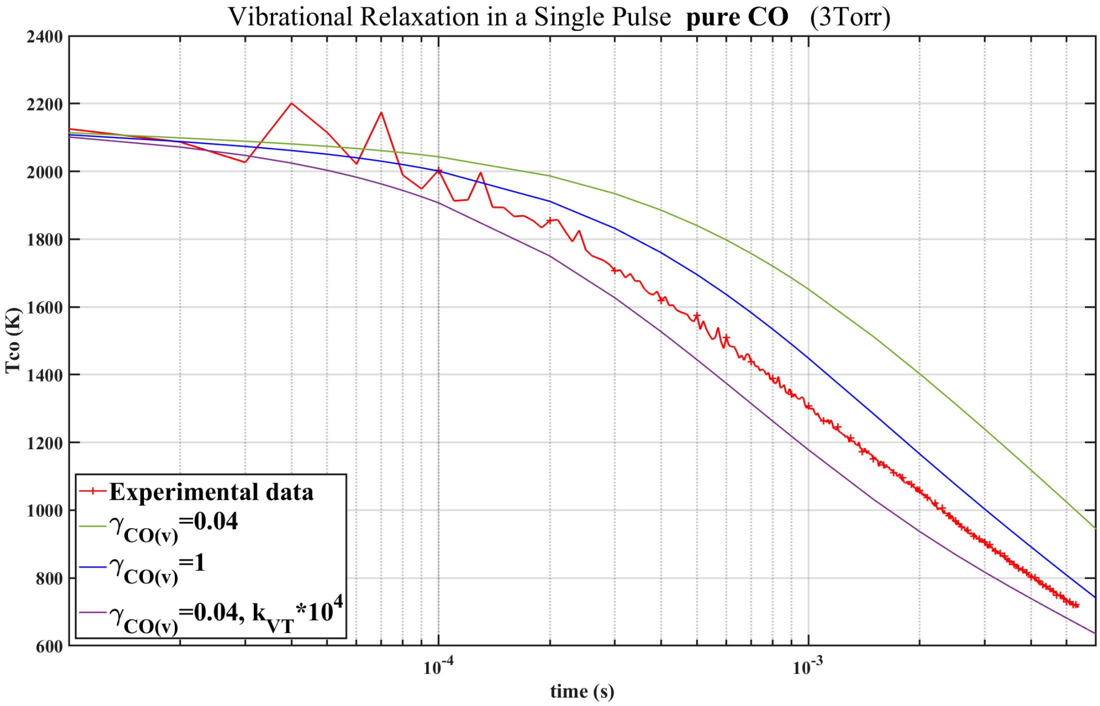

Figure 6.25: Simulation of the relaxation of the CO vibrational temperature in a pure CO Single Pulse experiment at 3Torr, 50mA. The experimental data is plotted in plain red line with '+' markers

of the pure CO post-discharge is shown on figure 6.25. For this simulation, several processes were used. First, the VT process:

$$CO(v=n) + CO \rightarrow CO(v=n-1) + CO \tag{6.12}$$

Several values are available in literature (Blauer et al. 1974,Roger C. Millikan 1965a,Cacciatore et al. 1981). In this work, a fit of the rate from Cacciatore et al. 1981 was used. A VV process was also included:

$$CO(v=n) + CO(v=m) \rightarrow CO(v=n-1) + CO(v=m+1) \tag{6.13}$$

The rate of this process was taken from Fromentin et al. 2023, originally taken from Hooker et al. 1963. Finally, the wall deactivation of CO(v) is taken into account:

$$CO(v) + wall \rightarrow CO + wall \tag{6.14}$$

Several values are found for the wall deactivation probability γ_v. In Black et al. 1974, γ_v for pyrex is estimated between 0.0186s^{-1} and 0.04^{-1}. The wall deactivation is however difficult to estimate in the pure CO single pulse experiment. At the end of the 6 hour long experiment the reactor wall was completely black and the plasma could barely be seen through the deposit. Less than 0.01% of the CO in the reactor is dissociated during one 5ms pulse, the coating is due to the accumulation over approximately 55000 pulses. This carbon coating accumulated over the experiment probably changes the γ_v value from the one of pyrex to the one of pure carbon. At the end of the experiment, the reactor was cleaned with a pure O_2 plasma. The walls returned to their original state after 30s of pure O_2 plasma exposure, confirming that pure carbon was indeed deposited on the walls. The experiment is plotted on figure 6.25 in red plain line with '+' markers. Three simulation curves are plotted. The first curve, in green, simulates the predicted evolution of Tco using γ_v=0.04 and shows that the relaxation is too long compared to the experiment. On the second curve, in blue, the wall deactivation probability γ_v is raised to

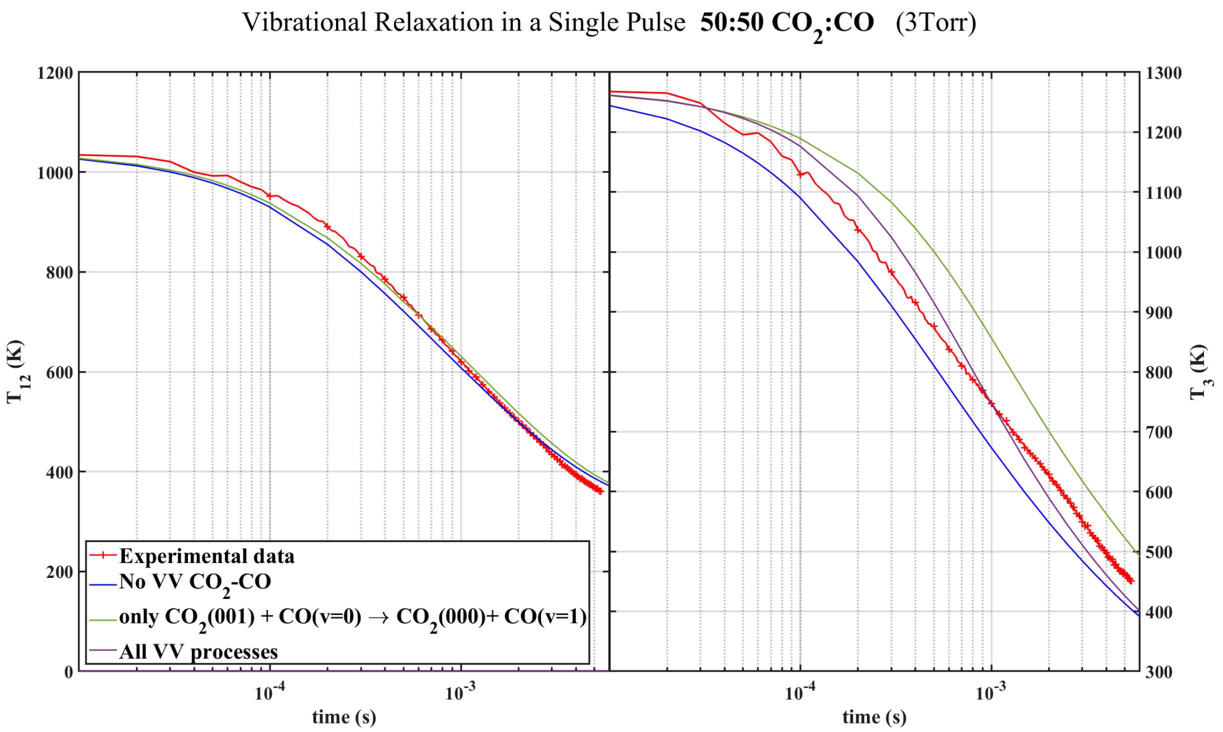

Figure 6.26: Simulation of the relaxation of T$_{12}$ (left) and T$_3$ (right) during the post-discharge phase of the 50:50 CO$_2$:CO single pulse experiment at 3Torr, 50mA. The experimental data is plotted in red

1, meaning that all vibrationally excited CO molecules reaching the wall lose their vibrational excitation. This improves the results but still does not allow to match the experiment. The third curve (in purple) shows the effect of increasing the rate of the VT process 6.12 by 10^4. In this case, the vibrational deexcitation is overestimated, but this shows that the rate chosen for 6.12 could be too small. Reality probably lies somewhere in between: the wall deactivation probability is probably high and the rate of CO VT is likely too low.

The simulation of the 50:50 CO$_2$:CO case is showed on figure 6.26.

Four processes are taken into account for this simulation:

$$\text{VT: } CO_2(001) + CO \rightarrow CO_2(mn^l0) + CO \tag{6.15}$$

$$CO(v = n) + CO_2 \rightarrow CO(v = n - 1) + CO_2 \tag{6.16}$$

$$\text{VV: } CO_2(\nu_1\nu_2 0) + CO(v = n) \rightarrow CO_2(\nu_1 - 1\nu_2 - 20) + CO(v = n + 1) \tag{6.17}$$

$$CO_2(00n) + CO(v = m) \rightarrow CO_2(00n - 1) + CO(v = m + 1) \tag{6.18}$$

The rate of reaction 6.15 is a fit from the values proposed in D. F. Starr et al. 1975 and in John C. Stephenson et al. 1972. The rate of 6.16 is taken from the recent work of Fromentin et al. 2023. For 6.17, the rate is fitted from data available in Kustova et al. 2020. Finally, the rate of process 6.18 was also fitted from data available in Kustova et al. 2020 and D. F. Starr et al. 1975. In this case, T$_{12}$, T$_3$ and Tco are simulated in 3 situations: the first (plotted in plain blue lines on all three figures), does not include any VV transfer between CO$_2$ and CO. The second (plotted in green) includes only process 6.18 for the VV transfer. The last one (plotted in purple) includes both processes 6.17 and 6.18. The experimental data is plotted in red with '+' markers. No clear "best" case can be identified" for T$_{12}$, plotted on the first graph of figure 6.26. All the simulation slightly underestimate the relaxation until 1 or 2 ms after the end of the pulse and the beginning of the post-discharge (depending on the cases), when the experiment and simulation cross. The relaxation on longer time scale is then overestimated in

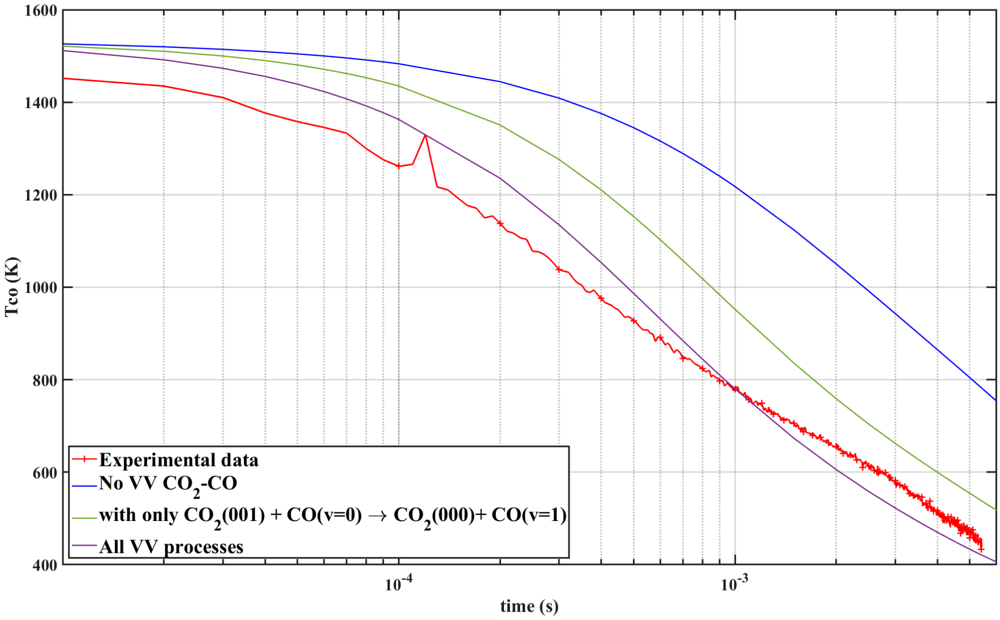

Figure 6.27: Simulation of the relaxation of Tco during the post-discharge phase of the 50:50 CO_2:CO single pulse experiment at 3Torr, 50mA. The experimental data is plotted in red

all cases. For T_3, plotted on the second panel, the case including no VV underestimates the relaxation. The case with only the VV with $CO_2(\nu_3)$ overestimates it. The case with both processes yields the best results, though the simulation and the experiment cross about 1ms after the beginning of the post-discharge. For Tco, plotted on figure 6.27, the relaxation of CO is overestimated without VV. The estimation of the relaxation improves when including process 6.18, and improves even more when including both 6.17 and 6.18, though experiment and simulation still cross at 1ms. The matching between simulation and experiment is improved for both T_3 and Tco when including the VV processes, emphasizing their strong effect.

- The transfer of vibrational energy from CO(v) to CO_2 (ν_3) is visible in the single pulse data
- The simulation of the post-discharge in the pure CO single pulse is difficult becasue of the unknown vibrational deexcitation probability at the wall
- The value of the VT rate used for the pure CO case seems too small
- The inclusions of VT and VV processes (6.15-6.18)between CO and CO_2 is necessary to match experiment and simulation in the 50:50 CO_2:CO single pulse

6.9.5 CO-CH_4

The 50:50 CO-CH_4 single pulse measurement is shown on figure 6.28. The measurement in CO:CH_4 (plotted in purple) is very noisy and difficult to analyze. The noise has several sources. Because the peaks of CO are more scattered than the ones of CO_2 and less intense, the fitting of the rotational temperature using the CO rotational structure is more challenging and sensitive to the noise. Second, for unclear reasons, the discharge containing a large amount of CO generate much more noise on IR spectra during the pulse than the discharge containing CO_2. The noise is due to the discharge itself and cease in the post-discharge. The noise on the absorbance is 5 times higher in the discharge compared to 0.5ms after the end of the discharge , where the signal is very clear. A similar issue was observed in the CO-H_2 discharge. Overall,

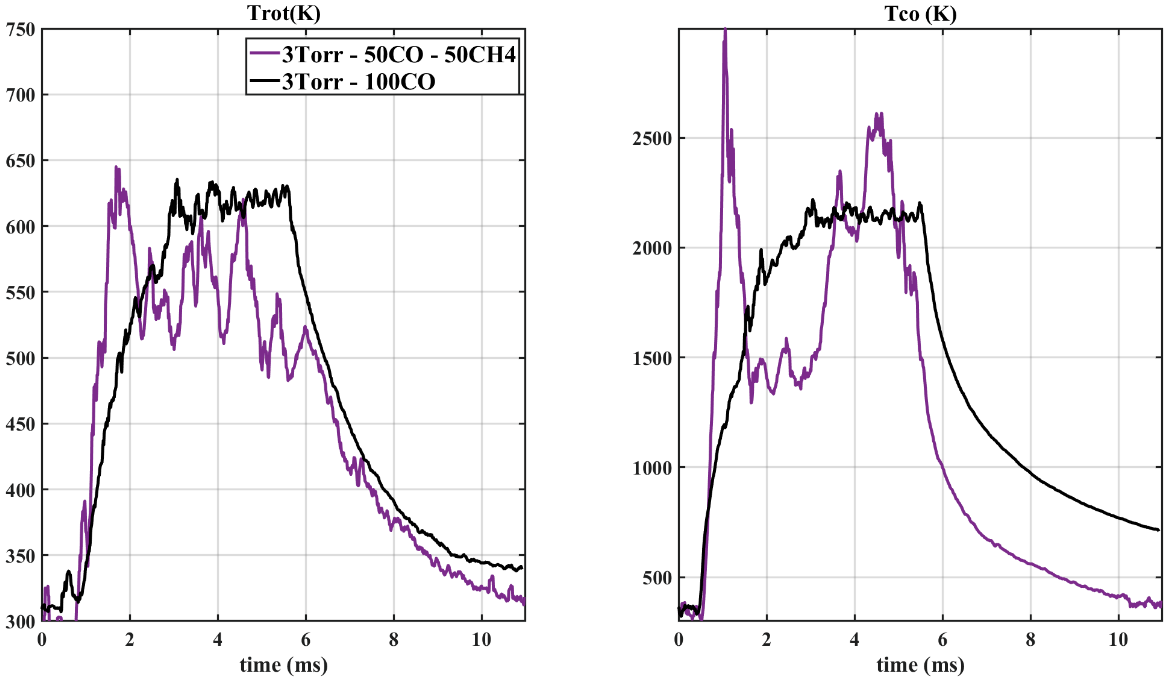

Figure 6.28: Evolution of the rotational (left) and vibrational temperatures of CO (right) during a 5ms pulse in the single pulse experiment in pure CO and in 50:50 CO:CH_4. The pressure is set to 3 Torr and the current to 50mA

the data during the pulses are too noisy to be trusted. The post-discharge data however can be analyzed since the noise level is then back to the usual one. The beginning of the post-discharge is not very clear: on the rotational temperature, it seems that the pulse is longer than in the pure CO case but on the CO vibrational temperature, the pulse seems shorter. The beginning of the post discharge is assumed to be at t=5.35ms, when the CO vibrational temperature sees a sudden sharp decrease. The Tco at that time is used as input for modelling the relaxation. The comparison of the experiment and the simulation is plotted on figure 6.29. The experimental data is plotted in red with '+' markers. The first curves, plotted in blue, include the VT process:

$$CO(v) + CH_4 \rightarrow CO(v=0) + CH_4 \tag{6.19}$$

whose rate is taken from Roger C. Millikan 1965a. As visible on the left of figure 6.29, when including only this process, the CO relaxation time is largely overestimated, taking about 10ms for relaxation. Because the vibrational excitation seems to be quenched somehow, two processes are added: a VV between CO and CH_4 and a CH_4 VT:

$$CO(v=n) + CH_4 \rightarrow CO(n-1) + CH_4(\nu_2, \nu_4) \tag{6.20}$$

$$CH_4(\nu_2, \nu_4 = 1) + CH_4 \rightarrow CH_4 + CH_4 \tag{6.21}$$

The rate of 6.20 (for v=1→v=0) was fitted from Roger C. Millikan 1965a and scaled with v for levels higher than v=1. The rate of (6.21) was fitted from Siddles et al. 1994. For CH_4, only the first two levels ($\nu_2 = 1$ & $\nu_4 = 1$) are included. Because CH_4 vibrational excitation was taken into account, CH_4 wall deactivation was included as well with the probability given in 6.3. These processes take into account the vibrational distribution of CH_4. Two curves are plotted on figure 6.29: in green with an initial vibrational temperature of CH_4 of 2000K, and the second in purple with an initial vibrational CH_4 temperature of 600K (which is the gas temperature in this condition. Using Tv_{CH_4}=600K=Trot yields better results, confirming that the CH_4 is at equilibrium. The vibrational temperature of CH_4 is plotted on figure 6.29. Interestingly, the vibrational pumping of CH_4 is not immediately lost to translations, leading to a brief moment

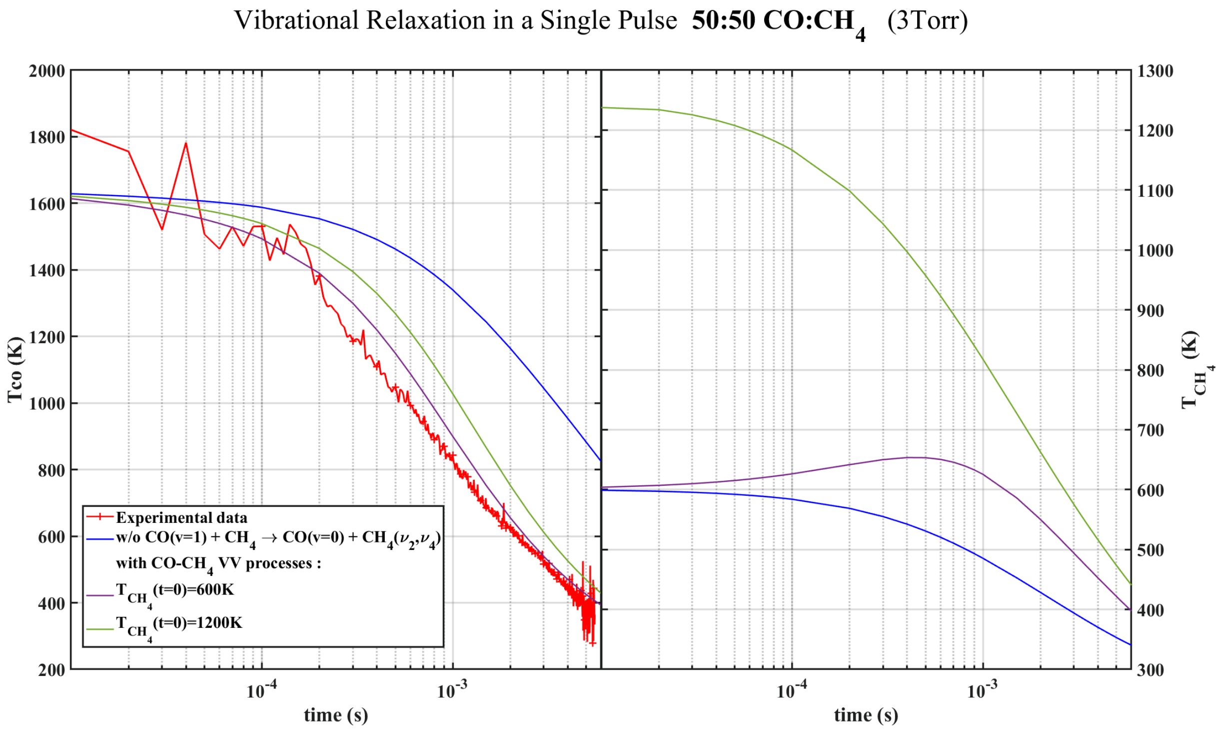

Figure 6.29: Simulation of the relaxation of Tco (left) and T$_{CH_4}$ (right) during the post-discharge of a 50:50 CO:CH$_4$ Single Pulse experiment. the experimental Tco is plotted in red, T$_{CH_4}$ was not measured

where CH$_4$ is out of equilibrium in the post-discharge. The CH$_4$ vibrational deexcitation is longer by several orders of magnitude than what had been measured in Butterworth et al. 2020, indicating that loss processes of CH$_4$ vibrations are probably neglected in this simple scheme.

- The discharge is very noisy and difficult to analyze
- The modelling of the post-discharge show that the decay is well reproduced when taking into account CH$_4$ vibrational excitation, with the CO-CH$_4$ VV and VT (Roger C. Millikan 1965a), the CH$_4$-CH$_4$ VT (Siddles et al. 1994) and the CH$_4$ wall deactivation

6.9.6 CO-H$_2$

The single pulse experiment in the CO-H$_2$ mixture is shown on figure 6.30. Only the 50:50 case at 3Torr, 50mA was investigated. The pulses in the mixture is once again very noisy: the end of the pulse is not clearly delimited, leaving some uncertainty on the validity of the measurement. The end of the pulse is determined using the pure CO case: the pulse duration being the same in both cases, the end should happen at the same time. In the CO:H$_2$ mixture, the rotational temperature initially increases before progressively going down 2ms after the beginning of the pulse. At the maximum of Trot (2ms after the beginning of the pulse), the temperature in the CO:H$_2$ mixture reaches 580K, the same value as in pure CO at the same time. By the end of the pulse, the temperature in pure CO reaches 630K, while it goes down to 440K in CO:H$_2$. It is hard to tell whether or not the decrease is real or is due to an experimental error. Tco also shows a similar issue with a maximum reaching 1720K (approximately 3ms after the beginning of the pulse) but going back down to 1140 K at the end of the 5ms. However the values measured in the afterglow 1ms after the end of the pulse do not show any noise (cleaner measurement in the afterglow are seen due to lack of electromagnetic noise of the pulse on the FTIR). It appears that the relaxation of Tco is much slower in CO:H$_2$ than in pure CO. A

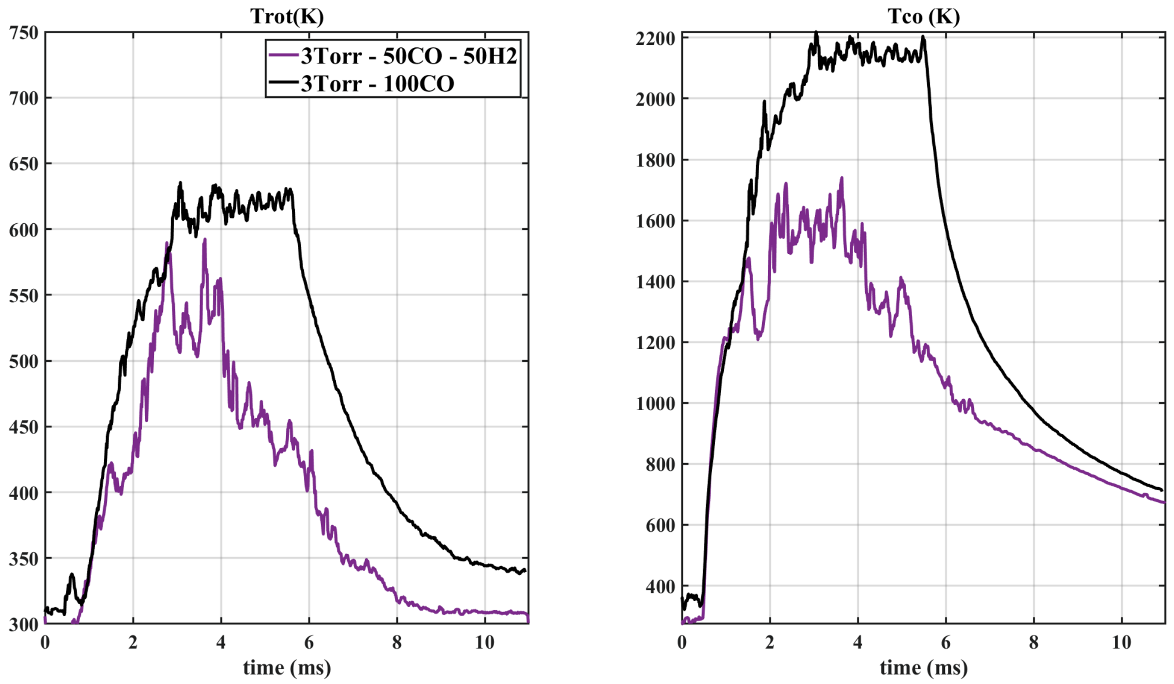

Figure 6.30: Evolution of Trot and Tco in the single pulse experiment in 50-50 CO-H$_2$ plasmas (at 3 Torr, 50mA)

comparison of the simulated and experimental post-discharges is shown on figure 6.31. For the CO:H$_2$ interactions, 4 processes were added in the simulation

$$\text{VT: } CO(v=n) + H_2 \rightarrow CO(v=n-1) + H_2 \tag{6.22}$$

$$CO + H_2(v=1) \rightarrow CO + H_2(v=0) \tag{6.23}$$

$$H_2(v=1) + H_2 \rightarrow H_2(v=0) + H_2 \tag{6.24}$$

$$\text{VV: } CO(v=n) + H_2(v=1) \rightarrow H_2(v=0) + CO(v=n+1) \tag{6.25}$$

The rates are taken from Blauer et al. 1974 for 6.22 (whose rate is in good agreement with Miller et al. 1977 and with Hooker et al. 1963), (6.23) and (6.24). The rate given for CO(v=1) was scaled to v for higher levels. Rate $k_{6.25}$ was taken from Matsui et al. 1975. Because the measurement is very noisy and the end of the pulse not well defined, it is not possible to match correctly the experiment and the simulation at the beginning of the post-discharge. The end of the post-discharge is less noisy and can be matched. For this measurement, the deactivation at the wall of vibrationally excited CO is included and the probability γ_v is kept at 0.04 s^{-1}, the value recommended for pyrex in Black et al. 1974. The deactivation of H$_2$ is also included using the probability given in table 6.3. Aside the experiment (in '+' markers), 3 cases are plotted. The first two test two different value of the vibrational temperature of H$_2$ with Tv$_{H_2}$=600K=Trot in blue and Tv$_{H_2}$=3000K in purple. the later matches the experiment better and was kept. This temperature is very high but the H$_2$ dissociation cross-section has a threshold of around 14eV, meaning that most electron in the discharge (whose mean electron energy is around 2eV) will only excite H$_2$ explaining how H$_2$ could have a very high vibrational temperature. A similar phenomenon is seen for nitrogen in nitrogen-containing plasmas. Process (6.25) is particularly interesting because it pumps the vibrations of CO and could partly explain the high CO temperature seen in the repetitive step-scan measurement. The last curve plotted is the case including all processes (with Tv$_{H_2}$=3000K) except the VT transfers CO(v)+H$_2$ (6.22). The end of the post-discharge seems better reproduced without the VT CO-H$_2$, indicating that the rate given in literature could be overestimated.

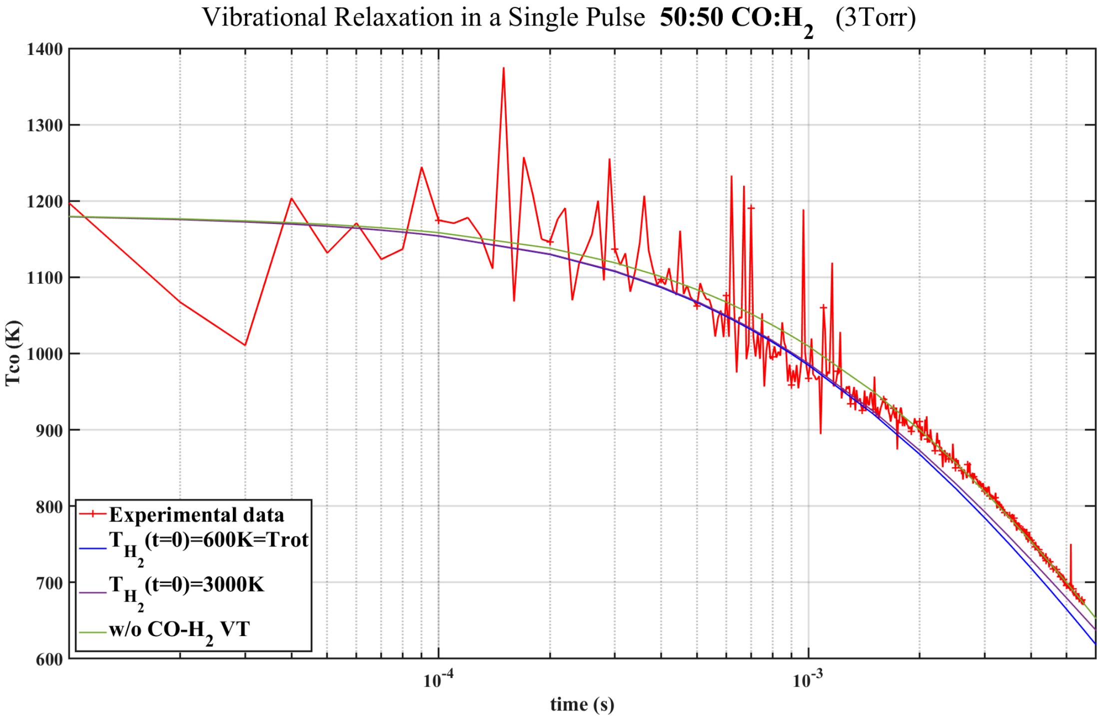

Figure 6.31: Simulation of the relaxation of Tco during the post-discharge of a 50:50 CO:H_2 Single Pulse experiment. the experimental Tco is plotted in red

- The modelling shows a small contribution to Tco from the H_2-CO VV transfer
- it is insufficient to explain the increase of Tco observed in the repetitive case
- The CO-H_2 VT rate (reaction 6.22) taken from Blauer et al. 1974 is probably overestimated

6.10 Summary and hypothesis

A few VT and VV processes were required to properly model the CO_2:CH_4 plasma relaxation in the step-scan experiment. These processes are gathered in table 6.4. The question of the increased Tco at 3Torr and 5Torr in the case of the repetitive step-scan experiment remains: which process increases Tco when increasing the initial CH_4 content in CO_2-CH_4 plasma above 1 Torr? Among the processes used here to model the post-discharge, two possible processes stand out, which are the pumping of CO and $CO_2(\nu_3)$ by H_2. The first process was found to be very small in the post-discharge and can be assumed to have a low rate during the discharge. The second was found to be necessary to properly reproduce CO_2 vibrational decay but does not explain alone how Tco increases in the repetitive experiment upon addition of CH_4 in the plasma. Given that nothing in the post-discharge can explain the increase of Tco at 3Torr, the process must be somehow related to electron excitation or dissociation processes forming molecules directly in high vibrational levels rather than to VV and VT processes.

Among the processes presented in table 6.4, it appears that the rate for losses of CO_2 vibrational quanta in the plasma are higher than for losses of CO vibrational quanta, which could contribute to keeping a high Tco while quenching CO_2, but still does not explain why Tco increases in some CO_2-CH_4 conditions compared to pure CO_2. A comparison of the EEDF in the various mixtures was carried out: the shape of the EEDF in CO_2-CH_4 plasmas could simply

Reaction	value at 600k (cm^3s^{-1})	source	Effect
$CO_2(000) + H_2(v=1) \rightarrow CO_2(001) + H_2$	2.10^{-13}	fit from Rosser Jr and Gerry 1971	CO_2 pumping
$CO_2(001) + CH_4 \rightarrow CO_2(\nu_1, \nu_2, 0) + CH_4$	3.10^{-13}	fit from Rosser Jr and Gerry 1971	CO_2 VT
$CO_2(001) + H_2 \rightarrow CO_2(\nu_1, \nu_2, 0) + H_2$	2.10^{-13}	fit from Rosser Jr and Gerry 1971	
$CO_2(001) + CO \rightarrow CO_2(\nu_1, \nu_2, 0) + CO$	3.10^{-14}	fit from Starr et al. 1974 & John C Stephenson et al. 1974	
$CO_2(001) + CO \rightarrow CO_2(000) + CO(v=1)$	5.10^{-13}	fit from Starr et al. 1974 & Kustova et al. 2020	CO_2-CO VV'
$CO_2(110) + CO(v=0) \rightarrow CO_2 + CO(v=1)$	7.10^{-15}	from Kustova et al. 2020	
$CO(v=0) + H_2(v=1) \rightarrow CO(v=1) + H_2(v=0)$	2.10^{-15}	fit from Matsui et al. 1975	CO vibrational pumping
$CO(v=1) + CO \rightarrow CO(v=0) + CO$	3.10^{-18}	fit from Hooker et al. 1963 & Blauer et al. 1974	CO VT
$CO(v) + H_2 \rightarrow CO(v=0) + H_2$	8.10^{-15}	fit from Hooker et al. 1963 & Miller et al. 1977	
$CO(v=1) + CH_4 \rightarrow CO(v=0) + CH_4$	8.10^{-21}	fit from Roger C. Millikan 1965a	
$CO_2 + CO(v=1) \rightarrow CO_2 + CO(v=0)$	1.10^{-18}	from Fromentin et al. 2023	
$CO(v=1) + CH_4(v=0) \rightarrow CO(v=0) + CH_4(v=1)$	5.10^{-14}	fit from Roger C. Millikan 1965a	CO VV'
$CO(v=1) + CO(v=0) \rightarrow CO(v=0) + CO(v=2)$	4.10^{-12}	fit from Hooker et al. 1963 & Blauer et al. 1974	CO VV transfer

Table 6.4: New quenching processes of CO and CO_2 taken into account in this work

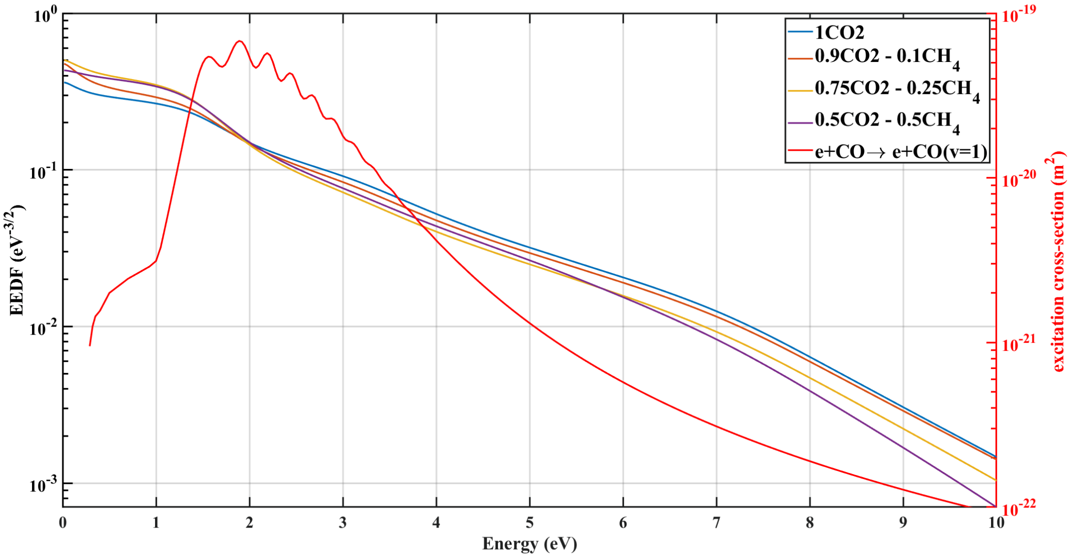

Figure 6.32: EEDF calculated in different plasmas corresponding to different initial mixtures. The pressure is 3Torr. The electron impact vibrational excitation cross-section of CO is plotted in red.

favours CO vibrational excitation. The EEDF were plotted for different initial mixtures on figure 6.32. The composition of the plasma at 3Torr was measured and used as input for the computation of the EEDF using LoKI-B. The reduced electric field was taken from the glow discharge measurement shown in chapter 4 and the temperatures measured during the step-scan experiment were used. The EEDF are plotted along with the vibrational excitation cross-section of CO. The four other EEDFs plotted are quite close at low energy and only diverge progressively after 1.5eV. Given that all the EEDFs are crossing close to the peak of the CO vibrational cross-section, no clear effect on Tco can be expected. The vibrational excitation rate coefficients (also computed by LoKI) in pure CO_2 and in 50:50 CO_2-CH_4 cases were compared and were found to be very close (1.35m^3s^{-1} vs 1.37m^3s^{-1}), insufficient to explain the observed excitation. The EEDFs were computed without taking into account the atomic O or H fractions (instead, the fractions of O_2 or H_2 were increased), but the low fractions should have limited impact on the EEDF. It was indeed verified in the previous chapter on actinometry that the variation of the atomic oxygen fraction in the computation has no significant effect on the EEDF and the atomic H_2 fraction was estimated below 1% of the gas density with actinometry. Because the increase of Tco is also pressure-dependant, the EEDFs were also plotted on figure 6.33 for different pressures in the 50:50 CO_2:CH_4 case. Similarly, the EEDFs for different pressures are close again at low energy and cross again close to the peak of the CO vibrational excitation cross-sections. The rates for the electron impact excitation was compared for all pressures and was found to be similar, once again not in agreement with the observed trend.

No straight-forward explanation of the increase of the observed vibrational excitation of CO can be found. The composition of the plasma is very unfavorable to CO excitation: the few percent of water present in the plasma should absolutely quench all form of vibrational excitation according to W.J.Witteman 1986. H_2 and the few atomic H should also largely contribute to strong vibrational quenching. Whatever the process explaining the high Tco is, it must be quite strong. In M.Damen et al. 2020, the repetitive experiment (with the same setup as presented here) measured the vibrational excitation in a 95:5 CO_2:H_2O mixture and showed that the vibrations of both CO and CO_2 are strongly decreased. The dissociation products of H_2O like OH or H were likely present in the plasma. These species can therefore be excluded from the list of potential vibrational excitation provider, along with the ones tested in the single pulse

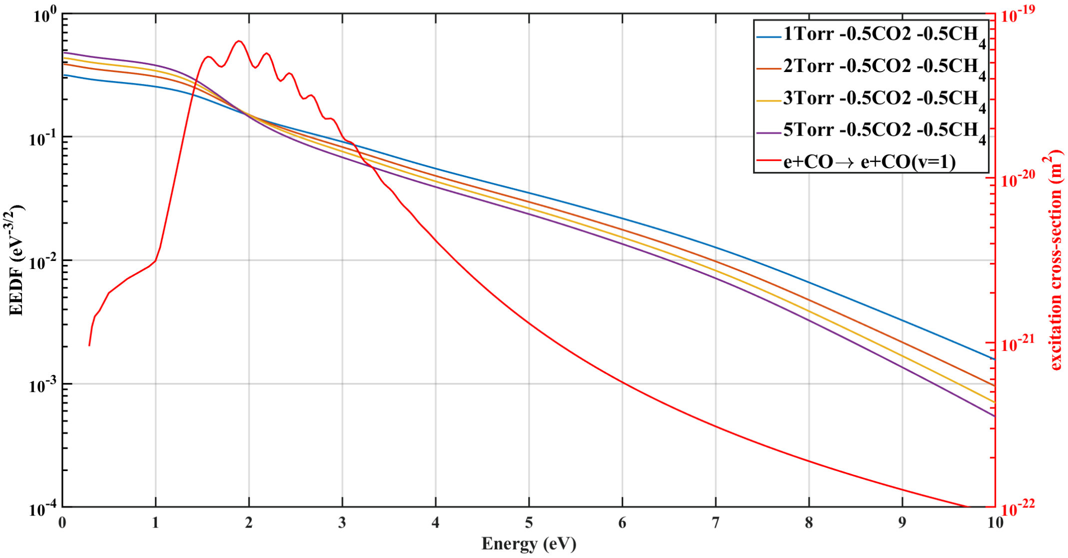

Figure 6.33: EEDF calculated for 4 different pressure for the 50:50 CO$_2$:CH$_4$ case. The pressure is varied between 1 and 5 Torr. The electron impact vibrational excitation cross-section of CO is plotted in red.

experiment: CH$_4$, H$_2$, H$_2$O, H$_2$, OH.

Pietanza, Colonna, Laricchiuta, et al. 2018 discussed the possibility to exchange CO electronic excitation into CO vibrational excitation through:

$$CO(a^3\Pi, w = 0) + CO \rightarrow CO(v = 27) + CO \tag{6.26}$$

Because of the high vibrational level, this process could lead to a strong increase of the CO vibrational temperature, but no experimental validation of this process was established so far. It is assumed that this process does not play an important role in pure CO$_2$ plasmas because of the quenching of the CO(a$^3\Pi$) state by CO$_2$ and O$_2$. In the CO$_2$-CH$_4$ plasmas, little O$_2$ is formed, meaning that the CO(a$^3\Pi$) would have less quenchers (assuming that CH$_4$ and its by-products like H$_2$ do not quench CO(a$^3\Pi$)), and the role of this process could be more important. It could therefore contribute to the high CO vibrational temperature observed. However, this phenomenon could be expected to be necessary to reproduce the decays in the post-discharge phase. Even if no CO(a$^3\Pi$) is formed in the post-discharge, CO(a$^3\Pi$) is formed during the pulse and would represent a reservoir for vibrational excitation. Secondly, as seen on figure 6.5 and 6.33, the increase of pressure should maintain a similar composition but reduce the number of electrons which can excite CO to the a$^3\Pi$ state. The ratio CO(a$^3\Pi$)/CO(X) should therefore decrease with increasing the pressure, which does not match the trend with pressure and does therefore not explain fully explain the evolution of the CO temperature. It could however partially explain the evolution of Tco.

Given the results of both the simplified model and the extended model, it is tempting to look further into the $O(1D) + CH_3 \rightarrow CO + H_2 + H$. Indeed, its ground-state counterpart $O(3P) + CH_3 \rightarrow CO + H_2 + H$ can produce vibrationally excited CO. Seakins et al. 1992 used time-resolved Fourier transform infrared spectroscopy to detect CO(v) produced after interaction of methyl radicals CH$_3$ with ground state oxygen atoms. The O were produced by photolysis of SO$_2$ (producing ground state atoms) while CH$_3$ was produced simultaneously by photolysis of acetone. While the experiment took place at room temperature, CO vibrational excitation up to v=8 was recorded and the CO vibrational temperature was fitted to 12700K. The high temperature suggested that CO was indirectly formed from a complex. The experiment was repeated in Marcy et al. 2001, where the CO(v=1) emission band was detected and used to trace CO during room-temperature measurements. The production channel of CO(v) was recorded and confirmed with a theoretical study which indicated that the production channel indeed went through the H+H_2CO, followed by H_2+HCO*, followed by production of excited CO. According to Preses et al. 2000, which studied the interaction of O and CH_3 using infrared TDLAS, the reaction could be enhanced by vibrationally excited CH_3 (which could be produced in our discharge after CH_4 + O(1D) according to Schlütter et al. 1993). Because the ground-state version of this process produces vibrationally excited CO, it could be imagined that the same process with an excited state, whose existence was suggested in the previous chapters, would also lead to vibrational excitation. It is unlikely that this process is the only cause of the increasing Tco in CO_2-CH_4 plasmas at 3Torr, but it highlight that the increased excitation could be due to one (or several) of the numerous chemical processes taking place in CO_2-CH_4 plasma.

The chemistry in the reactor was simulated using the simplified model presented in chapter 4. The main processes producing CO are presented on figure 6.34 and are :

$$e + CO_2 \rightarrow e + CO + O(1D) \tag{6.27}$$

$$2HCO \rightarrow CH2O + CO \tag{6.28}$$

$$CH_3 + O(1D) \rightarrow CO + H_2 + H \tag{6.29}$$

$$CH_2 + CO_2 \rightarrow CH_2O + CO \tag{6.30}$$

The first one, well known, does not give rise to vibrational excitation. This was confirmed by all our previous studies in pure CO_2. Nothing in literature indicated that the second one produced vibrationally excited CO. The third one was already discussed. The last channel (6.30) can produce excited CO. The vibrational distribution of CO after reaction (6.30) was studied in Hsu et al. 1977: CO_2 was mixed with CH_2 and CO(v) up to v=4 was measured, with an average vibrational energy of 1.9Kcal/mole (0.08eV/molecule). A similar distribution was observed in Shaub et al. 1981. A. H. Laufer and Bass 1977 conducted similar experiment and detected CO(v=2). A. H. Laufer and Bass 1977 estimated that 15% of CO produced was vibrationally excited. The channel (6.30) could therefore contribute to CO vibrational heating. Because of the possible pumping of CO(v) by H_2(v), a similar analysis was done for H_2. The main processes forming H_2 in the plasma are :

$$CH_3 + O(1D) \rightarrow CO + H_2 + H \tag{6.31}$$

$$CH_2 + H \rightarrow CH + H_2 \tag{6.32}$$

$$CH_2O + H \rightarrow H_2 + HCO \tag{6.33}$$

$$e + CH_4 \rightarrow e + CH_2 + H_2 \tag{6.34}$$

and wall recombination. Among these processes, only 6.32 was found to promote vibrational excitation of H_2 in litterature. Numerical studies of the reaction in Garcia et al. 2019 showed that the reaction could release energy in the vibrations of both CH and H_2. The energy could then be transferred to CO via VV processes. The rates of the three processes allegedly producing vibrationally excited CO or H_2 would increase with increasing initial CH_4, which is consistent with the experimental observations.

The question of the trend of CO temperature with pressure remains. The contribution of processes (6.30) and (6.29) to the CO balance in the reactor are plotted on figure 6.34. The contribution of channel (6.30) to CO production increases with pressure but the contribution of (6.29) decreases with pressure. Following the vibrational distribution measured for both of these processes, the latter has the strongest contribution and the vibrational excitation would scale with this one if CO(v) were really produced. The pressure trend could then hypothetically be explained by a competition of processes. On one hand, the CO is vibrationally excited by electron impact processes (similarly for all pressures as seen with the EEDFs) and chemical processes (whose contribution decreases with pressure): the CO vibrational excitation decreases

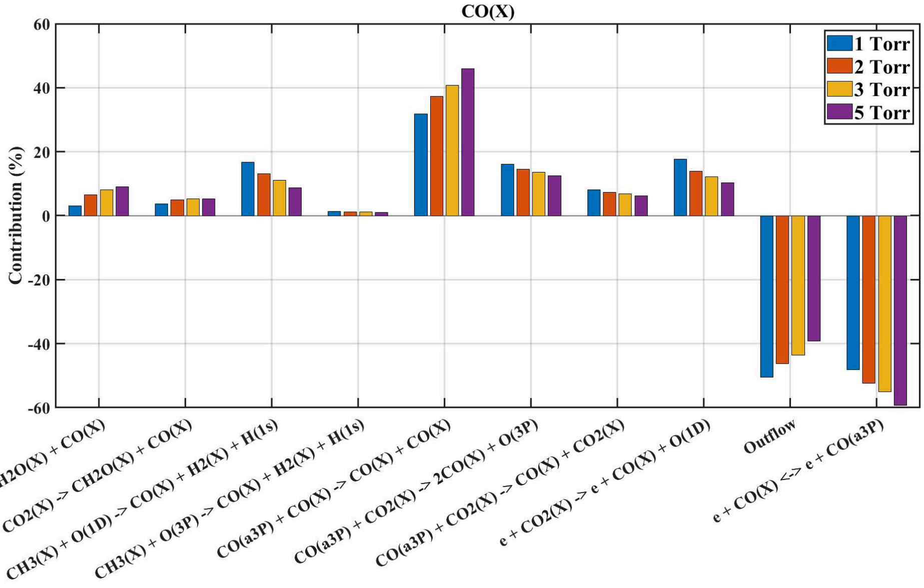

Figure 6.34: Contribution of the main CO loss and creation to CO balance. The contribution of the formation processes are positive, the one of the losses are negative. Each color is a different pressure

with pressure. On the other hand, the excitation is largely quenched by wall deactivation (whose relative importance compared to gas phase deexcitation decreases with pressure) and VT processes (which increase with temperature thus indirectly with pressure). In other words, at 1Torr wall deactivation quenches the chemically induced vibrational excitation, but not at 3Torr due to the relative contribution of the wall deactivation being less important than the one of the gas phase processes. At 3 Torr, the gas temperature low enough so that the VT processes can not quench all CO vibrational excitation. At 5Torr, The VT processes and the wall deactivation quench the chemically and electronically induced vibrational excitation. No similar effect is seen on CO_2 because the main source of CO_2 in the experiment in the flow, which constantly cools down the CO_2 vibrations.

This is highly hypothetical and proposed only for the sake of proposing an explanation to this experimental observation. It is based on a few processes (one of them having been only ever described in the previous chapter of this thesis) and certainly neglects some numerous pathways of these plasma. Shedding light on the vibrational excitation in CO_2-CH_4 plasma would require a complete and careful modelling. To this aim, the modeling effort of the single pulse measurements must be pursued.

6.11 Conclusion

The aim of this chapter was to study the vibrational excitation in CO_2-CH_4 plasma to understand the interactions of the vibrations of CO_2 and CO, previously studied in depth with the CH_4 and its by-products. To this aim, the vibrational temperatures of CO_2 and CO were measured during plasma pulses of 5ms with FTIR spectroscopy in various mixtures. A first configuration was studied: the repetitive experiment, which is a pulsed plasma. This experiment, containing all the species that would be found in a applicative CO_2 conversion experiment, allowed to draw the general conclusions: first, the rotational temperature, at equilibrium with the gas temperature, decreases in CO_2-CH_4 plasma which was attributed to an increase of the thermal conductivity. This increase was however in competition with efficient VT processes, sometimes leading to unexpected variations. The VT processes were indeed found to be very strong in CO_2-CH_4 plasmas, efficiently quenching T_{12}, T_3 and Tco, in good agreement with literature. This means that it is impossible to achieve CO_2 dissociation through purely vibrational ladder climbing in CO_2-CH_4, though DRM could still benefit from the out-of-equilibrium kinetics of CO_2-CH_4 plasmas. Despite the strong VT, an increase of the CO vibrational temperature compared to pure CO_2 plasmas was noted for 2 and 3Torr. To understand the source of this excitation, the Single Pulse experiment was used, in which the interaction of the molecules without their dissociation product is measured. This experiment provided data adapted for benchmarking a model. The post-discharge data in particular are very valuable, because they allow the study of the vibrational transfers without electron impact excitation. The interaction of CO_2 with CH_4, H_2 and CO, as well as CO with CH_4 and H_2 were modeled by Tiago Silva and allowed to fix rates for the VT processes. The wall losses were also included and proved to be an important vibrational loss channel. The measurements also highlighted that for a proper description of the vibrational kinetics of CO_2 and CO, the VV transfers and the vibrational kinetics of CH_4 and H_2 had to be taken into account: CO_2 and CO could both transfer vibrational quanta to CH_4 vibrations or be pumped by H_2 vibrations. These processes were however insufficient to explain the increase of Tco observed in the repetitive case. A possible explanation of the high Tco resides in the chemically induced vibrational excitation of CO_2. It can be reasonably supposed that the critical process $CH_3 + O(1D)$, identified in both the simplified and the extended chemical kinetic models leads to production of vibrationally excited CO (because its ground-state counterpart does). The pressure dependent vibrational excitation of Tco would then be due to competing electronically and chemically induced vibrational excitation on one hand and VT and wall deactivation on the other hand. This hypothesis does however seem fragile. Because of the complexity of CO_2-CH_4 plasmas and their numerous pathways, only a modeling effort can efficiently determine the most probable pathways. The modelling, started in this work must be pursued to include the plasma On phase of the discharge in the single pulse case. The correct comprehension of the rotational heating mechanisms will prove challenging, as they already are in pure CO_2 plasmas. The simplified model developed in chapter on the glow discharge will be very helpful as it will allow to determine the chemical pathways and to identify the most important species. The second step is the modelling of the post-discharge phase in the repetitive case, which will require the addition to the model of the VT and VV processes with the numerous species of CO_2-CH_4 plasmas. The final steps will be the modelling of the whole system, combining all processes included up to there. An additional effort should be put on the understanding of the $CH_3 + O(1D)$ reaction. As discussed, this reaction was not described in literature so far and the modeling of CO_2-CH_4 plasma did not allow to properly estimate its rate. Modeling in CH_4:O_2 plasma using the simplified model could probably bring additional proof of the existence of the process and constrain the rate better. Ideally, a dedicated experiment would be to measure the rate could be imagined. O(1D) could be produced by photolysis of O_3 and CH_3 by photolysis of acetone. The density of CO(v) could be followed by time-resolved FTIR spectroscopy. This experiment could determine if this process really exist, the branching ratio with which CO is produced from it and if it really does produces CO(v).

CHAPTER 7

Conclusion

CO_2-CH_4 plasma are a very interesting object of study because of their complex chemistry and of the great number of physical phenomenons taking place. They are still mostly misunderstood, but the present work sheds lights on some of their aspects. The main question driving this work was:

What are the basic physical phenomenon happening in CO_2-CH_4 plasma ?

The answer does not hold in a simple textbox! Two main points were studied in this work: the chemical kinetics and the vibrational kinetics.

Diagnostics Before studying CO_2-CH_4 plasma, efforts on developing OES-based techniques were made. The actinometry, a simple and convenient OES-based diagnostic was studied parametrically to determine how to draw the best results. It was used to measure O atom densities in O_2 discharges (with traces of Ar) and compared with results obtained with Cavity Ring-Down Spectroscopy. Because actinometry relies on line intensity ratio, testing it directly offers too many combinations. The choice of data for one atom can then depend on the data of the other andf this might occult error compensation when doing the ratio. To avoid this, another comparison method was developed: using the O atom density and the temperatures obtained from the CRDS data, the EEDF was computed with the Boltzmann solver LoKI. The intensity of each line was computed for various set of collision data. The most sensitive parameters/collision data are the choice of the set used for the computation of the EEDF and the choice of the excitation cross-section for the studied radiating level. Tests in pure O_2 were ran first. Two sets of cross-section for the EEDF were tested and no fully satisfying results were found. The Biagi set allowed for a good match of measured and simulated intensities but it is not validated against swarm parameters, raising question over the validity of the set. The IST set, which reproduces the swarm parameters did not allow to reach good agreement between experiment and simulation at first. The matching was however greatly improved by removing the atomic oxygen from the EEDF. Unfortunately, no common feature was observed on the EEDF of the best simulation cases, preventing from deducing what key feature improves simulation. Several excitation cross-section were tested and the cross-sections proposed in Laher and Gilmore 1990 seemed to yield the best results, both in terms of values and trends. O_2-Ar mixtures were then tested, with different Ar percentages. First, the simulated values of the line intensities progressively got worse and worse upon addition of Ar, indicating that the description of the tail of the EEDF in the mixture is likely inaccurate in O_2:Ar mixtures. Second, a sharp increase was seen in the simulation at low pressure (0.5Torr, corresponding to the highest reduced electric field) which was not found in the experimental data. Unfortunately, no point at low pressure was taken in pure oxygen so in the present condition, it is difficult to know if the very strong simulated trend observed in O_2-Ar plasma at low pressure is due to the computation of the EEDF in mixture or if this problem stems from a flaw in the model itself. More points are required to clear this particular point. Despite this, the actinometry calculations (i.e the ratio of lines) were carried out to measure the O fractions in these mixtures and gave surprisingly good results: the values were off by a factor 2 to 3 (so the order of magnitude was right) and the trends were very accurately reproduced thanks to the error compensation when doing the ratio, in O_2 plasma and in CO_2 plasma, showing that actinometry was still a very convenient diagnostic. The cross-section given in Pagnon 1995 were tested despite being very different from their original sources. They gave very good results for the O fraction but less accurate trends. It was also demonstrated that using some particular lines, actinometry can be performed with a poorly resolved spectrometer (using the peak intensity). The example of a USB spectrometer was demonstrated. Other applications of the USB spectrometer were put forward, such as the estimation of the rotational temperature through the fitting of a vibrational transition of the Angstrom system at 480nm, or the calculation of the CO vibrational temperature by fitting of several bands of the CO Angstrom system. This last technique still poses problems as an unexplained correction factor must be taken into account but it has demonstrated excellent trends. The fitting of the CO vibrational temperature using the 3rd positive system of the CO is also currently being tested and has yielded values very close to the FTIR measurements.

Chemical kinetics The chemistry of CO_2-CH_4 plasma was investigated first using a low pressure glow discharge. FTIR measurements of the composition of the plasma were taken in a large range of pressure, flow and gas mixtures and were completed by electric field measurement and optical emission spectroscopy. The rotational temperature, at equilibrium with the gas temperature was drawn from the OES and combined with the electric field measurements to obtain the reduced electric field. These data served as basis for the validation of a 0D kinetic model using the LoKI solver. A kinetic scheme based on the one already existing in pure CO_2 was developed, including molecules with up to 1 carbon atom (CO_2, CO, CH_4, CH_3, CH_2, CH, C, H, H_2, H_2O, OH, HCO...). A first iteration was assembled using only values available in literature but did not give satisfactory agreement with the measurements, which led to the some modifications in the scheme. The production of the CH_5^+ ion, usually considered main ion in the plasma, was changed: it is usually the main ion in modelling work because of a single reaction ($CH_4^+ + CH_4 \rightarrow CH_3 + CH_5^+$), whose rate commonly used is unusually high and was measured once in the 1970's. The removal of this single creation process changed the main ion to CH_4^+ and largely improved the self-consistently simulated value of the reduced electric field. The CH_4 electron impact dissociation rate used in the model proved to be insufficient to match measurements. The electron impact dissociation cross-section of CH_4 was multiplied by a factor 2 (remaining in agreement with available values in literature), which improved the simulation results. It was then noted that the electronic excited state, which play a key role in pure CO_2 plasma, were poorly taken into account: only a few rates concerning O(1D) were included. These rates were typically 3 to 4 orders of magnitude higher than their ground-state counterpart. The reaction CH_3+O(1D) → CO + H_2 + H was added, using the rate of CH_3 + O(3P) multiplied by 1000. The addition of this reaction largely improved the simulation results and gave very good matching results on the whole range of pressure, flow and mixture tested. The main reaction pathway were drawn from the model and the influence of the excited state appeared as critical. Accounting for O(1D) revealed new reaction pathways, often attributed to the chemistry of the C_2H_Y molecules considered as intermediate species even though they might only be present in traces. This study highlighted that too few rates are available for excited states. CO($a^3\Pi$), essential in CO_2 plasma, has no rate for reactions involving hydrogenated species. More work is required to investigate further the role of electronically excited states.

The chemical kinetics was further investigated in a pulsed radiofrequency discharge in close configuration, which was more challenging because the reduced electric field and electron density could not be measured in this discharge. The evolution of the gas composition was followed over time with FTIR spectroscopy. CO and H_2 remained the main products in this experiment but

C_2H_6 was found to be an intermediate specie whose density reached up to 5% of the gas fraction. Several pressures and gas mixture were investigated, as well as various pulsing parameters to play on the characteristic times of different processes. The measurements highlighted two important results; First, CO was produced very quickly from CH_4 (almost as quickly as it was form CO_2) meaning that CH_4 or its by-products were very quickly oxidized. Second the destruction of C_2H_6 reformed CH_4, seldom seen in literature. The discharge was modeled using the kinetic scheme developed for the glow discharge, extended to include molecules with 2 carbon atoms. Because of the number of calculations required to simulate one measurement, only a few test cases were simulated and compared to the experiment. The reaction previously evoked for the glow discharge, $CH_3+O(1D) \rightarrow CO + H_2 + H$, appeared to be the only possible pathway to match the production speed of both CO and H_2, confirming that this reaction is very important. This cleared the question of the balance between excited state chemistry and C_2H_Y chemistry: the model in the glow had brought up alternative pathways relying on excited state, this second part explicitly clears that the excited states (particularly O(1D)) are critical and that C_2H_6 also plays an important role but only if it accumulates enough in the plasma. The reformation mechanism of CH_4 after destruction of C_2H_6 remains unclear so far. Indeed, this model and literature show that there are very few pathways to break C_2H_Y molecules into two CH_X molecules in CO_2-CH_4 plasma, which were all taken into account and could not explain the experimental observations. A possible explanation could be the action of the surface. Because it was shown in literature that H recombination on the surface is very fast and efficient, it was assumed that a surface processes involving H and C_2H_6 could lead to CH_4 reformation. A surface process was added to the model and could lead to a CH_4 reformation, though not at the level expected. The surface process added did not aim at describing precisely the plasma/surface interaction, which should be done with a proper surface model, but simply at showing that the surface could indeed possibly explain the observation. Additional work is required to develop a good surface model, which will be necessary in the prospect of using modeling for applications (which often rely on catalysts). Using the model, the reaction pathways in the RF were explored. A comparative study with CH_4 plasma showed that the size of the largest molecule in the plasma was likely due to the reduced electric field (because of the dehydrogenation of CH_4 it causes) and the temperature (because of the dehydrogenation of C_2H_Y it causes).

Vibrational Kinetics The vibrational excitation, supposedly optimal in pure CO_2 plasma to achieve dissociation at low energy cost, was studied in the glow discharge with FTIR spectroscopy. The vibrational temperatures of CO_2 and CO were measured during a pulse of 5ms in various conditions of mixture and pressure. In most of the cases, the rotational temperature as well as the vibrational temperatures of CO_2 and CO were decreased upon addition of CH_4 in the initial mixture. The decrease of the vibrational temperatures was attributed to strong VT processes between CO_2 (or CO) and the CH_4 and its dissociation by-products (H_2, H, H_2O). This assumption was supported by rates of the VT coefficients found in literature, for example for the VT of CO_2 with H_2O whose rate can be found 1000 time higher than the VT of CO_2 with CO_2. The decrease of the rotational temperature was attributed to the large thermal conductivity of the H_2 produced in the plasma which very efficiently carries the heat to the wall. This decrease is in competition with the heating due to the aforementioned VT processes, leading to unexpected trends for the temperature in some conditions. Surprisingly, the CO excitation was increased in one particular conditions and happened to be further from equilibrium than in pure CO_2 on the range 2-5 Torr. To understand the source of this excitation as well as to obtain values of the VT rate for all species (literature value are spread), single pulse experiment where the gas experiences only one pulse of 5ms before leaving the reactor were carried out. These experiment allow to control the composition of the gas during the pulse. The post-discharge of these experiment, where no electron impact excitation takes place, was modelled. For all mixtures measured, the wall deexcitation accounts for a large part of the vibrational loss, but VT rates could also be obtained and compared to literature values. Interestingly, the VV processes to H_2 and CH_4 had to be considered to reproduce correctly the CO_2 and CO vibrational relaxation. It was highlighted that the VV processes with H_2 actually benefit CO_2 and CO (marginally for CO). No insights on the cause of the increase of the CO vibrational excitation were obtained with the modelling. On the contrary, most of the results pointed that CO vibrations are efficiently quenched by the other species of the CO_2-CH_4 plasma. The increase was attributed to chemically induced excitation. Literature indeed shows that CH_3+O(3P)→ CO + H_2 + H could produce CO at a vibrational temperature of several thousand K. Using the kinetic scheme, it was found that in this case like in the glow discharge studied before, CH_3+O(1D) → CO + H_2 + H was a major contributor to CO production and is expected, like its ground-state counterpart, to produce highly excited CO. Other processes could create excited CO or excited H_2 which could in turn pump CO(v). The trend of CO vibrational excitation with pressure was attributed to a competition to wall deexcitation, VT processes and chemically induced vibrations. More work is required to confirm this hypothesis.

Next steps

Much work remains. To complete the work done here, several experiments and modelling work can be done. The main one is to find a way to measure the rate of the reaction of $CH_3 + O(1D) \rightarrow CO + H_2 + H$. An ideal experiment specifically dedicated to this could be imagined using photolysis to produce separately CH_3 and O(1D) and make them react. This experiment could also allow to measure the branching ratio of the products: indeed, if $CH_3 + O(1D)$ is similar to $CH_3 + O(3P)$, CH_2O could be produced as well. In the present case, it was supposed that the branching ratio was in favor of the production of CO, because the building-up experiment in the RF showed that CO was produced very fast and going through CH_2O could not match the CO production rate. Nevertheless, it would be interesting to confirm this assumption experimentally. The photolysis experiment is also ideal because it would allow to follow the vibrational excitation of CO and thus confirm the hypothesis that this chemistry can produce vibrationally excited molecules. However, such experiment seems rather complicated from a material point of view because it requires peculiar equipment. A more accessible but less direct experiment would be to use the glow discharges in different conditions. A high flow could be used to limit the residence time of the gas in the plasma and limit the formation of dissociation products. This is close to what was done in step-scan experiment, where the flow was 7.4sccm but the discharge had a duty cycle ration of 1/3, making the dissociation equivalent the one obtained with a flow of 22.4sccm. The model was run in these conditions and showed a good agreement with the compositions measured during the step-scan measurements, but more conditions are necessary to have a good estimation.

The glow discharge Another test could be done by doing experimental and simulation comparisons in a CH_4-O_2 glow discharge. This discharge would produce both CH_3 and O(1D). The present "simplified" kinetic model could be used for that discharge. However, a new problem would arise: the electron impact dissociation of oxygen leads to formation of both O(1D) and O(1S) (which caries approximately 2.7 eV). The production of O(1S) would have to be estimated, as well as the rates of reaction of O(1S) with CH_3 and all other species. If the discharge conditions are chosen so that the reduced electric field is not too high, the production of O(1S) could be very limited and O(1D) could be considered as the only excited state. The comparison of simulation and experiment could certainly bring much information on the interactions of this excited state with all the species in the plasma. Controlling the flow could once again help controlling the quantity of dissociation products in the reactor (such as water) and could bring valuable information, even more if the vibrational excitation of CO can be measured.

RF plasmas Building-up measurements in the RF discharge could also be done in CH_4-O_2 plasma. Of course, more measurement in CO_2-CH_4 in the fastest configuration to simulate (500 trains of 1 pulse of 50ms) would be a first step to provide more data to validate the "extended" kinetic scheme. Different CO_2-CH_4 mixture (with CH_4 percentage below 50) would be good to validate the rate of the CH_3 + O(1D) (by looking at the first 5 seconds) and to limit the influence of the surface (which seems to be much stronger for hydrogenated species) on the longer time-scales. Currently, as long as it has not been tested against a larger set of measurements, the "extended" scheme is still considered incomplete, though it already yields good results. This is why the "extended" scheme has not been applied to the glow discharge: as some doubts on the CH_4 formation mechanisms still remain, using the extended scheme for the glow discharge might suggest alternatives pathways to the one found (though unlikely, as the newly added reactions concerned C_2H_6, which doesn't have time to be formed in the glow due to the flow renewal), ut the validity of these pathways will be questionable. CH_4-O_2 measurements in the RF will also provide valuable information on the rates of O(1D) with all the CH_4 derivative. The RF analysis is currently limited by the absence of knowledge of the temporal profile of the reduced electric field, the electron density and of the temperature. The first one currently appears as an insoluble problem, at least experimentally. If the line ratios for E field estimation presented in the actinometry chapter ever yield interesting results, they will be the best solution. An idea of the value of the electron density can be obtained by hairpin probe measurements. This measurements are usually difficult above 1Torr but they are worth a shot. The temperature could be obtained by OES. Ideally each 50ms pulse trigger a spectrometer focused on the discharge. The spectra could be analyzed to draw the rotational temperature over the 25s of plasma On time of the building up experiment. This measurement is quite straight forward and would be very interesting to set-up.

OES Both the glow discharge and the RF measurements require OES measurements to be properly analyzed. An even higher comprehension could be reached if the optical emission diagnostics are developed to draw as much information as possible. Indeed, all measurements proposed here could provide extremely valuable information on the vibrational excitation of CO, which showed unexpected behaviour in CO_2-CH_4 plasmas. The measurement of Tco, very promising, must be implemented for by OES, whether by using the 3rd positive system or the Angstrom system, for CO_2-CH_4 and CH_4-O_2 plasmas. The technique must first be validated. To that aim, cross-measurements of Tco by FTIR and OES must be performed in CO_2 containing discharges. The present work covered a large range of parameters in pure CO_2 but parametric measurements in numerous mixtures can be tested for different effects. CO_2-N_2 are already very well-known discharges in which the N_2 act as a vibrational energy reservoir for CO(v) and CO_2 (ν_3). The vibrational temperatures in CO_2-N_2 discharges is usually higher that in pure CO_2 discharge. By varying the pressure and mixture, points with similar reduced electric field but very different vibrational temperatures could be investigated. Ar is very interesting for the study of CO_2 because it has a very limited quenching effect on the CO_2 vibrational excitation, according to preliminary measurements. A constant vibrational temperature can be sustained while increasing the Ar percentage in the mixture, hence varying the pressure and probably the reduced electric field. Finally, CO_2-O_2 mixture are also of high interest because contrarily to the previous case, atomic oxygen created by electron impact dissociation of O_2 in the discharge will effectively quench the CO_2 vibrational excitation. Because the vibrational excitation is a very minor contribution to CO_2 dissociation in the glow discharge, the vibrational excitation can be lowered while maintaining a certain dissociation degree. These 3 mixtures will allow to study the robustness of the Tco OES measurements in a large range of conditions where the important parameters will vary while being known. Conveniently, if these measurements are done using a USB spectrometer, the broadband intensity will be accessible in all of these conditions as well. These measurements can provide a large number of point to verify or invalidate the current hypothesis on the intensity of the CO_2 broadband emission.

Step-scan measurements and modelling The study of the vibrational kinetics must also be pursued with the step-scan and the single pulse experiments. Ideally, single pulses experiment would be taken in CO_2-H_2O and CO-H_2O mixtures to draw the rates of VT processes with water, which are reported in literature to be extremely high. This however require specific equipment and could be challenging. As for the modelling part, the next steps should be the both the modelling of the post-discharge in the repetitive step-scan experiment and the modelling of the discharge phase in the single pulse experiment. The post-discharge phase of the repetitive step-scan requires to have a good idea of the quenching of the vibrations by all molecules (thus the need to measure the VT with water). Experimental data on the quenching by radicals will likely be difficult to find or measure but the density of radicals in the plasma is very low compared to the main products. This must be coupled to the chemical kinetics modelling to have access to the evolution of the composition of the plasma over the pulse of 5ms. If the hypothesis of the chemically induced post-discharge is correct, it could be visible in the post-discharge (though the production of excited CO(v) relies on reaction between radicals, whose density will be weak in the post-discharge). The modeling of the single pulse discharge phase will rather help constrain the electron impact excitation cross-section and the rate of the VV coefficients. The modelling of the discharge will allow to conclude with certainty on the chemically induced vibrational excitation. On this particular matter, the excitation could be more visible if the number of pulses that the gas undergo in the reactor is higher than one. Simulations should be run to compute the optimal plasma duration for the reaction CH_3 + O(1D) to occurs enough to have a measurable impact but for the other products (suc as water) remain negligible. Once this optimal plasma duration is fixed, it can be translated into a flow at a given pressure. This would give the best measurement conditions to confirm or invalidate the hypothesis of chemically induced excitation.

Actinometry As interesting as the measurement of Tco, the atomic densities must be systematically investigated. It is unlikely that progress on the accuracy of actinometry will be made, but an order of magnitude is good enough. Ideally, a small amount of Ar would be added in the RF experiment and the spectra would include the O and H lines so that the atomic densities can be estimated all along the experiment. Ongoing test with Xe as actinometer done by Tiago Silva will conclude on whether or not this gas can be used as actinometer at low concentrations, limiting the influence on the plasma. To properly use actinometry, a few points must be cleared. A unanswered fundamental question dwells in the comparison of measured and simulated intensity of atomic lines: when comparing their evolution with pressure (and inderetly with reduced electric field), the simulation shows a stiffer trend than the measurement. Though this could be due to inaccuracy of the cross-sections, it is possible that the actinometry equations occult an important phenomenon. To verify this, actinometry measurements must be taken on larger range of pressure: the few points taken at low pressure (0.5Torr) indeed showed that the trend of the Ar lines were somewhat similar to the simulated lines, but that the oxygen lines trends did not match, but it couldn't be determined whether this as due to the significant amount of Ar in the EEDF or really to the actinometry equations. Hence, simultaneous OES and CRDS measurements must be taken in a pure O_2 plasma on a pressure range as large as possible. As mentioned, investigations are on-going to figure if the Xe could be a good actinometer, which would be interesting because the Xe lines are very intense even at low Xe content. However, Xe is extremely expensive, which might be limiting if actinometry is to be used frequently/ as a routine diagnostic. Other actinometers such as He and Kr could also be tested. O_2-Kr mixtures were tested in this work but spectrum showed presence of N_2 in the plasma, leading to uncertainty on these points. The calibration of the Kr flowmeter was also doubtful, preventing from analyzing these points. Nevertheless, Kr could be an equally good actinometer. Finally, injecting several rare gas at the same time could be very interesting: in low quantities, they will have little impact on the EEDF, and the collection of signals from the different rare gas could allow to estimate the electron temperature and eedf. This last development requires much work but could be applied using the USB spectrometer (given the good comparison between USB and well-resolved spectrometers) and could therefore provide an experimental estimation of EEDF in most of the OES measurements.

General directions of CO_2-CH_4 plasmas

Despite progress in the recent years and a larger and larger effort by the community, CO_2-CH_4 plasma are still ill-understood. This work aimed at describing the main fundamental processes of the CO_2-CH_4 plasma. Many things are missing for a complete and clear understanding of this plasma (like for any other type of plasma) but some elements in particular appear as crucial. The role of the excited state, often neglected, must be included as it appears to be essential. The rates of reactions including excited states must be measured or calculated with quantum mechanics calculations. The surfaces might also play a very important role. The interaction of hydrogenated species with surface appear to be very strong and reactions impossible in the gas phase appear feasible on the surface, even without catalysts. The interaction of the surfaces with the plasma will have to be described to optimize correctly CO_2-CH_4 plasma

Unfortunately, in the current economic context, the economic interest of CO_2-CH_4 plasmas and DRM is not as high as it was a few years ago. The overall reaction pathways is the following:

$$nCO_2 + nCH_4 + (2n+1)H_2 \rightarrow C_{2n}H_{4n+2} + nH_2O \tag{7.1}$$

For this process to have an ecological interest, the CH_4 needs to either be captured from a polluting source (in the best case) or be produced from methanisation, i.e be recycled from agro-industrial waste. Despite being a considerable contributor to climate change, very little effort is done nowadays to capture CH_4 from polluting sources (solutions can be found for cattle but are often expensive, but would be possible in some cases). DRM will have a strong interest as soon as efficient CH_4 recycling is generalized. The second option is not operable at a large scale, as methanisation capacities are still low worldwide compared to production of natural gas. In France, methane production capacities by methanisation represent only one percent of the total methane consumed. The price of biogas (i.e methane produced by methanation) was declining over the last years and was on the trajectory to align with the cheap imported natural gas. But the war in Ukraine increased the price of natural gas (by a factor 5 over the last year), stopping the decrease of the biogas price. There is for the moment no CH_4 source which would allow a economically beneficial DRM. Then, the H_2 required also needs to be 'green' (i.e produced from water electrolysis). Less than 1% of the H_2 produced worldwide is "green", the rest being produced by combustion of hydrocarbons. The price of green H_2 is currently higher than the so-called 'grey' hydrogen but is coming down. It will however take a few years before green H_2 is as cheap as grey H_2. Finally, the hydrocarbons products could in no way compete with the low-price fossile fuels. Their price is rising but it will take a few more years before gasoline becomes expensive enough to make room for ecological alternatives. In the current conditions CO_2-CH_4 plasma do not allow to reach economic rentability in the current context and might not be economically interesting before years. DRM is ideal for energy storage because it produces high energy density molecules which do not degrade over time and are easily transportable, but this problem is currently overlooked, and it will take some time before the stake of efficient energy storage (both over time and distance) emerges. CO_2-CH_4 plasma however remain an extremely interesting scientific object, a pinnacle of plasma science mixing complex physics and intricate chemistry, from which we can learn much and for this, deserve to be studied.

Annex: kinetic scheme

Reactions included in the "simplified" model

This is a table listing the reactions used in the kinetic scheme, along with the rate and the source of the rate

Table 7.1: Chemical reaction included in the "simplified" model. The rates are given in m^3/molecule s for 2nd order reactions or m^6/molecule^2 s for 3rd order reactions

Reaction	Rate coefficient (m^3/molecule s)	Source
$CH_4 + M \rightarrow CH_3 + H + M$	1.4e-18*exp(-45700/T)	Baulch et al. 2005
$CH_4 + H \rightarrow CH_3 + H_2$	4.36e-19*(T/300)$^{3.16}$*exp(-4405.5566/T)	Sutherland et al. 2005
$CH_3 + H_2 \rightarrow CH_4 + H$	6.86e-20*(T/300)$^{2.74}$*exp(-4739.9122/T)	Baulch et al. 1992
$CH_3 + CH_3 \rightarrow CH_4 + CH_2$	1.34e-18*exp(-8858.0191/T)	Kramida et al. 2021
$CH_3 + H \rightarrow CH_4$	9.2e-29*(T/300)$^{-8.82}$*exp(-4968.4286/T)	C.Olm et al. 2016
$CH_4 \rightarrow CH_3 + H$	3720000000*exp(-52246/T)	W. Tsang et al. 1986
$CH_4 + O \rightarrow CH_3 + OH$	2.26e-18*(T/300)$^{2.2}$*exp(-3819.8328/T)	Miyoshi 1993
$CH_4 + O(1D) \rightarrow CH_3 + OH$	1.35e-16	Atkinson 1992
$CH_3 + OH \rightarrow CH_4 + O$	3.22e-20*(T/300)$^{2.2}$*exp(-2239.4612/T)	Cohen et al. 1991
$CH_4 + OH \rightarrow CH_3 + H_2O$	1.36e-19*(T/300)$^{3.04}$*exp(-920.0794/T)	Bonard et al. 2002
$CH_3 + H_2O \rightarrow CH_4 + OH$	1.2e-20*(T/300)$^{2.9}$*exp(-7479.7041/T)	W. Tsang et al. 1986
$CH_4 + HCO \rightarrow CH_3 + H_2O$	1.36e-19*(T/300)$^{2.85}$*exp(-11299.537/T)	W. Tsang et al. 1986
$CH_3 + H_2O \rightarrow CH_4 + HCO$	8.25e-20*(T/300)$^{2.8}$*exp(-2950.2676/T)	W. Tsang et al. 1986
$CH_3 + CH_3 \rightarrow CH_4 + CH_2$	1.16e-19*(T/300)$^{1.34}$*exp(-8167.6589/T)	Han et al. 2011
$CH_3 + H_2O \rightarrow CH_4 + OH$	1.2e-20*(T/300)$^{2.9}$*exp(-7479.7041/T)	W. Tsang et al. 1986
$CH_4 + OH \rightarrow CH_3 + H_2O$	1.36e-19*(T/300)$^{3.04}$*exp(-920.0794/T)	Bonard et al. 2002
$CH_4 + CH_2 \rightarrow CH_3 + CH_3$	7.14e-18*exp(-5050.2135/T)	Bohland et al. 1985
$CH_4 + HCO \rightarrow CH_3 + H_2O$	1.36e-19*(T/300)$^{2.85}$*exp(-11299.537/T)	W. Tsang et al. 1986

Continued on next page

Table 7.1 – continued from previous page

Reaction	Rate coefficient	Source
$CH_3 + HCO \rightarrow CH_4 + CO$	2.01e-16	W. Tsang et al. 1986
$CH_4 + O(1D) \rightarrow H_2 + H_2O$	1.5e-17	Baulch et al. 1992
$CH_3 + H \rightarrow CH_2 + H_2$	2.05e-18*(T/300)$^{2.43}$*exp(-6008.7798/T)	Glarborg et al. 2018
$CH_2 + H_2 \rightarrow CH_3 + H$	3.59e-19*(T/300)$^{2.3}$*exp(-3699.561/T)	K.W.Lu et al. 2010
$CH_2 + H_2 \rightarrow CH_3 + H$	5e-21	W.Wang et al. 2018
$CH_3 + OH \rightarrow H_2O + CH_2$	1.2e-16*exp(-1399.9639/T)	Baulch et al. 1994
$CH_3 + OH \rightarrow H_2O + H_2$	2.59e-19*(T/300)$^{-0.53}$*exp(-5439.8942/T)	Dean et al. 1987
$H_2 + CH \rightarrow CH_3$	2.01e-16*(T/300)$^{0.15}$	Fulle et al. 1997
$CH_3 + O \rightarrow H_2O + H$	1.4e-16	Baulch et al. 1992
$CH_3 + O \rightarrow CO + H_2 + H$	2.8e-17	W.Wang et al. 2018
$CH_2 + H_2O \rightarrow CH_3 + OH$	1.6e-22	W. Tsang et al. 1986
$CH_2 + H_2O \rightarrow CH_3 + HCO$	1e-20	W. Tsang et al. 1986
$CH_2 + HCO \rightarrow CH_3 + CO$	3.01e-17	W. Tsang et al. 1986
$O_2 + CH_3 \rightarrow OH + H_2O$	5.65e-19*exp(-4500.5713/T)	Zellner et al. 1988
$CH_3 + O_2 \rightarrow H_2O + OH$	5.5e-19*exp(-4500.5713/T)	Baulch et al. 1992
$CH_2 + O \rightarrow CO + H_2$	6.64e-17	Franck et al. 1988
$CH_2 + O \rightarrow CO + H + H$	1.33e-16	Franck et al. 1988
$CH_2 + H \rightarrow CH + H_2$	1e-17*exp(899.6332/T)	Baulch et al. 1992
$CH + H_2 \rightarrow CH_2 + H$	3.11e-16*exp(-1650.1293/T)	Brownsword et al. 1997
$CH_2 + O_2 \rightarrow CO_2 + H_2$	2.99e-17*(T/300)$^{-3.3}$*exp(-1439.6536/T)	Dombrowsky 1992
$CH_2 + O_2 \rightarrow CO_2 + H + H$	9.99e-19*(T/300)$^{0.99}$*exp(135.9072/T)	Glarborg et al. 2018
$CH_2 + O_2 \rightarrow CO + H_2O$	4e-19	W. Tsang et al. 1986
$CH_2 + O_2 \rightarrow CO + OH + H$	1e-18	W. Tsang et al. 1986
$CH_2 + H \rightarrow CH + H_2$	9.78e-18*(T/300)$^{-0.03}$*exp(319.923/T)	Han et al. 2011
$CH + HCO \rightarrow CH_2 + CO$	3e-17	W. Tsang et al. 1986
$C + H_2 + M \rightarrow CH_2 + M$	6.89e-38	Husain et al. 1975
$CH_2 + OH \rightarrow H + H_2O$	3.01e-17	W. Tsang et al. 1986
$CH_2 + O \rightarrow HCO + H$	5.01e-17	Tsuboi et al. 1981
$HCO + H \rightarrow O + CH_2$	6.61e-17*exp(-51596.6083/T)	Tsuboi et al. 1981
$CH_2 + O_2 \rightarrow H_2O + O$	2.1e-18*(T/300)$^{2.42}$*exp(-807.0239/T)	Glarborg et al. 2018
$C + H_2 \rightarrow CH + H$	1.5e-16	W.Wang et al. 2018

Continued on next page

Table 7.1 – continued from previous page

Reaction	Rate coefficient	Source
$CH + H_2 \rightarrow CH + H_2$	1.31e-16*(T/300)$^{1.79}$*exp(-839.4973/T)	W.Wang et al. 2018
$CH_2 + CO_2 \rightarrow H_2O + CO$	3.9e-20	W. Tsang et al. 1986
$H_2 + OH \rightarrow H_2O + H$	1.55e-18*(T/300)$^{1.6}$*exp(-1659.751/T)	Baulch et al. 1992
$H_2O + H \rightarrow H_2 + OH$	6.82e-18*(T/300)$^{1.6}$*exp(-9720.368/T)	Baulch et al. 1992
$OH + H_2O + H \rightarrow H_2O + H_2O$	1.19e-36*(T/300)$^{-2.1}$	Javoy et al. 2003
$H_2O + H_2O \rightarrow OH + H_2O + H$	1.18e-14*exp(-53641.2292/T)	Javoy et al. 2003
$H_2O \rightarrow OH + H$	6.56e-16*exp(-53641.2292/T)	Javoy et al. 2003
$OH + H \rightarrow H_2O$	6.87e-37*(T/300)$^{-2}$	Baulch et al. 1992
$H_2 + HCO \rightarrow H_2O + H$	2.66e-19*(T/300)^{2}*exp(-8969.8719/T)	W. Tsang et al. 1986
$H_2O + H \rightarrow H_2 + HCO$	1.44e-17*exp(-1743.9413/T)	Oehlers et al. 2000
$H + CO_2 \rightarrow CO + OH$	2.51e-16*exp(-13350.1714/T)	W. Tsang et al. 1986
$CO + OH \rightarrow H + CO_2$	5.4e-20*(T/300)$^{1.5}$*exp(250.1654/T)	Baulch et al. 1992
$H + HCO \rightarrow CO + H_2$	1.5e-16	Baulch et al. 1992
$H_2O + O \rightarrow OH + OH$	1.84e-17*(T/300)$^{0.95}$*exp(-8570.5695/T)	Lifshitz et al. 1991
$OH + OH \rightarrow H_2O + O$	1.65e-18*(T/300)$^{1.14}$*exp(-50.5142/T)	Baulch et al. 1992
$O + HCO \rightarrow H + CO_2$	5e-17	Baulch et al. 1992
$O + HCO \rightarrow CO + OH$	5e-17	Baulch et al. 1992
$OH + HCO \rightarrow CO + H_2O$	5e-17	W. Tsang et al. 1986
$H_2 + O_2 \rightarrow OH + OH$	4.15e-17*(T/300)$^{0.44}$*exp(-34758.5543/T)	Karach 1999
$OH + OH \rightarrow H_2 + O_2$	3.32e-18*(T/300)$^{0.51}$*exp(-25377.3528/T)	Karach 1999
$HCO + H \rightarrow O + CH_2$	6.61e-17*exp(-51596.6083/T)	Tsuboi et al. 1981
$O + CH_2 \rightarrow HCO + H$	5e-17	Tsuboi et al. 1981
$CH + O_2 \rightarrow HCO + O$	1.66e-17	Jachimowski 1977
$CH + O_2 \rightarrow CO + OH$	8.3e-17	Lichtin et al. 1984
$CO + H \rightarrow HCO$	5.29e-40*exp(-370.4372/T)	Baulch et al. 1992
$HCO \rightarrow CO + H$	1.93e-17*(T/300)$^{0.96}$*exp(-7367.8513/T)	Varga et al. 2016
$HCO + M \rightarrow CO + H + M$	8.56e-16*(T/300)$^{-1.2}$*exp(-8924.1686/T)	Friedrichs et al. 2002
$H_2 + OH \rightarrow H + H_2O$	1.07e-18*(T/300)$^{1.78}$*exp(-1452.8835/T)	Nguyen et al. 2011
$H_2O + H \rightarrow H_2 + OH$	6.82e-18*(T/300)$^{1.6}$*exp(-9720.368/T)	Baulch et al. 1992
$O_2 + H \rightarrow OH + O$	1.62e-16*exp(-7470.0824/T)	Baulch et al. 1994
$OH + O \rightarrow O_2 + H$	1.81e-17*(T/300)$^{-0.32}$*exp(176.7996/T)	Robertson et al. 2006
$HCO + H \rightarrow H_2O$	7.77e-20*exp(2280.3536/T)	Tsuboi et al. 1981
$HCO + H + M \rightarrow H_2O + M$	3.21e-36*(T/300)$^{-2.57}$*exp(-215.2865/T)	Eiteneer et al. 1998
$H_2 + O \rightarrow H + OH$	3.44e-19*(T/300)$^{2.67}$*exp(-3159.5406/T)	Baulch et al. 1992
$H + OH + M \rightarrow H_2 + O + M$	4.38e-39*(T/300)$^{-2}$	W.Wang et al. 2018
$H + OH \rightarrow H_2 + O$	2.24e-17*exp(-4000.2405/T)	Wilson 1972
$OH + M \rightarrow H + O + M$	4e-15*exp(-50033.0747/T)	W. Tsang et al. 1986

Continued on next page

Table 7.1 – continued from previous page

Reaction	Rate coefficient	Source
$H + O + M \rightarrow OH + M$	4.36e-38*(T/300)$^{-1}$	W. Tsang et al. 1986
$H + O_2 \rightarrow OH + O$	1.62e-16*exp(-7470.0824/T)	Baulch et al. 1994
$H_2 + O \rightarrow OH + H$	3.44e-19*(T/300)$^{2.67}$*exp(-3159.5406/T)	Baulch et al. 1992
$H_2 + O(1D) \rightarrow OH + H$	1.2e-16	Matsumi 1993
$H_2O + O \rightarrow HCO + OH$	1.78e-17*(T/300)$^{0.57}$*exp(-1390.3422/T)	W. Tsang et al. 1986
$H_2O + HCO \rightarrow H_2O + OH$	8.54e-19*(T/300)$^{1.35}$*exp(-13109.6278/T)	W. Tsang et al. 1986
$H_2O + OH \rightarrow H_2O + HCO$	4.73e-18*(T/300)$^{1.18}$*exp(224.9083/T)	Baulch et al. 1992
$HCO + HCO \rightarrow H_2O + CO$	3.01e-06	W. Tsang et al. 1986
$CH + CO_2 \rightarrow CO + HCO$	9.68e-19	W.Wang et al. 2018
$H + OH + M \rightarrow H_2O + M$	4.38e-36*(T/300)$^{-2}$	W.Wang et al. 2018
$O(1D) + H_2O \rightarrow OH + OH$	2e-16	Baulch et al. 1992
$O + CH \rightarrow C + OH$	2.52e-17*exp(-2380.1792/T)	Murrell et al. 1986
$CO + OH \rightarrow CO_2 + H$	8.42e-16*(T/300)$^{-0.84}$*exp(-24896.2656/T)	Panteleev et al. 2018
$H + H_2 \rightarrow H + H + H$	4.67e-19*(T/300)$^{-1}$*exp(-55000/T)	Baulch et al. 1992
$H + H + M \rightarrow H_2 + M$	6.04e-51*(T/300)$^{-1}$	Baulch et al. 1992
$C_2 + H \rightarrow C + CH$	4.67e-22*(T/300)$^{0.5}$*exp(-30450/T)	Baulch et al. 1992
$CH + O \rightarrow CO + H$	6.59e-17	Baulch et al. 1992
$H_2O + O \rightarrow H_2 + O_2$	4.48e-18*(T/300)$^{0.97}$*exp(-34518.0107/T)	Karach 1999
$H_2 + O_2 \rightarrow H_2O + O$	4.15e-17*(T/300)$^{0.51}$*exp(-35480.1852/T)	Karach 1999
$CH + H \rightarrow C + H_2$	6.5e-16*(T/300)$^{0.01}$*exp(-2685.6696/T)	Han et al. 2011
$C + H_2 \rightarrow CH + H$	6.6e-22*exp(-1170/T)	Baulch et al. 1992
$CH + CO_2 \rightarrow H + CO + CO$	5.71e-18*exp(-345.1801/T)	Baulch et al. 1992
$H_2 + O(1D) \rightarrow H + OH$	2.87e-16	Tully 1975
$H_2O + O(1D) \rightarrow OH + OH$	2.19e-16*exp(-64.9468/T)	Dunlea et al. 2004
$CH + O_2 \rightarrow CO_2 + H$	1.2e-17	W.Wang et al. 2018
$CH + O_2 \rightarrow CO + OH$	8e-18	W.Wang et al. 2018
$CH + O_2 \rightarrow CO + H + O$	1.2e-17	W.Wang et al. 2018
$H + H + H_2O \rightarrow H_2O + H_2$	6.04e-51*(T/300)$^{-1}$	Baulch et al. 1992
$H + wall \rightarrow 0.5H_2$	0.01	Parametric study
$CH_2O + O(1D) \rightarrow H_2O + CO$	1.66e-16	W.Wang et al. 2018

Table 7.2: Ion reactions included in the "simplified" model

Reaction (m^3/molecule s)	Rate coefficient	Source
$CH_4(+, X) + Wall \rightarrow CH_4$	Effective ambipolar diffusion	

Continued on next page

Table 7.2 – continued from previous page

Reaction	Rate coefficient	Source
$CH_4(+,X) + O_2 \rightarrow CH_4 + O_2(+,X)$	3.9e-16	W.Wang et al. 2018
$CO_2(+,X) + CH_4 \rightarrow CH_4(+,X) + CO_2$	5.5e-16	W.Wang et al. 2018
$CO(+,X) + CH_4 \rightarrow CH_4(+,X) + CO$	7.93e-16	W.Wang et al. 2018
$CH_4(+,X) + CH_4 \rightarrow CH_5(+,X) + CH_3$	1.5e-15	D. Smith et al. 1977
$H + CH_5(+,X) \rightarrow CH_4(+,X) + H_2$	1.5e-16	McEwan et al. 1999
$H_2 + CH_4(+,X) \rightarrow CH_5(+,X) + H$	4.89e-17*(T/300)$^{-0.14}$*exp(-36.1/T)	D. Smith et al. 1977
$CH_4(+,X) + H \rightarrow CH_3(+,X) + H_2$	1e-17	Karpas et al. 1979
$CH_4(+,X) + O \rightarrow CH_3(+,X) + OH$	1e-15	W.Wang et al. 2018
$CH_3(+,X) + HCO \rightarrow CO + CH_4(+,X)$	4.4e-16*(T/300)$^{-0.5}$	Prasad et al. 1980
$CH_3(+,X) + CH_4 \rightarrow CH_4(+,X) + CH_3$	1.36e-16	W.Wang et al. 2018
$O(+,gnd) + CH_4 \rightarrow CH_4(+,X) + O$	8.9e-16	N. G. Adams et al. 1980
$H_2(+,X) + CH_4 \rightarrow CH_4(+,X) + H_2$	1.4e-15	Kim et al. 1975
$CH_4 + H(+,X) \rightarrow CH_4(+,X) + H$	1.5e-15	Huntress 1975
$C + CH_5(+,X) \rightarrow CH_4 + CH(+,X)$	1.2e-15	Prasad et al. 1980
$CH_5(+,X) + Wall \rightarrow CH_4 + H$	Effective ambipolar diffusion	
$e + CH_5(+,X) \rightarrow CH_2 + H_2 + H$	4.76e-14*(T/300)$^{-0.52}$	Semaniak et al. 1998
$e + CH_5(+,X) \rightarrow CH_3 + H_2$	1.4e-14*(T/300)$^{-0.52}$	Semaniak et al. 1998
$e + CH_5(+,X) \rightarrow CH_3 + H + H$	1.96e-13*(T/300)$^{-0.52}$	Semaniak et al. 1998
$e + CH_5(+,X) \rightarrow CH_4 + H$	5.5e-13*(T/300)$^{-0.3}$*exp(NaN/T)	Smith et al. 1984
$e + CH_5(+,X) \rightarrow CH + H_2 + H_2$	8.4e-15*(T/300)$^{-0.52}$	Semaniak et al. 1998
$CH_5(+,X) + CH_2 \rightarrow CH_3(+,X) + CH_4$	9.69e-16	Prasad et al. 1980
$H_2(+,X) + CH_4 \rightarrow CH_5(+,X) + H$	1.14e-16	Kim et al. 1975
$CH_5(+,X) + CH \rightarrow CH_2(+,X) + CH_4$	6.9e-16	Prasad et al. 1980
$CH_5(+,X) + C \rightarrow CH(+,X) + CH_4$	1.2e-15	W.Wang et al. 2018
$H_3(+,X) + CH_4 \rightarrow CH_5(+,X) + H_2$	2.4e-15	Bohme et al. 1980
$CH_3(+,X) + Wall \rightarrow CH_3$	Effective ambipolar diffusion	

Continued on next page

Table 7.2 – continued from previous page

Reaction	Rate coefficient	Source
$CH_3(+,X) + e \rightarrow CH_2 + H$	7.75e-14*(T/300)$^{-0.5}$	Brian et al. 1990
$CH_3(+,X) + e \rightarrow CH + H_2$	1.95e-13*(T/300)$^{-0.5}$	Brian et al. 1990
$CH_3(+,X) + e \rightarrow CH + H + H$	2e-13*(T/300)$^{-0.4}$	Brian et al. 1990
$O(+,gnd) + CH_4 \rightarrow OH + CH_3(+,X)$	1.1e-16	N. G. Adams et al. 1980
$H_2(+,X) + CH_2 \rightarrow CH_3(+,X) + H$	1e-15	Prasad et al. 1980
$H_2(+,X) + CH_4 \rightarrow CH_3(+,X) + H_2 + H$	2.3e-15	Kim et al. 1975
$H(+,X) + CH_3 \rightarrow CH_3(+,X) + H$	3.4e-15	Prasad et al. 1980
$H(+,X) + CH_4 \rightarrow CH_3(+,X) + H_2$	2.3e-15	Prasad et al. 1980
$CH_2(+,X) + HCO \rightarrow CO + CH_3(+,X)$	4.5e-16*(T/300)$^{-0.5}$	Prasad et al. 1980
$H_2 + CH_2(+,X) \rightarrow CH_3(+,X) + H$	1.6e-15	D. Smith et al. 1977
$H_3(+,X) + CH_2 \rightarrow CH_3(+,X) + H_2$	1.7e-15	Prasad et al. 1980
$O(-,gnd) + CH_3(+,X) \rightarrow O + CH_3$	7.51e-14*(T/300)$^{-0.5}$	Harada et al. 2008
$H_2(+,X) + Wall \rightarrow H_2$	Effective ambipolar diffusion	
$H(+,X) + Wall \rightarrow H$	Effective ambipolar diffusion	
$H_3(+,X) + Wall \rightarrow H_2 + H$	Effective ambipolar diffusion	
$H_2(+,X) + e \rightarrow H + H$	1.6e-14*(T/300)$^{-0.43}$	Brian et al. 1990
$H_3(+,X) + e \rightarrow H_2 + H$	2.34e-14*(T/300)$^{-0.52}$	McCall et al. 2004
$H_3(+,X) + e \rightarrow H + H + H$	4.36e-14*(T/300)$^{-0.52}$	McCall et al. 2004
$H(+,X) + HCO \rightarrow CO + H_2(+,X)$	9.4e-16*(T/300)$^{-0.5}$	Prasad et al. 1980
$H + CO(+,X) \rightarrow CO + H(+,X)$	7.5e-16	Federer et al. 1984
$H + H_2(+,X) \rightarrow H_2 + H(+,X)$	6.4e-16	Karpas et al. 1979
$H + O(+,gnd) \rightarrow O + H(+,X)$	5.66e-16*(T/300)$^{0.36}$*exp(NaN/T)	Stancil, P. C. et al. 1999
$O(-,gnd) + H_3(+,X) \rightarrow O + H_2 + H$	7.51e-14*(T/300)$^{-0.5}$	Harada et al. 2008
$H_2(+,X) + C \rightarrow CH(+,X) + H$	2.4e-15	Prasad et al. 1980
$H + H_2(+,X) \rightarrow H_2 + H(+,X)$	6.4e-16	Karpas et al. 1979
$H_2(+,X) + O_2 \rightarrow O_2(+,X) + H_2$	8e-16	Kim et al. 1975
$O(-,gnd) + H(+,X) \rightarrow O + H$	7.51e-14*(T/300)$^{-0.5}$	Harada et al. 2008
$H(+,X) + HCO \rightarrow CO + H_2(+,X)$	9.4e-16*(T/300)$^{-0.5}$	Prasad et al. 1980
$H(+,X) + HCO \rightarrow CO(+,X) + H_2$	9.4e-16*(T/300)$^{-0.5}$	Prasad et al. 1980

Continued on next page

Table 7.2 – continued from previous page

Reaction	Rate coefficient	Source
$H(+,X) + CH_2O \rightarrow CO(+,X) + H_2 + H$	1.06e-15*(T/300)$^{-0.5}$	Sen et al. 1992
$H(+,X) + CH_2 \rightarrow CH(+,X) + H_2$	1.4e-15	Prasad et al. 1980
$H_2(+,X) + C \rightarrow CH(+,X) + H$	2.4e-15	Prasad et al. 1980
$H_3(+,X) + C \rightarrow CH(+,X) + H_2$	2e-15	Prasad et al. 1980
$H(+,X) + CH \rightarrow CH(+,X) + H$	1.9e-15	Prasad et al. 1980
$H_2(+,X) + H_2 \rightarrow H_3(+,X) + H$	2.08e-15	Theard et al. 1974
$H_2(+,X) + HCO \rightarrow CO + H_3(+,X)$	1e-15*(T/300)$^{-0.5}$	Prasad et al. 1980
$H_2(+,X) + CO \rightarrow CO(+,X) + H_2$	6.44e-16	Kim et al. 1975
$C(+,X) + HCO \rightarrow CO + CH(+,X)$	4.8e-16*(T/300)$^{-0.5}$	Prasad et al. 1980
$H(+,X) + O_2 \rightarrow O_2(+,X) + H$	2e-15	David Smith et al. 1992
$H(+,X) + O \rightarrow O(+,gnd) + H$	6.86e-16*(T/300)$^{0.26}$*exp(224.3/T)	Stancil, P. C. et al. 1999
$CH_2(+,X) + Wall \rightarrow CH_2(+,X)$	Effective ambipolar diffusion	
$CH_2(+,X) + e \rightarrow C + H_2$	7.68e-14*(T/300)$^{-0.6}$	Larson et al. 1998
$CH_2(+,X) + e \rightarrow C + H + H$	4.03e-13*(T/300)$^{-0.6}$	Larson et al. 1998
$CH_2 + CO(+,X) \rightarrow CH_2(+,X) + CO$	4.3e-16	Prasad et al. 1980
$CH_2 + O(+,gnd) \rightarrow O + CH_2(+,X)$	9.7e-16	Prasad et al. 1980
$CH_2 + O_2(+,X) \rightarrow O_2 + CH_2(+,X)$	4.3e-16	Prasad et al. 1980
$H_2 + CH(+,X) \rightarrow H + CH_2(+,X)$	1.2e-15	McEwan et al. 1999
$H_2(+,X) + CH \rightarrow CH_2(+,X) + H$	7.1e-16	Prasad et al. 1980
$H_2(+,X) + CH_2 \rightarrow CH_2(+,X) + H_2$	1e-15	Prasad et al. 1980
$H(+,X) + CH_2 \rightarrow CH_2(+,X) + H$	1.4e-15	Prasad et al. 1980
$CH + H_2(+,X) \rightarrow H + CH_2(+,X)$	7.1e-16*(T/300)$^{-0.5}$	Prasad et al. 1980
$CH(+,X) + HCO \rightarrow CO + CH_2(+,X)$	4.6e-16	Prasad et al. 1980
$CH(+,X) + H_2 \rightarrow CH_2(+,X) + H$	1.2e-15	McEwan et al. 1999
$H_3(+,X) + CH \rightarrow CH_2(+,X) + H_2$	1.2e-15	Prasad et al. 1980
$CH(+,X) + Wall \rightarrow CH$	Effective ambipolar diffusion	
$CH(+,X) + e \rightarrow C + H$	1.5e-13*(T/300)$^{-0.42}$	Brian et al. 1990

Continued on next page

Table 7.2 – continued from previous page

Reaction	Rate coefficient	Source
$CH + CO(+,X) \rightarrow CO + CH(+,X)$	3.2e-16*(T/300)$^{-0.5}$	Prasad et al. 1980
$CH + O(+,gnd) \rightarrow O + CH(+,X)$	3.5e-16*(T/300)$^{-0.5}$	Prasad et al. 1980
$CH + O_2(+,X) \rightarrow O_2 + CH(+,X)$	3.1e-16*(T/300)$^{-0.5}$	Prasad et al. 1980
$H(+,X) + CH \rightarrow H + CH(+,X)$	1.9e-15*(T/300)$^{-0.5}$	Prasad et al. 1980
$H_2(+,X) + CH \rightarrow CH(+,X) + H_2$	7.1e-16*(T/300)$^{-0.5}$	Prasad et al. 1980
$CH(+,X) + CH_{2O \rightarrow CO+CH_3(+,X)}$	9.6e-16*(T/300)$^{-0.5}$	N. Adams et al. 1978
$CH(+,X) + HCO \rightarrow CO + CH_2(+,X)$	4.6e-16*(T/300)$^{-0.5}$	Prasad et al. 1980
$CH(+,X) + O_2 \rightarrow CO(+,X) + OH$	1e-17	N. Adams et al. 1978
$CH(+,X) + OH \rightarrow CO(+,X) + H_2$	7.5e-16*(T/300)$^{-0.5}$	Prasad et al. 1980
$C + OH(+,X) \rightarrow O + CH(+,X)$	1.2e-15	Prasad et al. 1980
$CH + OH(+,X) \rightarrow OH + CH(+,X)$	3.5e-16*(T/300)$^{-0.5}$	Prasad et al. 1980

Table 7.3: electron impact reactions included in the "simplified" model

electron impact reaction	**Source (LXCat Database)**
e + CH_2 → e + e + CH_2(+,X)	Morgan (Kinema Research Software)
e + CH_2 → e + e + CH(+,X) + H(1s)	Morgan (Kinema Research Software)
e + CH_2 → e + CH + H(1s)	Morgan (Kinema Research Software)
e + CH_2 → e + C + H_2	Morgan (Kinema Research Software)
e + CH_3 → e + e + CH_3(+,X)	Morgan (Kinema Research Software)
e + CH_3 → e + e + CH_2(+,X) + H(1s)	Morgan (Kinema Research Software)
e + CH_3 → e + e + CH(+,X) + H_2	Morgan (Kinema Research Software)
e + CH_3 → e + e + CH_2 + H(+,X)	Morgan (Kinema Research Software)
e + CH_3 → e + e + CH + H_2(+,X)	Morgan (Kinema Research Software)
e + CH_3 → e + CH_2 + H(1s)	Morgan (Kinema Research Software)
e + CH_3 → e + CH + H_2	Morgan (Kinema Research Software)
e + CH_3 → e + CH + 2H(1s)	Morgan (Kinema Research Software)
e + CH_4(+,X) → CH_3 + H(1s)	Morgan (Kinema Research Software)
e + CH_4(+,X) → CH_2 + H_2	Morgan (Kinema Research Software)
e + CH_4(+,X) → CH_2 + 2H(1s)	Morgan (Kinema Research Software)
e + CH_4(+,X) → CH + H(1s) + H_2	Morgan (Kinema Research Software)
e + CH_4(+,X) → C + 2H_2	Morgan (Kinema Research Software)
e + CH_4 → e + CH_3 + H(1s)	Community database
e + CH_4 → e + CH_2 + H_2	Community database
e + CH_4 → e + C + H_2 + H_2	Community database
e + CH_4 → e + CH + H_2 + H(1s)	Community database

Continued on next page

Table 7.3 – continued from previous page

electron impact reaction	Source (LXCat Database)
e + CH_4 → e + e + CH_4(+,X)	Community database
e + CH_4 → e + e + CH_3(+,X) + H(1s)	Community database
e + CH_4 → e + CH_2(+,X) + H_2	Community database
e + CH_4 → e +e + CH_3 + H(+,X)	Community database
e + CH_4 → e + e + H_2 + H_2 + C(+,X)	Community database
e + CH_4 → e + e + H(1s) + H_2 + CH(+,X)	Community database
e + CH_4 → e + e + CH_2 + H_2(+,X)	Community database
e + CH → e + e + CH(+,X)	Morgan (Kinema Research Software)
e + CH → e + C + H(1s)	Morgan (Kinema Research Software)
e + H_2O → H_2 + O(-,X)	Triniti
e + H_2O → OH + H(1s) + e	Biagi
e + H_2O → e + H(+,1s) + OH	Biagi
e + H_2O → e + H_2 + O(+,X)	Biagi
e + H_2O → e + H_2(+,X) + O	Biagi
e + H_2 → e + H(1s) + H(1s)	Itikawa
e + H_2 → e + e + H_2(+,X)	IST-Lisbon database
e + H(1s) → e + e + H(+,X)	IST-Lisbon database

Reactions included in the "extended" model

Table 7.4: Chemical reaction included in the "extended" model. The rates are in m^3/molecule s for 2nd order or m^6/molecule^2 s for 3rd order

Reaction	Rate coefficient (m^3/molecule s)	Source
$CH_3 + CH_3 \rightarrow C_2H_6$	5.66e-17*(T/300)$^{-0.37}$	Sangwan et al. 2015
$CH_3 + CH_3 + M \rightarrow C_2H_6 + M$	1.68e-30*(T/300)$^{-7}$*exp(-1390.4258/T)	Baulch et al. 1992
$C_2H_6 + M \rightarrow CH_3 + CH_3 + M$	4.5e-14*exp(-41930/T)	Baulch et al. 1992
$C_2H_6 \rightarrow CH_3 + CH_3$	1540000000000*(T/300)$^{-1.25}$*exp(-45706.038/T)	Baulch et al. 1992
$C_2H_6 + H \rightarrow CH_3 + CH_4$	8.9e-26	R. A. Back 1983
$C_2H_5 + H \rightarrow C_2H_6$	2.25e-16*(T/300)$^{0.16}$	Harding et al. 2005
$C_2H_6 \rightarrow C_2H_5 + H$	811000000000*(T/300)$^{-1.23}$*exp(-51359.1532/T)	Stewart et al. 1989
$C_2H_6 + CH_3 \rightarrow CH_4 + C_2H_5$	1.86e-20*(T/300)$^{3.44}$*exp(-5229.733/T)	Peukert et al. 2013
$CH_4 + C_2H_5 \rightarrow C_2H_6 + CH_3$	2.51e-21*(T/300)$^{4.14}$*exp(-6320.6639/T)	W. Tsang et al. 1986
$C_2H_6 + H \rightarrow H_2 + C_2H_5$	6.73e-16*(T/300)$^{-0.51}$*exp(-6744.0462/T)	Han et al. 2011
$H_2 + C_2H_5 \rightarrow C_2H_6 + H$	4.12e-21*(T/300)$^{3.6}$*exp(-4250.6615/T)	W. Tsang et al. 1986
$C_2H_6 + M \rightarrow C_2H_4 + H_2$	1.15e-13*exp(-41255.7133/T)	Brodsky et al. 1960
$C_2H_4 + H_2 \rightarrow C_2H_6$	5.75e-22*exp(-21650.2285/T)	Pease 1932

Continued on next page

Table 7.4 – continued from previous page

Reaction	Rate coefficient	Source
$C_2H_6 + O \rightarrow C_2H_5 + OH$	8.54e-18*(T/300)$^{1.5}$*exp(-2920.3753/T)	Baulch et al. 1992
$C_2H_6 + O(1D) \rightarrow C_2H_5 + OH$	6.29e-16	Matsumi 1993
$C_2H_5 + OH \rightarrow C_2H_6 + O$	9.85e-25*(T/300)$^{8.8}$*exp(-250.1804/T)	Cohen et al. 1991
$C_2H_5 + HCO \rightarrow C_2H_6 + CO$	2.01e-16	W. Tsang et al. 1986
$C_2H_5 + H_2O \rightarrow C_2H_6 + OH$	2.06e-20*(T/300)$^{1.44}$*exp(-10200.866/T)	W. Tsang et al. 1986
$C_2H_6 + OH \rightarrow C_2H_5 + H_2O$	1.06e-18*(T/300)^{2}*exp(435.4102/T)	Baulch et al. 1992
$C_2H_6 + C_2H_3 \rightarrow C_2H_4 + C_2H_5$	2.32e-21*(T/300)$^{4.49}$*exp(-2503.007/T)	Muszyńska et al. 2009
$C_2H_4 + C_2H_5 \rightarrow C_2H_6 + C_2H_3$	5.83e-20*(T/300)$^{3.13}$*exp(-9060.6206/T)	W. Tsang et al. 1986
$C_2H_6 + C_2H_2 \rightarrow C_2H_5 + C_2H_3$	1.6e-18*exp(-2297329.8051/T)	A. Laufer et al. 1983
$C_2H_6 + C_2H \rightarrow C_2H_2 + C_2H_5$	7.13e-18*(T/300)$^{2.11}$*exp(431.8018/T)	Dash et al. 2015
$C_2H_2 + C_2H_5 \rightarrow C_2H_6 + C_2H$	4.5e-19*exp(-11800.5773/T)	W. Tsang et al. 1986
$C_2H_6 + OH \rightarrow C_2H_5 + H_2O$	1.45e-18*(T/300)$^{2.08}$*exp(-519.6055/T)	Khaled et al. 2015
$C_2H_5 + H_2O \rightarrow C_2H_6 + OH$	2.06e-20*(T/300)$^{1.44}$*exp(-10200.866/T)	W. Tsang et al. 1986
$C_2H_6 + HCO \rightarrow CH_2O + C_2H_5$	4.18e-19*(T/300)$^{2.72}$*exp(-9180.8997/T)	W. Tsang et al. 1986
$CH_2O + C_2H_5 \rightarrow C_2H_6 + HCO$	8.19e-20*(T/300)$^{2.81}$*exp(-2950.445/T)	W. Tsang et al. 1986
$C_2H_6 + CH \rightarrow C_2H_4 + CH_3$	1.3e-16	Galland et al. 2003
$C_2H_5 + O \rightarrow CH_2O + CH_3$	2.67e-17	W. Tsang et al. 1986
$C_2H_5 + O \rightarrow C_2H_4 + OH$	6.31e-18*(T/300)$^{0.03}$*exp(198.4604/T)	Harding et al. 2005
$C_2H_5 + CH_3 \rightarrow CH_4 + C_2H_4$	1.91e-18	Baulch et al. 1992
$C_2H_5 + CH_2 \rightarrow C_2H_4 + CH_3$	3.01e-17	W. Tsang et al. 1986
$C_2H_5 + H \rightarrow CH_3 + CH_3$	5.99e-17	Baulch et al. 1992
$CH_3 + CH_3 \rightarrow C_2H_5 + H$	1.46e-17*(T/300)$^{0.1}$*exp(-5340.3897/T)	Stewart et al. 1989
$C_2H_5 + H \rightarrow C_2H_4 + H_2$	3.01e-18	W. Tsang et al. 1986
$C_2H_4 + H_2 \rightarrow C_2H_5 + H$	1.69e-17	W. Tsang et al. 1986
$C_2H_5 + OH \rightarrow C_2H_4 + H_2O$	4e-17	W. Tsang et al. 1986
$C_2H_4 + H \rightarrow C_2H_5$	1.25e-17*(T/300)$^{1.07}$*exp(-730.0938/T)	Curran 2006
$C_2H_4 + H + M \rightarrow C_2H_5 + M$	1.3e-35*exp(-380.0818/T)	Baulch et al. 1994
$C_2H_5 + M \rightarrow C_2H_4 + H + M$	1.66e-13	Warnatz 1981
$C_2H_5 \rightarrow C_2H_4 + H$	6860000*(T/300)$^{0.95}$	Curran 2006
$C_2H_5 + C_2H_3 \rightarrow C_2H_4 + C_2H_4$	1.07e-29	M. H. Back 1970
$C_2H_4 + C_2H_4 \rightarrow C_2H_5 + C_2H_3$	8e-16*exp(-35963.4352/T)	W. Tsang et al. 1986

Continued on next page

Table 7.4 – continued from previous page

Reaction	Rate coefficient	Source
$C_2H_5 + C_2H \rightarrow C_2H_4 + C_2H_2$	3.01e-18	W. Tsang et al. 1986
$C_2H_4 + OH \rightarrow C_2H_3 + H_2O$	2.85e-21*(T/300)$^{4.57}$*exp(287.4669/T)	C.Olm et al. 2016
$C_2H_3 + H_2O \rightarrow C_2H_4 + OH$	1.2e-20*(T/300)$^{2.9}$*exp(-7480.154/T)	W. Tsang et al. 1986
$C_2H_4 + CH_3 \rightarrow C_2H_3 + CH_4$	6.91e-18*exp(-5600.1924/T)	Baulch et al. 1992
$C_2H_3 + CH_4 \rightarrow C_2H_4 + CH_3$	2.13e-20*(T/300)$^{4.02}$*exp(-2749.579/T)	W. Tsang et al. 1986
$CH_3 + CH_2 \rightarrow C_2H_4 + H$	2.1e-16	B. Wang and Fockenberg 2001
$C_2H_4 + CO \rightarrow HCO + C_2H_3$	2.51e-16*exp(-45585.759/T)	W. Tsang et al. 1986
$HCO + C_2H_3 \rightarrow C_2H_4 + CO$	1.5e-16	W. Tsang et al. 1986
$C_2H_4 + O \rightarrow C_2H_3 + OH$	1.33e-18*(T/300)$^{1.91}$*exp(-1879.9615/T)	Mahmud et al. 1987
$C_2H_4 + O \rightarrow CH_3 + HCO$	5.51e-17*(T/300)$^{-1.72}$*exp(-1456.5793/T)	Xiaohu Li et al. 2017
$C_2H_4 + O \rightarrow CH_2O + CH_2$	8.08e-19*(T/300)$^{1.99}$*exp(-1438.5374/T)	Xiaohu Li et al. 2017
$C_2H_4 + H \rightarrow H_2 + C_2H_3$	9e-16*exp(-7500.6014/T)	Baulch et al. 1992
$H_2 + C_2H_3 \rightarrow C_2H_4 + H$	1.61e-19*(T/300)$^{2.63}$*exp(-4299.9759/T)	W. Tsang et al. 1986
$C_2H_3 + H \rightarrow C_2H_4$	2.02e-16*(T/300)$^{0.2}$	Harding et al. 2005
$C_2H_4 + M \rightarrow C_2H_3 + H + M$	4.3e-13*exp(-48592.7351/T)	Baulch et al. 1994
$CH_2O + C_2H_3 \rightarrow C_2H_4 + HCO$	8.07e-20*(T/300)$^{2.81}$*exp(-2950.445/T)	W. Tsang et al. 1986
$C_2H_4 + C_2H_2 \rightarrow C_2H_3 + C_2H_3$	4e-17*exp(-31873947.5583/T)	W. Tsang et al. 1986
$C_2H_3 + C_2H_3 \rightarrow C_2H_4 + C_2H_2$	3.5e-17	A. H. Laufer and Fahr 2004
$CH_3O + C_2H_3 \rightarrow C_2H_4 + CH_2O$	4e-17	W. Tsang et al. 1986
$C_2H_2 + H_2 \rightarrow C_2H_4$	5e-19*exp(-19605.4847/T)	W. Tsang et al. 1986
$C_2H_4 + M \rightarrow C_2H_2 + H_2 + M$	5.8e-14*exp(-35963.4352/T)	Baulch et al. 1994
$C_2H_4 \rightarrow C_2H_2 + H_2$	97500000*(T/300)$^{0.44}$*exp(-44743.8056/T)	W. Tsang et al. 1986
$CH_3O + CH_2 \rightarrow C_2H_4 + OH$	4e-17	W. Tsang et al. 1986
$C_2H_3 + O_2 \rightarrow CH_2O + HCO$	2.76e-17*(T/300)$^{-1.39}$*exp(-509.9832/T)	Mebel et al. 1996
$C_2H_3 + O_2 \rightarrow CH_2O + CO + H$	1.65e-17*(T/300)$^{-1.35}$*exp(-394.5153/T)	Matsugi et al. 2014
$C_2H_3 + O \rightarrow C_2H_2 + OH$	5.5e-18*(T/300)$^{0.2}$*exp(215.2995/T)	Harding et al. 2005
$C_2H_3 + OH \rightarrow CH_3 + HCO$	2.88e-16*(T/300)$^{-1.85}$*exp(-501.5636/T)	Knyazev 2017
$C_2H_3 + OH \rightarrow C_2H_2 + H_2O$	5e-17	W. Tsang et al. 1986
$C_2H_3 + OH \rightarrow CH_4 + CO$	6.84e-18*(T/300)$^{-1.33}$*exp(-298.292/T)	Knyazev 2017

Continued on next page

Table 7.4 – continued from previous page

Reaction	Rate coefficient	Source
$C_2H_3 + CH_3 \rightarrow CH_4 + C_2H_2$	1.5e-17*exp(384.893/T)	Stoliarov et al. 2000
$CH_4 + C_2H_2 \rightarrow C_2H_3 + CH_3$	5e-19*exp(-2749.579/T)	A. H. Laufer and Fahr 2004
$C_2H_3 + CH_2 \rightarrow C_2H_2 + CH_3$	3.01e-17	W. Tsang et al. 1986
$C_2H_3 + C_2H \rightarrow C_2H_2 + C_2H_2$	1.6e-18	W. Tsang et al. 1986
$C_2H_2 + C_2H_2 \rightarrow C_2H_3 + C_2H$	1.6e-17*exp(-42458.5037/T)	W. Tsang et al. 1986
$C_2H_3 + CH_3O \rightarrow CH_2O + C_2H_4$	4e-17	W. Tsang et al. 1986
$C_2H_2 + H_2 \rightarrow C_2H_3 + H$	4e-18*exp(-32715.9009/T)	W. Tsang et al. 1986
$C_2H_3 + H \rightarrow C_2H_2 + H_2$	2.01e-17	Baulch et al. 1992
$C_2H_2 + CH_3O \rightarrow CH_2O + C_2H_3$	1.2e-18*exp(-4529.7089/T)	W. Tsang et al. 1986
$CH_3 + CH \rightarrow H + C_2H_3$	5e-23	W. Tsang et al. 1986
$C_2H_2 + OH \rightarrow C_2H + H_2O$	4.5e-17*exp(-5281.5207/T)	W. Tsang et al. 1986
$C_2H + H_2O \rightarrow C_2H_2 + OH$	7.74e-20*$(T/300)^{3.05}$*exp(-376.564/T)	Carl et al. 2005
$C_2H_2 + OH \rightarrow CO + CH_3$	9.13e-17*exp(-6892.4447/T)	Vandooren et al. 1977
$CO + CH_3 \rightarrow C_2H_2 + OH$	6.31e-17*exp(-30437.9211/T)	Tsuboi et al. 1981
$C_2H_2 + CH_3 \rightarrow CH_4 + C_2H$	3.01e-19*exp(-8703.0799/T)	W. Tsang et al. 1986
$CH_4 + C_2H \rightarrow C_2H_2 + CH_3$	5.11e-19*$(T/300)^{2.44}$*exp(330.847/T)	Dash et al. 2015
$C_2H_2 + CO \rightarrow C_2H + HCO$	8e-16*exp(-53657.3628/T)	W. Tsang et al. 1986
$C_2H + HCO \rightarrow C_2H_2 + CO$	1e-16	W. Tsang et al. 1986
$C_2H_2 + O_2 \rightarrow HCO + HCO$	1e-17*exp(-26828.6814/T)	Gimenez-Lopez et al. 2016
$C_2H_2 + O \rightarrow CH_2 + CO$	3.5e-18*$(T/300)^{1.5}$*exp(-854.1867/T)	Warnatz 1981
$C_2H + OH \rightarrow C_2H_2 + O$	3.01e-17	W. Tsang et al. 1986
$C_2H_2 + H + M \rightarrow C_2H_3 + M$	3.31e-36*exp(-739.8941/T)	Baulch et al. 1992
$C_2H_2 + H \rightarrow C_2H_3$	1.4e-17*exp(-1300.5294/T)	Baulch et al. 1992
$C_2H_3 + M \rightarrow C_2H_2 + H + M$	1.9e-07*$(T/300)^{-7.5}$*exp(-22858.5178/T)	Baulch et al. 1992
$C_2H_2 + H \rightarrow H_2 + C_2H$	2.49e-16*$(T/300)^{1.21}$*exp(-15038.4986/T)	Han et al. 2011
$H_2 + C_2H \rightarrow C_2H_2 + H$	8.95e-19*$(T/300)^{2.57}$*exp(-129.9326/T)	A. H. Laufer and Fahr 2004
$C_2H + CH_2 \rightarrow C_2H_2 + CH$	3.01e-17	W. Tsang et al. 1986
$C_2H + O_2 \rightarrow CO + HCO$	4e-18	W. Tsang et al. 1986
$C_2H + O \rightarrow CO + CH$	2.4e-17*exp(-229.733/T)	Devriendt et al. 1997

Continued on next page

Table 7.4 – continued from previous page

Reaction	Rate coefficient	Source
$C_2H + OH \rightarrow CO + CH_2$	3.01e-17	W. Tsang et al. 1986
$CH_3 + O \rightarrow CH_3O$	1.22e-16*(T/300)$^{0.05}$*exp(-68.5723/T)	Harding et al. 2005
$CH_3 + O_2 \rightarrow CH_3O + O$	2.19e-16*exp(15759.5881/T)	Baulch et al. 1992
$CH_3 + OH \rightarrow CH_3O + H$	2.57e-18*(T/300)$^{-0.23}$*exp(7011.2122/T)	Dean et al. 1987
$CH_3O + H \rightarrow CH_3 + OH$	1.6e-16	Wing Tsang 1987
$CH_3O + CO \rightarrow CO_2 + CH_3$	2.6e-17*exp(5941.7256/T)	W. Tsang et al. 1986
$CH_3O + O \rightarrow CH_3 + O_2$	3.55e-17*exp(239.4014/T)	Cobos et al. 1985
$CH_3 + O_2 \rightarrow CH_3O + O$	2.19e-16*exp(15759.5881/T)	Baulch et al. 1992
$CH_3O + O \rightarrow CH_2O + OH$	1e-17*exp(NaN/T)	W. Tsang et al. 1986
$CH_3O + CH_3 \rightarrow CH_2O + CH_4$	4e-17	W. Tsang et al. 1986
$CH_3O + CH_2 \rightarrow CH_2O + CH_3$	3e-17	W. Tsang et al. 1986
$CH_3O + H \rightarrow CH_3 + OH$	1.6e-16	W. Tsang et al. 1986
$CH_3 + OH \rightarrow CH_3O + H$	6.45e-19*(T/300)$^{1.01}$*exp(6013.9069/T)	Jasper et al. 2007
$CH_3O + H \rightarrow CH_2O + H_2$	3.14e-16*(T/300)$^{-0.58}$*exp(855.3486/T)	Q. S. Li et al. 2004
$CH_3O + OH \rightarrow CH_2O + H_2O$	3.01e-17	W. Tsang et al. 1986
$CH_3O + HCO \rightarrow CH_2O + CH_2O$	3.01e-17	W. Tsang et al. 1986

Table 7.5: electron impact reactions included in the "simplified" model

electron impact reaction	Source (LXCat Database)
e + C_2H_2 → e + e + CH(+,X) + CH	Morgan
e + C_2H_2 → e + C_2H + H(1s)	Morgan
e + C_2H_2 → e + 2CH	Morgan
e + C_2H_2 → e + CH_2 + C	Morgan
e + C_2H_3 → e + e + C_2H_2 + H(+,X)	R. K. Janev et al. 2002, R. Janev et al. 2002, R. Janev et al. 2004
e + C_2H_3 → e + C_2H_2 + H(1s)	R. K. Janev et al. 2002, R. Janev et al. 2002, R. Janev et al. 2004
e + C_2H_3 → e + C_2H + H_2	R. K. Janev et al. 2002, R. Janev et al. 2002, R. Janev et al. 2004
e + C_2H_3 → e + C_2H + 2H(1s)	R. K. Janev et al. 2002, R. Janev et al. 2002, R. Janev et al. 2004
e + C_2H_4 → e + C_2H_3 + H(1s)	R. K. Janev et al. 2002, R. Janev et al. 2002, R. Janev et al. 2004
e + C_2H_4 → e + C_2H_2 + H_2	R. K. Janev et al. 2002, R. Janev et al. 2002, R. Janev et al. 2004
e + C_2H_4 → e + C_2H_2 + 2H(1s)	R. K. Janev et al. 2002, R. Janev et al. 2002, R. Janev et al. 2004

Continued on next page

Table 7.5 – continued from previous page

electron impact reaction	Source (LXCat Database)
e + C_2H_4 → e + C_2H + H_2 + H(1s)	R. K. Janev et al. 2002, R. Janev et al. 2002, R. Janev et al. 2004
e + C_2H_4 → e + CH_3 + CH	R. K. Janev et al. 2002, R. Janev et al. 2002, R. Janev et al. 2004
e + C_2H_4 → e + $2CH_2$	R. K. Janev et al. 2002, R. Janev et al. 2002, R. Janev et al. 2004
e + C_2H_4 → e + C + CH_4	R. K. Janev et al. 2002, R. Janev et al. 2002, R. Janev et al. 2004
e + C_2H_5 → e + e + CH_3(+,X) + CH_2	R. K. Janev et al. 2002, R. Janev et al. 2002, R. Janev et al. 2004
e + C_2H_5 → e + C_2H_4 + H(1s)	R. K. Janev et al. 2002, R. Janev et al. 2002, R. Janev et al. 2004
e + C_2H_5 → e + C_2H_3 + H_2	R. K. Janev et al. 2002, R. Janev et al. 2002, R. Janev et al. 2004
e + C_2H_5 → e + C_2H_3 + 2H(1s)	R. K. Janev et al. 2002, R. Janev et al. 2002, R. Janev et al. 2004
e + C_2H_5 → e + C_2H_2 + H_2 + H(1s)	R. K. Janev et al. 2002, R. Janev et al. 2002, R. Janev et al. 2004
e + C_2H_5 → e + C_2H + $2H_2$	R. K. Janev et al. 2002, R. Janev et al. 2002, R. Janev et al. 2004
e + C_2H_5 → e + CH_4 + CH	R. K. Janev et al. 2002, R. Janev et al. 2002, R. Janev et al. 2004
e + C_2H_5 → e + CH_2 + CH_3	R. K. Janev et al. 2002, R. Janev et al. 2002, R. Janev et al. 2004
e + C_2H_6 → e + e + CH_3(+,X) + CH_3	R. K. Janev et al. 2002, R. Janev et al. 2002, R. Janev et al. 2004
e + C_2H_6 → e + e + CH_2(+,X) + CH_4	R. K. Janev et al. 2002, R. Janev et al. 2002, R. Janev et al. 2004
e + C_2H_6 → e + C_2H_5 + H(1s)	R. K. Janev et al. 2002, R. Janev et al. 2002, R. Janev et al. 2004
e + C_2H_6 → e + C_2H_4 + H_2	R. K. Janev et al. 2002, R. Janev et al. 2002, R. Janev et al. 2004
e + C_2H_6 → e + C_2H_3 + H_2 + H(1s)	R. K. Janev et al. 2002, R. Janev et al. 2002, R. Janev et al. 2004
e + C_2H_6 → e + C_2H_2 + $2H_2$	R. K. Janev et al. 2002, R. Janev et al. 2002, R. Janev et al. 2004
e + C_2H_6 → e + CH_4 + CH_2	R. K. Janev et al. 2002, R. Janev et al. 2002, R. Janev et al. 2004
e + C_2H_6 → e + CH_3 + CH_3	R. K. Janev et al. 2002, R. Janev et al. 2002, R. Janev et al. 2004
e + C_2H → e + e + C + CH(+,X)	R. K. Janev et al. 2002, R. Janev et al. 2002, R. Janev et al. 2004
e + C_2H → e + C + CH	R. K. Janev et al. 2002, R. Janev et al. 2002, R. Janev et al. 2004

Bibliography

Masson-Delmotte, Valerie et al. (2019). *Global warming of 1.5C* (cit. on p. 1).

Ritchie, Hannah et al. (2020). *CO_2 and other Greenhouse Gas Emissions*. URL: https://ourworldindata.org/co2-and-other-greenhouse-gas-emissions (cit. on pp. 1, 2).

ClimateWatch (n.d.). URL: https://www.climatewatchdata.org/ (cit. on p. 2).

Administration, US. Energy Information (n.d.). *U.S. Energy-Related Carbon Dioxide Emissions, 2020*. URL: https://www.eia.gov/environment/emissions/carbon/ (cit. on p. 2).

ADEME (n.d.). *'Le Captage et Stockage géologique du CO2 (CSC) en France'*. URL: 'https://presse.ademe.fr/wp-content/uploads/2020/07/captage-stockage-geologique-co2_csc_avis-technique_2020.pdf' (cit. on p. 3).

Morillo-Candas, Ana-Sofia (Dec. 2019). "Investigation of fundamental mechanisms of CO2 plasmas". Theses. Université Paris Saclay (COmUE). URL: https://hal-polytechnique.archives-ouvertes.fr/tel-03014566 (cit. on pp. 3, 5, 73, 75, 90, 136, 151, 167, 190, 193, 195, 218).

Q.Wang et al. (2020). "Molecularly engineered photocatalyst sheet for scalable solar formate production from carbon dioxide and water". In: *Nat Energy* 5, pp. 703–710. DOI: https://doi.org/10.1038/s41560-020-0678-6 (cit. on p. 4).

Chen, Jiaxin et al. (2018). "The potential of microalgae in biodiesel production". In: *Renewable and Sustainable Energy Reviews* 90, pp. 336–346. ISSN: 1364-0321. DOI: https://doi.org/10.1016/j.rser.2018.03.073 (cit. on p. 4).

Romero, Manuel et al. (2012). "Concentrating solar thermal power and thermochemical fuels". In: *Energy Environ. Sci.* 5 (11), pp. 9234–9245. DOI: 10.1039/C2EE21275G (cit. on p. 4).

Varvoutis, Georgios et al. (2022). "Recent Advances on CO2 Mitigation Technologies: On the Role of Hydrogenation Route via Green H2". In: *Energies* 15.13. ISSN: 1996-1073. DOI: 10.3390/en15134790 (cit. on pp. 4, 9).

A.Fridman (2008). *Plasma Chemistry*. Cambridge University Press (cit. on pp. 4, 6, 131, 189).

Treanor, C.E. et al. (1968). "Vibrational relaxation of anharmonic oscillators with exchange-dominated collisions". In: *J. Phys. Chem.* 48, pp. 1798–1807 (cit. on p. 5).

Morillo-Candas, A S, C Drag, et al. (July 2019a). "Oxygen atom kinetics in CO2 plasmas ignited in a DC glow discharge". In: *Plasma Sources Science and Technology* 28.7, p. 075010. DOI: 10.1088/1361-6595/ab2b84 (cit. on pp. 5, 8, 18, 19, 103, 105, 114, 121, 156).

Adamovich, I. V. et al. (1996). "Vibrational Relaxation, Nonequilibrium Chemical Reactions, and Kinetics of No Formation behind Strong Shock Waves". In: *Molecular Physics and Hypersonic Flows*. Ed. by Mario Capitelli. Dordrecht: Springer Netherlands, pp. 85–104. ISBN: 978-94-009-0267-1. DOI: 10.1007/978-94-009-0267-1_5 (cit. on pp. 5, 18, 161).

W.J.Witteman (1986). *The CO_2 laser*. Springer (cit. on pp. 6, 7, 18, 200, 206, 214, 227).

Asisov, R.I. et al. (1985). "Plasmachemical methods of energy carrier production". In: *International Journal of Hydrogen Energy* 10.7. WHEC-V Papers not Included in the Proceedings, pp. 475–477. ISSN: 0360-3199. DOI: https://doi.org/10.1016/0360-3199(85)90075-8.

URL: https://www.sciencedirect.com/science/article/pii/0360319985900758 (cit. on p. 6).

Snoeckx, R. and A. Bogaerts (2017). “Plasma technology – a novel solution for CO2 conversion?” In: *Chemical Society Reviews* 46, pp. 5805–5863. DOI: 10.1039/C6CS00066E (cit. on p. 6).

Guerra, Vasco et al. (Oct. 2017). “The case for in situ resource utilisation for oxygen production on Mars by non-equilibrium plasmas”. In: *Plasma Sources Science and Technology* 26.11, 11LT01. DOI: 10.1088/1361-6595/aa8dcc. URL: https://doi.org/10.1088/1361-6595/aa8dcc (cit. on p. 7).

Premathilake, Dilshan et al. (2019). “Oxygen Generation by Carbon Dioxide Glow Discharge and Separation by Permeation Through Ultrathin Silver Membranes”. In: *Earth and Space Science* 6.4, pp. 557–564. DOI: https://doi.org/10.1029/2018EA000521 (cit. on p. 7).

Guerra, V. et al. (2022). “Plasmas for in situ resource utilization on Mars: Fuels, life support, and agriculture”. In: *Journal of Applied Physics* 132.7, p. 070902. DOI: 10.1063/5.0098011 (cit. on p. 7).

Kelly, Sean et al. (2022). “Producing oxygen and fertilizer with the Martian atmosphere by using microwave plasma”. In: *Chem* 8.10, pp. 2797–2816 (cit. on p. 7).

Morillo-Candas, A S, T Silva, et al. (Jan. 2020). “Electron impact dissociation of CO2”. In: *Plasma Sources Science and Technology* 29.1, 01LT01. DOI: 10.1088/1361-6595/ab6075 (cit. on pp. 7, 8, 16, 135–137, 140, 149).

L.D.Pietanza et al. (2021). “Advances in non-equilibrium CO2 plasma kinetics: a theoretical and experimental review”. In: *Eur. Phys. J. D* 75.237. DOI: https://doi.org/10.1140/epjd/s10053-021-00226-0 (cit. on pp. 8, 190, 211).

Klarenaar, B L M, R Engeln, et al. (Oct. 2017). “Time evolution of vibrational temperatures in a CO2 glow discharge measured with infrared absorption spectroscopy”. In: *Plasma Sources Science and Technology* 26.11, p. 115008. DOI: 10.1088/1361-6595/aa902e (cit. on pp. 8, 72, 76, 90, 148, 191, 193, 194, 196).

Klarenaar, B L M, A S Morillo-Candas, et al. (Mar. 2019). “Excitation and relaxation of the asymmetric stretch mode of CO2 in a pulsed glow discharge”. In: *Plasma Sources Science and Technology* 28.3, p. 035011. DOI: 10.1088/1361-6595/aada5e (cit. on p. 8).

Silva, T et al. (Jan. 2018). “Kinetic study of low-temperature CO2 plasmas under non-equilibrium conditions. I. Relaxation of vibrational energy”. In: *Plasma Sources Science and Technology* 27.1, p. 015019. DOI: 10.1088/1361-6595/aaa56a (cit. on pp. 8, 194, 209, 210, 214, 216).

Grofulović, M et al. (Nov. 2018). “Kinetic study of CO2 plasmas under non-equilibrium conditions. II. Input of vibrational energy”. In: *Plasma Sources Science and Technology* 27.11, p. 115009. DOI: 10.1088/1361-6595/aadb60 (cit. on pp. 8, 16, 20, 194, 210).

Silva, Tiago, Ana Sofia Morillo-Candas, et al. (2021). “Modeling the time evolution of the dissociation fraction in low-pressure CO2 plasmas”. In: *Journal of CO_2 Utilization* 53, p. 101719. DOI: https://doi.org/10.1016/j.jcou.2021.101719 (cit. on pp. 8, 136, 149).

Silva, A F et al. (Dec. 2020). “A reaction mechanism for vibrationally-cold low-pressure CO2 plasmas”. In: *Plasma Sources Science and Technology* 29.12, p. 125020. DOI: 10.1088/1361-6595/abc818 (cit. on pp. 8, 88, 100–103, 110, 119, 155, 193, 198).

Terraz, L et al. (2019). “Influence of N2 on the CO2 vibrational distribution function and dissociation yield in non-equilibrium plasmas”. In: *Journal of Physics D: Applied Physics* 53.9, p. 094002 (cit. on p. 8).

Budde, Maik et al. (Sept. 2022). “Electron-neutral collision cross sections for Hsub2/subO: I. Complete and consistent set”. In: *Journal of Physics D: Applied Physics* 55.44, p. 445205. DOI: 10.1088/1361-6463/ac8da3 (cit. on pp. 8, 17, 101).

M.Damen et al. (2020). “Vibrational quenching by water in a CO2 glow discharge measured using quantum cascade laser absorption spectroscopy”. In: *Plasma Sources Sci. Technol.* 29, p. 095017. DOI: https://doi.org/10.1088/1361-6595/abad54 (cit. on pp. 8, 207, 227).

Pietanza, L D, G Colonna, and M Capitelli (Oct. 2022). “Non-equilibrium plasma kinetics of CO2 in glow discharges: a comparison with existing modeling and experimental results”. In:

Plasma Sources Science and Technology 31.10, p. 104001. DOI: 10.1088/1361-6595/ac9083 (cit. on pp. 8, 190, 194).

Naidis, G V et al. (Nov. 2022). "Modeling of vibrational excitation dynamics in a nanosecond CO2 discharge". In: *Journal of Physics D: Applied Physics* 55.1, p. 015202. DOI: 10.1088/1361-6463/ac9c10. URL: https://dx.doi.org/10.1088/1361-6463/ac9c10 (cit. on pp. 8, 9).

Biondo, Omar et al. (Aug. 2022). "Insights into the limitations to vibrational excitation of CO2: validation of a kinetic model with pulsed glow discharge experiments". In: *Plasma Sources Science and Technology* 31.7, p. 074003. DOI: 10.1088/1361-6595/ac8019. URL: https://dx.doi.org/10.1088/1361-6595/ac8019 (cit. on pp. 8, 190, 194).

Trenchev, G. et al. (2019). "Atmospheric pressure glow discharge for CO2 conversion: Model-based exploration of the optimum reactor configuration". In: *Chemical Engineering Journal* 362, pp. 830–841. ISSN: 1385-8947. DOI: https://doi.org/10.1016/j.cej.2019.01.091. URL: https://www.sciencedirect.com/science/article/pii/S1385894719301111 (cit. on p. 8).

Renninger, Stephan et al. (2020). "High efficiency CO2-splitting in atmospheric pressure glow discharge". In: *Journal of CO2 Utilization* 42, p. 101322. ISSN: 2212-9820. DOI: https://doi.org/10.1016/j.jcou.2020.101322. URL: https://www.sciencedirect.com/science/article/pii/S2212982020308234 (cit. on p. 8).

Rond, C et al. (2008). "Spectroscopic measurements of nonequilibrium CO2 plasma in RF torch". In: *Chemical Physics* 354.1-3, pp. 16–26 (cit. on pp. 8, 79).

Morillo-Candas, Ana Sofia et al. (2020a). "Time Evolution of the Dissociation Fraction in rf CO2 Plasmas: Impact and Nature of Back-Reaction Mechanisms". In: *The Journal of Physical Chemistry C* 124.32, pp. 17459–17475. DOI: 10.1021/acs.jpcc.0c03354 (cit. on p. 8).

Rooij, G. J. van et al. (2015). "Taming microwave plasma to beat thermodynamics in CO2 dissociation". In: *Faraday Discuss.* 183 (0), pp. 233–248. DOI: 10.1039/C5FD00045A. URL: http://dx.doi.org/10.1039/C5FD00045A (cit. on p. 8).

Britun, Nikolay and Jaroslav Hnilica (2020). "Optical spectroscopy for sputtering process characterization". In: *Journal of Applied Physics* 127.21, p. 211101. DOI: 10.1063/5.0006586 (cit. on pp. 8, 31).

Soldatov, Sergey et al. (2021). "Time-Resolved Optical Emission Spectroscopy Reveals Nonequilibrium Conditions for CO2 Splitting in Atmospheric Plasma Sustained with Ultrafast Microwave Pulsation". In: *ACS Energy Letters* 6.1, pp. 124–130. DOI: 10.1021/acsenergylett.0c01983 (cit. on p. 8).

Maillard, Jean et al. (2022). "Time-resolved Optical Emission Spectroscopy measurements of electron density and temperature in CO2 Nanosecond Repetitively Pulsed discharges". In: *AIAA SCITECH 2022 Forum*, p. 2368 (cit. on p. 9).

Ceppelli, M et al. (Nov. 2021). "Time-resolved optical emission spectroscopy in CO2 nanosecond pulsed discharges". In: *Plasma Sources Science and Technology* 30.11, p. 115010. DOI: 10.1088/1361-6595/ac2411 (cit. on pp. 9, 71).

Montesano, Cesare, Sara Quercetti, et al. (2020). "The effect of different pulse patterns on the plasma reduction of CO2 for a nanosecond discharge". In: *Journal of CO2 Utilization* 39, p. 101157. ISSN: 2212-9820. DOI: https://doi.org/10.1016/j.jcou.2020.101157 (cit. on p. 9).

Pokrovskiy, G V et al. (Mar. 2022). "Fast gas heating and kinetics of electronically excited states in a nanosecond capillary discharge in CO2". In: *Plasma Sources Science and Technology* 31.3, p. 035010. DOI: 10.1088/1361-6595/ac5102 (cit. on p. 9).

Dębek, Radosław et al. (2019). "A review on plasma-catalytic methanation of carbon dioxide – Looking for an efficient catalyst". In: *Renewable and Sustainable Energy Reviews* 116, p. 109427. ISSN: 1364-0321. DOI: https://doi.org/10.1016/j.rser.2019.109427 (cit. on p. 9).

Costa, Patrick Da et al. (2021). “Ni-based catalysts for plasma-assisted CO2 methanation”. In: *Current Opinion in Green and Sustainable Chemistry* 32, p. 100540. ISSN: 2452-2236. DOI: `https://doi.org/10.1016/j.cogsc.2021.100540` (cit. on p. 9).

Sivachandiran, L. et al. (2020). “CO2 reforming in CH4 over Ni/-Al2O3 nano catalyst: Effect of cold plasma surface discharge”. In: *Applied Surface Science* 501, p. 144175. ISSN: 0169-4332. DOI: `https://doi.org/10.1016/j.apsusc.2019.144175` (cit. on p. 9).

J.Amouroux et al. (2011). “Carbon dioxide: a raw material and a future chemical fuel for a sustainable energy industry”. In: *Journal of Physical Chemistry C* (cit. on p. 9).

Kano, Masaki et al. (2012). “Reforming of Carbon Dioxide to Methane and Methanol by Electric Impulse Low-Pressure Discharge with Hydrogen”. In: *Plasma Chemistry and Plasma Processing* 32, pp. 177–185. DOI: `https://doi.org/10.1007/s11090-011-9333-0` (cit. on p. 9).

Kelly, Seán et al. (2019). “CO2 Decomposition in CO2 and CO2/H2 Spark-like Plasma Discharges at Atmospheric Pressure”. In: *ChemSusChem* 12.16, pp. 3785–3791. DOI: `https://doi.org/10.1002/cssc.201901744` (cit. on p. 9).

Liu, Jing-Bao et al. (May 2019). “Insight into gliding arc (GA) plasma reduction of COsub2/sub with Hsub2/sub: GA characteristics and reaction mechanism”. In: *Journal of Physics D: Applied Physics* 52.28, p. 284001. DOI: `10.1088/1361-6463/ab1bb1` (cit. on p. 9).

Ashford, Bryony et al. (2022). “Plasma-catalytic CO2 hydrogenation to ethane in a dielectric barrier discharge reactor”. In: *Journal of CO2 Utilization* 57, p. 101882. ISSN: 2212-9820. DOI: `https://doi.org/10.1016/j.jcou.2022.101882`. URL: `https://www.sciencedirect.com/science/article/pii/S2212982022000014` (cit. on p. 10).

Arora, Shalini et al. (2016). “An overview on dry reforming of methane: strategies to reduce carbonaceous deactivation of catalysts”. In: *RSC Adv.* 6 (110), pp. 108668–108688. DOI: `10.1039/C6RA20450C`. URL: `http://dx.doi.org/10.1039/C6RA20450C` (cit. on p. 10).

Pavlov, Alexander A. et al. (2000). “Greenhouse warming by CH4 in the atmosphere of early Earth”. In: *Journal of Geophysical Research: Planets* 105.E5, pp. 11981–11990. DOI: `https://doi.org/10.1029/1999JE001134`. URL: `https://agupubs.onlinelibrary.wiley.com/doi/abs/10.1029/1999JE001134` (cit. on p. 10).

Centi et al. (November 2009). “Opportunities and prospects in the chemical recycling of carbon dioxide to fuels”. In: *Catalysis Today* 148.3-4, pp. 191–205. DOI: `https://doi.org/10.1016/j.cattod.2009.07.075` (cit. on p. 10).

Bogaerts, A. et al. (2016). “Plasma based CO_2 and CH_4 conversion: A modeling perspective”. In: *Plasma Process Polym* 14. DOI: `10.1002/ppap.201600070` (cit. on pp. 10, 15).

W.Wang et al. (2018). “Modeling Plasma-based CO2 and CH4 Conversion in Mixtures with N2, O2, and H2O: The Bigger Plasma Chemistry Picture”. In: *J. Phys. Chem. C* 122.16, pp. 8704–8723. DOI: `https://doi.org/10.1021/acs.jpcc.7b10619` (cit. on pp. 10, 15, 143, 242–245).

C.Bai (2019). “Numerical investigation on the CH4/CO2 nanosecond pulsed dielectric barrier discharge plasma at atmospheric pressure”. In: *AIP Advances* 9, p. 035023. DOI: `10.1063/1.5063519` (cit. on pp. 10, 15, 16, 102, 112, 116, 119–121, 179, 180, 184).

Pan, Jie et al. (2022). “Numerical modeling and mechanism investigation of nanosecond-pulsed DBD plasma catalytic CH_4 dry reforming”. In: *J. Phys. D: Appl. Phys* 55, p. 035202. DOI: `https://doi.org/10.1088/1361-6463/ac2ad8` (cit. on pp. 10, 15).

Maroni, Plinio (2005). “Bond- and mode-specific reactivity of methane on Ni(100)”. PhD thesis (cit. on p. 11).

Owens, Alec et al. (2016). “A highly accurate ab initio potential energy surface for methane”. In: *The Journal of Chemical Physics* 145.10, p. 104305. DOI: `10.1063/1.4962261` (cit. on pp. 10, 12).

Butterworth, Tom et al. (Sept. 2020). “Plasma induced vibrational excitation of CHsub4/sub—a window to its mode selective processing”. In: *Plasma Sources Science and Technology* 29.9, p. 095007. DOI: `10.1088/1361-6595/aba1c9` (cit. on pp. 12, 102, 195, 223).

Nikitin, Andrei V. et al. (2011). “Rotational and vibrational energy levels of methane calculated from a new potential energy surface”. In: *Chemical Physics Letters* 501.4, pp. 179–186. ISSN: 0009-2614. DOI: https://doi.org/10.1016/j.cplett.2010.11.008. URL: https://www.sciencedirect.com/science/article/pii/S0009261410014715 (cit. on p. 12).

Pham, T. et al. (2020). “Microwave-assisted dry reforming of methane for syngas production: a review”. In: *Environ Chem Lett* 18, pp. 1987–2019. DOI: https://doi.org/10.1007/s10311-020-01055-0 (cit. on pp. 12, 15).

Ozkan, A. et al. (2015). “CO2–CH4 conversion and syngas formation at atmospheric pressure using a multi-electrode dielectric barrier discharge”. In: *Journal of CO2 Utilization* 9, pp. 74–81. ISSN: 2212-9820. DOI: https://doi.org/10.1016/j.jcou.2015.01.002 (cit. on p. 12).

Pham, M.H. et al. (2011). “Activation of methane and carbon dioxide in a dielectric-barrier discharge-plasma reactor to produce hydrocarbons—Influence of La2O3/-Al2O3 catalyst”. In: *Catalysis Today* 171.1, pp. 67–71. ISSN: 0920-5861. DOI: https://doi.org/10.1016/j.cattod.2011.03.015 (cit. on p. 13).

Wang, Qi, Bin-Hang Yan, et al. (2009). “Dry Reforming of Methane in a Dielectric Barrier Discharge Reactor with Ni/Al2O3 Catalyst: Interaction of Catalyst and Plasma”. In: *Energy & Fuels* 23.8, pp. 4196–4201. DOI: 10.1021/ef900286j (cit. on p. 13).

Wang, Qi, Yi Cheng, et al. (2009). “Dry reforming of methane in an atmospheric pressure plasma fluidized bed with Ni/-Al2O3 catalyst”. In: *Catalysis Today* 148.3. Special Issue of the 10th International Conference on CO2 Utilization, Tianijn, China, May 17-21, 2009, pp. 275–282. ISSN: 0920-5861. DOI: https://doi.org/10.1016/j.cattod.2009.08.008. URL: https://www.sciencedirect.com/science/article/pii/S0920586109005574 (cit. on p. 13).

Wang, Huaqin et al. (2019). “Non-thermal plasma enhanced dry reforming of CH4 with CO2 over activated carbon supported Ni catalysts”. In: *Molecular Catalysis* 475, p. 110486. ISSN: 2468-8231. DOI: https://doi.org/10.1016/j.mcat.2019.110486. URL: https://www.sciencedirect.com/science/article/pii/S2468823119303219 (cit. on p. 13).

Mei, D.H. et al. (2017). “CO2 reforming with methane for syngas production using a dielectric barrier discharge plasma coupled with Ni/-Al2O3 catalysts: Process optimization through response surface methodology”. In: *Journal of CO2 Utilization* 21, pp. 314–326. ISSN: 2212-9820. DOI: https://doi.org/10.1016/j.jcou.2017.06.020. URL: https://www.sciencedirect.com/science/article/pii/S2212982017302093 (cit. on p. 13).

Kameshima, Seigo et al. (2015). “Pulsed dry methane reforming in plasma-enhanced catalytic reaction”. In: *Catalysis Today* 256. Plasmas for enhanced catalytic processes (ISPCEM 2014), pp. 67–75. ISSN: 0920-5861. DOI: https://doi.org/10.1016/j.cattod.2015.05.011 (cit. on pp. 13, 17).

Xu, Junqiang, Huan Tian, et al. (2022). “A coupling bimetallic Ni–La/MCM-41 catalyst enhanced by radio frequency (RF) plasma for dry reforming”. In: *New J. Chem.* 46 (5), pp. 2326–2334. DOI: 10.1039/D1NJ05029J (cit. on p. 13).

Xu, Junqiang, Yalin Liu, et al. (2022). “Ni-based catalysts with coke resistance enhance by radio frequency discharge plasma for CH4/CO2 reforming”. In: *International Journal of Hydrogen Energy* 47.8, pp. 5240–5249. ISSN: 0360-3199. DOI: https://doi.org/10.1016/j.ijhydene.2021.11.131 (cit. on p. 13).

Liu, Shuang et al. (2020a). “Review of Plasma-Assisted Catalysis for Selective Generation of Oxygenates from CO2 and CH4”. In: *ACS Catalysis* 10.4, pp. 2855–2871. DOI: 10.1021/acscatal.9b04811 (cit. on pp. 13, 189).

Wang, Li et al. (Aug. 2017). “One-Step Reforming of CO2 and CH4 into High-Value Liquid Chemicals and Fuels at Room Temperature by Plasma-Driven Catalysis”. In: *Angewandte Chemie* 129. DOI: 10.1002/ange.201707131 (cit. on p. 14).

Li, Di et al. (2020). “Direct conversion of CO2 and CH4 into liquid chemicals by plasma-catalysis”. In: *Applied Catalysis B: Environmental* 261, p. 118228. ISSN: 0926-3373. DOI: https://doi.org/10.1016/j.apcatb.2019.118228. URL: https://www.sciencedirect.com/science/article/pii/S0926337319309750 (cit. on pp. 14, 17).

Jwa, E. et al. (2013). “Plasma-assisted catalytic methanation of CO and CO2 over Ni–zeolite catalysts”. In: *Fuel Processing Technology* 108. Special Issue of APCRE11, pp. 89–93. ISSN: 0378-3820. DOI: https://doi.org/10.1016/j.fuproc.2012.03.008. URL: https://www.sciencedirect.com/science/article/pii/S0378382012001014 (cit. on p. 14).

Scapinello, M. et al. (2016). “Conversion of CH4 /CO2 by a nanosecond repetitively pulsed discharge”. In: *J. Phys. D: Appl. Phys.* 49, p. 075602. DOI: https://doi.org/10.1088/0022-3727/49/7/075602 (cit. on p. 14).

Montesano, Cesare, Marzia Faedda, et al. (2021). “CH4 reforming with CO2 in a nanosecond pulsed discharge. The importance of the pulse sequence”. In: *Journal of CO2 Utilization* 49, p. 101556. ISSN: 2212-9820. DOI: https://doi.org/10.1016/j.jcou.2021.101556 (cit. on pp. 14, 185).

Wang, Xiaoling et al. (2019). “Nanosecond pulsed plasma assisted dry reforming of CH4: The effect of plasma operating parameters”. In: *Applied Energy* 243, pp. 132–144. ISSN: 0306-2619. DOI: https://doi.org/10.1016/j.apenergy.2019.03.193 (cit. on p. 14).

S.Zhang et al. (2022). “Optical emission spectroscopy measurement of plasma parameters in a nanosecond pulsed spark discharge for CO_2-CH_4 dry reforming”. In: *Spectrochimica Acta Part A: Molecular and Biomolecular Spectrocscopy* 267, p. 120590. DOI: https://doi.org/10.1016/j.saa.2021.120590 (cit. on p. 14).

Liu, Z. et al. (2020). “Phase-Resolved Measurement of Atmospheric-Pressure Radio-Frequency Pulsed Discharges in Ar/CH4/CO2 Mixture”. In: *Plasma Chem Plasma Process* 40, pp. 937–953. DOI: https://doi.org/10.1007/s11090-020-10071-5 (cit. on pp. 14, 132).

H.Li et al. (2020). “Optical and Mass Spectrometric Measurements of the CH4CO2 Dry Reforming Process in a Low Pressure, Very High Density, and Purely Inductive Plasma”. In: *J. Phys. Chem. A* 124, 72717282. DOI: https://dx.doi.org/10.1021/acs.jpca.0c04033 (cit. on pp. 14, 132).

Tao, Xumei et al. (2011). “CH4–CO2 reforming by plasma – challenges and opportunities”. In: *Progress in Energy and Combustion Science* 37.2, pp. 113–124. ISSN: 0360-1285. DOI: https://doi.org/10.1016/j.pecs.2010.05.001. URL: https://www.sciencedirect.com/science/article/pii/S0360128510000390 (cit. on p. 14).

Jasiński, M. et al. (2013). “Atmospheric pressure microwave plasma source for hydrogen production”. In: *International Journal of Hydrogen Energy* 38.26, pp. 11473–11483. ISSN: 0360-3199. DOI: https://doi.org/10.1016/j.ijhydene.2013.05.105. URL: https://www.sciencedirect.com/science/article/pii/S0360319913013013 (cit. on p. 15).

Hrycak, B et al. (2019). “Hydrogen production via synthetic biogas reforming in atmospheric-pressure microwave (915 MHz) plasma at high gas-flow output”. In: *Plasma Chemistry and Plasma Processing* 39.3, pp. 695–711 (cit. on p. 15).

Chun, Se Min et al. (2019). “CO2 Microwave Plasma—Catalytic Reactor for Efficient Reforming of Methane to Syngas”. In: *Catalysts* 9.3. ISSN: 2073-4344. DOI: 10.3390/catal9030292. URL: https://www.mdpi.com/2073-4344/9/3/292 (cit. on p. 15).

de Dios García, Ignacio et al. (2021). “Syngas production via microwave-assisted dry reforming of methane”. In: *Catalysis Today* 362. 1st International Conference on Unconventional Catalysis, Reactors and Applications: Catalysis Beyond the Reactor, pp. 72–80. ISSN: 0920-5861. DOI: https://doi.org/10.1016/j.cattod.2020.04.045. URL: https://www.sciencedirect.com/science/article/pii/S092058612030239X (cit. on p. 15).

Zhang, Fusen et al. (2022). “Fe/HZSM-5 synergizes with biomass pyrolysis carbon to reform CH4–CO2 to syngas in microwave field”. In: *International Journal of Hydrogen Energy* 47.21. Sustainable Hydrogen Energy Technologies, pp. 11153–11163. ISSN: 0360-3199. DOI: https://doi.org/10.1016/j.ijhydene.2022.01.158 (cit. on p. 15).

Zhu, Mingrui et al. (2022). “Surface induced gas-phase redistribution effects in plasma-catalytic dry reforming of methane: numerical investigation by fluid modeling”. In: *J. Phys. D: Appl. Phys* 55, p. 355201. DOI: https://doi.org/10.1088/1361-6463/ac74f7 (cit. on p. 15).

Tu, X. et al. (2012). “Plasma-catalytic dry reforming of methane in an atmospheric dielectric barrier discharge: Understanding the synergistic effect at low temperature”. In: *Applied*

Catalysis B: Environmental 125, pp. 439–448. ISSN: 0926-3373. DOI: https://doi.org/10.1016/j.apcatb.2012.06.006 (cit. on p. 15).

Bie, C. De et al. (2015). "The Dominant Pathways for the Conversion of Methane into Oxygenates and Syngas in an Atmospheric Pressure Dielectric Barrier Discharge". In: *J. Phys. Chem. C* 119, 233122350. DOI: http://dx.doi.org/10.1021/acs.jpcc.5b06515 (cit. on pp. 15, 112, 116, 118–122, 143, 154, 155, 179, 180, 183, 184).

Snoeckx, Ramses et al. (2013). "Plasma-Based Dry Reforming: A Computational Study Ranging from the Nanoseconds to Seconds Time Scale". In: *The Journal of Physical Chemistry C* 117.10, pp. 4957–4970. DOI: 10.1021/jp311912b (cit. on p. 15).

Snoeckx, R., Y. X. Zeng, et al. (2015). "Plasma-based dry reforming: improving the conversion and energy efficiency in a dielectric barrier discharge". In: *RSC Adv.* 5 (38), pp. 29799–29808. DOI: 10.1039/C5RA01100K. URL: http://dx.doi.org/10.1039/C5RA01100K (cit. on p. 15).

Cleiren, Emelie et al. (2017). "Dry Reforming of Methane in a Gliding Arc Plasmatron: Towards a Better Understanding of the Plasma Chemistry". In: *ChemSusChem* 10.20, pp. 4025–4036. DOI: https://doi.org/10.1002/cssc.201701274 (cit. on pp. 15, 119, 183).

Van Alphen, S. et al. (2021). "Effect of N2 on CO2-CH4 conversion in a gliding arc plasmatron: Can this major component in industrial emissions improve the energy efficiency?" In: *Journal of CO2 Utilization* 54, p. 101767. DOI: https://doi.org/10.1016/j.jcou.2021.101767 (cit. on pp. 15, 17, 93, 116).

Mei, Danhua et al. (2022). "CH4 reforming with CO2 using a nanosecond pulsed dielectric barrier discharge plasma". In: *Journal of CO2 Utilization* 62, p. 102073. ISSN: 2212-9820. DOI: https://doi.org/10.1016/j.jcou.2022.102073. URL: https://www.sciencedirect.com/science/article/pii/S2212982022001925 (cit. on pp. 16, 119).

Hake, R.D. et al. (1967). "Momentum-transfer and inelastic-collision cross-section for electrons in O2, CO and CO2". In: *Physical Review* 158, pp. 70–84. DOI: https://doi.org/10.1103/PhysRev.158.70 (cit. on p. 16).

Polak, L. et al. (1976). "Electron impact induced electronic excitation and molecular dissociation". In: *International Journal for Radiation Physics and Chemistry* 8, pp. 257–282. DOI: https://doi.org/10.1016/0020-7055(76)90070-X (cit. on p. 16).

Alves, L L (Dec. 2014). "The IST-LISBON database on LXCat". In: *Journal of Physics: Conference Series* 565.1, p. 012007. DOI: 10.1088/1742-6596/565/1/012007. URL: https://dx.doi.org/10.1088/1742-6596/565/1/012007 (cit. on pp. 16, 101).

Bouwman, D. et al. (2021). "Neutral dissociation of methane by electron impact and a complete and consistent cross section set". In: *Plasma Sources Sci. Technol.* 30, p. 075012. DOI: https://doi.org/10.1088/1361-6595/ac0b2b (cit. on p. 16).

Baulch, D.L. et al. (1992). "Evaluated kinetic data for combustion modeling". In: *J. Phys. Chem.* 21, p. 411 (cit. on pp. 17, 119, 166, 181, 183, 184, 241–244, 249–253).

Tsang, W. et al. (1986). "Chemical kinetic data base for combustion chemistry. Part I. Methane and related compounds". In: *J. Phys. Chem. Ref. Data* 15 (cit. on pp. 17, 108, 119, 160, 174, 241–244, 249–253).

Liu, Shuang et al. (2020b). "Review of Plasma-Assisted Catalysis for Selective Generation of Oxygenates from CO2 and CH4". In: *ACS Catalysis* 10.4, pp. 2855–2871. DOI: 10.1021/acscatal.9b04811 (cit. on p. 17).

Konnov, Alexander A. (2015). "On the role of excited species in hydrogen combustion". In: *Combustion and Flame* 162.10, pp. 3755–3772. ISSN: 0010-2180. DOI: https://doi.org/10.1016/j.combustflame.2015.07.014 (cit. on p. 17).

Lefkowitz, J. (2015). "Species and temperature measurements of methane oxidation in a nanosecond repetitively pulsed discharge". In: *Phil. Trans. R. Soc A* 373, p. 20140333. DOI: https://dx.doi.org/10.1098/rsta.2014.0333 (cit. on pp. 17, 126, 127, 139, 176).

Mao, Xingqian et al. (2019). "Numerical modeling of ignition enhancement of CH4/O2/He mixtures using a hybrid repetitive nanosecond and DC discharge". In: *Proceedings of the Combustion Institute* 37.4, pp. 5545–5552. ISSN: 1540-7489. DOI: https://doi.org/10.1016/j.proci.2018.05.106 (cit. on p. 17).

Starik, A M et al. (May 2012). “Comprehensive analysis of combustion enhancement mechanisms in a supersonic flow of CHsub4/sub–Osub2/submixture with electric-discharge-activated oxygen molecules”. In: *Plasma Sources Science and Technology* 21.3, p. 035015. DOI: `10.1088/0963-0252/21/3/035015` (cit. on p. 17).

Kozák, Tomáš et al. (June 2014). “Splitting of COsub2/subby vibrational excitation in non-equilibrium plasmas: a reaction kinetics model”. In: *Plasma Sources Science and Technology* 23.4, p. 045004. DOI: `10.1088/0963-0252/23/4/045004`. URL: `https://doi.org/10.1088/0963-0252/23/4/045004` (cit. on pp. 17, 161).

Booth, J P et al. (May 2019). “Oxygen (3P) atom recombination on a Pyrex surface in an O2 plasma”. In: *Plasma Sources Science and Technology* 28.5, p. 055005. DOI: `10.1088/1361-6595/ab13e8` (cit. on p. 18).

A.Rousseau, G. Cartry et al. (2001). “Surface recombination of hydrogen atoms studied by a pulsed plasma excitation technique”. In: *Journal of Applied Physics* 89, p. 2074. DOI: `https://doi.org/10.1063/1.1325000` (cit. on pp. 18, 103, 114).

Czerwiec, T et al. (Dec. 2005). “Nitrogen dissociation in a low pressure cylindrical ICP discharge studied by actinometry and mass spectrometry”. In: *Journal of Physics D: Applied Physics* 38.24, pp. 4278–4289. DOI: `10.1088/0022-3727/38/24/003` (cit. on p. 24).

Ricard, André et al. (2007). “Determination of N-, H- and O-Atom Densities in N2–H2 and in N2–O2 Gas Mixtures by Optical Actinometry in Flowing Microwave Discharges and by NO Titration in Post-Discharges”. In: *Plasma Processes and Polymers* 4.S1, S965–S968. DOI: `https://doi.org/10.1002/ppap.200732308` (cit. on p. 24).

Lopaev, D V et al. (Jan. 2017). “Actinometry of O, N and F atoms”. In: *Journal of Physics D: Applied Physics* 50.7, p. 075202. DOI: `10.1088/1361-6463/50/7/075202` (cit. on pp. 24, 78).

Pagnon, D et al. (Sept. 1995). “On the use of actinometry to measure the dissociation in Osub2/subDC glow discharges: determination of the wall recombination probability”. In: *Journal of Physics D: Applied Physics* 28.9, pp. 1856–1868. DOI: `10.1088/0022-3727/28/9/014` (cit. on pp. 24, 26, 30, 57, 58).

Tsutsumi, T. et al. (2017). “Investigation of the radially resolved oxygen dissociation degree and local mean electron energy in oxygen plasmas in contact with different surface materials”. In: *Journal of Applied Physics* 121.14, p. 143301. DOI: `10.1063/1.4979855` (cit. on pp. 24, 27, 36, 62).

Britun, Nikolay, Alexandr Belosludtsev, et al. (Jan. 2017). “Ground state atomic oxygen in high-power impulse magnetron sputtering: a quantitative study”. In: *Journal of Physics D: Applied Physics* 50.7, p. 075204. DOI: `10.1088/1361-6463/aa560c`. URL: `https://doi.org/10.1088/1361-6463/aa560c` (cit. on pp. 24, 31).

Morillo-Candas, A S, C Drag, et al. (July 2019b). “Oxygen atom kinetics in CO_2 plasmas ignited in a DC glow discharge”. In: *Plasma Sources Science and Technology* 28.7, p. 075010. DOI: `10.1088/1361-6595/ab2b84` (cit. on pp. 24, 26, 27, 30, 31, 33, 35).

Dyatko, N.A. et al. (1998). “Actinometric method for measuring hydrogen-atom density in a glow discharge plasma”. In: *Plasma Physics Reports* 24.12, pp. 1041–1050. DOI: `101134/1952662` (cit. on p. 24).

Gicquel, A. et al. (1998). “Validation of actinometry for estimating relative hydrogen atom densities and electron energy evolution in plasma assisted diamond deposition reactors”. In: *Journal of Applied Physics* 83.12, pp. 7504–7521. DOI: `10.1063/1.367514` (cit. on p. 24).

Krištof, J et al. (June 2016). “Diagnostics of low-pressure hydrogen discharge created in a 13.56 MHz RF plasma reactor”. In: *Physica Scripta* 91.7, p. 074009. DOI: `10.1088/0031-8949/91/7/074009` (cit. on pp. 24, 26, 61).

Bernatskiy, A.V. et al. (Sept. 2015). “Detection of water impurities in plasma by optical actinometry”. In: *Bull. Lebedev Phys. Inst.* 42, pp. 273–276. DOI: `10.3103/S1068335615090055`. URL: `https://doi.org/10.3103/S1068335615090055` (cit. on p. 24).

Bernatskiy, A V, V N Ochkin, et al. (Sept. 2016). “Multispectral actinometry of water and water-derivative molecules in moist, inert gas discharge plasmas”. In: 49.39, p. 395204. DOI: 10.1088/0022-3727/49/39/395204 (cit. on pp. 24, 30).

Bernatskiy, A V, V V Lagunov, et al. (June 2016). “Study of water molecule decomposition in plasma by diode laser spectroscopy and optical actinometry methods”. In: *Laser Physics Letters* 13.7, p. 075702. DOI: 10.1088/1612-2011/13/7/075702. URL: https://doi.org/10.1088/1612-2011/13/7/075702 (cit. on p. 24).

Booth, J-P, A Chatterjee, O Guaitella, D Lopaev, et al. (June 2022). “Quenching of O2(b) by O(3P) atoms. Effect of gas temperature”. In: *Plasma Sources Science and Technology* 31.6, p. 065012. DOI: 10.1088/1361-6595/ac7749 (cit. on pp. 25, 29).

Kramida, A et al. (2021). NIST Atomic Spectra Database (ver. 5.9), [Online]. Available: https://physics.ni
[2022, October 2]. National Institute of Standards and Technology, Gaithersburg, MD. (Cit. on pp. 27, 241).

Jelenak, Z. M. et al. (May 1993). “Electronic excitation of the 750- and 811-nm lines of argon”. In: *Phys. Rev. E* 47 (5), pp. 3566–3573. DOI: 10.1103/PhysRevE.47.3566. URL: https://link.aps.org/doi/10.1103/PhysRevE.47.3566 (cit. on p. 27).

Niemi, K et al. (Apr. 2005). “Absolute atomic oxygen density measurements by two-photon absorption laser-induced fluorescence spectroscopy in an RF-excited atmospheric pressure plasma jet”. In: *Plasma Sources Science and Technology* 14.2, pp. 375–386. DOI: 10.1088/0963-0252/14/2/021 (cit. on pp. 27, 35, 36).

Berden, Giel et al. (2009). *Cavity ring-down spectroscopy: techniques and applications*. John Wiley & Sons (cit. on p. 27).

Booth, J.P et al. (2000). “Ultraviolet cavity ring-down spectroscopy of free radicals in etching plasmas”. In: *Chemical Physics Letters* 317.6, pp. 631–636. ISSN: 0009-2614. DOI: https://doi.org/10.1016/S0009-2614(99)01424-4. URL: https://www.sciencedirect.com/science/article/pii/S0009261499014244 (cit. on p. 27).

Stancu, G D, F Kaddouri, et al. (Mar. 2010). “Atmospheric pressure plasma diagnostics by OES, CRDS and TALIF”. In: *Journal of Physics D: Applied Physics* 43.12, p. 124002. DOI: 10.1088/0022-3727/43/12/124002. URL: https://dx.doi.org/10.1088/0022-3727/43/12/124002 (cit. on p. 27).

Laher, Russ R. et al. (1990). “Updated Excitation and Ionization Cross Sections for Electron Impact on Atomic Oxygen”. In: *Journal of Physical and Chemical Reference Data* 19.1, pp. 277–305. DOI: 10.1063/1.555872 (cit. on pp. 30, 33, 36, 58).

Drag, C et al. (July 2021). “Measurement of the two-photon excitation cross-section of the 6p′[3/2]sub2/sub and 6p′[1/2]sub0/sub levels of Xe I at the wavelengths 224.3 and 222.6 nm”. In: *Plasma Sources Science and Technology* 30.7, p. 075026. DOI: 10.1088/1361-6595/abfbeb. URL: https://doi.org/10.1088/1361-6595/abfbeb (cit. on p. 31).

Julienne, P. S. et al. (1976). “Cascade and radiation trapping effects on atmospheric atomic oxygen emission excited by electron impact”. In: *Journal of Geophysical Research (1896-1977)* 81.7, pp. 1397–1403. DOI: https://doi.org/10.1029/JA081i007p01397 (cit. on p. 32).

Davis, J. et al. (Nov. 1974.). “Distorted wave calculations for gaunt factors, cross sections, and rate coefficients of selected al- lowed, forbidden, and spin exchange transitions”. In: *Memo. Rep. 2939, Naval Res. Lab., Washington, D.C.* (cit. on p. 32).

Gulcicek, Erol E. et al. (1987). “Absolute differential and integral electron excitation cross sections of the atomic oxygen ^{3}P and 5 P states at 30 eV”. In: *Journal of Geophysical Research: Space Physics* 92.A4, pp. 3445–3448. DOI: https://doi.org/10.1029/JA092iA04p03445 (cit. on pp. 32, 33).

Gulcicek, E. E. et al. (1988). “Absolute differential and integral electron excitation cross sections for atomic oxygen, 6, the 3P -> 3P and 3P → 5P transitions from 13.87 to 100 eV”. In: *Journal of Geophysical Research: Space Physics* 93.A6, pp. 5885–5889. DOI: https://doi.org/10.1029/JA093iA06p05885 (cit. on pp. 32, 33).

Barklem, P. S. (2007). “Electron-impact excitation of neutral oxygen”. In: *A&A* 462.2, pp. 781–788. DOI: `10.1051/0004-6361:20066341`. URL: `https://doi.org/10.1051/0004-6361:20066341` (cit. on p. 33).

Tayal, S. S. et al. (Oct. 2016). “*B*-spline *R*-matrix-with-pseudostates approach for excitation and ionization of atomic oxygen by electron collisions”. In: *Phys. Rev. A* 94 (4), p. 042707. DOI: `10.1103/PhysRevA.94.042707` (cit. on p. 33).

Vaughan, S. O. et al. (1988). “Absolute experimental differential and integral electron excitation cross sections for atomic oxygen: 4. The (^{3}P → 3s^{3}P°), (^{3}P → 2s 2p 5 ^{3}P°), (^{3}P → 4d ^{3}P°) Autoionizing Transitions (878, 792, and 770 Å) and five members of the (^{3}P → nd ^{3}D°) Rydberg series (1027 Å)”. In: *Journal of Geophysical Research: Space Physics* 93.A1, pp. 289–293. DOI: `https://doi.org/10.1029/JA093iA01p00289` (cit. on p. 33).

Kanik, I et al. (June 2001). “Electron-impact studies of atomic oxygen: I. Differential and integral cross sections experiment and theory”. In: *Journal of Physics B: Atomic, Molecular and Optical Physics* 34.13, pp. 2647–2665. DOI: `10.1088/0953-4075/34/13/308`. URL: `https://doi.org/10.1088/0953-4075/34/13/308` (cit. on p. 33).

Viegas, P et al. (June 2021). “Resolving discharge parameters from atomic oxygen emission”. In: *Plasma Sources Science and Technology* 30.6, p. 065022. DOI: `10.1088/1361-6595/ac04bd` (cit. on p. 33).

Fiebrandt, Marcel et al. (Apr. 2020). “Determination of atomic oxygen state densities in a double inductively coupled plasma using optical emission and absorption spectroscopy and probe measurements”. In: *Plasma Sources Science and Technology* 29.4, p. 045018. DOI: `10.1088/1361-6595/ab7cbe` (cit. on p. 33).

Caplinger, James E et al. (Jan. 2020). “The importance of cascade emission and metastable excitation in modeling strong atomic oxygen lines in laboratory plasmas”. In: *Plasma Sources Science and Technology* 29.1, p. 015011. DOI: `10.1088/1361-6595/ab5e5f` (cit. on p. 33).

Bretagne, J et al. (May 1986). “Relativistic electron-beam-produced plasmas. I. Collision cross sections and loss function in argon”. In: *Journal of Physics D: Applied Physics* 19.5, pp. 761–777. DOI: `10.1088/0022-3727/19/5/010` (cit. on p. 33).

Hayashi, M. (Nov. 1981). *Recommended values of transport cross sections for elastic collision and total collision cross section of electrons in atomic and molecular gases* (cit. on p. 33).

Zatsarinny, Oleg et al. (Feb. 2014). “Electron-impact excitation of argon at intermediate energies”. In: *Phys. Rev. A* 89 (2), p. 022706. DOI: `10.1103/PhysRevA.89.022706`. URL: `https://link.aps.org/doi/10.1103/PhysRevA.89.022706` (cit. on p. 33).

Chutjian, A. et al. (May 1981). “Electron-impact excitation of electronic states in argon at incident energies between 16 and 100 eV”. In: *Phys. Rev. A* 23 (5), pp. 2178–2193. DOI: `10.1103/PhysRevA.23.2178` (cit. on p. 33).

Chilton, J. Ethan et al. (Jan. 1998). “Measurement of electron-impact excitation into the $3p^54p$ levels of argon using Fourier-transform spectroscopy”. In: *Phys. Rev. A* 57 (1), pp. 267–277. DOI: `10.1103/PhysRevA.57.267`. URL: `https://link.aps.org/doi/10.1103/PhysRevA.57.267` (cit. on pp. 33–35).

Filipovic, D M et al. (Feb. 2000a). “Electron-impact excitation of argon: I. The 4s´[½]sub1/sub, 4p[½]sub1/suband 4p´[½]sub0/substates”. In: *Journal of Physics B: Atomic, Molecular and Optical Physics* 33.4, pp. 677–691. DOI: `10.1088/0953-4075/33/4/306` (cit. on p. 33).

— (May 2000b). “Electron-impact excitation of argon: II. The lowest resonance 4s[sup3/sup/sub2/sub]sub1/suban metastable 4s[sup3/sup/sub2/sub]sub2/suband 4s’[Â½]sub0/substates”. In: *Journal of Physics B: Atomic, Molecular and Optical Physics* 33.11, pp. 2081–2094. DOI: `10.1088/0953-4075/33/11/308` (cit. on p. 33).

Puech, V et al. (Dec. 1986). “Collision cross sections and electron swarm parameters in argon”. In: *Journal of Physics D: Applied Physics* 19.12, pp. 2309–2323. DOI: `10.1088/0022-3727/19/12/011`. URL: `https://doi.org/10.1088/0022-3727/19/12/011` (cit. on pp. 33, 35, 58).

Frost, L. S. et al. (Dec. 1964). “Momentum-Transfer Cross Sections for Slow Electrons in He, Ar, Kr, and Xe from Transport Coefficients”. In: *Phys. Rev.* 136 (6A), A1538–A1545. DOI:

10.1103/PhysRev.136.A1538. URL: https://link.aps.org/doi/10.1103/PhysRev.136.A1538 (cit. on p. 33).

Schaper, M. et al. (1969). "Absolutbestimmung der Gesamtanregungsquerschnitte der Edelgase durch Elektronenstoss". In: *Beitrage aus der Plasmaphysik* 9.1, pp. 45–57. DOI: https://doi.org/10.1002/ctpp.19690090105 (cit. on p. 34).

Ballou, James K. et al. (Oct. 1973). "Electron-Impact Excitation of the Argon Atom". In: *Phys. Rev. A* 8 (4), pp. 1797–1807. DOI: 10.1103/PhysRevA.8.1797 (cit. on p. 34).

Gousset, G et al. (Mar. 1991). "Electron and heavy-particle kinetics in the low pressure oxygen positive column". In: *Journal of Physics D: Applied Physics* 24.3, pp. 290–300. DOI: 10.1088/0022-3727/24/3/010 (cit. on pp. 34, 101).

Price, D A et al. (July 1972). "Ionization in oxygen-hydrogen mixtures". In: *Journal of Physics D: Applied Physics* 5.7, pp. 1249–1259. DOI: 10.1088/0022-3727/5/7/309 (cit. on p. 34).

— (Aug. 1973). "Current growth in oxygen". In: *Journal of Physics D: Applied Physics* 6.12, pp. 1514–1524. DOI: 10.1088/0022-3727/6/12/314 (cit. on p. 34).

Corbin, R. J. et al. (Dec. 1974). "Electron avalanches in oxygen and in mixtures of O_2 and H_2: Determination of the first Townsend coefficient α". In: *Phys. Rev. A* 10 (6), pp. 2273–2279. DOI: 10.1103/PhysRevA.10.2273 (cit. on p. 34).

Yanguas-Gil, Angel et al. (May 2005). "An update of argon inelastic cross sections for plasma discharges". In: *Journal of Physics D: Applied Physics* 38.10, pp. 1588–1598. DOI: 10.1088/0022-3727/38/10/014 (cit. on p. 35).

Meler, U. et al. (1986). "H and O atom detection for combustion applications: study of quenching and laser photolysis effects". In: *Chemical Physics Letters* 126.6, pp. 567–573. ISSN: 0009-2614. DOI: https://doi.org/10.1016/S0009-2614(86)80175-0. URL: https://www.sciencedirect.com/science/article/pii/S0009261486801750 (cit. on p. 35).

Dagdigian, Paul J. et al. (1988). "Collisional transfer between and quenching of the 3p 3P and 5P states of the oxygen atom". In: *Chemical Physics Letters* 148.4, pp. 299–308. ISSN: 0009-2614. DOI: https://doi.org/10.1016/0009-2614(88)87276-2. URL: https://www.sciencedirect.com/science/article/pii/0009261488872762 (cit. on p. 35).

Tejero-del-Caz, A. (2019). "The LisbOn KInetics Boltzmann solver". In: *Plasma Sources Sci. Technol.* 28, p. 043001. DOI: https://doi.org/10.1088/1361-6595/ab0537 (cit. on pp. 36, 101, 155).

— (2021). "On the quasi-stationary approach to solve the electron Boltzmann equation in pulsed plasmas". In: *Plasma Sources Sci. Technol.* 30, p. 065008. DOI: https://doi.org/10.1088/1361-6595/abf858 (cit. on pp. 36, 101).

Booth, J-P, A Chatterjee, O Guaitella, J Santos Sousa, et al. (Nov. 2020). "Determination of absolute O(3P) and O2(a1Dg) densities and kinetics in fully modulated O2 dc glow discharges from the O2(X3Sg) afterglow recovery dynamics". In: *Plasma Sources Science and Technology* 29.11, p. 115009. DOI: 10.1088/1361-6595/abb5e7 (cit. on pp. 38, 39).

Bittner, J. et al. (1988). "Quenching of two-photon-excited H(3s, 3d) and O(3p 3P2,1,0) atoms by rare gases and small molecules". In: *Chemical Physics Letters* 143.6, pp. 571–576. ISSN: 0009-2614. DOI: https://doi.org/10.1016/0009-2614(88)87068-4 (cit. on p. 61).

Donnelly, V M (Sept. 2004). "Plasma electron temperatures and electron energy distributions measured by trace rare gases optical emission spectroscopy". In: *Journal of Physics D: Applied Physics* 37.19, R217. DOI: 10.1088/0022-3727/37/19/R01 (cit. on p. 64).

A. Kramida et al. (2022). NIST Atomic Spectra Database (ver. 5.10), [Online]. Available: `https://physics.nist.gov/asd` [2022, November 18]. National Institute of Standards and Technology, Gaithersburg, MD. (Cit. on p. 68).

Pearse, Reginald William Blake et al. (1976). *The identification of molecular spectra.* Vol. 297. Chapman and Hall London (cit. on pp. 68, 69).

Poncin-Epaillard, Fabienne et al. (2002). "Characterization of CO2 plasma and interactions with polypropylene film". In: *Plasmas and polymers* 7.1, pp. 1–17 (cit. on p. 68).

Robinson, D et al. (1958). “Intensity Measurements on the O2+ Second Negative, CO Ångström and Third Positive and NO γ and β Molecular Band Systems”. In: *Proceedings of the Physical Society (1958-1967)* 71.6, p. 957 (cit. on p. 68).

Slanger, TG et al. (1971). “CO (a 3Π), Its Production, Detection, Deactivation, and Radiative Lifetime”. In: *The Journal of Chemical Physics* 55.5, pp. 2164–2173 (cit. on p. 68).

Conway, Robert R (1981). “Spectroscopy of the Cameron bands in the Mars airglow”. In: *Journal of Geophysical Research: Space Physics* 86.A6, pp. 4767–4775 (cit. on p. 68).

Wallace, Lloyd (1962). “Band-Head Wavelengths of C2, ch, cn, co, nh, no, 02, oh, and Their Ions.” In: *The Astrophysical Journal Supplement Series* 7, p. 165 (cit. on p. 68).

Cicala, G et al. (Mar. 2009). “Study of positive column of glow discharge in nitrogen by optical emission spectroscopy and numerical simulation”. In: *Plasma Sources Science and Technology* 18.2, p. 025032. DOI: `10.1088/0963-0252/18/2/025032`. URL: `https://dx.doi.org/10.1088/0963-0252/18/2/025032` (cit. on p. 68).

Gauyacq, D et al. (1979). “The emission spectrum of the CO2+ ion: rovibronic analysis of the band system”. In: *Canadian Journal of Physics* 57.10, pp. 1634–1649 (cit. on p. 69).

R.Snoeckx et al. (2017). “Plasma technology – a novel solution for CO2 conversion?” In: *Chemical Society Reviews* 46, pp. 5805–5863. DOI: `10.1039/C6CS00066E` (cit. on pp. 69, 132).

Silva, Tiago, Nikolay Britun, et al. (Mar. 2014). “Optical characterization of a microwave pulsed discharge used for dissociation of CO2”. In: *Plasma Sources Science and Technology* 23.2, p. 025009. DOI: `10.1088/0963-0252/23/2/025009` (cit. on pp. 69, 71).

Y.Du et al. (2017). “CO(B1Sigma–>A1Pi) Angstrom System for Gas Temperature Measurements in CO2 Containing Plasmas”. In: *Plasma Chem Plasma Process* 37, pp. 29–41. DOI: `DOI10.1007/s11090-016-9759-5` (cit. on pp. 69, 71).

S.Yamada et al. (2021). “Nonequilibrium characteristics in the rotational temperature of CO excited states in microwave discharge CO2 plasma”. In: *Japanese Journal of Applied Physics 60* 60, p. 046005. DOI: `https://doi.org/10.35848/1347-4065/abee04` (cit. on p. 69).

Kovács, István et al. (1969). *Rotational structure in the spectra of diatomic molecules.* Akadémiai Kiadó Budapest (cit. on p. 71).

D.Coster et al. (1934). “Predissociation in the Angström Bands of CO”. In: *Physica* 1.1-6, pp. 155–160. DOI: `https://doi.org/10.1016/S0031-8914(34)90019-7` (cit. on p. 71).

Kpa, R et al. (2014). “Ångström (B1Σ+$\rightarrow$ A1Π) 0–1 and 1–1 bands in isotopic CO molecules: further investigations”. In: *Journal of Physics B: Atomic, Molecular and Optical Physics* 47.4, p. 045101 (cit. on p. 75).

Drake, DJ et al. (2009). “Characterization of a CO 2/N 2/Ar supersonic flowing discharge”. In: *Journal of applied physics* 106.8, p. 083305 (cit. on p. 75).

Ochkin, Vladimir N (2009). *Spectroscopy of low temperature plasma.* John Wiley & Sons (cit. on p. 76).

Stancu, G D, O Leroy, et al. (Sept. 2016). “Microwave air plasmas in capillaries at low pressure II. Experimental investigation”. In: *Journal of Physics D: Applied Physics* 49.43, p. 435202. DOI: `10.1088/0022-3727/49/43/435202` (cit. on p. 77).

Qin, Z. et al. (2017). “Radiative transition probabilities for the main diatomic electronic systems of N2, N2+, NO, O2, CO, CO+, CN, C2 and H2 produced in plasma of atmospheric entry”. In: *Journal of Quantitative Spectroscopy and Radiative Transfer* 202, pp. 286–301. ISSN: 0022-4073. DOI: `https://doi.org/10.1016/j.jqsrt.2017.08.010`. URL: `https://www.sciencedirect.com/science/article/pii/S002240731730328X` (cit. on p. 77).

Rogers, John et al. (Feb. 1970). “Radiative Lifetime of the B1+ State of CO∗”. In: *J. Opt. Soc. Am.* 60.2, pp. 278–279. DOI: `10.1364/JOSA.60.000278`. URL: `https://opg.optica.org/abstract.cfm?URI=josa-60-2-278` (cit. on p. 77).

Gupta, Sreenath B. et al. (2011). “On use of CO2 chemiluminescence for combustion metrics in natural gas fired reciprocating engines”. In: *Proceedings of the Combustion Institute* 33.2, pp. 3131–3139. ISSN: 1540-7489. DOI: `https://doi.org/10.1016/j.proci.2010.05.032`. URL: `https://www.sciencedirect.com/science/article/pii/S1540748910000866` (cit. on p. 79).

Pravilov, AM et al. (1978). “SPECTRAL DISTRIBUTION OF RATE CONSTANT OF CHEMILUMINESCENCE IN REACTION OF O (P-3)+ CO (+ HE)-STARCO2 (+ HE)+ HNU”. In: *ZHURNAL FIZICHESKOI KHIMII* 52.8, pp. 1863–1866 (cit. on p. 79).

Slack, M et al. (1985). “High temperature rate coefficient measurements of CO+ O chemiluminescence”. In: *Combustion and Flame* 59.2, pp. 189–196 (cit. on p. 79).

Kopp, Madeleine M et al. (2015). “Rate determination of the CO2* chemiluminescence reaction CO+ O+ M CO2*+ M”. In: *International Journal of Chemical Kinetics* 47.1, pp. 50–72 (cit. on p. 79).

Silva, T. et al. (Jan. 2020). “Dynamics of Gas Heating in the Afterglow of Pulsed CO2 and CO2–N2 Glow Discharges at Low Pressure”. In: *Plasma Chemistry and Plasma Processing* 40.3, pp. 713–725. DOI: 10.1007/s11090-020-10061-7. URL: https://doi.org/10.1007/s11090-020-10061-7 (cit. on pp. 92, 193).

M.Scapinello et al. (2016). “Conversion of CH4 /CO2 by a nanosecond repetitively pulsed discharge”. In: *J. Phys. D: Appl. Phys.* 49, p. 075602. DOI: https://doi.org/10.1088/0022-3727/49/7/075602 (cit. on p. 93).

Ghorbanzadeh, A.M. et al. (2007). “Carbon dioxide reforming of methane by pulsed glow discharge at atmospheric pressure: The effect of pulse compression”. In: *J. Appl. Phys.* 101, p. 123303. DOI: https://doi.org/10.1063/1.2745425 (cit. on p. 93).

Grofulović, Marija et al. (2016). “Electron-neutral scattering cross sections for CO2: a complete and consistent set and an assessment of dissociation”. In: *Journal of Physics D: Applied Physics* 49, p. 395207. DOI: doi:10.1088/0022-3727/49/39/395207 (cit. on pp. 101, 107).

Alves, Luis Lemos et al. (2016). “Electron scattering cross sections for the modelling of oxygen-containing plasmas”. In: *The European physical journal D* 70.6, pp. 1–9 (cit. on p. 101).

Ogloblina, Polina et al. (Dec. 2019). “Electron impact cross sections for carbon monoxide and their importance in the electron kinetics of CO2–CO mixtures”. In: *Plasma Sources Science and Technology* 29.1, p. 015002. DOI: 10.1088/1361-6595/ab4e72. URL: https://dx.doi.org/10.1088/1361-6595/ab4e72 (cit. on p. 101).

D.Bouwman et al. (2021). “Neutral dissociation of methane by electron impact and a complete and consistent cross section set”. In: *Plasma Sources Sci. Technol.* 30, p. 075012. DOI: https://doi.org/10.1088/1361-6595/ac0b2b (cit. on pp. 101, 107, 120).

Starr, D.F. et al. (1974). “Vibrational deactivation of carbon monoxide by hydrogen and nitrogen from 100 to 650 °K”. In: *J. Chem. Phys.* 61, p. 5421. DOI: https://doi.org/10.1063/1.1681897 (cit. on p. 102).

Millikan, Roger C. (1965a). “Vibration—Vibration Energy Exchange between Carbon Monoxide and Methane”. In: *J. Chem. Phys.* 43, p. 1439. DOI: https://doi.org/10.1063/1.1696952 (cit. on pp. 102, 206, 219, 222, 223, 226).

Hirschfelder, Joseph Oakland et al. (1964). “Molecular theory of gases and liquids”. In: *Molecular theory of gases and liquids* (cit. on pp. 103, 167, 211).

K.E.Shuler et al. (1949). “The Kinetics of Heterogeneous Atom and Radical Reactions. I. The Recombination of Hydrogen Atoms on Surfaces”. In: *J. Chem. Phys.* 17, p. 1212. DOI: https://doi.org/10.1063/1.1747144 (cit. on p. 103).

Self, S. A. et al. (1966). “Static Theory of a Discharge Column at Intermediate Pressures”. In: *The Physics of Fluids* 9.12, pp. 2486–2492. DOI: 10.1063/1.1761642 (cit. on p. 103).

Ferreira, C. M. et al. (1983). “Modelling of the low-pressure argon positive column”. In: *Journal of Applied Physics* 54.5, pp. 2261–2271. DOI: 10.1063/1.332380 (cit. on p. 103).

Coche, P et al. (May 2016). “Microwave air plasmas in capillaries at low pressure I. Self-consistent modeling”. In: *Journal of Physics D: Applied Physics* 49.23, p. 235207. DOI: 10.1088/0022-3727/49/23/235207. URL: https://dx.doi.org/10.1088/0022-3727/49/23/235207 (cit. on p. 103).

Makochekanwa, C. (2006). “Experimental observation of neutral radical formation from CH4 by electron impact in the threshold region”. In: *Physical Review A* 74, p. 042704. DOI: http://dx.doi.org/10.1103/PhysRevA.74.042704 (cit. on p. 107).

Baulch, D.L. et al. (1994). “Evaluated kinetic data for combustion modeling: Supplement I”. In: *J. Phys. Chem.* 23, p. 847 (cit. on pp. 108, 242–244, 250, 251).

Warnatz, J. (1981). *Combustion Chemistry: Rate coefficients in the C/H/O system.* Springer - Verlag (cit. on pp. 108, 250, 252).

D.Smith et al. (1977). “Reaction of simple hydrocarbon ions with molecules at thermal energies”. In: *Plasma Sources Sci. Technol.* 23 (2), pp. 123–135. DOI: https://doi.org/10.1016/0020-7381(77)80094-6 (cit. on pp. 112, 113).

Viehland, L.A. et al. (1995). “Transport Properties of Gaseous Ions over a Wide Energy Range, IV”. In: *Atomic Data and Nuclear Data Tables* 60.1, pp. 37–95. ISSN: 0092-640X. DOI: https://doi.org/10.1006/adnd.1995.1004. URL: https://www.sciencedirect.com/science/article/pii/S0092640X85710042 (cit. on p. 113).

F.H.Field et al. (1957). “Reactions of Gaseous Ions. I. Methane and Ethylene”. In: *J. Am. Chem. Soc.* 79 (10), pp. 2419–2429. DOI: https://doi.org/10.1021/ja01567a020 (cit. on p. 113).

J.R.Fincke et al. (2002). “Plasma Thermal Conversion of Methane to Acetylene”. In: *Plasma Chemistry and Plasma Processing* 22 (1). DOI: 10.1023/a:1012944615974 (cit. on pp. 117, 151).

Morillo-Candas, Ana Sofia et al. (2020b). “Time Evolution of the Dissociation Fraction in rf CO2 Plasmas: Impact and Nature of Back-Reaction Mechanisms”. In: *The Journal of Physical Chemistry C* 124.32, pp. 17459–17475. DOI: 10.1021/acs.jpcc.0c03354 (cit. on pp. 119, 132, 133, 138, 140, 148, 149, 153).

Liu, Jing-Lin et al. (2022). “Mechanism study on gliding arc (GA) plasma reforming: A combination approach of experiment and modeling”. In: *Plasma Processes and Polymers*, e2200077 (cit. on pp. 119, 179, 180, 184).

Janev, R K et al. (Oct. 2001). *Cross sections and rate coefficients for electron-impact ionization of hydrocarbon molecules.* URL: https://www.osti.gov/etdeweb/biblio/20234432 (cit. on pp. 120, 126).

Atkinson, R. (1992). “Evaluated Kinetic and Photochemical Data for Atmospheric Chemistry. Supplement IV, IUPAC Subcommittee on Gas Kinetic Data Evaluation for Atmospheric Chemistry”. In: *J. Phys. Chem. Ref. Data* 21, pp. 1125–1568 (cit. on pp. 126, 176, 241).

Capezzuto, Pio et al. (1976). “Contribution of vibrational excitation to the rate of carbon dioxide dissociation in electrical discharges”. In: *The Journal of Physical Chemistry* 80.8, pp. 882–888 (cit. on p. 132).

Spencer, Laura F et al. (2011). “Efficiency of CO2 dissociation in a radio-frequency discharge”. In: *Plasma Chemistry and Plasma Processing* 31.1, pp. 79–89 (cit. on p. 132).

V.A.Godyak et al. (1990). “In situ simultaneous radio frequency discharge power measurements”. In: *Journal of Vacuum Science Technology A* 8, p. 3833. DOI: doi:10.1116/1.576457 (cit. on pp. 133, 134).

Alphen, S. Van et al. (2021). “Effect of N2 on CO2-CH4 conversion in a gliding arc plasmatron: Can this major component in industrial emissions improve the energy efficiency?” In: *Journal of CO2 Utilization* 54, p. 101767. DOI: https://doi.org/10.1016/j.jcou.2021.101767 (cit. on p. 143).

Anokhin, E M et al. (July 2016). “Kinetic mechanism of plasma recombination in methane, ethane and propane after high-voltage nanosecond discharge”. In: *Plasma Sources Science and Technology* 25.4, p. 044006. DOI: 10.1088/0963-0252/25/4/044006. URL: https://dx.doi.org/10.1088/0963-0252/25/4/044006 (cit. on p. 156).

Schlütter, J. et al. (1993). “State selective investigation of the reactions O(1D)+CH4 (C2H6)→OH (CH2OH)+CH3(1(),2(),J,K) using resonant multiphoton ionization detection of CH3”. In: *Chemical Physics Letters* 213.3, pp. 262–268. ISSN: 0009-2614. DOI: https://doi.org/10.1016/0009-2614(93)85130-G (cit. on pp. 161, 229).

Kunze, Hans-Joachim (2009). *Introduction to plasma spectroscopy.* Vol. 56. Springer Science & Business Media (cit. on p. 162).

Piejak, R B et al. (Oct. 2005). “Hairpin resonator probe measurements in RF plasmas”. In: *Plasma Sources Science and Technology* 14.4, p. 734. DOI: `10.1088/0963-0252/14/4/012` (cit. on p. 162).

Matsumi, Y. (1993). “Isotopic branching ratios and translational energy release of H and D atoms in reaction of O(1D) atoms with alkanes and alkyl chlorides”. In: *J. Phys. Chem.* 97, pp. 6816–6821 (cit. on pp. 166, 176, 244, 250).

Back, R. A. (1983). “A search for a gas-phase free-radical inversion displacement reaction at a saturated carbon atom”. In: *Canadian Journal of Chemistry* 61.5, pp. 916–920. DOI: `10.1139/v83-164` (cit. on pp. 166, 249).

Li, Xinyi et al. (2021). “Enhanced lattice oxygen activity on glow discharge plasma irradiated SrCr/SiO2 and the performance in oxidative dehydrogenation of ethane with CO2”. In: *Molecular Catalysis* 509, p. 111658. ISSN: 2468-8231. DOI: `https://doi.org/10.1016/j.mcat.2021.111658` (cit. on pp. 167, 168).

Gómez-Ramírez, Ana et al. (2014). “Low Temperature Production of Formaldehyde from Carbon Dioxide and Ethane by Plasma-Assisted Catalysis in a Ferroelectrically Moderated Dielectric Barrier Discharge Reactor”. In: *ACS Catalysis* 4.2, pp. 402–408. DOI: `10.1021/cs4008528`. URL: `https://doi.org/10.1021/cs4008528` (cit. on p. 168).

Dean, A.M. et al. (1987). “Bimolecular QRRK analyss of methyl radical reactions”. In: *Int. J. Chem. Kinet* 19 (cit. on pp. 175, 176, 242, 253).

Miyoshi, A. (1993). “Reaction rates of atomic oxygen with straight chain alkanes and fluoromethanes at high temperatures”. In: *Chem. Phys. Lett.* 204, pp. 241–247 (cit. on pp. 176, 241).

Tully, J.C. (1975). “Reactions of O(1D) with atmospheric molecules”. In: *J. Chem. Phys* 62 (cit. on pp. 176, 244).

Fagerström, Kjell et al. (1994). “Pressure and temperature dependence of the gas-phase reaction between methyl and hydroxyl radicals”. In: *Chemical physics letters* 224.1-2, pp. 43–50 (cit. on p. 176).

Heijkers, Stijn et al. (2020). “Plasma-based CH4 conversion into higher hydrocarbons and H2: modeling to reveal the reaction mechanisms of different plasma sources”. In: *The Journal of Physical Chemistry C* 124.13, pp. 7016–7030 (cit. on pp. 180, 185).

Sillesen, Alfred et al. (1993). “Kinetics of the reactions H+ C2H4→ C2H5, H+ C2H5→ 2CH3 and CH3+ C2H5→ products studied by pulse radiolysis combined with infrared diode laser spectroscopy”. In: *Chemical physics letters* 201.1-4, pp. 171–177 (cit. on pp. 181, 183).

Harding, Lawrence B et al. (2005). “Predictive theory for hydrogen atom- hydrocarbon radical association kinetics”. In: *The Journal of Physical Chemistry A* 109.21, pp. 4646–4656 (cit. on pp. 181, 249–251, 253).

Kurylo, Michael J et al. (1970). “Absolute rates of the reactions H+ C2H4 and H+ C2H5”. In: *The Journal of Chemical Physics* 53.7, pp. 2776–2783 (cit. on p. 183).

Gao, Yuan et al. (2021). “Coupling bimetallic Ni-Fe catalysts and nanosecond pulsed plasma for synergistic low-temperature CO2 methanation”. In: *Chemical Engineering Journal* 420, p. 127693. ISSN: 1385-8947. DOI: `https://doi.org/10.1016/j.cej.2020.127693` (cit. on p. 183).

Thejaswini, H.C. et al. (2011). “Plasma chemical reactions in C2H2/N2, C2H4/N2, and C2H6/N2 gas mixtures of a laboratory dielectric barrier discharge”. In: *Advances in Space Research* 48.5, pp. 857–861. ISSN: 0273-1177. DOI: `https://doi.org/10.1016/j.asr.2011.04.020`. URL: `https://www.sciencedirect.com/science/article/pii/S027311771100281X` (cit. on p. 183).

Sanchez-Gonzalez, Rodrigo et al. (2007). “Methane and ethane decomposition in an atmospheric-pressure plasma jet”. In: *IEEE transactions on plasma science* 35.6, pp. 1669–1676 (cit. on p. 183).

Sangwan, Manuvesh et al. (2015). “Reaction CH3 + CH3 → C2H6 Studied over the 292–714 K Temperature and 1–100 bar Pressure Ranges”. In: *The Journal of Physical Chemistry A*

119.28. PMID: 25973698, pp. 7847–7857. DOI: 10.1021/acs.jpca.5b01276 (cit. on pp. 184, 249).

Stewart, P.H. et al. (1989). “Pressure and temperature dependence of reactions proceeding via a bound complex. 2. Application to 2CH3 → C2H5 + H”. In: *Combustion and Flame* 75.1, pp. 25–31. ISSN: 0010-2180 (cit. on pp. 184, 249, 250).

Hassouni, K et al. (2001). “Investigation of chemical kinetics and energy transfer in a pulsed microwave H2/CH4 plasma”. In: *Plasma Sources Science and Technology* 10.1, p. 61 (cit. on p. 185).

Kustova, E. et al. (2021). “Novel approach for evaluation of CO2 vibrational relaxation times”. In: *Chemical Physics Letters* 764, p. 138288. ISSN: 0009-2614. DOI: https://doi.org/10.1016/j.cplett.2020.138288 (cit. on p. 190).

Morillo-Candas, A S, B L M Klarenaar, et al. (Dec. 2020). “Effect of oxygen atoms on the vibrational kinetics of CO2 and CO revealed by the use of a large surface area material”. In: *Journal of Physics D: Applied Physics* 54.9, p. 095208. DOI: 10.1088/1361-6463/abc992. URL: https://dx.doi.org/10.1088/1361-6463/abc992 (cit. on p. 194).

De Vasconcelos, M.H. et al. (1977). “Vibrational relaxation time measurements in CH4 and CH4-rare gas mixtures”. In: *Physica A: Statistical Mechanics and its Applications* 86.3, pp. 490–512. ISSN: 0378-4371. DOI: https://doi.org/10.1016/0378-4371(77)90091-7. URL: https://www.sciencedirect.com/science/article/pii/0378437177900917 (cit. on p. 195).

Louviot, Maud et al. (2015). “Strong thermal nonequilibrium in hypersonic CO and CH4 probed by CRDS”. In: *The Journal of Chemical Physics* 142.21, p. 214305 (cit. on p. 195).

Pannier, Erwan et al. (2019). “RADIS: A nonequilibrium line-by-line radiative code for CO2 and HITRAN-like database species”. In: *Journal of Quantitative Spectroscopy and Radiative Transfer* 222-223, pp. 12–25. ISSN: 0022-4073. DOI: https://doi.org/10.1016/j.jqsrt.2018.09.027. URL: https://www.sciencedirect.com/science/article/pii/S0022407318305867 (cit. on p. 195).

Green, Don W et al. (2019). *Perry’s chemical engineers’ handbook*. McGraw-Hill Education (cit. on p. 198).

Thermal Conductivity and heat transfer (n.d.). URL: https://www.engineersedge.com/heat_transfer/thermal-conductivity-gases.htm (cit. on p. 198).

Lopez-Puertas, Manuel et al. (2001). *Non-LTE radiative transfer in the Atmosphere*. Vol. 3. World Scientific (cit. on pp. 201, 207, 208).

Millikan, Roger C (1965b). “Vibration—Vibration Energy Exchange between Carbon Monoxide and Methane”. In: *The Journal of Chemical Physics* 43.5, pp. 1439–1442 (cit. on pp. 206, 208).

Hooker, William J. et al. (1963). “Shock-Tube Study of Vibrational Relaxation in Carbon Monoxide for the Fundamental and First Overtone”. In: *The Journal of Chemical Physics* 38.1, pp. 214–220. DOI: 10.1063/1.1733464 (cit. on pp. 206, 219, 224, 226).

Richman, Dennis C. et al. (1975). “Vibrational energy transfer rates for the CO–CH4, CO–CF4, and CO–SF6 systems”. In: *The Journal of Chemical Physics* 63.5, pp. 2242–2244. DOI: 10.1063/1.431608 (cit. on p. 206).

Kovacs, MA (1973). “Vibrational relaxation of carbon monoxide by foreign gases”. In: *The Journal of Chemical Physics* 58.10, pp. 4704–4706 (cit. on p. 206).

Matsui, Hiroyuki et al. (1975). “Vibrational relaxation in H2–CO and D2–CO mixtures, measured via stimulated Raman-ir fluorescence”. In: *The Journal of Chemical Physics* 63.10, pp. 4171–4176 (cit. on pp. 206, 224, 226).

Yardley, James T. et al. (1970). “Vibrational Deactivation in Methane Mixtures”. In: *The Journal of Chemical Physics* 52.3, pp. 1450–1453. DOI: 10.1063/1.1673149. URL: https://doi.org/10.1063/1.1673149 (cit. on p. 206).

Mehl, Rosemary et al. (1978). “Interspecies vibrational energy flow in CO2 or N2O mixtures with the series of deuterated methanes”. In: *The Journal of Chemical Physics* 69.12, pp. 5349–5354 (cit. on pp. 206, 208).

Siddles, R.M. et al. (1994). “The vibrational deactivation of the bending modes of CD4 and CH4 measured down to 90 K”. In: *Chemical Physics* 188.1, pp. 99–105. ISSN: 0301-0104. DOI: `https://doi.org/10.1016/0301-0104(94)00248-7`. URL: `https://www.sciencedirect.com/science/article/pii/0301010494002487` (cit. on pp. 206, 212, 214, 222, 223).

Buchwald, MI and GJ Wolga (1975). “Vibrational relaxation of CO2 (001) by atoms”. In: *The Journal of Chemical Physics* 62.7, pp. 2828–2832 (cit. on p. 206).

Moore, C Bradley et al. (1967). “Vibrational energy transfer in CO2 lasers”. In: *The Journal of Chemical Physics* 46.11, pp. 4222–4231 (cit. on pp. 207, 208).

Rosser Jr, WA, AD Wood, et al. (1969). “Deactivation of vibrationally excited carbon dioxide (ν 3) by collisions with carbon dioxide or with nitrogen”. In: *The Journal of Chemical Physics* 50.11, pp. 4996–5008 (cit. on p. 207).

Rosser Jr, WA and ET Gerry (1969). “De-excitation of Vibrationally Excited CO2*(ν 3) by Collisions with He, O2, and H2O”. In: *The Journal of Chemical Physics* 51.5, pp. 2286–2287 (cit. on p. 207).

— (1971). “De-excitation of Vibrationally Excited CO2 (001) by Collisions with CO2, H2, NO, and Cl2”. In: *The Journal of Chemical Physics* 54.9, pp. 4131–4132 (cit. on pp. 207, 216, 226).

Rosser Jr, WA, RD Sharma, et al. (1971). “Deactivation of vibrationally excited carbon dioxide (001) by collisions with carbon monoxide”. In: *The Journal of Chemical Physics* 54.3, pp. 1196–1205 (cit. on p. 207).

Cheo, P (1968). “Relaxation of CO_2 laser levels by collisions with foreign gases”. In: *IEEE Journal of Quantum Electronics* 4.10, pp. 587–593 (cit. on pp. 207, 208).

Wang, Baoshan, Yueshu Gu, et al. (1999). “Rapid vibrational quenching of CO (V) by H2O and C2H2”. In: *The Journal of Physical Chemistry A* 103.37, pp. 7395–7400 (cit. on pp. 207, 208).

Glass, GP et al. (1982). “Vibrational relaxation of carbon monoxide in collisions with atomic hydrogen”. In: *The Journal of Physical Chemistry* 86.6, pp. 908–913 (cit. on p. 207).

Starr, DF et al. (1974). “Vibrational deactivation of carbon monoxide by hydrogen and nitrogen from 100 to 650° K”. In: *The Journal of Chemical Physics* 61.12, pp. 5421–5425 (cit. on pp. 207, 208, 226).

Song, L. et al. (Nov. 2015). “QUANTUM CALCULATION OF INELASTIC CO COLLISIONS WITH H. III. RATE COEFFICIENTS FOR RO-VIBRATIONAL TRANSITIONS”. In: *The Astrophysical Journal* 813.2, p. 96. DOI: `10.1088/0004-637X/813/2/96` (cit. on p. 207).

Stephenson, John C et al. (1974). “Vibrational energy transfer in CO from 100 to 300 K”. In: *The Journal of Chemical Physics* 60.9, pp. 3562–3566 (cit. on pp. 207, 226).

Shmelev, V M et al. (Aug. 1975). “CO2 + N2 + CO + H2O gas-dynamic laser”. In: 4.8, p. 944. DOI: `10.1070/QE1975v004n08ABEH010494` (cit. on p. 207).

Shmelev, Vladimir Mikhailovich et al. (1981). “Gasdynamic CO laser utilizing hydrogen-containing active media”. In: *Soviet Journal of Quantum Electronics* 11.4, p. 487 (cit. on pp. 207, 208).

Cassady, PE et al. (1979). “Performance potential of advanced GDL concepts”. In: *AIAA Journal* 17.8, pp. 845–853 (cit. on p. 207).

Rosenberg Jr, CW von et al. (1971). “Vibrational relaxation of CO in nonequilibrium nozzle flow, and the effect of hydrogen atoms on CO relaxation”. In: *The Journal of Chemical Physics* 54.5, pp. 1974–1987 (cit. on pp. 207, 208).

Balakrishnan, N et al. (2002). “Quantum-mechanical study of rotational and vibrational transitions in CO induced by H atoms”. In: *The Astrophysical Journal* 568.1, p. 443 (cit. on pp. 207, 208).

Yang, Benhui et al. (2010). “Rotational Quenching of CO due to H2 Collisions”. In: *The Astrophysical Journal* 718.2, p. 1062 (cit. on p. 207).

Walker, Kyle M. et al. (Sept. 2015). “QUANTUM CALCULATION OF INELASTIC CO COLLISIONS WITH H. II. PURE ROTATIONAL QUENCHING OF HIGH ROTATIONAL LEVELS”. In: *The Astrophysical Journal* 811.1, p. 27. DOI: `10.1088/0004-637X/811/1/27` (cit. on p. 207).

Forrey, Robert C. et al. (2015). "Mutual vibrational quenching in CO+H2 collisions". In: *Chemical Physics* 462. Inelastic Processes in Atomic, Molecular and Chemical Physics, pp. 71–78. ISSN: 0301-0104. DOI: `https://doi.org/10.1016/j.chemphys.2015.07.001` (cit. on p. 207).

Blauer, J et al. (1974). "A survey of vibrational relaxation rate data for processes importantto CO2-N2-H2O infrared plume radiation". In: *7th Fluid and PlasmaDynamics Conference*, p. 536 (cit. on pp. 207, 208, 210, 217–219, 224–226).

Buchwald, MI and SH Bauer (1972). "Vibrational relaxation in carbon dioxide with selected collision partners. I. Water and heavy water". In: *The Journal of Physical Chemistry* 76.22, pp. 3108–3115 (cit. on p. 208).

Capitelli, Mario et al. (2013). *Plasma kinetics in atmospheric gases*. Vol. 31. Springer Science & Business Media (cit. on p. 210).

Black, Graham et al. (1974). "Measurements of vibrationally excited molecules by Raman scattering. II. Surface deactivation of vibrationally excited N2". In: *The Journal of Chemical Physics* 60.9, pp. 3526–3536. DOI: `10.1063/1.1681570` (cit. on pp. 211, 219, 224).

Arnold, J. et al. (1993). "CARS studies on the heterogenous relaxation of vibrationally excited hydrogen and deuterium". In: *Chemical Physics Letters* 203.2, pp. 283–288. ISSN: 0009-2614. DOI: `https://doi.org/10.1016/0009-2614(93)85402-A` (cit. on p. 211).

Bott, Jerry F (1976). "Vibrational energy exchange between H2 (v= 1) and D2, N2, HCl, and CO2". In: *The Journal of Chemical Physics* 65.10, pp. 3921–3928 (cit. on pp. 216–218).

Miller, Richard G. et al. (1977). "V–V energy transfer in H2-additive gas mixtures using a stimulated Raman vibrational fluorescence technique". In: *The Journal of Chemical Physics* 66.11, pp. 5150–5158. DOI: `10.1063/1.433777` (cit. on pp. 217, 224, 226).

Grimley, A. J. et al. (1979). "Electronic to vibrational energy transfer from I(52P1/2). III. H2, HD, and D2". In: *The Journal of Chemical Physics* 70.10, pp. 4724–4729. DOI: `10.1063/1.437260` (cit. on p. 217).

Cacciatore, Mario et al. (1981). "Semiclassical calculation of VV and VT rate coeffecients in CO". In: *Chemical Physics* 58.3, pp. 395–407. ISSN: 0301-0104. DOI: `https://doi.org/10.1016/0301-0104(81)80074-2`. URL: `https://www.sciencedirect.com/science/article/pii/0301010481800742` (cit. on p. 219).

Fromentin, Chloe et al. (2023). "In preparation". In: (cit. on pp. 219, 220, 226).

Starr, D. F. et al. (1975). "Vibrational energy transfer in CO2–CO mixtures from 163 to 406°K". In: *The Journal of Chemical Physics* 63.11, pp. 4730–4734. DOI: `10.1063/1.431259` (cit. on p. 220).

Stephenson, John C. et al. (1972). "Temperature Dependence of Nearly Resonant Vibration → Vibration Energy Transfer in CO2 Mixtures". In: *The Journal of Chemical Physics* 56.3, pp. 1295–1308. DOI: `10.1063/1.1677362` (cit. on p. 220).

Kustova, E. et al. (2020). "Multi-temperature vibrational energy relaxation rates in CO2". In: *Physics of Fluids* 32.9, p. 096101. DOI: `10.1063/5.0021654` (cit. on pp. 220, 226).

Pietanza, L D, G Colonna, A Laricchiuta, et al. (Sept. 2018). "Non-equilibrium electron and vibrational distributions under nanosecond repetitively pulsed CO discharges and afterglows: II. the role of radiative and quenching processes". In: *Plasma Sources Science and Technology* 27.9, p. 095003. DOI: `10.1088/1361-6595/aad7f2`. URL: `https://dx.doi.org/10.1088/1361-6595/aad7f2` (cit. on p. 228).

Seakins, Paul W et al. (1992). "A laser flash photolysis/time-resolved FTIR emission study of a new channel in the reaction of methyl+ oxygen atom: production of carbon monoxide (v)". In: *The Journal of Physical Chemistry* 96.11, pp. 4478–4485 (cit. on p. 228).

Marcy, Timothy P. et al. (2001). "Theoretical and Experimental Investigation of the Dynamics of the Production of CO from the CH3 + O and CD3 + O Reactions". In: *The Journal of Physical Chemistry A* 105.36, pp. 8361–8369. DOI: `10.1021/jp010961f` (cit. on p. 229).

Preses, Jack M. et al. (2000). "A Measurement of the Yield of Carbon Monoxide from the Reaction of Methyl Radicals and Oxygen Atoms". In: *The Journal of Physical Chemistry A* 104.29, pp. 6758–6763. DOI: `10.1021/jp000404d` (cit. on p. 229).

Hsu, David S. Y. et al. (1977). “The production of vibrationally excited CO from the reaction of CH2 with O2 and CO2”. In: *International Journal of Chemical Kinetics* 9.3, pp. 507–509. DOI: `https://doi.org/10.1002/kin.550090318` (cit. on p. 229).

Shaub, WM et al. (1981). “Dynamics and mechanisms of CO production from the reactions of CH2 radicals with O (3P) and O2”. In: 18.1, pp. 811–818 (cit. on p. 229).

Laufer, Allan H. and Arnold M. Bass (1977). “Reaction between triplet methylene and CO2: rate constant determination”. In: *Chemical Physics Letters* 46.1, pp. 151–155. ISSN: 0009-2614. DOI: `https://doi.org/10.1016/0009-2614(77)85184-1` (cit. on p. 229).

Garcia, Ernesto et al. (2019). “Kinetics Of The H + CH2 → CH + H2 Reaction At Low Temperature”. In: *The Journal of Physical Chemistry A* 123.34. PMID: 31373813, pp. 7408–7419. DOI: `10.1021/acs.jpca.9b06212` (cit. on p. 229).

Baulch, D.L. et al. (2005). “Evaluated kinetic data for combustion modeling: Supplement II”. In: *J. Phys. Chem.* 34, p. 757 (cit. on p. 241).

Sutherland, J.W et al. (2005). “Rate Constants for H + CH4, CH3 + H2, and CH4 Dissociation at High Temperature”. In: *Int J. Chem. Kinet.* 33, p. 669 (cit. on p. 241).

C.Olm et al. (2016). “Development of an Ethanol Combustion Mechanism Based on a Hierarchical Optimization Approach”. In: *Int J. Chem. Kinet.* 48, pp. 423–441 (cit. on pp. 241, 251).

Cohen, N. et al. (1991). “Chemical Kinetic Data Sheets for High-Temperature Reactions. Part II”. In: *Journal of Physical and Chemical Reference Data* 20.6, pp. 1211–1311. DOI: `10.1063/1.555901` (cit. on pp. 241, 250).

Bonard, A. et al. (2002). “Kinetics of OH Radical Reactions with Methane in the Temperature Range 295-660 K and with Dimethyl Ether and Methyl-tert-butyl Ether in the Temperature Range 295-618 K”. In: *J. Phys. Chem. A* 106, pp. 4384–4389 (cit. on p. 241).

Han, P.P et al. (2011). “Reaction Rate of Propene Pyrolysis”. In: *J. Comput. Chem* 32, pp. 2745–2755 (cit. on pp. 241, 242, 244, 249, 252).

Bohland, T. et al. (1985). “Kinetics of the reactions between CH2(X3B1)-radicals and saturated hydrocarbons in the temperature range 296 K - 707K”. In: *Ber. Bunsenges. Phys. Chem* 89 (cit. on p. 241).

Glarborg, P. et al. (2018). “Modeling nitrogen chemistry in combustion”. In: *Prog. Energy Combust. Sci.* 67, pp. 31–68 (cit. on p. 242).

K.W.Lu et al. (2010). “Shock Tube Study on the Thermal Decomposition of CH3OH”. In: *J. Phys. Chem. A* 114, pp. 5493–5502 (cit. on p. 242).

Fulle, D. et al. (1997). “Bimolecular QRRK analyss of methyl radical reactions”. In: *J. Chem. Phys.* 106, pp. 8691–8698 (cit. on p. 242).

Zellner, R. et al. (1988). “Computational study of the CH3 + O2 chain branching reaction”. In: *J. Chem. Phys.* 92 (cit. on p. 242).

Franck, P. et al. (1988). “Acetylene oxidation: the reaction of C2H2 + O at high temperatures”. In: *Symp. Int. Combust. Proc.* 21, pp. 885–893 (cit. on p. 242).

Brownsword, R.A. et al. (1997). “Kinetics over a wide range of temperature (13-744 K): rate constants for the reactions of CH(v=O) with H2 and D2 and for the removal of CH(v=1) by H2 and D2”. In: *J. Chem. Phys.* 106, pp. 7662–7677 (cit. on p. 242).

Dombrowsky Ch.AND Wagner, H.Gg. (1992). “Investigation of the 3CH2 + O2 reaction in shock wave”. In: *Ber. Bunsenges. Phys. Chem.* 96, pp. 1048–1055 (cit. on p. 242).

Husain, David et al. (1975). “Kinetic investigation of ground state carbon atoms, C (2 3 Pj)”. In: *Journal of the Chemical Society, Faraday Transactions 2: Molecular and Chemical Physics* 71, pp. 525–531 (cit. on p. 242).

Tsuboi, T. et al. (1981). “Shock Tube Study on Homogeneous Thermal Oxidation of Methanol”. In: *Combust. Flame* 42 (cit. on pp. 242, 243, 252).

Javoy, S. et al. (2003). “Elementary reaction kinetics studies of interest in H2 supersonic combustion chemistry”. In: *Experimental Thermal and Fluid Science* 27.4. Second Mediterranean Combustion Symposium, pp. 371–377. ISSN: 0894-1777. DOI: `https://doi.org/10.1016/S0894-1777(02)00241-8` (cit. on p. 243).

Oehlers, C. et al. (2000). “An Investigation of the D/H AdditionElimination and H Atom Abstraction Channels in the Reaction D + H2CO in the Temperature Range 296 K T 780 K”. In: *The Journal of Physical Chemistry A* 104.45, pp. 10500–10510. DOI: 10.1021/jp0012496 (cit. on p. 243).

Lifshitz, Assa et al. (1991). “Rate constants for the reaction, O+H2O→OH+OH, over the temperature range, 1500–2400 K, by the flash photolysis-shock tube technique: A further consideration of the back reaction”. In: *Symposium (International) on Combustion* 23.1. Twenty-Third Symposium (International) on Combustion, pp. 59–67. ISSN: 0082-0784 (cit. on p. 243).

Karach S.P.AND Osherov, V.I (1999). “Ab Initio Analysis of the Transition States on the Lowest Triplet H2O2 Potential Surfac”. In: *J. Chem. Phys* 110, pp. 11918–11927 (cit. on pp. 243, 244).

Jachimowski, Casimir J (1977). “An experimental and analytical study of acetylene and ethylene oxidation behind shock waves”. In: *Combustion and Flame* 29, pp. 55–66 (cit. on p. 243).

Lichtin, D.A. et al. (1984). “NH(A3 → X3) Chemiluminescence from the CH(X2) + NO reaction”. In: *Chemical Physics Letters* 108.1, pp. 18–24. ISSN: 0009-2614. DOI: https://doi.org/10.1016/0009-2614(84)80360-7 (cit. on p. 243).

Varga, Tamás et al. (2016). “Development of a Joint Hydrogen and Syngas Combustion Mechanism Based on an Optimization Approach”. In: *International Journal of Chemical Kinetics* 48.8, pp. 407–422. DOI: https://doi.org/10.1002/kin.21006 (cit. on p. 243).

Friedrichs, Gernot et al. (2002). “Quantitative detection of HCO behind shock waves: The thermal decomposition of HCO”. In: *Physical Chemistry Chemical Physics* 4.23, pp. 5778–5788 (cit. on p. 243).

Nguyen, Thanh Lam et al. (2011). “Ab Initio Reaction Rate Constants Computed Using Semiclassical Transition-State Theory: HO + H2 → H2O + H and Isotopologues”. In: *The Journal of Physical Chemistry A* 115.20. PMID: 21539339, pp. 5118–5126. DOI: 10.1021/jp2022743 (cit. on p. 243).

Robertson, Robert et al. (2006). “Temperature Dependence of O + OH at 136377 K Using Ozone Photolysis”. In: *The Journal of Physical Chemistry A* 110.21. PMID: 16722682, pp. 6673–6679. DOI: 10.1021/jp055863z (cit. on p. 243).

Eiteneer, B. et al. (1998). “Determination of rate coefficients for reactions of formaldehyde pyrolysis and oxidation in the gas phase”. In: *J. Phys. Chem. A* 102, pp. 5196–5205 (cit. on p. 243).

Wilson W.E., Jr (1972). “A critical review of the gas-phase reaction kinetics of the hydroxyl radical”. In: *J. Phys. Chem. Ref. Data* 1, pp. 535–573 (cit. on p. 243).

Murrell, J.N. et al. (1986). “Predicted rate constants for the exothermic reactions of ground state oxygen atoms and CH radicals”. In: *J. Mol. Struct. THEOCHEM* 139 (cit. on p. 244).

Panteleev, S. et al. (2018). “Molecular Dynamics Study of Combustion Reactions in a Supercritical Environment. Part 2: Boxed MD Study of CO plus OH -> CO2 + H Reaction Kinetics”. In: *J. Phys. Chem. A* 122, p. 897 (cit. on p. 244).

Dunlea, E.J. et al. (2004). “Measurement of the rate coefficient for the reaction of O(1D) with H2O and re-evaluation of the atmospheric OH production rate”. In: *Phys. Chem. Chem. Phys* 6, pp. 3333–3340 (cit. on p. 244).

Smith, D. et al. (1977). “Reaction of simple hydrocarbon ions with molecules at thermal energies”. In: *International Journal of Mass Spectrometry and Ion Physics* 23.2, pp. 123–135. ISSN: 0020-7381. DOI: https://doi.org/10.1016/0020-7381(77)80094-6. URL: https://www.sciencedirect.com/science/article/pii/0020738177800946 (cit. on pp. 245, 246).

McEwan, Murray J. et al. (Mar. 1999). “New H and H2 Reactions with Small Hydrocarbon Ions and Their Roles in Benzene Synthesis in Dense Interstellar Clouds”. In: *The Astrophysical Journal* 513.1, p. 287. DOI: 10.1086/306861. URL: https://dx.doi.org/10.1086/306861 (cit. on pp. 245, 247).

Karpas, Z. et al. (1979). “An ion cyclotron resonance study of reactions of ions with hydrogen atomsa)”. In: *The Journal of Chemical Physics* 70.6, pp. 2877–2881. DOI: 10.1063/1.437823 (cit. on pp. 245, 246).

Prasad, SS et al. (1980). “A model for gas phase chemistry in interstellar clouds. I-The basic model, library of chemical reactions, and chemistry among C, N, and O compounds”. In: *The Astrophysical Journal Supplement Series* 43, pp. 1–35 (cit. on pp. 245–248).

Adams, Nigel G. et al. (1980). “An experimental survey of the reactions of NHn+ ions (n=0 to 4) with several diatomic and polyatomic molecules at 300 K”. In: *The Journal of Chemical Physics* 72.1, pp. 288–297. DOI: 10.1063/1.438893 (cit. on pp. 245, 246).

Kim, J. K. et al. (1975). “Ion cyclotron resonance studies on the reaction of H2+ and D2+ ions with various simple molecules and hydrocarbons”. In: *The Journal of Chemical Physics* 62.7, pp. 2820–2825. DOI: 10.1063/1.430817 (cit. on pp. 245–247).

Huntress, W.T. (1975). “Reaction of protons with methane in the Jovian ionosphere”. In: *Planetary and Space Science* 23.2, pp. 377–378. ISSN: 0032-0633. DOI: https://doi.org/10.1016/0032-0633(75)90141-5. URL: https://www.sciencedirect.com/science/article/pii/0032063375901415 (cit. on p. 245).

Semaniak, J. et al. (May 1998). “Dissociative Recombination and Excitation of CH5+: Absolute Cross Sections and Branching Fractions”. In: *The Astrophysical Journal* 498.2, p. 886. DOI: 10.1086/305581. URL: https://dx.doi.org/10.1086/305581 (cit. on p. 245).

Smith, D et al. (1984). “Dissociative recombination coefficients for H3 (+), HCO (+), N2H (+), and CH5 (+) at low temperature-Interstellar implications”. In: *The Astrophysical Journal* 284, pp. L13–L16 (cit. on p. 245).

Bohme, D. K. et al. (1980). “Determination of proton affinities from the kinetics of proton transfer reactions. VII. The proton affinities of O2, H2, Kr, O, N2, Xe, CO2, CH4, N2O, and CO”. In: *The Journal of Chemical Physics* 73.10, pp. 4976–4986. DOI: 10.1063/1.439975 (cit. on p. 245).

Brian, J. et al. (1990). “The dissociative recombination of molecular ions”. In: *Physics Reports* 186.5, pp. 215–248. ISSN: 0370-1573. DOI: https://doi.org/10.1016/0370-1573(90)90159-Y. URL: https://www.sciencedirect.com/science/article/pii/037015739090159Y (cit. on pp. 246, 247).

Harada, Nanase et al. (Sept. 2008). “Modeling Carbon Chain Anions in L1527”. In: *The Astrophysical Journal* 685.1, p. 272. DOI: 10.1086/590468. URL: https://dx.doi.org/10.1086/590468 (cit. on p. 246).

McCall, B. J. et al. (Nov. 2004). “Dissociative recombination of rotationally cold H_3^+”. In: *Phys. Rev. A* 70 (5), p. 052716. DOI: 10.1103/PhysRevA.70.052716. URL: https://link.aps.org/doi/10.1103/PhysRevA.70.052716 (cit. on p. 246).

Federer, W. et al. (June 1984). “Reaction of O^+, CO^+, and CH^+ Ions with Atomic Hydrogen”. In: *Phys. Rev. Lett.* 52 (23), pp. 2084–2086. DOI: 10.1103/PhysRevLett.52.2084. URL: https://link.aps.org/doi/10.1103/PhysRevLett.52.2084 (cit. on p. 246).

Stancil, P. C. et al. (1999). “Charge transfer in collisions of O+ with H and H+ with O”. In: *Astron. Astrophys. Suppl. Ser.* 140.2, pp. 225–234. DOI: 10.1051/aas:1999419. URL: https://doi.org/10.1051/aas:1999419 (cit. on pp. 246, 247).

Sen, AD et al. (1992). “Formaldehyde reactions in dark clouds”. In: *The Astrophysical Journal* 391, pp. 141–143 (cit. on p. 247).

Theard, Lowell P. et al. (1974). “Ion-molecule reactions and vibrational deactivation of H2+ ions in mixtures of hydrogen and helium”. In: *The Journal of Chemical Physics* 60.7, pp. 2840–2848. DOI: 10.1063/1.1681453 (cit. on p. 247).

Smith, David et al. (1992). “A selected ion-flow tube study of the reactions of O+, H+ and HeH]+ with several molecular gases at 300 K”. In: *International Journal of Mass Spectrometry and Ion Processes* 117, pp. 457–473. ISSN: 0168-1176. DOI: https://doi.org/10.1016/0168-1176(92)80108-D. URL: https://www.sciencedirect.com/science/article/pii/016811769280108D (cit. on p. 247).

Larson, Å. et al. (Sept. 1998). “Branching Fractions in Dissociative Recombination of CH2+”. In: *The Astrophysical Journal* 505.1, p. 459. DOI: `10.1086/306164`. URL: `https://dx.doi.org/10.1086/306164` (cit. on p. 247).

Adams, N.G. et al. (1978). “Reactions of CH+n ions with molecules at 300 K”. In: *Chemical Physics Letters* 54.3, pp. 530–534. ISSN: 0009-2614. DOI: `https://doi.org/10.1016/0009-2614(78)85278-6`. URL: `https://www.sciencedirect.com/science/article/pii/0009261478852786` (cit. on p. 248).

Peukert, S. L. et al. (2013). “Direct Measurements of Rate Constants for the Reactions of CH3 Radicals with C2H6, C2H4, and C2H2 at High Temperatures”. In: *The Journal of Physical Chemistry A* 117.40. PMID: 23968575, pp. 10228–10238. DOI: `10.1021/jp4073153` (cit. on p. 249).

Brodsky, AM et al. (1960). “863. The principles governing high-temperature ethane cracking”. In: *Journal of the Chemical Society (Resumed)*, pp. 4443–4454 (cit. on p. 249).

Pease, Robert N. (1932). “THE HOMOGENEOUS COMBINATION OF ETHYLENE AND HYDROGEN. A SECOND-ORDER ASSOCIATION REACTION”. In: *Journal of the American Chemical Society* 54.5, pp. 1876–1882. DOI: `10.1021/ja01344a020` (cit. on p. 249).

Muszyńska, Marta et al. (2009). “Kinetics of the Hydrogen Abstraction C2H3• + Alkane → C2H4 + Alkyl Radical Reaction Class”. In: *The Journal of Physical Chemistry A* 113.29. PMID: 19569659, pp. 8327–8336. DOI: `10.1021/jp903762x` (cit. on p. 250).

Laufer, A.H. et al. (1983). “Computations and estimates of rate coefficients for hydrocarbon reactions of interest to the atmospheres of the outer solar system”. In: *Icarus* 56.3, pp. 560–567. ISSN: 0019-1035 (cit. on p. 250).

Dash, Manas Ranjan et al. (2015). “Abstraction and addition kinetics of C2H radicals with CH4, C2H6, C3H8, C2H4, and C3H6: CVT/SCT/ISPE and hybrid meta-DFT methods”. In: *Phys. Chem. Chem. Phys.* 17 (5), pp. 3142–3156 (cit. on pp. 250, 252).

Khaled, Fethi et al. (2015). “An experimental and theoretical study on the kinetic isotope effect of C2H6 and C2D6 reaction with OH”. In: *Chemical Physics Letters* 641, pp. 158–162. ISSN: 0009-2614. DOI: `https://doi.org/10.1016/j.cplett.2015.10.057`. URL: `https://www.sciencedirect.com/science/article/pii/S0009261415008209` (cit. on p. 250).

Galland, Nicolas et al. (2003). “Experimental and Theoretical Studies of the Methylidyne CH(X2) Radical Reaction with Ethane (C2H6): Overall Rate Constant and Product Channels”. In: *The Journal of Physical Chemistry A* 107.28, pp. 5419–5426. DOI: `10.1021/jp027465r` (cit. on p. 250).

Curran, H. J. (2006). “Rate constant estimation for C1 to C4 alkyl and alkoxyl radical decomposition”. In: *International Journal of Chemical Kinetics* 38.4, pp. 250–275. DOI: `https://doi.org/10.1002/kin.20153` (cit. on p. 250).

Back, M. H. (1970). “Mechanism of the bimolecular reactions of ethylene and propylene”. In: *International Journal of Chemical Kinetics* 2.5, pp. 409–418. DOI: `https://doi.org/10.1002/kin.550020506` (cit. on p. 250).

Wang, Baoshan and Christopher Fockenberg (2001). “Direct Measurement of the Rate Constant for the CH2(X3B1) + CH3 Reaction at 300 K”. In: *The Journal of Physical Chemistry A* 105.37, pp. 8449–8455. DOI: `10.1021/jp011350q` (cit. on p. 251).

Mahmud, Khaled et al. (1987). “A high-temperature photochemistry kinetics study of the reaction of oxygen (3P) atoms with ethylene from 290 to 1510 K”. In: *Journal of Physical Chemistry* 91.6, pp. 1568–1573 (cit. on p. 251).

Li, Xiaohu et al. (2017). “Theoretical kinetics of O + C2H4”. In: *Proceedings of the Combustion Institute* 36.1, pp. 219–227. ISSN: 1540-7489. DOI: `https://doi.org/10.1016/j.proci.2016.06.053` (cit. on p. 251).

Laufer, Allan H. and Askar Fahr (2004). “Reactions and Kinetics of Unsaturated C2 Hydrocarbon Radicals”. In: *Chemical Reviews* 104.6. PMID: 15186181, pp. 2813–2832. DOI: `10.1021/cr030039x` (cit. on pp. 251, 252).

Mebel, A. M. et al. (1996). "Ab Initio and RRKM Calculations for Multichannel Rate Constants of the C2H3 + O2 Reaction". In: *Journal of the American Chemical Society* 118.40, pp. 9759–9771. DOI: `10.1021/ja961476e` (cit. on p. 251).

Matsugi, Akira et al. (2014). "Yield of Formyl Radical from the Vinyl + O2 Reaction". In: *International Journal of Chemical Kinetics* 46.5, pp. 260–274. DOI: `https://doi.org/10.1002/kin.20823` (cit. on p. 251).

Knyazev, Vadim D. (2017). "Kinetics and mechanism of the reaction of recombination of vinyl and hydroxyl radicals". In: *Chemical Physics Letters* 685, pp. 165–170. ISSN: 0009-2614. DOI: `https://doi.org/10.1016/j.cplett.2017.07.040`. URL: `https://www.sciencedirect.com/science/article/pii/S0009261417307108` (cit. on p. 251).

Stoliarov, Stanislav I. et al. (2000). "Experimental Study of the Reaction between Vinyl and Methyl Radicals in the Gas Phase. Temperature and Pressure Dependence of Overall Rate Constants and Product Yields". In: *The Journal of Physical Chemistry A* 104.43, pp. 9687–9697. DOI: `10.1021/jp992476e` (cit. on p. 252).

Carl, Shaun A. et al. (2005). "Pulsed laser photolysis and quantum chemical-statistical rate study of the reaction of the ethynyl radical with water vapor". In: *The Journal of Chemical Physics* 122.11, p. 114307. DOI: `10.1063/1.1861887` (cit. on p. 252).

Vandooren, J. et al. (1977). "Reaction mechanisms of combustion in low pressure acetylene-oxygen flames". In: *Symposium (International) on Combustion* 16.1, pp. 1133–1144. ISSN: 0082-0784. DOI: `https://doi.org/10.1016/S0082-0784(77)80402-5`. URL: `https://www.sciencedirect.com/science/article/pii/S0082078477804025` (cit. on p. 252).

Gimenez-Lopez, Jorge et al. (2016). "Experimental and Kinetic Modeling Study of C2H2 Oxidation at High Pressure". In: *International Journal of Chemical Kinetics* 48.11, pp. 724–738. DOI: `https://doi.org/10.1002/kin.21028` (cit. on p. 252).

Devriendt, Katia et al. (1997). "Direct Identification of the C2H(X2+) + O(3P) → CH(A2) + CO Reaction as the Source of the CH(A2→X2) Chemiluminescence in C2H2/O/H Atomic Flames". In: *The Journal of Physical Chemistry A* 101.14, pp. 2546–2551. DOI: `10.1021/jp963434i` (cit. on p. 252).

Tsang, Wing (1987). "Chemical Kinetic Data Base for Combustion Chemistry. Part 2. Methanol". In: *Journal of Physical and Chemical Reference Data* 16.3, pp. 471–508. DOI: `10.1063/1.555802` (cit. on p. 253).

Cobos, CJ et al. (1985). "High-pressure falloff curves and specific rate constants for the reaction methyl+ molecular oxygen. dblharw. CH3O2. dblharw. CH3O+ atomic oxygen". In: *The Journal of Physical Chemistry* 89.20, pp. 4332–4338 (cit. on p. 253).

Jasper, Ahren W. et al. (2007). "Kinetics of the Reaction of Methyl Radical with Hydroxyl Radical and Methanol Decomposition". In: *The Journal of Physical Chemistry A* 111.19. PMID: 17388366, pp. 3932–3950. DOI: `10.1021/jp067585p` (cit. on p. 253).

Li, Qian Shu et al. (2004). "Direct ab initio dynamics study on the rate constants and kinetics isotope effects of CH3O+H→CH2O+H2 reaction". In: *The Journal of Chemical Physics* 121.19, pp. 9474–9480. DOI: `10.1063/1.1807391` (cit. on p. 253).

Janev, R. K. et al. (2002). "Collision processes of CHy and CHy+ hydrocarbons with plasma electrons and protons". In: *Physics of Plasmas* 9.9, pp. 4071–4081. DOI: `10.1063/1.1500735` (cit. on pp. 253, 254).

— (2002). *Collision processes of hydrocarbon species in hydrogen plasmas: II. The ethane and propane families*. Forschungszentrum, Zentralbibliothek (cit. on pp. 253, 254).

— (2004). "Collision processes of C 2, 3 H y and C 2, 3 H y+ hydrocarbons with electrons and protons". In: *Physics of Plasmas* 11.2, pp. 780–829 (cit. on pp. 253, 254).

ECOLE
DOCTORALE

Titre : Etude experimentale et numérique des mécanismes fondamentaux d'un plasma de CO_2-CH_4

Mots clés : CO_2, CH_4, plasmas froids, Reformage à sec du méthane, Diagnostics infrarouges, actinometrie

Résumé : Le CO_2 est le principal gaz à effet de serre responsable du réchauffement climatique. Afin de limiter ses effets, il est nécessaire de le recycler en produits à valeur ajoutée. Le reformage à sec du Méthane (CO_2 + CH_4 $\rightarrow$ 2CO + 2H2) par plasma est une piste prometteuse pour transformer le CO_2 en hydrocarbure avec un faible coût énergétique. Cette thèse étudie la chimie complexe des plasmas de CO_2 – CH_4, encore mal comprise car très complexe, en comparant des mesures expérimentales dans une décharge simple avec des simulations numériques 0D. Une décharge radiofréquence, plus appropriée pour la conversion, est étudiée par la suite de la même manière. Enfin, les vibrations du CO_2, clés pour limiter le coût énergétique de conversion, sont également étudiées. Ce travail apporte des éléments sur la compréhension des phénomènes fondamentaux qui régissent le plasma, ouvrant la porte à son optimisation pour des applications futures.

Title : An experimental and numerical investigation of the fundamental mechanisms of a CO_2-CH_4 plasma

Keywords : CO_2, CH_4, cold plasma, Dry Reforming of Methane, DRM, Infrared Diagnostics, Actinometry

Abstract : CO_2 is the main greenhouse gas responsible for global warming. In order to limit its effects, it is necessary to recycle it into value-added products. The dry reforming of methane (CO_2 + CH_4 $\rightarrow$ 2CO + 2H2) by plasma is a promising way to transform CO_2 into hydrocarbon with a low energy cost. This thesis studies the complex chemistry of CO_2 - CH_4 plasmas, still poorly understood because of its complexity, by comparing experimental measurements in a simple discharge with 0D numerical simulations. A radiofrequency discharge, more suited for conversion, is then studied in the same way. Finally, the vibrations of CO_2, key to limit the energy cost of conversion, are also studied. This work brings elements on the understanding of the fundamental phenomena that govern the plasma, paving the way to its optimization for future applications.

Institut Polytechnique de Paris
91120 Palaiseau, France